



HAL
open science

Evolution of galaxy dynamics as a function of environment over the last 10 Gyrs with MUSE-VLT

Wilfried Mercier

► **To cite this version:**

Wilfried Mercier. Evolution of galaxy dynamics as a function of environment over the last 10 Gyrs with MUSE-VLT. Galactic Astrophysics [astro-ph.GA]. Université Paul Sabatier - Toulouse III, 2022. English. NNT : 2022TOU30264 . tel-04104122

HAL Id: tel-04104122

<https://theses.hal.science/tel-04104122v1>

Submitted on 23 May 2023

HAL is a multi-disciplinary open access archive for the deposit and dissemination of scientific research documents, whether they are published or not. The documents may come from teaching and research institutions in France or abroad, or from public or private research centers.

L'archive ouverte pluridisciplinaire **HAL**, est destinée au dépôt et à la diffusion de documents scientifiques de niveau recherche, publiés ou non, émanant des établissements d'enseignement et de recherche français ou étrangers, des laboratoires publics ou privés.



THÈSE

En vue de l'obtention du

DOCTORAT DE L'UNIVERSITÉ DE TOULOUSE

Délivré par : *l'Université Toulouse 3 Paul Sabatier (UT3 Paul Sabatier)*

Présentée et soutenue le *30/11/2022* par :

Wilfried MERCIER

**Évolution de la dynamique des galaxies en fonction de leur environnement
au cours des dix derniers milliards d'années avec MUSE-VLT**

JURY

SOUCAIL GENEVIÈVE
FÖRSTER-SCHREIBER NATASCHA
PUECH MATHIEU
KRAJNOVIĆ DAVOR
SWINBANK MARK
JABLONKA PASCALE
CONTINI THIERRY
EPINAT BENOIT

Astronome
Scientifique senior
Astronome
Scientifique senior
Professeur
Professeur
Directeur de recherche CNRS
Astronome adjoint

Présidente
Rapporteur
Rapporteur
Examineur
Examineur
Examineur
Directeur de Thèse
Co-directeur de Thèse

École doctorale et spécialité :

SDU2E : Astrophysique, Sciences de l'Espace, Planétologie

Unité de Recherche :

Institut de Recherche en Astrophysique et Planétologie (UMR 5277)

Directeur(s) de Thèse :

Contini Thierry et Epinat Benoit

Rapporteurs :

Förster-Schreiber Natascha et Puech Mathieu

*A mon grand-père
A qui cette Thèse est dédiée.*

Remerciements

Effectuer une thèse est un processus étrange dont rares sont ceux, à ma connaissance, qui en sont sortis intacts. Pour ma part, j'ai la chance de pouvoir dire que mon expérience a été incroyable. Les raisons sont certainement multiples mais certaines, évidentes, méritent d'être citées. Tout d'abord, il me semble clair, avec le recul, qu'on ne peut pas complètement réussir sa thèse sans l'aide d'un encadrement de grande qualité. Sur ce point, le mien a été irréprochable, à la fois dans les interactions professionnelles et personnelles, et je tiens à remercier encore une fois chaleureusement mes encadrants, Thierry et Benoît, pour ces quatre années passées avec eux. Un grand merci de m'avoir donné l'opportunité de travailler, d'apprendre et de mieux comprendre ce domaine si complexe qu'est l'astrophysique des galaxies, et en particulier leur dynamique à partir de données IFU que j'affectionne tout particulièrement. Merci également de m'avoir permis de développer ma recherche dans ce domaine et de m'avoir insufflé une rigueur et une certaine forme d'esprit critique vis-à-vis de son propre travail et de celui des autres; peut-être plus utile maintenant que jamais dans les temps qui courent. Un énorme merci également pour les opportunités inestimables de voyages et de rencontres qui m'ont été offertes lors de conférences, d'écoles ou d'autres événements. Ma thèse a débuté sur le sommet de Paranal, peut-être ce soir-là où le vent s'était levé ; souvenirs oniriques de travailler, marcher, se baigner au milieu du désert chilien, observer un ciel nocturne étranger, voir pour la première fois les nuages de Magellan, d'un côté les montagnes, de l'autre l'océan. De même, avoir la possibilité de venir jusqu'à Hawaii, de travailler au CFHT, marcher sur des coulées de lave, se baigner en plein milieu du mois de Janvier, ou encore grimper au sommet du Mauna Kea; tout cela est inestimable. Encore une fois, merci infiniment !

Plus généralement, je tiens à remercier toutes les personnes avec qui j'ai pu échanger ou collaborer aux cours de ces dernières années, que ce soit à l'IRAP ou ailleurs. Plus spécifiquement, je souhaite remercier le consortium MUSE et ses membres pour m'avoir donné la chance de faire parti de cette superbe aventure et de m'avoir permis de rencontrer nombres de personnes incroyables qui, je suis sûr, se reconnaîtront en lisant ces lignes. Un remerciement particulier à Valentina avec qui nous avons collaboré depuis le tout début de mon stage sur MAGIC et avec qui cela a toujours été un plaisir de discuter. Au-delà du cadre de la recherche, je veux aussi remercier chaleureusement l'association "Les étoiles brillent pour tous", l'équipe en charge du module doctoral et en particulier mes acolytes, Léo et Merwan, pour ces supers moments passés ensemble. Merci également à mes deux ex-stagiaires, Hugo et Maxime, qui ont fourni tous les deux un travail remarquable, avec qui cela a toujours été un plaisir d'interagir et pour lesquels je souhaite un futur brillant.

Enfin, sur un plan plus personnel, je souhaite remercier ma famille, ainsi que ma copine sans qui tout cela n'aurait pu avoir lieu ou du moins qui se serait déroulé de manière totalement différente.

Tout d’abord, un grand merci à Lina d’avoir été et d’être restée là pendant tout ce temps, ainsi que d’avoir apporté beaucoup de joie et de bonne humeur, cela malgré la distance au départ et par la suite certains moments difficiles, incluant cet effroyable passage qu’est la rédaction du manuscrit. Un énorme merci à ma famille, en particulier mes parents et mes grands-parents qui m’ont fait confiance depuis de nombreuses années vis-à-vis de cet objectif un peu irréaliste qu’est d’obtenir une thèse en Astrophysique. Nul doute que tout cela aurait été immensément plus difficile sans leur soutien. Ainsi, au-delà d’un travail personnel évident, cette thèse est avant tout, à mon sens, un effort et une réussite collectifs. Malheureusement, tous n’auront pas été en mesure d’être là jusqu’au bout, mais je suis certain que chacun en tire néanmoins une grande fierté, peu importe où ils se trouvent. Pour conclure, un merci spécial à mon camarade, mon meilleur ami, mon “frérot” comme on dit dans la famille, et avec qui j’ai grandi, mon toutou Kirby.

Toulouse, le 09/02/2023
Wilfried Mercier

Abstract

Understanding the morphological and dynamical evolution of galaxies across cosmic time is one of the key goals of modern extragalactic astrophysics. Our current view is that galaxies are objects that evolve secularly and build their stellar mass through star formation which is sustained by cold gas accretion from the cosmic web. However, this picture is not sufficient to explain entirely their evolution. Environmental processes can also affect their morphology, kinematics, or gas content, as well as quench star formation, and can thus be driving mechanisms to explain the transition from high to low redshift. Thus, important recent efforts have been put into probing the effect of the environment on galaxies. In this endeavour, 3D spectroscopy can help because it provides spatially resolved properties across the galaxies' extent. MUSE is one of the most powerful 3D spectrographs thanks to its large field-of-view and high sensitivity when combined with adaptive optics.

During this Thesis, I have used data from the deep MUSE-gAlaxy Groups In Cosmos survey (MAGIC) which targets galaxy groups/clusters in the COSMOS field, as well as foreground and background field galaxies. MAGIC is ideal to probe the impact of the environment at $0.2 \lesssim z \lesssim 1.5$ for a large sample of galaxies with high completeness and down to low stellar masses ($M_* \approx 10^9 M_\odot$). From this survey, I modelled the morphology of about 900 galaxies by performing a bulge-disk decomposition to extract key morphological parameters (e.g. bulge-to-disk flux ratio, disk inclination, etc.) and the ionised gas kinematics from the MUSE cubes using the [O II] doublet as kinematics tracer and taking into account beam-smearing for 600 galaxies. I also integrated a mass modelling where I constrained the kinematics using prior information from the bulge-disk decomposition to recover more precise dark matter fractions. This has allowed me to contribute to a first analysis of the Tully-Fisher relation at $z \sim 0.7$, followed by my first paper on the analysis of major scaling relations as a function of environment. From these works, I showed that galaxies are affected by their host structure at $z \sim 0.7$ in terms of morphology and star-formation rate but not in terms of their dynamics. I continued with another analysis of the impact of the environment on the galaxies' stellar angular momentum. The first results suggest that there is a visible impact of the environment on the angular momentum, mostly associated to massive galaxies found in the densest parts of the structures. Because these galaxies also host massive bulges, the current interpretation is that they have probably suffered from a depletion of angular momentum ($\sim 20\%$) by building up their bulge component while reaching the inner parts of the structures. Furthermore, I have also worked on the development of a new methodology that produces resolved stellar mass maps using pixel-per-pixel SED fitting techniques and a corresponding machine learning application that I am currently refining. My Thesis has shown the powerful capabilities of MAGIC to probe the impact of the environment on galaxy evolution. This effort will be pushed forward in the near future thanks to

already existing and new MUSE surveys such as the HUDF, MUSE-WIDE, MXDF, and MUSCATEL. For the latter, I will be able to produce the galaxies' stellar mass maps and use them to get better constraints on the galaxies' ionised gas kinematics and on their dark matter content. Furthermore, these new developments combined with my expertise in morpho-kinematics analyses will also be beneficial for future data from next-generation instruments with the JWST or ERIS-VLT and on the longer term with HARMONI and MOSAIC on the ELT.

Résumé

Comprendre l'évolution morphologique et dynamique des galaxies au cours du temps cosmique est l'un des objectifs principaux de l'astrophysique extragalactique moderne. Notre compréhension actuelle est que les galaxies sont des objets qui évoluent séculairement et qui assemblent leur masse via la formation stellaire entretenue par l'accrétion de gaz froid de la toile cosmique. Cependant, cette image n'est pas suffisante pour expliquer entièrement leur évolution. Des processus environnementaux peuvent aussi affecter leur morphologie, cinématique et contenu en gaz, ainsi que supprimer leur formation stellaire, et donc jouer un rôle majeur pour expliquer la transition de haut à bas redshift. Ainsi, des efforts importants ont récemment été réalisés pour sonder l'effet de l'environnement sur les galaxies. Dans ce but, la spectroscopie 3D peut aider car elle procure des données spatialement résolues des propriétés physiques des galaxies. MUSE est l'un des spectrographes 3D les plus performants grâce à son grand champ de vue et sa haute sensibilité quand il est combiné avec l'optique adaptative.

Durant cette thèse, j'ai utilisé des données issues du relevé profond "MUSE gAlaxy Groups In Cosmos survey (MAGIC)" ciblant des groupes/amas de galaxies dans le champ COSMOS, ainsi que des galaxies d'avant et d'arrière plan. MAGIC est idéal pour sonder l'impact de l'environnement à $0.2 \lesssim z \lesssim 1.5$ pour un grand échantillon de galaxies avec une haute complétude et jusqu'à de faibles masses stellaires ($M_* \approx 10^9 M_\odot$). Parmi ces données, j'ai modélisé la morphologie d'environ 900 galaxies en réalisant une décomposition bulbe-disque afin d'extraire les paramètres principaux (ratio de flux bulbe-disque, inclinaison du disque, etc.) et la cinématique du gaz ionisé via les cubes MUSE en utilisant le doublet [O II] comme traceur cinématique et en prenant en compte l'effet du "beam smearing" pour 600 galaxies. J'ai aussi implémenté une modélisation de masse où j'ai contraint la cinématique en utilisant les informations issues de la décomposition bulbe-disque afin d'obtenir des fractions de matière noire plus précises.

Cela m'a permis de contribuer à une première analyse de la relation de Tully-Fisher à $z \sim 0.7$, suivie de mon premier papier sur l'analyse de plusieurs relations d'échelles majeures en fonction de l'environnement. A partir de ces travaux, j'ai montré que les galaxies sont affectées par leur structure à $z \sim 0.7$ au travers de leur morphologie et de leur formation stellaire mais pas de leur dynamique. J'ai poursuivi avec une autre analyse de l'impact de l'environnement sur le moment angulaire stellaire des galaxies. Les premiers résultats suggèrent qu'il y a un impact visible de l'environnement sur le moment angulaire, associé principalement aux galaxies massives localisées dans les zones les plus denses des structures. Etant donné que ces galaxies possèdent des bulbes massifs, l'interprétation actuelle est qu'elles ont probablement souffert d'une déplétion de leur moment angulaire ($\sim 20\%$) durant le processus de formation du bulbe alors qu'elles atteignaient les parties centrales des structures. Qui plus est, j'ai aussi travaillé au développement d'une nouvelle méthode pour produire des cartes de masse résolues via une technique de "SED fitting"

pixel par pixel et via une application de “machine learning” que j’affine actuellement. Ma thèse a montré les capacités de MAGIC pour sonder l’effet de l’environnement sur l’évolution des galaxies. Cet effort se poursuivra dans le future proche grâce à d’autres relevés MUSE existants et à venir comme le HUDF, MUSE-WIDE, MXDF et MUSCATEL. Pour ce dernier, j’aurai la possibilité de produire des cartes de masse résolues et de les utiliser pour mieux contraindre la cinématique du gaz ionisé et la fraction de matière noire dans les galaxies. Ces nouveaux développements combinés avec mon expertise dans les analyses morpho-cinématiques seront aussi utiles pour de futures données issues d’instruments de prochaine génération avec le JWST ou ERIS-VLT et sur le plus long terme avec HARMONI et MOSAIC sur l’ELT.

Contents

Remerciements	i
Abstract	iii
Résumé	v
List of Figures	6
List of Tables	7
List of Codes	9
Notations and mathematical symbols	11
List of spectroscopic features	13
Foreword	15
Introduction en français	19
1 Introduction	23
1.1 Useful concepts of modern cosmology	23
1.1.1 The FLRW metric	24
1.1.2 The expansion of the Universe	25
1.1.3 Notion of redshift	26
1.1.4 Impact on astrophysical quantities	27
1.2 A concise history of our understanding of galaxies	29
1.2.1 The dawn of extragalactic astronomy	29
1.2.2 A quick march towards our current view of galaxies	30
1.2.3 Last steps towards modern extragalactic astrophysics	33
1.3 Galaxy evolution across cosmic time	35
1.3.1 Properties of local galaxies	35
1.3.2 Galaxies in the distant Universe	38
1.3.3 Impact of galaxies's environment	40
1.4 The Dark Matter enigma	43
1.4.1 Dark Matter or modified gravity ?	44

1.4.2	Current questions regarding Dark Matter	45
2	Spectroscopy in extragalactic astronomy	47
2.1	Principles of spectroscopy	48
2.2	The rise of Integral Field Spectroscopy	49
2.2.1	Pioneering concepts: TIGER, OASIS, and SAURON	49
2.2.2	First-generation instruments	52
2.2.3	The MUSE revolution	53
2.2.4	Miscellaneous current and next-generation instruments	58
3	The MAGIC survey	61
3.1	Survey design and observing strategy	61
3.2	MUSE data and main survey properties	64
3.2.1	MUSE data for the MAGIC sample	64
3.2.2	Redshift determination	65
3.2.3	Survey completeness	68
3.2.4	PSF and LSF measurements	69
3.2.4.1	LSF variation with wavelength	71
3.2.4.2	PSF modelling	71
3.2.5	Derivation of galaxies' physical parameters	73
3.2.5.1	Early derivations with FAST	73
3.2.5.2	Star formation rates from the [OII] doublet	73
3.2.5.3	New derivation with CIGALE	75
3.2.5.4	Comparison of physical parameters between the different modellings	78
3.3	Structure identification and density estimation	83
3.3.1	Structure identification with a FoF algorithm	83
3.3.2	Local and global density estimators	84
4	Morphological modelling	87
4.1	Morphology of disk galaxies	88
4.1.1	Sérsic model	88
4.1.2	Sky projection: the curse of astrophysicists	89
4.1.2.1	Projection for a razor-thin disk	91
4.1.2.2	Projection of thick disks: the case of the double exponential disk	92
4.1.2.3	From single to double exponential disk	95
4.2	Impact of bulges	97
4.3	Multi-component decomposition	99
4.3.1	Bulge-disk decomposition	99
4.3.2	Global effective radius	101
4.4	Morphological modelling of galaxies in the MAGIC sample	102
4.4.1	Modelling with GALFIT	102
4.4.2	Automatic modelling for a large number of galaxies	105

5	Dynamical modelling	109
5.1	Kinematics of a test particle	110
5.1.1	Kinematics in cylindrical coordinates	110
5.2	Mass modelling	111
5.2.1	Mass modelling for a kinematics tracer in a plane	112
5.2.2	Asymmetric drift correction	112
5.2.2.1	Asymmetric drift correction for thick disks	113
5.2.3	Circular velocity for a spherical distribution of mass	114
5.2.4	Examples of mass models	114
5.2.4.1	Hernquist bulge	115
5.2.4.2	Freeman’s disk	115
5.2.4.3	Double exponential disk	116
5.2.4.4	NFW dark matter profile	118
5.2.4.5	Of the choice of DM profiles for dynamical models of intermediate redshift galaxies	118
5.3	Ionised gas kinematics with IFU data	122
5.3.1	Extraction of kinematics maps	122
5.3.1.1	Sub-cube extraction	122
5.3.1.2	Emission line fitting	123
5.3.1.3	Maps cleaning	124
5.3.2	Theory behind the kinematics modelling	125
5.3.2.1	Line-of-sight velocity	125
5.3.2.2	Instrumental impact on the velocity field	126
5.3.2.3	Instrumental impact on the velocity dispersion map	128
5.3.2.4	Brief comments on modelling the kinematics	129
5.3.3	Gas kinematics and dynamical modelling of the MAGIC sample	131
5.3.3.1	Contribution to MOCKING	131
5.3.3.2	Kinematics maps extraction	132
5.3.3.3	Dynamical modelling	133
6	Scaling relations in the MAGIC survey	137
7	Angular momentum in the MAGIC survey	173
8	Detailed study of dark matter	199
8.1	Resolved maps from multi-band HST photometry	200
8.1.1	Fundamental principles of SED fitting	206
8.1.1.1	Multi-band photometric observations	206
8.1.1.2	Key concepts: IMF, SSPs, SFH, and dust attenuation	208
8.1.1.3	Fitting galaxies’ SEDs with LEPHARE and CIGALE	210
8.1.2	Application to resolved SED fitting	211
8.1.2.1	Pre-processing steps	211
8.1.2.2	Handling flux uncertainties	212
8.1.2.3	Pixel-per-pixel SED fitting with LEPHARE and CIGALE	214
8.1.3	A python library to easily produce resolved maps from pixel-per-pixel SED fitting	216

8.1.4	A quick look at the impact of resolved maps on morphological and kinematics models	221
8.2	Machine learning application with Self Organising Maps	224
8.2.1	A general overview of Self Organising Maps	224
8.2.1.1	Key concepts for the SOM	225
8.2.1.2	Learning phase	228
8.2.2	Using the SOM for predictions	229
8.2.3	Optimisation of the SOM	229
8.2.4	The need for a fast implementation	230
8.2.5	Current implementation of the SOM	231
8.2.6	First results and perspectives	232
	Concluding remarks and perspectives	237
	Conclusions et perspectives	241
	Observatories, instruments, and surveys	263
	Glossary	271
	Publication list	1
	Appendix A Major MUSE surveys	5
A.1	Main GTO MUSE surveys	5
A.2	Main non-GTO MUSE surveys	6
	Appendix B MAGIC field-of-views	9
	Appendix C Jeans' equations	25
C.1	From Boltzmann's to Jeans' equations	25
C.2	Jeans' equations in Cartesian coordinates	26
C.3	Jeans' equations in cylindrical coordinates	27
C.4	Isothermal sheet thickness profile	28
	Appendix D Impact of convolution on the variance	29

List of Figures

1.1	Examples of Hubble’s galaxy types	31
1.2	Colour bimodality in the local Universe	36
2.1	Original design of the TIGER Integral Field Spectrograph	50
2.2	Examples of early velocity fields from TIGER, OASIS, and SAURON	51
2.3	Illustration of the field splitting and image slicing for MUSE	54
2.4	Illustration of a raw and processed MUSE observation	55
2.5	Redshift interval for the main spectral features detected with MUSE	56
3.1	Example of a MUSE observation in MAGIC	62
3.2	Examples of MUSE spectra	66
3.3	Redshift distribution of the MAGIC survey	67
3.4	Completeness of the MAGIC survey	69
3.5	Illustration of the fitting procedure for the MUSE PSF	70
3.6	Comparison between the different SFR estimates from CIGALE	76
3.7	Main Sequence and physical parameters for galaxies in MAGIC	79
3.8	Comparison between the stellar mass from CIGALE and that from FAST	80
3.9	Comparison of the MS relations built with different stellar masses and SFRs	81
4.1	Example of an azimuthally averaged surface brightness profile	88
4.2	Geometry for the sky projection of a disk	90
4.3	Projection of a double exponential disk	93
4.4	Impact of thickness on central surface brightness	95
4.5	Impact of a single Sérsic fit to a galaxy with a non-negligible bulge contribution	98
4.6	Flux distribution and B/T as a function of radius	100
4.7	Example of current summary file for GALFIT	105
5.1	Examples of various mass models	116
5.2	Impact of the DM choice on dynamical models	121
5.3	Illustration of the kinematics maps extraction with CAMEL	123
5.4	Illustration of the cleaning process for the kinematics maps	124
5.5	Illustration of the instrumental impact on the kinematics maps	127
8.1	First batch of HST images for the test sample used for resolved SED fitting	204
8.2	Second batch of HST images for the test sample for resolved SED fitting	205

8.3	HST filters' throughput used for the resolved SED modelling	206
8.4	Illustration of the impact of redshift and filters on a galaxy's SED	207
8.5	Examples of resolved stellar maps from LEPHARE and CIGALE	215
8.6	GALFIT fit for galaxy ID1 using a stellar mass map versus the F160W map.	221
8.7	MOCKING fit for galaxy ID1 using a stellar mass map versus the F160W map.	223
8.8	Illustration of the learning phase for SOMs	227
8.9	Example of a resolved stellar mass map using the SOM	233
8.10	Performance of the SOM with noisy data	234
B.1	MUSE observation for COSMOS group 23	10
B.2	MUSE observation for COSMOS group 26	11
B.3	MUSE observation for COSMOS group 28	12
B.4	MUSE observation for COSMOS group 30	13
B.5	MUSE observation for COSMOS group 32	14
B.6	MUSE observation for COSMOS group 34	15
B.7	MUSE observation for COSMOS group 35	16
B.8	MUSE observation for COSMOS group 51	17
B.9	MUSE observation for COSMOS group 61	18
B.10	MUSE observation for COSMOS group 79	19
B.11	MUSE observation for COSMOS group 84	20
B.12	MUSE observation for COSMOS group 87	21
B.13	MUSE observation for COSMOS group 114	22
B.14	MUSE observation for COSMOS group 172	23

List of Tables

- 3.1 Summary of the main characteristics of each MUSE field from Epinat et al. (in prep.). 63
- 3.2 Models and grid of parameters for the SED modelling with CIGALE of galaxies in
MAGIC 77

- 8.1 Main characteristics of the test sample used for resolved SED fitting 202
- 8.2 Zero point and PSF FWHM values for the HST bands. 212

List of Codes

- 4.1 Example of GALFIT FEEDME file. 104
- 4.2 Example of GALFIT CONSTRAINTS file. 104
- 4.3 GALFIT python wrapper code example. 107
- 5.1 Example of a CAMEL configuration file for galaxy 114_CGR79. 132
- 5.2 Example of a MOCKING configuration file for galaxy 114_CGR79. 135
- 8.1 First part of the example of a python script to perform SED fitting. 218
- 8.2 Second part of the example of a python script to perform SED fitting that is specific to LEPHARE. 219
- 8.3 Third part of the example of a python script to perform SED fitting that is specific to CIGALE. 220

Notations and mathematical symbols

Notation/Symbol Description

$\vec{\nabla}, \vec{\nabla}_{\vec{v}}$	Gradient with respect to spatial and velocity coordinates, respectively. The latter is used chiefly in Appendix C to compute Jeans' equations.
$f(\vec{x}, \vec{v}, t)$	Distribution function in phase space used to derive Jeans' equations.
$\overline{\overline{\sigma^2}}$	Stress tensor appearing in Jeans' equations. Its diagonal terms correspond to the velocity dispersion squared along the three directions.
$\langle \vec{x} \rangle$	Average of vector \vec{x} in velocity space given a distribution function f .
γ, Γ	Lower incomplete and complete gamma functions.
R_{eff}	Effective or half-light/half-mass radius, that is which encloses half of the total light/mass of the galaxy.
R_d, R_{22}	Disk scale length and radius of maximum rotation for a Freeman's disk. They are connected to the disk effective radius through the following relations: $R_d = R_{eff,d}/b_1$ and $R_{22} = 2.2R_d$ with $b_1 \approx 1.6783$.
ρ, ρ_M	3D light and mass distribution, respectively.
Σ, Σ_M	Intrinsic surface brightness and mass surface density, respectively. This is the surface brightness of a galaxy seen face-on.
Σ_{obs}	Observed surface brightness. This is the surface brightness of a galaxy when projected on the sky.
$h(\vec{r})$	Thickness profile for thick disks. For a razor-thin disk $h(\vec{r}) = \delta(z)$.
q, q_0	Observed and intrinsic axis ratios. The former is the combination of both the intrinsic axis ratio and the projection effects of the galaxy on the plane of the sky.

Notation/Symbol Description

i, i_0	Observed inclination derived from the observed axis ratio and intrinsic inclination. For a razor-thin disk $q = \cos i$ and $i = i_0$. An inclination of 0° (90°) corresponds to a face-on (edge-on) galaxy. For other geometries, the observed axis ratio must be corrected beforehand to compute the intrinsic inclination.
$F(< R),$ $M(< R)$	Flux and mass integrated in an aperture of radius R , respectively. The integration can be carried out from observations in a circular or elliptical aperture on the plane of the sky or from models in a sphere of radius R .
F_λ, F_ν	Flux density in units of wavelength or frequency.
D_A, D_L	Angular diameter and luminosity distances.
z, z_c, z_{sys}	Total, cosmological, and systemic redshift. The latter is associated to the bulk velocity of the galaxy along the line-of-sight when modelling their kinematics.
Φ	Gravitational potential.
V_R, V_z, V_θ, V_c	Radial, vertical, rotation and circular velocities, respectively. The circular velocity does not take into account the effect of asymmetric drift correction.
V_{ac}	Asymmetric drift correction that lowers the observed rotation velocity due to non streaming motions.
$V_{\theta, \text{corr}}$	Asymmetric drift corrected rotation velocity.
σ_V, σ_R	Velocity dispersion along the line-of-sight and along the radial direction, respectively.
V_b	Rotation velocity generated by a bulge mass distribution.
$V_{\text{RT}}, V_d, V_{\text{DE}}$	Rotation velocities generated by disk distributions. The first corresponds to a razor-thin disk, the second to a double exponential disk approximation, and the last to a double exponential disk corrected in the inner parts.
V_h	Rotation velocity generated by a DM halo.
f_{DM}	Fraction of DM with respect to the total mass of the galaxy.

List of spectroscopic features

- [NII] Nitrogen two, two forbidden emission lines at 6548 Å and 6583 Å close to H α . 51, 122
- [OIII] Oxygen three, a group of forbidden emission lines whose brightest line is observed at 5007 Å produced by the transition of an electron in a doubly ionised oxygen atom. 51, 57, 60, 65, 71, 72, 122
- [OII] Oxygen two, a bright doublet of emission lines observed at 3726 Å and 3729 Å produced by the transition of an electron in a singly ionised oxygen atom. 57, 60, 64, 65, 67–69, 71–74, 77, 78, 80, 82, 83, 87, 122, 124, 131–133, 137, 138, 201
- [SII] Sulphur two, two forbidden emission lines at 6716 Å and 6731 Å redward of H α . 122
- Balmer break A sudden drop in flux shortward of 3646 Å due to completely ionised electrons from the second energy level of the hydrogen atom by photons with higher energy. 57, 65
- CIII] Carbon three, two UV semi-forbidden lines at 1907 Å and 1909 Å. 57
- CaII H Second calcium-II doublet line, also known as Fraunhofer H line, a rest-frame violet absorption line at 3968 Å first observed by Joseph von Fraunhofer in the spectrum of the Sun. 57, 65
- CaII K First calcium-II doublet line, also known as Fraunhofer K line, a rest-frame violet absorption line at 3933 Å first observed by Joseph von Fraunhofer in the spectrum of the Sun. 57, 65
- D4000 The flux or flux density ratio between a red-wise and a blue-wise narrow band around a rest-frame wavelength of 4000 Å. 65
- G-band A broad absorption line at 4301 Å caused by CH molecules and less significantly by iron. 57, 65
- H α H-alpha, a rest-frame red emission/absorption line of the Balmer series at 6562 Å due to the transition of an electron in an hydrogen atom from its third energy level to its second's. Its brightness, rest-frame wavelength, and relation to star forming regions make it an ideal tracer of star formation in galaxies. 33, 37, 44, 54, 57, 60, 65, 68, 73, 74, 122

- H β** H-beta, a rest-frame blue-green emission/absorption line of the Balmer series at 4861 Å due to the transition of an electron in an hydrogen atom from its fourth energy level to its second's. 51, 60, 65, 122
- H δ** H-delta, a rest-frame violet emission/absorption line of the Balmer series at 4101 Å due to the transition of an electron in an hydrogen atom from its sixth energy level to its second's. 122
- H γ** H-gamma, a rest-frame blue emission/absorption line of the Balmer series at 4341 Å due to the transition of an electron in an hydrogen atom from its fifth energy level to its second's. 122
- Ly α** Lyman alpha, a rest-frame ultraviolet emission line at 1215 Å due to the transition of an electron in an hydrogen atom from its second energy level to the ground level, discovered by Theodore Lyman, and observed in high redshift galaxies. 5, 6, 33, 57, 58, 64, 67–69
- Lyman break** A sudden drop in flux shortward of 911 Å due to higher energy photons being completely absorbed by neutral gas. 57, 65
- Mg II** Magnesium two, a NUV resonant doublet at 2796 Å and 2803 Å. 6, 7, 57

Foreword

This work is dedicated to the study of the morphological and dynamical evolution of galaxies across cosmic time with the help of the Multi-Unit Spectroscopic Explorer (MUSE). During these three years, my main focus has been to study the impact of the environment on the physical, morphological, and dynamical properties of galaxies in the MUSE-gAlaxy Groups In Cosmos (MAGIC) sample at intermediate redshift ($0.2 \lesssim z \lesssim 1.5$). MAGIC is a deep survey specifically designed to efficiently probe the impact of the environment on the dynamics of galaxies. Using this data combined with HST images, I have contributed to four papers, two of which have been published (Abril-Melgarejo et al. 2021; Mercier et al. 2022) and two are almost complete (analysis of the angular momentum discussed in Chapter 7 and the MAGIC survey paper in Chapter 3). These papers have allowed us to put the strongest constraints up to date on the impact of the environment at intermediate redshift on major scaling relations. In turn, these results provide insights into the interplay of the morphology and the dynamics of galaxies with their host environment.

Originally, the plan was to perform a first self-consistent analysis of the impact of the environment on the dynamics of galaxies in the MAGIC survey and then to apply the same method to the MUSE Cosmic Assembly survey Targeting Extragalactic Legacy fields (MUSCATEL) survey. However, due to social strikes across Chile and an unexpected pandemics across the globe, VLT operations had to shut down which has produced delays in the acquisition of MUSCATEL. Hence, the plan shifted towards a different trajectory. The new idea was to focus my efforts on MAGIC for the time being by improving our current methodology (i.e. implementing mass models, see Chapter 5) so that it would be ready when MUSECATEL would become available. These new developments shall be even more important for the next generation of integral field spectrographs that will provide spatially resolved kinematics observations with unprecedented resolution and sensitivity at high redshift.

In this manuscript, I provide a summary of all the work that I have carried out over the last three years, either alone or with the help of Master students whose internship I supervised (see Chapter 8). I start the discussion with an introduction that is split in two different chapters. In Chapter 1, I give a general overview of the current field of extragalactic astronomy. Because I feel that one cannot completely grasp the modern questions that are tackled by current research without keeping in mind the historical development of the field and of its ideas, I give, after a brief discussion about cosmology, a quick historical overview of the development of extragalactic astrophysics from its very beginning up to this day. In Chapter 2, I rather focus on the instrumental side by discussing the development of integral field spectroscopy. In particular, I discuss in details the main instrument that I have been using, MUSE, and also a few other similar instruments currently operational or that shall become so in the near- or mid-term future.

Because this work has relied so far entirely on MAGIC, I give a thorough description of the survey design and of the characteristics of the data. In Chapter 3, I provide the key characteristics of the survey (redshift determination, completeness, Point Spread Function, Line Spread Function, structure identification, etc.) and I give a first quick discussion of the physical properties of the sample of galaxies at $z < 1.5$. Then, I switch to more theoretical aspects in Chapters 4 and 5 where I present the methodology used to model the morphology and the kinematics of intermediate redshift galaxies in MAGIC. For the morphological modelling, I focus on the bulge-disk decomposition used in the analysis of the scaling relations (see Chapter 6) and of the angular momentum (see Chapter 7) where I emphasise the importance of such a decomposition for galaxies with massive bulges. I also present a python code that I developed at the beginning of my Thesis to automatise the morphological modelling performed with GALFIT. For the kinematics part, I discuss the theory behind the mass models that I incorporated and used for the first time in the kinematics fitting tool MOCKING. I also discuss how I fitted the galaxies' resolved kinematics starting from the MUSE cubes and how I took instrumental effects such as beam smearing into account to recover the galaxies' intrinsic rotation and velocity dispersion. As mentioned previously, Chapters 6 and 7 present the two main analyses that I have carried out during this Thesis. The first chapter includes my published analysis of three scaling relations (Main Sequence relation, size-mass relation, and Tully Fisher relation) as a function of environment in the MAGIC survey and the second chapter includes a still ongoing but nearly finished analysis of the angular momentum in MAGIC using a novel approach that combines our best-fit kinematics models from [Mercier et al. \(2022\)](#) with high-resolution HST images to get the most accurate angular momentum estimate for a large sample with our current dataset. In the last chapter of this Thesis (see Chapter 8) I present ongoing developments regarding the production of spatially resolved maps of physical parameters (e.g. stellar mass or star formation rate - SFR) using pixel-per-pixel spectral energy distribution fitting (see Sect. 8.1) and using machine learning techniques (see Sect. 8.2). In both cases, I discuss the maturity of the method at the moment, the difficulty we have encountered and the solutions that we have proposed, and I show a few examples of current results before mentioning future applications. Finally, I finish this manuscript by mentioning the perspectives of this work in the near-future with plans for further analyses in MAGIC and MUSECATEL, as well as further improvements of our method in preparation for next-generation integral field spectrographs installed on the future Extremely Large Telescopes such as HARMONI or MOSAIC.

In parallel to the work described in this Thesis, I have also contributed throughout the last three years to a few additional analyses as co-author (see the list of publications for a short description of my contribution). First, I have contributed at the beginning of this Thesis mainly on the sample selection and on the galaxies' morphology in the first analysis of the Tully-Fisher relation in MAGIC ([Abril-Melgarejo et al. 2021](#)). My second important contribution, still in MAGIC, is concerning the survey paper (Epinat et al., in prep.). This includes mainly the MUSE point spread function modelling and characterisation as a function of the observed wavelength and all the work related to the modelling and the morphology and kinematics of the [O II] emitters in the sample (bulge-disk decomposition, [O II] fluxes measurements, kinematics mass modelling, [O II] star formation rates, etc.). I have also contributed to other analyses that use MUSE data apart from MAGIC that are related to my field of expertise. Among these, I can cite my short contributions to the analyses of the ionised gas angular momentum in the HUBBLE Ultra Deep Field in [Bouché et al. \(2021\)](#) and of the impact of gas flows on the mass-metallicity and the SFR-mass-metallicity relations (Langan et al., in prep.), and my more significant contributions to

the measurements of spectroscopic redshifts for a large sample of galaxies in a survey covering massive lensing clusters (Richard et al. 2021) and to the morphological modelling of the nine $z \sim 1$ star-forming galaxies in the MUSE Extreme Deep Field for which we constrained the shape of their dark matter profile (Bouché et al. 2022).

Introduction (foreword in French)

Ce travail est dédié à l'étude de l'évolution morphologique et dynamique des galaxies au cours du temps cosmique avec l'aide de l'instrument « Multi-Unit Spectroscopic Explorer » (MUSE). Durant ces trois années, mon attention s'est portée sur l'étude de l'impact de l'environnement sur les propriétés physiques, morphologiques et dynamiques des galaxies dans le relevé « MUSE-gAlaxy Groups In Cosmos » (MAGIC) à redshift intermédiaire ($0.2 \lesssim z \lesssim 1.5$). MAGIC est un relevé profond conçu spécifiquement pour sonder efficacement l'impact de l'environnement sur la dynamique des galaxies. A l'aide de ces données combinées avec des images HST, j'ai contribué à quatre articles, dont deux ont été publiés (Abril-Melgarejo et al. 2021; Mercier et al. 2022) et deux sont quasiment terminés (analyse du moment angulaire discutée au Chapitre 7 et description du relevé MAGIC au Chapitre 3). Ces articles nous ont permis de poser les plus fortes contraintes à ce jour sur l'impact de l'environnement à redshift intermédiaire sur plusieurs relations d'échelles majeures des galaxies. En conséquence, ces résultats nous renseignent sur les interactions entre la morphologie et la dynamique des galaxies avec leur environnement.

Le plan initial était d'effectuer une première analyse auto-cohérente de l'impact de l'environnement sur la dynamique des galaxies dans le relevé MAGIC, puis d'appliquer la même méthode pour le nouveau relevé « MUSE Cosmic Assembly survey Targeting Extragalactic Legacy fields » (MUSCATEL). Cependant, suite à des manifestations au Chili et à l'arrivée inattendue d'une pandémie mondiale, les opérations du VLT ont dû être arrêtées ce qui a produit des délais dans l'acquisition de MUSCATEL. De fait, le plan s'est orienté vers un objectif différent. La nouvelle idée était de concentrer mes efforts sur MAGIC en améliorant notre méthodologie (c'est-à-dire d'implémenter des modèles de masse, voir Chapitre 5) de telle sorte que cela serait prêt quand les données MUSCATEL deviendraient disponibles. Ces nouveaux développements seront d'autant plus importants pour la prochaine génération de spectrographes à intégrale de champs qui fourniront des observations cinématiques spatialement résolues avec une résolution et une sensibilité à haut redshift inégalées.

Dans ce manuscrit, je résume le travail que j'ai effectué au cours des ces trois dernières années, soit seul, soit avec l'aide d'étudiants en Master donc j'ai supervisé les stages (voir Chapitre 8). Je commence par une introduction séparée en deux chapitres différents. Dans le Chapitre 1, je donne une vue d'ensemble du champs de recherche actuel qu'est l'astronomie extragalactique. Parce que je considère qu'on ne peut pas complètement appréhender les questions modernes qui sont étudiées par la recherche actuelle sans avoir en tête les développements historiques de la discipline et de ses idées, je fournis, après une brève introduction à la cosmologie, un résumé rapide du développement de l'astrophysique extragalactique depuis son commencement jusqu'à aujourd'hui. Dans le Chapitre 2, je me concentre plutôt sur le côté instrumental en discutant le développement de la spectroscopie à intégrale de champs. En particulier, je discute en détails l'instrument principal

que j'ai utilisé, MUSE, ainsi que quelques autres instruments actuellement opérationnels ou qui le seront à court ou moyen terme. Parce que ce travail n'aurait pas pu avoir lieu sans MAGIC, je fournis une description détaillée du relevé. Dans le Chapitre 3, je donne les caractéristiques principales du relevé (détermination des redshifts, complétude, fonction d'étalement du point - PSF, fonction d'étalement de la raie, identification des structures, etc.) et je fournis une discussion rapide des propriétés physiques de l'échantillon de galaxies à $z < 1.5$. Ensuite, je me concentre sur des aspects plus théoriques dans les Chapitres 4 et 5 où je présente la méthodologie utilisée pour modéliser la morphologie et la cinématique des galaxies à redshift intermédiaire dans MAGIC. Pour la modélisation morphologique, je me concentre sur la décomposition bulbe-disque utilisée dans l'analyse des relations d'échelles (voir Chapitre 6) et du moment angulaire (voir Chapitre 7) où je mets en avant l'importance d'une telle décomposition pour des galaxies avec des bulbes massifs. Je présente aussi un code python que j'ai développé au tout début de ma Thèse et qui automatise la modélisation morphologique faite avec GALFIT. Concernant la partie cinématique, je discute la théorie derrière les modèles de masse que j'ai incorporés et utilisés pour la première fois dans le code d'ajustement cinématique MOCKING. Je discute aussi comment j'ai ajusté la cinématique résolue des galaxies à partir des cubes de données MUSE et comment j'ai pris en compte les effets instrumentaux comme le « beam-smearing » pour obtenir la rotation et la dispersion de vitesse intrinsèques des galaxies. Comme mentionné précédemment, les Chapitres 6 et 7 présentent les deux analyses principales que j'ai effectué durant cette Thèse. Le premier des deux chapitres inclut mon analyse publiée de trois relations d'échelles (séquence principale, relation masse-taille et relation de Tully-Fisher) en fonction de l'environnement dans le relevé MAGIC, et le second inclut une analyse quasiment terminée du moment angulaire dans MAGIC en utilisant une approche novatrice qui combine nos modèles cinématiques issus de [Mercier et al. \(2022\)](#) avec les images à haute résolution HST pour obtenir l'estimation la plus précise du moment angulaire pour un grand échantillon de galaxies. Dans le dernier chapitre de cette Thèse (voir Chapitre 8), je présente des développements en cours concernant la construction de cartes de paramètres physiques (ex : masse stellaire, ou taux de formation stellaire - SFR) spatialement résolue à l'aide d'une technique d'ajustement de distribution d'énergie spectrale pixel par pixel (voir Sect. 8.1) et d'une application d'apprentissage machine (voir Sect. 8.2). Dans les deux cas, je discute de la maturité des méthodes dans leurs états actuels, des difficultés rencontrées et des solutions qui ont été proposées. Je montre aussi quelques exemples de résultats avant de mentionner les applications futures. Finalement, je termine ce manuscrit en discutant les perspectives de ce travail dans le futur proche avec mes plans pour de nouvelles analyses avec MAGIC et MUSCATEL, ainsi que de futures améliorations de notre méthode en préparation de la prochaine génération de spectrographes à intégral de champs qui seront installés sur les télescopes extrêmement grands tel que HARMONI ou MOSAIC.

En parallèle du travail décrit dans cette Thèse, j'ai aussi contribué au cours de ces trois dernières années à plusieurs analyses supplémentaires en tant que co-auteur (voir la liste de publications pour une courte description de ma contribution). En premier lieu, j'ai contribué au tout début de cette Thèse à la sélection de l'échantillon ainsi qu'à la caractérisation de la morphologie des galaxies lors de la première analyse de la relation de Tully-Fisher dans MAGIC ([Abril-Melgarejo et al. 2021](#)). Ma seconde contribution importante, toujours en rapport avec MAGIC, concerne le papier décrivant le relevé (Epinat et al., in prep.). Cela inclut principalement la modélisation et la caractérisation de la PSF de MUSE en fonction de la longueur d'onde observée, ainsi que tout ce qui touche à la modélisation morphologique et cinématique des émetteurs [O II] dans l'échantillon (décomposition bulbe-disque, mesure des flux [O II], modélisation de masse, taux de formation

stellaire [O II], etc.). J'ai aussi contribué à d'autres analyses qui utilisent des données MUSE au-delà de MAGIC et qui sont en rapport avec mon domaine d'expertise. Parmi celles-ci, je peux citer d'abord mes contributions mineures aux analyses du moment angulaire du gaz ionisé dans le « HUBBLE Ultra Deep Field » de [Bouché et al. \(2021\)](#) et de l'impact de l'accrétion et de l'éjection de gaz dans les galaxies sur les relations de masse-métallicité et de SFR-masse-métallicité (Langan et al., in prep.). Ensuite, je peux mentionner mes contributions plus importantes sur la mesure des redshifts spectroscopiques pour un grand échantillon de galaxies dans un relevé ciblant des amas de galaxies avec de forts effets de lentille gravitationnelle ([Richard et al. 2021](#)) et sur la modélisation morphologique de neuf galaxies à formation d'étoiles à $z \sim 1$ dans le relevé « MUSE Extreme Deep Field » pour lesquelles nous avons pu contraindre les profils de halo de matière noire ([Bouché et al. 2022](#)).

Chapter 1

A quick introduction to galaxy morpho-dynamical evolution

Extragalactic astrophysics is a complex field of research with many specialities. This Thesis is mainly concerned with the dynamical evolution of galaxies across cosmic time but, to understand it plainly, one must relate it to the evolution of other key aspects related to galaxies such as their morphology or physical properties. Besides, our understanding of galaxy evolution has tremendously changed throughout the last century and it is therefore enlightening to remind ourselves where this field of research stood one hundred years ago and to compare it where it is now. Hence, in this Chapter, I provide an overview of our current understanding of galaxy evolution.

I start with a short theoretical section concerning the cosmological context in extragalactic astrophysics. In particular, Sect. 1.1 allows me to write down the important cosmological concepts that are linked to observational extragalactic astrophysics (e.g. redshift, fluxes, distance measurements, etc.) and that are used throughout this Thesis. In Sect. 1.2, I proceed with a relatively condensed summary of the historical developments that led to our modern view of galaxies. In Sect. 1.3, I describe our current understanding of galaxy properties and their evolution across cosmic time, separating those found in the local Universe in Sect. 1.3.1 from high-redshift galaxies in Sect. 1.3.2, and from the impact of their host environment in Sect. 1.3.3. Finally, I conclude this chapter by quickly mentioning in Sect. 1.4 the current evidence and questions regarding the presence of Dark Matter (DM) in galaxies and galaxy clusters.

1.1 Useful concepts of modern cosmology

Galaxies are objects embedded in a Universe evolving with cosmic time. In order to study the evolution of their intrinsic properties such as their shape, mass, size, stellar populations, amount of cold gas, etc., we need to take into account the impact of our Universe's cosmology on these properties. The goal of this Thesis is to study the dynamical evolution of galaxies and not to use them as tracers of our cosmological model. Therefore, I will not give a detailed account of the underlying principles and derivations of the current cosmological model. Instead, I will focus on how the current Λ Cold Dark Matter (Λ CDM) cosmological model impacts measurements of key

physical quantities useful for my analysis (e.g. distance, size, luminosity, etc.).

1.1.1 The FLRW metric

Modern cosmology is built on the foundations of General Relativity (GR) even though a similar solution, though not behaving precisely in the same way, could also be derived in the framework of classical mechanics. In order to understand how the Universe evolves and how it affects galaxies' properties, one needs to find an expression of curvature of space-time encapsulated in its metric. In GR the metric is described as a second-rank tensor $g_{\mu\nu}$ which can be thought of as a matrix with two dimensions. Because the framework of GR is in four-space (time plus spatial three-space) the metric has 16 components that reduces to ten because it is symmetric ($\forall \mu, \nu, g_{\mu\nu} = g_{\nu\mu}$). A common way to write it is through the line element ds that describes an infinitesimal displacement along all directions (including time): $ds^2 = g_{\mu\nu} dx^\mu dx^\nu$, where I have used Einstein's summation convention where an implicit sum is to be understood when the same symbol appears as a subscript and superscript in a product. For instance, in 3D Euclidian geometry, the metric writes $ds^2 = dx^2 + dy^2 + dz^2$ whereas on a two-sphere it rather writes $ds^2 = R^2 d\theta^2 + R^2 \sin^2 \theta d\phi^2$ where R is the radius of curvature of the sphere and (θ, ϕ) are the usual spherical coordinates. The two key hypotheses at the basis of our modern Λ CDM cosmological model are the *homogeneity* and *isotropy* of the Universe which are summarised in the cosmological principle that states that we are not located at any special location in our Universe. A typical evidence supporting such hypotheses at least to first order is the large homogeneity of the Cosmic Microwave Background (CMB). If we further assume that there exists a set of fundamental observers whose motion makes them always see the Universe as isotropic and that are equipped with clocks measuring the same proper time called cosmic time, then the metric in a curved, homogeneous, isotropic, and expanding Universe becomes the Friedmann–Lemaître–Robertson–Walker metric (FLRW) that writes (e.g. [Longair 2008](#))

$$\begin{aligned} ds^2 &= dt^2 - \frac{a^2(t)}{c^2} \left[dr^2 + R_c^2(t_0) \sin^2 \left(\frac{r}{R_c(t_0)} \right) (d\theta^2 + \sin^2 \theta d\phi^2) \right] \\ &= dt^2 - \frac{a^2(t)}{c^2} \left[\frac{dr_1^2}{1 - \kappa r_1^2} + r_1^2 (d\theta^2 + \sin^2 \theta d\phi^2) \right], \end{aligned} \quad (1.1)$$

where c is the speed of light, t is the aforementioned cosmic time, $R_c(t_0)$ is the curvature of space-time at present time t_0 , r is the comoving distance along the line-of-sight (LOS), that is the distance from us not taking into account the expansion of the Universe, $a(t)dr$ is the infinitesimal element of proper distance (also called physical distance) along the LOS at time t (i.e. taking into account the expansion of the Universe), and $a(t)r_1 d\theta$ and $a(t)r_1 \sin \theta d\phi$ are the elements of proper distance at time t along the two perpendicular directions with respect to the LOS. The second expression is a bit more common than the first one and is obtained by defining a new proper length $r_1 = R_c(t_0) \sin(r/R_c(t_0))$ and the Gaussian curvature of space-time $\kappa = 1/R_c^2(t_0)$. In both expressions $a(t)$ is a unitless scale factor that encompasses the expansion of the Universe, that is it tells us how to convert a comoving distance into a physical one and vice versa. A common convention is to set $a(t_0) = 1$, that is the scale factor of the Universe is unity at present time. As an indication, I note that in Eq. 1.1 r and r_1 have units of distances but there exists another convention for which the transformation $|\kappa|r_1^2 \rightarrow r_1^2$ is applied to Eq. 1.1 so that $a(t)$ becomes

$R(t) = a(t)R_c(t_0)$ and κ becomes $k \in \{-1, 0, 1\}$. When $k = -1, 0,$ and 1 the geometry is said to be hyperbolic, flat, and spherical, respectively.

1.1.2 The expansion of the Universe

Equation 1.1 provides us with the geometry of space-time but it does not tell us anything about how the structure of the Universe evolves with time. To know how fast the Universe expands or contracts we need to derive the expression for the scale factor $a(t)$. This is only possible using the 16 Einstein's equations that write

$$R_{\mu\nu} - \frac{1}{2}g_{\mu\nu}R + \Lambda g_{\mu\nu} = -\frac{8\pi G}{c^2}T_{\mu\nu}, \quad (1.2)$$

where $R_{\mu\nu}$, $g_{\mu\nu}$, and $T_{\mu\nu}$ are second-rank tensors, with $R_{\mu\nu}$ the Ricci tensor, $g_{\mu\nu}$ the metric, and $T_{\mu\nu}$ the stress-energy tensor. In Eq. 1.2, R is the Ricci scalar that can be derived from the Ricci tensor and the metric, c is the speed of light, and G is the gravitational constant. In what follows I do not provide further details about GR and the derivation of Einstein's equations because it is beyond the scope of this Thesis. More information can be found in any textbook on GR and/or cosmology. Nevertheless, I can add the few following information: (i) the Ricci tensor $R_{\mu\nu}$ is connected to the metric and so to the curvature of space-time and (ii) the stress-energy tensor $T_{\mu\nu}$ describes the density, flux, pressure, and stress of a given fluid and acts as the source of gravity in Einstein's equations. Using the FLRW metric and assuming a perfect fluid whose stress-energy tensor writes $T^{\mu\nu} = (\rho + P/c^2)u^\mu u^\nu + Pg^{\mu\nu}$, with ρ its total mass density (including radiation), P its pressure and u the four-velocity vector, Einstein's equations reduce to the two following Friedmann-Lemaître equations (Friedmann 1922, 1924; Lemaître 1927):

$$\frac{\ddot{a}}{a} = -\frac{4\pi G}{3} \left(\rho + \frac{3P}{c^2} \right) + \frac{\Lambda}{3} \quad (1.3)$$

$$H^2 + \frac{kc^2}{a^2} = \frac{8\pi G\rho}{3} + \frac{\Lambda}{3}, \quad (1.4)$$

where $H(t) = \dot{a}(t)/a(t)$ is called the Hubble constant and Λ is the cosmological constant from which the Λ CDM model takes its name. Without a cosmological constant, the solution with $k < 0$ corresponds to an open Universe that expands forever and that with $k > 0$ corresponds to a closed Universe that expands first and then collapses onto itself after some time. The solution with $k = 0$ is called an Einstein-de Sitter Universe and corresponds to the critical case where there is just enough matter to reduce its expansion but not enough to trigger its collapse. The corresponding critical density is given by

$$\rho_c = \frac{3H^2}{8\pi G}. \quad (1.5)$$

Contrary to the matter and radiation contents represented by P and ρ that will always decelerate the expansion of the Universe, the cosmological constant can act as an acceleration term if it is positive. In particular, the first Friedmann-Lemaître equation tells us that if $\Lambda > 4\pi(\rho + 3P)$ then the Universe will be accelerated (as long as $P > -\rho/3$). Thus, since the discovery of the acceleration of the expansion of the Universe (Riess 1998; Perlmutter et al. 1999), the cosmological constant has been added into Einstein's and Friedmann-Lemaître equations to take into account the effect of dark energy.

1.1.3 Notion of redshift

An important notion in extragalactic astronomy is that of redshift. It corresponds to the shift of a spectrum with respect to its rest-frame wavelength position because of the motion of the galaxy and of the expansion of the Universe. Thus, in essence a galaxy's spectrum can be blue- or red-shifted, but since at large enough distances the expansion of the Universe takes over, we only refer to it as redshift. By definition, it writes

$$z = \frac{\lambda_{\text{obs}} - \lambda_{\text{em}}}{\lambda_{\text{em}}}, \quad (1.6)$$

where λ_{obs} is the observed wavelength and λ_{em} the emitted one. Hence, we have the two following scaling relations:

$$\begin{aligned} \lambda_{\text{obs}} &= (1 + z)\lambda_{\text{em}} \\ \nu_{\text{em}} &= (1 + z)\nu_{\text{obs}}, \end{aligned} \quad (1.7)$$

where $\nu = c/\lambda$ is the frequency. In special relativity, the redshift due to the velocity v along the line of sight writes

$$\begin{aligned} 1 + z &= \sqrt{\frac{1 + v/c}{1 - v/c}} \\ &\underset{v \ll c}{\approx} 1 + \frac{v}{c}, \end{aligned} \quad (1.8)$$

which reduces to the classical expression for low velocities with respect to the speed of light. In cosmology, its expression is different because it must take into account the expansion of the Universe encapsulated in the scale factor $a(t)$. Its expression can be easily derived from the FLRW metric considering that a packet of photons emitted at time t_{em} during a time interval Δt_{em} is received at time t_{obs} during an interval Δt_{obs} . The light propagates radially towards us along a null geodesic (i.e. $ds^2 = d\theta^2 = d\phi^2 = 0$) so that we have $cdt = a(t)dr$. The front of the wave packet propagates from the space-time position (t_{em}, r) to $(t_{\text{obs}}, 0)$ and the rear of the wave packet propagates from $(t_{\text{em}} + \Delta t_{\text{em}}, r)$ to $(t_{\text{obs}} + \Delta t_{\text{obs}}, 0)$. Thus, for both the front and the rear of the wave packet we can integrate $cdt/a(t)$ on one side and dr on the other. Because they share the same integral along r , we can equate them to obtain

$$\begin{aligned} \int_{t_{\text{em}}}^{t_{\text{obs}}} dt/a(t) &= \int_{t_{\text{em}} + \Delta t_{\text{em}}}^{t_{\text{obs}} + \Delta t_{\text{obs}}} dt/a(t) \\ &\approx \int_{t_{\text{em}}}^{t_{\text{obs}}} dt/a(t) + \frac{\Delta t_{\text{obs}}}{a(t_{\text{obs}})} - \frac{\Delta t_{\text{em}}}{a(t_{\text{em}})}, \end{aligned} \quad (1.9)$$

which is valid for small Δt_{obs} and Δt_{em} . Thus, we get the cosmological time dilation expression

$$\frac{\Delta t_{\text{obs}}}{\Delta t_{\text{em}}} = \frac{a(t_{\text{obs}})}{a(t_{\text{em}})}. \quad (1.10)$$

Given that by convention $a(t_{\text{obs}}) = a(t_0) = 1$, it reduces to $\Delta t_{\text{em}} = a(t_{\text{em}})\Delta t_{\text{obs}}$. If Δt_{obs} and Δt_{em} are understood as the period of the wave, then we have $\nu_{\text{em}} = \nu_{\text{obs}}/a(t_{\text{em}})$, which gives

$$1 + z_c = 1/a(t_{\text{em}}), \quad (1.11)$$

where z_c is the cosmological redshift of the source.

There is one last aspect that needs be discussed. Indeed, the redshift of a galaxy is not simply the result of the expansion of the Universe but can be affected by further motions. For instance, a galaxy can have its own proper motion along the LOS, it can be located in a group or in a cluster of galaxies which will have their own bulk velocity as well, or it can rotate which will change the value of the redshift depending on whether we measure it in a part of the galaxy that rotates faster or slower. Thus, we need to derive a law of composition for redshifts to combine all these effects together. To do so, let us imagine a galaxy at a cosmological redshift z_c and an observer located at the same redshift. For this observer, the galaxy has a LOS velocity that produces a second redshift z_1 , so that the light emitted by the galaxy at a wavelength λ_{em} will appear at the wavelength $\lambda_1 = (1 + z_1)\lambda_{\text{em}}$. On the other hand, the light will appear for us as if emitted in the frame of the observer at the wavelength λ_1 and will be redshifted to the observed wavelength $\lambda_{\text{obs}} = (1 + z_c)\lambda_1 = (1 + z_c)(1 + z_1)\lambda_{\text{em}}$. If the global redshift can be split into multiple components, then we can generalise the previous result and obtain the law of composition for redshifts

$$\lambda_{\text{obs}} = \prod_i (1 + z_i)\lambda_{\text{em}}. \quad (1.12)$$

1.1.4 Impact on astrophysical quantities

Now that we have quickly discussed the theory behind cosmology, we still need to derive how key physical quantities useful for this Thesis are affected by the expansion of the Universe. As already discussed in Sect. 1.1.1, we can assign a distance to an object without taking into account the expansion of the Universe: its comoving distance r . To transform it into a physical distance we must apply the scale factor to take into account the expansion of the Universe, $a(t)r$, and we call it its proper distance. But these two distances are not the only ones we can define. There are at least two more that can be useful in combination with other physical quantities: the angular diameter distance and the luminosity distance.

The angular diameter distance D_A corresponds to the distance that must be used to derive the physical size of an object or the physical separation between two close objects at the same cosmological redshift (noted d) with an apparent angular size or separation $\Delta\theta$ on the plane of the sky through the Euclidian formula

$$d = D_A \Delta\theta. \quad (1.13)$$

To derive it, one can use the FLRW metric and consider the line element along the direction θ . The physical size will be given by integrating it, which gives

$$\begin{aligned} d &= a(t)R_c(t_0) \sin\left(\frac{r}{R_c(t_0)}\right) \Delta\theta \\ &= \frac{r_1}{1 + z_c} \Delta\theta, \end{aligned} \quad (1.14)$$

where r_1 is defined in Eq. 1.1 and reduces to the usual Euclidian distance $r_1 \approx r$ when $r \ll R_c(t_0)$. Thus, the angular diameter distance scales with radius as

$$D_A = \frac{r_1}{1 + z_c}. \quad (1.15)$$

In cosmology the angular diameter distance increases up to a turnover point ($z \approx 1.5$ for Λ CDM) and then decreases again. Thus, for an object with a fixed physical size this means that its angular size on the plane of the sky will first decrease up to the turnover point and then will increase again. Hence, contrary to our intuition in Euclidean geometry where the further away an object is from us the smaller is its angular extent, high-redshift galaxies can appear larger than lower redshift counterparts with the same physical size.

On the other hand, the luminosity distance comes from working out the impact of cosmology on the flux that we observe. Indeed, let us consider an isotropic source with intrinsic luminosity $L = \Delta E_{\text{em}}/\Delta t_{\text{em}}$, where ΔE_{em} is the emitted energy in an interval Δt_{em} . At present time, its luminosity will be distributed over a spherical area of $4\pi a^2(t_0)r^2 = 4\pi r^2$, since $a(t_0) = 1$ by convention, so that a telescope at a comoving distance r from the source and with an area \mathcal{A} will receive a fraction $\mathcal{A}/(4\pi r^2)$ of the total emitted luminosity. At the same time, the received luminosity L_{obs} is just the product of the telescope area by the observed flux, hence we have

$$\begin{aligned} L_{\text{obs}} &= F \times \mathcal{A} \\ &= \frac{\Delta E_{\text{obs}}}{\Delta t_{\text{obs}}} \times \frac{\mathcal{A}}{4\pi r^2}. \end{aligned} \quad (1.16)$$

But, we know from Eq. 1.7 that the observed photons' frequency and therefore energy both scale as $\Delta E_{\text{obs}} = \Delta E_{\text{em}}/(1 + z)$ and from Eqs. 1.10 and 1.11 that the observed time interval within which the photons will be received scales as $\Delta t_{\text{obs}} = (1 + z)\Delta t_{\text{em}}$. Thus, we find the relation

$$F = \frac{L}{4\pi D_L^2}, \quad (1.17)$$

where we have defined the luminosity distance as

$$D_L = r(1 + z). \quad (1.18)$$

Furthermore, I will also use the concept of flux density in what follows. In this Thesis, I call flux density the flux per unit wavelength (noted F_λ) or per unit frequency (noted F_ν). Its unit will either be in $\text{erg s}^{-1} \text{\AA}^{-1} \text{cm}^{-2}$ for F_λ or in $\text{erg s}^{-1} \text{Hz}^{-1} \text{cm}^{-2}$ for F_ν . The derivation of the impact of cosmology on the observed flux density is very similar to that of the flux. The only difference is that it is divided either by a frequency or by a wavelength so that, based on Eq. 1.7, we have

$$F_{\nu,\text{obs}}(\nu_{\text{obs}}) = F_{\nu,\text{em}}(\nu_{\text{em}}/(1 + z)) \times (1 + z) \quad (1.19)$$

$$F_{\lambda,\text{obs}}(\lambda_{\text{obs}}) = \frac{F_{\lambda,\text{em}}(\lambda_{\text{em}}(1 + z))}{1 + z} \quad (1.20)$$

We see that in both cases we have a shift of the frequency or wavelength range as well as a scale factor that is either larger than or less than unity depending on whether we consider F_ν or F_λ .

1.2 A concise history of our understanding of galaxies

1.2.1 The dawn of extragalactic astronomy

Among the topics in Astronomy, extragalactic astrophysics is a quite recent field of research, in some way that is barely one hundred years old. A certainly important reason for such a late development in the study of galaxies is that there are actually only a handful which are visible with the naked eye on the celestial sphere. The most visible of all is our Galaxy, the Milky Way. Beside it, our closest companion, the Andromeda galaxy (M31), is supposed to be visible in the northern hemisphere and so is the Triangulum galaxy (M33). However, even though they are supposed to be very luminous, they span large areas on the sky which make them hardly visible without the aid of optical systems. Additionally, in the southern hemisphere two bright and easily visible galaxies can also be seen: the Small and the Large Magellanic Clouds. But apart from these close and bright objects, no other galaxy can be seen without the use of binoculars or refractive/reflective telescopes. However, this picture changed throughout the eighteenth and nineteenth centuries when astronomers such as Charles Messier or John Herschel started to make catalogues of such objects that were called at the time nebulae.

As the number of observed nebulae grew with time, the question of their distance to us became unavoidable. Given that precise distance measurements were lacking up to 1925, two competing ideas faced each other regarding this question. Some astronomers thought that the nebulae were objects located within our own Galaxy, whereas others rather thought that they were *Island Universes* to use the terminology devised by Immanuel Kant but inspired by the earlier works of Emanuel Swedenborg and Thomas Wright ([Swedenborg 1734](#); [Wright & Rafinesque 1837](#)), that is external systems composed of stars similar to the Milky Way, hence extragalactic objects. Thus, it is not totally inaccurate to say that, before a first conclusive answer was brought by Edwin Hubble in 1925, the size of the Universe, or rather our comprehension of it, did not extend beyond the visible boundaries of the Milky Way. One of the reasons behind the longevity of the debate is that the class of nebulae that were observed at the time did not only incorporate objects that we would refer to nowadays as galaxies but also globular clusters and planetary nebulae that are both indeed found in the Galaxy. Besides, the debate was definitely exacerbated by the fact that, until the very end of the nineteenth century, observations of nebulae were restricted to scarce hand-drawings and a handful of not-so-conclusive spectra. In 1914 and in subsequent years, spectroscopic observations of galaxies such as M31, M81, or M33 made, among other astronomers, by Vesto Melvin Slipher showed that some of the nebulae had radial and rotation velocities much greater than those of stars in the Milky Way (e.g. [Slipher 1913](#)). Actually, the velocities were so large that it was found that these objects, if they were indeed part of the Galaxy, could not be gravitationally bound. However, this did not yet prove that they were located well beyond the confines of the Milky Way. A definite proof that at least some of these objects are indeed located far away and are therefore similar to our Galaxy in terms of size and luminosity was given by Edwin Hubble for the first time in 1925 ([Hubble 1925](#)). His evidence came from the measurements of the magnitudes and periods of oscillation of 47 variable stars in M33 and 36 in M31 that he associated with Cepheid stars. A few years before, it had been shown by Henrietta Leavitt that Cepheids have a period of oscillation that correlates with their intrinsic luminosity ([Leavitt 1908](#); [Leavitt & Pickering 1912](#)). Hence, by measuring M33 and M31 Cepheids' period, Hubble could derive their intrinsic luminosity and compare it with their observed flux to determine their distance. Under the assumptions that there is no significant absorption in both galaxies, that the variable stars do belong to them, and that Cepheids are ubiquitous in the Universe he found a

distance of 285 kpc for both M33 and M31, much beyond the 5 kpc that were thought to be the radius of the Milky Way at the time (Shapley & Curtis 1921). Even with a more modern upper limit for the size of our Galaxy of roughly 45 kpc this would still mean that after Hubble’s discovery the size of the Universe had expanded by at least a factor of nine and its volume by nearly a thousand. More details about the long march from the nebulae to the galaxy world across the eighteenth, nineteenth, and early twentieth centuries and the subsequent birth of the field of extragalactic astrophysics can be found in Gordon (1969) and Longair & Giacconi (2007).

1.2.2 A quick march towards our current view of galaxies

From this moment, the field of extragalactic astrophysics really began and the discoveries that followed accelerated at an impressive rate. I will come back to some specific points in later sections but I can nevertheless give a brief account of the major steps forward that led towards our current understanding of galaxy evolution. To begin with, in parallel to resolving the great debate regarding the nature and the distances of nebulae/galaxies, Hubble had also devised a visual classification (Hubble 1926) based on observations of 400 galaxies and so apparently did Knut Lundmark the same year (Lundmark 1926). Both classifications were similar in the sense that they split galaxies in three distinct groups with ramifications for each: ellipticals, spirals, and irregulars. Examples taken from Hubble (1926) for these three classes are shown in Fig. 1.1. As discussed in Hubble’s footnote, the classification was adopted so as to be as descriptive as possible, that is to classify galaxies based on their observable morphological features rather than on a putative early understanding of galaxy evolution. Yet, from his own point of view and influenced by James Jeans’ theory, Hubble not only saw it as a classification scheme but also as a sort of evolutionary track with objects starting as elliptical systems and evolving into spirals within which the gas was thought to collapse to form stars. This view regarding the evolution of galaxies led him to emphasise the role of nebular gas in galaxies and thus influenced him in keeping to use the term “extragalactic nebulae” whereas other astronomers such as Lundmark rather recognised the importance of stars and therefore called them instead galaxies. By the 1950s the latter term had taken over and would be solely used in following publications (Smith 2009). The details of the classification and the physical properties associated to each class of galaxies are discussed further in Sect. 1.3.1. Though simple in nature, this classification has been and is still widely used nowadays, mainly for studies at low redshift (see Sect. 1.3.2 for a discussion regarding the morphology of galaxies at high redshift), and is commonly referred to as the Hubble fork diagram¹. Parallely to the development of the Hubble diagram and of the settling of the great debate, early works by Slipher had already shown that a majority of galaxies were receding from us with large velocities (Slipher 1913, 1915). Alternatively, in 1927, George Lemaître published a paper within which he used Einstein’s GR to derive the dynamics of an expanding Universe (Lemaître 1927). Using Slipher’s velocity measurements and recently published Hubble’s distances for the same galaxies he observed for the first time a correlation between distance and velocity (i.e. the further away a galaxy, the faster it recedes from us) that seemingly proved the expansion of the Universe. However, his work did not meet great international success given that the original paper was published in a Belgian journal and that Lemaître himself removed the part concerning

¹Updated classifications have been proposed since then, including for instance that of van den Bergh (1976) where lenticular galaxies form a sequence parallel to that of spirals, that of Kormendy & Bender (1996) where ellipticals are classified according to their isophotal shape, that of Kormendy & Bender (2012) that combines the two previous classifications, or that of Cappellari et al. (2011b) which takes into account the galaxy stellar kinematics.

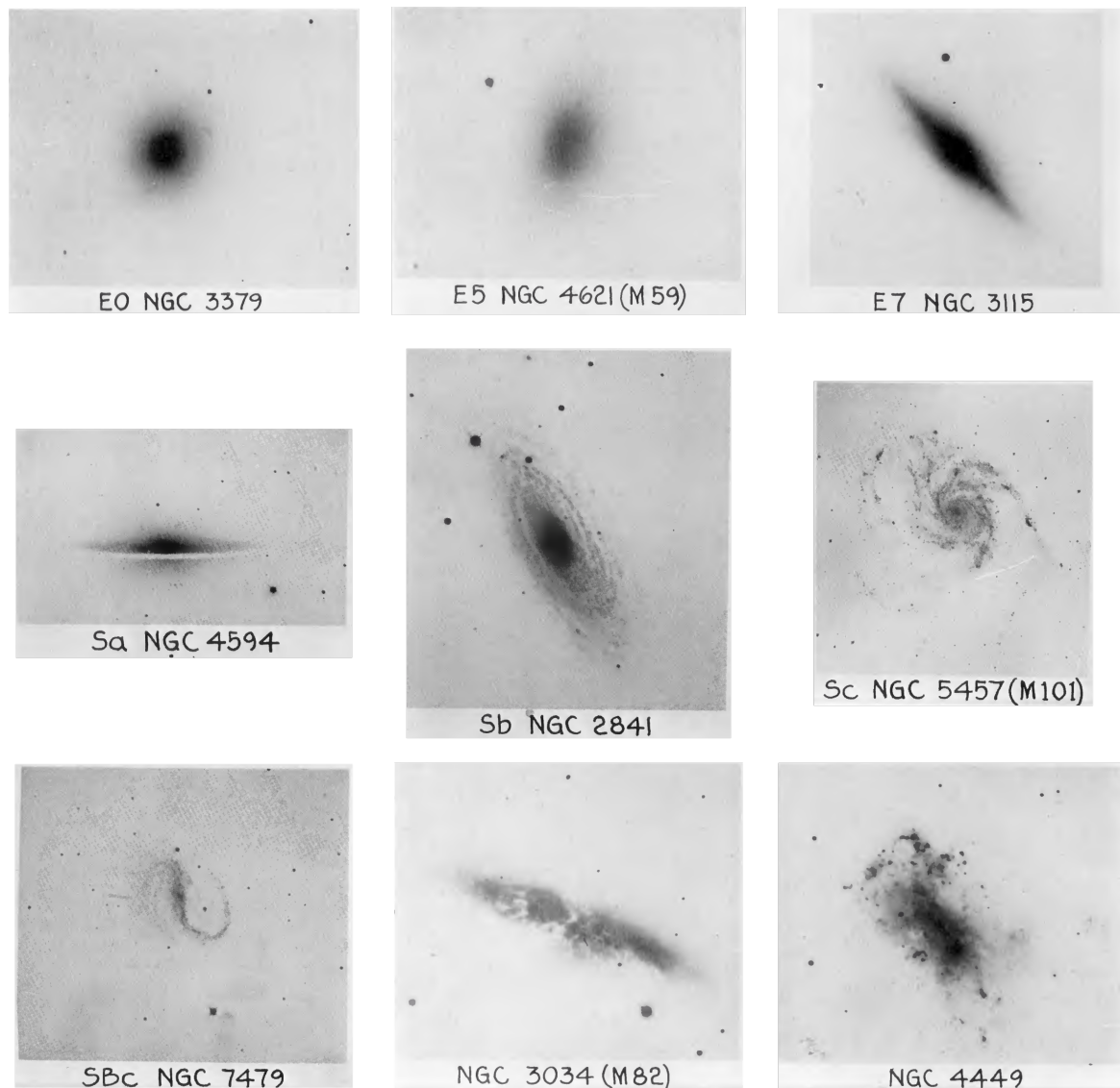


Figure 1.1: Montage illustrating various Hubble's types. Ellipticals are shown on the first line from less to more disk-like, spirals are shown on the second line from little to important spiral structure, an example of barred spiral galaxy is shown on the bottom left (NGC 7479), and two irregular galaxies are shown on the last line (NGC 3034 and NGC 4449). Images are taken from Hubble's original publication (Hubble 1926).

the observed correlation between distance and velocity in the 1931 English translation (Lemaître 1931; Livio 2011). Hence, a few years later, Hubble would publish his own analysis also using Slipher’s velocities and his own updated distance measurements (Hubble 1929) to re-discover the same correlation, now dubbed the Hubble-Lemaître law. The constant of proportionality on the other hand would retain the latter name and be labelled in the years to follow as the Hubble constant (noted H_0), that is a constant that describes the current rate of expansion of the Universe. Around the same time, studies of the spatial distribution of galaxies around the Milky Way started to be done (e.g. Shapley & Ames 1926) and showed the existence of clusters of galaxies, focussing particularly on the Virgo cluster. Then, by the 1930s astronomers started to realise that absorption by material along the LOS, especially near the Galactic plane, had to be taken into account (Trumpler 1930; Joy 1939, e.g.) and in 1933 Fritz Zwicky proposed a first argument for the existence of a large missing mass in galaxy clusters (Zwicky 1933, see also Sect. 1.4.1 for a more thorough discussion).

Quickly afterwards would the second world war (WWII) begin which, as some authors have argued (e.g. Longair 2019), has certainly played a crucial role in the developments of physics and modern astrophysics. For instance, it is in the wake of WWII and at the dawn of the Space Race that the industry of space rockets that was crucial for the birth of space-based astronomy would massively develop. In a similar fashion, the large investments made on radio techniques and on the development of infrared detectors, both primarily for the sake of war and intelligence, would later greatly benefit the fields of radio and infrared astronomy, respectively. Indeed, in the 1950s, what was then thought of as “radio stars” would be found to actually be, at least for some of them, extragalactic sources (Baade & Minkowski 1954a,b). Thus, it became obvious that to study galaxies, optical observations would not suffice but that the whole spectrum would have to be taken into account. During the same decade, Gérard de Vaucouleurs would suggest for the first time the existence of super-clusters of galaxies (de Vaucouleurs 1958) and the first radio studies of neutral gas (HI) using the 21 cm line would begin, first on the Milky Way and then on nearby galaxies (e.g. Ewen & Purcell 1951; Kerr & Hindman 1953; Raimond & Volders 1957). Later on, the 1960s saw an increased interest among the astronomical community in the active nuclei of galaxies with regards to their evolution (e.g. Markarian 1963; Ambartsumian 1968). It is during this same period that the European Southern Observatory (ESO) was founded partly to compete with American observatories that were the leading astronomical facilities of the time and partly to open up the southern sky to this field of research. It would nevertheless take another decade before first light would be achieved in Chile where the observing sites had been chosen.

Across the 1970s and 1980s, both observational and theoretical developments were made concerning the clustering of galaxies on very large scales, with evidence on both sides supporting that galaxy clusters assembled into a large scale structure (Zeldovich 1978; Einasto et al. 1980), nowadays referred to as the cosmic web. Furthermore, investigations of the optical properties of galaxies in rich clusters at $z \approx 0.3$ compared to those in the vicinity of the Milky Way showed that the former had bluer galaxies in their central parts (e.g. Butcher & Oemler 1978). Subsequent photometric and spectroscopic analyses at slightly higher redshift confirmed previous observations of what would be known as the Butcher–Oemler effect (e.g. MacLaren et al. 1988; Butcher & Oemler 1984). The explanation for this effect was that either “high” redshift galaxies located in clusters had suffered from an enhancement of star-formation at $z \approx 0.3 - 0.4$ (MacLaren et al. 1988) or that local galaxies had seen their star formation quenched with respect to those located in the field at the same redshift (Butcher & Oemler 1984). Hence, these observations shed the first lights on the importance of the impact of the environment on the

evolution of galaxies. Perhaps even more importantly, the 1970s saw a number of kinematics studies using neutral (HI) and ionised ($H\alpha$) gas of nearby galaxies that showed that they have flat rotation curves up to large distances (e.g. Rogstad & Shostak 1972; Roberts & Rots 1973; Bosma 1978, 1981a,b; Rubin et al. 1978a,b, 1980), hence suggesting that there might be a DM component in galaxies similarly to galaxy clusters. By the end of the 1970s, the Canada-France-Hawaii Telescope (CFHT) was also inaugurated at Mauna Kea in Hawaii which allowed for observations with very good seeing conditions. It is with the help of this telescope that the first serendipitous detection of a gravitational arc in the Abell cluster A370 would be done (Soucail et al. 1987; Soucail 1987). During the same period, Tully et al. (1975) discovered a correlation between galaxy luminosity and spectral line width, a proxy for the rotation velocity, that would later be known as the Tully-Fisher relation (TFR). A similar relation would also be found for elliptical galaxies, but with the velocity dispersion instead of the rotation velocity, approximately at the same time (Faber & Jackson 1976), now referred to as the Faber-Jackson relation. It is also during this decade that another important scaling relation, the mass-metallicity relation (MZR), would be found (e.g. Lequeux et al. 1979; Skillman et al. 1989) which further showed the importance of feedback processes on the evolution of galaxies, as already discussed a few years back in theoretical papers (e.g. Larson 1974; White & Rees 1978a).

During the 1990s, efforts were made into observing high-redshift galaxies to constrain their evolution. Early deep photometric and/or spectroscopic ground-based surveys (Broadhurst et al. 1988; Cowie et al. 1991, e.g.) were mostly limited to intermediate redshifts ($z \approx 0.3 - 0.4$, roughly 5 Gyr of galaxy evolution) but a leading observing method at the time was to use background quasi-stellar objects (QSOs) to observe foreground galaxies through the absorption of their neutral gas (e.g. Steidel & Hamilton 1993; Pettini et al. 1994). At the same period was launched the Hubble Space Telescope (HST), the first large space telescope with a primary mirror of 2.4 m built in collaboration between the National Aeronautics and Space Administration (NASA) and the European Space Agency (ESA). Early HST observations (e.g. Dressler et al. 1994b,a; Dickinson 1995) showed that even with low integration times it was possible to get deep images unveiling a large number of galaxies. Furthermore, these initial studies highlighted that by $z \sim 1$ the galaxies in clusters could still be classified between spirals and ellipticals, as in the local Universe. However, they also noted that there was a significant fraction of irregular and seemingly interacting galaxies. In parallel, using the ultraviolet (UV) filters aboard the HST, Giavalisco et al. (1995) managed to observe a Ly α -emitting galaxy at $z = 3.4$, proving that it was possible to resolve high-redshift galaxies with HST. The complex picture regarding the high-redshift Universe that emerged from the aforementioned early analyses incited the telescope's committee to perform a deep observation of a single field devoid of any already detected bright objects or low-redshift galaxy clusters for ten consecutive days (Williams et al. 1996). This field that would profoundly affect extragalactic astrophysics is most famously known as the Hubble Deep Field (HDF).

1.2.3 Last steps towards modern extragalactic astrophysics

Following the release of the HDF and subsequent observations such as the Hubble Ultra Deep Field (HUDF), further major breakthroughs in our understanding of galaxy evolution were made. As for the previous section, I cannot cite them all but I can give a flavour of what we have learned since the early 2000s. To begin with, by mid-2000s multi-wavelength photometric and spectroscopic observations combined with various Star Formation Rate (SFR) estimates and Spectral Energy Distribution (SED) models suggested that there is a tight correlation between

stellar mass and SFR (e.g. [Noeske et al. 2007](#); [Elbaz et al. 2007](#); [Daddi et al. 2007](#)). This relation is now referred to as the star-forming Main Sequence (MS) and, as discussed in more details in [Sect. 1.3](#), it is still extensively studied in the literature (e.g. [Whitaker et al. 2014](#); [Boogaard et al. 2018](#); [Mercier et al. 2022](#)). To explain these new scaling relations and older ones such as the MZR that hold at both low and high redshift, the “bathtub model” ([Bouché et al. 2010](#); [Lilly et al. 2013](#)) was developed in which stellar mass growth and star formation are induced by a continuous accretion of gas and regulated by feedback processes at the same time. Variations of this model exist between authors concerning the importance of different feedback processes and how to implement the effect of the environment but it has nevertheless shown how simple regulation mechanisms can produce such scaling relations. The early 2000s also saw an increased interest in supermassive black-holes as a possible early feedback process for high-redshift galaxies (e.g. [Silk & Rees 1998](#); [Di Matteo et al. 2005](#)) and to explain the observed black hole mass-velocity dispersion relation (e.g. [Ferrarese & Merritt 2000](#); [Tremaine et al. 2002](#)). Roughly ten years after the HST became operational two additional space-based American telescopes were launched, the first observing in the infrared (IR) and named SPITZER and the second in the UV and named Galaxy Evolution Explorer (GALEX). Combined with HST, these three telescopes greatly increased our understanding of the star formation history of galaxies across cosmic time (e.g. [Calzetti et al. 2007](#)). In particular, these new data allowed to confirm early results (e.g. [Lilly et al. 1996](#); [Madau et al. 1996](#)) that the comoving SFR density is larger at higher redshift up to a turnover point around $z \sim 2$ beyond which it decreases again (e.g. [Hopkins 2004](#); [Hopkins & Beacom 2006](#)). The advent of large ground- and space-based photometric surveys also allowed the study of the morphological evolution of galaxies. During the 2000s it was found that galaxies’ stellar mass correlates with their size but, according to later studies (e.g. [Trujillo & Aguerrí 2004](#); [Trujillo et al. 2006](#); [van der Wel et al. 2014b](#)), that the zero point of the relation strongly evolves with redshift. Combined with statistical modellings of the projected shape of galaxies on the plane of the sky (e.g. [van der Wel et al. 2014a](#); [Zhang et al. 2019](#)), these observations clearly showed that the morphology of galaxies has substantially changed with cosmic time and that high-redshift galaxies do not settle as easily on the Hubble diagram as local galaxies do.

The twenty-first century also saw a tremendous increase in kinematics studies of galaxies across cosmic time. Prior to this era, these were fairly limited to relatively small samples of low-redshift galaxies almost exclusively observed with long-slit spectroscopy since 3D spectroscopy was only in its infancy (see [Sect. 2.2.1](#) for a discussion on the topic). Nevertheless, by the end of the 1990s first “high” redshift kinematics observations were made (e.g. [Vogt et al. 1996](#); [Simard & Pritchett 1998](#)) that showed that (i) rotating disks are already present at $z \sim 1$, (ii) there is a TFR at these redshifts similar to the local Universe, though with more scatter, and (iii) that there is a significant (around 30%) fraction of galaxies that are kinematically disturbed (at least their gas component). The following decades saw the development of Very Large Telescopes (VLTs) to which were associated Multi-Object Spectrographs (MOS) and 3D spectroscopes that either allowed to observe large sample of galaxies with multi-slit spectroscopy or smaller samples of galaxies with spatially resolved (i.e. 2D) kinematics. The first relatively large surveys that came out of these instruments confirmed early arguments regarding the presence of rotating and kinematically disturbed gas disks in high-redshift galaxies (e.g. [Förster Schreiber et al. 2006b](#), [2009a](#); [Law et al. 2009](#); [Contini et al. 2012](#); [Epinat et al. 2012](#); [Contini et al. 2016](#)). In particular, the presence of a large proportion of dispersion-dominated objects triggered interesting discussions on whether the large dispersion values were intrinsic or instrumental-driven (e.g. [Shapiro et al. 2008](#); [Puech et al. 2007, 2008a](#); [Newman et al. 2013](#)). These observations also led to

the discussion of whether the TFR evolved with cosmic time (e.g. Puech et al. 2008a; Vergani et al. 2012; Contini et al. 2016), but no clear trend could be found. The ubiquity of high velocity dispersions and morphologically disturbed galaxies at high redshift also raised the question of whether galaxy mergers were more common in the early Universe. Kinematics studies clearly helped in showing that the merger fraction was higher at higher redshift up to a turnover point at $z \sim 3$ (e.g. Puech et al. 2012; López-Sanjuan et al. 2013a; Ventou et al. 2017, 2019).

Our modern picture of extragalactic astrophysics and of the formation and evolution of galaxies would not have reached its current state without the quick development of cosmological and zoom-in simulations. Early simulations that integrated baryonic components were first developed during the 1990s (e.g. White & Frenk 1991; Katz et al. 1992; Kauffmann et al. 1993), though they were either limited to rather small volumes or required the use of semi-analytical models. These were much further developed across the 2000s and 2010s so that they have now become key tools to understand the evolution of galaxies. For instance, we can cite ILLUSTRIS and its follow-up project The Next Generation Illustris Simulations (ILLUSTRISTNG) (Vogelsberger et al. 2014; Springel et al. 2018) that are hydrodynamical simulations, MILLENIUM (Springel et al. 2005) which is the first semi-analytical simulation from the Virgo consortium that was followed by their second hydrodynamical simulation Evolution and Assembly of GaLaxies and their Environments (EAGLE) (Schaye et al. 2015; Crain et al. 2015), or the Feedback In Realistic Environments (FIRE) simulation (Hopkins et al. 2014) that has been designed to resolve the interstellar medium (ISM) and star formation. These simulations have shown or confirmed, among many other things, the importance of DM haloes for galaxies build-up, the importance of gas inflows from the cosmic web to fuel star formation on Gyr timescales, or that multiple feedback processes are required (e.g. active galactic nucleus - AGN, radiative, supernovae, etc.) to recover the observed scaling relations at both low and high redshift.

1.3 Galaxy evolution across cosmic time

In this section, I briefly discuss the properties of galaxies at low (Sect. 1.3.1) and high (Sect. 1.3.2) redshift. Some parts will be reminiscent of Sect. 1.2 but the objective of this section is different. In Sect. 1.2, I tried to give an historical perspective on the evolution of the field of extragalactic astrophysics and how quickly our understanding of galaxy evolution has changed in a relatively short amount of time. On the other hand, in this section I will rather give a broad depiction of our current view of galaxies and how this is linked to their evolution across cosmic time.

1.3.1 Properties of local galaxies

As already quickly discussed in Sect. 1.2.2, galaxies in the local Universe are usually classified, mostly for historical reasons, using an updated version of the Hubble diagram. Nevertheless, this classification scheme is far from perfect, for instance because it does not include irregular, peculiar, and dwarf galaxies, or because the classification of ellipticals is not physical but rather mostly depends on the galaxies' inclination on the plane of the sky (e.g. van den Bergh 1976). Hence, other classifications have been suggested in the meantime in terms of morphology (e.g. de Vaucouleurs 1974; van den Bergh 1976; Kormendy & Bender 1996, 2012) or kinematics (e.g. Cappellari et al. 2011a,b). Still, for simplicity only the Hubble diagram will be considered in what follows. The two main classes that populate this diagram are elliptical and spiral galaxies that are also usually called, for historical reasons as well, early-type and late-type galaxies, respectively.

As mentioned, other types of galaxies exist, though they are less common at low redshift. For instance, we can cite irregular galaxies that cannot be associated to neither elliptical nor spiral galaxies, peculiar galaxies that typically include merging galaxies or in interaction, dwarf galaxies that can resemble ellipticals, spirals, or irregulars but that are smaller, less massive and less bright, or low-surface brightness galaxies that are equivalent to the ellipticals and spirals but with an overall low surface brightness that renders their detection difficult. Even though this classification was initially built on morphological (and magnitude) criteria, there are actually key physical differences between the various classes that hint at the fact that these populations either have not followed the same evolutionary track or that they are not at the same stage of their evolution.

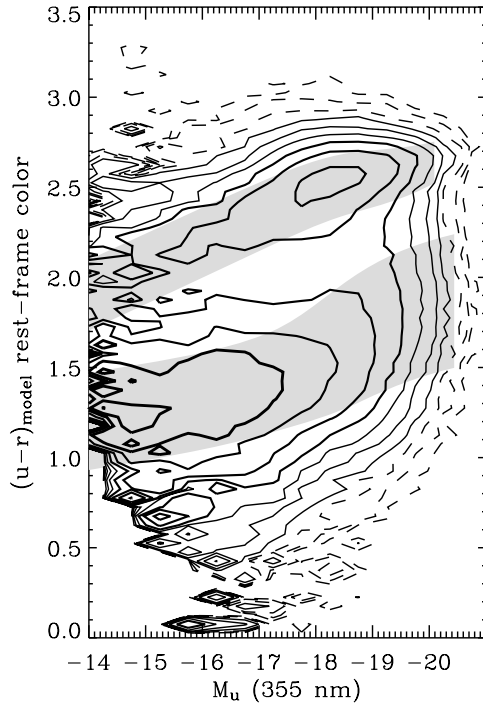


Figure 1.2: Example of a colour-magnitude diagram adapted from [Baldry et al. \(2006\)](#) that shows the colour bimodality observed in the local Universe. The vertical axis shows the u-band minus r-band rest-frame galaxy colour and the horizontal axis shows the absolute magnitude in the u-band. Hence, redder galaxies are found on the top of the plot and brighter galaxies on the right. The blue sequence is visible on the lower left part of the plot around a colour of roughly 1.2 mag (hence bluer and fainter) and the red sequence on the top right part of the plot around a colour of roughly 2.5 mag (redder and brighter). Galaxies located between the two sequences are said to belong to the green valley.

To begin with, let us consider ellipticals and spirals since they form the bulk of galaxies in the local Universe. Elliptical galaxies are characterised by a smooth surface brightness distribution that is typically described by a de Vaucouleurs profile ([de Vaucouleurs 1948](#)). These galaxies mainly contain old and metal-rich stars with little cold gas and thus little to no star-formation at all which therefore render their colour quite red compared to spiral galaxies. Their smooth surface brightness can easily be fitted with elliptical isophotes, hence their name. Even though these galaxies have a very low amount of cold gas, it was nevertheless found that they possess a significant fraction of hot gas that emits in the X-rays (e.g. [Roberts et al. 1991](#)). From a kinematics point-of-view, elliptical galaxies are found to have little but non-zero rotation (e.g. [Cappellari et al. 2007](#); [Emsellem et al. 2007](#)) and exhibit strong correlations between (i) their stellar velocity dispersion and luminosity or stellar mass, known as the Faber-Jackson relation, and (ii) their stellar velocity dispersion and size. Both relations were found to actually be projections of a more fundamental relation dubbed the fundamental plane ([Djorgovski & Davis 1987](#)). On the other hand, spiral galaxies are thin disk-like structures with usually a small but

non-zero thickness. They tend to have more inner structure than ellipticals since they exhibit spiral arms and tend to have a bar and a bulge in their inner parts. Galaxies that have the structure of a disk but the smooth surface brightness distribution of ellipticals are called lenticular galaxies. The bulge component is a key characteristic that most spirals, though not all, have. Contrary to the disk and in particular to the spiral arms that are dominated by massive blue young stars, the bulge is made of a larger variety of stars, including old ones. Additionally, spiral galaxies have a large fraction of cold gas either under its molecular phase (H_2), mainly located in the arms and in star-forming regions, or under its atomic phase (HI) which is much more extended than the stellar disk. Combined with the prevalence of massive young stars that produce ionising photons, these facts make spiral galaxies much more star-forming than ellipticals. The kinematics of spiral galaxies is typically that of a rotating disk. Contrary to what would be expected, the rotation curves of disk galaxies are ubiquitously found to be flat at large radii, as shown by early investigations of rotation curves derived from $H\alpha$ and HI observations (e.g. Rogstad & Shostak 1972; Roberts & Rots 1973; Rubin et al. 1978a; Bosma 1978, 1981a,b). As already discussed, these observations were interpreted as the fact that spiral galaxies must contain massive DM haloes that dominate the stellar and gas dynamics at large distances. One of their most important kinematics scaling relations is the TFR that was initially discovered as a correlation between the luminosity of a galaxy and its rotation velocity (either derived from the stars or the gas) at large distances (a proxy for the DM halo mass, Tully et al. 1975). Later on, it was found that this relation also holds when using stellar masses instead of luminosities. Spiral and elliptical galaxies also obey additional scaling relations (e.g. size-mass or mass-metallicity) and in particular one that is linked to their evolution: the mass-SFR relation (e.g. Noeske et al. 2007; Elbaz et al. 2007; Daddi et al. 2007). Indeed, star-forming galaxies, hence mostly spirals, tend to follow a scaling law in the stellar mass-SFR plane called the MS. Instead, ellipticals mostly populate a red sequence below this sequence. This separation in two populations in the mass-SFR diagram is also seen in colour histograms and colour-magnitude diagrams as shown in Fig. 1.2. In the local Universe, bright galaxies, hence mostly ellipticals, dominate the luminosity and mass budgets (e.g. Schechter 1976) but, in terms of numbers, most of the galaxies are actually low-mass objects. Furthermore, it was found with recent large spectroscopic surveys, in particular that of the Sloan Digital Sky Survey (SDSS), that there is a clear correlation between the galaxies' stellar mass and their gas-phase metallicity (e.g. Tremonti et al. 2004) consistent with galactic winds impacting more importantly low-mass galaxies that have shallower gravitational potentials.

Other types of galaxies also exist in the local Universe. For instance, in the mass-SFR diagram discussed above, starburst galaxies are found to lie above the MS. These galaxies usually have blue spectra that are indicative of the presence of massive hot stars and high star-formation, thought to be mainly produced by recent mergers between gas-rich progenitors. Another type of galaxies that has become more and more studied in recent years because of their dynamical properties are dwarf galaxies. Historically speaking, dwarfs were just low-luminosity, and therefore low-mass, counterparts of ellipticals, spirals, and irregulars (e.g. Baade 1944; Sandage & Binggeli 1984). However, they are interesting in various aspects. First, the fact that such low-mass objects still exist in the local Universe means that they must have had a relatively moderate mass assembly which must be taken into account when constraining the physical processes at the origin of the mass build-up of the whole galaxy population. Second, these systems do not always scale along the same scaling laws as their more massive counterparts. For instance, one of the historical reasons why dwarfs were considered as a separate class was that the more massive they become, the higher their surface brightness, which is the exact opposite

behaviour of more massive elliptical and spiral galaxies (e.g. [Kormendy 1985](#)). Lastly, dwarfs form a population of DM-dominated objects which make them perfect candidates to study the properties and the distribution of DM (e.g. [Gilmore et al. 2007](#)).

1.3.2 Galaxies in the distant Universe

It was found quite early that galaxies at high-redshift are different from their local counterparts in many aspects. To begin with, the Hubble classification between spirals and ellipticals becomes more difficult to use in the distant Universe. The reason is certainly a combination of the facts that (i) we are probing galaxies at an earlier phase of their evolution before they settled along the Hubble sequence and (ii) high-redshift galaxies are also smaller and fainter because of cosmology, hence sub-structures such as spiral arms are more difficult to detect for these objects. Indeed, it is now clear that galaxies have significantly evolved across cosmic time. For instance, as already discussed in Sect. 1.2.3, the morphology of galaxies has greatly changed from high to low redshift with a larger fraction of morphologically disturbed objects found at high redshift (e.g. [Brinchmann et al. 1998](#)), with disks that tend to be much thicker for high-mass galaxies, and with galaxies that have prolate rather than oblate (i.e. elongated rather than flattened along the axis of symmetry) shapes at low stellar mass (e.g. [van der Wel et al. 2014a](#); [Zhang et al. 2019](#)). In addition, studies of the evolution of the comoving SFR density across cosmic time have shown that galaxies have experienced an increase in star formation activity up to a peak around $z \sim 2 - 3$ and then a reduction to the current value measured at $z = 0$ (e.g. [Madau & Dickinson 2014](#); [Gruppioni et al. 2020](#)). The question of what caused this peak or rather why the SFR density was reduced after that turnover point is still open. Given that the SFR is linked to the amount of cold gas located in galaxies but also to the efficiency to convert this gas into new stars, different mechanisms have been suggested. For instance, feedback processes (e.g. AGN, stellar winds, etc.) might have removed a fraction of the gas, thus reducing, potentially momentarily if the gas is then re-accreted, the star formation activity. Other mechanisms rather linked to the environment of galaxies have also been proposed such as ram-pressure stripping, thermal evaporation, or galaxy harassment ([Gunn & Gott 1972](#); [Cowie & Songaila 1977](#), see Sect. 1.3.3). Beside the evolution of their SFR, galaxies have also changed in terms of mass and size and that differently if they are star-forming or quiescent. Indeed, the stellar mass function of star-forming galaxies has mainly increased for its low-mass end whereas that of quiescent galaxies has increased across the entire mass range (e.g. [Ilbert et al. 2010](#); [Muzzin et al. 2013](#)). These two populations are necessarily linked to each other since star-forming galaxies will populate the quiescent population once quenched. Such results are also consistent with recent studies of the evolution of the merger fraction with cosmic time using close pair counts (e.g. [López-Sanjuan et al. 2013a](#); [Tasca et al. 2014](#); [Ventou et al. 2017](#)) and simulations (e.g. [Puech et al. 2012](#); [Snyder et al. 2017](#); [Ventou et al. 2019](#)) that show that the merger fraction increases to nearly 20% (compared to a few percent at $z = 0$) with redshift up to $z \approx 3$ and slowly decreases beyond. Furthermore, both populations of galaxies have also increased in size across cosmic time, with quiescent galaxies showing a steeper increase with redshift (e.g. [van der Wel et al. 2014a](#)). These two evolutions (stellar mass and size) can also be seen as the result of the fact that galaxies at high redshift follow a similar size-mass relation as those at low redshift, hence that an increase in stellar mass seems to produce an increase in size. The stellar mass evolution can also be linked to that of the SFR through the mass-SFR relation, with high-redshift star-forming galaxies also found to be located along a MS. In order for the MS to have survived across billion years timescales, it means

that the physical processes that produce it in the local Universe must have already played an important role at earlier cosmic times. However, because star-formation was higher in the past we see an evolution of the zero-point of the relation with redshift (e.g. [Speagle et al. 2014](#)) that holds at low stellar masses (e.g. [Whitaker et al. 2014](#); [Boogaard et al. 2018](#)). Linked to the size, mass, and SFR evolutions with redshift, there is also a visible gas-phase metallicity evolution. Even though measuring precisely the metallicity at high redshift is not simple, large samples at $z \sim 2$ have been assembled that show that galaxies in the distant Universe had a lower metallicity than in the local Universe (e.g. [Erb et al. 2006](#); [Wuyts et al. 2014, 2016](#)). Furthermore, high redshift estimates of the cold gas fraction (both under atomic and molecular phase, e.g. see [Tacconi et al. 2020](#); [Walter et al. 2020](#)) have also shown that distant galaxies were much more cold gas-rich than at the current epoch (by a factor of roughly two in HI and five in H₂ between $z = 0$ and $z \approx 2$).

Galaxies have also evolved dynamically throughout cosmic time. In the local Universe, galaxy disks that are dynamically supported by their own rotation are ubiquitous but at higher redshift the picture becomes more complex. As discussed quickly in Sect. 1.3.1, a first striking feature of the observed velocity fields of a non-negligible fraction of intermediate and high redshift galaxies is their lack of rotation in their gas component (e.g. [Förster Schreiber et al. 2006b, 2009a](#); [Epinat et al. 2009](#); [Law et al. 2009](#); [Contini et al. 2012](#); [Epinat et al. 2012](#); [Contini et al. 2016](#)). This has led to substantial dynamical classifications between rotationally supported, dispersion dominated, and kinematically disturbed galaxies using the ionised gas as kinematics tracer (e.g. [Flores et al. 2006](#); [Yang et al. 2008](#); [Epinat et al. 2009](#); [Contini et al. 2016](#)). The proportion of galaxies between the three classes is roughly one third each, though the exact numbers depend on the selection function of the survey and the criteria used for the classification. At the same time, this also means that at $z \gtrsim 2$ a significant fraction of galaxies are already rotationally supported disk systems, which implies that their dynamical assembly and relaxation must have happened quickly (at most roughly 3 Gyr at $z \gtrsim 2$). Besides, there is no strong evidence that the TFR zero-point for rotationally supported galaxies evolves with cosmic time. Hence, because the rotation velocity is tightly linked to the galaxies' gravitational potential, this shows that there must have been a strong interplay between the distribution of DM and the baryons as the galaxies accreted cold gas.

Based on current evidence (see below) and on our understanding of galaxy formation and evolution, we would expect high-redshift galaxies to be less massive and more gas-rich than in the local Universe (hence the DM fraction should be either equal to or higher than that at $z = 0$), but also not yet dynamically relaxed given that the higher gas fractions seen at high redshift should produce larger velocity dispersion values as well. Such an effect on the dispersion has indeed been observed (e.g. [Stott et al. 2016](#)) but it has also raised the question of whether the measured velocity dispersions are overestimated or not, that is whether instrumental effects (beam smearing, for more details see Sect. 5.3) whose impact is expected to be stronger at higher redshift where the spatial resolution is lower are correctly taken into account or not (e.g. [Epinat et al. 2010, 2012](#); [Di Teodoro & Fraternali 2015](#); [Bouché et al. 2015](#)). Similarly, the question of the evolution of the DM fraction with redshift is still open. Recent observations do suggest that high-redshift galaxies require a DM component when modelling their gas kinematics (e.g. [Lang et al. 2017](#); [Genzel et al. 2017, 2020](#); [Tiley et al. 2019b](#); [Bouché et al. 2022](#); [Sharma et al. 2021](#); [Price et al. 2021](#)), but some have nevertheless highlighted that they might have lower DM fractions than in the local Universe (e.g. [Lang et al. 2017](#); [Genzel et al. 2017, 2020](#); [Sharma et al. 2021](#); [Price et al. 2021](#); [Sharma et al. 2021](#)). This observed decrease in DM fraction seems to be inversely correlated with the density of the stellar disk and the mass of the bulge component (e.g. see [Genzel et al. 2020](#)). A few different explanations can be given. First, some authors, such as [Tiley et al. \(2019b\)](#), have suggested that

the observed trend might be a spurious effect induced by the stacking technique that makes the average rotation curve appear to fall, hence giving the impression that high-redshift galaxies are depleted in DM with respect to their low-redshift counterparts. A second important explanation is related to the radius where the DM fraction is estimated. Indeed, the aforementioned studies usually use the ionised or molecular gas components to probe the kinematics but neither are found in the outer parts of the galaxies. In practice, this means that the DM fraction is typically estimated around the half-light radius of the stellar disk component of the galaxies. On the contrary, the bulk of the mass of the DM halo is expected to be distributed at much larger distances (e.g. Courteau & Dutton 2015). Furthermore, galaxies are also expected to build-up their stellar mass with cosmic time and therefore to grow in size, meaning that the DM fraction of high-redshift galaxies will be estimated closer to the centre (where the mass of the DM halo is negligible) than their low-redshift counterparts. Hence, we can imagine a scenario where a galaxy builds up its stellar mass with cosmic time while retaining the mass and shape of its DM halo. In this scenario, the DM fraction estimated at the virial radius of the halo will be high at high redshift since little stellar mass will have had enough time to build up. However, it will decrease with cosmic time since only the stellar mass will increase with decreasing redshift. On the other hand, if the DM fraction is estimated at the stellar half-light radius of the galaxy, its value will be initially relatively low as it will be estimated close to the centre where little DM mass is found while most of the stellar mass will be concentrated. But, as the galaxy builds up its stellar mass, its half-light radius will increase so that the DM fraction will be evaluated further out where the bulk of the DM mass is located, hence increasing the measured DM fraction. Therefore, lower DM fractions observed at high redshift with respect to local galaxies such as reported for instance in Lang et al. (2017), Genzel et al. (2017, 2020), Sharma et al. (2021), or Price et al. (2021) are not necessarily inconsistent with the current model of galaxy formation and evolution as long as the radius where the DM fraction is estimated is properly taken into account (for a discussion on the topic, see also Sect. 4.4 of Förster Schreiber & Wuyts 2020).

1.3.3 Impact of galaxies’s environment

As discussed in Sect. 1.3.2, galaxies follow their own secular evolution driven by the accretion of cold gas that is transformed into new stars and regulated by feedback processes. This picture combined with more violent events such as galaxy mergers is supposed to drive their evolution over long timescales in terms of physical properties (e.g. stellar mass, metallicity, SFR, etc.), morphology (build-up of the Hubble sequence with the formation of disks and ellipticals), and kinematics (increase in the fraction of rotationally supported disk systems with large amounts of DM). Nevertheless, the secular evolution of galaxies is not sufficient in itself to explain their observed properties. Indeed, it has now become clear that a major component of galaxy evolution is the impact of their host environment at both low and high redshift. Studies that discuss the effect of the environment focus on four main types: (i) galaxy clusters that are the most massive virialised structures in the Universe (e.g. Muzzin et al. 2009; Balogh et al. 2017), (ii) galaxy groups (e.g. More et al. 2012; Abril-Melgarejo et al. 2021; Mercier et al. 2022), an intermediate type of structure that is smaller than galaxy clusters and that can either be isolated or a substructure of clusters, (iii) the cosmic web that is made of galaxy clusters and groups but also of filaments linking the clusters together (e.g. Umehata et al. 2019; Bacon et al. 2021; Daddi et al. 2021), and (iv) the field, that is the remaining space where there is no detected structures. Ideally, field galaxies would be located in low-density regions called cosmic voids, but in practice

it depends upon how the classification between field, groups, clusters, or filaments, was done. Among the four types of environment, the cosmic web is the most difficult of all to observe because of its low surface-brightness emission (e.g. Bacon et al. 2021) and was therefore until recently mostly a prediction from cosmological simulations without clear observational counterparts (e.g. Haider et al. 2016; Galárraga-Espinosa et al. 2020), except from the large-scale distribution of galaxies in large spectroscopic surveys such as the SDSS (e.g. Chen et al. 2015; Krolewski et al. 2019; Darragh Ford et al. 2019; Sarron et al. 2019). Throughout recent years, efforts have also been pushed into observing and characterising the properties of the progenitors of low redshift galaxy clusters, called proto-clusters, before they virialised (e.g. Darvish et al. 2020; Champagne et al. 2021).

As discussed further below, based on observational and theoretical arguments, it has been discussed that galaxy clusters could play an important role in quenching star formation and morphologically transforming galaxies. The two main channels through which a galaxy is likely to be affected by the galaxy cluster it is infalling into are (i) through hydrodynamical mechanisms between the relatively cold gas found in the ISM and in the circum-galactic medium (CGM) of the galaxy and the much hotter intra-cluster medium (ICM) and (ii) through gravitational interactions with one or multiple galaxies already located or infalling into the cluster, or directly with the cluster’s gravitational potential (for a review on the topic, see Cortese et al. 2021). The former mechanisms have been proposed to offer pathways through which galaxies can suffer from starvation (also called strangulation), that is the cessation of cold gas accretion from the CGM, which is a prerequisite to quench star formation. The typical physical mechanisms that have been suggested are (i) ram-pressure stripping (Gunn & Gott 1972) which removes the gas located in galaxies because of the pressure exerted by the ICM. Its effect is more efficient for low-mass galaxies, denser structures (i.e. for clusters more than groups), and in the outer parts of galaxies. And (ii) thermal evaporation (Cowie & Songaila 1977) where the cold gas found in a galaxy is heated by the hot ICM which allows it to evaporate and fill the CGM. Such hydrodynamical mechanisms have been predominantly observed in the local Universe (e.g. Boselli et al. 2006; Boissier et al. 2012; Longobardi et al. 2020), though there has been quite recently a first serendipitous discovery at $z \sim 0.7$ in the MUSE-gAlaxy Groups In Cosmos (MAGIC) survey (Boselli et al. 2019), and they are thought to be the driving mechanisms behind the formation of the so-called jellyfish galaxies (e.g. Mercer et al. 2007; Smith et al. 2010; Ebeling et al. 2014; McPartland et al. 2016; Poggianti et al. 2017). On the other hand, gravitational interactions can be summarised into the so-called galaxy harassment effect which is the combined effect of tidal gravitational interactions between an infalling galaxy, the cluster, and the other galaxies found therein across multiple fly-bys. Gravitational mechanisms are important, in particular to account for the morphological transition seen in clusters and to explain the higher fraction of irregular galaxies found in these structures. Note that the aforementioned mechanisms can also affect galaxies in groups. However, some of these mechanisms that can be predominant in galaxy clusters (e.g. ram-pressure stripping) can become marginal in groups because of the groups’ lower gas density and/or shallower gravitational potential. This might be different in proto-clusters where, according to current simulations (e.g. Chiang et al. 2017), galaxy groups are expected to affect the properties (e.g. SFR) of their galaxy members before the clusters formed (i.e. pre-processing; see for instance Fujita 2004).

Multiple studies have tried to detect a visible impact of the environment on galaxies’ physical properties in order to discriminate between different underlying mechanisms. For instance, the stellar mass function (SMF) has been compared between galaxies located in clusters and galaxies

found in the field. Such studies at both low and high redshift have highlighted from the shape of the galaxy stellar mass function that galaxy clusters contain an excess of massive galaxies and tend to be depleted in low-mass galaxies (e.g. Peng et al. 2010; van der Burg et al. 2020) compared to field galaxies at the same redshift. At the same time, galaxies in clusters have on average systematically lower SFR values at fixed stellar mass (e.g. Calvi et al. 2018; Old et al. 2020b,a; Mercier et al. 2022) and nearly all massive galaxies found in the inner parts of galaxy clusters are quenched. These facts have therefore raised the question of whether quenching is environmentally or stellar mass driven in clusters. In the local Universe, it has been shown (e.g. Peng et al. 2010) that the stellar mass is the driving mechanism for massive galaxies but that environmental quenching becomes more important for low-mass galaxies. Still, there is a significant population of star-forming galaxies in clusters and in groups and some of the quenched galaxies are not located far below the MS. Therefore, this suggests that, if the environment does help in quenching star formation, it must have happened on relatively short timescales (e.g. Muzzin et al. 2012; Mercier et al. 2022). Similarly, recent intermediate redshift studies such as McNab et al. (2021) or Baxter et al. (2022) have shown that massive galaxies at $z \sim 1$ were certainly quenched prior to their infall into the cluster and that it was also the case for lower-mass galaxies, though they also suffered from additional quenching by their cluster during their infall. Furthermore, higher redshift studies ($z \sim 3$) such as those of Sarron & Conselice (2021) and Lemaux et al. (2022) have rather found that the fraction of quenched galaxies in groups and clusters decreases with increasing redshift and that the global SFR of these galaxies at fixed stellar mass increases with increasing redshift. These last contradictory results can be reconciled with what is observed in the local Universe by remarking that most high-redshift clusters are not virialised yet. Hence, these studies show that the environment seems to mostly affect the evolution of galaxies prior to the virialisation of the structures, that is through pre-processing in high-redshift groups that will assemble into the clusters seen at low redshift.

Finally, galaxy clusters and galaxy groups might also affect the dynamics of galaxies but the evidence is rather scarce for the moment. From a theoretical perspective, there have been some claims that gravitational interactions between galaxies in the outskirts of clusters might strip them of a significant fraction of their stellar content and produce DM dominated dwarfs that are observed in the local Universe (D’Onghia et al. 2009). If there is a significant fraction of irregular galaxies found in clusters, then we may expect to find imprints in their gas and stellar kinematics either by increasing the velocity dispersion or by producing out-of-equilibrium motions with respect to the bulk rotation of the galaxy. As already discussed before, it is true that samples of galaxies at higher redshift have a larger fraction of objects with large velocity dispersion or no clear signs of rotation in their gas kinematics (kinematically disturbed objects, e.g. Förster Schreiber et al. 2006b, 2009a; Epinat et al. 2009; Law et al. 2009; Contini et al. 2012; Epinat et al. 2012; Contini et al. 2016). However, it is less clear whether this is due to the galaxies still being in a transitional dynamical state, or whether this is due to merger events that happened recently in their past, or whether the galaxies’ environment plays a significant role through the aforementioned physical mechanisms associated to galaxy clusters and galaxy groups (e.g. Mendes de Oliveira et al. 1998; Epinat et al. 2009; Feng et al. 2020). Large surveys specifically designed to target galaxies in the field, in groups, and in clusters at intermediate and/or high redshift and with resolved kinematics information, such as the MAGIC survey (Epinat et al., see also Chapter 3), will certainly help to answer such questions. Ordered rotation in galaxies might also be affected by their environment, for instance through the removal of their gas or stellar content (ram-pressure stripping, gas evaporation, etc.; for a review on the topic see Cortese et al. 2021),

by suppressing feedback processes (and therefore affecting the shape of DM haloes in their inner parts, e.g. [Freundlich et al. 2020](#)), or by changing the distribution of baryons (e.g. asymmetric features or contraction of the distribution, [Maltby et al. 2010](#); [Kuchner et al. 2017](#); [Matharu et al. 2019](#); [Mercier et al. 2022](#)). An ideal scaling relation to investigate this effect is the TFR since it links the stellar and the dynamical contents of galaxies. Indeed, if the environment affects the gas or stellar kinematics of the galaxies through one of the aforementioned mechanisms then the effect should be visible in the TFR when comparing galaxies located in low- and high-density environments. However, until recently only a handful of studies had tried to do so, probably because of the difficulty to assemble large representative spectroscopic samples of galaxies both in the field and in clusters or group of galaxies with resolved kinematics data. A few notable exceptions are the first analysis performed by [Pelliccia et al. \(2019\)](#) using long-slit spectroscopy and our two analyses presented in [Abril-Melgarejo et al. \(2021\)](#) and [Mercier et al. \(2022\)](#). Though results may seem conflicting, our current interpretation based on our latest results is that there is no discernable impact of the environment on the TFR at $z \sim 0.7$, hence at this redshift galaxies in galaxy clusters or large groups exhibit neither lower nor higher mass fractions of baryons than in the field. Perhaps even more importantly, our two analyses ([Abril-Melgarejo et al. 2021](#); [Mercier et al. 2022](#)) have shown how systematic effects induced by the comparison carried out between different surveys can propagate to the dynamical analysis and strongly impact the conclusions if not carefully taken into account. In this regard, MAGIC with its unique design combined with the powerful capabilities of Multi-Unit Spectroscopic Explorer (MUSE) (see Sect. 2.2.3) is the ideal survey to reduce these systematics to their minimum and to provide the best constraints on the impact of the environment on galaxies' dynamics at intermediate redshift.

1.4 The Dark Matter enigma

A particularly important quantity that is needed to explain observations in extragalactic astrophysics and in cosmology is DM. Indeed, current estimates of the cosmological parameters find that nearly 85% of the total mass in the Universe, thus excluding dark energy that dominates the energy budget, is composed of DM ([Planck Collaboration et al. 2020, 2021](#)). At the same time, DM has become a key component in dynamical models of galaxies and galaxy clusters without which it is nearly impossible to explain the large velocities of the gas and the stars in the galaxies or the amplitude of the gravitational lensing visible in massive galaxy clusters (a typical textbook example would be the bullet cluster, e.g. in [Clowe et al. 2004](#)). Furthermore, our current model of galaxy formation and evolution greatly makes use of DM to explain the early formation of DM dominated structures onto which baryons would be accreted to form proto-galaxies and then galaxies (e.g. for an early model of this type see [White & Rees 1978b](#)). Thus, DM seems ubiquitous in our current understanding of the Universe and yet its nature still remains a mystery. An opposite view of this “missing mass problem” is to rather consider it as a proof of the limits of the current laws of physics, especially concerning gravity. Throughout the years, various theories have thus been proposed to modify Newtonian gravity on the scales of galaxies and galaxy clusters but their difficulty to conciliate DM-dominated systems (e.g. dwarf or low-surface brightness galaxies, see [de Blok & McGaugh 1997](#); [Boldrini 2021](#)) with seemingly DM-poor systems (e.g. [Mancera Piña et al. 2022](#)) has raised doubts as to whether such models are sufficient to explain DM.

1.4.1 Dark Matter or modified gravity ?

Historically speaking, early proofs of the gravitational effect of DM came from the pioneering work of Fritz Zwicky on the Coma Cluster (Zwicky 1933, 1937). His argument was that, based on the virial theorem and on the measurement of the radial velocities of the galaxies located in the cluster, there was just not enough luminous mass (by a factor of roughly 400, though overestimated because he was not aware at the time of the existence of hot gas located between galaxies) in the galaxies to explain the apparently large velocity dispersion. Hence, he concluded that there must be some invisible matter that must dominate the mass budget. During the 1970s, multiple kinematics studies of local galaxies using H α and cold gas (HI, e.g. Rogstad & Shostak 1972; Roberts & Rots 1973; Rubin et al. 1978a,b, 1980; Bosma 1978, 1981a,b) and of the Milky Way using dwarf companions (e.g. Ostriker et al. 1974) shed light on the fact that the rotation curves of galaxies remain constant beyond a certain point, indicating the presence of large amount of unseen mass. Beside their rotation curves, the galaxy disks were also found to be cold, that is with very little velocity dispersion. It was shown by Ostriker & Peebles (1973) that such disks could not remain stable alone in numerical simulations over a Hubble time (i.e. a characteristic time-scale of the Universe) and that they built-up bar instabilities unless a large spherical halo with a mass at least equal to that of the disk was added. Though the evidence had become clear, the nature of this invisible mass was not yet elucidated. For instance, Ostriker et al. (1974) suggested that it was due to a large number of very faint stars that extended well beyond the optical radius seen in photographic plates, but other theories were proposed based on white dwarfs, black holes, or massive baryonic particles. Throughout the 1980s, the leading theory was that this missing mass was composed of massive neutrinos but disagreements between observations and simulations and the impossibility to measure a neutrino mass consistent with the required cosmological value led to a loss of interest. In parallel, a set of new theories where the missing mass would be made of non-baryonic massive particles were developed. These theories were labelled as Warm Dark Matter (WDM) and Cold Dark Matter (CDM) and had the advantage to much better match the temperature fluctuations seen in the CMB and the observed clustering of galaxies (e.g. Davis & Djorgovski 1985). Nevertheless, there were still discrepancies and to match even better the clustering new models were developed, among those was suggested the idea of adding a cosmological constant to the CDM model. Definite proof of the accelerated expansion of the Universe through the observations of type Ia supernovae and thus of the need of a non-zero cosmological constant (Riess 1998; Perlmutter et al. 1999) further strengthened the theory and led to the establishment of our current standard model of cosmology (Λ CDM). It has become clear from the large amount of rotation curves and 2D velocity fields that have been studied in the literature, such as the Spitzer Photometry and Accurate Rotation Curves (SPARCS), Calar Alto Legacy Integral Field Area Survey (CALIFA), or Sydney-AAO Multi-object Integral field spectrograph (SAMi) samples in the local Universe (Lelli et al. 2016; Sánchez et al. 2016; Croom et al. 2012) or the Mass Assembly Survey with SINFONI in VVDS (MASSIV) described in Contini et al. (2012) at high redshift, that nearly every galaxy contains significant amounts of DM even at high redshift. In parallel, further evidence for the presence of an invisible mass in galaxy clusters has been found in various ways. For instance this was done through the measurement of the velocity dispersion of galaxies moving through clusters (as Zwicky did), which requires enough unseen mass for the galaxies to remain gravitationally bound to the structure, through the measurement of the temperature of the hot X-ray emitting gas located in the ICM, which requires enough mass so that the gas remains in hydrostatic equilibrium, or through the gravitational lensing effect of some clusters on background sources

(e.g. Richard et al. 2021). More historical details about evidence for the missing mass problem can be found for instance in Sanders (2010). Alternatively to the development of the DM theory, other alternative theories of gravity started to be developed during the 1980s, the most famous being the Modified Newtonian dynamics (MOND) first described in Milgrom (1983). A common feature in such theories is that they describe the missing mass problem by changing the laws of gravity and thus the dynamics of a system. This introduces a typical acceleration a_0 that acts as an additional constant above which Newtonian dynamics is recovered and below which the effective acceleration that appears in Newton's first law of gravity is proportional to the square of the intrinsic acceleration (i.e. for $a \ll a_0$ we have $F \propto ma^2$, with m the gravitational mass and a the intrinsic acceleration). Thus, for any mass distribution which can be reduced to a point mass when seen sufficiently far away we find that $GM/r^2 \propto a^2 \propto V^4/r^2$, which corresponds to a flat rotation curve at large radii. Despite the clear appeal of alternative theories of gravity there have been a few difficulties that have slowed down their development. A first point that needs to be taken into account is that they must be applicable on scales for which DM is necessary. This includes galaxies and galaxy clusters but also cosmological scales since DM is required to produce the large scale structure of the Universe, the so-called cosmic web. A second important point is that, by construction, such theories predict that the dynamics of the systems is tightly linked to their baryonic content (stars, gas, dust, etc.). Hence, there must be an additional effort made to explain outliers where such links are not observed such as, for instance, the recent DM-poor galaxy presented in Mancera Piña et al. (2022)² or the bullet cluster whose observed mass distribution does not match the total mass distribution derived with gravitational lensing. Therefore, for the time being the leading theory has remained that the missing mass in galaxies and galaxy clusters is linked to DM. Nevertheless, this does not mean that a compelling alternative theory of gravity might hypothetically emerge in the near-future and provide us with an answer to mystery that is DM from a dynamical standpoint.

1.4.2 Current questions regarding Dark Matter

Even if Λ CDM and therefore DM have become nowadays the leading theories, this does not mean that there are no remaining questions concerning them for which we do not have definite answers yet. The most obvious unanswered question regarding DM is concerning its nature itself. If DM is indeed composed of still undetected new particles, then the answer is ultimately likely to come from particle physics. Nevertheless, extragalactic astrophysics remains a privileged laboratory that can be used to put constraints on which type of particles might be appropriate for DM. The details how this is achieved actually go beyond the scope of this Thesis, and also to some degree of my current understanding, but I can nevertheless mention one survey that I am aware of, MUSE-FAINT (Zoutendijk et al. 2020), that used observations of ultra-faint dwarf galaxies to put constraints on various models of DM: massive astrophysical compact halo object (MACHOs), self-interacting and fuzzy DM, and axion-like particles (Zoutendijk et al. 2020, 2021a,b; Regis et al. 2021). However, current questions regarding DM do not reduce solely to its nature. For instance, one of such key question is whether structure formation happened quicker than what Λ CDM predicts. Evidence that it might be so are the too large number of very luminous galaxies

²Note that some galaxies may seem to be outliers not because of the theory used but because of uncertainties propagating to the dynamical modelling, including the galaxy inclination, the distribution of stars and gas, or the mass-to-light ratio of the various baryonic components in the galaxy (e.g. stellar disk, stellar bulge, cold gas disk, etc.).

in the Local Volume and a too low number of galaxies in the Local Void, as well as the existence of massive clusters at high redshifts (e.g. [Mortonson et al. 2011](#)). Another current challenge is concerning the missing satellite problem of the Milky Way which states that there may be not enough (low-mass) satellites around it compared to predictions from Λ CDM simulations ([Moore et al. 1999](#); [Strigari & Wechsler 2012](#)).

There exist other discrepancies between observations and Λ CDM simulations, in particular towards the formation of bulgeless and low-surface brightness galaxies, but one question that is particularly important with respect to my field of expertise is regarding the cusp-core problem. This is a long-standing issue between observations and predictions from DM-only simulations that do not agree on the slope of the DM profiles in the inner parts. Early simulations of the collapse of DM haloes such as those performed by [Navarro et al. \(1997\)](#) clearly showed that the inner logarithmic slope ($d \log \rho / d \log r$, with ρ the density) could be fitted by a universal value of minus unity which led to the establishment of the now famous Navarro-Frenk-White (NFW) profile. Thus, simulations predicted that DM haloes are cuspy. On the other hand, early mass models performed on the rotation curves of local galaxies showed that they must have a constant density in the inner parts, hence that they have a core (e.g. [Moore 1994](#); [Burkert & Silk 1997](#); [Salucci 2001](#)). This result still holds nowadays with nevertheless some measurements that might point out towards cuspy DM haloes but still with a shallower slope than what Λ CDM predicts (e.g. [Chemin et al. 2011](#)), though more recent results would suggest that core profiles are preferred over cuspy ones (e.g. [Korsaga et al. 2018, 2019a,b](#)). At higher redshift, the picture is more complex because of stronger instrumental effects that affect kinematics observations (see Sect. 5.2.4.5 for a discussion on that topic with our data). Still, a few years back a seminal analysis performed by [Genzel et al. \(2020\)](#) using rotation curves showed evidence that galaxies at $z \approx 2$ host core DM profiles. During the following year, we further strengthened this evidence in [Bouché et al. \(2022\)](#) by performing mass models on 2D velocity fields of $z \approx 1$ galaxies using data from the MUSE Extremely Deep Field (MXDF). The current explanation that is given to solve the apparent discrepancy in the inner slope is that DM haloes are originally cuspy by nature, but that there must exist at least one mechanism that sufficiently heats the halo so that it removes some DM particles in the inner parts, thus transforming the cuspy initial profile into a core one. Suggested physical processes that can heat DM particles enough are (i) dynamical friction induced by the passage of, for instance, a satellite galaxy, a globular cluster, or even just a collection of gas clouds (e.g. [El-Zant et al. 2001](#); [Romano-Díaz et al. 2008](#); [Nipoti & Binney 2014](#)) or (ii) feedback processes from supernovae, from an AGN, or from stellar winds (e.g. [Read & Gilmore 2005](#); [Madau et al. 2014](#); [El-Zant et al. 2016](#); [Dutton et al. 2016](#); [Freundlich et al. 2020](#)). Hence, even if we have fundamentally found some plausible solutions to the cusp-core problem, the questions of which mechanism plays a leading role and whether these explanations are enough at high redshift where DM profiles have had less time to be affected by baryonic processes are still a matter of debate.

Chapter 2

Spectroscopy in extragalactic astronomy

There are two main types of observations (in terms of electromagnetic radiation) that can be carried out in extragalactic astronomy: imaging and spectroscopy. Both are actually two pieces of the same puzzle. Imaging can be seen as providing spatial information over a spectrum that has been integrated over a sufficiently large spectral window, whereas spectroscopy can rather be seen as the opposite, that is as a spectrum that is spectrally resolved but spatially integrated over a given aperture. Because the various constituents of a galaxy (e.g. stars, gas, dust, etc.) do not emit in the same way, we can recover their spectral signatures and infer from them some physical properties such as the presence of some chemical species, their relative abundance, the amount of extinction due to dust, or the gas and/or stellar velocity just to cite a few. Therefore, spectra are key observations because they are fundamental to extract major physical quantities useful to study the evolution of galaxies that would otherwise be very difficult, if not impossible at all, to obtain. Furthermore, the spectra of galaxies are also affected by their motion and by the expansion of the Universe. Thus, they are also key observations to derive, when possible, precise cosmological redshifts that are in turn useful to correctly derive galaxies' physical properties that depend on their distance to us such as their stellar mass or SFR.

In this section, I therefore give a brief overview of spectroscopy as it is used in extragalactic astronomy. I will restrict the discussion to the optical and IR since these are the parts of the spectrum that I have worked with during this Thesis. In particular, I will focus on integral field spectroscopy which is the observing technique that I have been using the most during this Thesis. I begin in Sect. 2.1 with a description of the fundamental principles behind modern spectroscopy such as how spectra are currently obtained and I give a brief overview of the physics behind the main spectroscopic features seen in galaxy spectra. Then, in Sect. 2.2 I focus on integral field spectroscopy. I give an historical overview of the development of the discipline, from the early instruments to the current and next generation instruments that are or shall be installed on future telescopes. In particular, I focus my discussion on MUSE which is the main instrument that I have been using during this Thesis.

2.1 Principles of spectroscopy

The first astronomical application of spectroscopy was performed by J. R. von Fraunhofer at the beginning of the nineteenth century by observing the Sun and then other stars which led him to discover the presence of absorption lines now known as Fraunhofer lines. Since then, the field of spectroscopy has greatly changed and is now not limited to the sole study of nearby stars.

Historically, spectroscopic studies such as the one performed by J. R. von Fraunhofer were limited to integrated spectra, that is spectra taken within a given aperture. These had the advantage of allowing to observe relatively faint objects since their total light was integrated but at the cost of a loss of spatial information. The core concept of spectroscopy is to disperse the incoming light but there are multiple techniques that allow doing so. The oldest one is through the use of a prism that will disperse the light in different directions because of the variation of the prism's material index of refraction with wavelength. A second technique is to use a dispersion grating which is an optical component made of a series of equally spaced ridges (reflective grating) or slits (transmissive grating) that will diffract the incoming light when passing through a slit or when being reflected on a ridge. The result is a diffraction pattern due to the superposition of the waves from each slit/ridge with a succession of light intensity peaks and valleys. The important point is that the position of the peaks and valleys (defined by their order) are determined by the distance between each slit/ridge in the grating and by the wavelength of the incoming light. Thus, gratings act as dispersive systems and produce a spectrum for each order (except the zeroth one). However, there are two caveats with such systems: (i) consecutive orders will partially overlap with each other because of the wavelength dependence of the dispersion and (ii) for a given order, there is a maximum wavelength beyond which the light cannot be dispersed any more by the grating.

Dispersion gratings that are optimised to focus the light for a given order and central wavelength are called blazed or echelette gratings. A last technique that uses both previous concepts is called a grism. It corresponds to a prism with one of its face manufactured as a dispersion grating.

The lack of spatial resolution in integrated spectra quickly led astronomers to use dispersive systems in combination with slits. This technique, called long-slit spectroscopy, consists in placing a slit before the dispersive system so that the resulting spectrum is dispersed onto the detector perpendicular to the slit orientation. This way, it is possible to obtain some spatial information but only in 1D. Despite their relative simplicity compared to more complex designs discussed below, long-slit spectrographs have been and are still widely used, as is the case for instance with the DEep Imaging Multi-Object Spectrograph (DEIMOS) described in [Faber et al. \(2003\)](#) and used for the Observations of Redshift Evolution in Large-Scale Environments (ORELSE) survey ([Lubin et al. 2009](#)). The main difficulty with long-slit spectroscopy when observing galaxies is that one must place the slit in advance on the target which requires to know its position and the slit orientation. For instance, to measure the velocities within a galaxy the ideal case is when the slit is positioned along the galaxy's major axis to minimise projection effects, which therefore requires to have this information prior to placing the slit. Historically, one way to circumvent this issue and to produce spatially resolved observations of galaxies with long-slit spectroscopy was to scan the slit along a given direction while keeping the same orientation. However, such observations lacked precision and were laborious, thus not very efficient. In the mean-time, two other scanning methods had been developed that relied on the principle of interference rather than diffraction: Fourier Transform Spectroscopy (FTS) and Fabry-Pérot spectroscopy. The former uses a Michelson interferometer to make the incoming light interfere with itself which produces an interference pattern on the detector. By varying the distance between the two arms

of the instrument and recording the interference pattern, one recovers an output signal at each position in the field that is the Fourier transform of the input spectrum. The latter technique uses two parallel semi-reflective blades that only let pass through wavelengths that are in resonance with the distance between the two blades, thus selecting only a fraction of the full spectrum. By changing the distance between the blades, it is thus possible to scan the full spectrum.

During the 1980s and 1990s, new optical designs were suggested to overcome the issues imposed by scanning devices. These designs that involved the use of fibres coupled with arrays of micro-lenses or image slicers would become what is nowadays called integral field spectroscopy. An historical overview of these new instruments is given in Sect. 2.2.

2.2 The rise of Integral Field Spectroscopy

In what follows, I provide a short historical overview of the development of the field of Integral Field Spectroscopy from early proof of concepts with the development of the *Traitement Intégral des Galaxies par l'Etude de leurs Raies* (TIGER) spectrograph, going through the different generations of instruments, to MUSE that is discussed in Sect. 2.2.3. I conclude this section by mentioning other current valuable Integral Field Spectrograph (IFS) instruments and what might be expected from the next generation that will be installed on the future Extremely Large Telescopes (ELTs).

2.2.1 Pioneering concepts: TIGER, OASIS, and SAURON

The early concept of Integral Field Spectroscopy was suggested by George Courtès in 1980 during the “Premier colloque national du comité français du télescope spatial: Applications de la photométrie bidimensionnelle à l’Astrophysique” (First colloquium of the french committee of the space telescope: applications from 2D photometry to Astrophysics) in Toulouse (Lachieze-Rey 1980). A second publication, in English this time and much easier to find, was published in 1982 (Courtes 1982) where two IFS designs were presented, both implementing an array of lenses. The first design uses an array of lenses located at the focus of the telescope that splits the field-of-view (FoV) into multiple parts. After passing through an optical system composed of a prism or a grism, the spectra are cast onto a detector. The second design is an improved version of a previous concept that was proposed and developed by Vanderriest (1980). The idea is to use optical fibres, to split the FoV, whose ends are re-arranged into a line that feeds a slit spectrograph. George Courtès noticed that because of the fibres’ design a significant fraction of the incoming flux is lost with this system and he therefore improved it by adding an array of lenses before the fibres. This way, each lens focuses the light onto the central parts of the fibres where the flux loss is marginal. During the 1980s, the first design was developed by a collaboration between the observatories of Lyon and Marseille. This first prototype, named TIGER¹, was run for the first time at the CFHT in 1987 (Bacon et al. 1995) and operated on a regular basis from 1990 to 1996. TIGER was truly the first operational IFS instrument in the world that integrated George Courtès’ idea. It acted as the first proof-of-concept that showed to the world the feasibility and the powerful capabilities of such an instrument compared to already existing devices (long-slit scanning, Fabry-Pérot, etc.) and it therefore paved the way for the

¹As explained in Bacon et al. (1995) the name is actually a pun since the instrument shared the same cage as another instrument named PUMA.

development of modern 3D spectroscopy. It had a quite small FoV of either $7'' \times 7''$ or $10'' \times 10''$ in spectrographic mode and observed in the visible part of the spectrum with a spectral resolving power varying from $R \sim 350$ to $R \sim 2000$ depending on the filter used. Thus, TIGER was mainly used to study compact objects such as galactic nuclei (e.g. [Bacon et al. 1994](#); [Durret et al. 1994](#)), though science topics diversified throughout the years (T Tauri stars, quasars, gravitational lenses, etc.) as the design of the instrument and its associated reduction software converged to their final forms (see [Emsellem 1999](#)).

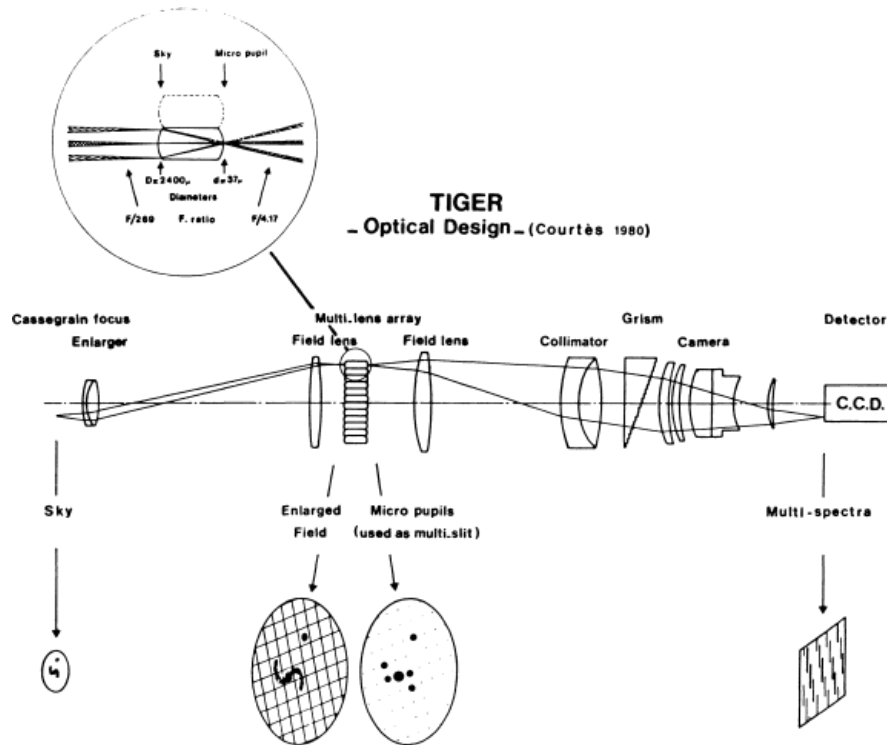


Figure 2.1: Original design of the TIGER Integral Field Spectrograph from [Bacon et al. \(1988\)](#) based on a first concept proposed by [Courtes \(1982\)](#). The combination of an array of micro-lenses with a grism allows to split the FoV and produce one spectrum per spatial element.

The development of the Adaptive Optics (AO) bonnette for the CFHT and the requirements to collect a large number of spectra on a small FoV with a large spatial sampling led to the decommissioning of TIGER that was replaced by the Optically Adaptive System for Imaging Spectroscopy (OASIS) spectrograph. This new IFS instrument built by the observatory of Lyon under the supervision of Roland Bacon was specifically designed to be used with the bonnette. After preliminary tests at the Observatory of Haute-Provence (OHP), the instrument was shipped to Hawaii where it ran for the first time in 1997 and in 1998 for the beginning of the scientific phase where it observed among other things T Tauri stars (e.g. [Lavalley 2000](#)), the stellar dynamics of galactic nuclei and bars (e.g. [Emsellem 1999](#); [Bacon et al. 2001](#)), radio galaxies (e.g. [Rocca-Volmerange et al. 2000](#)), as well as quasars (e.g. [Ledoux et al. 1998](#)). In 2002, the

instrument was decommissioned and brought back to Lyon before being installed on the William Herschel Telescope (CFHT) in 2003 (Rutten 2000). When installed on the CFHT, its hexagonal FoV varied from $2.7'' \times 3.7''$ to $12'' \times 16.7''$ over roughly 1100 spatial elements with a spectral resolving power going from $R \sim 1100$ to $R \sim 4300$ (depending on the spectral configuration) in the optical.

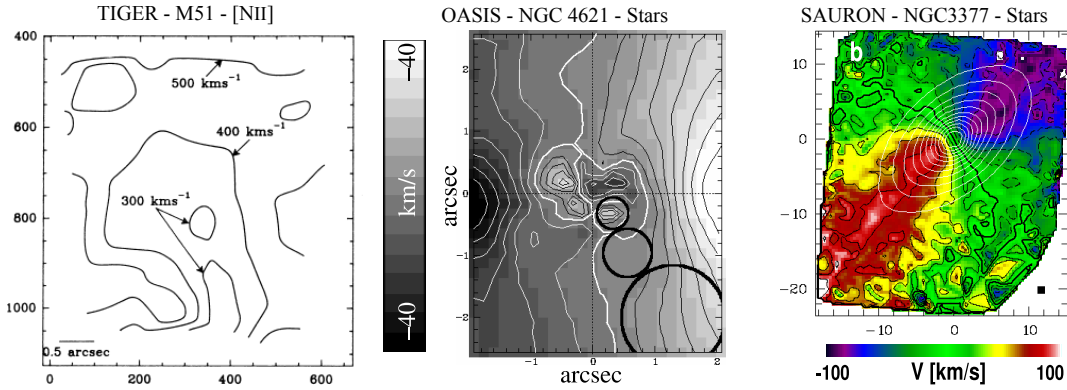


Figure 2.2: Examples of early velocity fields from TIGER ([NII] gas kinematics for M51, Bacon et al. 1988), OASIS (stellar kinematics for NGC 4621, Wernli et al. 2002), and SAURON (stellar kinematics for NGC 3377, Bacon et al. 2001). We can see the variation in spectral resolution and the transition from the small FoV IFS instruments, TIGER and OASIS, to a larger FoV with SAURON.

Following the conception of TIGER and OASIS a collaboration between the observatories of Lyon, Leiden, and the University of Durham decided to build another IFS instrument in the footsteps of OASIS but dedicated to the study of the stellar and gas dynamics of nearby galaxies. Indeed, even if OASIS could study galaxy kinematics, its small FoV limited it to the inner regions such as the nucleus or the bar. Thus, the Spectroscopic Areal Unit for Research on Optical Nebulae (SAURON) instrument was commissioned on the WHT early 1999 (Miller et al. 2000; Bacon et al. 2001) and operated until 2014. It was a large FoV and quite high throughput (about 35% for the optics, 14% in total) IFS instrument also using an array of 1520 square micro-lenses. Two observing modes were provided by the instrument: (i) a low spatial resolution mode with spatial pixels (spaxels) of nearly $1'' \times 1''$ spanning a large FoV of $33'' \times 41''$ and (ii) a high spatial resolution mode with spaxels of $0.26'' \times 0.26''$ spanning a smaller FoV of $9'' \times 11''$. Even though the optics were optimised to observe between 4500 \AA and 7000 \AA , it was commissioned with a single filter in the range $4180 \text{ \AA} - 5400 \text{ \AA}$ which contains bright emission and absorption lines for nearby galaxies such as $H\beta$ or $[\text{OIII}]\lambda 5007$. Because it was specifically designed to study the galaxies' kinematics, the instrument also had low spectral sampling of nearly 1 \AA per spectral pixel (spexel) and a Line Spread Function - LSF Full Width at Half Maximum (FWHM) of nearly three spaxels. As a comparison, this is equivalent to the spectral sampling of OASIS in its high spectral resolution configuration which had a spectral coverage twice narrower (or equivalently a sampling twice lower than that of the medium resolution configuration which had roughly the same spectral coverage as SAURON). Its main science objective was the dynamical analysis of a sample of 72 nearby spiral, lenticular, and elliptical galaxies that led to the SAURON project with, as of December 2022, roughly 70 papers starting with Bacon et al. (2001) and including the

ATLAS^{3D} series (e.g. see [Cappellari et al. 2011a](#)).

Examples of early velocity fields for the three instruments are shown in Fig. 2.2 (left: TIGER, middle: OASIS, and right: SAURON). The leftmost velocity field was obtained from the first observations made with TIGER on the nucleus of M51 ([Bacon et al. 1988](#)), the middle one from [Wernli et al. \(2002\)](#) was observed a few years after the beginning of the observing runs with OASIS and shows the existence of a counter-rotating core with respect to the rotation of the galaxy's disk in NGC 4621, and the rightmost velocity field was an early result for the first observations carried out with SAURON on NGC 3377 ([Bacon et al. 2001](#)). Apart from a clear variation in spectral resolution, we can also see how the instruments evolved from small FoVs focussed on the nuclear regions of galaxies to larger FoVs that can observe the larger disk kinematics.

2.2.2 First-generation instruments

The forefathers of the IFS instruments showed how promising integral field spectroscopy could become using the design with an array of micro-lenses. At the same time, improvements in the conception of fibre bundles and the development of MOS such as the Visible Multi-Object Spectrograph (VIMOS), presented in [Le Fevre et al. \(1998\)](#), also motivated the scientific community to install a first generation of IFS instruments on large telescopes such as the Very Large Telescope (VLT), the KECK telescopes or the Gemini Observatory (Gemini). In addition, independently of the work achieved by the teams in Lyon and Marseille, another one at the Max-Planck-Institut für extraterrestrische Physik (MPE) developed a new design, observing in the IR, and based on the concept of an image slicer that, as the name suggests, slices the FoV into stripes that are then fed into a long-slit grism spectrograph. This instrument, named 3D-MPE, was deployed as early as 1993 in various locations from the WHT to the 2.2 m MPG-ESO telescope in La Silla, Chile ([Cameron et al. 1993](#); [Krabbe et al. 1995](#)) and was the foundation for the modern SINFONI instrument. SINFONI was a first-generation IFS instrument in collaboration between MPE and ESO that was installed on the UT4 platform of the VLT. The instrument made use of the image slicing technique and of its own natural guide star AO system (applicable for the 3'' and 0.8'' modes only, see below). It was specifically designed to individually study distant objects and therefore it observed in the IR with a narrow FoV of either 8'' × 8'', 3'' × 3'', or 0.8'' × 0.8'' (pixel scale of 125 × 250 mas, 50 × 100 mas, or 12.5 × 25 mas, respectively; see [Thatte et al. 1998](#)). It led to significant surveys such as the Spectroscopic Imaging survey in the Near-infrared with SINFONI (SINS) and the zCOSMOS-SINFONI (zC-SINF) survey that studied the dynamics of a sample of high redshift (e.g. [Förster Schreiber et al. 2006a, 2009b, 2014, 2018](#); [Cresci et al. 2009](#); [Shapiro et al. 2009](#); [Mancini et al. 2011](#); [Newman et al. 2012, 2014](#); [Tacchella et al. 2015](#)), the MASSIV that probed 84 star-forming galaxies in the range $0.9 \leq z \leq 1.8$ (e.g. [Epinat et al. 2009](#); [Contini et al. 2012](#); [Epinat et al. 2012](#); [Vergani et al. 2012](#); [López-Sanjuan et al. 2013b](#); [Divoy et al. 2014](#)), and the Lyman-break galaxies Stellar populations and Dynamics (LSD) and Assessing the Mass-Abundance redshift[-Z] Evolution (AMAZE) surveys that were designed to study the chemical content of high redshift ($z \gtrsim 3$) Lyman-break galaxies (LBGs) (e.g. [Maiolino et al. 2008](#); [Mannucci et al. 2009](#); [Gnerucci et al. 2011](#)).

Another first-generation instrument that hosts an IFS but this time on the UT2 platform is the Fibre Large Array Multi-Element Spectrograph (FLAMES). FLAMES is a fibre facility installed in 2002 ([Pasquini et al. 2002](#)) whose goal was to perform MOS spectroscopy over a large FoV of 25' in diameter. It hosts two different spectrographs, one of which is GIRAFFE, a medium to

high-resolution spectrograph that observes in the visible but with three different modes:

- (i) MEDUSA that performs spectroscopy for 132 targets simultaneously over the entire FoV,
- (ii) the IFU mode that can perform integral field spectroscopy for 15 different targets using deployable Integral Field Units (IFUs) but with small FoVs of roughly $3'' \times 3''$, and
- (iii) ARGUS, a single IFU with a larger FoV of $12'' \times 7''$ (Pasquini et al. 2000). The IFU mode of FLAMES-GIRAFFE is particularly interesting because it used for the first time multiple IFUs to probe a larger FoV (Flores et al. 2004). Both the IFU and ARGUS modes nevertheless provide low spatial sampling with only 20 spaxels for the former and 14×22 spaxels for the latter. Its most significant survey is the Intermediate MAss Galaxy Evolution Sequence (IMAGES) survey that probed 63 galaxies at $0.4 < z < 0.75$ to study their dynamics (e.g. Flores et al. 2004, 2006; Puech et al. 2006a,b, 2007, 2008b, 2010, 2014; Yang et al. 2008; Neichel et al. 2008; Rodrigues et al. 2008).

One last first-generation instruments that has also contributed significantly to the field of extragalactic astrophysics and to integral field spectroscopy is OH-Suppressing Infra-Red Imaging Spectrograph (OSIRIS). It is an IFS instrument specifically designed to be used on the KECK telescopes with its AO system. It saw its first light in 2005 and operated in the IR. Its design is similar to most of the other IFS instruments in the sense that it also uses an array of micro-lenses with fibre bundles. Its FoV is not larger than any other IFS instrument in operation at the time but the fact that it is used at the KECK telescopes with its AO system makes the observations diffraction limited. Thus, it provided high resolution observations with a spatial sampling varying from $0.1''$ per spaxel for the coarsest mode to $0.02''$ per spaxel for the finest one (Larkin et al. 2000, 2006) and with a Point Spread Function - PSF FWHM of about $0.1''$ (e.g. Wright et al. 2007). For instance, Wright et al. (2007); Law et al. (2009); Wright et al. (2009, 2010); Law et al. (2018) used it to study the spatially resolved kinematics of a small sample of $z \sim 2 - 3$ galaxies as a function of their morphology and AGN activity.

2.2.3 The MUSE revolution

After the success of the first generation of IFS instruments installed on large telescopes there was a need for a second generation with improved capacities in terms of FoV and sensitivity to study statistically significant samples of intermediate and high redshift galaxies. These new instruments, such as the K-band Multi Object Spectrograph (KMOS) and MUSE, were designed in a context where large photometric and spectro-photometric surveys such as the The Two Micron All Sky Survey (2MASS) (Skrutskie et al. 2006), the All-Wavelength Extended Groth Strip International Survey (AEGIS) (Davis et al. 2007), the Great Observatories Origins Deep Survey (GOODS) (Dickinson et al. 2003), the Cosmic Evolution Survey (COSMOS) (Scoville et al. 2007), or the SDSS (Gunn & Knapp 1993) had already shed light on the large scale structure of the Universe. Similarly, these surveys had already started probing the global properties of galaxies as a function of redshift and environment. Nevertheless, the study of the physical processes taking place on resolved scales were still limited to relatively small samples of galaxies from previous IFS instruments. Thus, in the course of 2001, ESO defined four main scientific objectives that required specific instruments, two of which were (i) a near-infrared (NIR) MOS instrument to study high-redshift galaxies and (ii) a 3D spectrograph with a large FoV. The former instrument that was selected for this call is KMOS (see Sect. 2.2.4) and the latter is MUSE, which was suggested by Roland Bacon (Monnet 2002).

MUSE is a multi-IFU IFS instrument with a FoV of $1' \times 1'$ in wide-field mode and a high

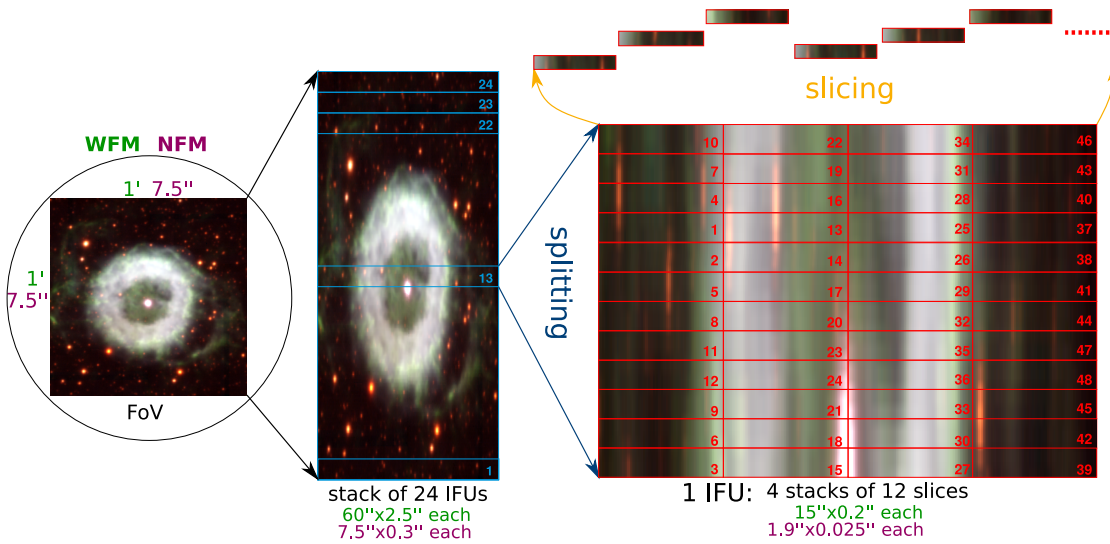


Figure 2.3: Illustration of the field splitting and image slicing for MUSE taken from [Weilbacher et al. \(2020\)](#). The original FoV is shown on the left-hand side, the field splitting in 24 parts in the middle, and the final image slicing in 48 parts that is done for each of the 24 IFUs on the right-hand side. Each slice is then fed to a spectrograph and its resulting spectrum is imaged on the corresponding CCD.

sensitivity that was designed to study large samples of intermediate and high redshift galaxies. It was built by the MUSE consortium that gathers the Leibniz Institute for Astrophysics Potsdam (AIP), Centre de Recherche Astrophysique de Lyon (CRAL), Eidgenössische Technische Hochschule Zürich (ETH), Institut de Recherche en Astrophysique et Planétologie (IRAP), Institute for Astrophysics and Geophysics (IAG), Leiden University, and ESO. Similarly to SINFONI, it also implements an image slicer rather than an array of micro-lenses to feed the FoV into multiple spectrographs ([Henault et al. 2003](#)). Its large FoV which is one of the key characteristics of the instrument is further achieved through the use of a field splitter and 24 IFUs as illustrated in Fig. 2.3. The way this is done is roughly speaking as follows: 1. the FoV is split into 24 sub-fields that are each fed to a single IFU, 2. each sub-field is cut into 48 slices following the pattern shown in Fig. 2.3, and 3. each slice is sent into the spectrograph that disperses its light vertically into the corresponding Charged-Coupled Device (CCD). These steps produce 24 output images of 4224×4240 pixels as shown on the left-hand side of Fig. 2.4. Each image has the 48 spectra dispersed vertically into four quadrants. The cross splitting the quadrants in the middle corresponds to the overscan region of the CCD whereas the two strips on both sides are pre-scan regions. Both are required by the CCD to read the data. Such raw data cannot be used directly and a full reduction pipeline must be applied to go from these 24 images to the final data cube (see the right-hand side of Fig. 2.4 for a narrow-band image around $H\alpha$ for the same observation). Since I directly worked on already reduced MUSE data and that I never performed the reduction steps myself during this Thesis, I will not discuss it further and I will redirect the interested reader to [Weilbacher et al. \(2020\)](#) where the latest reduction pipeline is described in details. Technically, MUSE can operate in two modes: wide-field and narrow-field mode. The difference

between the two is that the narrow-field mode operates over a narrower FoV of $7.5'' \times 7.5''$ with a spatial sampling of 25 mas per spaxel that is similar to space-based optical observations. This mode can be interesting for observations that require a finer spatial scale without a higher spectral resolving power over a narrower FoV but with the high sensitivity of MUSE and its IFS instrument capacities (e.g. to study AGNs such as in [Winkel et al. 2022](#)). Nevertheless, the most widely used mode is the wide-field one which is what I have been using. Therefore, in what follows, I will not discuss further the narrow-field mode. The output of the wide-field mode is a data cube of $1' \times 1'$ with a spatial sampling equal to $0.2''$ per spaxel, spanning a wavelength range that goes from 4650 \AA to 9300 \AA with a spectral sampling of 1.25 \AA per spaxel.

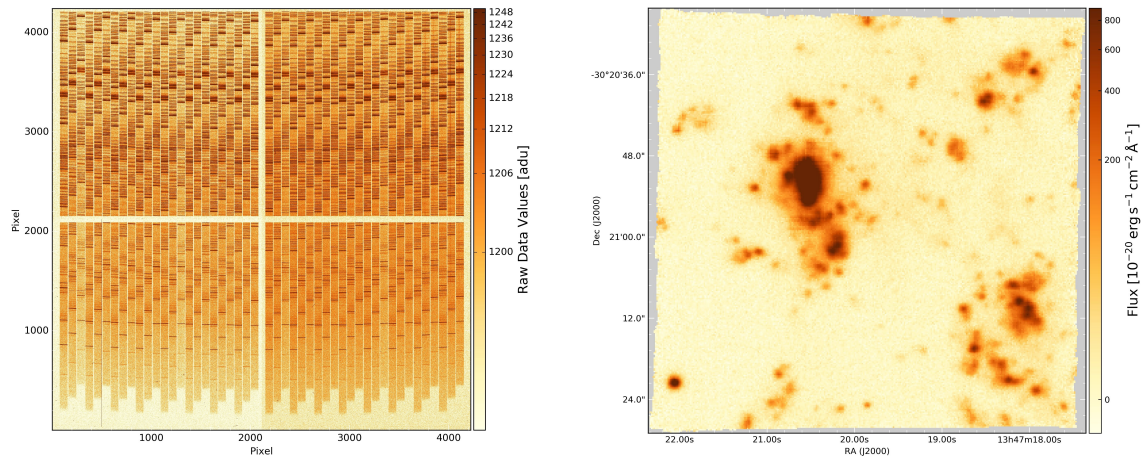


Figure 2.4: Illustration of a raw (left-hand side) and fully processed (right-hand side) MUSE observation taken from [Weilbacher et al. \(2020\)](#). The raw image is the output of the tenth IFU’s CCD whereas the processed image corresponds to the entire FoV around the $H\alpha$ wavelength. The central cross and the sides of the raw image correspond to the overscan and pre-scan of the CCD, respectively. There are 48 spectra aligned vertically in the raw image with the blue end at the bottom and the red end at the top.

Another interesting aspect of MUSE is that since summer 2017 it can operate with the AO module GALACSI ([Ströbele et al. 2012](#)) using four sodium laser guide-stars installed on the UT4 platform of the VLT. After being emitted, the light of the lasers will be absorbed and re-emitted by the sodium layer of the atmosphere that will be then observed by specific sensors on the ground. The wavefront distortion due to the turbulence in the lower parts of the atmosphere will then be computed so that a real-time correction is constantly applied to the primary mirror of the telescope. Without AO, MUSE already performs well with a PSF FWHM at around 6000 \AA in good atmospheric conditions which is around $0.7''$. With AO and if the turbulence is mostly in the lower parts of the atmosphere, the PSF FWHM can reach around $0.4''$ at the same wavelength. Actually, the spatial resolution will be slightly worse at bluer wavelengths and slightly better at redder ones because of once again the turbulence that will more severely affect the blue part of the spectrum (see for instance Fig. 2 of [Bacon et al. 2015](#)). A second key characteristics of the instrument that has already been mentioned before is its high sensitivity. Combined with its large FoV, this gives MUSE the possibility to observe a large number of galaxies over relatively

short integration times and to probe low-mass galaxies down to $10^7 M_{\odot}$ that could hardly be observed and studied in a statistically significant manner with previous IFS instruments. Furthermore MUSE observes continuously across its FoV, contrary to complementary instruments such as KMOS that rather observes galaxies individually over smaller FoVs but across a larger patrol field, which means one can perform blind source detection across the FoV without prior selection (except the field location) as was done for instance in the MUSE Hubble Ultra Deep Field (MUSE-HUDF) and in the MXDF respectively described in [Bacon et al. \(2017\)](#) and [Bacon et al. \(2021\)](#). All these characteristics therefore render MUSE a particularly powerful instrument to study the evolution of galaxies at intermediate to high redshift.

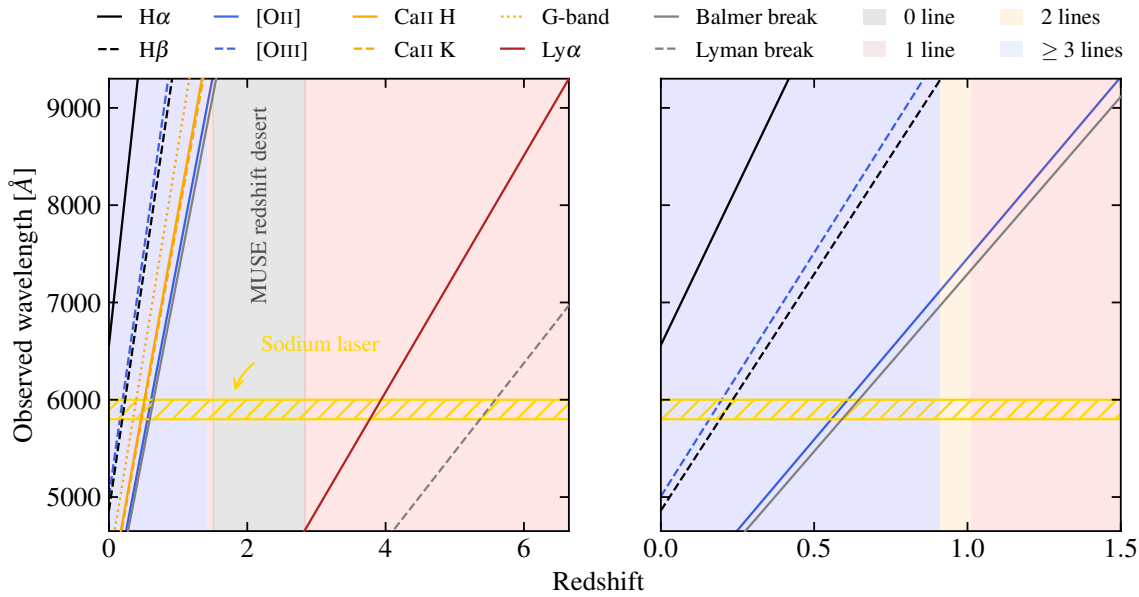


Figure 2.5: Redshift interval for the main emission and absorption lines as well as spectral features detected with MUSE. The left-hand side plot shows the full redshift range over which detections can be made and the right-hand side plot focusses on the $[O II]$ emitters range. The oxygen lines are shown in blue, the Balmer lines in black, the absorption lines in orange, and $Ly\alpha$ in red. The Balmer and Lyman breaks are also indicated with grey lines. The background color indicates whether no line (grey), a single line (red), two lines (orange), or three or more lines (blue) are available in the given spectral window. The background colors on the right-hand side are different because they only take into account emission lines whereas on the left-hand side the colors also take into account the absorption lines (but not the breaks). As an indication, the spectral window that is unavailable because of the sodium laser when the AO system is used is shown as the horizontal hatched yellow region.

MUSE is sensitive to two main types of galaxies: (i) those with a bright stellar continuum that are visible across the entire wavelength range and (ii) those with bright emission lines, independently of the continuum, that are usually associated to high star formation or to an AGN activity. A galaxy can obviously have both a strong continuum and emission lines at the same

time, so the two types are not mutually exclusive. Besides, those with a strong enough continuum can also have stellar absorption lines and, in the right conditions, fainter emission or absorption lines can also be detected. I do not show examples of MUSE spectra in this section because a few that are relevant for the MAGIC survey are already presented and discussed in Chapter 3. In practice, both emission and absorption lines, combined with a few spectroscopic features (e.g. Balmer break) when they are visible, are used to derive a spectroscopic redshift. The details of how this is done can be found in Sect. 3.2.2 for the MAGIC survey and in the relevant survey papers (see below) for the others. Nevertheless, the reliability of the derived spectroscopic redshift and the detection itself, especially in the case of emission line galaxies, highly depends on the number of strong enough spectroscopic features that fall within the MUSE wavelength range. Incidentally, such features being limited in number and located at fixed rest-frame wavelengths, they restrict the redshift intervals within which galaxies might be securely detected. I show in Fig. 2.5 the observed wavelength of the main emission and absorption lines, as well as the Balmer break and the Lyman break, as a function of redshift. This figure therefore shows the redshift window over which such features may be detected. At low and intermediate redshifts, the main absorption lines are the Balmer lines, CaII H λ 3968.47, CaII K λ 3933.68, and the G-band from CH molecules, and bright emission lines are also the Balmer lines, [OII] $\lambda\lambda$ 3727, 3729, and [OIII]. We can see that the redshift range where most of the lines are detected is below $z = 1.5$. In particular, when H α disappears the [OII] doublet enters the wavelength range around $z \approx 0.2$. This interval ($0.2 \lesssim z \lesssim 1.5$) is what we will refer to in the next chapters as the [OII] emitters redshift range since it is usually the brightest line available in this range that I used to model the dynamics of galaxies (see Chapters 3 and 5 for more details). At higher redshift ($z \gtrsim 3$), Ly α becomes detectable because it is a bright line with a complex and easily identifiable profile that originates from the propagation of resonant Ly α photons in neutral gas within the interstellar medium and/or in the vicinity of galaxies. However, between redshifts $z = 1.5$ and $z \approx 3$ we see that there are neither bright emission nor absorption lines available which renders the determination of secure spectroscopic redshifts difficult. This spectral window is referred to as the MUSE redshift desert. A few fainter lines such as Mg II $\lambda\lambda$ 2796, 2803 and C III] $\lambda\lambda$ 1907, 1909 are nevertheless available, so it is still possible to measure a few redshifts in this range.

The powerful capabilities of MUSE compared to previous generations of IFS instruments have led to numerous studies on a plethora of topics since the instrument saw its first light in 2014 (Bacon et al. 2014). Thus, it would be beyond the scope of my current knowledge to give a full account of every subject that has been addressed using MUSE. Therefore, in what follows, I only cite a few important broad topics that have used both Guaranteed Time Observation (GTO) and non-GTO data. These topics include among many others: (i) probing the dust and gas structure of planetary nebulae (e.g. Walsh et al. 2016; Monreal-Ibero & Walsh 2020), (ii) performing spectroscopy and studying the dynamics of a large number of stars found in globular clusters (e.g. Husser et al. 2016; Kamann et al. 2016, 2018; Voggel et al. 2016), (iii) studying the stellar kinematics of local and intermediate redshift galaxies (e.g. Emsellem et al. 2014; Krajnović et al. 2015, 2018; Guérou et al. 2016; Guérou et al. 2017), (iv) studying the dynamics and/or angular momentum of intermediate redshift galaxies (e.g. Contini et al. 2016; Swinbank et al. 2017; Bouché et al. 2021), (v) probing the evolution of galaxy mergers across cosmic time (e.g. Ventou et al. 2017, 2019), (vi) constraining the low-mass end of the galaxy MS relation (e.g. Boogaard et al. 2018), (vii) studying inflows and outflows in galaxies using background quasars (e.g. Bouché et al. 2016; Schroetter et al. 2016, 2019, 2021; Zabl et al. 2019, 2021), (viii) putting constraints on the nature of dark matter (e.g. Zoutendijk et al. 2020, 2021a; Bouché et al. 2022), (ix) studying

Ly α haloes at high redshift (e.g. Swinbank et al. 2015; Wisotzki et al. 2016; Patr icio et al. 2016; Diener et al. 2017; Leclercq et al. 2017; Matthee et al. 2020; Maseda et al. 2020; Kusakabe et al. 2020), (x) the serendipitous discovery of a giant ionised gas structure in the COSMOS field (Epinat et al. 2018), (xi) using galaxy clusters as magnifying lenses to study background galaxies (e.g. Richard et al. 2015, 2021; Karman et al. 2015, 2017; Bina et al. 2016; Lagattuta et al. 2017; Mahler et al. 2018; de La Vieuville et al. 2019), (xii) looking at the effect of environment on small samples of galaxies (e.g. Fossati et al. 2016; Sheen et al. 2017; Consolandi et al. 2017; Boselli et al. 2019), (xiii) studying gas-stripping in a statistically significant sample of local galaxies (e.g. Poggianti et al. 2017; Bellhouse et al. 2017; Fritz et al. 2017, and subsequent papers of the series), or (xiv) probing the impact of the environment on the dynamics of a large sample of intermediate redshift galaxies (Abril-Melgarejo et al. 2021; Mercier et al. 2022). Furthermore, several important GTO and non-GTO surveys carried out extragalactic observations with MUSE, including for instance the MUSE Hubble Deep Field South (MUSE-HDFS), MUSE-HUDF, MXDF, or MUSE-WIDE designed to study galaxy evolution at intermediate and high redshift, or more importantly the MAGIC survey (see Chapter 3) that was designed to probe the effect of the environment on galaxy dynamical properties at intermediate redshift (see Appendix A for a more complete and detailed list of major MUSE survey as of December 2022).

2.2.4 Miscellaneous current and next-generation instruments

MUSE is not the only second-generation IFS instrument currently observing in the world. Other instruments with their own key characteristics also exist and it is fair that I mention them before finishing this chapter by discussing the next-generation of such instruments that will be installed on the future ELTs. As already quickly discussed, KMOS is a second-generation IFS instrument operating in the IR that was built by various institutes in the United Kingdom and in Germany in collaboration with ESO. It was commissioned in 2012 and is installed on the UT1 platform of the VLT. Similarly to MUSE, it uses the image slicing technique but its particularity is that it builds upon the concept first introduced with GIRAFFE of using deployable IFUs to observe multiple galaxies at the same time in a large FoV of 7.2' in diameter (Tomono et al. 2003; Sharples et al. 2004). Its wavelength range makes it perfect to study the resolved physical processes taking place in intermediate and high redshift galaxies. At the same time, its design with deployable IFUs allows to study the impact of the environment on galaxies in a wide variety of environments by simultaneously probing galaxies in the inner parts of galaxy groups or galaxy clusters and in their outskirts (Sharples et al. 2005). KMOS was one of the first IFS instruments to provide large surveys of galaxies with resolved spectroscopic data such as K-band Multi Object Spectrograph 3D (KMOS3D) (Wisnioski et al. 2015, 2019) and KMOS Redshift One Survey (KROSS) (Stott et al. 2016) which have led to important studies concerning the dynamics of galaxies, including the evolution of angular momentum across cosmic time (e.g. Burkert et al. 2016; Swinbank et al. 2017; Harrison et al. 2017) or the redshift evolution of the Tully-Fisher relation (e.g.  bler et al. 2017; Tiley et al. 2019a, 2021). Another current IFS instrument is Mapping Nearby Galaxies at APO (MANGA) that provides the eponymous survey (Bundy et al. 2015) and which is operational since the fourth data release of the SDSS. It is composed of 17 IFUs made of fibre bundles that observe local galaxies in the SDSS from the UV to the NIR with medium spectral resolving power. The quality of its data product and the ever-increasing number of observed galaxies has led to numerous studies, in particular regarding galaxy evolution (e.g. Jin et al. 2016; Belfiore et al. 2017; Graham et al. 2018; Law et al. 2022). Similarly to MANGA, another current

instrument dedicated to providing integral field spectroscopy for thousands of galaxies at low-redshift is SAMI, first described in [Croom et al. \(2012\)](#). It is composed of 13 different IFUs that use fibre bundles to observe galaxies over $15''$ FoVs in diameter. Its current eponymous survey targets galaxies located in groups and in the field and is thus ideal to probe the impact of the environment in the local Universe (e.g. [Allen et al. 2015](#); [Green et al. 2018](#); [Scott et al. 2018](#); [Croom et al. 2021](#)).

Even more recently, the James Webb Space Telescope (JWST) was finally launched and as of July 2022 is fully operational and working. Among the on-board instruments are found JWST Mid-Infrared Instrument (MIRI) ([Wright et al. 2004](#)) and JWST Near-Infrared Spectrograph (NIRSPEC) that both include an integral field spectroscopic mode ([Rieke et al. 2015](#)). MIRI provides observations between roughly $5\mu\text{m}$ and $28\mu\text{m}$ using four IFUs that split the wavelength range in four sections and each section is further split in three gratings. The four IFUs observe at the same time but with a single grating, thus three observations of the same source are required to have a complete wavelength coverage. It has a small FoV that varies between $3.2'' \times 3.7''$ ($\sim 0.2''$ per spaxel) for the shortest wavelengths and $6.6'' \times 7.6''$ ($\sim 0.3''$ per spaxel) for the longest ones ([Wells et al. 2015](#)). On the other hand, NIRSPEC contains a single IFU that operates between $0.6\mu\text{m}$ ($\sim 0.9\mu\text{m}$ for medium spectral resolution) and $5.3\mu\text{m}$ and always observes a $3'' \times 3''$ ($0.1''$ per spaxel). For the low spectral resolution mode ($R \sim 100$) the full wavelength range is recorded, but for the two medium-resolution modes ($R > 1000$) the wavelength range is split in four different gratings ([Closs et al. 2008](#)).

Integral field spectroscopy having already had a tremendous impact on the field of extragalactic astrophysics it seems logical to expect that next-generation IFS instruments should be planned to be located on the future ELTs operational around the 2030s and 2040s. For instance, ESO has plans to incorporate IFS instruments on its future Extremely Large Telescope (ELT), first through its first-light instrument High Angular Resolution Monolithic Optical and Near-infrared Integral field spectrograph (HARMONI), described in [Tecza et al. \(2009\)](#) and [Thatte et al. \(2010\)](#), and then through a second generation MOS instrument with IFS capabilities called MOSAIC ([Evans et al. 2014](#)). HARMONI will be an IFU operating in the visible and in the NIR through various spectral channels with medium or high spectral resolving power. Combined with powerful AO systems specifically designed for the ELT, it will be optimised to obtain high-resolution diffraction-limited observations of high redshift galaxies. On the other hand, MOSAIC will be a second-generation MOS instrument that will also observe in the optical and in the NIR. Similarly to GIRAFFE and KMOS it will also host multiple IFUs that can be arranged in a 40 arcmin^2 FoV. Similarly, IFS instruments are also planned on the future Thirty Meter Telescope (TMT). One of the first light instruments will be Infrared Imaging Spectrograph (IRIS) that will observe in the NIR with medium spectral resolving power and over a relatively large FoV of $34'' \times 34''$ ([Larkin et al. 2010](#)). Thanks to the TMT and the use of a specific AO system, it shall provide diffraction-limited observations similar to what HARMONI will achieve. Apart from the ELTs, the VLTs will also be updated in the near-future with new-generation instruments including IFS instruments. To begin with, the current plan at ESO is to install onto one of the four telescopes of the VLT a new MUSE-like instrument optimised to observe in the blue part of the spectrum between roughly 350 nm and 600 nm : BLUEMUSE ([Richard et al. 2019](#)). The point of this instrument that will greatly benefit from the design of MUSE is to probe the part missing in MUSE data over a larger FoV and with a medium spectral resolving power. Finally, there is also a new spectrograph currently installed on the VLT with IFS capabilities that will soon start science operations in April 2023. This instrument, called Enhanced Resolution

Imager and Spectrograph (ERIS) (Davies et al. 2018), will observe in the IR and has an integral field spectroscopic observing mode called ERIS-SPIFFIER that is an upgraded version of SPIFFI, the IFU of SINFONI. Combined with powerful AO modes and two resolving powers (medium at $R \sim 5000$ and high at $R \sim 10\,000$), the instrument shall be able to probe the dynamics of individual high-redshift galaxies ($z \gtrsim 5$) with high spatial and spectral resolutions using emission lines such as [OII], [OIII], or $H\beta$, as well as the optical disk of intermediate redshift galaxies using $H\alpha$ with better spatial sampling and spatial and spectral resolution than MUSE.²

²Further plans for future fibre-based IFS instruments include for instance HECTOR on the Anglo-Australian Telescope (Bryant et al. 2016) or SPECTEL, a project for a dedicated large FoV 10 m-class telescope for dedicated 3D spectroscopic observations (Ellis & Dawson 2019).

Chapter 3

The MAGIC survey

The data used in [Abril-Melgarejo et al. \(2021\)](#) and [Mercier et al. \(2022\)](#) (see also Chapter 6) and in the analysis of the angular momentum presented in Chapter 7 are all part of the MAGIC survey. Therefore, before delving into the analysis of the impact of the environment on galaxy scaling relations at $z \sim 0.7$ in Chapter 6 and on their angular momentum in Chapter 7, we briefly present in this section the survey design, the main characteristic of the observed structures and of their galaxies, and we refer the reader to [Epinat et al. \(in prep.\)](#) for a complete description of the survey.

3.1 Survey design and observing strategy

The MAGIC survey is a MUSE GTO observing program (PI: T. Contini) whose goal is to study the impact of the environment on the morpho-dynamical properties of galaxies, including their dynamics, around redshift $z \approx 0.7$. To this end, 17 deep MUSE observations were carried out in the COSMOS field ([Scoville et al. 2007](#)), or more specifically in the area covered by the spectroscopic survey zCOSMOS ([Lilly et al. 2007](#)), each centred on at least one already known structure. Each observation was obtained during dark nights and under good seeing conditions with a PSF FWHM below $0.8''$. The locations of the fields were chosen so as to maximise the number of dense groups in each FoV based on the zCOSMOS group catalogue of [Knobel et al. \(2009, 2012\)](#) (groups between $z \approx 0.25$ and $z \approx 0.85$), and further refined with the COSMOS2015 photometric catalogue of [Laigle et al. \(2016\)](#) and the COSMOS-WALL catalogue of [Iovino et al. \(2016\)](#). Targeting structures already detected in previous works was necessary in order to maximise the detection rate and the sample statistics since blind observations with MUSE would have been otherwise too costly and much less efficient given the size of its FoV. Thus, there were 14 galaxy groups that were chosen for target selection of the 17 MUSE fields for a total on-source exposure time of 67 h, half of which were carried out in wide-field mode with the new ESO VLT Ground Layer Adaptive Optics (GLAO) facility GALACSI ([La Penna et al. 2016](#)). In this Thesis and in [Epinat et al. \(2018\)](#); [Boselli et al. \(2019\)](#); [Abril-Melgarejo et al. \(2021\)](#); [Mercier et al. \(2022\)](#); [Epinat et al. \(in prep.\)](#) each MUSE field was labelled after the name of the main targeted group given in the last version of the zCOSMOS group catalogue of [Knobel et al. \(2012\)](#). Their label writes CGRXXX, where XXX is the number of the group, which is the contraction of COSMOS GROUP NUMBER XXX. Similarly, we will label galaxies as

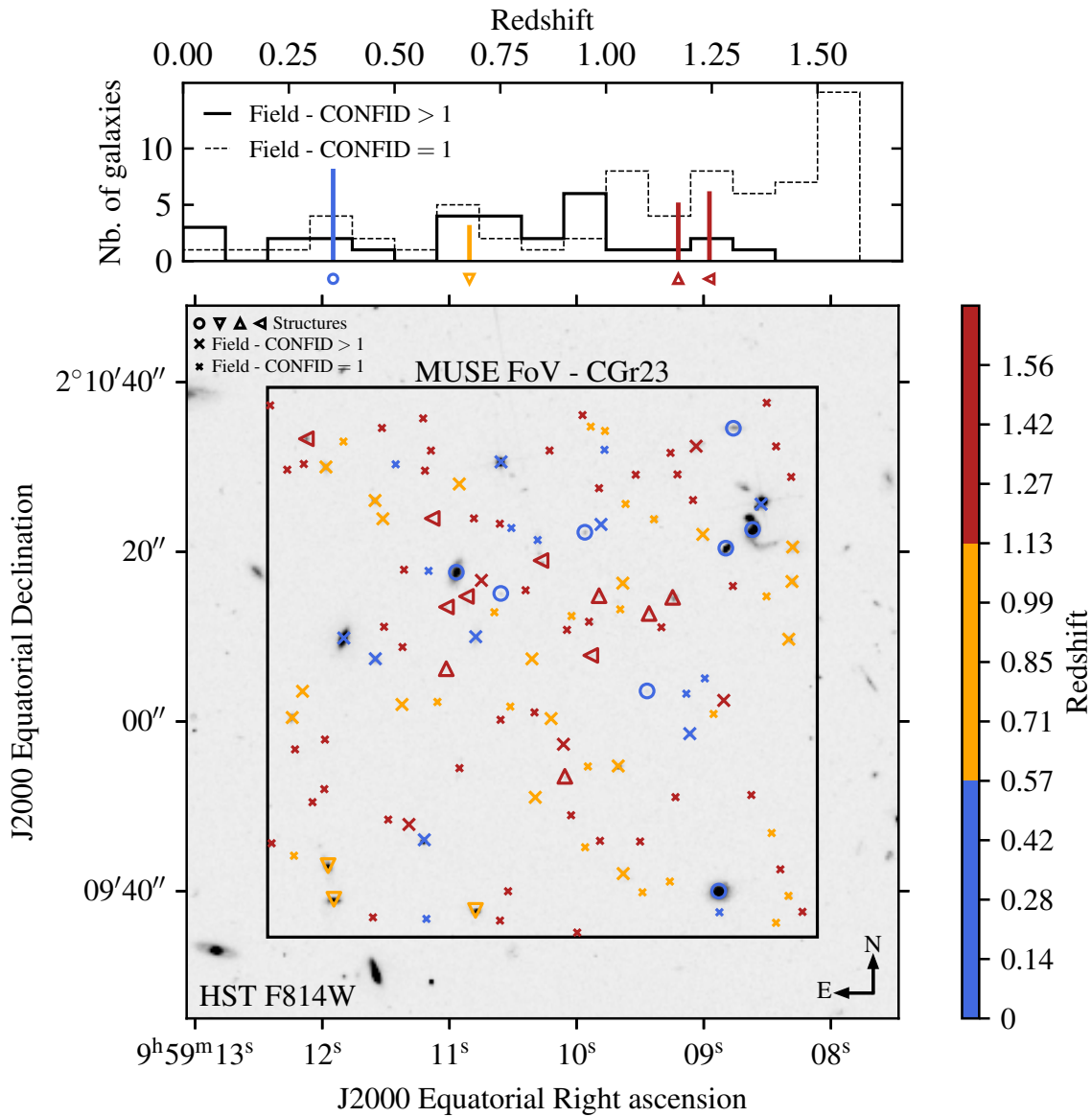


Figure 3.1: HST image of the MUSE observation CGR23. The main MUSE FoV is represented as a square with dimensions roughly equal to $1' \times 1'$, with north and east pointing up and left, respectively. The galaxies observed in the FoV are colour-coded according to their MUSE spectroscopic redshift. Field galaxies are shown with crosses whereas each structure is shown with its own marker (see the top left part of the main plot). Field galaxies with low redshift confidence flag (CONFID) are shown with smaller markers (by definition there are no such galaxies in the structures). On the top is shown the redshift histogram for field galaxies, segregated between low (black dashed line) and high (black solid line) CONFID value. The structures are shown with vertical lines with the same colour as that of the galaxies in the main plot and below each line is shown the corresponding symbol used in the main plot.

Table 3.1: Summary of the main characteristics of each MUSE field from Epinat et al. (in prep.).

Field	R.A.	Dec.	θ	Exposure	FWHM ₇₀₀₀	$\partial\text{FWHM}_{\text{PSF}}/\partial\lambda$	β_{PSF}
(1)	J2000 (2)	J2000 (3)	$^{\circ}$ (4)	h (5)	" (6)	"/ μm (7)	(8)
CGR23	149°47'34"	2°10'7"	0	1.00	0.615	-0.342	2.592
CGR26	150°29'30"	2°4'16"	35	1.00	0.586	-0.270	2.707
CGR28	150°13'32"	1°48'45"	-10	4.35	0.569	-0.368	2.594
CGR30	150°8'30"	2°3'60"	0	9.75	0.588	-0.282	2.606
CGR32-M1	149°55'14"	2°31'53"	30	4.35	0.480	-0.405	2.206
CGR32-M2	149°56'4"	2°31'24"	30	4.35	0.490	-0.406	2.037
CGR32-M3	149°55'10"	2°30'49"	30	4.35	0.546	-0.498	2.241
CGR34	149°51'24"	2°29'26"	-4	5.25	0.571	-0.236	2.825
CGR35	150°0'21"	2°27'23"	30	4.69	0.555	-0.447	2.448
CGR51	149°58'52"	1°47'55"	-30	1.00	0.577	-0.339	2.714
CGR61	149°43'34"	1°55'8"	-40	1.00	0.596	-0.344	3.320
CGR79	149°49'7"	1°49'19"	-20	4.35	0.501	-0.345	2.474
CGR84-M1	150°3'3"	2°35'48"	0	5.25	0.532	-0.249	2.568
CGR84-M2	150°3'35"	2°36'46"	0	4.35	0.608	-0.526	2.068
CGR87	150°1'31"	2°21'29"	-20	2.68	0.540	-0.368	2.191
CGR114	149°59'55"	2°15'32"	-15	4.38	0.588	-0.400	2.340
CGR172	150°10'16"	2°31'24"	0	4.69	0.481	-0.483	2.074

Notes: (1) MUSE field name, (2) equatorial right ascension (J2000), (3) equatorial declination (J2000), (4) FoV rotation angle with respect to the North (positive towards East), (5) total on-source exposure time, (6) FWHM at 7000 Å for a Moffat PSF, (7) linear gradient of the PSF FWHM with wavelength, and (8) beta parameter of the Moffat PSF profile.

YYY_CGRXXX, where YYY corresponds to the galaxy's ID. However, there are actually five slight exceptions to this rule when it was decided to do a mosaic of potentially extended groups. The first set of exception comes from the fact that one of the observed structures is not a dense group but a galaxy cluster: CGR32 (more than 100 members). This structure therefore required three MUSE FoVs to map it entirely and these individual fields are labelled as CGR32-MX with X running from one to three and where M stands for mosaic. Nevertheless, unless specified otherwise, their galaxy labels will always write YYY_CGR32 independently of which field they belong to (IDs are unique for the three combined MUSE fields so that there are no duplicates). The second set of exceptions is for CGR84. Indeed, similarly to CGR32, it was found that the density measured from the COSMOS2015 catalogue was high well beyond the structure's location so that a mosaic of two fields was used. The northernmost one was labelled CGR84-M1 and the southernmost CGR84-M2. In [Abril-Melgarejo et al. \(2021\)](#) and [Mercier et al. \(2022\)](#), and therefore in Chapter 6 as well, these two fields were labelled as CGR84 and CGR84-N instead (previous nomenclature) for the southern and northern structures, respectively.

An example of a MUSE field (CGR23) observed as part of the MAGIC survey is shown in Fig. 3.1 and the remaining of the fields are illustrated in Appendix B (see Fig. B.1 to B.14). The main MUSE FoV (or FoVs in the case of CGR32 and CGR84) is represented for each field as a black

square with north and east respectively oriented up and left. Field objects (galaxies and stars), that is those not associated to any structure (see Sect. 3.3 for how the structures were detected), are always represented as crosses and galaxies in structures are shown with various symbols (one symbol per structure, see the legend on the top left corner of each figure). Field galaxies are further separated between low confidence flag for the redshift estimate (CONFID, see Sect. 3.2.2 below) represented with small crosses and high CONFID value with large crosses (by definition there are only high CONFID galaxies in the structures, see Sect. 3.3). Furthermore, galaxies are colour-coded according to their redshift with the maximum value set to $z = 1.56$ to highlight the distribution of [OII] emitters, being the main population of galaxies studied in the MAGIC survey and in this Thesis¹. However, let us keep in mind that galaxies above $z = 1.56$ can be distributed well beyond this value, among which are found Ly α emitters located beyond redshift $z = 2.9$. Additionally, on top of each figure is shown the redshift histograms for the objects found in the FoVs. Field objects with high CONFID are represented with a black solid line whereas low CONFID objects are shown with a black dashed line. On the other hand, structures are represented as vertical lines with the same colour as that associated to their redshift. Furthermore, to help the reader easily identify the structures, below each vertical line is shown the symbol used to represent the corresponding structure in the HST image. As can be seen from Fig. B.1 to B.14, a large variety of structures can be found in the different MUSE fields. Field galaxies that are [OII] emitters tend to be spread out quite evenly between $z \approx 0.2$ and $z \approx 1.5$ for the majority of the fields, whereas galaxies in structures are mostly located in large structures in the redshift range $0.5 \leq z \leq 0.9$. Nevertheless, smaller structures (less than ten members or so) are also found above and below this range. We will go back in more details to the structure identification and their main characteristics in Sect. 3.3.

3.2 MUSE data and main survey properties

In this section, we briefly describe the data reduction process which was done for most of the MUSE fields before the start of this Thesis. We also quickly discuss in Sect. 3.2.2 how spectroscopic redshifts were determined from the MUSE spectra and how they are distributed for field galaxies and those located in structures.

3.2.1 MUSE data for the MAGIC sample

At the start of this Thesis, data reduction had already been done for 14 out the 17 MUSE fields. The last observations of CGR35, CGR87, and CGR172 being obtained in the first few months of this work, the data reduction was performed quickly afterwards so that science-ready data cubes for these fields were available as early as the beginning of the year 2020. Similarly to what was done in the MUSE-HDFS survey (Bacon et al. 2015), the final data cube for each field was obtained by combining Observing Blocks (OBs) composed of four 900 s exposures. Between each exposure a small dithering pattern and a 90° rotation of the FoV were performed so that every pixel, except perhaps those near the centre, would fall into different channels (see Sect. 2.2.3). Among the 17 MUSE fields, 12 have integration times larger than

¹Note that in this Thesis [OII] emitters refer to galaxies whose redshift falls in the $0.2 \lesssim z \lesssim 1.5$ range where the [OII] doublet could theoretically be detected. Thus, it includes galaxies for which the [OII] doublet is indeed detected as well as galaxies that do not possess it in their spectrum. For instance, this includes quenched galaxies at $0.2 \lesssim z \lesssim 1.5$ whose redshift is determined from their absorption lines and features.

4 h 20 min, one is slightly above two and a half hours and four fields only have one hour. The location of the FoVs, as well as their rotation angle with respect to the north, and their on-source exposure time are summarised in Table. 3.1. Each OB was processed through the MUSE standard pipeline described in [Weilbacher et al. \(2020\)](#) that includes all the common steps to process raw data from 3D spectrographs such as but not limited to producing bad pixel tables, bias frames, dark frames, flat-fields, flux calibration, sky subtraction. Sky subtraction was applied on each exposure separately before aligning and then combining them using stars in the FoV and was further improved by applying the Zurich Atmosphere Purge (ZAP) software ([Soto et al. 2016](#)) on the final data cube. For more details about the data reduction process, see the survey paper ([Epinat et al., in prep.](#)).

3.2.2 Redshift determination

Contrary to what was done in the MUSE-HDFS and MUSE-HUDF surveys ([Bacon et al. 2015, 2017](#)), galaxies in the MAGIC survey were not blindly detected since multi-band photometric observations were required to derive key physical parameters such as their stellar mass or SFR. Instead, any object listed in the COSMOS2015 catalogue of [Laigle et al. \(2016\)](#) that fell in one of the MUSE FoVs was added to the MAGIC catalogue and had its redshift and physical properties derived. Recently, this step was further refined by using the newest COSMOS2020 catalogue of [Weaver et al. \(2022\)](#). Because this last step was done quite recently, these new galaxies do not appear in [Abril-Melgarejo et al. \(2021\)](#), [Mercier et al. \(2022\)](#), and in Chapter. 6 but are taken into account in the analysis of the angular momentum presented in Chapter 7. In both COSMOS2015 and COSMOS2020 catalogues the 3σ limiting magnitude measured in an aperture of $3''$ is $z_{\text{app}}^{++} < 25.9$ (25.7 in COSMOS2020, see [Laigle et al. 2016](#); [Weaver et al. 2022](#)). This means that galaxies brighter than this limit are present in the COSMOS catalogue and are therefore also part of the MAGIC catalogue. Thus, the MAGIC survey is technically speaking almost magnitude-limited in the sense that the flux limit does not come from the MUSE observations themselves but from COSMOS. Nevertheless, as will be quickly discussed in Sect. 3.2.3, this is not particularly problematic as the MAGIC survey is nearly complete up to an upper apparent magnitude of roughly 24.5 in the z^{++} band, that is within the detection limit of the COSMOS catalogue.

Beforehand, galaxies in the MAGIC survey only had photometric redshifts from COSMOS, except those observed with the VIMOS multi-object spectrograph as part of the zCOSMOS and COSMOS-WALL observations. However, MUSE is a 3D spectrograph which means that for any object in the catalogue a spectrum can be extracted and a (potentially tentative) redshift can be measured. Thus, for each object a PSF-weighted spectrum was extracted and a redshift was measured similarly to what was done in [Bacon et al. \(2015, 2017\)](#) and [Inami et al. \(2017\)](#) for the MUSE-HDFS and MUSE-HUDF surveys. To be more precise, this was achieved with the help of the redshift finding algorithm Manual and Automatic Redshifting Software (MARZ) described in [Hinton et al. \(2016\)](#) using absorption and emission lines and continuum features. Depending on the redshift of the galaxy, the main absorption lines are the Balmer lines, CaII H, CaII K, and the G-band from CH molecules. The main emission lines are also the Balmer lines (chiefly $H\alpha$ but also $H\beta$), [OII], [OIII], whereas continuum features are the Balmer break, the Lyman break, and D4000. We refer the reader to Fig. 2.5 for more details as to which lines and features are available depending on the redshift of the galaxies and whether AO is used or not. For each object a redshift was assigned with a given confidence flag (hereafter CONFID) ranging from zero to three:

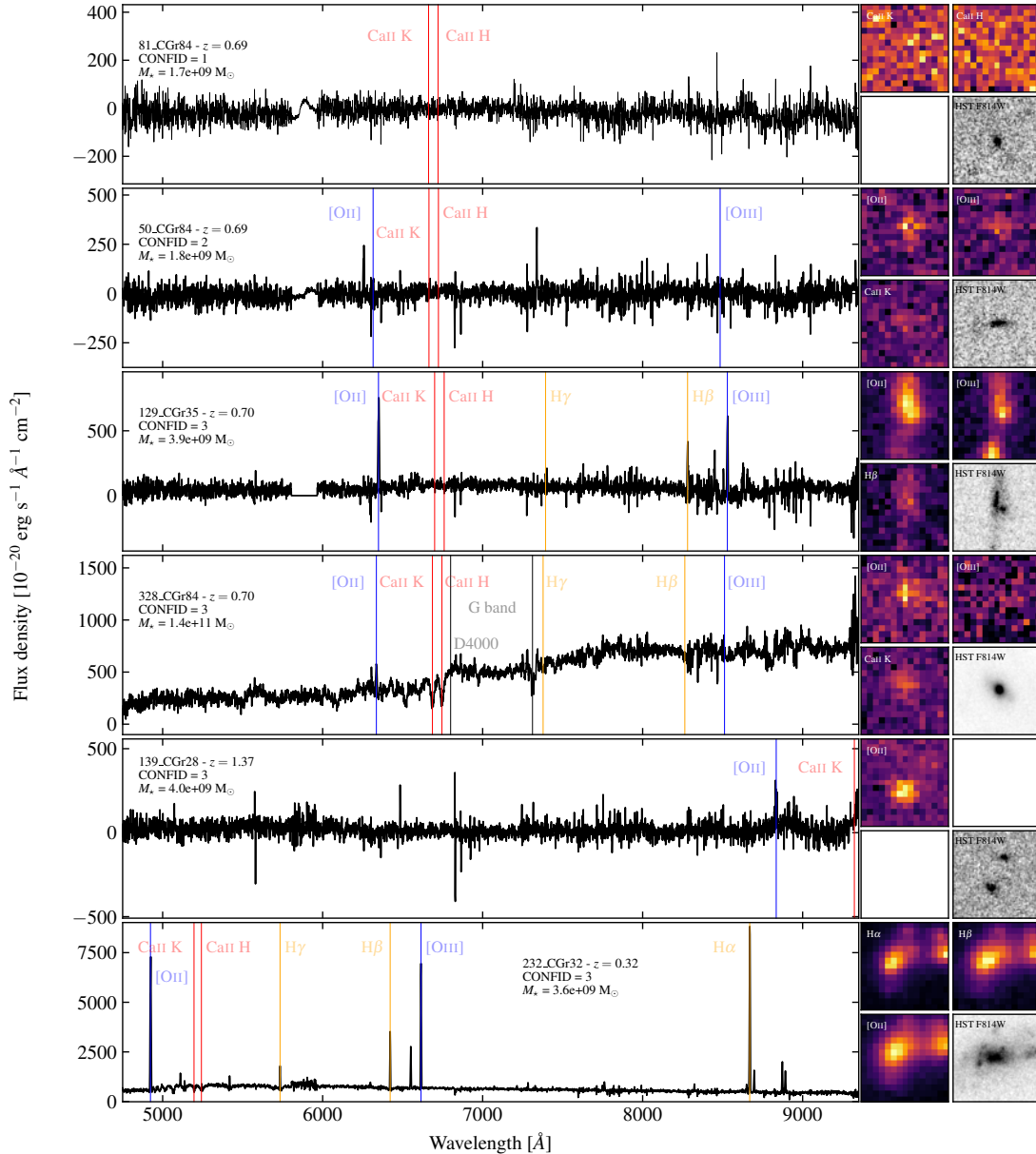


Figure 3.2: Examples of MUSE spectra and their main spectral features extracted in a $3''$ aperture for six different types of galaxies. From top to bottom: (i), (ii), and (iii) 81_CGr84, 50_CGr84, and 129_CGr35, three galaxies with similar redshift ($z \approx 0.7$) and stellar mass ($M_* \approx 10^9 M_\odot$) and with a low, intermediate, and high spectroscopic redshift confidence flag (CONFID), respectively, (iv) 328_CGr84, a galaxy similar to 129_CGr35 but with a high stellar mass, (v) 139_CGr28, a galaxy similar to 129_CGr35 but found at higher redshift, and (vi) a galaxy similar to 129_CGr35 but found at lower redshift. To the right of each spectrum are shown three MUSE narrow band images for different absorption and emission lines taken by collapsing the cube in a window of ten spectral pixels (spexels) around the line after removing the continuum and the corresponding HST image in the F814W band. All images have a dimension of $3'' \times 3''$. The gap visible between roughly 5800 \AA and 6000 \AA for the three first galaxies on the top is due to the sodium laser of the AO system. We can see how much more resolved become the spectral features when going from a low to a high CONFID value as well as how it becomes more and more difficult to detect strong emission lines when a galaxy get close to the MUSE desert that starts at $z \approx 1.5$.

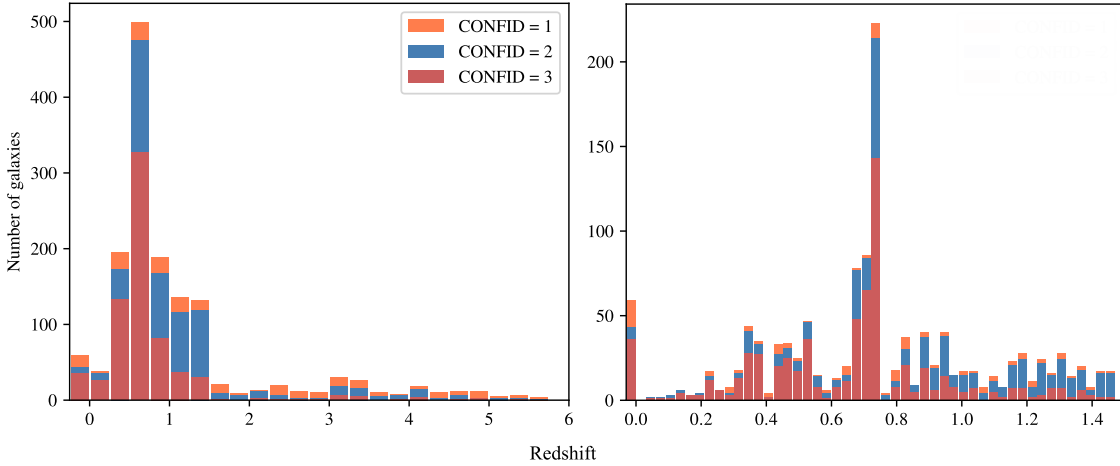


Figure 3.3: Redshift distribution of the whole MAGIC survey from Epinat et al. (in prep.) including galaxies and stars (shown in the negative bin), for different confidence flags (CONFID): (1) tentative, (2) confident, and (3) highly confident. An inset zoomed-in on the [O II] emitters redshift range is also shown with smaller redshift bins to highlight the location of the structures. The bulk of the galaxies are located in the redshift range $0.2 \lesssim z \lesssim 1.5$ which corresponds to the redshift at which the [OII] doublet falls in the MUSE wavelength range ([OII] emitters). Beyond $z \approx 1.5$ there is a sheer drop in detection because of the MUSE redshift desert. The detections rise slightly again after $z \approx 2.9$ because $\text{Ly}\alpha$ enters the wavelength range. Overall, most [OII] emitters have confident MUSE spectroscopic redshifts (CONFID ≥ 2).

a value of zero means that no spectroscopic redshift was assigned, a value of one represents a tentative redshift that was chosen without any strong spectroscopic features visible, a value of two represents a confident redshift measurement that is based on a few faint lines or on a single strong feature (e.g. bright emission line), and a value of three corresponds to a highly confident redshift measurement that was based on multiple strong features (usually multiple bright absorption and emission lines). Examples of different spectra are shown in Fig. 3.2. I represent from top to bottom three galaxies with similar redshift $z \approx 0.7$ and stellar mass $M_* \approx 10^9 M_\odot$ but with different CONFID values (81_CGR84, 50_CGR84, and 129_CGR35), as well as galaxy 328_CGR84 that is similar to 129_CGR35 in terms of redshift and CONFID but with a much higher stellar mass around $10^{11} M_\odot$ and two more galaxies, 139_CGR28 and 232_CGR32, also similar to 129_CGR35 in terms of stellar mass and CONFID with the first found at a higher redshift ($z \approx 1.4$) and the second at a lower redshift ($z \approx 0.3$). MUSE narrow-band images are also shown on the right-hand side of each spectrum centred on various absorption or emission lines and computed by collapsing the cube in a ten spexels window around each line after removing the continuum. As an indication, I also show the corresponding HST images of the galaxies in the F814W band. We can clearly see how spectral features become much more visible, and in particular how emission lines become brighter, as we go from CONFID = 1 to CONFID = 3. Additionally, we also see the wealth of emission lines available for relatively low redshifts and how bright emission and absorption lines fall out the MUSE range when we reach the beginning of the redshift desert at $z \approx 1.5$.

The redshift distribution of the entire MAGIC survey is shown in Fig. 3.3 with the highest CONFID shown in red and the lowest in orange, including galaxies but also stars represented in the negative redshift bin. The bulk of the galaxies are [OII] emitters, as expected given that all of the targeted groups fall within this redshift range and because it is one of the brightest emission lines available after H α . The [OII] emitters represent a key population of emission line galaxies that was targeted by the MAGIC survey and which has been used in Abril-Melgarejo et al. (2021); Mercier et al. (2022) and in Chapters 6 and 7 to derive the galaxies' kinematics and study the impact of the environment on their dynamical properties. Beyond $z \approx 1.5$ a sheer drop in detection is visible in Fig. 3.3 which is due to the galaxies entering the MUSE redshift desert (see Sect. 2.2.3). Beyond $z \approx 2.9$, the detection rises moderately because of the Ly α line entering the MUSE wavelength range. Nevertheless, the growth is not as significant as for the MUSE-HDFS and MUSE-HUDF surveys. This is because, as was previously stated, no blind detection was performed (except in a single field, CGR30) which significantly reduces the number of observed Ly α emitters. Besides, every field in the MAGIC survey is shallower than both the MUSE-HDFS and the MUSE-HUDF, thus further hindering the ability to detect such high-redshift objects. Overall, most of the derived MUSE spectroscopic redshifts are secure with CONFID values larger than or equal to two. For the entire redshift range, the objects with a CONFID equal to one only amount to roughly 16%. When restricting to [OII] emitters only, this number drops below 9%, showing the strength of MUSE in deriving precise spectroscopic redshifts in this redshift range.

3.2.3 Survey completeness

The goal of this short section is not to give a full account of the completeness of the full MAGIC survey but rather to highlight the values that we get for the main population of galaxies that were targeted, that is [OII] emitters. A more thorough description will be given in the survey paper (Epinat et al., in prep.). The completeness is shown in Fig. 3.4 for the entire redshift range as a function of the apparent z^{++} magnitude (z_{app}^{++}). In our case, the completeness was defined as the number of galaxies with secure spectroscopic redshifts ($\text{CONFID} \geq 2$) divided by the total number of galaxies with a photometric redshift, and this in bins of redshift and apparent magnitude. Thus, the completeness is a measure of our capacity to securely measure the galaxies' redshifts. A value of unity means that 100% of the galaxies in the bin found in the photometric catalogue had their spectroscopic redshift precisely measured, whereas a null value means that no spectroscopic redshift could be correctly measured in the bin. We can see that the survey is nearly complete (at least above 80%) for the [OII] emitters redshift range up to an apparent upper magnitude of $z_{\text{app}}^{++} \approx 24.5$. Above this value, it quickly drops close to a few percent and to zero beyond the COSMOS limiting magnitude. The very high completeness for the [OII] emitters combined with the fact that the [OII] doublet is a bright emission line therefore make them the perfect galaxy population in the MAGIC survey to study the impact of the environment on their dynamical properties. Note that the completeness in the [OII] emitters range is different from the fraction of star-forming galaxies with the [OII] doublet detected. Indeed, as already stated in footnote 1 of this chapter, the [OII] emitters sample corresponds to galaxies in the redshift range $0.25 \leq z \leq 1.5$ where the [OII] doublet can be theoretically detected. Thus, among this sample are found star-forming galaxies that have the [OII] doublet in their spectrum as well as passive galaxies that do not have it but whose redshift can be determined from their absorption lines. As an indication, among the 1142 galaxies that are part of the [OII] emitters sample, 20% do not have any [OII] doublet detected at all and this number rises to 40% when including galaxies whose

[OII] doublet detection is below the 3σ level. As an indication, this corresponds to a flux detection limit of roughly² $2 \times 10^{-18} \text{ erg s}^{-1} \text{ cm}^{-2}$ which can be converted into a [OII]-derived SFR lower limit of roughly $0.1 M_{\odot} \text{ yr}^{-1}$ at the median redshift of the structures in MAGIC (i.e. $z \approx 0.7$, see Sect. 3.2.5.2 for the details of the derivation of the SFR from the [OII] doublet flux).

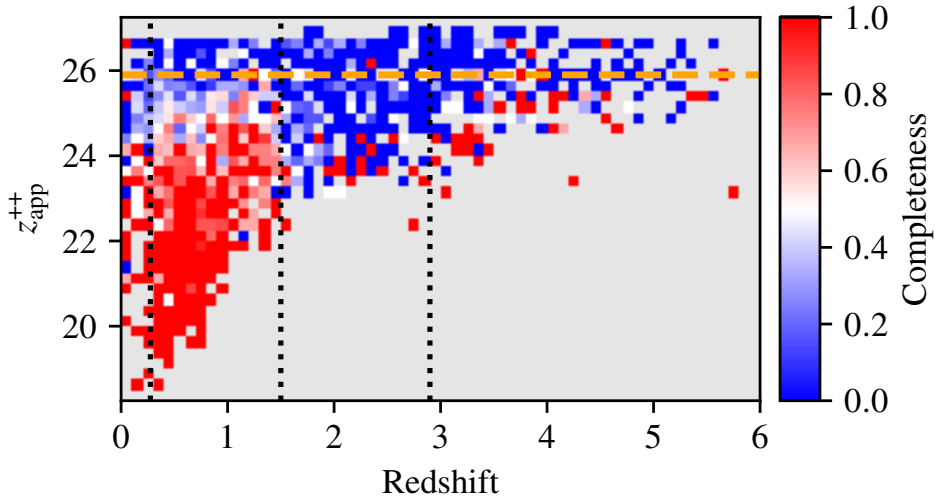


Figure 3.4: Completeness of the MAGIC survey as a function of redshift and apparent (z_{app}^{++}) magnitude in the z^{++} band adapted from Epinat et al. (in prep.). The orange dashed line represents the limiting magnitude of COSMOS and the black dotted vertical lines show, from left to right, the minimum redshift for [O II] emitters, the maximum redshift for [O II] emitters, and the minimum redshift for Ly α emitters to be detected in the MUSE wavelength range. Up to a $z_{\text{app}}^{++} \approx 24.5$ the completeness is very high for the [O II] emitters range.

Complementarily to what is shown in Fig. 3.3, the completeness drops to zero beyond $z = 1.5$ because of the [OII] doublet leaving the MUSE wavelength range and the galaxies entering the MUSE redshift desert. Past $z \approx 2.9$, it rises significantly again, though only for the intrinsically brightest sources, due to the Ly α line entering the wavelength range.

3.2.4 PSF and LSF measurements

An important aspect of dynamical studies such as those carried out as part of the MAGIC survey require a precise knowledge of both the PSF and the LSF. Indeed, in our MUSE data the LSF will affect each spixel by broadening the absorption and emission lines, whereas the PSF will blend in each spixel the signal coming from every other spixel in the cube. When extracting and modelling the stellar or gas kinematics of a galaxy out of a data cube, both the PSF and the LSF impact the velocity field and velocity dispersion map and it is referred to as beam smearing (see Sect. 5.3.2 for a discussion of its impact on kinematics maps and models).

²This value was estimated in Mercier et al. (2022) but there is a typo in the text with the minus sign missing. The correct value is the one given in this Thesis.

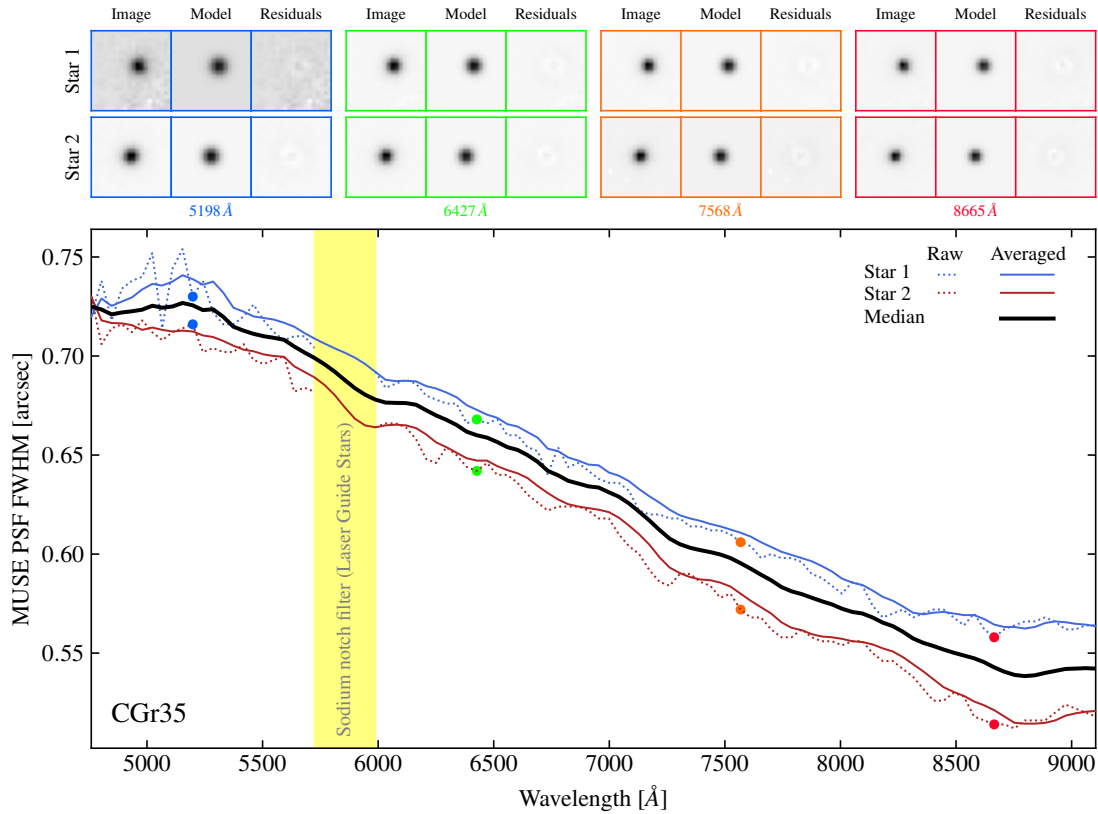


Figure 3.5: Illustration of the fitting procedure to measure the wavelength dependence of the MUSE PSF FWHM for CGR35. Examples of GALFIT Gaussian fits for the two stars found in the field are shown on the top for four different wavelengths. Below is shown the raw (dotted lines) and the rolling-averaged wavelength variation of the PSF FWHM for the two stars, as well as the median curve used to derive the linear trend (thick black solid line). The FWHM values measured from the examples of the two stars are shown as circles with the same colour as the frames of the images. The raw lines are cut between roughly 5700 \AA and 6000 \AA since no data was available in this range because of the sodium notch filter (due to AO, shown in light yellow). The rolling-averaged curves were interpolated before deriving the median curve.

3.2.4.1 LSF variation with wavelength

The MUSE LSF was the easiest of the two quantities to parametrise. To do so, we used the prescription of [Bacon et al. \(2015\)](#) and [Guérou et al. \(2017\)](#) who fitted with a Gaussian profile sky emission lines spread throughout the MUSE wavelength range in the MUSE-HDFS and UDF-10 (MUSE-HUDF) data cubes. As discussed in Sect. 3.1 of [Guérou et al. \(2017\)](#), for both data cubes the LSF FWHM variation with wavelength is well described by a similar second order polynomial given by

$$\text{FWHM}_{\text{LSF}}(\lambda) = \lambda^2 \times 5.866 \times 10^{-8} - \lambda \times 9.187 \times 10^{-4} + 6.040, \quad (3.1)$$

where FWHM_{LSF} and λ are both in angstrom, with λ the observed wavelength. Equation 3.1 was found to be very robust when measured from one spaxel to another, with variations of the order of 0.05 Å, and for two different data cubes obtained from observations carried at different observing periods. Thus, we did not try to model once again the LSF in MAGIC and used Eq. 3.1 throughout.

3.2.4.2 PSF modelling

The modelling of the PSF is a bit trickier because it is expected to change from one cube to another and must therefore be modelled independently for each MUSE field. Furthermore, it is also expected to vary with wavelength and might as well change depending on where the galaxies are located in the FoV. However, the lack of bright stars at multiple enough locations in the cubes made it difficult, if not impossible at all, to precisely measure any spatial variation of the PSF. Therefore, only the wavelength dependence was modelled and it was assumed to be constant at a given wavelength throughout the MUSE FoV.

Initially, the PSF was measured in [Abril-Melgarejo et al. \(2021\)](#) for all the MUSE fields except for CGR35, CGR87, and CGR172 since the observations for these three fields were not over yet at the time. Because the only galaxies studied in [Abril-Melgarejo et al. \(2021\)](#) were all located in groups and because earlier results from the MUSE-HDFS ([Bacon et al. 2015](#)) and MUSE-HUDF ([Bacon et al. 2017](#)) surveys showed that the PSF FWHM dependence with wavelength can be approximated by a linearly decreasing function, the way it was first measured was to (i) find all the bright, but non-saturated, stars located in the fields, (ii) select every group studied in the analysis, (iii) for each group extract, for each star in the FoV, narrow-band images around the observed wavelengths of [OII] and [OIII], and then (iv) fit each narrow-band with a Gaussian profile to retrieve the PSF FWHM at two different wavelengths. In [Mercier et al. \(2022\)](#), the value of the MUSE PSF FWHM at the observed wavelength of [OII] (being the emission line used for the kinematics) was computed for each galaxy by interpolating in-between or extrapolating beyond the two values measured in [Abril-Melgarejo et al. \(2021\)](#), assuming a linearly decreasing relation. In addition, CGR35, CGR87, and CGR172 were also incorporated into the analysis and therefore required their MUSE PSF to be measured as well. A quick description of how it was done is given in Sect. 2.1 of the paper and in Chapter 6, but we describe it in slightly more details below.

Since the approach was different from [Abril-Melgarejo et al. \(2021\)](#) in the sense that we were now looking at galaxies in structures and in the field throughout the whole redshift range of [OII] emitters ($0.2 \lesssim z \lesssim 1.5$), I decided to use a more robust method to derive the FWHM dependence with wavelength for these fields. After identifying bright but non-saturated stars, as well as a low

surface brightness unresolved object located at $z \approx 2.67$ for CGR87, 100 sub-data cubes with dimensions 10×10 pixels³ were extracted for each star (and for the unresolved object). The sub-data cubes were then collapsed into narrow-band images with a fixed redshift slice of $\Delta z = 0.01$ that converts to a wavelength slice of $\Delta\lambda = \Delta z \times \lambda$. Each narrow-band was fitted independently of the others using GALFIT with symmetric (i) Gaussian and (ii) Moffat profiles with free β parameter. Since results did not differ significantly between both models and to remain consistent with what was done in [Abril-Melgarejo et al. \(2021\)](#) the Gaussian model was kept. For each MUSE field, the wavelength dependence of the PSF FWHM was measured by (i) applying a rolling-average to the FWHM-wavelength curve of each star to remove small scale variations, (ii) median combining the averaged curves of all the stars in each field, and then (iii) fitting each median line with a linearly decreasing function. This procedure is illustrated for CGR35 in Fig. 3.5. Examples of GALFIT fits performed on two stars for four different wavelength values are shown on the top and the PSF wavelength dependence is shown below. In particular, the initial raw dependence is shown with dotted lines, the 5700 Å to 6000 Å range missing because of the sodium notch filter due to AO observations, the rolling-averaged curves as thin solid lines, and the median relation as the thick black solid line.

Even if the linear fit does not capture the full complexity of the wavelength dependence of the MUSE PSF FWHM, the clear advantage of using this method over the one used in [Abril-Melgarejo et al. \(2021\)](#) is that the relation that is derived does not depend on potential fluctuations that would happen at the [OII] and [OIII] wavelengths, therefore rendering it much more robust. Thus, as part of the MAGIC survey paper (Epinat et al., in prep.), it was decided to update the MUSE PSF values using the method described above at the exceptions of (i) extracting narrow-band images in an aperture of $6'' \times 6''$, (ii) collapsing them in a fixed wavelength interval of 100 Å, and (iii) modelling the stars with a flat background plus a Gaussian/Moffat profile, the latter being retained in the end. Thus, at present all MUSE fields have had their PSF measured in a consistent way and these values are the ones used in the analysis of the angular momentum in Chapter. 7. The parameters for the parametrisation of the PSF are given in columns (6), (7), and (8) of Table. 3.1. Column (6) represents the FWHM at a wavelength of 7000 Å (FWHM_{7000}) and column (7) represents the linear gradient of the FWHM with wavelength ($\partial\text{FWHM}_{\text{PSF}}/\partial\lambda$). Thus, the parametrisation writes

$$\text{FWHM}_{\text{PSF}}(\lambda) = \frac{\partial\text{FWHM}_{\text{PSF}}}{\partial\lambda} \times (\lambda - 0.7) + \text{FWHM}_{7000}, \quad (3.2)$$

where λ is the observed wavelength in μm . Column (8) provide the β parameter of the Moffat profile. For the three latest MUSE fields CGR35, CGR87, and CGR172, the difference between this new modelling and the previous one is negligible since they are nearly identical. For the other fields, it leads to differences in FWHM of at most $0.3''$ at the blue end of the spectrum and $0.2''$ at the red end. Furthermore, because the PSF FWHM was updated after the analysis carried out in [Mercier et al. \(2022\)](#), we checked whether this would affect the best-fit kinematics parameters, in particular the circular velocity (see Sect. 5.2.1 and Chapter 6). Apart from a few galaxies that had poorly constrained kinematics parameters in the first place, no significant impact could be found.

³MUSE pixels, $0.2''$ across

3.2.5 Derivation of galaxies' physical parameters

Galaxies' key physical parameters such as their stellar mass or their SFR were derived from SED fitting using the photometric bands available in the COSMOS catalogue of [Laigle et al. \(2016\)](#) in combination with their MUSE spectroscopic redshift. SED fitting is a complicated modelling process that relies on many assumptions and libraries. The point of this section is to briefly describe how the physical parameters were derived before discussing the physical properties of field galaxies and those in structures. More details can be found in Sect. 8.1.1 where the models, their parameters, and their underlying assumptions used in SED fitting, especially in the case of the Code Investigating GALaxy Emission (CIGALE), will be discussed.

3.2.5.1 Early derivations with FAST

In [Epinat et al. \(2018\)](#), [Boselli et al. \(2019\)](#), and [Abril-Melgarejo et al. \(2021\)](#), these parameters were derived using the SED fitting code FAST ([Kriek et al. 2009](#)). In total, 29 out of the 32 bands of the COSMOS2015 catalogue were used and each galaxy's SED was modelled using a synthetic library generated from the Single Stellar population (SSP) models of [Conroy & Gunn \(2010\)](#) with a [Chabrier \(2003\)](#) initial mass function (IMF), a [Calzetti et al. \(2000\)](#) extinction law, and an exponentially declining star formation history (SFH). These physical parameters were also used in [Mercier et al. \(2022\)](#) except for the SFR. Indeed, when compared with that given in the COSMOS catalogue, computed with the Photometric Analysis for Redshift Estimate (LEPHARE)⁴ code, the SFR values had an average difference of about 0.8 dex, which was three to four times larger than the discrepancy observed in stellar mass. Besides, the MS relation obtained with FAST is quite discretised and galaxies seem to be capped to an upper limiting line. Thus, because stellar masses seemed consistent between the two SED modellings but not the SFRs, because of the sparsity of the $M_\star - \text{SFR}$ grid, and because of the presence of this limiting line, we decided to not rely on the SFR values from FAST.

3.2.5.2 Star formation rates from the [OII] doublet

In [Mercier et al. \(2022\)](#), the SFRs were computed from the [OII] doublet luminosity using the [Kennicutt \(1992, 1998\)](#) relation after correcting for Galactic and intrinsic dust extinctions:

$$\text{SFR} \text{ [M}_\odot \text{ yr}^{-1}] = (1.4 \pm 0.4) \times 10^{-41} L_{[\text{OII}]} \text{ [erg s}^{-1}], \quad (3.3)$$

where $L_{[\text{OII}]}$ is the [OII] luminosity corrected for extinction. This relation relies on a [Salpeter \(1955\)](#) IMF but it is possible to convert it to other IMFs. For instance, to recover the SFR with a [Kroupa \(2002\)](#) IMF Eq. 3.3 must be multiplied by a factor of 1.5 ([Gilbank et al. 2010](#)) and in the case of a [Chabrier \(2003\)](#) IMF Eq. 3.3 must be multiplied by a factor of 0.62 ([Boogaard et al. 2018](#)). Ideally, we would have used $\text{H}\alpha$ to compute the SFR as it is more robust ([Kennicutt 1998](#)) but the line is not available for the entire redshift range for the [OII] emitters. Besides, modulo a larger scatter, the [OII] doublet is also a good tracer of star formation. The luminosity is linked to the flux of the galaxy through the usual equation

$$L_{[\text{OII}]} = 4\pi D_L^2 F_{[\text{OII}],\text{corr}}, \quad (3.4)$$

⁴<https://www.cfht.hawaii.edu/~arnouts/LEPHARE/lephare.html>

where D_L is the luminosity distance (see Sect. 1.1.4) and $F_{[\text{OII}],\text{corr}}$ is the flux corrected of extinction. Following Kennicutt (1998), the correction of the observed flux $F_{[\text{OII}]}$ ⁵ must be computed by taking into account the Galactic extinction $A_{[\text{OII}],\text{MW}}$ at the observed [OII] wavelength and the intrinsic extinction of the galaxy computed at the rest-frame $\text{H}\alpha$ wavelength ($A_{\text{H}\alpha}$) using the formula

$$F_{[\text{OII}],\text{corr}} = F_{[\text{OII}]} \times 10^{0.4(A_{\text{H}\alpha} + A_{[\text{OII}],\text{MW}})}. \quad (3.5)$$

In Eq. 3.5, we must use the intrinsic extinction at the rest-frame wavelength of $\text{H}\alpha$ rather than at that of [OII], as might be expected, because of the way the [OII] fluxes were calibrated in Kennicutt (1998). For both extinctions, one needs a model to go from an observed or derived quantity (e.g. from SED fitting) such as the extinction in the V band to the value at the required wavelength. We decided to use a Cardelli et al. (1989) law for the Galactic extinction. We do not write explicitly its expression because it is a complex polynomial function by segments whose coefficients vary depending on which part of the spectrum it is evaluated. It provides a parametrisation of the ratio between the Galactic extinction $A(\lambda)$ at a given wavelength and that in the V band (A_V) as a function of wavelength. Thus, one needs to know A_V to derive the Galactic extinction at the wavelength of the observed [OII] doublet. This was done by using a total-to-selective extinction ratio $R_V = 3.1$, as is usual for the Milky Way, and the colour excess between the B and V bands $E(B - V)$ provided by FAST. By definition, the V band extinction and the colour excess are linked through the following relation:

$$A_V = R_V \times E(B - V), \quad (3.6)$$

where $E(B - V)$ is defined as

$$\begin{aligned} E(B - V) &= A_B - A_V \\ &= (m_B - M_B) - (m_V - M_V) \\ &= (m_B - m_V) - (M_B - M_V), \end{aligned} \quad (3.7)$$

with A_B the extinction in the B band and where the symbol m represents an apparent magnitude and the symbol M an absolute magnitude corrected for extinction. The k-correction does not appear in Eq. 3.7 because the dust in the Milky Way affects the redshifted light and not the intrinsic one. Since the extinction in the B band is higher in our Galaxy than in the V band, the flux in the B band will be more severely affected and the apparent magnitude in this band will therefore increase more significantly producing an excess of colour, hence the name.

We could have done a similar derivation for the intrinsic extinction using the A_V value provided by FAST and a model for the extinction law such as a Calzetti et al. (2000) curve but, as for the SFR, the large uncertainties on this parameter dissuaded us from using it. Instead, we relied on a prescription given by Gilbank et al. (2010, 2011) that empirically parametrises the $\text{H}\alpha$ extinction as a function of stellar mass for the [OII] doublet when used to derive the SFR with the Kennicutt law. This parametrisation writes

$$A_{\text{H}\alpha} = 51.201 - 11.199 \log_{10} \left(\frac{M_\star}{M_\odot} \right) + 0.615 \log_{10}^2 \left(\frac{M_\star}{M_\odot} \right), \quad (3.8)$$

⁵The total flux is measured from the best-fit double Gaussian fit performed on the [OII] doublet. See Sect. 5.3.1.2 for more details.

for stellar masses above $10^9 M_{\odot}$ and a constant value below.

3.2.5.3 New derivation with Cigale

For the survey paper (Epinat et al., in prep.) and following the release of the new COSMOS2020 version of the catalogue (Weaver et al. 2022), the physical parameters were derived again with the latest photometric measurements using CIGALE⁶. A description of the main parameters and their range of values is shown in Table 3.2. Briefly, for this modelling the SSPs that were used are those of Bruzual & Charlot (2003) using a Salpeter (1955) IMF with a fixed metallicity of 0.02 dex. The SFH that was used is called a truncated delayed exponential law (see Ciesla et al. 2018, 2021) and it corresponds to a delayed exponential law (i.e. $SFH \sim t \times \exp\{-t/\tau\}$, with τ the e-folding time of the SFH) followed by a truncation episode of constant star formation that can be lower (quenching) or larger (burst) than the value of the SFH just before the episode. This phenomenological model allows to reduce biases when measuring the stellar mass and the SFR of quenched and starburst galaxies from SED modelling (Ciesla et al. 2018, 2021). Thus, the truncation episode was forced to happen at the very end of the SFH, with an age below 100 Myr (see Table. 3.2 for the full list of values). Finally, we used a modified starburst attenuation law (Boquien et al. 2019) which, for the parameters that were used, reduces to a Charlot & Fall (2000) law with a total-to-selective extinction ratio $R_V = 3.1$ and a colour excess varying from 0.001 to 0.7.

Two important parameters that come out of SED fitting are the galaxies' stellar mass and their SFR. In CIGALE, the stellar mass is not a free parameter as in for instance LEPHARE but is derived by scaling the SFH to the data (for more details, see Boquien et al. 2019). Similarly, the SFR is not fitted directly but is a product of the modelling. What is truly fitted are the free parameters of the SFH that will determine the value of the SFR. By default, CIGALE provides three different values: (i) the instantaneous SFR (noted SFR_{inst}) which corresponds to the SFH evaluated during the last 1 Myr time-step, (ii) an average value computed over a short period of 10 Myr, and (iii) an average value computed over a longer period of 100 Myr. A comparison between the three different values is shown in Fig. 3.6. It is clear that the instantaneous SFR and the average value over 10 Myr are similar for most of the galaxies. The main reason is certainly that below 10 Myr the truncation episode that leads either to a burst or to a quenching of star formation has already happened for the majority of the galaxies. But, the SFH becomes constant afterwards and therefore there is no further changes in SFR. Only for galaxies that are modelled with a late truncation episode does this change, though the effect remains moderate. On the other hand, the discrepancy is much larger when using the average value over 100 Myr. Indeed, this corresponds to the time when the truncation is allowed to take place for the first time. Thus, this value will be sensitive to both the smooth part of the SFH and to the truncation. This is visible in Fig. 3.6 where the 100 Myr average value is larger than the instantaneous one for most of the galaxies given that CIGALE models most of them with a quenching phase. Star formation rates can be derived in various ways (emission line, ultra-violet or blue bands, emission in the infrared, etc.) but none of these methods provides an SFR estimate over a period as short as 1 Myr. The 10 Myr average value can be seen as a good compromise since it roughly corresponds to the timescale over which the SFR is measured when using emission lines. However, as is shown in Fig. 3.6, it is quite sensitive to the late truncation episode so one has somehow to trust that such an episode occurred in order to use it. Lastly, the 100 Myr average value is also a SFR proxy candidate which is much

⁶<https://cigale.lam.fr/>

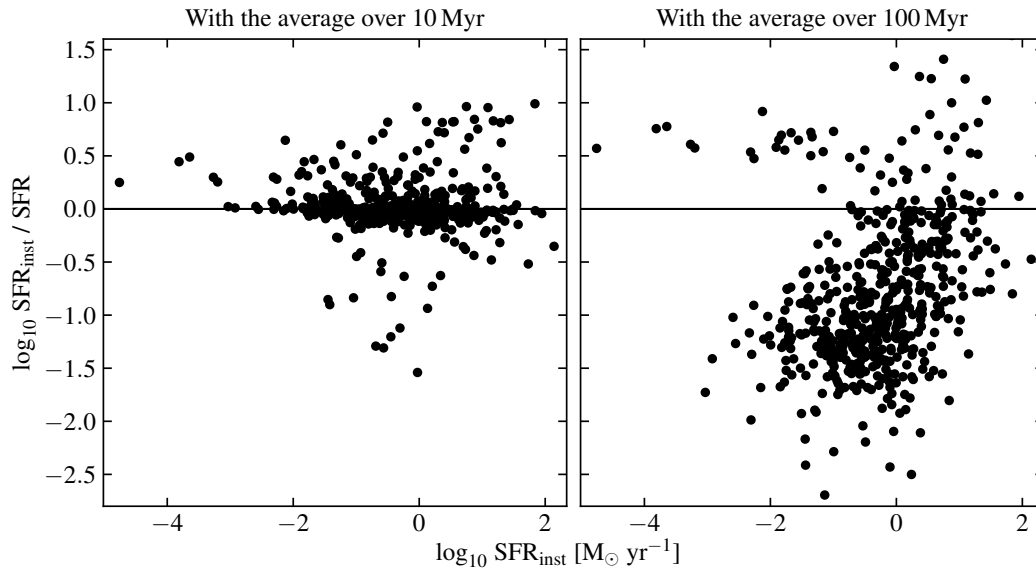


Figure 3.6: Comparison between the instantaneous SFR derived by CIGALE during the last 1 Myr time-step and the average values derived during the last 10 and 100 Myr. We only show [O II] emitters with $\text{CONFID} \geq 2$. For most galaxies the instantaneous value and that averaged over 10 Myr are similar. However, there is a large discrepancy when using the 100 Myr averaged value. This indicates that for most galaxies the truncation episode happens between the last 100 Myr and 10 Myr of the SFH and is usually modelled as a quenching phase.

less affected by the late truncation phase and more by the smooth part of the SFH. Thus, it can also be seen as a good compromise at the cost of having higher SFR values on average. Therefore, in what follows, we will use the two average values and we will drop the instantaneous SFR.

Table 3.2: Models and grid of parameters for the SED modelling with CIGALE of galaxies in MAGIC

Parameter	Values	Description
(1)	(2)	(3)
Truncated delayed SFH		
Age (Gyr)	1e-03, 2e-03, 8e-03, 2.3e-02, 6.7e-02, 0.2e-01, 0.6, 1.6, 4.5, 12.9	Age of the oldest stars that contribute to the SED
τ (Gyr)	1e-03, 3e-03, 9e-03, 2.7e-02, 8.1e-02, 0.24, 0.73, 2.2, 6.6, 20	e-folding time of the exponential part of the SFH
Age trunc. (Myr)	1, 12, 23, 34, 45, 56, 67, 78, 89, 100	Age of the truncation episode
SFR ratio	1e-04, 2.2e-03, 4.6e-02, 1, 2.2e+01, 4.6e+02, 1e+04	Ratio of SFR after and before the truncation episode
Bruzual et Charlot (2003) SSP		
IMF	Salpeter	Initial Mass Function used in the modelling
Metallicity	0.02	Metallicity values
Modified starburst attenuation law		
$E(B - V)$	1e-3, 8e-2, 0.16, 0.23, 0.32, 0.39, 0.47, 0.55, 0.62, 0.7	Colour excess of the nebular lines and of the stellar continuum
R_V	3.1	Total to selective extinction ratio.

Notes: (1) Parameter name, (2) range of values used in the modelling, and (3) short description. Only the SFH, SSP, and attenuation law models and their parameters are shown in this table, the other models (nebular and dust template) having default values. The dust template model used is that of [Dale et al. \(2014\)](#).

When stellar mass is plotted against the SFR it is referred to as the MS. In Fig. 3.7 we show the MS for the entire MAGIC sample ($\text{CONFID} \geq 2$), that is including galaxies beyond the [OII] emitters range. Field galaxies and those in structures (see Sect. 3.3) are shown separately as squares and circles with a black contour, respectively. Additionally, I used the MS/red sequence separation line from [Abril-Melgarejo et al. \(2021\)](#) to highlight the difference between the population of star-forming galaxies that lie along the MS (shown in blue) and that of passive/quenched galaxies (shown in red - it also contains a few green valley galaxies). Before applying the separation, I normalised the SFRs to a redshift $z_0 = 0.7$ as in [Mercier et al. \(2022\)](#) to remove the intrinsic redshift dependence of the relation. This normalisation writes

$$\log_{10} \text{SFR}_z = \log_{10} \text{SFR} - 2.8 \log_{10} \left(\frac{1+z}{1+z_0} \right), \quad (3.9)$$

where SFR_z is the normalised SFR and where the factor of 2.8 is derived from [Speagle et al. \(2014\)](#) and is more adapted for our stellar mass range than the value of 1.4 used in [Abril-Melgarejo et al. \(2021\)](#). However, the SFR values shown in the plot are those directly coming out of CIGALE. Above the main plot are also shown histograms for four different physical parameters. From left to right we have (i) the main stellar population age, (ii) the ratio of the SFR before and after the episode of burst/quenching of star formation, (iii) the SFR measured in the last CIGALE time step of 10 Myr, and (iv) the total stellar mass of the galaxies. Item number (ii), that is the SFR ratio, measures by how much the smooth exponentially declining SFH is changed when the burst/quenching episode happens. If it is below unity, it means that a quenching phase was modelled by CIGALE at the end of the SFH and, if it is above unity, it rather means that a burst phase was modelled. However, the significance of whether the galaxy experienced or not a burst/quenching phase is not as simple as just looking at the SFR ratio given that it also depends on the value of the SFH just before the episode happened.

A few points can be noted. First, the environment within which galaxies reside (field versus structures) is different between the MS and red sequence populations in the sense that passive galaxies are mostly found in structures whereas star-forming galaxies are an equal mix of galaxies in the field and in structures. Secondly, the red sequence population does not have the same physical parameter distribution than the MS population with on average: (i) older galaxies (peaking at an age of about 2 – 3 Gyr versus 300 Myr for MS galaxies), (ii) lower SFR values (by definition), and (iii) it is mostly populated by massive galaxies (the majority above $10^{10} M_{\odot}$). In addition, galaxies on the MS exhibit a much wider distribution of ages, dominating the young population and the low SFR ratios with the bulk of the objects modelled with a quenching episode in their SFH (negative values, see histogram in [Fig. 3.7](#)). On the other hand, galaxies on the red sequence are mostly modelled with old stellar populations and with a SFR ratio that peaks near unity. These differences arise because passive galaxies are modelled with old SFHs that smoothly increase with time, reaching their peak value and then smoothly decreasing to low SFRs. A non-negligible fraction (of the order of 10%) is also modelled with a quenching phase in their last billion years. On the other hand, star-forming galaxies have a much wider range of SFHs which, depending on their position on the MS, can be modelled with or without a burst/quenching phase. Among the objects that do have this phase, some experience a high exponential growth of their SFH followed by a quick quenching phase, while others experience a weak exponential growth of their SFH, then followed by a very strong burst episode. In both cases, these types of SFH certainly allow CIGALE to produce blue SEDs since the old stellar population required to produce the red part of the spectrum would not have had time to dominate the emission yet.

3.2.5.4 Comparison of physical parameters between the different modellings

In [Abril-Melgarejo et al. \(2021\)](#), both the stellar mass and the SFR derived from FAST were used to separate galaxies between star-forming and passive objects. In [Mercier et al. \(2022\)](#), we kept using the stellar mass from FAST but computed a new estimate of the SFR using the [OII] doublet and in the survey paper ([Epinat et al., in prep.](#)), as well as in the analysis of the angular momentum performed in [Chapter 7](#), we derived again new values of the stellar mass and the SFR using CIGALE. Among the two parameters, the stellar mass is probably the most important one

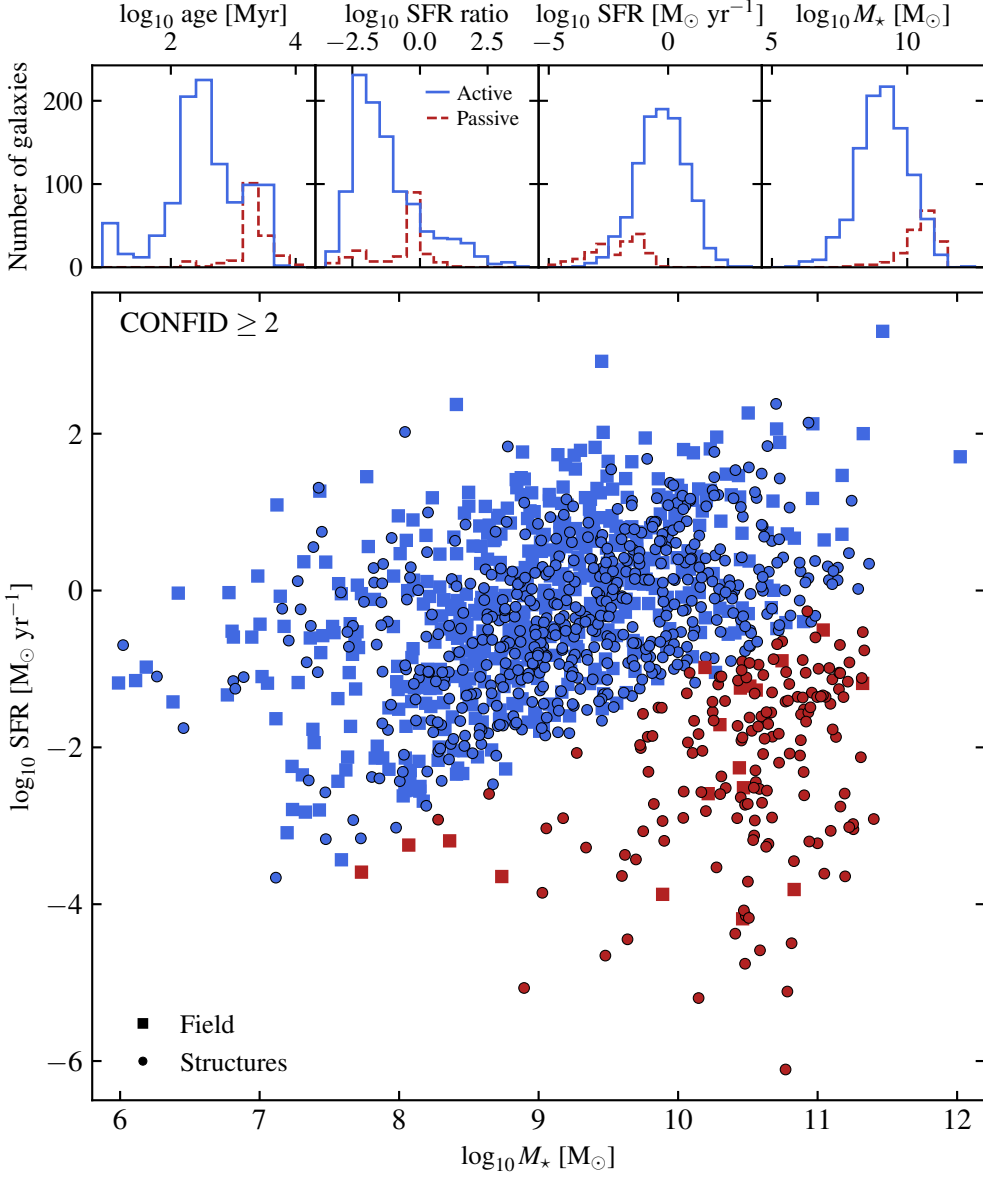


Figure 3.7: Main sequence relation obtained from the SFR and the stellar mass values derived with CIGALE for the full MAGIC sample ($\text{CONFID} \geq 2$) and histograms for, from left to right, (i) the age of the galaxy, (ii) the ratio of the SFR before and after the burst/quenching episode, (iii) the instantaneous SFR, and (iv) the galaxies’ stellar mass. As an indication, I show field galaxies with square symbols and galaxies in structures (see Sect. 3.3) with circles with a black contour. Furthermore, galaxies are separated between star-forming (blue symbols in the MS and a blue solid line in the histograms) and passive systems (red symbols in the MS and a red dashed line in the histograms). To split the sample between star-forming and passive galaxies I used the separation given in [Abril-Melgarejo et al. \(2021\)](#) after normalising the SFRs to $z_0 = 0.7$ using the same expression as in [Mercier et al. \(2022\)](#). This normalisation corrects for the redshift evolution of the MS and is well suited for the stellar mass range that is probed. For illustration purposes, the raw values of the SFR and stellar mass are shown.

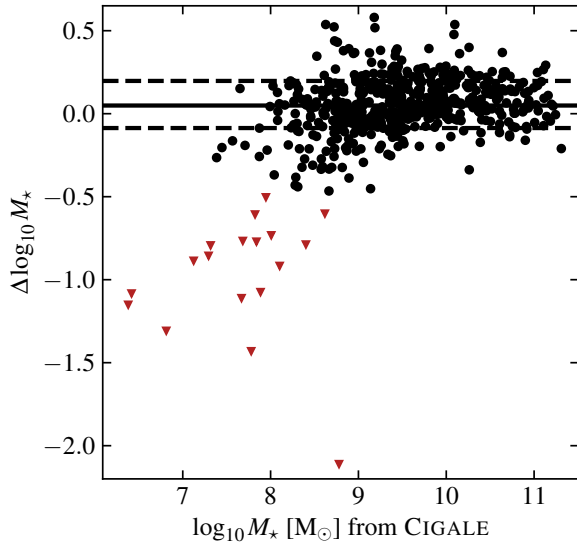


Figure 3.8: Comparison between the stellar mass derived from CIGALE and that from FAST. Only the [OII] emitters with $\text{CONFID} \geq 2$ are shown. A positive difference means that CIGALE overestimates the stellar mass with respect to FAST. Overall, values are consistent within plus or minus 0.1 dex and with a small median bias of 0.05 dex (median value represented as a plain line and the 25th and 75th quantiles as dashed lines). Only low-mass objects according to CIGALE were modelled as more massive galaxies by FAST which is certainly due to different SFHs. Objects with a difference below -0.5 dex have been identified with downward pointing red triangles.

for the analysis since it explicitly appears in the mass models (see Sect. 5.2.4 for examples) and in the various scaling relations that have been investigated (see Chapters 6 and 7). On the contrary, the SFR does not impact the dynamical models. Thus, as long as the stellar mass is well constrained, a large uncertainty on the SFR should not be too problematic to derive the galaxies' dynamics⁷. Only when the SFR appears explicitly in a scaling relation it becomes important to constrain it efficiently. This was the case in [Mercier et al. \(2022\)](#) and in Chapter 6 where the MS relation, the size-mass relation, and the TFR were investigated. Hence, I show in what follows a comparison of the stellar mass estimated with CIGALE and with FAST and I discuss how the MS relation is impacted when using different stellar mass and SFR estimates.

The difference in stellar mass between CIGALE and FAST as a function of that of CIGALE is shown in Fig. 3.8 (a positive difference means that the value from CIGALE is larger), focussing on the [OII] emitters with secure spectroscopic redshifts ($\text{CONFID} \geq 2$) only. For the bulk of the galaxies, CIGALE and FAST find consistent stellar masses within at most 0.5 dex, except towards the lowest CIGALE-derived stellar masses where FAST derives larger values (downward pointing red triangles in the figure). The median difference between the two codes is only of 0.05 dex when excluding outliers at low CIGALE stellar masses, whereas the 25th and 75th quantiles are found at -0.09 dex and 0.2 dex, meaning that most galaxies are found within plus or minus 0.15 dex from the median value. This shows that on average CIGALE tends to produce slightly larger (by roughly 25%) stellar masses than FAST. These differences can certainly be explained by different SFH and IMF models being used, in particular given that a [Salpeter \(1955\)](#) IMF should produce on average higher stellar masses than a [Chabrier \(2003\)](#) IMF. Furthermore, such a discrepancy between two SED fitting codes is consistent with the literature (e.g. [Walcher et al. 2011](#)). Concerning the larger discrepancy observed at low stellar masses, we can compare it with Fig. 3.9 that shows the MS relation using the different stellar mass and SFR estimates at our disposal. In particular, we can focus on the top left plot that shows the MS for CIGALE using the 10 Myr

⁷Though, a sample selection based on the SFR can have an indirect impact on the analysis.

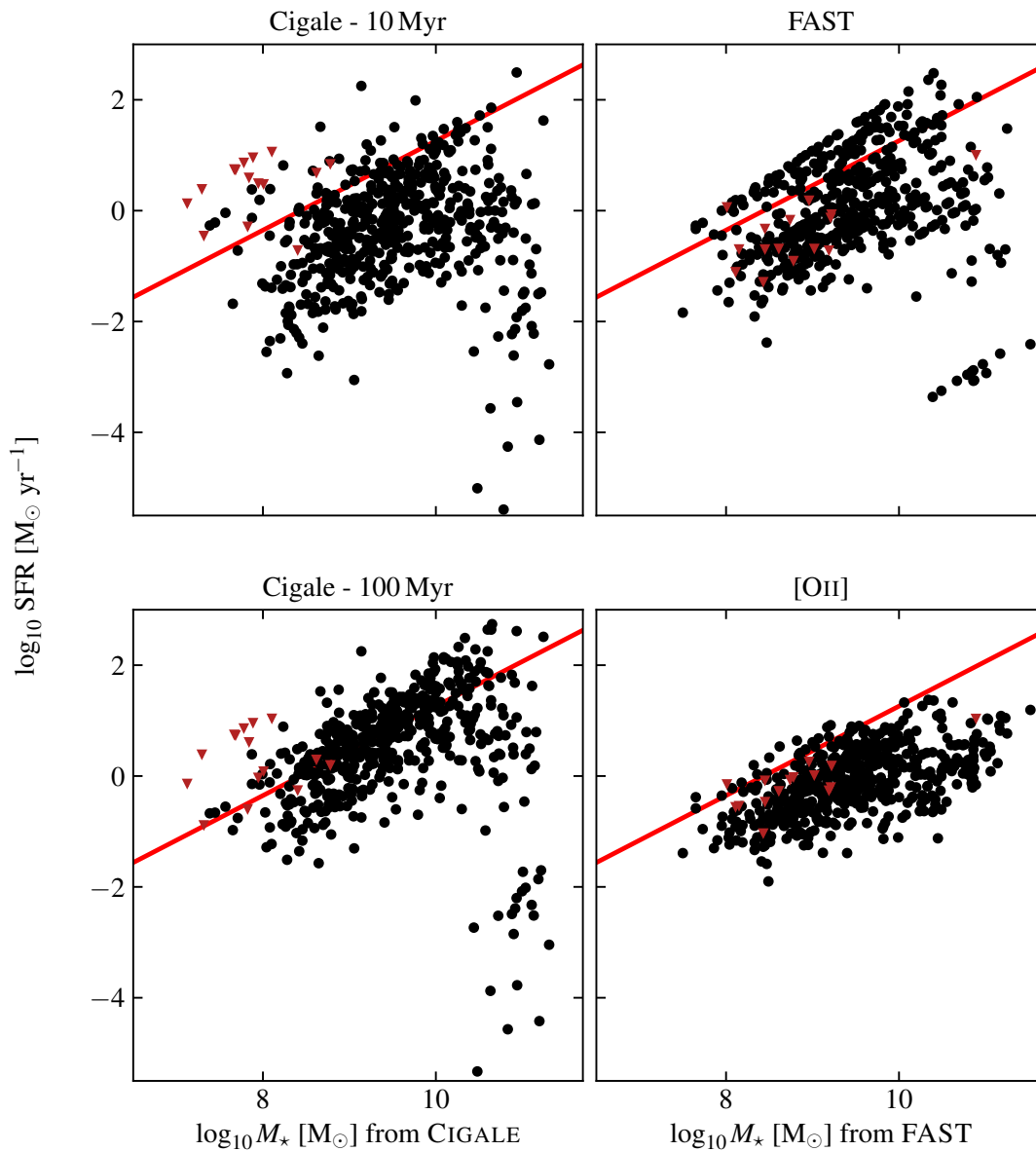


Figure 3.9: Comparison of four different MS relations that we can build when using the various stellar mass and SFR estimates presented in Sect. 3.2.5. Only the [O II] emitters with secure spectroscopic redshifts are shown ($\text{CONFID} \geq 2$). On the left is shown the MS relation using the stellar mass and SFR from CIGALE (top: average over 10 Myr, bottom: average over 100 Myr). The top right plot shows the MS using the values from FAST and the bottom right plot shows the relation when using the stellar mass from FAST and the SFR derived from the [O II] doublet. The same thick red line was added to each plot to guide the eye. It corresponds to the best-fit line of CIGALE’s 100 Myr relation obtained by fitting the MS after removing the red sequence while taking into account the uncertainties on both the stellar mass and the SFR during the fit. All SFRs and stellar masses were estimated in the same aperture of $3''$ on the plane of the sky. Galaxies with a large stellar mass difference identified in Fig. 3.8 are also shown with the same downward pointing red triangle symbol.

average SFR estimate, as well as the top right plot that shows the MS using the values from FAST. Similarly to Fig. 3.8, the galaxies with the largest discrepancy ($\Delta \log_{10} M_{\star} < -0.5$) are identified with downward pointing red triangles. With CIGALE, these objects are above the MS whereas with FAST they are located throughout. Thus, the difference observed in stellar mass for these objects is most likely the result of using two different parametrisations of the SFH, FAST lacking a burst/quenching phase contrary to CIGALE.

As previously mentioned, Fig. 3.9 represents four different MS relations that can be built using the different stellar mass and SFR estimates. The top right plot shows the relation derived with FAST that was used in [Abril-Melgarejo et al. \(2021\)](#). The bottom right plot represents the relation that uses the SFR estimated from the [OII] doublet and the stellar mass from FAST that was used in [Mercier et al. \(2022, see also Chapter 6\)](#). On the left are shown the MS relations using the parameters from CIGALE (the top plot uses the 10 Myr average SFR and the bottom the 100 Myr average values). These MS relations have not been normalised to correct for their redshift evolution. In each of these relations we recover the shape of the typical MS with low-mass galaxies that tend to have lower SFR values than high-mass galaxies, but both the slope, zero point, and the scatter of the MS significantly change from one relation to another, as discussed in more details below. Focussing first on the two MS relations using the parameters from CIGALE, we see a positive vertical offset of the zero point of about 1 dex when using the 100 Myr average SFR values with respect to the 10 Myr average, consistent with what is visible on the right-hand side of Fig. 3.6. In both cases the red sequence is clearly apparent below the MS, with galaxies spread along 3-4 dex of SFR values. However, the scatter along the vertical direction in the MS is larger by at least 0.3 dex when using the 10 Myr average SFR, certainly because of the burst/quenching phase that spreads galaxies above and below the relation that was built by the smooth part of the SFH. We see on the top right plot the discretisation of the $M_{\star} - \text{SFR}$ grid that produces strong correlation lines. This affects particularly the top of the MS where no galaxies are found above the upper limiting line discussed in Sect. 3.2.5.1, as well as the red sequence. Furthermore, FAST's SFR values were derived using a [Chabrier \(2003\)](#) IMF, whereas we used a [Salpeter \(1955\)](#) IMF for CIGALE. This should affect the shape of the MS and in particular the estimate of the SFR. According to [Boogaard et al. \(2018\)](#), if the number of massive stars ($> 10 M_{\odot}$) is assumed to remain the same between the two IMFs, then converting from a [Chabrier \(2003\)](#) to a [Salpeter \(1955\)](#) IMF can be done by diving the SFR by a factor of 0.62. Hence, the MS from FAST can be compared in an IMF-independent way to the other MS relations in Fig. 3.9 by vertically offsetting it by roughly 0.2 dex. Note that this value is quite consistent with the 0.3 dex zero point difference observed between this MS and that from CIGALE when using the 100 Myr average SFR values. Finally, the relation in the bottom right plot is probably the most different of the four. As for FAST, this MS has a zero point lower by roughly 0.3 dex with respect to CIGALE's 100 Myr average SFR relation, though this difference cannot be accounted for by IMF differences since it uses the same [Salpeter \(1955\)](#) IMF as CIGALE. Furthermore, this relation also has a lower slope of about 0.7 when the other relations rather find a slope of 0.8 and it tends to have a SFR scatter lower by 0.1 dex on average with respect to CIGALE's MS. One of the reasons for such a difference might have been the [Gilbank et al. \(2010, 2011\)](#) parametrisation of $A_{\text{H}\alpha}$ that was used to derive the SFR. However, since it provides larger extinction values for higher stellar masses, it should actually produce a larger slope with respect to CIGALE's MS, which is the opposite of what is observed. The two most striking features in this relation are (i) its low scatter (as already discussed above) and (ii) the lack of a red sequence. These two points can be explained by the fact that we are considering a sample of [OII] emitters, thus star-forming galaxies. Hence, even

galaxies that have accumulated a significant fraction of old stars so that their spectrum is sufficiently red to fall on CIGALE’s red sequence should still have enough star formation to produce a bright [OII] doublet. Therefore, they should still appear on the MS when using this SFR tracer. Besides, galaxy-per-galaxy variations in dust extinction that might affect their vertical location on the MS and its scatter are smoothed by the [Gilbank et al. \(2010, 2011\)](#) parametrisation since it only provides an average parametrisation of $A_{H\alpha}$ with stellar mass.

3.3 Structure identification and density estimation

To properly constrain the impact of the environment on galaxy properties and galaxy evolution, the environment must be accurately quantified first. To this end, many techniques have been proposed that allow to identify which galaxies belong to structures and which galaxies do not (i.e. field galaxies). Such techniques include among others Voronoi tessellation, Delaunay triangulation (e.g. [Marinoni et al. 2002](#)), weighted adaptive kernel smoothing, n^{th} nearest neighbours, or Friends of Friends (FoF) algorithms (e.g. [Knobel et al. 2012](#); [Iovino et al. 2016](#)). Some methods are purely based on either photometric or spectroscopic observations whereas others such as the Voronoi tessellation Monte-Carlo mapping technique described in [Lemaux et al. \(2017, 2022\)](#) and [Hung et al. \(2020, 2021\)](#) combine both observations. Because, as discussed in [Darvish et al. \(2015\)](#), different estimators yield similar but still slightly different results, we used multiple estimators to define the structures and estimate their density. I mention that this work was not carried out by myself but by B. Epinat and B. Lemaux. However, I have extensively used the results of the FoF algorithm for the analysis of the scaling relations in [Mercier et al. \(2022\)](#) and in Chapter 6 and for the analysis of the angular momentum in the MAGIC survey (see Chapter 7). Hence, it is important that I provide a brief account of how this was achieved.

3.3.1 Structure identification with a FoF algorithm

The first step was to determine which galaxies are associated to structures and which galaxies belong to the field. Following [Bacon et al. \(2015\)](#), we used a FoF algorithm to detect structures in our MUSE fields. Classically, FoF algorithms define structures through an iterative process given two tunable parameters that are the transverse and longitudinal (i.e. along the line-of-sight) separations. In our case, the former is given by the physical distance between galaxies on the plane of the sky and the latter by the difference of MUSE spectroscopic redshifts between two galaxies. When galaxies are gravitationally bound to the same structure, then this redshift difference is related to their relative motion along the LOS in the structure. Hence, the two parameters used for the FoF algorithm to detect structures are a transverse proper (i.e. physical) distance and a LOS velocity separation. The algorithm then iterates by finding the “friends” of each galaxy in the input catalogue, that is galaxies that respect the projected distance and velocity separations criteria, then find the “friends” of “friends” using the same criteria, and so on until the structures are determined. Classically, the two parameters of the FoF algorithm have to be tuned from simulations beforehand to account for the survey target selection and success rate (e.g. [Knobel et al. 2012](#); [Iovino et al. 2016](#)). In our case, and as discussed previously, we do not have any pre-selection, we have a high completeness in the [OII] emitters range (i.e. below $z \approx 1.5$) where we want to detect the structures, and we have low uncertainties on the velocity difference between two galaxies ($\Delta v \approx 20 \text{ km s}^{-1}$). Besides, our goal is to characterise small groups, where low-mass galaxies may be found, as much as large groups and clusters. Therefore,

we ran the FoF algorithm on the entire MAGIC sample⁸, selecting galaxies that have a secure spectroscopic redshift ($\text{CONFID} \geq 2$), without any magnitude cut. Based on the prescription given in [Knobel et al. \(2012\)](#) that applies for galaxy groups with more than six members, we used a transverse separation of 450 kpc and a velocity separation of 500 km s^{-1} .

3.3.2 Local and global density estimators

Once the structures have been identified, we can estimate the density at each location in the FoV. The first way to do so is through the derivation of local density estimators that compute a density estimate locally at a given position in the FoV taking into account the spatial distribution in the structure. In our case, we have used two different estimates that do not rely on the same data.

First, we have considered the Voronoi tessellation Monte-Carlo mapping technique ([Lemaux et al. 2017, 2022](#); [Hung et al. 2020, 2021](#)) that combines photometric and spectroscopic information but that does not take into account the output of the FoF algorithm. Second, we have derived a somewhat similar but finer density estimate that also uses Voronoi tessellation but for each detected group separately and that uses MUSE and zCOSMOS ([Lilly et al. 2007](#)) spectroscopic redshifts. Both methods have advantages and caveats that are discussed below and thus they provide complementary information.

The Voronoi tessellation Monte-Carlo mapping technique is interesting because it can be applied on photometric and spectroscopic data and thus over a larger FoV than our MUSE observations, which allows to mitigate the oversampling of spectroscopic redshifts in our MUSE FoVs. To apply the method, we used photometric information from the COSMOS catalogue of [Laigle et al. \(2016\)](#) and spectroscopic information from the zCOSMOS and VIMOS Ultra-Deep Survey (VUDS) spectroscopic catalogues ([Lilly et al. 2007](#); [Le Fèvre et al. 2015](#)). Only these catalogues were considered because, contrary to other catalogues (e.g. COSMOS-Wall, [Iovino et al. 2016](#)), they provide a homogeneous sampling in redshift space. The way the method works is by assigning to each source a redshift and an associated uncertainty drawn from a random distribution. Then, redshift slices in the range $0.2 \leq z \leq 1.5$ are produced with a step of 150 km s^{-1} and for each slice Voronoi tessellations are performed. A first density map is computed as the inverse of the cell's area which is then transformed into a grid with rectangular cells with 75 kpc wide pixels in physical distance. This process is repeated 100 times and the final density is computed as the mean map. Because sampling may differ from one redshift slice to another, it is more useful to use the overdensity $\delta(z)$ rather than the density which is defined as $1 + \delta(z) = \Sigma(z)/\Sigma_{\text{med}}(z)$, where $\Sigma(z)$ is the density map centred at redshift z and $\Sigma_{\text{med}}(z)$ is the median value of the map at the same redshift. The clear advantage of this method is that we can assign an overdensity value for each galaxy. This includes field galaxies but also galaxies that are located near the edges of the MUSE FoV. However, its disadvantages are that (i) it does not use MUSE spectroscopic redshifts and (ii) it only provides a density estimate in a redshift slice rather than associated to a given structure.

Hence, to correct for these two caveats we derived a second local density estimator which uses MUSE spectroscopic redshifts. This estimator also relies on Voronoi tessellation but, in this case, there is no more need to perform Monte Carlo realisations because the galaxies associated to structures in MAGIC all have secure spectroscopic redshifts. The clear advantage of this method compared to the previous one is that we can perform the Voronoi tessellation and compute the local density for each structure separately, therefore taking into account the output of the FoF. In

⁸That is on the entire catalogue rather than on each MUSE field separately.

particular, this means that we have a density estimate galaxy-per-galaxy whereas the previous method averaged it over 75 kpc wide pixels. Its caveats are that (i) we do not have a density estimate for field galaxies and (ii) we underestimate the density for galaxies near the sides of the MUSE FoVs because we certainly miss a few galaxies that belong to the structure but that are located beyond the FoVs. To help circumvent the latter point, we also have computed the same estimator but including galaxies in zCOSMOS that are located beyond the FoVs.

Finally, we also consider a last estimator that probes global rather than local environment. This estimator combines the projected distance of a galaxy with respect to the structure's centre (R_{proj}) with its line-of-sight velocity with respect to the structure's systemic velocity (Δv , e.g. [Noble et al. 2013](#); [Pelliccia et al. 2019](#)). This estimator writes

$$\eta = \frac{R_{\text{proj}}}{R_{200}} \times \frac{|\Delta v|}{\sigma_V}, \quad (3.10)$$

where $R_{200} = \sqrt{3}\sigma_V/[10H(z)]$ is the radius where the density of the structure is equal to 200 times the critical density of the Universe, with $H(z)$ the Hubble parameter at redshift z , and $\sigma_V = c \times \Delta z/(1+z)$ is the velocity dispersion of the structure, with Δz the difference in redshift between the galaxy and the structure (see [Epinat et al.](#) for more details). Infalling galaxies that are still located far away from the structure's centre and that have large velocities with respect to the systemic velocity will therefore have small η values whereas already accreted galaxies located in the inner parts and with low velocity will have larger values. Hence, assuming the density is higher in the central parts, η can also be used as a proxy for the density at the galaxy's location. Because it uses the projected distance and the galaxy's velocity, it is also a complementary estimator to the two previous local estimators. However, η requires to define a structure and its centre (in our case taken as the barycentre of the galaxies' associated to the structure by the FoF algorithm) which is not possible for field galaxies. Hence, this estimator is solely restricted to galaxies located in structures found by the FoF algorithm.

Chapter 4

Morphological modelling

The main goal of this thesis is to perform the analysis of the impact of the environment on the dynamical properties of intermediate redshift galaxies in the MAGIC survey. In [Mercier et al. \(2022\)](#) and in [Chapter 6](#) I studied the impact of the environment on scaling relations and in [Chapter 7](#) I discuss the angular momentum of galaxies in MAGIC. For both analyses, a crucial aspect was to model the galaxies' morphology to extract key morphological parameters. This step was performed during the first year of this thesis. There were actually two different, though not entirely estranged, reasons why this modelling was important: (i) to disentangle the contribution to the observed surface brightness of the disk and of the bulge components and (ii) to reliably model the morphology to constrain afterwards the contribution of the stars to the total gravitational potential of the galaxy in order to produce mass models for the kinematics modelling (see [Chapter 5](#) for more details). Indeed, the first point is important because even at intermediate redshift ($z \approx 1$) star-forming disk galaxies tend to host two main components: first, the stellar disk in itself and second, an inner spherical or spheroidal bulge component. Thus, deriving accurate morphological parameters for both components was important, especially in [Mercier et al. \(2022\)](#) where we made use of the fraction of flux found in the bulge with respect to the disk to select a sample of star-forming galaxies and of the disk size to study the size-mass relation. The second point is as important as the first, if not even more, because, as is discussed in [Sect. 5.3.3](#), we used the parameters derived from the morphological modelling to constrain the ionised gas kinematics in order to derive more precise DM fractions.

Thus, in this chapter I describe how I performed the morphological modelling for nearly 900 [OII] emitters in the MAGIC survey. I begin with a presentation of the main disk model that I have been using and its main characteristics in [Sect. 4.1](#). I also go through an important aspect that is sky projection and how it can affect the shape of galaxies seen on the plane of the sky. In particular, I focus on its effect on two different disk models: (i) the razor-thin disk and (ii) the double exponential disk. In [Sect. 4.2](#), I quickly argue, illustrated with an example, why taking into account the contribution of the bulge component during the morphological modelling is important and, in [Sect. 4.3](#), I discuss the multi-component decomposition that was done in [Abril-Melgarejo et al. \(2021\)](#) and [Mercier et al. \(2022\)](#). Lastly, I present in [Sect. 4.4](#) the morphological modelling performed on the MAGIC sample during this thesis and I mention a small python wrapper that I developed at the beginning of my PhD to automatise the modelling with GALFIT for a large number of galaxies.

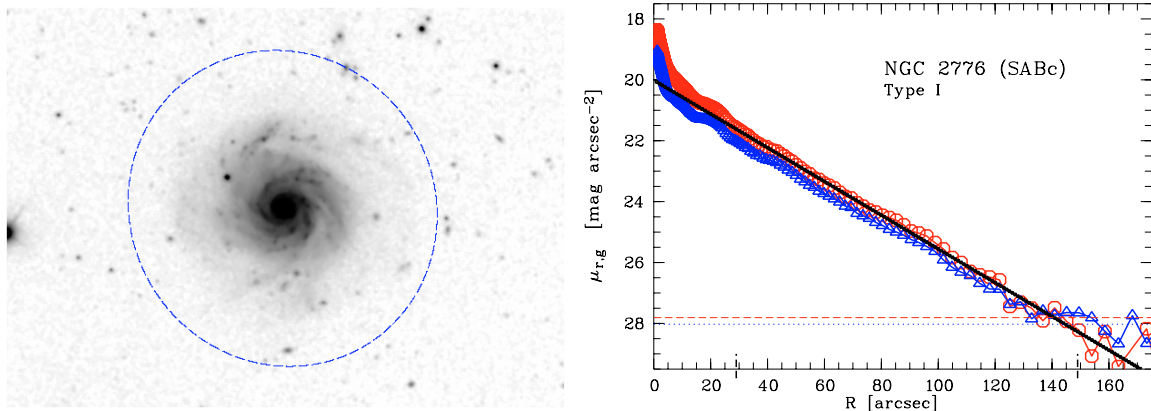


Figure 4.1: Example of an azimuthally averaged surface brightness profile for NGC2776 from [Pohlen & Trujillo \(2006\)](#). Left: r' band SDSS image with the dashed blue line representing the noise limit. Right: surface brightness profile in the g' band (blue triangles) and in the r' band (red triangles), with the best-fit exponential disk profile shown in black.

4.1 Morphology of disk galaxies

Various models for the surface brightness distribution of disks of galaxies have been suggested in the literature over the years. Some were based on observations of galaxies in the local Universe e.g. [Sérsic 1963](#)) whereas others have been theoretically derived so as to find a potential-density pair which solves Poisson equation (see Sect. 5.2). For instance, this is the case for [Kuzmin \(1956\)](#) solution of the eponymous Kuzmin’s disk.

4.1.1 Sérsic model

Among all the surface brightness models one in particular, the Sérsic profile ([Sérsic 1963](#)), has been used in numerous studies to represent the surface brightness distribution Σ of both disk-like and elliptical galaxies at various redshifts (e.g. [Trujillo et al. 2007](#); [Maltby et al. 2010](#); [Mowla et al. 2019](#); [Costantin et al. 2022](#)). This axisymmetric model is usually written as

$$\Sigma(R) = \Sigma_{eff} \exp \left\{ -b_n \left[\left(\frac{R}{R_{eff}} \right)^{1/n} - 1 \right] \right\}, \quad (4.1)$$

where R_{eff} , called the effective or half-right radius, corresponds to the distance where the integrated flux reaches half of the total flux, and Σ_{eff} is the surface brightness evaluated at R_{eff} . In Eq. 4.1, the term b_n is a function of the Sérsic index n and is the solution of the following equation ([Graham et al. 2005](#)):

$$\Gamma(2n) = 2\gamma(2n, b_n), \quad (4.2)$$

where Γ and γ are the complete and lower incomplete gamma functions, respectively. The central surface density of such a model is given by

$$\Sigma(0) = \Sigma_{eff} e^{b_n}, \quad (4.3)$$

and the flux F integrated up to radius R can be computed as

$$F(< R) = 2\pi n \Sigma_{eff} R_{eff}^2 e^{b_n} \gamma \left(2n, b_n \left(\frac{R}{R_{eff}} \right)^{1/n} \right) / b_n^{2n}. \quad (4.4)$$

This model is therefore entirely described by three parameters only and has the advantage to represent quite accurately the surface brightness profile of various types of galaxies. Indeed, the disk component of galaxies is well represented by an exponential disk model given by setting n to unity. In this case Eq. 4.1 simplifies to

$$\Sigma(R) = \Sigma_{eff} \exp \left\{ -b_1 \left[\frac{R}{R_{eff}} - 1 \right] \right\}, \quad (4.5)$$

where $b_1 \approx 1.6783$. Equation 4.5 is sometimes written with the disk scale length $R_d = R_{eff,d}/b_1$ instead which corresponds to the e-folding length of the profile.

Another model, usually used to represent elliptical galaxies or the bulge component of disk-like galaxies, is the de Vaucouleurs profile (de Vaucouleurs 1948) and corresponds to a Sérsic profile with $n = 4$, that is

$$\Sigma(R) = \Sigma_{eff} \exp \left\{ -b_4 \left[\left(\frac{R}{R_{eff}} \right)^{1/4} - 1 \right] \right\}, \quad (4.6)$$

where $b_4 \approx 7.6692$. Additionally, the Sérsic profile also reduces to a Gaussian profile when $n = 1/2$. Thus, the Sérsic profile is really well suited to fit the global (average) morphology of galaxies independently of whether they are more disk-like or more elliptical. For more complicated cases such as galaxies with bulges, bars, spiral arms, rings, tails, and so on either more complex surface brightness models are required or in some cases multiple Sérsic profiles can be combined together (see Sec. 4.3).

4.1.2 Sky projection: the curse of astrophysicists

Generally speaking, what really matters to understand the evolution of galaxies is their intrinsic properties, but these are not directly observed. For instance, understanding in detail the dynamical evolution of a galaxy would require at the very least measurements of its 3D stellar and/or gas distribution as well as its velocity vector at each position in 3D space. Unfortunately, there is an effect that affects virtually any observed quantity and inevitably leads to a loss of crucial information: line-of-sight integration also known as sky projection. Effectively, what this means is that any observed quantity is the combination of the contribution of each emitting material element along the line of sight. This effect is technically speaking an utter hindrance because it completely blurs any spatially resolved information along the line of sight and renders extremely difficult, if not impossible, the inversion process. In practice, sky projection affects any quantity derived from flux measurements such as the morphology of galaxies obtained from photometric observations in a single or in multiple bands. Additionally, it also affects the derived galaxies kinematics. Indeed, because we cannot measure proper motions on the plane of the sky and spatially resolve stars in galaxies at intermediate to high redshift, as can be done with GAIA

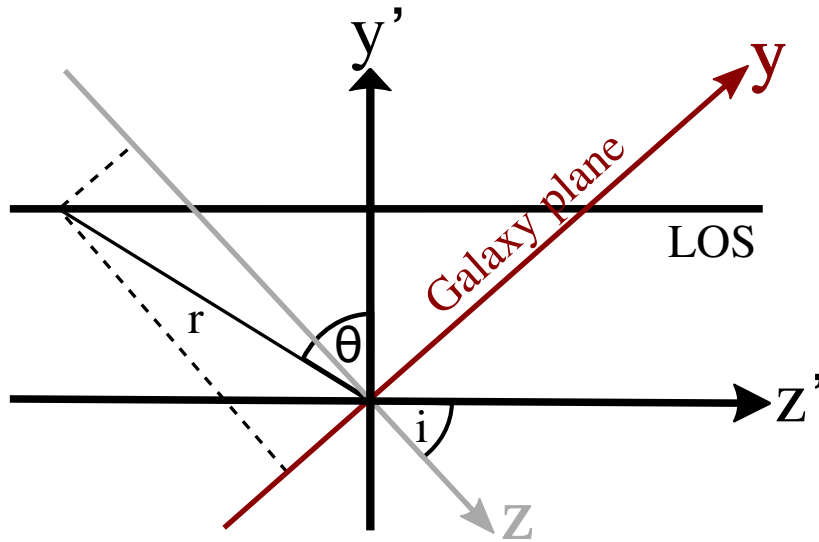


Figure 4.2: Schematics of the geometry used to integrate a razor-thin and thick disk distributions (see Sects. 4.1.2.1 and 4.1.2.2). The axis $x = x'$ (not shown on the figure but going in to have oriented axes) is the axis of rotation, with $x - y$ the plane of the galaxy and $x' - y'$ the plane of the sky, and z' is the direction of the line-of-sight. The angle i represents the inclination of the galaxy. This geometry leads to the coordinate transformations given by Eqs. 4.11 and 4.12.

in the Milky Way and in its vicinity, we are bound to measure the velocity along the line of sight using the Doppler shift. The shift, as well as the shape of the emission or absorption line that is used to derive the velocity, will be affected by both the stellar light distribution of the emitting material and its velocity vector along the line-of-sight.

The impact of sky projection is thus very important and does somewhat hinders our ability to understand in acute details the dynamics of galaxies. In this sense, and because it is not limited to the sole field of extragalactic astrophysics, there is no overstatement in calling sky projection/line-of-sight integration the curse of astrophysicists. In what follows, we discuss how sky projection can affect the modelling of the morphology of galaxies.

Let us assume that the stellar light emitted in 3D space by a galaxy can be represented by its stellar light distribution $\rho(\vec{r})$, and that the galaxy is located sufficiently far away so that its light rays reach us parallel to each other. If z' represents the line of sight distance with respect to the plane of the sky that passes through the center of the galaxy (see Fig. 4.2 for a schematics representing the geometry of the problem), then the observed surface brightness profile at position (x', y') on the plane of the sky writes

$$\Sigma_{\text{obs}}(x', y') = \int_{z' \in \mathbb{R}} dz' \rho(\vec{r}). \quad (4.7)$$

Note that Eq. 4.7 is correct as long as the medium is optically thin, otherwise $\rho(\vec{r})$ must be understood as the stellar light distribution already attenuated by the medium the light rays will have to pass through; for instance by taking into account dust absorption and/or scattering. For a spherically symmetric distribution, that is $\rho(\vec{r}) = \rho(r)$, Eq. 4.7 simplifies to Abel integral equation

which can be inverted, most of the time numerically, to derive ρ as a function of Σ_{obs} (for a derivation of the inverse of Abel integral equation, see Appendix B of [Binney & Tremaine 2008](#)).

4.1.2.1 Projection for a razor-thin disk

For more complicated distributions, solving analytically Eq. 4.7 is usually not possible, and so is inverting it to recover ρ given Σ_{obs} . However, there is a family of distributions, used extensively in the literature, for which Eq. 4.7 admits an analytical solution: razor-thin disks. A disk is said to be razor-thin when it has no thickness, in which case its stellar light distribution and surface brightness profile are related through the following equation

$$\rho(\vec{r}) = \Sigma(x, y)\delta(z), \quad (4.8)$$

where δ is a Dirac distribution, z is the vertical distance with respect to the plane $x - y$, and Σ is the surface density in the plane of the disk. If ρ represents the 3D stellar light distribution we will call Σ the intrinsic surface brightness distribution and if ρ represents the 3D mass distribution we will rather call Σ the surface mass density. Since stellar mass is not a direct observable and because I mainly focussed on modelling the surface brightness and stellar light distribution of galaxies during this thesis, I will exclusively use the term surface brightness throughout the following parts.

If the galaxy is seen face-on, that is $z' = z$ (see Fig. 4.2), then Eq. 4.7 can be easily solved and one finds that $\Sigma_{\text{obs}} = \Sigma$. In other terms, for a face-on razor-thin disk galaxy the observed surface brightness is identical to the intrinsic one. On the other hand, when the galaxy is seen edge-on the integral will be carried out perpendicularly to the z direction so that we will get $\Sigma_{\text{obs}} \propto \delta(z)$. Hence an edge-on razor-thin disk will have its flux distributed along a line (that is a null surface) so that its surface brightness should diverge. For a galaxy which is neither face-on, nor edge-on, we need to consider the geometry of the problem to solve Eq. 4.7. For a razor-thin disk, the geometry is shown in Fig. 4.2 with the sky represented as the plane $x' - y'$, where x' is not shown on the figure since it is orthogonal to the plane $y' - z'$. The disk, contained in the plane $x - y$, is inclined by an angle i around the axis $x = x'$. If we define r as the distance of a point in the (y', z') plane and θ as the oriented angle between the r and y' axes ($-\pi/2 < \theta < \pi/2$), then we have

$$y' = r \cos \theta, \quad z' = r \sin \theta, \quad (4.9)$$

$$y = r \cos(\theta - i), \quad z = r \sin(\theta - i). \quad (4.10)$$

Since the integral is computed along a line of constant y' , we can insert Eq. 4.9 into Eq. 4.10 after developing the cosine and sine terms to get

$$y = z' \sin i + y' \cos i, \quad (4.11)$$

$$z = z' \cos i - y' \sin i. \quad (4.12)$$

For a razor-thin disk, Eq. 4.7 writes

$$\Sigma_{\text{obs}}(x', y') = \int_{z' \in \mathbb{R}} dz' \Sigma(x, y)\delta(z). \quad (4.13)$$

From Eq. 4.12, we have $dz = dz' \cos i$, which means the integral in Eq. 4.13 will only be evaluated at $z = 0$ where $y = y' / \cos i$. Thus, we get

$$\Sigma_{\text{obs}}(x', y') = \frac{\Sigma(x', y' / \cos i)}{\cos i}. \quad (4.14)$$

The isophotes of Σ_{obs} on the plane of the sky will be given by the set of points $P = (x', y')$ such that $\Sigma_{\text{obs}}(x', y')$ is constant. From Eq. 4.14, the isophotes of Σ_{obs} are therefore given by

$$\{P = (x', y') \mid \Sigma(x', y' / \cos i) = C\}, \quad (4.15)$$

where the braces represent a set (in this case of points) and $C = \Sigma_{\text{obs}}(x', y') \cos i$ is a constant term that defines the isophotal value. If the intrinsic surface brightness follows cylindrical symmetry, that is $\Sigma(x, y) = \Sigma(R)$, then the isophotes are given by the equation

$$x'^2 + \left(\frac{y'}{\cos i}\right)^2 = R^2 \quad (4.16)$$

where R is a constant term. This corresponds to an ellipse whose axis ratio $q = b/a$, with a and b respectively the semi-major and semi-minor axes, and ellipticity $e = \sqrt{1 - q^2}$ are respectively given by

$$q = \cos i \quad \text{and} \quad e = \sin i. \quad (4.17)$$

In Eq. 4.14, we recover the fact that the observed surface brightness must be equal to the intrinsic one when the galaxy is seen face-on and that it diverges for edge-on galaxies. In what follows, we will see that Eq. 4.17 is not valid any more when considering disks with non-zero thickness.

4.1.2.2 Projection of thick disks: the case of the double exponential disk

Razor-thin disks are a very common assumption that is made in many morphological and kinematical studies. Nevertheless there has been increasing evidence that disk-like galaxies tend to have significant thickness profiles, especially when going towards higher redshifts. Indeed, studies of the 3D shape of galaxies as a function of cosmic time have been carried out for instance by [van der Wel et al. \(2014a\)](#) and [Zhang et al. \(2019\)](#) using SDSS and HST data in the Cosmic Assembly Near-infrared Deep Extragalactic Legacy Survey (CANDELS) field. By modelling the apparent axis ratio distribution with an ellipsoid model for the shape of their star forming galaxies they found that galaxy disks become thicker with larger stellar masses and at higher redshift up to $z = 2.5$. Thus, the assumption of razor-thin disks may be inappropriate when modelling the morphology of intermediate to high redshift galaxies and may therefore bias the morphological parameters derived from this simple assumption, especially regarding the disk inclination.

In the most general case, in order to derive the surface brightness distribution of a thick disk, one has to solve Eq. 4.7. However, it is common practice to make a few assumptions when modelling the thickness profile of disk-like galaxies. One of the main assumptions that is made is that it is possible to separate the intrinsic surface brightness profile Σ from the thickness profile h (e.g. [van der Kruit & Searle 1981a](#); [Bizyaev & Mitronova 2002](#); [Mosenkov et al. 2015](#); [Bizyaev et al. 2020](#)), that is the stellar light distribution writes

$$\rho(\vec{r}) = \Sigma(x, y)h(\vec{r}), \quad (4.18)$$

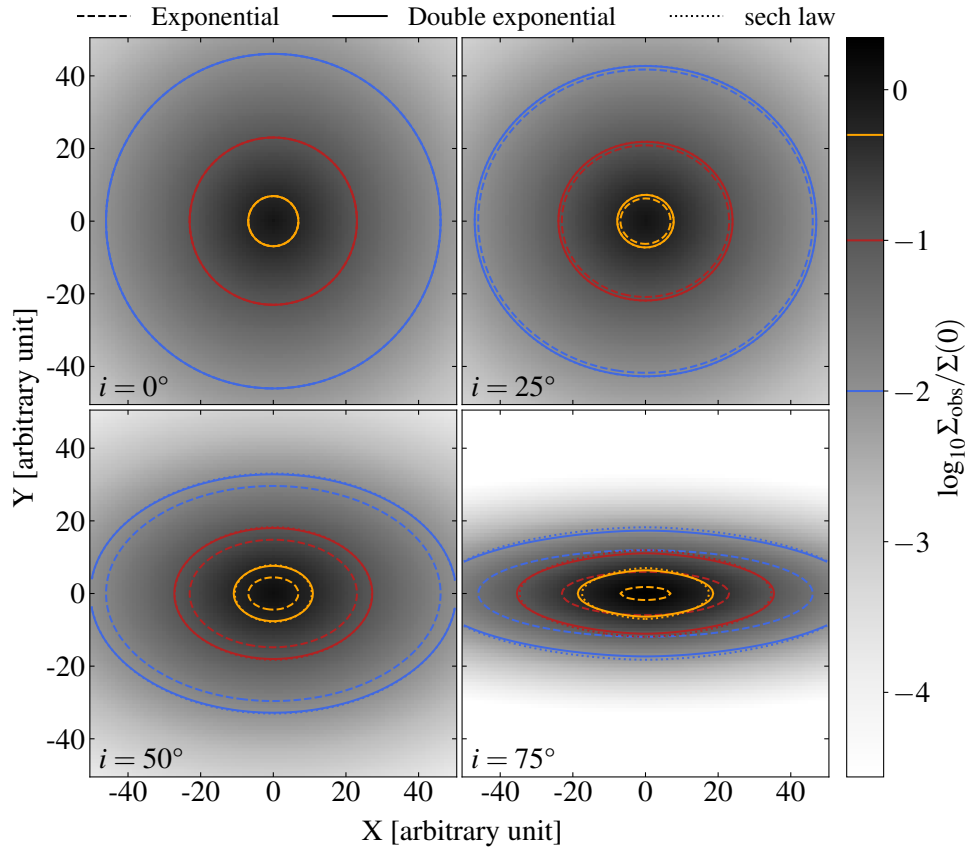


Figure 4.3: Examples of sky projection for a double exponential disk as a function of the disk inclination: 0° (top left), 25° (top right), 50° (bottom left), and 75° (bottom right). Normalised surface brightness contours are shown at half (orange), one tenth (red), and one hundredth (blue) the central value for single exponential (dashed line), double exponential (solid line), and sech law (dotted line) profiles. All profiles share the same disk scale length of ten pixels, scale height of 2 pixels ($q_0 = 0.2$), and central surface brightness.

where the following integral always holds:

$$\int_{z \in \mathbb{R}} dz h(\vec{r}) = 1. \quad (4.19)$$

Equation 4.19 is just a different way to say that the the integral of the stellar light distribution along the line of sight for a face-on galaxy yields the intrinsic surface brightness profile of the galaxy (that is independent of projection effects) independently of the shape of the thickness profile. Because of Eq. 4.19 h must be integrable and normalised, and thus cannot be constant. At the very least, it has to be a function of z , the vertical distance with respect to the disk $x - y$ plane but, in essence, it could also vary with x and y . The question of the variation of the

thickness profile with the distance R to the centre was discussed as early as [van der Kruit & Searle \(1981a\)](#), though at the time they could not find any significant dependence with R . On the other hand, [Bizyaev et al. \(2014\)](#) did find non-negligible radial gradients of the scale height when modelling a sample of edge-on galaxies in the SDSS. However, given the uncertainties on their modelling and the impact of dust extinction and dust scattering, they were only able to measure significant radial gradients for galaxies with massive bulges. Therefore, as they discuss in their analysis, the radial dependence they measure has probably nothing to do with an intrinsic variation of the disk scale height with R , but more with a contamination of the bulge component. Thus, let us simplify the shape of the thickness profile and assume in what follows that it is only a function of z , that is $h(\vec{r}) = h(z)$. The question we need to ask ourselves now is: what is its shape? A first answer can be given from the theoretical side by assuming that the distribution of light along z at a given position R corresponds to an isothermal sheet: this is the so-called sech law (e.g. [Spitzer 1942](#)). Its expression can be derived from the Jean's equations in cylindrical coordinates (see Appendix C.4 for a quick derivation) and is given by

$$h(z) = \frac{1}{4h_z} \operatorname{sech}^2\left(\frac{z}{2h_z}\right), \quad (4.20)$$

where we have defined $h_z = z_0/2$ the scale height of the disk, with z_0 defined in Appendix C.4, and where we have normalised Eq. C.23 so that it obeys Eq. 4.19. In the case of a thin disk or far enough from the disk plane, that is when $|z| \gg h_z$, we have $\operatorname{sech}(x) \approx 2 \exp\{-|x|\}$ and the sech law simplifies to ([van der Kruit & Searle 1981b](#))

$$h(z) = \frac{1}{2h_z} \exp\left\{-\frac{|z|}{h_z}\right\}, \quad (4.21)$$

where we have also normalised it to obey Eq. 4.19. When combined with an exponential disk for the surface brightness distribution we obtain the so-called double exponential disk:

$$\rho(R, z) = \frac{\Sigma(0)}{2h_z} \exp\left\{-\frac{R}{R_d} - \frac{|z|}{h_z}\right\}, \quad (4.22)$$

and we call $q_0 = h_z/R_d$ the intrinsic axis ratio of the disk.

The sky projection of a double exponential disk is described in details in Appendix E of [Mercier et al. \(2022\)](#), so we directly provide below the solution. Assuming an optically thin medium, the sky projected surface brightness distribution of a double exponential disk writes

$$\Sigma_{\text{obs}}(x', y') = \frac{\Sigma(0)}{2q_0 \sin i} \int_{\mathbb{R}} dv \exp\left\{-\sqrt{\alpha^2 + v^2} - |\beta v - \gamma|\right\}, \quad (4.23)$$

where $v = y/R_d$, with y related to the line-of-sight coordinate z' through Eq. 4.11, and where we have defined the following variables:

$$\alpha = \frac{x'}{R_d}, \quad \beta = \frac{1}{q_0 \tan i}, \quad \gamma = \frac{y'}{h_z} \left(\sin i + \frac{\cos^2 i}{\sin i} \right). \quad (4.24)$$

Generally speaking, Eq. 4.23 cannot be solved analytically and has to be integrated numerically. Nevertheless there exists an analytical solution along the minor axis y' given by

$$\begin{aligned}\Sigma_{\text{obs}}(0, y') &= \frac{\Sigma(0)}{2q_0 \sin i} \int_{\mathbb{R}} dv \exp\{-|v| - |\beta v - \gamma|\} \\ &= \frac{\Sigma(0)}{q_0 \sin i} \frac{e^{-\gamma} - \beta e^{-\gamma/\beta}}{1 - \beta^2}.\end{aligned}\tag{4.25}$$

We show in Fig. 4.3 an example of sky projection for a double exponential disk with $R_d = 10$ pixels and $h_z = 2$ pixels computed through numerical integration. As a comparison, we show surface brightness contours for this profile (solid line) and for a single exponential disk (dashed line) and a sech law (dotted line) both with similar parameters. When viewed face-on, the three profiles match perfectly as can be expected from Eq. 4.19. However, the more inclined the disk the larger the difference between the single exponential disk model (i.e. razor-thin) and the double exponential disk becomes. In particular, we see that for a given set of intrinsic disk model parameters the projected single exponential disk will appear more concentrated than the double exponential disk. Furthermore, the isophotes of a projected double exponential disk are not elliptical contrary to a razor-thin disk since the intrinsic thickness of the disk will contribute to the shape of the isophotes on top of the sky projection. Nevertheless, even up to quite high inclinations ($i \lesssim 80^\circ$) the elliptical isophote approximation remains acceptable. Finally, we can see that for any surface brightness contour and inclination value the sech law profile gives almost the same isophotes as the double exponential disk, which shows that the approximation which was made to derive Eq. 4.21 was appropriate.

4.1.2.3 From single to double exponential disk

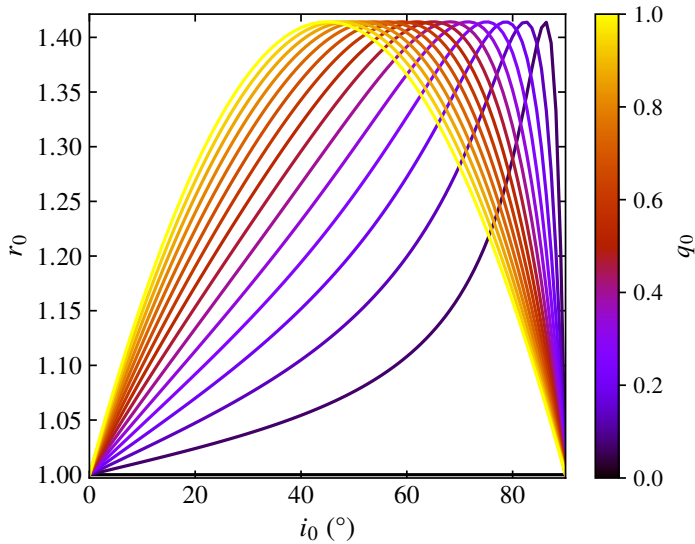


Figure 4.4: Ratio of the intrinsic central surface brightness to the value measured by a single exponential fit as a function of the intrinsic disk inclination i_0 and axis ratio q_0 . This ratio was computed using the approximation of an oblate spheroid system to relate the intrinsic axis ratio to the intrinsic inclination.

Rarely will a surface brightness fit be performed by numerically integrating a 3D model along the line-of-sight since it can be prone to numerical artefacts, might suffer from degeneracies, and

would certainly increase the computation time. For all these reasons, 2D fitting softwares such as GALFIT (see Sect. 4.4.1 for a quick description) only provide surface brightness distributions which can be projected onto the sky assuming a razor-thin disk geometry. Nevertheless, we saw in Sect. 4.1.2.2 that a double exponential profile projected onto the sky has isophotes which are nearly elliptical. Therefore, if one knows or at least assumes a given axis ratio, it might be possible to recover the intrinsic disk parameters of the double exponential profile given a single exponential razor-thin disk fit onto the observed surface brightness distribution.

If one knows q_0 , then there are three main parameters that need to be recovered: the intrinsic central surface brightness $\Sigma(0)$, the disk scale length, and the intrinsic inclination of the disk i_0 . Estimating the impact on the disk scale length is not straightforward since it would involve integrating Eq. 4.23 to compute the e-folding length of the projected surface brightness distribution, which can only be done numerically and would depend upon the other parameters. Nevertheless, for face-on or mildly inclined galaxies, the disk scale length from the single exponential fit should give a fairly reasonable estimate of the intrinsic value. Regarding the central surface brightness, it is possible to compute the analytical correction that is required to go from the single exponential fit value to the intrinsic one. To do so, one must (i) compute the relation between the observed central surface brightness and the intrinsic one ($\Sigma_{\text{exp}}(0)$) for a single exponential fit, which is given by evaluating Eq. 4.14 at $x' = y' = 0$, and (ii) compute the same relation but in the case of a projected double exponential disk, which is given by evaluating Eq. 4.25 at $y' = 0$. The correction writes

$$\frac{\Sigma(0)}{\Sigma_{\text{exp}}(0)} = \frac{q_0 \sin i_0 + \cos i_0}{q}, \quad (4.26)$$

where q and q_0 are respectively the observed (from the single exponential fit) and intrinsic axis ratio. Equation 4.26 can only be solved if the intrinsic axis ratio and inclination of the disk are known a priori but, if the former can usually be assumed, the latter is usually what one wants to derive. Thus, to compute the central surface brightness correction, one needs to derive the correction for the inclination first. Similarly to the disk scale length, there is no analytical formula that links the observed axis ratio to the intrinsic inclination given the other parameters.

Therefore, in [Mercier et al. \(2022\)](#) we approximated the dependence of the intrinsic inclination to the observed and intrinsic axis ratio by considering that the double exponential disk could be approximated by an oblate spheroid with similar q_0 . Then, it follows from [Bottinelli et al. \(1983\)](#) that we have the following relation:

$$\cos^2 i_0 = \frac{q^2 - q_0^2}{1 - q_0^2}, \quad (4.27)$$

in which case Eq. 4.26 reduces to

$$\frac{\Sigma(0)}{\Sigma_{\text{exp}}(0)} = \frac{q_0 \sin i_0 + \cos i_0}{\sqrt{q_0^2 \sin^2 i_0 + \cos^2 i_0}}. \quad (4.28)$$

I show in Fig. 4.4 the ratio from Eq. 4.28 as a function of the intrinsic axis ratio and inclination. For perfectly face-on and edge-on galaxies, the measured central surface brightness from a single exponential fit is not biased. However, for other inclinations and for non-zero intrinsic thickness values the central surface brightness derived from a single Sérsic fit will underestimate the intrinsic value. The correction that needs to be applied will vary with i_0 depending on q_0 and reach a maximum value equal to $\sqrt{2}$.

4.2 Impact of bulges

Assuming the disk component of galaxies can be approximated by a razor-thin disk, their inclination can be derived by either measuring the ellipticity of their isophotes and then using Eq. 4.17 or by directly fitting a sky projected 2D model to the observed surface brightness using Eq. 4.14. In particular, a common practice (e.g. Trujillo et al. 2007; Longhetti et al. 2007; Kormendy et al. 2009; Law et al. 2012; van der Wel et al. 2012, 2014b) is to fit a single Sérsic profile with a free Sérsic index n to account for both disk-like ($n \approx 1$) and elliptical ($n \approx 4$) galaxies, as well as those with in-between shapes. However, this approximation may break as soon as the contribution of other components to the overall surface brightness distribution can no longer be neglected, in particular that of the central bulge. Therefore, fitting a single Sérsic profile to a galaxy with a non-negligible bulge contribution may bias the measure of the disk parameters. To get a rough estimate of how and how much the bulge component might affect the results of a single Sérsic fit performed to recover the disk parameters, I generated a grid of galaxy models using GALFIT (for more details and for an example of a modelling performed with GALFIT see Sect. 4.4). Each model was generated by combining an exponential disk profile for the disk component with a symmetrical de Vaucouleurs profile to represent the surface brightness distribution of a spherically symmetric bulge, and was convolved with a PSF represented by a circular Moffat profile with a FWHM of 3 pixels and a powerlaw slope of 1.9, similar to the PSF used to model the morphology of galaxies from HST F814W images in the MAGIC survey (Abril-Melgarejo et al. 2021; Mercier et al. 2022). Once the models generated, they were fitted with a single Sérsic profile with all its parameters let free, including its Sérsic index n . Because using a single bulge-disk model would not be representative of the type of systematics which may arise when fitting with a single Sérsic profile, I generated instead a grid of models with different bulge and disk parameters. The most important parameters which control the bulge-to-total flux ratio (B/T) are the bulge and disk total magnitudes and effective radii. In particular, only the difference between the bulge total magnitude and that of the disk will affect B/T rather than their exact values. Therefore, without loss of generality, I set the disk total magnitude to 20, with the magnitude photometric zero point set to an arbitrary value of 30, and varied the other aforementioned parameters. The following grid was used:

- Bulge total magnitude: 18, 20, 20.5, 21, 22, and 23 dex.
- Bulge effective radius: 15, 10, 5, 3, and 2 pixels.
- Disk effective radius: 30, 25, 20, 15, 10, and 5 pixels.
- Disk axis ratio: 0.17, 0.5, 0.77, 0.94, and 1, which corresponds to razor-thin disk inclinations of 0, 20, 40, 60, and 80°, respectively.

The reason for choosing these values was twofold: (i) to be consistent with the typical sizes and B/T values found in the morphological analysis of the MAGIC survey (see Chapter 3), (ii) so that there would be approximately 25% of the models falling in one of the following B/T bins: $B/T < 15\%$, $15\% \leq B/T \leq 50\%$, $50\% \leq B/T \leq 75\%$, and $B/T > 75\%$. In total, this corresponds to 900 bulge-disk models generated and then fitted with GALFIT. We show in Fig. 4.5 the variation of various best-fit parameters as a function of the true disk axis ratio and B/T. The parameters for each individual fit are shown as small markers whereas the median value for each B/T and axis ratio bins are shown as large markers with a dashed line. From left to right and top

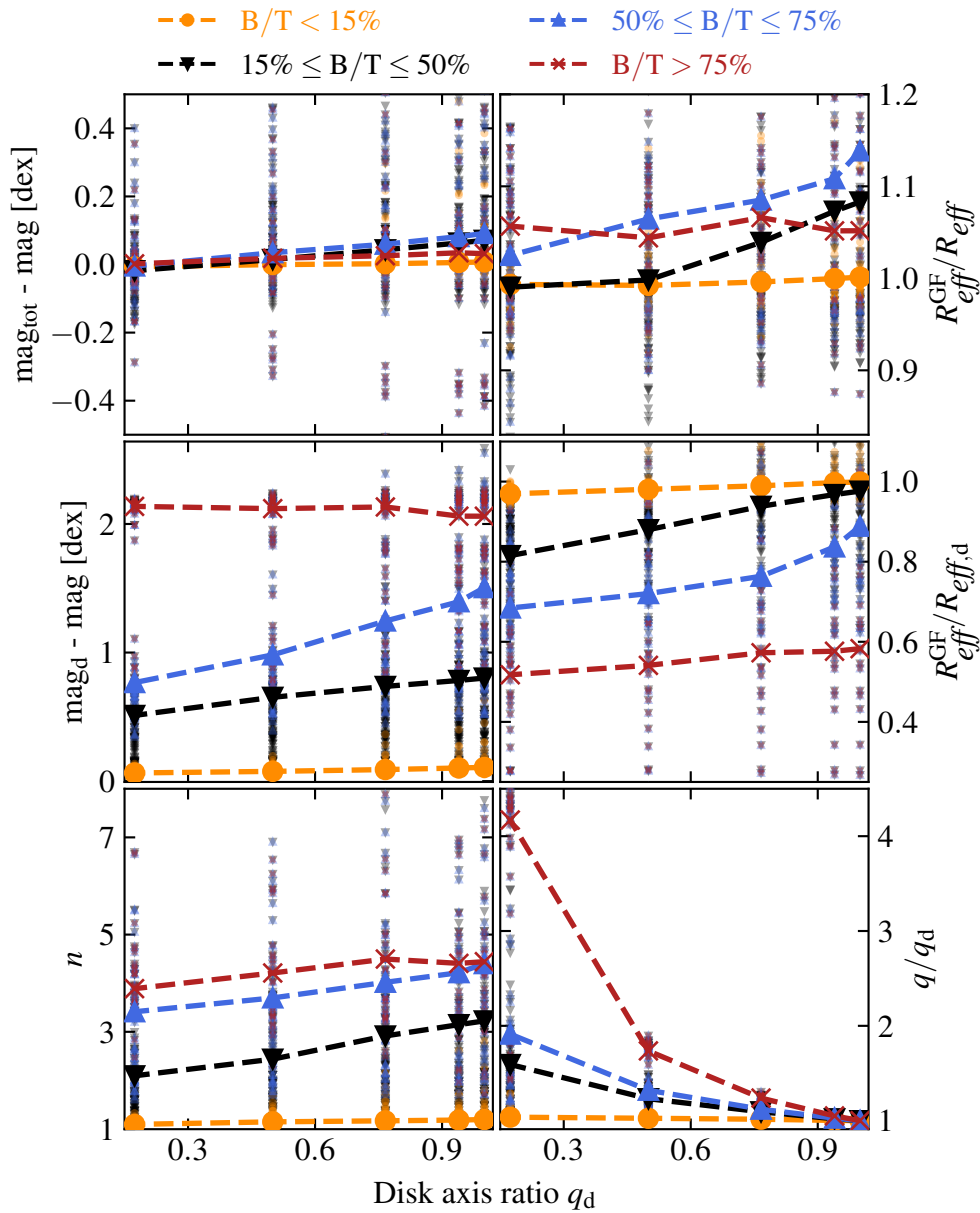


Figure 4.5: Variation of the best-fit parameters for various composite galaxy models with non negligible bulge contribution as a function of the true disk axis ratio and bulge-to-total flux ratio (B/T). Each model was fitted with GALFIT using a single Sérsic profile with free Sérsic index. The B/T values for each model are shown as small markers whereas the median values for each B/T are shown as large markers with dashed lines. From left to right and top to bottom: (i) difference between the true total magnitude (disk and bulge, noted mag_{tot}) and that of the best-fit model (mag), (ii) ratio between the model effective radius ($R_{\text{eff}}^{\text{GF}}$) and the true global effective radius (noted R_{eff} , see Sect. 4.3.2 for its definition), (iii) difference between the true disk magnitude (mag_{d}) and that of the best-fit model, (iv) ratio between the model effective radius and the true disk effective radius $R_{\text{eff,d}}$, (v) best-fit Sérsic index, and (vi) ratio between the model axis ratio q and the true disk axis ratio q_{d} . Even if the global parameters (total magnitude and global effective radius) are quite well recovered, a single Sérsic fit overestimates the flux contained in the disk and its axis ratio while it underestimates its size, especially for large bulge contributions.

to bottom (i) difference between the true total magnitude (noted mag_{tot}), including the disk and the bulge components, and that of the best-fit model (noted mag), (ii) ratio between the single Sérsic model effective radius $R_{\text{eff}}^{\text{GF}}$ and the true global effective radius R_{eff} which corresponds to the radius which contains half of the total light, that is including the disk and the bulge components (see Sect. 4.3.2 for how it is computed in practice), (iii) difference between the true disk magnitude (mag_{d}) and that of the best-fit model, (iv) ratio between the model effective radius and the true disk effective radius $R_{\text{eff,d}}$, (v) best-fit Sérsic index, and (vi) ratio between the model axis ratio q and the true disk axis ratio q_{d}

The first row of Fig. 4.5 shows how well does a single Sérsic fit recover the global properties of a bulge-disk model that are the total magnitude and the global effective radius. On average a single Sérsic fit recovers almost the same total magnitude and finds an effective radius which is slightly biased towards larger values though still close to the correct one. As we go towards larger B/T, then the scatter in these two plots increases significantly even though the median values are not as much affected. The second and third rows focus on the other hand on the efficiency of using the single Sérsic fit parameters as proxies for the disk properties. We can see that, for small bulge contributions, a single Sérsic fit converges towards a near exponential model with small bias and scatter for each parameter. But, the larger the bulge contribution the more biased and the more scattered the parameters become. This is especially relevant for the axis ratio since it is a morphological parameter that needs to be precisely constrained to properly model the dynamics of galaxies (see Sect. 5.3 for a discussion on that topic). Indeed, we see that the more elliptical the disk component (i.e. low q_{d}), the more underestimated is its axis ratio estimate q when fitting with a single Sérsic profile.

4.3 Multi-component decomposition

4.3.1 Bulge-disk decomposition

One way to circumvent the biases which arise when modelling with a single Sérsic profile the surface brightness distribution of galaxies is to use multiple components. When doing so, the most general form the total surface brightness Σ can take is

$$\Sigma_{\text{obs}}(x, y) = \sum_i \Sigma_{\text{obs},i}(x, y), \quad (4.29)$$

where $\Sigma_{\text{obs},i}$ corresponds to the projected surface brightness distribution of the component i . When the multi-component decomposition simplifies to a combination of a bulge and a disk, a common practice (e.g. Laurikainen et al. 2010; Abril-Melgarejo et al. 2021; Chu et al. 2021; Bouché et al. 2022; Costantin et al. 2022; Mercier et al. 2022; Quilley & de Lapparent 2022) is to model each component as an axisymmetric Sérsic profile. To remove degeneracies the disk is usually chosen to be an exponential disk and the bulge can either be a Sérsic profile with free Sérsic index or a de Vaucouleurs profile. In the latter case, the total surface brightness writes

$$\Sigma(R) = \Sigma_{\text{eff,d}} \exp \left\{ -b_1 \left[\frac{R}{R_{\text{eff,d}}} - 1 \right] \right\} + \Sigma_{\text{eff,b}} \exp \left\{ -b_4 \left[\left(\frac{R}{R_{\text{eff,b}}} \right)^{1/4} - 1 \right] \right\}, \quad (4.30)$$

where $(\Sigma_{\text{eff,d}}, R_{\text{eff,d}})$ and $(\Sigma_{\text{eff,b}}, R_{\text{eff,b}})$ are the disk and bulge Sérsic parameters, respectively. For disk-like galaxies, the bulge component will only dominate in the inner parts. Nevertheless, this

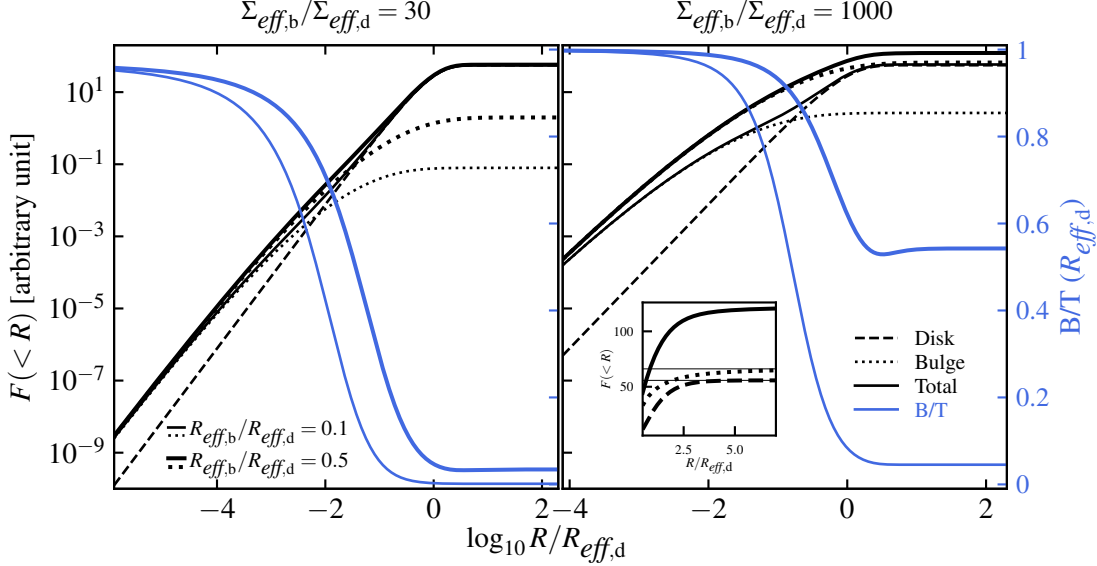


Figure 4.6: Variation of the flux distribution (black lines) and bulge-to-total flux ratio (B/T, blue lines) with radius for a weak bulge (left-hand plot) and a strong bulge (right-hand plot). For each plot, two cases are shown: (i) a small bulge with $R_{eff,b}/R_{eff,d} = 0.1$ represented as thin lines and (ii) a larger bulge with $R_{eff,b}/R_{eff,d} = 0.5$ represented as thick lines. The bulge flux distribution is shown as dotted lines and the total flux distribution (bulge and disk) as solid lines. The same disk model was used throughout and its flux distribution is represented as a thin dashed line in both plots. The bump visible for the thick blue line on the right-hand plot is due to the fact that the bulge is sufficiently bright and large so that its flux distribution reaches its plateau after that of the disk, as is shown on the inset in the right plot.

does not mean that the bulge contribution becomes null at large radii. Indeed, using Eq. 4.4 we can write the bulge-to-total flux ratio integrated up to radius R as

$$B/T(R) = \frac{B/D(R)}{1 + B/D(R)}, \quad (4.31)$$

where the bulge-to-disk ratio B/D is given by

$$B/D(R) = \frac{4b_1^2 \Sigma_b(0) R_{eff,b}^2 \gamma \left(8, b_4 \left(\frac{R}{R_{eff,b}} \right)^{1/4} \right)}{b_4^8 \Sigma_d(0) R_{eff,d}^2 \gamma \left(2, b_1 \frac{R}{R_{eff,d}} \right)}. \quad (4.32)$$

From the series expansion of the incomplete gamma function evaluated for small values of x given by $\gamma(s, x) \approx x^s/s$, we get that B/T near $R = 0$ is given by

$$B/T(R \rightarrow 0) = [1 + \Sigma_d(0)/\Sigma_b(0)]^{-1}. \quad (4.33)$$

Thus, the bulge-to-total flux ratio computed at the centre is just a different way to write the ratio of the central surface brightnesses between the disk and the bulge components. At infinity, B/T is given by

$$B/T(R \rightarrow \infty) = \left[1 + \frac{2b_4^8 \Sigma_d(0) R_{eff,d}^2}{(8!)b_1^2 \Sigma_b(0) R_{eff,b}^2} \right]^{-1}, \quad (4.34)$$

where $2b_4^8/[(8!)b_1^2] \approx 210.75$. Therefore, the only way to have a null bulge contribution at large distances is that either the disk contribution is infinite while that of the bulge is finite, or that the central surface brightness and/or effective radius of the bulge component are equal to zero, that is that there is no bulge at all. Similarly, even if the bulge usually dominates in the inner parts (i.e. $\Sigma_b(0) > \Sigma_d(0)$), this does not necessarily mean that B/T will reach a value close to one. However, in practice bulges have quite small radii compared to that of the disk component¹. This means that, most of the time, galaxies with a non-negligible bulge contribution at large radii will have B/T almost equal to one near the centre.

A few examples of B/T values computed at different distances for various bulge and disk parameters are shown in Fig. 4.6. The B/T values are shown as blue solid lines whereas the black lines represent the flux distribution of the bulge component (dotted), the disk component (dashed), and the sum of the two (solid). The left-hand plot represents the case of a galaxy with a weak bulge contribution and the right plot shows the case of a strong bulge contribution. In both plots, thick lines represent galaxies with a large bulge ($R_{eff,b}/R_{eff,d} = 0.5$) and thin lines galaxies with a small bulge ($R_{eff,b}/R_{eff,d} = 0.1$). As previously stated and as shown in Fig. 4.6, for typical galaxies without massive bulges, B/T gets close to zero far enough from the centre. In the case of the most massive bulge with the largest size (thick blue line, right plot), we can see a bump in B/T after $R \approx 2R_{eff,d}$ which means the contribution of the bulge component slightly increases again after this radius. This bump is actually physical and not an artefact (assuming such massive and large bulges would exist in nature in the first place). The explanation is that, near the centre the bulge dominates, as can be seen in Fig. 4.6, but at the same time the disk contribution increases since its inner slope is larger than that of the bulge and therefore B/T decreases. However, because the bulge is large, it reaches the plateau of its flux distribution after that of the disk component. Thus what happens is that, till the disk has not reached its plateau, B/T decreases but, once it is on the plateau, the flux of the bulge keeps mildly rising while that of the disk remains constant, therefore slightly increasing the value of B/T before the bulge reaches its own plateau and B/T remains nearly constant afterwards.

4.3.2 Global effective radius

An interesting quantity to derive is the radius R_n which encloses nth percent of the total flux. If measured on the plane of the sky, then this can easily be done using an isophotal fitting approach (e.g. [Jedrzejewski 1987](#); [Stone et al. 2021](#)), albeit taking care of the background signal and of the flux from nearby objects. However, we know that galaxies are composed of multiple components which have different geometries (e.g. spherical bulge or razor-thin disk). Isophotal fitting will therefore bias the measurement of the radius, especially when galaxies have a non-negligible bulge contribution.

¹At least in the case of the MAGIC survey, see for instance Fig. A.2 of [Mercier et al. \(2022\)](#) or in Chapter 6.

This issue disappears when one fits the surface brightness distribution with a multi-component decomposition because the geometry of each component is directly taken into account into the fit, which means that the recovered individual surface brightness profiles are intrinsic. Assuming a multi-component decomposition as described in Eq. 4.29, cylindrical symmetry for the individual surface brightness profiles (i.e. $\Sigma_i(x, y) = \Sigma_i(R)$), and that all components share the same centre, one can find R_n by solving the following equation

$$\sum_i \int_0^{R_n} dRR \Sigma_i(R) = \frac{n}{100} \times \sum_i \int_{\mathbb{R}} dRR \Sigma_i(R). \quad (4.35)$$

When $n = 50$, the solution to this equation is called the global half-light or effective radius (noted R_{eff}). Generally speaking, Eq. 4.35 can be solved by computing the two integrals numerically. However, in the case of a bulge-disk decomposition similar to Eq. 4.30, one can use the expression of the flux of a Sérsic profile integrated within a radius R given by Eq. 4.4 to derive the following analytical form:

$$F_{tot,d} \left[\gamma \left(2, b_1 \frac{R_{eff}}{R_{eff,d}} \right) - 0.5 \right] + \frac{F_{tot,b}}{\Gamma(8)} \left[\gamma \left(8, b_4 \left(\frac{R_{eff}}{R_{eff,b}} \right)^{1/4} \right) - \Gamma(8)/2 \right] = 0, \quad (4.36)$$

where $F_{tot,b}$ and $F_{tot,d}$ are the bulge and disk total fluxes, respectively. If one defines the total magnitude of a component i as $\text{mag}_i = -2.5 \log_{10} F_{tot,i} + \text{zpt}$, where zpt is a zero point that is the same for all the components and normalises by the total flux, then Eq. 4.36 writes

$$f(R_{eff})/f(\infty) = 0, \quad (4.37)$$

where the function f is defined as

$$f(x) = 10^{-\text{mag}_d/2.5} \left[\gamma \left(2, b_1 \frac{x}{R_{eff,d}} \right) - 0.5 \right] + 10^{-\text{mag}_b/2.5} \left[\gamma \left(8, b_4 \left(\frac{x}{R_{eff,b}} \right)^{1/4} \right) / \Gamma(8) - 0.5 \right], \quad (4.38)$$

and Eq. 4.37 can be solved by searching for its unique zero located between $R_{eff,d}$ and $R_{eff,b}$. Indeed, if R_{eff} is larger than both $R_{eff,d}$ and $R_{eff,b}$, then the flux at R_{eff} will be the sum of $F_d(R_{eff}) > F_{d,tot}/2$ and $F_b(R_{eff}) > F_{b,tot}/2$. Thus, its value will be larger than the expected $F_{tot}/2$ value. Therefore, R_{eff} cannot be greater than $\max(R_{eff,d}, R_{eff,b})$, and the same argument can be given when R_{eff} is less than both $R_{eff,d}$ and $R_{eff,b}$. Additionally, it can be proven that there is a unique zero that is a solution of Eq. 4.37 by noticing that f is a monotonously increasing function of x whose normalised form $f(x)/f(\infty)$ is bounded between -1 for $x = 0$ and 1 for $x = \infty$.

4.4 Morphological modelling of galaxies in the MAGIC sample

4.4.1 Modelling with Galfit

In [Mercier et al. \(2022\)](#), we modelled the surface brightness distribution of more than a thousand galaxies in the MAGIC sample by performing a bulge-disk decomposition using the morphological

modelling tool GALFIT² (Peng et al. 2002). GALFIT is a powerful, fast, and versatile forward modelling tool that can fit any number of components on images using various models that can be projected onto the sky. A custom PSF model can be provided by the user and masks can be applied to reduce the influence of nearby objects on the fit. Running GALFIT only requires to write an input file (called FEEDME) which contains the models, the initial values of their parameters, and a few metadata. A second optional file (called CONSTRAINTS) can be given to provide additional constraints between parameters. We provide below an example of typical FEEDME and CONSTRAINTS files that were used to model the galaxies in the MAGIC sample. In addition to the bulge and disk components we also added a sky background model which produces a sky gradient in both x and y directions. This model can be useful to remove the contribution to the disk and bulge components of a potential sky background in the image or that of a nearby source which would induce a sky gradient in its direction. For all the components, two values must be provided for each parameter, except for the centre position which needs four (two for the x coordinate and two for the y coordinate). The first value corresponds to the initial guess and the second one defines whether the parameter must be fixed (0) or free (1). In our case, the free parameters are (i) the centre positions, (ii) the total magnitudes, (iii) the effective radii, (iv) the disk axis ratio, (v) the disk PA, and (vi) the sky model parameters. On the other hand, the Sérsic indices of the disk and the bulge were fixed to $n = 1$ and $n = 4$ and the bulge axis ratio and PA were fixed to $q = 1$ and $PA = 0^\circ$, respectively. Furthermore, a few constraints were placed: (i) the offset between the disk and the bulge components was fixed to its initial value. Because both models were initialised to the same position, in practice this means that we forced the disk and the bulge to share the same centre, (ii) to limit potential degeneracies, we forced the centre to only be able to move in a box whose side length is equal to ten pixels, (iii) we set limits on the total magnitudes and effective radii of the disk and bulge components. These limits forced GALFIT to try different bulge-disk combinations before potentially converging to a single disk or single bulge model. If a galaxy has a negligible disk or bulge component, GALFIT will try to find the combination of parameters which minimises its contribution to the surface brightness distribution. In practice, this means its total magnitude will converge to the maximum value and its size is likely to converge to either its upper or lower bound. With an upper magnitude of 100 dex for a magnitude zero point of 30 dex, this effectively means that for our HST data the model will have a null contribution to the surface brightness and to the total flux.

²<https://users.obs.carnegiescience.edu/peng/work/galfit/galfit.html>

```

1 =====
2 # IMAGE PARAMETERS
3 A) input.fits           # Input data image (FITS file)
4 B) output.fits        # Name for the output image
5 D) psf.fits           # Input PSF image for convolution
6 G) example.constraints # File with parameter constraints
7 H) 0 134 0 134        # Image region to fit (xmin xmax ymin ymax)
8 I) 134 134            # Size of convolution box (x y)
9 J) 30.0               # Magnitude photometric zeropoint
10 O) regular            # Display type (regular, curses, both)
11 P) 0                 # 0=normal run; 1,2=make model/imgblock;
12                     # 3=normal run and separate components
13 =====
14
15 # Disk component
16 O) sersic             # Object type
17 1) 70.0 70.0 1 1     # position x, y [pixel]
18 3) 22.0 1            # total magnitude
19 4) 15.00 1           # effective radius R_e [pixel]
20 5) 1.00 0            # Sersic exponent
21 9) 0.30 1            # axis ratio (b/a)
22 10) 90.0 1           # position angle [Degrees: Up=0, Left=90]
23 Z) 0                 # Skip this model in output image?
24
25 # Bulge component
26 O) sersic             # Object type
27 1) 70.0 70.0 1 1     # position x, y [pixel]
28 3) 22.0 1            # total magnitude
29 4) 5.00 1            # effective radius R_e [pixel]
30 5) 4.00 0            # Sersic exponent
31 9) 1.00 0            # axis ratio (b/a)
32 10) 0.0 0            # position angle [Degrees: Up=0, Left=90]
33 Z) 0                 # Skip this model in output image?
34
35 # sky
36 O) sky               # Object type
37 1) 1.00 1            # sky background [ADU counts]
38 2) 0.000 1           # dsky/dx (sky gradient in x)
39 3) 0.000 1           # dsky/dy (sky gradient in y)
40 Z) 0                 # Skip this model in output image?

```

Code 4.1: Example of GALFIT FEEDME file.

Component	parameter	constraint
1_2	x	offset
1_2	y	offset
1	x	-5.0 5.0
1	y	-5.0 5.0
1	mag	10.0 to 100.0
2	mag	10.0 to 100.0
1	re	0.5 to 100.0
2	re	0.5 to 100.0

Code 4.2: Example of GALFIT CONSTRAINTS file.

4.4.2 Automatic modelling for a large number of galaxies

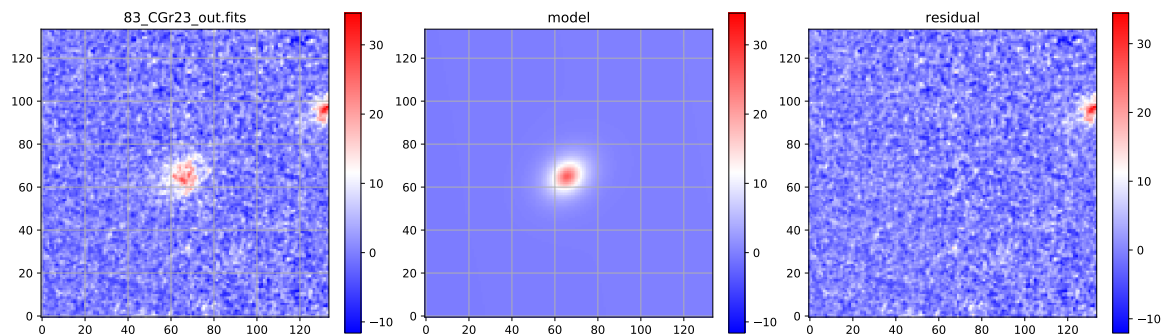


Figure 4.7: Example of a current summary file for galaxy 83_CGr23 generated by my python wrapper for automatic modelling of a large number of galaxies with GALFIT. From left to right: HST image, GALFIT best-fit model, and residuals. Flux units are arbitrary. This type of summary file is automatically generated at the end of the fitting process for each object that was fitted and was used in [Mercier et al. \(2022\)](#) to quickly identify galaxies that needed improved morphological models.

One of my first steps was to model the morphology of a large sample of mainly star forming galaxies from the MAGIC survey. From the 2730 objects in the initial MAGIC catalogue, including nearby stars, intermediate, and high-redshift galaxies ($z > 1.5$), we selected 1142 [O II] emitters with reliable spectroscopic redshifts³. The bulge-disk decomposition performed on these 1142 [O II] emitters is similar to what was described in Sect. 4.4.1 and a full description can be found in [Mercier et al. \(2022\)](#).

Since GALFIT was designed to model in details the morphology of galaxies by manually creating configuration files and iterating through the models and their parameters, using it directly on such a large number of galaxies is not entirely well suited. Thus, to accelerate and automatise the modelling process I developed a python wrapper around GALFIT⁴ which allows to easily model any number of galaxies using a common set of models with similar initial parameter values. This wrapper was built to be as versatile as possible and therefore is not restricted to bulge-disk decompositions only, but can be used with any combination of models provided in GALFIT and for any kind of photometric data. At the end of the modelling, summary pdf files are created to quickly visualise the modelling and assert whether a model needs to be improved or not. An example of such a summary file for galaxy 83_CGr23 is shown in Fig. 4.7. Because of the way it was built, this wrapper makes it as easy to model a large number of galaxies as single objects without having to manually tune any configuration file. This code was successfully used in [Mercier et al. \(2022\)](#) where I performed a bulge-disk decomposition on HST ACS F814W images of the 1142 [O II] emitters in the MAGIC sample. After removing low signal-to-noise ratio (S/N) objects and very small objects, we managed to get reliable bulge-disk decompositions for 890 galaxies⁵.

³[O II] emitters are defined as intermediate redshift galaxies for which we might be able to detect the [O II] $\lambda\lambda 3727, 3729$ doublet in the MUSE wavelength range, that is, located in the redshift range $0.25 \lesssim z \lesssim 1.5$

⁴<https://github.com/WilfriedMercier/wilfried/tree/master/galfit>

⁵The morphological models can be found as supplementary material of [Mercier et al. \(2022\)](#) at the following address: <https://www.aanda.org/articles/aa/olm/2022/09/aa43110-22/aa43110-22.html>

Below is shown an example of a python code which uses this GALFIT wrapper to produce FEEDME and CONSTRAINTS files similar to what is illustrated in the code snippets [4.1](#) and [4.2](#), which runs GALFIT onto those files, and which produces a pdf summary file once the fit is done:

```

1 from galfit import run_galfit
2
3 # Sky model
4 sky = {'name' : 'sky'}
5
6 # Header properties:
7 # - do not include the input/output and constraint file names
8 # - psf must be the same for all objects
9 header = {'psfImage' : 'psf.fits'}
10
11 # Sersic models:
12 # - objects will have the same initial parameters
13 disk = {'name' : 'sersic', 'x' : 70, 'y' : 70, 'n' : 1, 'fixedParams' : ['n'],
14         're' : 15, 'mag' : 22, 'b0vera' : 0.3, 'PA' : 90}
15
16 bulge = {'name' : 'sersic', 'x' : 70, 'y' : 70, 'n' : 4, 'fixedParams':['n', 'PA',
17         'b0vera'], 're' : 5, 'mag' : 22}
18
19 # Constraints
20 absRangeM = {'type':'absoluteRange', 'value':[10, 100]}
21 absRangeRe = {'type':'absoluteRange', 'value':[0.5, 100]}
22 relRange = {'type':'relativeRange', 'value':[-5, 5]}
23 offset = {'type':'offset', 'value':0.0}
24
25 constraint = [{'components' : [1, 2], 'parameter':'x',
26                 'constraint' : offset},
27               {'components' : [1, 2], 'parameter':'y',
28                 'constraint' : offset},
29               {'components' : 1, 'parameter':'x',
30                 'constraint' : rRange},
31               {'components' : 1, 'parameter':'y',
32                 'constraint' : rRange},
33               {'components' : 1, 'parameter':'mag',
34                 'constraint' : absRangeM},
35               {'components' : 2, 'parameter':'mag',
36                 'constraint' : absRangeM},
37               {'components' : 1, 'parameter':'re',
38                 'constraint' : absRangeRe},
39               {'components' : 2, 'parameter':'re',
40                 'constraint' : absRangeRe},
41               ]
42
43 inputNames = ['input.fits']
44 outputNames = ['output.fits']
45 feedmeNames = ['input.feedme']
46 constraintNames = ['input.constraints']
47
48 run_galfit(feedmeNames, header=header, pathIn='./'
49            listProfiles = [disk, bulge, sky],
50            inputNames = inputNames,
51            constraintNames = constraintNames,
52            outputNames = outputNames,
53            constraints = constraint)

```

Code 4.3: GALFIT python wrapper code example.

Chapter 5

Dynamical modelling

For the dynamical analysis of the galaxies in the MAGIC survey performed in [Abril-Melgarejo et al. \(2021\)](#) and [Mercier et al. \(2022\)](#) (see also Chapter 6), and for the analysis of the angular momentum in Chapter 7, I had to derive the galaxies' ionised gas kinematics, more specifically the kinematics that is traced by the [O II] doublet, being one of the brightest emission lines visible in the MUSE cubes in the redshift range $0.2 \lesssim z \lesssim 1.5$. For this, I used the moment maps formalism described in [Epinat et al. \(2010\)](#) that assumes that the gas is located in a rotating razor-thin disk. For the star-forming galaxies at intermediate redshift that I studied, this approximation is appropriate because such galaxies mostly have disk geometries. Besides, the gas being collisional it is expected that, with enough time, it should collapse into a rotating disk through a redistribution of angular momentum. This hypothesis is therefore common in kinematics studies found in the literature (e.g. [Epinat et al. 2010](#); [Übler et al. 2017](#); [Bouché et al. 2022](#)). There are at least two major difficulties with such a modelling: (i) the line-of-sight integration (as for the morphology) that removes the 3D information that would be required to have a complete modelling of the 3D gas or stellar kinematics and (ii) the low spatial and/or spectral resolution of our MUSE data around and beyond $z = 1$ which limits the complexity of the models we can use. Therefore, to perform such models we must rely on assumptions. The razor-thin disk geometry of the gas is certainly one of them that is appropriate for most galaxies. The fact that we only consider rotation during the modelling is another. Some authors have nevertheless started investigating new models beyond the simple rotating disk assumption (e.g. [Bizyaev et al. 2017](#); [Wang & Lilly 2022](#); [Lopez-Coba et al. 2022](#)) but these remain nevertheless fairly limited yet.

Thus, I describe in this chapter the different steps that I took to produce and fit resolved kinematics map models for almost 600 [O II] emitters using a forward modelling method that involves mass models. I start in Sects. 5.1 and 5.2 by describing the very general theoretical background behind the kinematics and mass modelling that I performed. These two sections, even if they have been used to derive the ionised gas kinematics only, are technically speaking applicable to stellar kinematics as well. More specifically, in Sect. 5.1 I derive the kinematics of a test particle under the influence of generic forces, especially in the context of cylindrical coordinates. In Sect. 5.2, I turn towards mass modelling and I show how the kinematics of a test particle can be related to the gravitational potential of a given mass distribution under the assumption of equilibrium. I discuss the effect of the asymmetric drift correction on the rotation velocity and I provide detailed examples of mass models that were used in [Mercier et al. \(2022\)](#). I

also quickly mention whether the choice of parametrisation for the DM halo profile has an important impact or not on our modelling of the velocity fields for our MUSE data of intermediate redshift galaxies and on the derived DM mass fraction. In Sect. 5.3, I explain how the kinematics maps extraction works and how I did it for the MAGIC sample. I also describe the theory behind the moment maps formalism that is used to model the galaxies' velocity fields, taking into account the instrumental effects on both the velocity fields and the velocity dispersion maps. Finally, I conclude this chapter by mentioning how the modelling was performed in practice for the MAGIC survey and how it changed between the analyses performed in [Abril-Melgarejo et al. \(2021\)](#) and [Mercier et al. \(2022\)](#) and that of the angular momentum presented in Chapter 7.

5.1 Kinematics of a test particle

To begin with, we will consider a test particle whose position $\vec{r}(t)$ can vary in time under the influence of various forces. For instance, the motion of the test particle can be impacted by the gravitational potential generated by the mass distribution of the galaxy within which it is embedded, as well as that of nearby objects, but also by other kind of forces such as those generated by outflows from AGN feedback and/or star formation, pressure gradients, and so on. In very general terms, the kinematics of a test particle can be described by Newton's equation

$$\frac{\partial \vec{V}}{\partial t}(\vec{r}) = \vec{F}(\vec{r}), \quad (5.1)$$

where $\partial \vec{V} / \partial t$ is the total acceleration, with \vec{V} the velocity vector, and \vec{F} is the sum of the different forces contributing to the kinematics. In Eq. 5.1 and in what follows we always make the dependence on time implicit. Since Eq. 5.1 is too general to be used directly, in what follows we will simplify it by making some assumptions about the forces at play and the geometry of the problem.

5.1.1 Kinematics in cylindrical coordinates

Because of the symmetries found in some galaxies, in particular their disk component, it is common practice, without loss of generality, to write the velocity vector in cylindrical coordinates (R, θ, z) . In these coordinates, R and θ represent the radial distance and azimuthal angle in a plane at fixed z , respectively, and z represents the vertical distance with respect to the plane $z = 0$. In this coordinate system, and with the corresponding basis vectors $(\hat{e}_R, \hat{e}_\theta, \hat{e}_z)$, we can write the velocity vector as

$$\vec{V}(\vec{r}) = V_R(\vec{r}) \hat{e}_R + V_\theta(\vec{r}) \hat{e}_\theta + V_z(\vec{r}) \hat{e}_z, \quad (5.2)$$

where $V_R(\vec{r}) = \dot{R}$ corresponds to radial motions, $V_\theta(\vec{r}) = R\dot{\theta}$ to rotation and $V_z(\vec{r}) = \dot{z}$ to vertical motions. Similarly, the total acceleration writes

$$\frac{\partial \vec{V}}{\partial t}(\vec{r}) = a_R(\vec{r}) \hat{e}_R + a_\theta(\vec{r}) \hat{e}_\theta + a_z(\vec{r}) \hat{e}_z, \quad (5.3)$$

where the three components a_R , a_θ and a_z can be written as

$$\begin{aligned}
a_R &= \dot{V}_R - V_\theta^2/R, \\
a_\theta &= V_R V_\theta/R + \dot{V}_\theta, \\
a_z &= \dot{V}_z,
\end{aligned} \tag{5.4}$$

and where we have made implicit the dependence on \vec{r} . A few points are worth mentioning. To begin with, we see that vertical forces (i.e. along \hat{e}_z) will only affect the vertical velocity component, whereas radial and azimuthal forces can affect both the radial and azimuthal components of the velocity vector. Besides, if all the forces cancel each other out along the vertical axis it only implies that V_z will be constant in time, but not necessarily in space. If we consider the special case where the contribution of forces cancel each other out along \hat{e}_θ , for instance to study the kinematics of a test particle located in an axisymmetric disk, and if we further assume that the radial velocity component is constant (potentially null) then the velocity of the test particle is purely circular and given by

$$V_\theta = \sqrt{-R a_R}. \tag{5.5}$$

We note that Eq. 5.5 remains correct even if there are azimuthal forces, that is along \hat{e}_θ , as long as $\dot{V}_R = 0$. However, then there would also be a non-zero velocity component along the radial direction to take into account and/or V_θ would become time-dependent (see the second line of Eq. 5.4).

5.2 Mass modelling

In this section, we assume that we want to derive the kinematics of a test particle embedded in a galaxy. Generally speaking, this galaxy could be isolated or have companion objects such as other galaxies in its vicinity. Each object will have its own mass distribution, made of various constituents (e.g. stars, gas, dust, DM halo, etc.), which can be decomposed into multiple components (e.g. bulge, disk, halo, etc.). Each component of each galaxy will have its own mass distribution $\rho_{M,i}$, which will generate a gravitational potential Φ_i following Poisson equation

$$\nabla^2 \Phi_i(\vec{r}) = -4\pi G \rho_{M,i}(\vec{r}), \tag{5.6}$$

where G is the gravitational constant and ∇^2 is the Laplacian operator. For a given mass distribution $\rho_{M,i}$, assuming one can solve Eq. 5.6, then the corresponding acceleration $\vec{a}_i = \vec{F}_i/m$, with m the mass of the test particle, is given by

$$\vec{a}_i(\vec{r}) = -\vec{\nabla} \Phi_i(\vec{r}), \tag{5.7}$$

where $\vec{\nabla}$ is the gradient operator. Thus, to derive the kinematics of a test particle in a given mass distribution, one has to solve Eq. 5.5 in combination with Eq. 5.7. Because the total mass distribution ρ_M is nothing more than the sum of the individual mass distributions, so will be the total gravitational potential Φ , that is we have

$$\rho_M(\vec{r}) = \sum_i \rho_{M,i}(\vec{r}) \quad \text{and} \quad \Phi(\vec{r}) = \sum_i \Phi_i(\vec{r}). \tag{5.8}$$

5.2.1 Mass modelling for a kinematics tracer in a plane

Because we wrote the equation of motion of a test particle in cylindrical coordinates in Sect. 5.1.1, it can be useful to also rewrite Eq. 5.7 in the same way, for instance if the kinematics tracer that is used is located in a plane. This is given by

$$\vec{\nabla}\Phi(\vec{r}) = \frac{\partial\Phi}{\partial R}(\vec{r}) \hat{e}_R + \frac{1}{R} \frac{\partial\Phi}{\partial\theta}(\vec{r}) \hat{e}_\theta + \frac{\partial\Phi}{\partial z}(\vec{r}) \hat{e}_z. \quad (5.9)$$

The radial acceleration will be given by $-\partial\Phi/\partial R$, so that if we assume that $\dot{V}_R = 0$ we find the solution

$$V_\theta(\vec{r}) = \sqrt{R \frac{\partial\Phi}{\partial R}(\vec{r})}. \quad (5.10)$$

Note that V_θ appearing in Eq. 5.10 is sometimes noted V_c or V_{circ} instead and referred to as the circular velocity. Thus, using Eq. 5.8 we get the law of velocity addition for the circular velocity:

$$V_\theta^2(\vec{r}) = \sum_i V_{\theta,i}^2(\vec{r}), \quad (5.11)$$

where $V_{\theta,i}$ is the circular velocity that is solution of Eq. 5.10 for the mass distribution $\rho_{M,i}$.

5.2.2 Asymmetric drift correction

Equation 5.10 is a common starting point for kinematic studies using mass models since it relates the theoretical rotation or circular velocity to a given mass distribution. However, it is also common to find in such studies a correction for the circular velocity called asymmetric drift. This corrective term is included so as to take into account the impact of a radial pressure gradient to the kinematics. The asymmetric drift correction to the circular velocity can be derived from Jean's equations under the main assumption of cylindrical symmetry (e.g. see Chapter 4 of [Binney & Tremaine 2008](#)). Nevertheless, its mathematical form can be recovered without invoking Jean's equations. Following [Dalcanton & Stilp \(2010\)](#) and [Bouché et al. \(2022\)](#), the acceleration \vec{a}_P generated by such a pressure gradient can be written as

$$\vec{a}_P(\vec{r}) = -\frac{1}{\rho_M} \frac{\partial P}{\partial R}(\vec{r}) \hat{e}_R, \quad (5.12)$$

with P the pressure and where the negative sign comes from the fact that a positive pressure gradient will induce an inward force, and a negative gradient will induce an outward force. In this case, Eq. 5.10 is rewritten as

$$V_{\theta,\text{corr}} = \sqrt{R \frac{\partial\Phi}{\partial R}(\vec{r}) - \frac{R}{\rho} \frac{\partial P}{\partial R}(\vec{r})}, \quad (5.13)$$

where $V_{\theta,\text{corr}}$ is the asymmetric drift corrected circular velocity, that is the rotation velocity that is affected by both the gravitational potential and the pressure gradient. Noting that $d \log R = dR/R$ and assuming that $P = \rho_M \sigma_R^2$, with σ_R the velocity dispersion along the radial direction, we get

$$V_{\theta,\text{corr}}^2 = V_\theta^2 + V_{\text{ac}}^2, \quad (5.14)$$

where V_{ac} is the asymmetric drift correction given by

$$V_{\text{ac}} = \sqrt{-\sigma_R^2 \left[2 \frac{\partial \log \sigma_R}{\partial \log R} + \frac{\partial \log \rho_M}{\partial \log R} \right]}, \quad (5.15)$$

and where we have made implicit the dependence on \vec{r} . Equations 5.14 and 5.15 are the most general expressions of the asymmetric drift correction usually found in the literature¹. To determine the correction, one has to know *a priori* the mass density of the kinematics tracer used (stars, ionised or cold gas), but also the radial component of the velocity dispersion. Because the dispersion is usually measured along the line of sight from spectroscopic data (noted σ_V), deriving σ_R is not straightforward. A common assumption is isotropy, that is $\sigma(\vec{r}) = \sigma_R = \sigma_V$. We note that in this expression σ only corresponds to the velocity dispersion related to the pressure gradient. However, in practice, the velocity dispersion which can be measured from kinematics data is the result of multiple physical processes (e.g. stellar or AGN feedback, accretion, mergers, etc.). Thus, directly using σ_V in Eq. 5.14 might lead to an overestimate of the asymmetric drift correction, which in turn could lead to biases in the estimate of the circular velocity.

5.2.2.1 Asymmetric drift correction for thick disks

In the case where the mass distribution of the kinematics tracer is located in a disk as given by Eq. 4.18, Eq. 5.15 simplifies to

$$V_{\text{ac}} = \sqrt{-\sigma_R^2 \left[2 \frac{\partial \log \sigma_R}{\partial \log R} + \frac{\partial \log \Sigma_M}{\partial \log R} + \frac{\partial \log h_z}{\partial \log R} \right]}, \quad (5.16)$$

where Σ_M is the mass density of the kinematics tracer in the plane of the disk, that is the equivalent of the surface brightness distribution but in terms of mass. For a double exponential disk model or even a sech law the thickness profile h_z is independent of R so that its derivative in Eq. 5.16 vanishes. To further simplify the expression of the asymmetric drift correction, the assumption of constant velocity dispersion is usually made, in which case Eq. 5.16 becomes

$$V_{\text{ac}} = \sigma_R \sqrt{-\frac{\partial \log \Sigma_M}{\partial \log R}}. \quad (5.17)$$

If the mass density is described by a Sérsic profile then Eq. 5.17 is simply given by

$$V_{\text{ac}} = \sigma_R \sqrt{\frac{b_n}{n} \left(\frac{R}{R_{\text{eff}}} \right)^{1/n}}, \quad (5.18)$$

where R_{eff} is the effective radius of the Sérsic profile. This simplifies even further for an exponential disk as it becomes

$$V_{\text{ac}} = \sigma_R \sqrt{\frac{R}{R_d}}, \quad (5.19)$$

¹Similar expressions can be derived from Jeans' equations by assuming that $\sigma_\phi = \sigma_R$ and $\overline{v_R v_z} = 0$. See Appendix C for the notation and Sect. 4.8.2 of Binney & Tremaine (2008) for the derivation.

where R_d is the disk scale length of the kinematics tracer mass distribution. Other expressions for the asymmetric drift correction that depend on other hypotheses (h_z and/or σ_R dependent on R , spheroidal mass distribution, etc.) can be found in the literature. These expressions go beyond the scope of the kinematics modelling and analysis performed in [Mercier et al. \(2022\)](#) (see Sect. 6) and in this Thesis and therefore we refer the interested reader to Appendix A of [Bouché et al. \(2022\)](#) for more details and references.

5.2.3 Circular velocity for a spherical distribution of mass

Spherical mass distributions are useful first approximations used to describe multiple components in galaxies, whether that be a bulge or a stellar or DM halo. Such distributions are interesting from a kinematical point of view because their circular velocity can be easily derived. Indeed, let us write Poisson's equation in cylindrical coordinates, assuming the gravitational potential is spherically symmetric as should be appropriate for distributions:

$$\frac{1}{r^2} \frac{\partial}{\partial r} \left(r^2 \frac{\partial \Phi}{\partial r} \right) = 4\pi G \rho_M. \quad (5.20)$$

Multiplying by r^2 and integrating along r from the center to some radius R we get

$$R^2 \frac{\partial \Phi}{\partial r} \Big|_R = GM(< R), \quad (5.21)$$

where $M(< R)$ is the integrated mass up to radius R . If Eq. 5.21 is evaluated in the plane of the galaxy disk, that is at $z = 0$, then we recover on the left hand side of the equation R times the circular velocity so that, for any spherically symmetric mass distribution, it writes

$$V_\theta = \sqrt{\frac{GM(< R)}{R}}. \quad (5.22)$$

We note that Eq. 5.22 can also be used inversely, that is to compute the integrated mass within some radius given V_θ as long as the mass distribution remains spherically symmetric.

5.2.4 Examples of mass models

There exist multiple mass models that can be used to model the dynamics of galaxies. Some can be derived from analytical mass density-gravitational potential pairs (e.g. Kuzmin's disk) whereas others must be computed numerically for a given mass distribution. In the latter case and for an arbitrary mass density, one has to find first the corresponding gravitational potential and then compute the circular velocity. In [Mercier et al. \(2022\)](#), we used and described four different mass models: (i) a spherically symmetric Hernquist's model ([Hernquist 1990](#)) to describe the bulge component of galaxies, (ii) a razor-thin exponential disk model, also referred to as Freeman's disk ([Freeman 1970](#)), (iii) a double exponential disk, and (iv) a spherically symmetric NFW ([Navarro et al. 1996](#)) halo for the DM distribution. For details about the derivation of the circular velocity for each mass distribution we invite the reader to refer to Appendix D of [Mercier et al. \(2022\)](#) which can also be found in Chapter 6 of this Thesis. An example adapted from galaxy 104_CGR79 of the shape of the circular velocity, mass density, and cumulative mass profiles for the Hernquist's model, double exponential disk, and NFW halo is shown in Fig 5.1.

5.2.4.1 Hernquist bulge

The Hernquist’s model is an interesting mass distribution that is used to describe galaxy bulges since, as it was shown in [Hernquist \(1990\)](#), once projected onto the plane of the sky, and under the assumption of spherical symmetry, it fits quite well the usual circular de Vaucouleurs profile used to model the surface brightness distribution of the bulge component in galaxies. It writes

$$\rho_M(r) = \frac{M_b}{2\pi} \frac{a}{r} \frac{1}{(r+a)^3}, \quad (5.23)$$

where r is the radial distance with respect to the center of the profile, M_b the total bulge mass and $a = r_{1/2,M}/(1 + \sqrt{2})$ its scale radius with $r_{1/2,M}$ the half-mass size. Integrating Eq. 5.23 to get the mass and then using Eq. 5.22, the circular velocity in the plane of the disk writes

$$V_b(R) = 2V_{b,\max} \frac{\sqrt{ar}}{a+r}, \quad (5.24)$$

where $V_{b,\max} = 0.5 \times \sqrt{GM_b/a}$ is the maximum circular velocity reached at $r = a$.

A caveat of Eqs. 5.23 and 5.24 is that they require M_b and a to be known which are parameters of the mass density rather than parameters of the surface brightness distribution which is what is observed/fitted in practice. Therefore, in [Mercier et al. \(2022\)](#) we computed a mapping between Hernquist and de Vaucouleurs parameters by generating a grid of Hernquist’s models whose parameters are appropriate for the galaxies in the MAGIC sample, sky projected them, and then fitted them with de Vaucouleurs profile. The observed correlation between the two Hernquist parameters $F_b = M_b/\Upsilon$ and a , Υ being the mass-to-light ratio (M/L) assumed to be constant throughout the galaxy, and the two de Vaucouleurs parameters Σ_{eff} and R_{eff} were then fitted with the two following scaling relations:

$$\log_{10} a [\text{kpc}] = -0.454 + 0.725 \log_{10} R_{eff,b}[\text{kpc}] \quad (5.25)$$

$$\log_{10} F_b/\Sigma_{eff,b} [\text{cm}^2] = 1.194 + 1.750 \log_{10} R_{eff,b}[\text{kpc}]. \quad (5.26)$$

For typical bulge sizes around 1 – 2 kpc the relative difference between the true maximum bulge induced circular velocity and that inferred using the mapping given in Eqs. 5.25 and 5.26 is, at its lowest, below 10%. On the other hand, bulges with very small and very large sizes should have larger relative differences, however such bulges are typically associated with small fluxes since they are either too large to be physical or too small to be resolved in our HST data.

5.2.4.2 Freeman’s disk

A very common disk model used in the literature is the so-called Freeman’s disk. This model assumes a razor-thin disk with an exponential surface brightness distribution (see Eq. 4.8) and has an analytical expression for its circular velocity that was derived by [Freeman \(1970\)](#) based on a previous work by [Toomre \(1963\)](#). The velocity writes

$$V_{RT}(R) = V_{RT,\max} \times \frac{yf(y)}{1.075 f(1.075)}, \quad (5.27)$$

where the subscript RT stands for razor-thin, $f(y) = \sqrt{I_0(y)K_0(y) - I_1(y)K_1(y)}$, $y = R/(2R_d)$, and with I_i and K_i modified Bessel functions of the first and second kind, respectively. In Eq. 5.27,

the maximum circular velocity is reached at $R = 2.15R_d$ and can be found numerically by finding the zero of the derivative of the rotation velocity as given in Freeman (1970). It is equal to

$$V_{\text{RT,max}} = 2.15f(1.075) \sqrt{\pi G R_d \Sigma_M(0)}, \quad (5.28)$$

with $\Sigma_M(0) = \Upsilon \Sigma(0)$ the central surface mass density of the disk. The factor 1.075 in Eqs. 5.27 and 5.28 just comes from the fact that the function $f(y)$ is evaluated at the radius of maximum velocity.

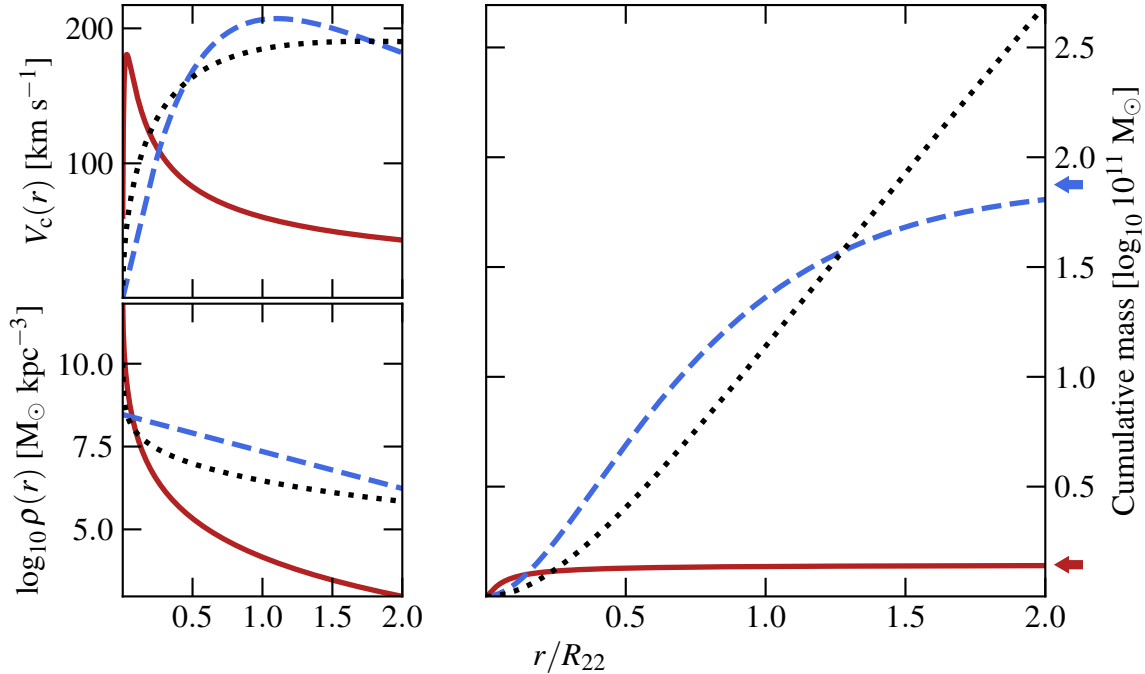


Figure 5.1: Illustration of the various mass models discussed in Sect. 5.2.4. In each figure is represented a Hernquist profile (red line, see Sect. 5.2.4.1), a double exponential disk (blue dashed line, see Sect. 5.2.4.3 and Eq. 4.22), and a NFW profile (black dotted line, see Sect. 5.2.4.4). On the top left are shown the rotation curves, on the bottom left the mass density profiles, and on the right hand-side the cumulative mass profiles. The mass density profile for the double exponential disk is taken in the plane of the disk. The total mass of the bulge and disk component are indicated with red and blue arrows, respectively. The NFW profile reaches a virial mass $M_{200} \approx 2 \times 10^{12} M_\odot$ at its virial radius $R_{200} \approx 47R_{22}$, making the galaxy DM-dominated with a DM fraction of about 91% at R_{200} .

5.2.4.3 Double exponential disk

In the case of a double exponential disk as described by Eq. 4.22, there is no known analytical formula for the circular velocity. However, an analytical approximation was derived in the case of

thin disks, that is with small scale height h_z , in Bovy J. online book “Dynamics and Astrophysics of Galaxies. Princeton University Press, Princeton, NJ” (in preparation)²:

$$V_d^2(R) = V_{\text{RT}}^2(R) - V_{\text{corr,max}}^2 \times \frac{R e^{1-R/R_d}}{R_d}, \quad (5.29)$$

The maximum of the correction $V_{\text{corr,max}}$ is reached at R_d and is given by

$$V_{\text{corr,max}} = \sqrt{2\pi G h_z \Sigma_M(0)/e}. \quad (5.30)$$

Equations 5.29 and 5.30 give a fairly reasonable approximation to the real rotation curve generated by the potential of a double exponential disk in the plane of the disk for small h_z . For most of the radial range this approximation gives a circular velocity that is off from the real value by around 2%, except in the inner parts where the difference rises significantly. More specifically, the main caveat of Eq. 5.29 is that V_d^2 becomes negative as soon as the correction factor becomes greater than the razor-thin disk circular velocity squared appearing on the right hand side of the equation, which always happens in the inner parts. This is not too problematic if one just sets the circular velocity to zero once this happens but the issue is now that the circular velocity reaches zero before reaching the center of the galaxy, which is unphysical for axisymmetric models. The straightforward solution to this problem would be to numerically compute the circular velocity without relying on Eq. 5.29 but (i) with a much longer computational time and (ii) at the cost of numerical stability given that it would involve two integrals with Bessel functions (see Eq. D.11 in Mercier et al. 2022).

The solution I adopted was to apply a correction in the inner parts to the approximation given by Eq. 5.29. Indeed, near the center the rotation curve of a flattened mass distribution is expected to rise quickly so that the approximation of a linearly rising rotation curve in the inner parts should be appropriate enough and would certainly be better than assuming a null velocity throughout. This derivation is presented in Appendix D.5 of Mercier et al. (2022) (see also Sect. 6) and was done by finding a scaling relation between the intrinsic axis ratio $q_0 = h_z/R_d$ of the galaxy and the radius R_0 at which the tangential line to the rotation curve given by Eq. 5.29 passes through the center of the galaxy. The relation reads

$$\log(R_0/R_d) = 0.76679 + 0.86230x - 0.13703x^2 - 0.02308x^3 + 0.00452x^4 + 0.00102x^5, \quad (5.31)$$

where $x = \log q_0$.³ The choice of a fifth order polynomial fit was based mostly on the shape of the observed relation and on the need to keep a low error (typically below 2%) in the range of q_0 values we were interested in. Therefore, the rotation curve for the double exponential disk we adopted in Mercier et al. (2022) writes

$$V_{\text{DE}} = \begin{cases} V_d(R_0) \times R/R_0 & \text{if } R < R_0, \\ V_d(R) & \text{otherwise,} \end{cases} \quad (5.32)$$

where the subscript DE stands for double exponential, R_0 is solution of Eq. 5.31, and V_d is the circular velocity derived by J. Bovy and given by Eqs. 5.29 and 5.30. On top of what has been previously said, Eq. 5.32 also has the advantage of being continuous and differentiable everywhere.

²See Eq. 8.73 in Chapter 8 at <https://galaxiesbook.org/>.

³Note that there are a few typos in Appendix D.5 of Mercier et al. (2022). The equation to solve to find R_0 given q_0 is indeed Eq. D.24 of the paper with $y_0 = R_0/(2R_d)$. The correct expression for the solution is the one given in Eq. 5.31 of this Thesis.

5.2.4.4 NFW dark matter profile

Multiple models of DM exist in the literature either cores or cusps in their central parts, for instance the NFW (Navarro et al. 1996), Einasto (Einasto 1965), Burkert (Burkert 1995), or Dekel-Zhao (Freundlich et al. 2020) profiles just to cite a few. In Mercier et al. (2022) we have decided to use a spherically symmetric NFW profile to model the DM halo component that has strong effects on the dynamics of galaxies. This mass density profile writes

$$\rho(r) = \delta_c \rho_{\text{crit}} \frac{r_s}{r(1 + r/r_s)^2}, \quad (5.33)$$

where $r_s = r_{200}/c$ is the scale radius, with r_{200} the virial radius of the halo where the mean overdensity is equal to 200 and c the halo concentration, $\rho_{\text{crit}} = 3H_0^2/(8\pi G)$ the Universe closure density and δ_c the halo characteristic overdensity (for more details, see Navarro et al. 1996). The corresponding circular velocity writes

$$V_h(r) = \frac{V_{h,\text{max}}}{0.46499} \sqrt{\frac{\log(1 + r/r_s)}{r/r_s} - \frac{1}{1 + r/r_s}}, \quad (5.34)$$

where $V_{h,\text{max}}$ is the maximum circular velocity reached at $r \approx 2.163 r_s$ (similarly to the Freeman's disk it has to be derived numerically). This DM halo model has the disadvantage that, if integrated to infinity, its total mass diverges. Thus, its total mass as well as its extent are to be taken at the virial radius of the halo where the structure is supposed to be the outermost bound. Hence, one has to be careful when using an NFW profile to not integrate it beyond its virial radius when computing its dynamical effect. Hopefully for us, DM haloes are found to be sufficiently large so that their extent goes beyond the galaxies' optical radius where the ionised gas kinematics is effectively measured in our MUSE data.

5.2.4.5 Of the choice of DM profiles for dynamical models of intermediate redshift galaxies

Throughout the years it has become increasingly obvious that the dynamics and the observable matter content of galaxies cannot be reconciled unless an additional DM component is added. Two main families of DM exist in the literature, differing in the slope in the inner parts. The first, derived from DM-only simulations, is called cuspy and it typically corresponds to models such as the NFW profile that have a non-zero slope in their inner parts so that the DM density is infinite at the center. The second family corresponds to core profiles and is favoured by observations, for instance the pseudo isothermal sphere (Begeman 1987). A third family, widely used in the literature to study the cusp-core problem, are parametric models with varying inner and/or outer slopes. Typical parametric DM profiles are that of Einasto, Zhao (Zhao 1997), or Dekel-Zhao. These profiles behave very differently near the center even though they all share a similar behaviour at large radii with constant or slowly declining rotation curves. Thus, it could be expected that their impact on the dynamics of galaxies is significant, especially in the inner parts. However, we argue that the choice of the DM profile, and therefore the shape of the halo near the center, is not particularly significant to model the kinematics of intermediate redshift galaxies given our MUSE data. This point is particularly relevant in this case and in the study performed in Mercier et al. (2022) since the goal was never to study the shape of the DM haloes but rather to compute their mass far enough from the central parts.

To illustrate that point, one of the most massive disk-dominated galaxies with a non negligible bulge contribution was selected from the MAGIC sample: galaxy ID 104_CGR79. This galaxy was found to have massive disk and bulge components of $M_d(R_{22}) \approx 7.0 \times 10^{10} M_\odot$ and $M_b(R_{22}) \approx 2.5 \times 10^{10} M_\odot$, respectively, with a dominating DM component⁴. Its size and mass therefore make it a perfect candidate to check the impact of different DM parametrisations on the goodness of fit of the velocity field. To do so, the velocity field extracted from the MUSE cube was fitted using a mass model combining a double exponential disk with intrinsic axis ratio $q_0 \approx 0.2$ (see Eq. 9 of [Mercier et al. 2022](#) for more details on how to derive the disk thickness), a Hernquist bulge, and four different types of spherically symmetric DM haloes: (i) a cuspy NFW profile, as was done in [Mercier et al. \(2022\)](#), (ii) a parametric Einasto model which can be either cuspy or cored, (iii) a pseudo isothermal sphere which is a cored profile, and (iv) a Hubble modified model ([Reynolds 1913](#); [Hubble 1930](#); [Rood et al. 1972](#); [Binney & Tremaine 2008](#)) which is cored as well. I skip the details of how the kinematics modelling was performed or how the kinematic maps were extracted from the MUSE cube since these will be covered in details in Sect. 5.3.

The results of the four different fits are shown in Fig. 5.2. The first row shows the various best-fit DM rotation curves for the NFW (solid line), Einasto (dashed line), pseudo isothermal sphere (dotted line), and Hubble modified (dashed-dotted line) profiles. As an indication, I also show the disk (blue solid line) and bulge (red solid line) rotation curves used in the fit, the radius R_{22} where the dynamical mass was measured (vertical blue dashed line), and the extent of the MUSE data (R_{last} - vertical red solid line). The second and third row represent the best-fit velocity fields and residuals, respectively. Almost all the rotation curves display a similar inner slope, except for NFW. This comes from the fact that only the NFW profile is cuspy (the Einasto profile converges towards a cored profile with $\alpha \approx 0.6$). Beyond R_{last} , where the rotation curves are extrapolated, the profiles show different behaviours depending on whether they decline with radius (NFW, Einasto, and Hubble modified) or if they remain constant (pseudo isothermal sphere). Nevertheless, the velocity fields and their residuals are strikingly similar no matter the difference in the inner parts. Similarly, the DM masses computed within R_{22} are nearly identical with $M_{\text{DM}} \approx 1.49, 1.47, 1.47,$ and $1.53 \times 10^{11} M_\odot$ for the NFW, Einasto, pseudo isothermal sphere, and Hubble modified models, respectively. The main explanation for the fact that these profiles yield similar velocity fields and DM masses is the impact of instrumental effects on the forward velocity field model that smooths out the steep velocity gradient in the inner parts. This effect, also known as beam smearing, will be discussed more attentively in Sect. 5.3.

It is important to note that even though all these models provide similar fits and dynamical masses at R_{22} for this galaxy, some might be favoured with respect to the others using additional independent constraints. One of such constraints that could be used is the stellar-to-halo mass relation (SHMR) that links the stellar mass of the galaxies to their typical halo mass. This relation can be constrained either from simulations (e.g. abundance matching or halo occupation distribution) or from empirical models of galaxy formation (for a review on the topic see [Wechsler & Tinker 2018](#)). In this specific case, extrapolating the best-fit dark matter profiles to their virial radius provides virial masses (M_{vir}) of the order of $10^{12} M_\odot$, except for the pseudo isothermal sphere that reaches rather $7 \times 10^{12} M_\odot$. Furthermore, this gives a stellar-to-halo mass ratio $M_*/M_{\text{vir}} \approx 6\%$ for all the profiles (except the pseudo isothermal sphere) which is slightly above the value of 1-2% that is expected for a halo of mass $M_{\text{vir}} \approx 10^{12} M_\odot$ given the various SHMRs at $z \approx 1$ found in the literature (e.g. [Guo et al. 2010](#); [Behroozi et al. 2013](#); [Kravtsov et al. 2018](#)).

⁴Approximately $1.5 \times 10^{11} M_\odot$ at R_{22} based on a fit performed in [Mercier et al. \(2022\)](#) with a NFW profile for the DM component

Only the pseudo isothermal sphere model does recover a mass ratio around 1% consistent with the SHMR. Hence, if the objective is to probe the shape of DM halo profiles at intermediate and high redshift, the SHMR could be used in combination with such forward kinematic models to favour or disfavour some profiles (e.g. [Bouché et al. 2022](#), where it was used to show evidence for core profiles at $z \approx 1$). Alternatively, authors such as [Li et al. \(2020\)](#) have also tried to directly implement the SHMR as a prior in their Bayesian framework when modelling galaxy rotation curves. Because the constraint is directly implemented in the modelling when marginalising over the fitted parameters, it allows to recover best-fit DM halo profiles that are consistent with the SHMR. In this Thesis, the goal was not to constrain the shape of the DM halo profiles but rather (i) to recover the intrinsic circular velocity of the ionised gas and (ii) to derive the DM fraction, both within the optical radius of the galaxies. Because our MUSE data are restricted to the optical size of the galaxies and since we did not want to extrapolate our kinematics measurements at large distances where we would need additional data (e.g. HI), we did not use the SHMR in the modelling.

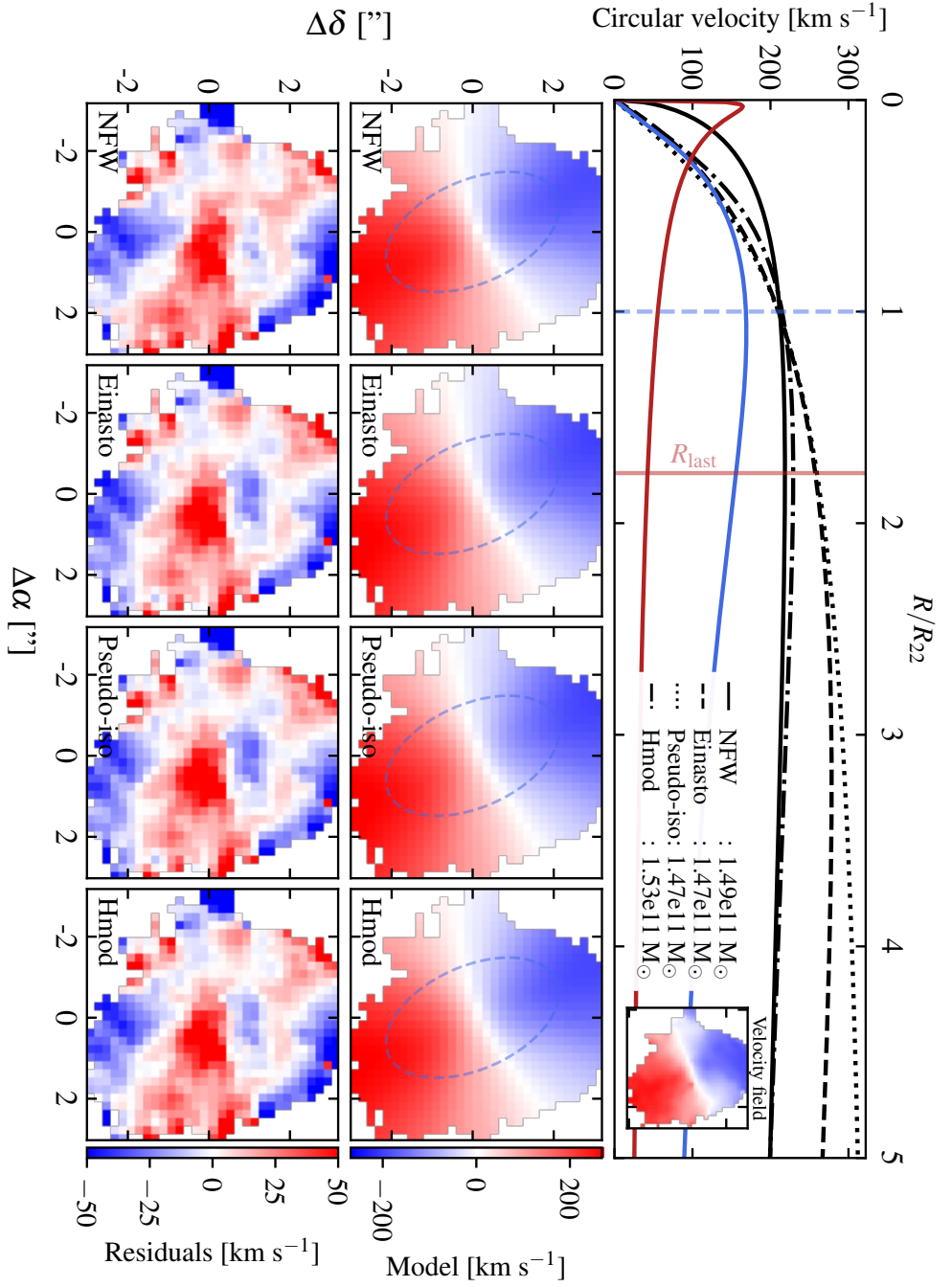


Figure 5.2: Example of various dynamical fits performed on the same galaxy 104_CGR79. The top row shows the different best-fit DM rotation curves using the following profiles: NFW (solid line), Einasto (dashed line), pseudo isothermal sphere (dotted line), and Hubble modified (dashed-dotted line). The bulge and disk components used in the fit are also shown as solid blue and red lines, respectively. The vertical dashed blue line represents the position where the DM mass for each model was computed and the red solid line represents the extent of the MUSE velocity field, that is beyond which the rotation curves are extrapolated. The second row represents the best-fit velocity fields for each model and the last row shows the residuals of each fit. As a comparison, we also show the MUSE velocity field as an inset in the first row and the radius where the DM mass is computed as an ellipse in the second row.

5.3 Ionised gas kinematics with IFU data

In what follows, I will describe how I modelled the galaxies' ionised gas kinematics for the [OII] emitters in the MAGIC survey. To begin with, I will discuss in Sect. 5.3.1 how I extracted the galaxies' kinematics maps from their MUSE cubes using the line fitting tool CAMEL⁵ and then I will quickly go through the theory behind the modelling of the gas velocity field in Sect. 5.3.2. Finally, I will conclude in Sect. 5.3.3 by discussing how this methodology was used in [Mercier et al. \(2022\)](#) and in Chapter 6 in combination with mass models using the kinematics fitting tool MOCKING⁶.

5.3.1 Extraction of kinematics maps

The first part of the kinematics modelling is to extract the kinematics maps from the MUSE cubes. This step was done for the MAGIC survey during the first year of my PhD using the line fitting tool CAMEL. CAMEL is a python code developed by [Epinat, B. \(Epinat et al. 2009, 2012\)](#) that is dedicated to fitting emission lines from data cubes in order to derive kinematics maps such as velocity fields, velocity dispersion maps, line fluxes, and so on. The whole process works by writing one configuration file per set of emission lines that has to be fitted simultaneously. The configuration file contains all the information CAMEL requires to perform the fit. Several lines can be fitted simultaneously using the same constraints for the velocity and eventually the velocity dispersion, as well as additional constraints on the flux between a set of lines (e.g. Balmer lines, doublet flux ratio, etc.). Emission lines that are integrated by default in CAMEL are H α , H β , H γ , H δ , [OII], [OIII], [NII], and [SII] $\lambda\lambda$ 6716, 6731, but it is also possible to add any additional line using the EXTRAL keyword.

5.3.1.1 Sub-cube extraction

To begin with, a sub-data cube centred on the galaxy's location is extracted from the MUSE cube using the following information given in the configuration file: (i) the redshift of the galaxy, (ii) the emission lines to fit, (iii) the spatial dimensions of the sub-data cube, and (iv) the spectral dimension of the sub-data cube. The spatial dimensions of the sub-cube can be defined through the use of the four following keywords: XMIN, XMAX, YMIN, and YMAX. Similarly, the spectral range can be defined in the configuration file with the keywords ZMIN and ZMAX.

To improve the fitting process, it is possible to clip as well as spatially and/or spectrally smooth the cube. For the clipping, three values must be provided: (i) the σ value of the σ -clipping, (ii) the number of passes, and (iii) the size of the box within which the median value is computed. The clipping is performed channel per channel using the usual σ -clipping method of replacing by the median value in the given channel all the spaxels that are σ times above the median. The latter can either be computed in the entire channel or in a box of a given size. The process is repeated until the clipping condition is not met any more or if the maximum number of passes is reached. By default, a 10σ -clipping is performed with three passes and a box to compute the median value of 3×3 spaxels. On the other hand, for both spatial and spectral smoothing the user only has to provide the FWHM of the Gaussian window used by CAMEL. By default, it does not apply any spectral smoothing but does apply a sub-PSF (at least for a MUSE cube) spatial smoothing of 2 spaxels.

⁵<https://gitlab.lam.fr/bepinat/CAMEL>

⁶<https://gitlab.lam.fr/bepinat/MockIng>

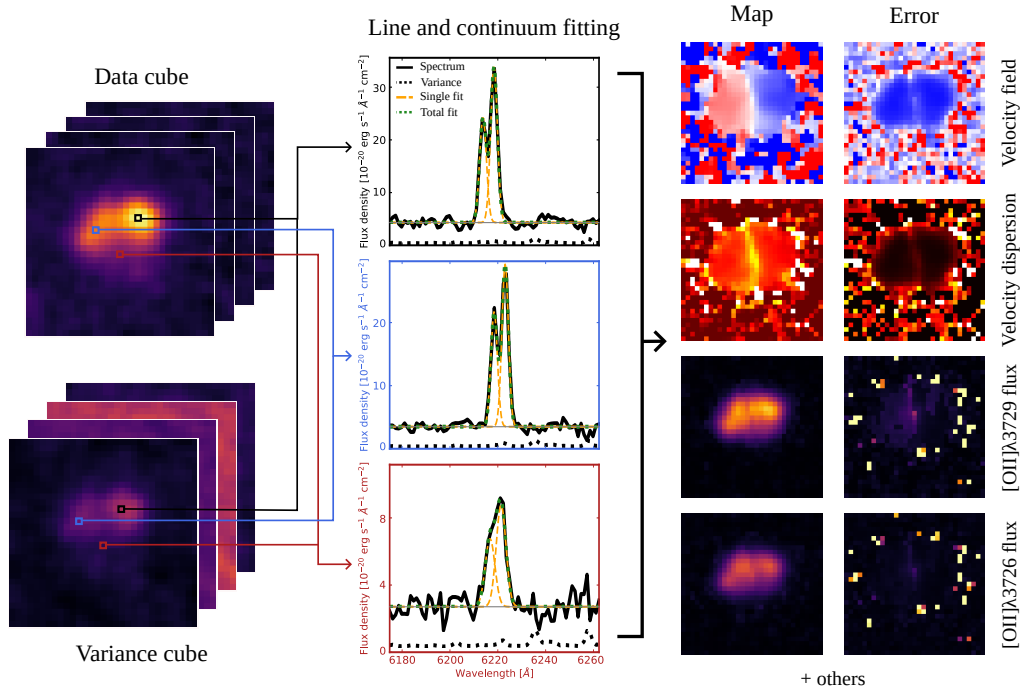


Figure 5.3: Illustration of the extraction process of the kinematics maps from a MUSE cube using CAMEL for galaxy 104_CGR79. On the left-hand side is shown the sub-data and variance cubes extracted by CAMEL with three different spaxels that are highlighted. Their spectra (solid line) around the [O II] doublet with their single (orange dashed line) and total (green dotted line) best-fit Gaussian lines are represented in the middle of the figure. The variance spectrum used during the fit is also shown with a black dotted line. On the right-hand side is shown a few important kinematics maps extracted from the cube by CAMEL for all the spaxels: the velocity field, velocity dispersion map, and the two flux maps. The corresponding error maps are also represented on their right with the same scale.

5.3.1.2 Emission line fitting

Once sub-data cubes are extracted, CAMEL will fit spaxel by spaxel each emission line using Gaussian profiles combined with a continuum modelled as a polynomial function. The degree of the polynomial can be provided by the user (zero by default) and CAMEL will automatically set the zeroth degree to the median value of the spaxel's spectrum. All the lines given in the configuration file will then be fitted at the same time by adjusting the redshift of the spaxel as well as the lines' amplitude and width. Furthermore, CAMEL uses by default an option that forces the lines to all have the same velocity dispersion. The user also has the possibility to provide additional keywords to further improve the fit such as giving lower and upper bounds on the dispersion of the line (`WMIN`, `WMAX`), the redshift range used to fit the lines (`ZRMIN`, `ZRMAX`) or the redshift range used to search for the best redshift (`REDMIN`, `REDMAX`).

After fitting each spaxel separately, taking into account the variance cube to weight the fits, CAMEL will produce various kinematics maps, the most important ones being: (i) the integrated

lines' fluxes, (ii) their velocity offset with respect to the given systemic redshift, (iii) their velocity dispersion, (iv) their S/N, and (v) the uncertainty associated to any of these values, except for the S/N. Other kinematics maps that are less important for the kinematics modelling but that can still be useful are also produced such as the best-fit central wavelength of the line, its width in spexels rather than in velocity, a model cube that only contains the best-fit Gaussian profiles, a continuum cube that only contains the best-fit continuum polynomial fit or a white light image. The process of fitting emission lines from the sub-data and variance cubes is illustrated in Fig. 5.3. Examples of spectral fits performed by CAMEL on the [OII] doublet is shown in the middle column for three spaxels with, from top to bottom, decreasing S/N. Each spectrum is represented as a solid black line, its uncertainty as a black dotted line, the two single line fits as orange dashed lines and the total fit of the doublet as a green dotted line. Doublet, such as [O II], are treated by CAMEL differently than singlets in the sense that the width of each line in the doublet is always forced to be equal to the that of the other one. The right-most two columns of Fig. 5.3 represent the raw kinematics maps (parameter and then uncertainty) that came out of the fitting process with on the first row the velocity field, on the second the velocity dispersion map, and on the third and last rows the flux of each line in the doublet.

5.3.1.3 Maps cleaning

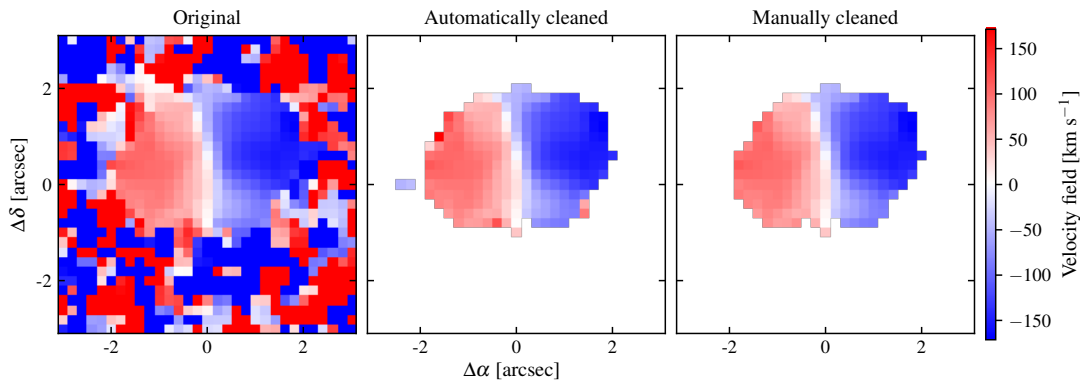


Figure 5.4: Illustration of the cleaning process for the kinematics maps using the velocity field of 114_CGR79 as an example.

A last but important step after the maps were extracted is to clean them. Indeed, a velocity field as presented in the right-most part of Fig. 5.3 will not be correctly fitted during the kinematics modelling process because of the contribution of all the pixels around that have large velocities. Most of these pixels tend to have a velocity which is equal to the lower or upper bound of the velocity offset allowed during the fit of the line. Their origin can be twofold: (i) they are noise dominated or (ii) there are sky residuals that were produced during the data reduction of the cube, in which case it was not the emission line that was fitted and therefore the pixel's velocity is not meaningful. This is more likely to happen when the fitted line falls in the reddest part of the spectrum beyond roughly 8000 Å (where sky lines are the most numerous and the brightest), that is at $z \gtrsim 1$ for [OII] emitters.

In [Abril-Melgarejo et al. \(2021\)](#) and [Mercier et al. \(2022\)](#) (see also Chapters 6 and 7), this cleaning process was done in two steps. First, we performed an automatic cleaning by keeping spaxels with a S/N larger than five and with a line width larger than 80% of the LSF FWHM computed using Eq. 3.1. The first criterion ensures that we are not keeping spaxels with a large noise contribution to the flux and the second criterion removes those that contain sky residuals. We used a conservative threshold of 80% for the latter criterion to ensure that we might not be removing spaxels with signal but with a low velocity dispersion given that there is an avoidable uncertainty on both the LSF and on our estimate of the line width that can both affect the dispersion value. Second, we visually inspected the velocity fields and the spectra for each remaining spaxel and removed (i) the few that were isolated from the bulk of the velocity field (typically 3-4 spaxels at most) and (ii) those that were connected to the velocity field but that had large velocity discontinuities with respect to their neighbours. These latter spaxels typically correspond to sky residuals that were not removed because of the conservative 80% threshold on the line width used during the automatic cleaning step that was discussed above. This step was done with `PYQUBEVIS`⁷, a light-weight visualisation tool that allows to open at the same time a kinematics map and its corresponding cube to easily inspect the spectrum associated to each spaxel. As an illustration, we show the cleaning process for galaxy 104_CGr79 applied to its velocity field in Fig. 5.4.

5.3.2 Theory behind the kinematics modelling

Below we describe quickly the formalism that is used in `MOCKING` to model the velocity field extracted from the MUSE cubes. Because these derivations were not done during this Thesis and because the details are already given in full account in [Epinat et al. \(2008, 2010\)](#), we only provide as minimum information to describe the theory behind the kinematics modelling and we refer the interested reader to the appendices of these two papers for more information.

5.3.2.1 Line-of-sight velocity

The baseline for modelling a velocity field is to correctly model the LOS velocity in each spaxel. In this chapter, we have already discussed how one can go from a given mass distribution to derive a rotation velocity under the assumption of dynamical equilibrium. However, this rotation or circular velocity is not enough to model a velocity field. Indeed, the only component of the velocity that is accessible for intermediate to high redshift galaxies is the component projected along the line-of-sight: the LOS velocity. In general terms, for a kinematics tracer located in a plane (e.g. gaseous disk) and assuming the same cylindrical coordinates as in Sect. 5.1.1, the LOS velocity writes

$$V_{\text{LOS}} = V_s + V_\theta \cos \theta \sin i + V_R \sin \theta \sin i + V_z \cos i, \quad (5.35)$$

where V_s is the systemic velocity of the galaxy, i is the inclination of the disk ($i = 0^\circ$ means face-on and $i = 90^\circ$ means edge-on) and θ is the azimuthal angle in the plane of the disk. The conversion from intrinsic galactic coordinates (R, θ) to those on the plane of the sky (R', ψ) is given by ([Epinat et al. 2008](#))

⁷<https://gitlab.lam.fr/bepinat/PyQubeVis>

$$R \cos \theta = R' \cos \psi, \quad (5.36)$$

$$R \sin \theta = R' \sin \psi / \cos i, \quad (5.37)$$

$$R = R' \sqrt{\cos^2 \psi + \sin^2 \psi / \cos^2 i}, \quad (5.38)$$

where $R' = \sqrt{x'^2 + y'^2}$ is the distance on the plane of the sky to the centre of the galaxy, with x' and y' the spaxel's position with respect to the galaxy centre (y' positive to the north and x' positive to the west), and ψ is the counter-clockwise azimuthal angle with respect to the galaxy's major axis that measures the position of the spaxel on the plane of the sky and that writes

$$R' \cos \psi = y' \cos \text{PA} - x' \sin \text{PA}, \quad (5.39)$$

$$R' \sin \psi = -x' \cos \text{PA} - y' \sin \text{PA}, \quad (5.40)$$

with PA the position angle of the disk plane with respect to the North⁸. If there is only rotation, as is usually assumed, then Eq. 5.35 is simplified with $V_R = V_z = 0$ and we can use the above set of equations to compute the LOS velocity for any pixel given a rotation curve model. However, this is not sufficient in itself as there are strong instrument effects that impact the velocity fields and velocity dispersion maps of intermediate and high redshift galaxies.

5.3.2.2 Instrumental impact on the velocity field

The complete description of how the instrumental impact is taken into account when modelling the velocity field can be found in Appendix A of [Epinat et al. \(2010\)](#). However, since it is an important aspect of the dynamical modelling, I provide a full account below. To begin with, we note $S(x', y', \lambda)$ the total flux density at position (x', y') on the plane of the sky and at an observed wavelength λ . It contains both the continuum and the line flux density noted $F_\lambda(x', y', \lambda)$. The flux of the line $F(x', y')$ is simply given by integrating F_λ along the spectral dimension and the high-resolution velocity field corresponds to the first order moment of the line, that is

$$\bar{V}(x', y') = \frac{\int_{\lambda \in \mathbb{R}^+} d\lambda F_\lambda(x', y', \lambda) v(\lambda)}{F(x', y')}, \quad (5.41)$$

where $v(\lambda)$ is the velocity offset that corresponds to the line being located at an observed wavelength λ . Equation 5.41 is therefore just saying that we measure the LOS velocity as the average velocity offset weighted by the flux of the line. An example of such a model is shown on the first row and leftmost column of Fig. 5.5 for galaxy 114_CGR79.

First, we consider the effects of the spectral resolution and binning. For the former, its effect will be to convolve the line flux density F_λ with the LSF, while for the latter it will be equivalent to integrating the convolved flux density within a spectral window whose dimensions corresponds to those of the spaxels. Hence, we have

$$S_2(x', y', \lambda_i) = F_{\lambda,2}(x', y', \lambda_i) + C_2(x', y', \lambda_i), \quad (5.42)$$

⁸The notation has been slightly altered compared to [Epinat et al. \(2008\)](#) to be more consistent with previous chapters.

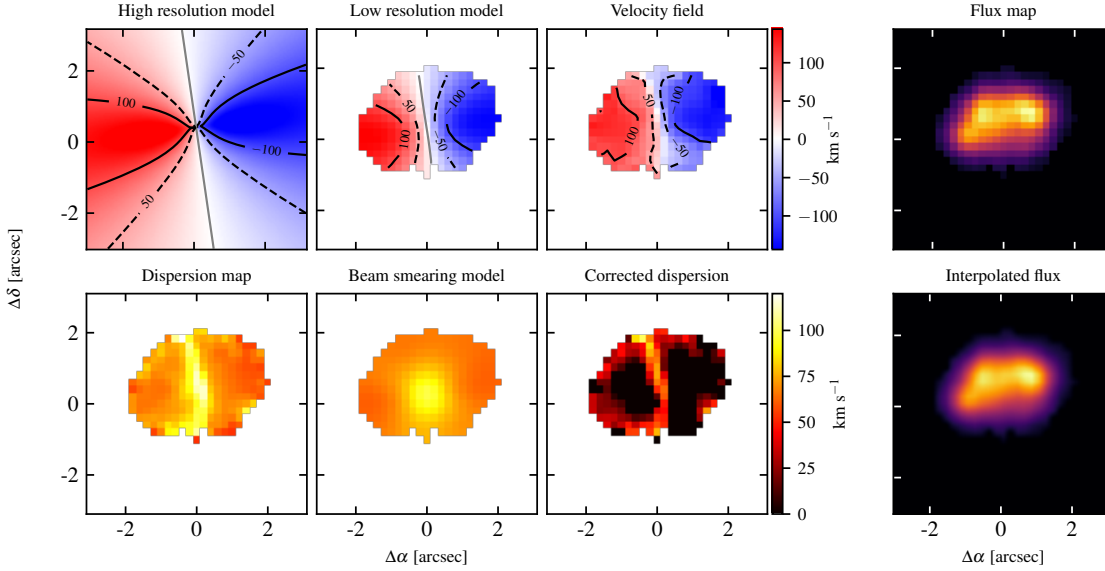


Figure 5.5: Illustration of the instrumental impact on the kinematics maps for galaxy 114_CGR79. The first row shows the velocity field, the second row the velocity dispersion, and the last column the [O II] flux map at the original resolution and after interpolating with an oversampling factor of four. To illustrate the effect of the PSF on the shape of the velocity field, we represent four iso-velocity curves at -50 , -100 , 0 , 50 , and 100 km s^{-1} on the high-resolution model (i.e. without PSF nor spatial binning, leftmost column), low-resolution model (after PSF and binning, second column), and on the velocity field extracted from the cube (third column).

where $F_{\lambda,2}$ is the convolved plus spectrally binned line flux density and C_2 is the same for the continuum⁹. If we derive the velocity field by integrating over a small spectral window around the line, we might consider the continuum to be constant in which case it will still remain constant after the convolution and the binning. Since there is no flux loss during either steps, the line flux can be computed by summing up the contribution of $F_{\lambda,2}$ in each spectral channel λ_i . Thus, we can approximate the expression for the velocity field given in Eq. 5.41 by changing the integral into a sum as

$$\bar{V}(x', y') \approx \sum_i \frac{F_{\lambda,2}(x', y', \lambda_i) v(\lambda_i)}{F(x', y')}. \quad (5.43)$$

Now, we turn to the first of the two spatial impacts of the instruments: the PSF. Similarly to the LSF, the PSF will also convolve the flux density but spatially this time. We note this new spatially convolved line flux density $F_{\lambda,3}(x', y', \lambda_i)$. The integrated flux, computed by summing up the contribution of $F_{\lambda,3}$ in each channel λ_i will also be impacted by the PSF and thus we note it $F_0(x', y')$. We can derive the expression for the velocity field when using $F_{\lambda,3}$ this time. To do so, we start again from Eq. 5.43 and we replace $F_{\lambda,2}$ by $F_{\lambda,3}$. Because we do not measure F any more

⁹Following [Epinat et al. \(2010\)](#), S_1 corresponds to the spectrum only affected by the spectral convolution.

but F_0 , we also need to replace the normalisation by the new value. This writes

$$\begin{aligned}
\bar{V}_0(x', y') &= \sum_i \frac{[F_{\lambda,2} \otimes \text{PSF}](x', y', \lambda_i) v(\lambda_i)}{F_0(x', y')} \\
&= \left[\left(F(x', y') \sum_i \frac{F_{\lambda,2}(x', y', \lambda_i) v(\lambda_i)}{F(x', y')} \right) \otimes \text{PSF} \right] (x', y') / F_0(x', y') \\
&= \frac{[(\bar{V}F) \otimes \text{PSF}](x', y')}{F_0(x', y')}, \tag{5.44}
\end{aligned}$$

where \otimes denotes the spatial convolution operation and \bar{V} is defined in Eq. 5.41. The first line in Eq. 5.44 is just its expression when using $F_{\lambda,3}$ and F_0 instead of $F_{\lambda,2}$ and F . It is possible to rewrite it into the second line because $v(\lambda_i)$ is independent on both x' and y' and because F is independent of λ_i . The last line is then just the second line rewritten using Eq. 5.43.

Finally, there is one last instrument effect to take into account: spatial binning. It will be equivalent to integrating $F_{\lambda,3}$ within a spatial window corresponding to the dimensions of a spaxel. We note this new line flux density $F_{\lambda,4}(x'_j, y'_j, \lambda_i)$, where (x'_j, y'_j) are now the discrete spaxels' coordinates. The integrated flux will also be impacted and we note it $F_1(x'_j, y'_j)$. Exactly in the same way as for the derivation of Eq. 5.44, we can compute the expression for this new velocity field when replacing $F_{\lambda,2}$ by $F_{\lambda,4}$ in the numerator of Eq. 5.43 and F by F_1 in its denominator. The only difference with Eq. 5.44 is that there will be two additional integrals since the flux in each spaxel will be integrated over its surface because of the binning. The final expression writes

$$\bar{V}_1(x'_j, y'_j) = \frac{\int_{x'_j-\Delta x}^{x'_j+\Delta x} dx' \int_{y'_j-\Delta y}^{y'_j+\Delta y} dy' [(\bar{V}F) \otimes \text{PSF}](x', y')}{F_1(x'_j, y'_j)}, \tag{5.45}$$

where the size of a spaxel along the x' and y' directions is equal to $2\Delta x$ and $2\Delta y$, respectively. Such a model is represented for 114_CGR79 on the first row and second column from the left in Fig. 5.5. It also corresponds to the best-fit model that was found by MOCKING. Thus we also show as a comparison the velocity field extracted from the MUSE cube with CAMEL on the third column.

5.3.2.3 Instrumental impact on the velocity dispersion map

The same procedure can be applied to derive the instrumental impact on the velocity dispersion map. Here, the point is not to model the velocity dispersion as for the velocity field but rather to correct it from instrumental effects. The velocity dispersion $\sigma(x', y')$ corresponds to the width of the line and therefore is defined as the second order moment of the flux density:

$$\begin{aligned}
\sigma^2(x', y') &= \frac{\int_{\lambda \in \mathbb{R}_+} d\lambda F_\lambda(x', y', \lambda) [v(\lambda) - \bar{V}(x', y')]^2}{F(x', y', \lambda)} \\
&= \bar{V}^2(x', y') - \overline{V^2}(x', y'), \tag{5.46}
\end{aligned}$$

We already know how \bar{V} is impacted by the LSF and PSF convolutions and the spectral and spatial binning, so we only need to derive their impact on $\overline{V^2}$. As before, we can approximate its

value by considering the LSF convolved and spectrally binned spectrum and summing along the spectral channels instead of integrating:

$$\overline{V^2}(x', y') \approx \frac{\sum_i F_{\lambda,2}(x', y', \lambda_i) v^2(\lambda_i)}{F(x', y')}. \quad (5.47)$$

The effect of the PSF will also write similarly by replacing \overline{V} by $\overline{V^2}$ in Eq. 5.44 and so will the spatial binning. Thus, once all the instrumental effects are taken into account and using Eq. 5.46, the square of the velocity dispersion writes

$$\sigma_1^2(x'_j, y'_j) = \frac{\int_{x'_j-\Delta x}^{x'_j+\Delta x} dx' \int_{y'_j-\Delta y}^{y'_j+\Delta y} dy' \left[(\overline{V^2} F) \otimes \text{PSF} \right] (x', y')}{F_1(x'_j, y'_j)} - \left[\frac{\int_{x'_j-\Delta x}^{x'_j+\Delta x} dx' \int_{y'_j-\Delta y}^{y'_j+\Delta y} dy' \left[(\overline{V} F) \otimes \text{PSF} \right] (x', y')}{F_1(x'_j, y'_j)} \right]^2, \quad (5.48)$$

which reduces to

$$\sigma_1^2(x'_j, y'_j) = \frac{\iint_{x'_j, y'_j} dx' dy' [\sigma^2 F \otimes \text{PSF}] (x', y')}{F_1(x'_j, y'_j)} + \frac{\iint_{x'_j, y'_j} dx' dy' [\overline{V^2} F \otimes \text{PSF}] (x', y')}{F_1(x'_j, y'_j)} - \left[\frac{\iint_{x'_j, y'_j} dx' dy' [\overline{V} F \otimes \text{PSF}] (x', y')}{F_1(x'_j, y'_j)} \right]^2, \quad (5.49)$$

where the integrals are still to be understood within a spaxel. The first term in Eq. 5.49 corresponds to the velocity dispersion truly impacted by instrumental effects (LSF, PSF, and binning) whereas the other terms are purely instrumental effects that are referred to as beam smearing. It is caused by the velocity shear and the PSF that mixes signal from neighbouring spaxels with different velocities and therefore spuriously increases the velocity dispersion measured from the line width.

5.3.2.4 Brief comments on modelling the kinematics

We now have everything to model a velocity field taking into account the instrumental effects using Eq. 5.45. We also have an expression given by Eq. 5.49 that tells us how we can correct the velocity dispersion map extracted from a cube to recover the beam-smearing corrected map. Beside requiring a precise knowledge of the LSF and the PSF, each equation requires two important information: (i) a high-resolution velocity field \overline{V} and (ii) the high-resolution flux map F . When modelling the velocity field with `MOCKING` the former is easy to get given that it corresponds to the model being generated. However, this is not true for the flux map that must be known *a priori*. If there is no high-resolution flux map available for the kinematics tracer being used, then `MOCKING` will compute an approximation by interpolating a low-resolution map. The interpolated flux map that was used during the modelling of 114_CGR79 is shown on the second

row and rightmost column of Fig. 5.5, with the original flux map extracted from the cube shown above. This interpolation was performed with an oversampling factor of four.

Once the best-fit high-resolution velocity field model has been found by MOCKING, it will compute the beam smearing component appearing in Eq. 5.49 and it will subtract it quadratically from the velocity dispersion map to recover the “true” velocity dispersion. The beam smearing correction is represented on the second row of Fig. 5.5 with the original velocity dispersion map on the leftmost column, the beam smearing model that was derived using the high resolution velocity field and the interpolated high-resolution flux map on the second column, and the beam smearing and LSF corrected dispersion map on the third column. We see that the beam smearing is higher where the flux and the velocity shear are large (by a factor of roughly 1.5 with respect to the outer parts of the map), which is near the centre. In addition, about half the spaxels have a null velocity dispersion after the correction was applied. The reason is that the correction is actually larger than the measured value from the line fit and therefore MOCKING clips it to zero. It is unlikely that the intrinsic gas dispersion is exactly zero in these pixels, though it is probably not very high (below roughly 30 km s^{-1} , e.g. see Appendix A of Boselli et al. 2021). What is more likely is that because we do not have access to the real high-resolution flux distribution, we are probably overestimating the flux in these pixels when using the interpolated map. Another possibility is due to the fact that we use the high-resolution velocity field model to derive the beam smearing but, as can be seen from the iso-density contours in Fig. 5.5, even the best-fit model does not perfectly fit the velocity field. Thus, the velocity shear is also an approximation of the underlying shear which will therefore also impact the derivation of the beam smearing. A last explanation for this apparent overcorrection could be that we are overestimating the value of the LSF since we have removed it quadratically from the velocity dispersion map.

Before presenting the application of the dynamical modelling to the MAGIC survey, I must first quickly discuss the efficiency of our method compared to other methods found in the literature. Indeed, our modelling relies on the moment map formalism (Epinat et al. 2008, 2010) which requires to extract kinematics maps from a data cube first and then fit them using the formalism. There exists another type of modelling that does not require the extraction of kinematics maps since it directly fits the data cube: 3D fitting codes such as Galaxy parameters and kinematics (GALPAK^{3D}) described in Bouché et al. (2015) or 3D-Based Analysis of Rotating Object via Line Observation (^{3D}BAROLO) described in Di Teodoro & Fraternali (2015). There are actually pros and cons for both methods and it is important to cite them. As discussed in Bouché et al. (2015) and as shown in subsequent analyses that used GALPAK^{3D} (e.g. Bouché et al. 2021), 3D fitting codes are more efficient than our method to model the kinematics of low S/N and thus very low-mass galaxies. The main reason is that the moment map formalism requires kinematics maps which must be extracted by fitting spaxel-per-spaxel one or more emission lines in the cube. Thus, for low S/N spaxels this will lead to uncertainties which will propagate to the kinematics model. Nevertheless, there are also some limitations to full 3D fitting codes. The main one is that such codes must produce a 3D galaxy model, hence a mock data cube, to fit the observed data. Therefore, this requires to produce (i) a kinematics model with underlying assumptions (e.g. rotation only, model of rotation curves, etc.), as is the case in our modelling, (ii) a model of the surface brightness distribution of the kinematics tracer that is fitted in the cube, and (iii) a model of the intrinsic velocity dispersion. For tilted ring models, which is what is used in ^{3D}BAROLO, there no need to model the surface brightness distribution directly since it is a free parameter that is fitted in each ring. However, it does assume that the surface brightness is the same along the ring. On the contrary, our method does not need to make assumptions on the spatial distribution

of the kinematics tracer that is used nor on the velocity dispersion. The only assumption that we make concerning the distribution of the ionised gas ([OII] doublet in our case) used as kinematics tracer is that it is located in a disk, which is also an assumption made in other codes such as GALPAK^{3D}. Furthermore, for both types of codes the net result is to recover the intrinsic kinematics by taking into account the impact of beam smearing and to produce model kinematics maps. Few analyses have tried to compare the results between 2D and 3D kinematics fitting codes but those that have done so (e.g. Contini et al. 2016) did find consistent results between the two techniques. The only cases where such codes might yield different results are typically nearly face-on and barely resolved galaxies where the large uncertainty on the inclination renders such modellings difficult. In particular, our method has the advantage of producing a beam smearing and LSF corrected velocity dispersion map without making assumptions on its spatial distribution.

5.3.3 Gas kinematics and dynamical modelling of the MAGIC sample

5.3.3.1 Contribution to MockKinG

At the beginning of the Thesis, the kinematics fitting code MOCKING was still in development. Instead, two prior codes written in Interactive Data Language (IDL) between 2008 and 2009 (Epinat et al. 2008, 2010) and which incorporated most of the features in the current code were available. The first focussed on local galaxies whereas the second was designed to model high-redshift galaxies by including the effect of beam smearing. These codes, especially the one specialised in modelling high-redshift galaxies, had been extensively tested and used in previous kinematics studies (e.g. Epinat et al. 2008, 2010, 2012; Vergani et al. 2012; Contini et al. 2016) and more recently in our previous analysis of the impact of the environment on a sub-sample of galaxies in MAGIC presented in Abril-Melgarejo et al. (2021)¹⁰. Meanwhile, there was an increasing need to rewrite the code in Python in a more modern and flexible manner that would be adapted to handle both local and high-redshift galaxies. A first version of this new code had been written by J. Dumoulin during his Master project at Laboratoire d’Astrophysique de Marseille (LAM) in 2016 and, in the following years, a few additional features were added by B. Epinat such as the possibility to have multiple rotation curve components for a single object. Therefore, one of the first aspects during this Thesis was to perform tests using galaxies from the MAGIC survey to compare the new results with the previous ones from the IDL code. I used the same rotation curve model (flat model, described in Sect. 5.3.3.3) as well as the same MUSE PSF and LSF FWHM values. MOCKING was available since the start with two different fitting techniques (see Sect. 5.3.3.3 for more details): a gradient descent-like algorithm and a Bayesian inference technique. On the contrary, the previous IDL code only worked with the former technique. Hence, the first test that was carried out was to compare the outputs of the two codes using the gradient descent-like algorithm. Then, the second test consisted in comparing the outputs of MOCKING between the gradient descent-like and Bayesian approaches for the same sample of galaxies in MAGIC. The result of the comparison is shown in Appendix A of Mercier et al. (2022) (see also Chapter 6). We found nearly identical results between MOCKING (in gradient descent mode) and the previous IDL code, as was expected given that the two codes fit the data in the same way. We also found consistent results (of the order of 10%) between the Bayesian and gradient descent-like approaches with MOCKING (as shown in Fig. A.1 of Mercier

¹⁰It is also this code that I used to perform a first kinematics analysis of the field galaxies in MAGIC during my Master project

et al. 2022), with the Bayesian approach that seemed less prone to converge towards a local minimum solution in cases where the velocity field is perturbed. These tests allowed the code to be used for the first time in Boselli et al. (2021) and Adamczyk (2021).

In parallel, I started implementing mass models in MOCKING. In particular, the focus was put on properly integrating a rotation curve model for a double exponential disk as discussed in Sect. 5.2.4.3. After further tests, this new model was used for the first time in the analyses of the galaxy scaling relations discussed in Mercier et al. (2022) and in Chapter 6 and of the stellar angular momentum in MAGIC presented in Chapter 7.

5.3.3.2 Kinematics maps extraction

In Mercier et al. (2022) and in Chapter 6 we used the kinematics fitting tool MOCKING that implements the moment maps formalism presented in Sect. 5.3.2 to model the dynamics of the galaxies in the MAGIC survey. This required first to extract the kinematics maps using the [OII] doublet with CAMEL (see Sect. 5.3.1) for the 890 galaxies that are part of the morphological sample, that is [OII] emitters in the MAGIC sample for which it was possible to model the morphology with GALFIT. This was done in an automatic fashion with CAMEL by extracting sub-data cubes of dimensions 30×30 MUSE spaxels around the observed wavelength of the [OII] doublet, which was then spatially smoothed with a Gaussian profile with a sub-resolution FWHM of 2 spaxels. The continuum was fitted with a constant value and the doublet with two Gaussian profiles with the same velocity offset and line width. An example of configuration file used by CAMEL to extract the maps for the galaxy 114_CGR79 is shown below:

```

1 FITSFILE= CGr79_d.fits           / Path of the cube FITS file
2 OUTPUT  = CGr79_d_114_o2        / Output directory
3 SKYFILE  = CGr79_d.fits         / Sky spectrum cube FITS file
4 HALPHA   = False                / Fit Halpha ? (default:TRUE)
5 OII      = True                 / Fit OII ? (default:FALSE)
6 COMMW    = True                 / Use a common width ? (default:FALSE)
7 REDSHIFT = 0.6684               / Initial redshift
8 REDMIN   = 0.665617408317857    / Minimum redshift for line fit
9 REDMAX   = 0.671182591682143    / Maximum redshift for line fit
10 ZRMIN    = 0.6572696332714281   / Minimum redshift for spectral range around lines
11 ZRMAX    = 0.6795303667285719   / Maximum redshift for spectral range around lines
12 INITW    = 50.0                 / Initial line width in km/s
13 WMIN     = 30.0                 / Minimum line width in km/s
14 WMAX     = 250.0                / Maximum line width in km/s
15 DFIT     = 100.0                / Bin to fit the line center in km/s
16 DGCTNUM  = 0                    / Polynomial degree for the continuum fit
17 SCLIP    = 10                   / Sigma-clipping threshold to clean the cube
18 XYCLIP   = 3                    / Box width for the median for the sigma-clipping
19 NCLIP    = 3                    / Number of passes for clipping (default:3)
20 WSMOOTH  = 0                    / Spectral smoothing
21 SSMOOTH  = 2.0                  / Spatial smoothing FWHM in pixel (default:0)
22 XMIN     = 197.0                / X minimum value for spatial cut of the input cube
23 XMAX     = 227.0                / X maximum value for spatial cut of the input cube
24 YMIN     = 251.0                / Y minimum value for spatial cut of the input cube
25 YMAX     = 281.0                / Y maximum value for spatial cut of the input cube
26 ZMIN     = 1180.0               / Z minimum value for spectral cut of the input cube
27 ZMAX     = 1250.0               / Z maximum value for spectral cut of the input cube

```

Code 5.1: Example of a CAMEL configuration file for galaxy 114_CGR79.

After the maps were extracted, they were cleaned as described in Sect. 5.3.1.3. Since not every galaxy in the [OII] emitters redshift range necessarily has enough [OII] signal to be detected, the cleaning phase led to the removal of 297 galaxies from the morphological sample, thus producing a kinematics sample of 593 galaxies. Because the cleaning of spurious spaxels is mostly driven by S/N considerations, as discussed in [Mercier et al. \(2022\)](#), it is roughly similar to removing galaxies whose integrated [OII] flux is equal to $2 \times 10^{-18} \text{ erg s}^{-1} \text{ cm}^{-2}$ at the median redshift of the groups in MAGIC ($z \approx 0.7$).

5.3.3.3 Dynamical modelling

Finally, the last step was to perform the kinematics modelling with MOCKING. First, in [Abril-Melgarejo et al. \(2021\)](#), we used a simple flat model for the rotation curve that writes

$$V_{\theta}(R) = \begin{cases} V_t \times R/R_t & \text{if } R < R_t \\ V_t & \text{otherwise,} \end{cases} \quad (5.50)$$

where V_t is the plateau velocity and R_t is the transition radius between the linearly rising part and the outer plateau. Even though this model is not physically motivated, it is robust to model and to recover the galaxies' rotation velocity at intermediate redshift (e.g. [Wright et al. 2007](#); [Epinat et al. 2009, 2010, 2012](#); [Contini et al. 2016](#)). The ionised gas was assumed to be located in a rotating razor-thin disk. To remove any degeneracies between the velocity field centre's location and the systemic velocity of the galaxy, as well as between V_t and the gas disk's inclination, we fixed both the centre's position and the inclination to the values derived with GALFIT during the morphological modelling. Furthermore, we also fixed the kinematics parameters of the stellar disk and bulge components when performing a mass modelling by assuming that they are robustly constrained from the morphological modelling. All the other parameters (rotation curve parameters of the DM halo component, kinematics position angle (PA), and systemic velocity) were let free during the fitting process. MOCKING implements two methods to perform the fit: (i) CAT_MPFIT¹¹, a python implementation of MPFIT ([Markwardt 2009](#)) that is a gradient descent kind of technique based on the Levenberg-Marquardt algorithm and (ii) a python implementation of MULTINEST ([Feroz & Hobson 2008](#); [Buchner et al. 2014](#)) that is a Bayesian inference tool based on a multi-nodal nested sampling algorithm. As discussed in Sect. 5.3.3.1, we originally used the former algorithm but, after comparing the results between the two methods in [Mercier et al. \(2022\)](#), we relied on the latter in subsequent modellings as it is less prone to finding a local rather than a global minimum.

A first modelling was performed in [Mercier et al. \(2022\)](#) using the same assumptions as in [Abril-Melgarejo et al. \(2021\)](#) but implementing a mass modelling approach (see Sect. 5.2.1). We used a double exponential disk model for the stellar disk component as described in Sect. 5.2.4.3, a Hernquist's model (see Sect. 5.2.4.1) for the stellar bulge, and we also included an unconstrained NFW DM halo (see Sect. 5.2.4.4). By definition the only constraint on the DM halo is the kinematics itself so that we let free its maximum rotation velocity $V_{h,\text{max}}$ and its scale radius R_s during the kinematics modelling. In practice, we should have also included the contribution of the cold gas components (in particular the molecular gas in the inner regions) that have a non-negligible impact, especially at intermediate and high redshift (e.g. [Tacconi et al. 2020](#)). To do so, we would have needed to have an idea of its spatial distribution and total mass either from

¹¹<https://www-astro.physics.ox.ac.uk/~cappellari/software/>

additional observations (e.g. ALMA) or from scaling laws (e.g. Kennicutt–Schmidt relation). Afterwards, we could have included it as an additional component to the kinematics model (e.g. razor-thin disk). Another option would have been to assume a spatial distribution for the cold gas (e.g. the same exponential distribution as that of the stellar disk or a flat distribution as in [Bouché et al. 2022](#)) and then to let the amplitude of this component free to vary (i.e. add the M/L of the gas component as an additional free parameter). Because we had no constraints on the gas mass and distribution in the galaxies of the MAGIC survey, we have decided in [Mercier et al. \(2022\)](#) to not take explicitly into account the contribution of the cold gas to the ionised gas kinematics. In practice, this means that it will be implicitly included in the DM halo component during the fitting process and that it must be accounted for during the analysis when estimating the mass of the NFW profile if one wants to estimate the mass of the DM component alone (e.g. see Sect.7.4 of [Mercier et al. 2022](#)).

Examples of such models can be found in Sect. 5 of [Mercier et al. \(2022\)](#) and in Chapter 6¹². Finally, the same modelling was performed once more for the analysis of the angular momentum (see Chapter 7). Indeed, after the derivation of new stellar mass estimates with CIGALE, as well as more precise MUSE PSF profiles using Moffat profiles (both for the survey paper, see [Epinat et al.](#), in prep.), it was decided to perform again the kinematics modelling using these latest values in order to have the best constraints on the galaxies’ kinematics parameters. Besides, the morphology was updated for 17 galaxies in the kinematics sample for the analysis of the angular momentum, mainly to derive better constraints on their bulge component. Since the morphological models directly affect the mass modelling, these galaxies also required to update their kinematics models. An example of a MOCKING configuration file for galaxy 114_CGR79 is shown below. This file corresponds to the latest modelling, including the mass models and the Moffat profile for the PSF.

¹²The full morpho-dynamical models can also be found as supplementary material of [Mercier et al. \(2022\)](#) at the following address: <https://www.aanda.org/articles/aa/olm/2022/09/aa43110-22/aa43110-22.html>

```

1 config fit:
2   method: multinest # multinest or mpfit
3   multinest:
4     evidence_tolerance: 0.5
5     max_iter: 0
6     max_modes: 100
7     mode_tolerance: -1.0e+60
8     n_iter_before_update: 100
9     n_live_points: 50
10    null_log_evidence: -1.0e+90
11    pltstats: false
12    sampling_efficiency: 0.8
13  verbose: false
14  files:
15    disp: CGr79_d_114_o2_ssmooth_disp_common_mclean5.0.fits # Dispersion map
16    errvel: CGr79_d_114_o2_ssmooth_evel_common_mclean5.0.fits # Error on Vfield
17    psf: null # PSF image (null=Gaussian/Moffat)
18    vel: CGr79_d_114_o2_ssmooth_vel_common_mclean5.0.fits # Vfield
19  name: CGr79_d_114 # ID
20  objects:
21    obj1: # Only one object implemented for now
22    components: # Free number of components
23    comp1:
24      model: bovy_corr # Name of the model in MocKinG - here Bovy curve
25      params:
26        q0: # Disk thickness required for a corrected Bovy curve
27          desc: q0 # Parameter name in the output file
28          fixed: 1 # 1 for fixed, 0 for free
29          limits:
30            - 0.17890397942393682 # Lower bound
31            - 0.17890397942393682 # Upper bound
32          value: 0.17890397942393682 # Initial value
33        rd: # Disk scale length
34          desc: rd
35          fixed: 1
36          limits:
37            - 2.189654476613038
38            - 2.189654476613038
39          value: 2.189654476613038
40        vm_RT: # Razor-thin maximum velocity
41          desc: vm_RT
42          fixed: 1
43          limits:
44            - 165.89090254236532
45            - 165.89090254236532
46          value: 165.89090254236532
47        vm_corr: # Maximum velocity of the correction
48          desc: vm_corr
49          fixed: 1
50          limits:
51            - 68.40760325005385
52            - 68.40760325005385
53          value: 68.40760325005385
54    comp2:
55      model: hernquist # Hernquist bulge model
56      params:
57        rt: # Radius where vm is reached
58          desc: a
59          fixed: 1
60          limits:
61            - 0.1699294100661157
62            - 0.1699294100661157
63          value: 0.1699294100661157
64        vm: # Maximum rotation velocity
65          desc: vm_hern
66          fixed: 1
67          limits:
68            - 121.70174860901213
69            - 121.70174860901213

```

```

70     value: 121.70174860901213
71 comp3:
72 model: nfw # NFW DM halo profile
73 params:
74   rt:
75     desc: rt # Radius where vm is reached
76     fixed: 0
77     limits:
78       - 0.5
79       - 20.0
80     value: 2.0
81   vm:
82     desc: vm # Maximum rotation velocity
83     fixed: 0
84     limits:
85       - 0.0
86       - 500.0
87     value: 80.0
88 dispersion info: # Info to model the dispersion (not implemented)
89 sig: 0.0
90 slope: 0.0
91 files: # Additional files - here [OII] flux map
92 flux: CGr79_d_114_o2_ssmooth_flux_common_OII_mclean5.0.fits
93 params:
94   inc: # Disk inclination
95     desc: inc
96     fixed: 1 # Fixed from morphology
97     limits:
98       - 60.24700720525112
99       - 60.24700720525112
100    value: 60.24700720525112
101   pa: # Kinematics position angle
102     desc: pa
103     fixed: 0 # Free to be adjusted
104     limits:
105       - -270.0
106       - 270.0
107     value: -67.05
108   vs: # Systemic velocity
109     desc: vs
110     fixed: 0 # Free to be adjusted
111     limits:
112       - -100.0
113       - 100.0
114     value: 0.0
115   xc: # X coordinate of the centre
116     desc: xc
117     fixed: 1 # Fixed
118     limits:
119       - 14.91
120       - 14.91
121     value: 14.91
122   yc: # Y coordinate of the centre
123     desc: yc
124     fixed: 1 # Fixed
125     limits:
126       - 16.71
127       - 16.71
128     value: 16.71
129 resol params: # PSF parameters if no PSF model is provided
130 beta: 2.4744437919453612 # Beta for the Moffat profile
131 oversample: 4 # Oversampling factor for the flux map
132 psfx: 2.639845311641693 # Spatial PSF FWHM in pixels
133 psfz: 53.04698637996095 # Spectral resolution in km/s
134 smooth: 2.0 # Additional smoothing applied beforehand

```

Code 5.2: Example of a MOCKING configuration file for galaxy 114_CGr79.

Chapter 6

Impact of the environment on galaxies' scaling relations in the MAGIC survey at $z \sim 0.7$

This chapter presents my first analysis as first author using MUSE data from the MAGIC survey. This work started at the beginning of this Thesis and was based on a preliminary analysis performed during my Master internship. It also followed on the work carried out by [Abril-Melgarejo et al. \(2021\)](#) in which I have also contributed. The manuscript was started to be written early of the second year for a first draft that was sent to the MUSE consortium at the end of November 2021. It was officially accepted by the *Astronomy & Astrophysics* journal on 14 April 2022.

In the previous analysis from [Abril-Melgarejo et al. \(2021\)](#), we focussed on a subsample of galaxies found in dense groups and we compared its TFR between the MAGIC survey and other samples targeting less dense structures such as the KMOS3D survey ([Wisnioski et al. 2015](#); [Übler et al. 2017](#)), the KROSS survey described in [Stott et al. \(2016\)](#) and [Tiley et al. \(2019a\)](#), and the ORELSE survey ([Lubin et al. 2009](#); [Pelliccia et al. 2019](#)). In addition, the first analysis performed during my Master internship compared galaxies in the field and galaxies in structures but (i) the results were preliminary, (ii) it did not include the entire MAGIC sample as it was missing the MUSE fields CGR35, CGR87, and CGR172, and (iii) only the kinematics had been modelled, following the method described in [Abril-Melgarejo et al. \(2021\)](#), but not the morphology. Besides, as discussed in [Abril-Melgarejo et al. \(2021\)](#) comparing the TFR between different surveys is difficult because a lot of systematic effects than can affect its shape. Thus, the observed difference in the TFR zero point found in [Abril-Melgarejo et al. \(2021\)](#) between MAGIC and other surveys might have been intrinsic, in the sense that it would be a genuine impact of the environment which might be related to quenching or baryon contraction happening in the densest structures, or it might have been a spurious effect due to the fact that we were comparing data from different instruments, with a different sample selection, that might have been reduced in different ways, and whose kinematics might have been extracted and modelled in different manners.

Thus, it was decided to perform the same dynamical modelling for the entire sample of [OII] emitters (see footnote 1 in Sect. 3.1 for a definition) in the MAGIC survey with secure

spectroscopic redshifts ($\text{CONFID} \geq 2$). This way, any systematics due to the instruments, selection, data reduction, kinematics extraction, morphological or kinematics modelling, or even the estimation of the galaxies' stellar mass should be reduced as much as possible since every step is done in a self-similar fashion for both galaxies in the field and those in structures.

The first step was to model the morphology of the galaxies for the entire sample of [OII] emitters using the bulge-disk decomposition described in Sect. 4 of the paper as well as in Sect. 4.4 of this manuscript. Then, the galaxies' kinematics maps were extracted from the different MUSE cubes as discussed in Sect. 5.3.3.2 and their kinematics was modelled as in Sect. 5.3.3.3 (see also Sect. 5 of the paper). Originally, the same flat model as in [Abril-Melgarejo et al. \(2021\)](#) was used (see also Sect. 5.3.3.3 for its definition) but we decided to implement mass models by using the morphological models to constrain the ionised gas kinematics. These mass models are the basis for Sect. 5.2 discussed in this manuscript (see also Appendix D of the paper). Section 6 of the paper discusses the sample selection criteria and in Sect. 7 the analysis of the impact of the environment on three scaling relations is carried out: (i) the size-mass relation, (ii) the SFR-mass relation, also known as the MS relation, and (iii) the TFR. We decided to include the size-mass and the MS relations on top of the TFR for a few reasons. Firstly, because we had all the parameters to include them in the analysis. Secondly, because the two physical interpretations that were retained in [Abril-Melgarejo et al. \(2021\)](#) to explain the apparent discrepancy in the TFR zero point between the MAGIC survey and the others were (i) an effect of quenching on the densest structures in MAGIC that produces a lower stellar mass at fixed dynamical mass and (ii) an effect of baryon contraction that increases the rotation velocity at fixed stellar mass in MAGIC. To probe the former effect, the MS relation was necessary, and to probe the latter we needed the size-mass relation. Lastly, when using mass models the size-mass relation appears in the TFR. Thus, to disentangle the impact on the TFR of a contraction of baryons from a lower stellar mass fraction (see Eqs. 15 and 16 in the paper and Sect. 7.4 for a discussion), we needed to have robust constraints on the size-mass relation first.

This analysis shows that there are measurable offsets for the size-mass relation (to the 1σ statistical level) and for the MS relation (to the 2σ level) consistent with galaxies in the most massive structures being quenched and with slightly denser stellar disks (or similarly smaller disks at fixed stellar mass). However, contrary to [Abril-Melgarejo et al. \(2021\)](#), no statistically significant effect of the environment on the TFR could be measured. This indicates that our previous result was certainly a spurious effect induced by comparing different samples, as stated above.








This work also has some limitations that need to be stated, the most important one concerning the dynamical modelling of the DM halo and the interpretation of the DM fraction. Our approach has been to reduce as much as possible any degeneracies and uncertainties by constraining the contribution of baryons on the ionised gas kinematics. Because the only constraints we have are on the stellar disk and bulge, these are the only two baryonic components that are explicitly included in the mass modelling. Hence, we have chosen not to include any mass model for the cold gas components (HI and/or H₂) given that we have no constraints in MAGIC neither on their total mass, nor on their spatial distribution. Yet, it is possible to get a broad estimate of the fraction of cold gas in the galaxies using the SFR derived from the ionised gas and the Schmidt-Kennicutt relation ([Schmidt 1959](#); [Kennicutt 1998](#)), as was done in Sect. 7.4 of the paper. When doing so, we find that [OII] emitters at $z \sim 0.7$ in MAGIC tend to have on average 20% (standard deviation of the same order of magnitude) of their baryonic mass as cold gas, which means that intermediate redshift galaxies in our sample hold on average a non-negligible cold gas

component that should be taken into account in the modelling. Incidentally, our approach of not including explicitly the cold gas in the mass modelling means that these components (HI and CO) are implicitly included in the best-fit DM halo model that is found.

Therefore, caution should be taken when interpreting the DM masses and fractions that are derived from the best-fit NFW models since they also contain the cold gas components (see also the discussion in Sect. 5.2.4.5). An alternative would have been to assume a shape (e.g. based on observations in the local Universe) for the cold gas distribution and either fix the amplitude using the mass estimate described above (but at the cost of large uncertainties) or to let the amplitude as an additional free parameter. Such an approach was applied for instance in [Bouché et al. \(2022\)](#) where the HI component was neglected and the CO component was assumed to be located in a disk of constant surface density. This approach would have been more physically motivated but would have relied on many assumptions that would have rendered the interpretation of the results slightly more difficult. Indeed, it is not clear that we would have been able to properly constrain the amplitude and thus the total mass of cold gas in the galaxy by letting it be as a free parameter. If fixed, then our parametrisation would have relied on additional scaling laws which would have induced further uncertainties. Similarly, it is not completely clear if the cold gas components follow the stellar distribution or not. As an indication, [Martinsson et al. \(2013\)](#) found that the HI gas mostly follows an off-centred radial Gaussian distribution whereas the CO gas distribution is mostly constant up to a few stellar disk scale lengths.

My contribution to this paper is important everywhere from writing it entirely, performing the morphological and kinematics modellings, defining the sample selection, performing completely the analysis, checking the effect of selection on our results, checking their reliability when applying further selections in mass and redshift or when using updated kinematics models all the way through producing the physical interpretation for the three scaling relations. The only parts that I did not do myself are (i) the data reduction, (ii) the SED fitting, and (iii) the environment characterisation through the FoF algorithm.

Scaling relations of $z \sim 0.25$ – 1.5 galaxies in various environments from the morpho-kinematics analysis of the MAGIC sample^{★,★★,★★★}

W. Mercier¹, B. Epinat^{2,9}, T. Contini¹, V. Abril-Melgarejo^{2,7}, L. Boogaard³, J. Brinchmann^{3,4}, H. Finley¹,
D. Krajnović⁸, L. Michel-Dansac⁵, E. Ventou¹, N. Bouché⁵, J. Dumoulin², and J. C. B. Pineda⁶

¹ Institut de Recherche en Astrophysique et Planétologie (IRAP), Université de Toulouse, CNRS, UPS, CNES, 31400 Toulouse, France

e-mail: wilfried.mercier@irap.omp.eu

² Aix Marseille Univ., CNRS, CNES, LAM, Marseille, France

³ Leiden Observatory, Leiden University, PO Box 9513, 2300 RA Leiden, The Netherlands

⁴ Instituto de Astrofísica e Ciências do Espaço, Universidade do Porto, CAUP, Rua das Estrelas, 4150-762 Porto, Portugal

⁵ Univ. Lyon, Univ. Lyon1, Ens de Lyon, CNRS, Centre de Recherche Astrophysique de Lyon UMR5574, 69230 Saint-Genis-Laval, France

⁶ Escuela de Física, Universidad Industrial de Santander, A.A. 678, Bucaramanga, Colombia

⁷ Space Telescope Science Institute, 3700 San Martin Drive, Baltimore, MD 21218, USA

⁸ Leibniz-Institut für Astrophysik Potsdam (AIP), An der Sternwarte 16, 14482 Potsdam, Germany

⁹ Canada-France-Hawaii Telescope, CNRS, 96743 Kamuela, HI, USA

Received 14 January 2022 / Accepted 14 April 2022

ABSTRACT

Context. The evolution of galaxies is influenced by many physical processes, which may vary depending on their environment.

Aims. We combine *Hubble* Space Telescope (HST) and Multi-Unit Spectroscopic Explorer (MUSE) data of galaxies at $0.25 \lesssim z \lesssim 1.5$ to probe the impact of environment on the size-mass relation, the main sequence (MS) relation, and the Tully-Fisher relation (TFR).

Methods. We perform a morpho-kinematics modelling of 593 [O II] emitters in various environments in the COSMOS area from the MUSE-gAlaxy Groups In Cosmos survey. The HST F814W images are modelled with a bulge-disk decomposition to estimate their bulge-disk ratio, effective radius, and disk inclination. We use the [O II] $\lambda\lambda 3727, 3729$ doublet to extract the galaxies' ionised gas kinematics maps from the MUSE cubes, and we model those maps for a sample of 146 [O II] emitters, including bulge and disk components constrained from morphology and a dark matter halo.

Results. We find an offset of 0.03 dex (1σ significant) on the size-mass relation zero point between the field and the large structure sub-samples, with a richness threshold of $N = 10$ to separate between small and large structures, and of 0.06 dex (2σ) with $N = 20$. Similarly, we find a 0.1 dex (2σ) difference on the MS relation with $N = 10$ and 0.15 dex (3σ) with $N = 20$. These results suggest that galaxies in massive structures are smaller by 14% and have star formation rates reduced by a factor of 1.3–1.5 with respect to field galaxies at $z \approx 0.7$. Finally, we do not find any impact of the environment on the TFR, except when using $N = 20$ with an offset of 0.04 dex (1σ). We discard the effect of quenching for the largest structures, which would lead to an offset in the opposite direction. We find that, at $z \approx 0.7$, if quenching impacts the mass budget of galaxies in structures, these galaxies would have been affected quite recently and for roughly 0.7–1.5 Gyr. This result holds when including the gas mass but vanishes once we include the asymmetric drift correction.

Key words. galaxies: evolution – galaxies: kinematics and dynamics – galaxies: clusters: general – galaxies: groups: general – galaxies: high-redshift

1. Introduction

The evolution of galaxies is not a trivial process, as numerous physical mechanisms that act on different physical scales and timescales and with different amplitudes are at play. From an observational point of view, our understanding of galaxy

evolution has greatly improved over roughly the last 25 years thanks to: (i) extended multi-band imaging and spectroscopic surveys of the local Universe (e.g., SDSS and 2dFGRS); (ii) the advent of the *Hubble* Space Telescope (HST), associated with 8–10 m class telescopes (e.g., VLT and Keck), which allowed galaxies in the more distant Universe to be probed and studied by combining extremely deep images (e.g., HUDF and COSMOS) with large spectroscopic surveys (e.g., VVDS and zCOSMOS); and (iii) the development and continuous improvement of 3D spectrographs (e.g., SINFONI, KMOS, and MUSE), whose data have allowed distant galaxies be to studied in even more detail. The current paradigm for galaxy evolution is that galaxies must have first formed their dark matter (DM) haloes in the early stages of the Universe, and only later started assembling

* Full Appendix G is available at <https://www.aanda.org>

** Full Table F.1 is only available at the CDS via anonymous ftp to cdsarc.u-strasbg.fr (130.79.128.5) or via <http://cdsarc.u-strasbg.fr/viz-bin/cat/J/A+A/665/A54>

*** Based on observations made with ESO telescopes at the Paranal Observatory under programmes 094.A-0247, 095.A-0118, 096.A-0596, 097.A-0254, 099.A-0246, 100.A-0607, 101.A-0282, 102.A-0327, and 103.A-0563.

their baryonic mass, by continuous accretion via the circumgalactic medium of mainly cold gas from filaments located in the cosmic web (e.g., Kereš et al. 2005; Ocvirk et al. 2008; Bouché et al. 2013; Zabl et al. 2019), by galactic wind recycling (Davé 2009; Hopkins et al. 2012; Schroetter et al. 2019), or through galaxy mergers (López-Sanjuan et al. 2012; Ventou et al. 2017, 2019; Mantha et al. 2018; Duncan et al. 2019). In particular, this scenario is favoured to explain the high star formation rates (SFRs) measured in the past billion years, which would have rapidly depleted the galaxies' gas content and would have led the galaxies to an early quenching phase unless their gas reservoir was continuously replenished throughout cosmic time. Thus, the mass assembly of the baryonic components of galaxies must be tightly linked to the evolution of their DM content.

This picture is further supported by the fact that high redshift galaxies appear to be quite different from their local counterparts, indicative that they must have radically evolved in order to populate the *Hubble* sequence that we see today. Studies comparing the global properties of high and low redshift galaxies have indeed shown that the former tend to be on average smaller (Trujillo et al. 2007; van der Wel et al. 2014b; Mowla et al. 2019) and less massive (Ilbert et al. 2010; Muzzin et al. 2013) than the latter. At the same time, galaxies have shown a rise in their mean SFR throughout cosmic time up to a peak of star formation at redshift $z \sim 2$ before declining to the typical value of roughly $0.01 M_{\odot} \text{ yr}^{-1} \text{ Mpc}^{-3}$ measured today (Hopkins & Beacom 2006), and their molecular gas fraction is also found to be larger at high redshift (Tacconi et al. 2018; Freundlich et al. 2019; Walter et al. 2020). In addition to their global properties, galaxies also show clear signs of morphological and kinematics evolution. Several studies have highlighted the fact that the proportion of triaxial systems and thick disks increases as we go to higher redshifts, with low mass galaxies having a larger tendency to be triaxial (van der Wel et al. 2014a; Zhang et al. 2019). This would suggest a trend for star-forming galaxies to flatten as they evolve, going from prolate to oblate shapes. At the same time, intermediate to high redshift galaxies are found to have on average more complex and perturbed gas kinematics with a larger velocity dispersion than their local counterparts (Flores et al. 2006; Yang et al. 2008; Epinat et al. 2010). While understanding the evolution of the different galaxy populations down to the intricate details is a particularly tedious task, it has become clear that there must exist a finite set of physical mechanisms at play that drives the bulk of the evolution in order to explain the various scaling relations first discovered in the local Universe but which have been shown to hold at intermediate and high redshift. Among these we can cite the Schmidt-Kennicutt relation (e.g., Schmidt 1959; Kennicutt 1998a), the mass-size relation (e.g., Shen et al. 2003; Mowla et al. 2019), the main sequence (MS) relation (e.g., Noeske et al. 2007; Whitaker et al. 2014), the Tully-Fisher relation (TFR; e.g., Tully & Fisher 1977; Contini et al. 2016; Tiley et al. 2019; Abril-Melgarejo et al. 2021), and the mass-metallicity relation (e.g., Tremonti et al. 2004; Erb et al. 2006).

One key question is whether the transition seen from high to low redshift between morphologically disturbed, particularly active galaxies to mostly relaxed, massive low-star-formation systems is mainly driven by in situ physical phenomena such as supernova-driven galactic super winds and active galactic nucleus feedback or, on the contrary, is driven by the environment within which these galaxies lie. This question has led discussions about the impact of galaxy clusters to the physical properties, morphology, and kinematics of their constituent galaxies. The two main mechanisms that can affect star formation in galaxies located in clusters with respect to those in the lowest-density environ-

ments (hereafter 'field' galaxies) are bursts of star formation and quenching (e.g., see Peng et al. 2010, for an analysis of environment and mass quenching in the local Universe). While the latter is not specifically inherent to galaxy clusters, these massive structures tend to accelerate its effect either through hydrodynamical mechanisms, such as ram-pressure stripping (e.g., Gunn & Gott 1972; Boselli et al. 2019) and thermal evaporation (e.g., Cowie & McKee 1977; Cowie & Songaila 1977), or through gravitational mechanisms, such as galaxy harassment (e.g., Cortese et al. 2021).

Until quite recently, few studies had tried to investigate the well-known scaling relations as a function of the environment of galaxies, except for the MS relation. Indeed, the MS relation is probably one of the most studied scaling relations as a function of environment as it can be used to directly probe the impact of quenching on the evolution of galaxies. Following the recent data release announcement of the Gemini Observations of Galaxies in Rich Early ENvironments (GOGREEN) and Gemini CLuster Astrophysics Spectroscopic Survey (GCLASS) surveys (Balogh et al. 2020), aimed at probing the impact of dense environments on intermediate redshift ($0.8 < z < 1.5$) galaxy properties, Old et al. (2020a,b) explored the environmental dependence of the star-forming MS between massive clusters and field galaxies. Using the [O II] doublet flux as a proxy for the SFR, they found the SFR of cluster galaxies to be on average 1.4 times lower than that of their field sample, the difference being more pronounced for low stellar masses. Alternatively, Erfanianfar et al. (2016), using data from the Cosmic Evolution Survey (COSMOS), All-Wavelength Extended Groth Strip International Survey (AEGIS), Extended Chandra Deep Field-South (ECDFS), and Chandra Deep Field North (CDFN) fields, could not find any difference in the MS relation between field galaxies and those in structures in the redshift range $0.5 < z < 1.1$, but they did find a similar trend to that of Old et al. (2020b) in the lowest redshift regime ($0.15 < z < 0.5$). On the other hand, Nantais et al. (2020) could not find any significant difference between field and Spitzer Adaptation of the Red-Sequence Cluster Survey (SpARCS; Muzzin et al. 2009) cluster galaxies at redshift $z \sim 1.6$, which, according to the authors, could be explained either by the fact that galaxies might have been accreted too recently to show signs of quenching or by the fact that the clusters might be not mature enough yet at this redshift to produce measurable environmental effects on these galaxies.

The environmental impact on the size-mass relation began to be studied only in the last decade, by Maltby et al. (2010). Using galaxies from the Space Telescope A901/2 Galaxy Evolution Survey (STAGES) survey (Gray et al. 2009), they found no difference in the size-mass relation for massive galaxies ($M_{\star} > 10^{10} M_{\odot}$) and a significant offset for intermediate to low mass galaxies, consistent with field spiral galaxies being about 15% larger than those in clusters at $z \sim 0.16$. Alternatively, Kuchner et al. (2017) found a similar relation at high mass rather than at low mass for late-type galaxies at $z = 0.44$, where cluster galaxies were smaller than their field counterparts, and Matharu et al. (2019) found the same trend when comparing the size-mass relation between field and cluster galaxies at $z \sim 1$. However, Kelkar et al. (2015), using data from the ESO Distant Cluster Survey, could not find any difference between field and cluster galaxies in the redshift range $0.4 < z < 0.8$.

Finally, regarding the TFR, Pelliccia et al. (2019) searched for differences between two samples of galaxies in groups and clusters from the Observations of Redshift Evolution in Large-Scale Environments (ORELSE) sample (Lubin et al. 2009) using long-slit spectroscopy data to derive the galaxies' kinematics. They could not find any significant difference between the two TFRs and therefore claimed the environment had no impact.

More recently, [Abril-Melgarejo et al. \(2021\)](#) analysed a sample of $z \sim 0.7$ galaxies located in galaxy groups from the MUSE-gALaxy Groups In Cosmos (MAGIC) survey (Epinat et al., in prep.) using Multi-Unit Spectroscopic Explorer (MUSE) and HST data. By comparing their TFR with that from the K -band Multi Object Spectrograph 3D (KMOS3D; [Úbler et al. 2017](#)), KMOS Redshift One Survey (KROSS; [Tiley et al. 2019](#)), and ORELSE ([Pelliccia et al. 2019](#)) samples, they found a significant offset in the TFR zero point, which they attributed to a possible impact of the environment since these samples targeted different populations of galaxies (galaxies in groups and clusters versus galaxies in clusters and in the field). This result led them to two different interpretations of this offset:

- (i) A quenching of star formation visible in the massive structures that led to a decrease in stellar mass with respect to the field or
- (ii) A baryon contraction phase for the galaxies in groups and clusters that led to an increase in circular velocity for these galaxies.

However, they also indicated that comparing samples from different datasets, with physical quantities derived from different tools, methods, and models and with different selection functions, leads to many uncertainties that might compromise the interpretation. Thus, they argued that, in order to study the impact of the environment on the TFR in a robust way, one would need to self-consistently apply the same methodology and models to galaxies located in various environments (field, groups, and clusters), which is the goal of this paper.

Here we push beyond the previous analysis performed by [Abril-Melgarejo et al. \(2021\)](#) and investigate differences in three main scaling relations (size-mass, MS, and TFR) when using samples that target different environments, with HST and MUSE data from the MAGIC survey. Because this survey targets galaxies located in galaxy groups and clusters, as well as foreground and background galaxies in a similar redshift range without prior selection, we expect to probe the impact of the environment on these relations in detail and with reduced uncertainties by applying the same procedure to model the morphology with HST images and the kinematics with MUSE cubes using the [O II] doublet.

This paper is structured as follows. In Sect. 2 we present the HST and MUSE data. In Sect. 3 we introduce the initial MAGIC sample and the structure identification, and we explain how we derived the galaxies' global properties (stellar mass and SFR). In Sect. 4 we present the morphological modelling performed with GALFIT on the entire [O II] emitter sample with reliable redshifts, the aperture correction applied for the stellar mass, and the prescription we applied to derive an average disk thickness as a function of redshift. In Sect. 5 we describe the kinematics modelling using the [O II] doublet as a kinematics tracer, as well as the mass models used to constrain the kinematics from the stellar distribution. In Sect. 6 we discuss the selection criteria applied to select samples to study the size-mass relation, the MS relation, and the TFR. Finally, we focus in Sect. 7 on the analysis of the three scaling relations as a function of environment. Throughout the paper we assume a Λ cold dark matter cosmology with $H_0 = 70 \text{ km s}^{-1} \text{ Mpc}^{-1}$, $\Omega_M = 0.3$, and $\Omega_\Lambda = 0.7$.

2. MUSE and HST data

2.1. MUSE observations and data reduction

Galaxies studied in this paper are part of the MAGIC survey. This survey targeted 14 galaxy groups located in the COSMOS area ([Scoville et al. 2007b](#)) selected from the COSMOS

group catalogue of [Knobel et al. \(2012\)](#) in the redshift range $0.5 < z < 0.8$, and observed during Guaranteed Time Observations as part of an observing programme studying the effect of the environment on 8 Gyr of galaxy evolution (PI: T. Contini). Though more details will be given in the MAGIC survey paper (Epinat et al., in prep), we provide in what follows a summary of the data acquisition and reduction.

In total, 17 different MUSE fields were observed over seven periods. For each target, observing blocks (OBs) of four 900-s exposures were combined, including a small dithering pattern, as well as a rotation of the field of 90° between each exposure. The final combined data cubes have total exposure times ranging between 1 and 10 hours. Because kinematics studies are quite sensitive to spatial resolution, we required observations to be carried out under good seeing conditions with a point spread function (PSF) full width at half maximum (FWHM) lower than $0.8''$, except in cases where the adaptive optics (AO) system was used.

The MUSE standard pipeline ([Weilbacher et al. 2020](#)) was used for the data reduction on each OB individually. Observations with AO used the v2.4 version, whereas the others used v1.6, except for the MUSE observations of COSMOS group CGr30, which used v1.2. Default sky subtraction was applied on each science exposure before aligning and combining them using stars located in the field. To improve sky subtraction, the Zurich Atmosphere Purge software ([Soto et al. 2016](#)) was then applied to the final combined data cube. The reduction leads to data and variance cubes with spatial and spectral sampling of $0.2''$ and 1.25 \AA , respectively, in the spectral range $4750\text{--}9350 \text{ \AA}$.

As shall be discussed in more detail in Sect. 5, the kinematics maps, which are extracted from the MUSE data cubes, serve as a basis for the kinematics modelling. Among those kinematics maps are the ionised gas velocity field and velocity dispersion maps, which are highly affected by both the limited spectral (line spread function) and spatial (PSF) resolutions of MUSE data through beam smearing. Because extracting reliable kinematics parameters depends on correctly taking into account the impact of the beam smearing in the kinematics models of the galaxies, it is therefore important to know the values of the MUSE PSF and line spread function (LSF) FWHM at the wavelength of observation. The MUSE LSF is modelled using the prescription from [Bacon et al. \(2017\)](#) and [Guérou et al. \(2017\)](#) who derived the wavelength dependence of the MUSE LSF FWHM in the *Hubble* Ultra Deep Field (HUDF) and *Hubble* Deep Field South as

$$FWHM_{\text{LSF}} = \lambda^2 \times 5.866 \times 10^{-8} - \lambda \times 9.187 \times 10^{-4} + 6.040, \quad (1)$$

where $FWHM_{\text{LSF}}$ and λ are both in \AA .

Because of the atmospheric turbulence, we expect the PSF FWHM to be reduced with increasing wavelength. As was shown in [Bacon et al. \(2017\)](#), the change of the PSF with wavelength can be quite accurately modelled with a declining linear relation. To derive the slope and zero point of this relation in each MUSE field, we extracted as many stars as possible, only keeping those with a reliable MUSE redshift measurement of $z \sim 0$. For each star, 100 sub-cubes of spatial dimension 10×10 pixels were extracted at regular intervals along the MUSE wavelength range and later collapsed into narrow band images using a fixed redshift slice depth of $\Delta z = 0.01$, scaling with wavelength as $\Delta \lambda = \Delta z \times \lambda$. Each narrow band image was modelled with GALFIT ([Peng et al. 2002a](#)) using a symmetric

- (i) 2D Gaussian profile,

(ii) Moffat profile with a free β index.

We found consistent results between these two models, and therefore decided to use the Gaussian values in the following analysis. In order to remove small-scale variations while keeping the global declining trend of interest in the wavelength dependence of the PSF FWHM, we applied a rolling average with a window of five data points for all the stars. For each MUSE field, the median wavelength dependence of the PSF FWHM of the stars in the field was fitted with a linear relation. We find a median value of $0.65''$ for the MUSE PSF FWHM and 2.55 \AA for the LSF FWHM (roughly 50 km s^{-1}). The values of the slope and zero point retrieved from the best-fit models were later used in the kinematics modelling (see Sect. 5).

2.2. HST data

In addition to using MUSE observations to extract the ionised gas kinematics, we also made use of *Hubble* Space Telescope Advanced Camera for Surveys (HST-ACS) images and photometry to model the morphology of the galaxies (see Sect. 4.1). For each galaxy we extracted stamps of dimension $4'' \times 4''$ in the F814W filter from the third public data release of the HST-ACS COSMOS observations (Koekemoer et al. 2007; Massey et al. 2010). These images have the best spatial resolution available ($\leq 0.1''$, that is, $\sim 600 \text{ pc}$ at $z \sim 0.7$) for HST data in the COSMOS field with a spatial sampling of $0.03''/\text{pixel}$, as is required to extract precise morphological parameters, with an exposure time of 2028 s per HST tile. At the same time, this filter corresponds to the reddest band available (*I*-band) and therefore to the oldest stellar populations probed by HST data, being less affected by star-forming clumps and with smoother stellar distributions.

As for MUSE data, a precise knowledge of the HST PSF in this filter is required to extract reliable morphological parameters. To model the HST PSF FWHM, a circular Moffat profile was fitted onto 27 non saturated stars located in our MUSE fields. The theoretical values of the HST PSF parameters, retrieved from the best-fit Moffat profile, used in the morphological modelling (see Sect. 4.1) correspond to the median values of the 27 best-fit models parameters and are $FWHM_{\text{HST}} = 0.0852''$ and $\beta = 1.9$, respectively (Abril-Melgarejo et al. 2021).

3. Galaxy sample properties

3.1. Initial MAGIC sample

Observations carried out for the MAGIC survey targeted already known galaxy groups in the COSMOS field such that all the galaxies in these fields up to $z \sim 1.5$ were already detected from previous broadband photometry and listed in the COSMOS2015 catalogue of Laigle et al. (2016) up to a 3σ limiting magnitude of 27 in *z*++ band. The spectroscopic redshift of the objects in the COSMOS2015 catalogue located in the observed MUSE fields were estimated with the redshift finding algorithm Manual and Automatic Redshifting Software (MARZ; Hinton 2016) using both absorption and emission features. At the redshift of the targeted groups ($z \sim 0.7$) the strongest emission lines are [O II] $\lambda\lambda 3727, 3729$, [O II] $\lambda 5007$, and H β , and the main absorption lines are Ca II H $\lambda 3968.47$, Ca II K $\lambda 3933.68$, *G* band from CH molecules, and Balmer absorption lines. Following Inami et al. (2017), a PSF weighted spectrum was extracted for each source and a robust redshift determination was obtained using the strongest absorption and emission lines. In each case,

Table 1. Median properties for the different samples of galaxies defined in Sect. 6.2.

Sample	Selection	Number	$\log_{10} M_{\star}$ [M_{\odot}]	$R_{\text{eff,d}}$ kpc	B/D (R_{eff})	$\log_{10} \text{SFR}_z$ [$M_{\odot} \text{ yr}^{-1}$]
(1)	(2)	(3)	(4)	(5)	(6)	(7)
[O II] emitters		1142	$9.2^{+1.2}_{-1.1}$			
Morphological		890	$9.4^{+1.1}_{-1.0}$	$2.5^{+2.6}_{-1.3}$	$0.2^{+1.5}_{-0.2}$	
Kinematics		593	$9.3^{+0.9}_{-0.9}$	$2.6^{+2.6}_{-1.4}$	$0.1^{+1.0}_{-0.1}$	$-0.2^{+0.5}_{-0.5}$
MS	(i)	447	$9.3^{+0.7}_{-0.7}$	$2.8^{+2.4}_{-1.5}$	$0.0^{+0.3}_{-0.0}$	$-0.2^{+0.5}_{-0.5}$
TFR	(i) to (v)	146	$9.6^{+0.6}_{-0.6}$	$3.9^{+2.1}_{-1.2}$	$0.0^{+0.2}_{-0.0}$	$0.0^{+0.4}_{-0.4}$

Notes: (1) Sample name, (2) selection criteria applied from Sect. 6.1, (3) number of galaxies, (4) SED-based stellar mass, (5) disk effective radius, (6) bulge-to-disk flux ratio at radius R_{eff} , and (7) [O II]-based SFR corrected for redshift evolution via normalisation at redshift $z_0 \approx 0.7$. In this table, each sample is a sub-sample of the one located just above. Stellar masses and SFR values are given in an aperture of $3''$. Uncertainties correspond to the 16th and 84th percentiles.

a redshift confidence flag was assigned ranging from CONFID = 1 (tentative redshift) to CONFID = 3 (high confidence).

Initially, the catalogue contained 2730 objects, including stars in our Galaxy, intermediate, and high redshift ($z \geq 1.5$) galaxies, 51% of which having reliable spectroscopic redshifts (CONFID > 1). As described in Sect. 5, the kinematics of the galaxies is extracted from the [O II] doublet. Therefore, as a starting point, we decided to restrict the sample of galaxies to [O II] emitters with reliable redshifts only, that is, galaxies in the redshift range $0.25 \lesssim z \lesssim 1.5$ with CONFID > 1. The main reason for considering [O II] emitters only is that the bulk of galaxies located in the targeted groups is located at redshift $z \sim 0.7$ where the [O II] doublet is redshifted into the MUSE wavelength range and happens to be among the brightest emission lines. Thus, using this emission line combines the advantages of having a high signal-to-noise ratio (S/N) extended ionised gas emission, while probing galaxies within a quite large redshift range roughly corresponding to 8 Gyr of galaxy evolution. Using the aforementioned criteria onto the initial MAGIC sample and without applying any further selection, the [O II] emitters sample contains 1142 galaxies. The main physical properties of this sample, along with other samples defined later in the text, are shown in Table 1.

3.2. Structure identification and characterisation

A crucial point when one wants to look at the effect of the environment on galaxy properties and evolution is to efficiently characterise the environment where galaxies lie. Galaxies are usually split into three main categories depending on their environment

- (i) field galaxies that do not belong to any structure,
- (ii) galaxies in groups that are gravitationally bound to a small number of other galaxies, and
- (iii) galaxies in clusters that are gravitationally bound to a large number of galaxies.

Because there is no sharp transition between a galaxy group and a galaxy cluster, and also because it is not particularly relevant for this discussion to disentangle between these two cases, we refer to both in the following parts as structures.

The characterisation of the galaxies' environment and their potential membership to a structure was performed with a 3D friends-of-friends (FoF) algorithm. Structure membership assignment was performed galaxy per galaxy given that the sky projected and the line of sight velocity separations were both

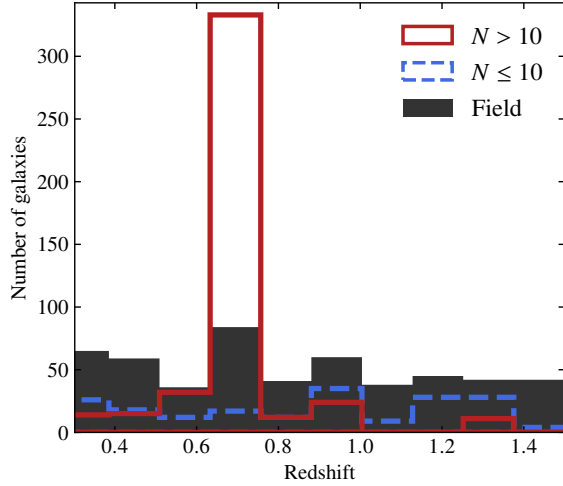


Fig. 1. Redshift distribution for the three initial sub-samples defined in Sect. 3.2. The samples of field galaxies (grey area) and galaxies in small structures (dashed blue line) have relatively flat distributions. The peak of the distribution for galaxies in large structures (red line) is located at redshift $z \sim 0.7$ and is driven by the largest structures ($40 \leq N \leq 100$) found in the COSMOS area of the MAGIC sample.

below two thresholds set to 450 kpc and 500 km s^{-1} , respectively, as was suggested by [Knobel et al. \(2009\)](#). We checked that varying the thresholds around the aforementioned values by small amounts did not change significantly the structure memberships (see MAGIC survey paper, [Epinat et al., in prep](#) for more details). As shown in Fig. 1, the bulk of the structures is located in the redshift range $0.6 < z < 0.8$ since most of them belong to the COSMOS wall ([Scoville et al. 2007a](#); [Iovino et al. 2016](#)), a large-scale filamentary structure located at redshift $z \approx 0.72$. Among these structures, those with at least ten members were studied in a previous paper ([Abril-Melgarejo et al. 2021](#)). In order to probe in detail the environmental dependence on galaxy properties, we use three sub-samples in the following sections:

- (i) the field galaxy sub-sample, which contains galaxies not assigned to any structure as well as galaxies that belong to structures with up to three members,
- (ii) the small structure sub-sample, which comprises galaxies that belong to structures that have between three and ten members,
- (iii) the large structure sub-sample, which contains galaxies in structures with more than ten members.

Within the [O II] emitters sample, 45% belong to the field, 20% are in small structures, and 35% are in the large structure sub-sample.

3.3. Stellar mass and star formation rates

Since galaxies are located in the COSMOS area, we used the same 32 photometric bands as in [Epinat et al. \(2018\)](#) and [Abril-Melgarejo et al. \(2021\)](#) found in [Laigle et al. \(2016\)](#) (COSMOS2015) catalogue to derive additional physical parameters such as stellar masses and SFRs. We used the spectral energy distribution (SED) fitting code FAST ([Kriek et al. 2009](#)) with a synthetic library generated from the stellar population synthesis models of [Conroy & Gunn \(2010\)](#) using a [Chabrier \(2003\)](#) initial mass function, an exponentially declining SFR, a [Calzetti et al. \(2000\)](#) extinction law, and fixing the redshift of the galaxy to the spectroscopic redshift derived from the MUSE spectrum. The

SED output parameters, including the stellar mass, SFR, and stellar metallicity, as well as their 1σ error, correspond to the values retrieved from the best-fit model of the SED, using the photometric bands values from [Laigle et al. \(2016\)](#) catalogue, and integrated within a circular aperture of diameter $3''$.

After performing a careful comparison between the stellar masses and SFR values computed with FAST and those given in the COSMOS2015 catalogue (computed using LEPHARE SED fitting code), we found consistent results for the stellar masses with, on average, a scatter of 0.2–0.3 dex. On the other hand, we found larger discrepancies between the SFR values, around 0.7–0.8 dex. Given that the origin of this discrepancy is unclear, and that SED-based SFR estimates usually have quite large uncertainties (e.g., [Wuyts et al. 2011](#); [Leja et al. 2018](#)), we decided to use emission lines instead to compute the SFR. Ultimately, one would want to use $H\alpha$ as tracer of star formation, but given the MUSE wavelength range, this would restrict the sample to $z \lesssim 0.4$ galaxies. Instead, following [Kennicutt \(1998b\)](#), we can use the [O II] doublet to compute the SFR in the entire [O II] emitters sample, as long as we can correct for Galactic and intrinsic extinctions, that is,

$$\text{SFR} [M_{\odot} \text{ yr}^{-1}] = (1.4 \pm 0.4) \times 10^{-41} L_{[\text{O II}]} [\text{erg s}^{-1}], \quad (2)$$

where SFR has not been normalised yet to account for the redshift evolution of the MS, $L_{[\text{O II}]} = 4\pi D_L^2 F_{[\text{O II}],\text{corr}}$ is the [O II] luminosity, with D_L the luminosity distance, and $F_{[\text{O II}],\text{corr}}$ the extinction corrected [O II] flux, which must be corrected for intrinsic extinction at the rest-frame $H\alpha$ wavelength ([Kennicutt 1992, 1998b](#)), computed as

$$F_{[\text{O II}],\text{corr}} = F_{[\text{O II}]} \times 10^{0.4(A_{H\alpha} + A_{[\text{O II}],\text{MW}})}, \quad (3)$$

with $F_{[\text{O II}]}$ the uncorrected [O II] flux integrated in an aperture of $3''$, $A_{H\alpha}$ the intrinsic extinction computed at the rest-frame $H\alpha$ wavelength, and $A_{[\text{O II}],\text{MW}}$ the Galactic extinction computed at the observed [O II] wavelength assuming a [Cardelli et al. \(1989\)](#) extinction law and $R_V = 3.1$. In order to compute the intrinsic extinction, one needs to know the extinction in a given band or at a given wavelength, for instance in the V band. This value is provided by FAST but, similarly to the SFR, it usually comes with large uncertainties. Given that the extinction plays an important role when deriving the SFR, we decided not to rely on the values from FAST. Instead, we used the prescription from [Gilbank et al. \(2010, 2011\)](#), which parametrises the extinction for $H\alpha$ using the galaxies stellar mass as

$$A_{H\alpha} = 51.201 - 11.199 \log_{10} \left(\frac{M_{\star}}{M_{\odot}} \right) + 0.615 \log_{10}^2 \left(\frac{M_{\star}}{M_{\odot}} \right), \quad (4)$$

for stellar masses $M_{\star} > 10^9 M_{\odot}$, and as a constant value below. When using the [O II]-based SFR in the analysis (Sect. 7), we checked that using the SED-based extinction rather than the prescription from [Gilbank et al. \(2010\)](#) to correct for intrinsic extinction did not change our conclusions.

The SFR-stellar mass plane for the kinematics sample (see Sect. 5.1), as well as the stellar mass and SFR distributions are shown in Fig. 2. In this figure and in what follows, we have taken out the zero point evolution of the MS by normalising the individual SFR values to redshift $z_0 = 0.7$ using the prescription

$$\log_{10} \text{SFR}_z = \log_{10} \text{SFR} - \alpha \log_{10} \left(\frac{1+z}{1+z_0} \right), \quad (5)$$

where SFR and SFR_z are the un-normalised and normalised SFR, respectively, and α is a scale factor. We used a value of

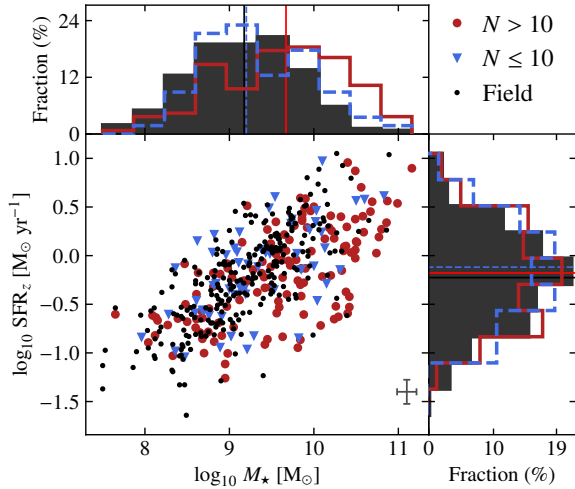


Fig. 2. SFR- M_* diagram for galaxies from the kinematics sample (see Sect. 6.1). Galaxies are separated between the field (black points), small structures (blue triangles), and large structures (red circles). The typical stellar mass and SFR error is shown on the bottom right. The SFR was normalised to redshift $z_0 = 0.7$. The SFR and mass distributions are shown as histograms to the top and right, respectively, with the median values for each sample represented as lines of similar colours.

$\alpha = 2.8$ from Speagle et al. (2014), which is larger than the value of $\alpha = 1.74$ derived and used in Boogaard et al. (2018) and Abril-Melgarejo et al. (2021). The main reason for normalising the redshift evolution with a larger slope is that the prescription from Boogaard et al. (2018) was derived on the low mass end ($\log_{10} M_*/M_\odot \lesssim 9$) of the MS. However, most of our galaxies have stellar masses larger than this threshold where the redshift evolution of the MS is much steeper (e.g., Whitaker et al. 2014).

4. Galaxy morphology

4.1. Morphological modelling

To recover the galaxies morphological parameters, we performed a multi-component decomposition using the modelling tool GALFIT on HST-ACS images observed with the F814W filter. In order to have a fair comparison with previous findings from Abril-Melgarejo et al. (2021), we used the same methodology to model the morphology of galaxies. Therefore, we performed a multi-component decomposition with

- (i) a spherically symmetric de Vaucouleurs profile¹ aimed at modelling the central parts of the galaxies (hereafter bulge) and
- (ii) a razor-thin exponential disk² describing an extended disk (hereafter disk).

In most cases, we expect the disk component to dominate the overall flux budget, except within the central parts where the bulge is usually concentrated. In very rare cases where the galaxies do not show any bulge component, GALFIT always converged towards a disk component only model. On the opposite, in the case of elliptically shaped galaxies, GALFIT usually converges towards a single de Vaucouleurs component. We do not systematically try to model additional features that may appear in very few cases, such as clumps, central bars, or spiral arms. When

¹ Sérsic profile with fixed Sérsic index $n = 4$, axis-ratio $b/a = 1$, and PA = 0° .

² Sérsic profile with a fixed Sérsic index $n = 1$.

clumps do appear, the multi-component decomposition is usually carried out without masking the clumps first. If the clumps seem to bias the morphological parameters of the main galaxy, a second run is done by either masking the clumps or adding other Sérsic profiles at their location. Unless there is no significant improvement in the robustness of the fitting process, the masked model is usually kept. Other cases may be galaxies in pairs or with small sky projected distances, which are modelled with an additional Sérsic profile at the second galaxy location, or out-of-stamps bright stars, which can contaminate the light distribution of some galaxies, in which case it is usually modelled with an additional sky gradient.

The aforementioned procedure was applied on the [O II] emitters sample. Among the 1142 galaxies, a few of them could not be reliably modelled with neither a bulge-disk decomposition nor a single disk or single bulge profile. Such galaxies turned out to be

- (i) low, or very low S/N objects for which the noise is contributing too much to the light distribution to extract reliable morphological parameters,
- (ii) very small galaxies for which the disk is barely resolved and the bulge not resolved at all.

After removing those cases, we get a morphological sample of 890 galaxies (i.e. 77% of the [O II] sample), which can be reliably modelled using this decomposition.

4.2. Morphological properties

The multi-component decomposition provides two scale parameters, the effective radius of the disk $R_{\text{eff,d}}$, and that of the bulge $R_{\text{eff,b}}$, but, in practice, we are more interested in the effective radius of the total distribution of light in the plane of the disk R_{eff} . Even though there is no analytical formula linking R_{eff} , $R_{\text{eff,d}}$, and $R_{\text{eff,b}}$, it can be shown from the definition of these three parameters that finding R_{eff} amounts to solving the following equation (see Appendix C for the derivation):

$$10^{-\text{mag}_d/2.5} \left[\gamma \left(2, b_1 \frac{R_{\text{eff}}}{R_{\text{eff,d}}} \right) - 0.5 \right] + 10^{-\text{mag}_b/2.5} \left[\gamma \left(8, b_4 \left(\frac{R_{\text{eff}}}{R_{\text{eff,b}}} \right)^{1/4} \right) / \Gamma(8) - 0.5 \right] = 0, \quad (6)$$

where mag_d and mag_b stand for the disk and bulge apparent total magnitudes as provided by GALFIT, respectively, $b_1 \approx 1.6783$, $b_4 \approx 7.6692$, Γ is the complete gamma function, and γ the lower incomplete gamma function. Equation (6) is solved for each galaxy using a zero search algorithm considering the two following additional arguments

- (i) it always admits a single solution,
- (ii) R_{eff} must be located between $R_{\text{eff,d}}$ and $R_{\text{eff,b}}$.

To get an estimate of the error on the effective radius, we generate for each galaxy 1000 realisations by perturbing the bulge and disk magnitudes and effective radii using the errors returned by GALFIT and assuming Gaussian distributions. For each realisation, we solve Eq. (6) and then compute the error as the 1σ dispersion around the median value. The majority of the galaxies in the morphological sample are disk dominated, 80% of them having a bulge-to-total flux ratio B/T (R_{eff}) < 0.5, with B/T as defined in Appendix C. As can be seen in Fig. 3, B/T distributions for galaxies from the morphological sample in the field, small, and large structure sub-samples are mostly similar, with very few bulge-dominated objects. There appears to be an excess of galaxies located in small structures with respect to field

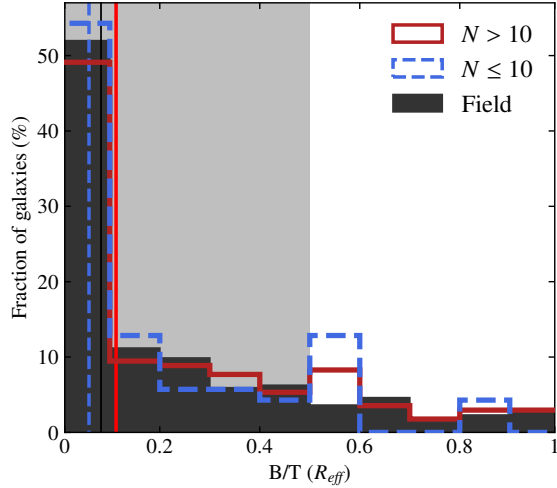


Fig. 3. Bulge-to-total flux ratio distribution computed at one effective radius for galaxies in the morphological sample located in various environments. The legend is similar to that of Fig. 1. The vertical lines correspond to the median B/T values for each sample. The grey area in the background indicates which galaxies were selected in the kinematics sample (see Sect. 5.1).

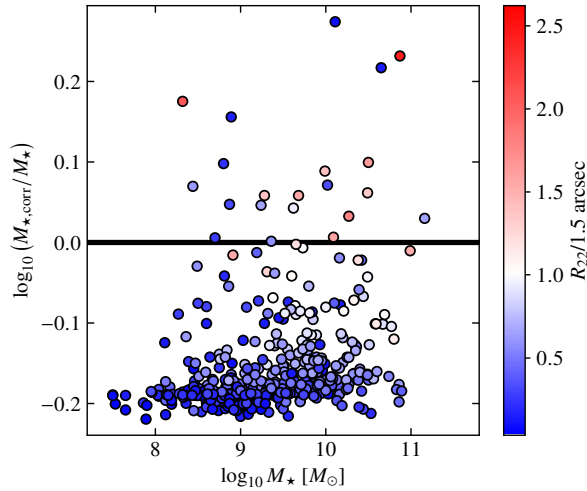


Fig. 4. Impact of stellar mass correction as a function of the SED-based stellar mass for galaxies from the morphological sample. Overall, the correction lowers the stellar mass, reducing it by as much as a factor of 1.5. We see that the smaller the disk radius, $R_{\text{eff,d}}$ (or equivalently R_{22}), the larger the stellar mass reduction, consistent with the fact that the SED-based stellar mass computed in an aperture of $3''$ usually overestimates the real value, though in practice this effect can be compensated for by sky projection and PSF effects.

galaxies in the range $0.5 \leq B/T \leq 0.6$ but, given the small number of galaxies in this bin (9), this excess may not be significant.

4.3. Stellar mass correction

As mentioned in Sect. 3.3, the galaxies stellar mass is retrieved from the SED fitting on the photometric bands in a circular aperture of $3''$ on the plane of the sky. On the other hand, the gas rotation velocity V_{22} (see Sect. 7), is usually derived at $R_{22} = 2.2 \times R_d$, where $R_d = R_{\text{eff,d}}/b_1$ is the disk scale length

defined as the e-folding length with respect to the central value. This means that the SED-based stellar mass corresponds to the integrated mass within a cylinder of diameter $3''$ orthogonal to the plane of the sky, whereas the kinematics is derived from the contribution of the mass located within a sphere of radius R_{22} . Therefore, directly comparing the kinematics with the SED-based stellar mass in scaling relations such as the TFR adds additional uncertainties due to projection effects (inclination), different sizes ($R_{\text{eff,d}}$, $R_{\text{eff,b}}$), and different bulge and disk contributions (B/D). Thus, we decided to apply a correction to the SED-based stellar mass estimate in the following way, assuming a constant mass-to-light ratio across the galaxy,

$$M_{\star,\text{corr}} = \frac{F_{\text{sph}}(R_{22})}{F_{\text{circ}}(1.5'')} M_{\star}, \quad (7)$$

where M_{\star} and $M_{\star,\text{corr}}$ are the uncorrected and corrected stellar masses measured in a $3''$ circular aperture on the plane of the sky and in a sphere of radius R_{22} around the galaxy centre, respectively. In Eq. (7), F_{sph} corresponds to the integrated flux in a sphere of radius R_{22} , while F_{circ} corresponds to the integrated flux in a $3''$ circular aperture on the plane of the sky.

In order to compute the mass correction, a high resolution 2D model was generated for each galaxy, projected on the sky given the axis ratio returned by GALFIT, and taking into account the impact of the MUSE PSF, whereas the flux in a sphere of radius R_{22} was integrated without taking into account the impact of the inclination, nor convoluting the surface brightness profile with the PSF. Taking into account the impact of the inclination and the PSF is important for the sky-projected model since the flux is integrated in a fixed aperture. Indeed, a higher inclination will result in the flux being integrated to larger distances along the minor axis, whereas higher PSF FWHM values will result in a loss of flux since it will be spread farther out. On the other hand, because the dynamical mass is derived in Sect. 5 from a forward model of the ionised gas kinematics taking into account the geometry of the galaxy and the impact of the PSF, the flux model integrated within a sphere of radius R_{22} must be fully free of projection and instrumental effects (i.e. inclination and PSF).

The impact of the stellar mass correction is shown in Fig. 4. For most galaxies the correction reduces the stellar mass, reaching at its maximum a factor of roughly 1.5. The main reason is that for $R_{22} < 1.5''$, the lower the disk effective radius, the more overestimated the SED-based stellar mass should be, though this argument must be mitigated by the fact that the inclination, the bulge contribution, and the PSF convolution can also play an important role in some cases, explaining why some galaxies have positive stellar mass corrections even with small disk effective radii.

4.4. Stellar disk inclination and thickness

In Sect. 4.1 we assumed that the surface brightness of the stellar disk can be represented by a razor-thin exponential profile, but in practice we expect most disk components to have non-zero thickness. Not taking into account this finite thickness can bias morphological and kinematics measurements, especially in the central parts, and the circular velocity. In turn, this can bias the derived dynamical parameters such as the baryon fraction. This effect becomes even more relevant when considering that the stellar disks thickness is expected to evolve with redshift and mass. By modelling the $q = b/a$ distribution, with a and b the apparent major and minor axes of the disk, respectively, for star-forming $z \leq 2.5$ galaxies in the Cosmic

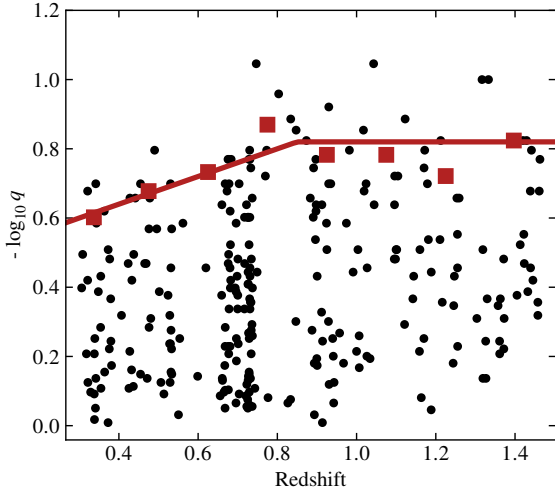


Fig. 5. Observed axis ratio, q , as a function of redshift for galaxies from the morphological sample (black points) after removing bulge-dominated galaxies and those with small disk sizes. The median values for the six most edge-on galaxies in redshift bins of width $\Delta z = 0.15$ are shown as red squares. The red line represents the thickness prescription that was applied. Independently of mass, galaxies tend to have thinner disks at larger redshifts, which may be due to the fact that we probe younger stellar populations at higher redshifts when observing in a single band.

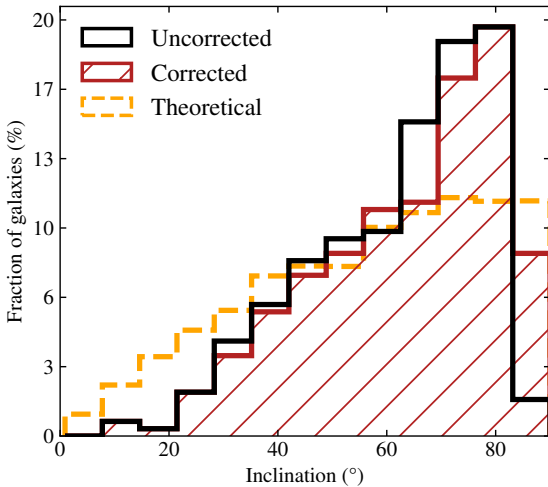


Fig. 6. Distribution of disk inclination for galaxies from the morphological sample, after removing bulge-dominated galaxies and those with small disk sizes. We show the distribution before correcting for the finite thickness of the disk (black line) and after the correction (red hatched area). The dashed orange line represents the binned theoretical distribution expected for randomly oriented disk galaxies. The correction tends to increase the fraction of edge-on galaxies. While being closer to the theoretical distribution at large inclinations, the corrected inclinations still do not match the distribution of randomly inclined galaxies.

Assembly Near-infrared Deep Extragalactic Legacy Survey (CANDELS) field and from the Sloan Digital Sky Survey (SDSS) catalogue, [van der Wel et al. \(2014a\)](#) found that galaxy disks become thicker with increasing stellar mass and at larger redshift. Similarly, [Zhang et al. \(2019\)](#), by looking at the q – $\log a$ plane, reached a fairly similar conclusion. On top of that, galaxies that exhibit a combination of a thin blue disk and a thick

red stellar disk are expected to have an observed thickness that varies with rest-frame wavelength. This effect can be observed in the catalogue of edge-on SDSS galaxies of [Bizyaev et al. \(2014\)](#), where the disk thickness of $z \lesssim 0.05$ galaxies tends to almost systematically increase when measured in the g , r , and i bands, respectively. In order to get an estimate of the disk thickness in our sample of galaxies, we used the methodology described in [Heidmann et al. \(1972\)](#) and [Bottinelli et al. \(1983\)](#). If galaxies located at a given redshift z , with a fixed stellar mass M_* , and emitting at a fixed rest-frame wavelength λ have a typical non-zero thickness $q_0(\lambda, z, M_*)$, then the observed axis ratio q for the majority of the galaxies should reach a minimum value equal to q_0 for edge-on galaxies. In our case, because the morphology is derived at a fixed observed wavelength $\lambda_{\text{obs}} \approx 8140 \text{ \AA}$ (F814W HST filter), this condition can be written as

$$q_0(\lambda_{\text{obs}}/(1+z), z, M_*) \lesssim q, \quad (8)$$

where λ_{obs} is the observed wavelength. The distribution of the observed axis ratio as a function of redshift is shown in Fig. 5. We see that the minimum observed axis ratio (i.e. highest $-\log_{10} q$) seems to decrease with redshift up to $z \approx 0.8$ – 0.9 and remains roughly constant afterwards. This trend, which seems inconsistent with the fact that the disk thickness has been previously observed to increase with redshift, can be explained by the fact that higher redshift galaxies are seen at a bluer rest-frame wavelength, which probes younger stellar populations, and probably thinner disks. Due to the lack of edge-on galaxies in various mass bins, we do not observe a clear dependence of q on stellar mass, and therefore decided to model only the redshift dependence of q . In order to avoid placing too much weight on outliers that may have thinner disks than the typical thickness expected at a given redshift, we separated galaxies in eight redshift bins and computed the median thickness of the six most edge-on galaxies in each bin. The dependence of the stellar disk thickness with redshift is given by

$$-\log_{10} q_0 = \begin{cases} 0.48 + 0.4z & \text{if } z \leq 0.85 \\ 0.48 & \text{otherwise.} \end{cases} \quad (9)$$

In the case of a razor-thin disk, the inclination i is related to the observed axis-ratio q through the relation $\cos i = q$. However, for a disk with non-zero thickness, the relation between i and q will depend on the exact geometry of the disk. Assuming our disk galaxies can be well approximated by oblate spheroidal systems, we have ([Bottinelli et al. 1983](#))

$$\cos^2 i = (q^2 - q_0^2)/(1 - q_0^2). \quad (10)$$

In Fig. 6, we show the distribution of the disk inclination for galaxies from the morphological sample (see Sect. 5.1) assuming razor-thin disks (black line), and after applying the thickness correction using Eqs. (9) and (10) (red hatched area). As expected, correcting for the disk thickness significantly increases the number of edge-on galaxies. Nevertheless, compared to the theoretical distribution (orange line), none of the distributions are consistent with randomly inclined galaxies. We find that we have an excess of galaxies in the range $60^\circ \lesssim i \lesssim 80^\circ$. The reason we are still missing some edge-on galaxies ($i > 80^\circ$) might be that we did not try to model the impact of the dust, which is known to affect edge-on galaxies more severely. Nevertheless, the inclination distribution we get is quite similar to the distributions found in other studies where they also lack edge-on galaxies ([Padilla et al. 2009](#); [Foster et al. 2017](#)).

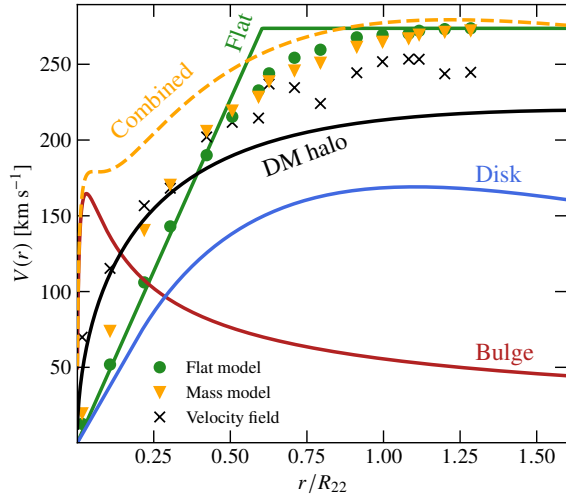


Fig. 7. Rotation curves for the flat (green line) and mass models (orange dashed) of galaxy 104-CGR79 at redshift $z = 0.53$. The components are the bulge (red), the thin disk (blue), and the DM halo (black). We also show the observed de-projected (but beam-smearred) rotation curves extracted along the major axis from the observed velocity field map (black crosses), from the best-fit velocity field flat model (green circles), and from the best-fit velocity field mass model (orange triangles). The largest difference between the flat and mass models is found in the inner parts, where the beam smearing is the strongest. The total dynamical mass differs slightly between models, with the flat one being 4% higher than the mass model one.

5. Galaxy kinematics

5.1. Kinematics modelling

Following the analysis in [Abril-Melgarejo et al. \(2021\)](#), we derived the ionised gas kinematics from the [O II] doublet only. For each galaxy, we extracted a sub-databcube with spatial dimensions 30×30 pixels around their centre and then performed a sub-resolution spatial smoothing using a 2D Gaussian kernel with a FWHM of 2 pixels in order to increase the S/N per pixel without worsening the databcube spatial resolution. From this smoothed version of the databcube, the [O II] doublet was fitted spaxel by spaxel by two Gaussian profiles with rest-frame wavelengths of 3727 \AA and 3729 \AA , respectively, assuming identical intrinsic velocity and velocity dispersion. Additionally, given the assumed photo-ionisation mechanisms producing the [O II] doublet ([Osterbrock & Ferland 2006](#)), we further constrained the flux ratio between the two lines as $0.35 \leq F_{[\text{O II}]\lambda 3727}/F_{[\text{O II}]\lambda 3729} \leq 1.5$. The aforementioned steps were performed with the emission line fitting python code CAMEL³, using a constant value to fit the continuum, and the MUSE variance cubes to weight the fit and estimate the noise. From this procedure, we recovered 2D maps for the following quantities: [O II] fluxes, S/N, velocity field, and velocity dispersion, as well as their corresponding spaxel per spaxel error estimation from the fit. To avoid fitting any noise or sky residuals that might appear in the flux and kinematics maps, especially in the outer parts of the galaxies, we cleaned the 2D maps in two successive steps: (i) through an automatic procedure, only keeping spaxels with $S/N \geq 5$ and $\text{FWHM}_{[\text{O II}]} \geq 0.8 \times \text{FWHM}_{\text{LSF}}(z)$, where $\text{FWHM}_{[\text{O II}]}$ and FWHM_{LSF} are the [O II] spatial PSF and spectral LSF FWHM, respectively, and (ii) by visually inspecting

the automatically cleaned velocity fields and manually removing remaining isolated spaxels or those with large velocity discontinuities with respect to their neighbours.

This led to the removal of 293 galaxies from the morphological sample (around 30%), mainly because they did not show any velocity field in their cleaned maps due to too low S/N per pixel. Because this cleaning process is mainly driven by S/N considerations, it is roughly similar to applying an [O II] integrated flux selection criterion of $F_{[\text{O II}]} \geq 2 \times 10^{18} \text{ erg s}^{-1} \text{ cm}^{-2}$.

The kinematics of the ionised gas in the remaining galaxies was modelled as a razor-thin rotating disk, using the method of line moments as described in [Epinat et al. \(2010\)](#). This method can quickly derive velocities maps by combining rotation curves⁴ from various components, taking into account the impact of spatial resolution on the derived velocity field, and the combined effect of the limited spatial and spectral resolutions on the velocity dispersion map. To derive the kinematics (circular velocity and velocity dispersion), we performed a mass modelling, taking into account prior knowledge from the morphological modelling. By using the best-fit GALFIT bulge and disk parameters from Sect. 4.1, and the disk thickness derived in Sect. 4.4, we fixed the rotation curves of the stellar disk and bulge components. Below we provide the main characteristics of the mass models used in the modelling, and we refer the reader to Appendix D for a detailed description of the models and rotation curves, as well as how implementing a finite thickness for the stellar disk impacts the estimate of the rotation of the gas. We assumed a double exponential density profile for the disk, which provides a surface brightness profile that is fairly similar to a single exponential distribution once projected onto the sky. In order to derive a density profile for the bulge component, one would need to numerically solve the inverse Abel transform for a de Vaucouleurs profile. But, because we required to have an analytical form for the bulge density, we decided to use instead a Hernquist profile ([Hernquist 1990](#)). As shown in Figs. D.4 and D.5, for the typical bulge parameters found in our sample, this functional form gives fairly reasonable surface brightness profiles once projected onto the sky. Finally, the DM halo was modelled using a Navarro-Frenk-White (NFW) profile ([Navarro et al. 1996](#)) with free parameters to account for constant or slowly declining observed rotation curves at large radii. This choice of DM parametrisation may not be entirely suitable with respect to observations that favour cored DM distributions. However, the core-cusp problem mainly affects the inner parts of the profiles. On the other hand, our goal is not to study the shape of DM haloes as a function of radius but rather to derive the ionised gas kinematics, the baryon, and the DM fractions where the inner shape of the DM halo has little impact on these quantities ([Korsaga et al. 2019](#)). In addition, because beam smearing strongly affects ground based observations of intermediate redshift galaxies, constraining robustly the inner DM halo distribution in detail remains a challenging problem but within reach (e.g., [Genzel et al. 2020](#); [Bouché et al. 2022](#)). The effect of beam smearing can be seen in Fig. 7 where we compare the best-fit rotation curves between a mass model and a simpler flat model for galaxy 104-CGR79. Even though the intrinsic rotation curves in the inner parts differ (dashed orange line versus green full line), the deprojected (but beam-smearred) rotation curves are almost the same.

⁴ We use the term rotation curve to refer to the circular velocity as a function of radius of models, and we explicitly write that it is observed otherwise.

³ <https://gitlab.lam.fr/bepinat/CAMEL>

For each galaxy, a 2D velocity field model is generated and fitted onto the velocity field extracted from the cube. Since beam smearing artificially increases the value of the velocity dispersion recovered from the cube, especially near the central parts, modelling it and quadratically removing it from the velocity dispersion map allows us to extract a much more reliable estimator of the overall velocity dispersion in each galaxy. Given the above description, the kinematics model requires the following parameters:

- (i) centre coordinates,
- (ii) inclination,
- (iii) kinematics position angle (PA),
- (iv) systemic redshift z_s ,
- (v) disk rotation curve parameters $V_{RT,max}$, $V_{corr,max}$, R_d (see Appendix D.3),
- (vi) bulge rotation curve parameters $V_{b,max}$, a (see Appendix D.6),
- (vii) DM halo rotation curve parameters $V_{h,max}$ and r_s (see Appendix D.8),
- (viii) PSF size.

However, there exists a strong degeneracy between the kinematics centre and z_s on one side, and the inclination of the disk and $V_{h,max}$ on the other side, which is even stronger when the data are highly impacted by beam smearing. Therefore, to remove this degeneracy we fixed the kinematics centre and inclination assuming they are identical to their morphological counterparts. As previously stated, we also fix the parameters of the disk and bulge components since we assume they are entirely constrained from the morphology. Thus, the centre coordinates, the inclination, the disk and bulge rotation curve parameters ($V_{RT,max}$, $V_{corr,max}$, R_d , $V_{b,max}$ and a) and the PSF model are fixed, whereas the kinematics PA, the systemic redshift, and the DM halo rotation curve parameters ($V_{h,max}$ and r_s) are free.

The kinematics modelling described above was performed with the new kinematics fitting code `MOCKING`⁵ using the python implementation of `MULTINEST` (Feroz & Hobson 2008; Buchner et al. 2014). `MULTINEST` is a Bayesian tool using a multi-nodal nested sampling algorithm to explore parameter space and extract inferences, as well as posterior distributions and parameter error estimation. To check our results, we ran `MOCKING` a second time but using this time the Levenberg-Marquardt algorithm, with the python implementation `CAT_MPFIT`⁶ of `MPFIT` (Markwardt 2009). Kinematics parameters were compared between these two methods as well as with earlier results obtained with an Interactive Data Language (IDL) code used in several previous studies (Epinat et al. 2009, 2010, 2012; Vergani et al. 2012; Contini et al. 2016; Abril-Melgarejo et al. 2021). A comparison of circular velocities obtained with `MULTINEST` and `MPFIT` can be found in Fig. A.1. We find consistent results between the methods, with `MULTINEST` providing more robust results. Thus, we use values from `MULTINEST` in the following parts. In addition, we performed a similar kinematics modelling but using an ad hoc flat model for the rotation curve as described in Abril-Melgarejo et al. (2021), in order to check the mass modelling and assess its reliability. After checking the morphological, kinematics, and mass models on the remaining galaxies, we decided to remove four additional objects:

- (i) 106-CGR84, 21-CGR114, and 101-CGR79 because they show signs of mergers in their morphology and kinematics, which may bias the measure of their dynamics, as well as their stellar mass estimate and thus their mass modelling,

- (ii) 13-CGR87 because it lies on the edge of the MUSE field with only half of its [O II] flux map visible.

Once these objects are removed, we get a kinematics sample of 593 galaxies with morphological and kinematics mass and flat models.

An example of a mass model with its corresponding flat model is shown in Fig. 7 for a disk-like galaxy with a non-zero (but weak) bulge contribution. The mass model rotation curve (orange dashed line) for the galaxy, which appears to be DM dominated, is consistent with the simpler flat model (green line), especially at R_{22} where the rotation velocity is inferred. Examples of full morpho-kinematics models for four types of galaxies are shown in Fig. 8 with, in the top-left corner, a galaxy with a close companion in its HST image and with a velocity field similar to that of a large fraction of galaxies in our sample, in the top-right corner an edge-on galaxy, in the bottom-left corner a large disk-dominated galaxy with visible arms and clumps, and in the bottom-right corner a small galaxy with a prominent bulge and a highly disturbed velocity field. These four examples give a decent overview of the types of galaxies, morphologies and kinematics we have to deal with in the MAGIC survey.

6. Sample selection

6.1. Selection criteria

Before analysing morpho-kinematics scaling relations as a function of environment, and following the discussion in Abril-Melgarejo et al. (2021; Sect. 3.6), we must first apply a few selection criteria to the kinematics sample depending on the scaling relation studied. The three relations analysed in this paper are the size-mass relation, MS relation, and TFR. Among the three, the TFR is the one that requires the most stringent criteria since we must ensure that we have good constraints on both the stellar mass and the kinematics measurements, which translates as having reliable constraints on the disk parameters (size, inclination), on the [O II] S/N, and on the dynamical modelling. On the other hand, we only require disk-dominated MS galaxies to analyse the size-mass and MS relations. Thus, we define a common sample for both the size-mass and MS relations, named the MS sample, by applying the following selection criterion:

- (i) $B/D (R_{eff}) \leq 1$,

where $B/D (R_{eff})$ is the bulge-to-disk flux ratio computed at one effective radius. This criterion ensures that we only have disk-dominated galaxies in the sample. In Abril-Melgarejo et al. (2021), we used a second selection criterion to remove red sequence galaxies located below the MS since we were only interested in star-forming galaxies. For the kinematics sample, applying this criterion would only remove two additional galaxies, since most of the red sequence galaxies also tend to be bulge dominated. Thus, we decided not to apply this criterion in the next parts. When applying the B/D selection, we end up with a MS sample of 447 galaxies.

Concerning the TFR, we must ensure that we have good constraints on the disk size, inclination, and [O II] S/N, as well as on the dynamical modelling, since they can all have significant impact on the kinematics and the derived dynamical masses. To ensure the TFR is not impacted by poor constraints on any of these parameters, we applied the following additional criteria on top of the B/D selection:

- (ii) $R_{eff,d} \geq 0.5 \times FWHM(z)$,
- (iii) $(S/N)_{tot} \geq 40 \times \sqrt{\pi [R_{eff,d}^2 + (FWHM(z)/2)^2]}$,

⁵ <https://gitlab.lam.fr/bepinat/MocKinG>

⁶ <https://www-astro.physics.ox.ac.uk/~mxc/software/>

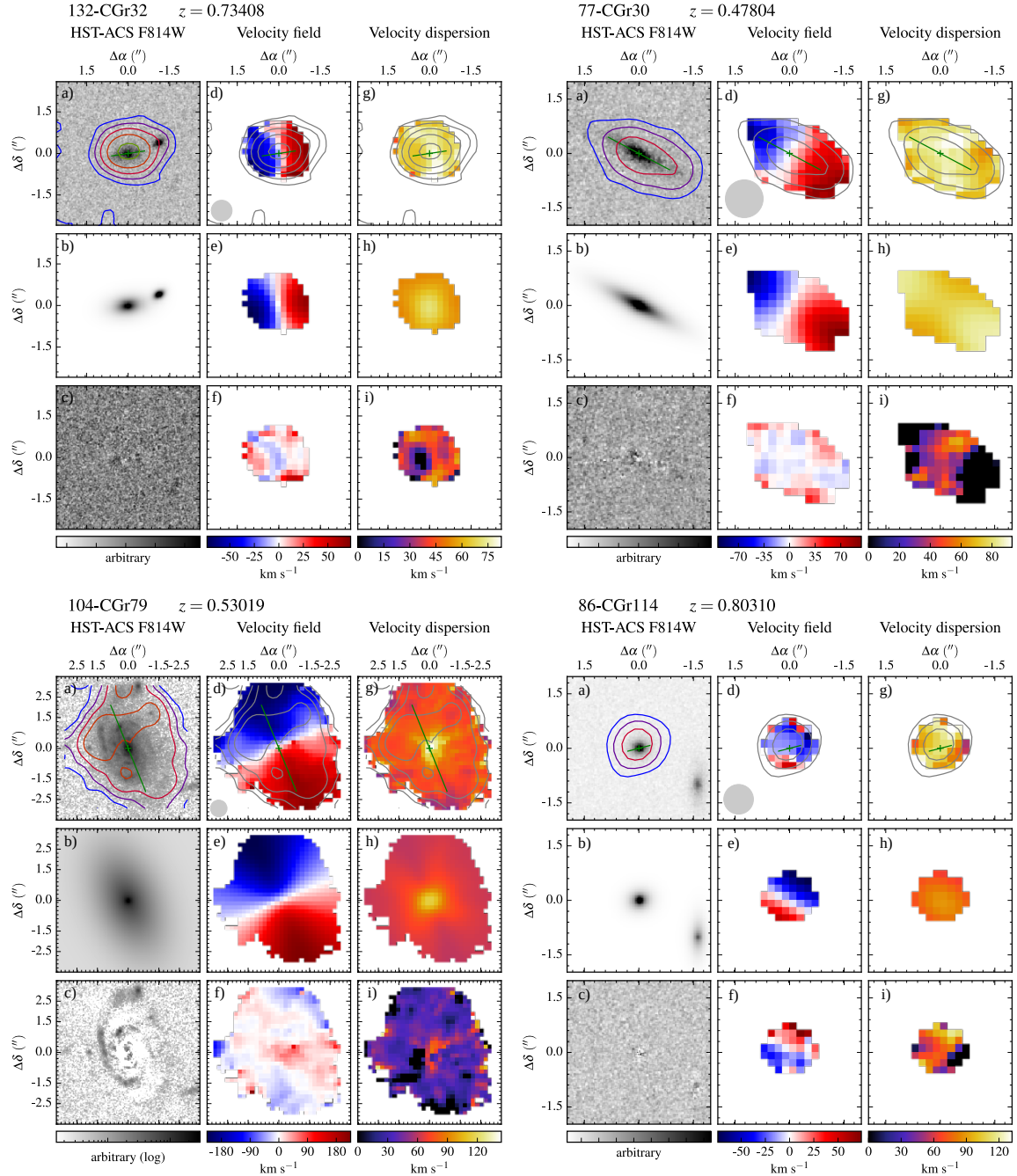


Fig. 8. Examples of morpho-kinematics modelling for galaxies with IDs 132-CGr32 and 104-CGr79 (both in large structures) and 77-CGr30 and 86-CGr114 (both in the field). In each panel, from *top to bottom* and *left to right*: (a) HST-ACS image, (b) GALFIT model, (c) HST residuals, (d) CAMEL velocity field, (e) MOCKING velocity field model, (f) velocity field residuals, (g) CAMEL velocity dispersion map, (h) MOCKING beam smearing model, including spectral resolution broadening, and (i) beam smearing and LSF corrected velocity dispersion map. The morpho-kinematics centre and the morphological PA are respectively shown in the HST image and the CAMEL maps as a green cross and a green line, whose length corresponds to R_{22} . The PSF FWHM is indicated as the grey disk in the velocity field. The [O II] surface brightness distribution is overlaid on top of the HST and MUSE [O II] flux maps, with contours at levels $\Sigma_{[\text{O II}]} = 2.5, 5, 10, 20, 40, \text{ and } 80 \times 10^{-18} \text{ erg s}^{-1} \text{ cm}^{-2} \text{ arcsec}^{-2}$.

- (iv) $25^\circ \leq i \leq 75^\circ$,
- (v) $f_\star \leq 1 - \Delta f_\star$,

where $R_{\text{eff},d}$ is the disk effective radius and $\text{FWHM}(z)$ the MUSE PSF FWHM computed at the [O II] doublet wavelength at the redshift of the galaxy (see Sect. 2.1), both in arcsec. In criterion

- (iv), i is the inclination after correcting for the finite thickness of the stellar disk, and in (v), $f_\star = M_{\star,\text{corr}} / (M_{\star,\text{corr}} + M_{\text{DM}})$ is the stellar fraction, with $M_{\star,\text{corr}}$ and M_{DM} the stellar and DM halo mass, respectively, both computed at R_{22} . The uncertainty on the stellar fraction Δf_\star is computed by propagating measurement and fit errors on both the stellar mass and the circular velocity.

Table 2. Median properties for various sub-samples of galaxies from the MS sample.

Sub-sample	Number	Proportion (%)	$\log_{10} M_{\star}$ [M_{\odot}]	$\log_{10} M_g$ [M_{\odot}]	$\log_{10} M_{\text{dyn}}$ [M_{\odot}]	$\log_{10} \text{SFR}_z$ [$M_{\odot} \text{ yr}^{-1}$]	$R_{\text{eff,d}}$ [kpc]
(1)	(2)	(3)	(4)	(5)	(6)	(7)	(8)
Field	256	57	$9.0^{+0.7}_{-0.7}$	$8.6^{+0.6}_{-0.6}$	$9.8^{+0.8}_{-0.9}$	$-0.1^{+0.6}_{-0.7}$	$2.6^{+2.4}_{-1.4}$
Small	56	13	$9.0^{+0.9}_{-0.5}$	$8.7^{+0.6}_{-0.4}$	$9.8^{+0.6}_{-0.8}$	$-0.2^{+0.8}_{-0.5}$	$2.8^{+2.2}_{-1.3}$
Large	135	30	$9.5^{+0.7}_{-0.9}$	$8.7^{+0.6}_{-0.7}$	$10.2^{+0.7}_{-1.0}$	$-0.2^{+0.6}_{-0.5}$	$3.3^{+2.5}_{-1.6}$
Small-5	293	66	$9.0^{+0.7}_{-0.6}$	$8.6^{+0.6}_{-0.6}$	$9.8^{+0.8}_{-0.9}$	$-0.1^{+0.6}_{-0.7}$	$2.6^{+2.4}_{-1.4}$
Large-5	154	34	$9.5^{+0.7}_{-0.9}$	$8.7^{+0.6}_{-0.6}$	$10.1^{+0.8}_{-0.9}$	$-0.2^{+0.6}_{-0.5}$	$3.2^{+2.5}_{-1.6}$
Small-10	312	70	$9.0^{+0.7}_{-0.6}$	$8.6^{+0.6}_{-0.6}$	$9.8^{+0.8}_{-0.9}$	$-0.1^{+0.6}_{-0.7}$	$2.6^{+2.3}_{-1.4}$
Small-15	345	77	$9.1^{+0.7}_{-0.7}$	$8.7^{+0.6}_{-0.6}$	$9.9^{+0.8}_{-1.0}$	$-0.1^{+0.8}_{-0.7}$	$2.7^{+2.4}_{-1.4}$
Large-15	102	23	$9.5^{+0.8}_{-0.8}$	$8.6^{+0.7}_{-0.6}$	$10.1^{+0.9}_{-0.9}$	$-0.2^{+0.5}_{-0.5}$	$3.2^{+2.6}_{-1.5}$
Small-20	370	83	$9.1^{+0.7}_{-0.7}$	$8.7^{+0.6}_{-0.6}$	$9.9^{+0.8}_{-1.0}$	$-0.1^{+0.6}_{-0.7}$	$2.8^{+2.4}_{-1.5}$
Large-20	77	17	$9.5^{+0.7}_{-0.9}$	$8.5^{+0.7}_{-0.7}$	$10.0^{+0.7}_{-0.9}$	$-0.3^{+0.5}_{-0.5}$	$3.2^{+2.1}_{-1.8}$

Notes: (1) Sub-sample name (we do not show the Large-10 sub-sample since it is identical to the Large one), (2) number of galaxies in each sub-sample, (3) proportion of galaxies in each sub-sample, (4) SED-based stellar mass, (5) gas mass derived from the extinction corrected [O II] flux, (6) dynamical mass from the mass models, including the stellar disk, stellar bulge, and DM halo, (7) [O II]-based SFR normalised at redshift $z_0 \approx 0.7$, and (8) disk effective radius. Masses are computed within $R_{22} = 2.2R_d$, with R_d the disk scale length. Uncertainties correspond to the 16th and 84th percentiles.

In (iii), the total S/N is computed as

$$(S/N)_{\text{tot}} = \sum_{x,y} F_{[\text{O II}]}(x,y) \left/ \sqrt{\sum_{x,y} \left[\frac{F_{[\text{O II}]}(x,y)}{S/N(x,y)} \right]^2} \right., \quad (11)$$

where $F_{[\text{O II}]}(x,y)$ and $S/N(x,y)$ correspond to the [O II] flux and S/N cleaned maps, respectively (see [Abril-Melgarejo et al. 2021](#)). Criterion (ii) is used to remove unresolved galaxies, that is, galaxies for which the stellar disk is smaller than the PSF, and criterion (iii) takes into account the dependence of the S/N on the effective radius, and is derived by assuming a constant surface brightness map, as well as a constant S/N map with a S/N per pixel of at least eight across one observed effective radius ($R_{\text{obs}}^2 = R_{\text{eff}}^2 + (\text{FWHM}(z)/2)^2$). As a consistency check, we also looked at how using a different threshold $(S/N)_{\text{tot}} \geq 30$ would impact the selection. This threshold adds 40 new galaxies, but the majority are either small with respect to their MUSE PSF FWHM or do not show clear velocity gradients. Thus, we decided to use criterion (ii) in the next parts. We show in Fig. 9, the galaxies distribution and selection in terms of S/N, $R_{\text{eff,d}}/\text{FWHM}$, and B/D for galaxies from the kinematics sample. Criterion (iv) removes face-on and edge-on galaxies because, for the former, uncertainties are too large to reliably constrain the rotation of the ionised gas and, for the latter, the mass models used in the kinematics modelling are much more loosely constrained.

Finally, criterion (v) identifies galaxies whose dynamical modelling failed, that is, for which we overestimated the contribution of baryons to the total rotation curve. This corresponds to 13 galaxies in the kinematics sample. Among them, we decided to remove ten galaxies, namely 85-CGR35, 28-CGR26, 257-CGR84, 113-CGR23, 83-CGR23, 38-CGR172, 130-CGR35, 110-CGR30, 105-CGR114, and 100-CGR172. These objects are shown as orange crosses in Fig. 9. Most of them tend to be quite small or with low S/N values even though they pass criteria (i) and (ii), but also have velocity fields with a quite low amplitude ($\sim 30\text{--}40 \text{ km s}^{-1}$). This means that any uncertainty on their morphological modelling and mass-to-light ratio will have a stronger

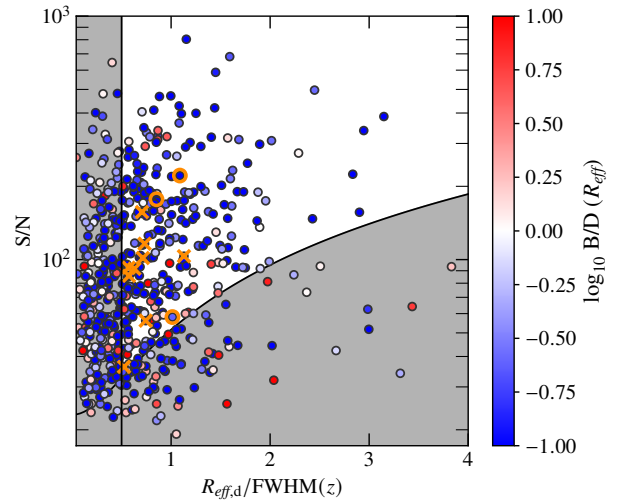


Fig. 9. S/N-disk effective radius-B/D selection plot for galaxies from the kinematics sample. The disk size selection criterion is represented as the vertical line. The S/N selection criterion depends on the FWHM, which varies with redshift and MUSE field. As an example, we show the S/N limit used for a typical FWHM of $0.65''$. Points are colour-coded according to their bulge-to-disk ratio computed at one effective radius. The grey areas give an idea of the galaxies eliminated by the size and S/N selection criteria. We also show the ten galaxies eliminated by selection criterion v (orange crosses) and the three we decided to keep (orange circles).

impact on their dynamical modelling. In addition, galaxies 85-CGR35 and 28-CGR26 have disturbed morphologies and/or kinematics, which may be due to past merger events or to a more complex morphology than the bulge-disk decomposition performed in Sect. 4.1. On the contrary, after carefully investigating their morphology and kinematics, we decided to keep galaxies 378-CGR32, 20-CGR84, and 19-CGR84 since they seemed to be intrinsically ‘baryon dominated’. After applying criteria (i) to (v), we end up with a TFR sample of 146 galaxies.

In Sect. 7 we may apply two additional selection criteria when it is necessary to have comparable parameter distributions between different environments:

- (vi) $\log_{10} M_{\star} [M_{\odot}] \leq 10$,
- (vii) $0.5 < z < 0.9$.

Criterion (vi) is used to have comparable samples in terms of stellar mass (see stellar mass distributions in Fig. B.4), whereas (vii) only keeps galaxies in a 1 Gyr interval around redshift $z \approx 0.7$ where most of the galaxies in the large structures are located. Thus, this criterion allows us to check that our results may not be impacted by a potential redshift evolution.

6.2. Summary of the different samples and sub-samples

To clarify the difference between the various samples used in this paper, we provide below a summary of their characteristics. We also show in Table 1 the distribution of their main physical parameters represented by their median value, 16th and 84th percentiles.

- (1) *[O II] emitters sample*: 1142 [O II] emitters with reliable spectroscopic redshift in the range $0.25 \lesssim z \lesssim 1.5$.
- (2) *Morphological sample*: 890 galaxies from the [O II] emitters sample with reliable bulge-disk decomposition.
- (3) *Kinematics sample*: 593 galaxies from the morphological sample with reliable kinematics.
- (4) *MS sample*: 447 disk-dominated galaxies from the kinematics sample selected in B/D only. This sample is used to study the size-mass and MS relations.
- (5) *TFR sample*: 146 disk-dominated galaxies from the MS sample with selection criteria from (i) to (v) applied to only keep galaxies with well constrained kinematics. This sample is used to study the TFR.

We show in Table 2 the median properties for each environment-based sub-sample of galaxies from the MS sample later used in the analysis. Among these, we show the field, small, and large structure ones defined in Sect. 3.2. Alternatively, when analysing the TFR in Sect. 7.4, we also split the entire sample into two sub-samples only: a field and small structure sub-sample on the one hand, and a large structure sub-sample on the other hand. This separation is performed because using the previously defined sub-samples would lead to too few galaxies in the small structures to reliably constrain their TFR. In the following and in Table 2, we refer to these sub-samples as Small- N and Large- N , where N corresponds to the richness threshold used to classify galaxies in either the field and small structure or large structure sub-samples. We note that the terms ‘small’ and ‘large’ used to name the sub-samples never refer to the size nor the mass of the structures, only to the number of galaxy members.

The main properties shown in Table 2 are the total number and the proportion of galaxies in each sub-sample, the stellar, gas, and dynamical masses computed within $R_{22} = 2.2R_d$, with R_d the disk scale length, the extinction corrected [O II]-based SFR, and the median disk effective radius $R_{\text{eff,d}}$. All the sub-samples have mostly similar gas mass and SFR distributions. However, the sub-samples that target the largest structures tend to have on average larger disk sizes and stellar masses. Their dynamical masses are slightly larger as well, though the difference between small and large structures at a fixed threshold is roughly 0.3–0.4 dex, similar to the difference seen in stellar masses, indicative that these massive structures do not host, on average, more massive DM haloes. Interestingly, when using the largest threshold values $N = 15, 20$, the large structure sub-samples have larger stellar masses ($\Delta \log_{10} M_{\star} \approx 0.5$ dex),

but similar dynamical masses with respect to the small structure sub-samples. One of the key difference visible in Fig. 2 is the stellar mass distribution. The large structure sub-sample is more extended than the field and the small structure sub-samples towards larger stellar masses, so that almost all the galaxies beyond $M_{\star} > 10^{10} M_{\odot}$ are located in the large structures. These massive galaxies also tend to have the largest SFR values, though their impact on the SFR distribution is not as clearly visible as in the stellar mass distribution.

The MAGIC catalogue containing the main morpho-kinematics and physical properties for galaxies from the MS sample is available at the Centre de Données astronomiques de Strasbourg (CDS). We provide in Table F.1 a description of the columns appearing in the catalogue. Appendix G contains the morpho-kinematics maps as shown in Fig. 8 for all galaxies in the TFR sample.

7. Analysis

We focus the analysis on the size-mass relation, the MS relation, and the TFR. We consider the MS and TFR samples and separate galaxies into three different sub-samples, targeting different environments. For the size-mass relation, we use the corrected stellar mass $M_{\star,\text{corr}}$, which better traces the disk and bulge masses within a sphere of radius R_{22} (see Sect. 4.3), and the disk scale length $R_d = R_{\text{eff,d}}/b_1$ for the size of our galaxies, where $R_{\text{eff,d}}$ is the disk effective radius and $b_1 \approx 1.6783$. We also use $M_{\star,\text{corr}}$ for the TFR, as well as the total circular velocity V_{22} derived at R_{22} from the best-fit mass and flat models for the velocity. This R_{22} value corresponds to where the peak of rotation for the disk component is reached and is typically used in similar studies (Pelliccia et al. 2019; Abril-Melgarejo et al. 2021). Lastly, for the MS, we use the SED-based stellar mass M_{\star} derived in an aperture of $3''$ and the extinction corrected and normalised [O II] SFR as described in Sect. 3.3. Each scaling relation is fitted with the form

$$\log_{10} y = \beta + \alpha(\log_{10} x - p), \quad (12)$$

where y is the dependent variable, x is the independent variable, and p is a pivot point equal to the median value of $\log_{10} x$ when using the full samples (MS or TFR). For each relation, we decided to always use stellar mass as the independent variable, so that the pivot point is $p = 9.2$. As pointed out in Williams et al. (2010), Pelliccia et al. (2017), this is justified for the TFR as fitting the opposite relation yields a slope biased towards lower values, while for the size-mass and MS relations we find more robust fits and smaller dispersion.

In order to have fits not biased by points with underestimated errors in x and y , we quadratically added an uncertainty on the error of both independent and dependent variables in each scaling relation. Based on Abril-Melgarejo et al. (2021), we decided to quadratically add an uncertainty of 0.2 dex on the stellar mass and the SFR, and of 20 km s^{-1} on the velocity, consistent with typical uncertainties and systematics found in the literature. For the size estimate, we added a slightly lower uncertainty of 0.065 dex, which corresponds to a relative error of roughly 15%, slightly below the more or less 30% scatter Kuchner et al. (2017) found when comparing size measurements between Subaru and HST data.

We used two different tools to perform the fits. The first one is LTSFIT (Cappellari et al. 2013), a python implementation of the Least Trimmed Square regression technique from Rousseeuw & Van Driessen (2006), and the second one is MPFITEXY (Williams et al. 2010) IDL wrapper of MPFIT. Both

Table 3. Comparison of fit parameters for the scaling relations with various selection criteria.

Relation	Selection	Number	α	β
(1)	(2)	(3)	(4)	(5)
Size-Mass		447(10)	0.33 ± 0.02	0.22 ± 0.01
	(ii)	270 (11)	0.16 ± 0.01	0.34 ± 0.01
	(iii)	389 (4)	0.35 ± 0.02	0.21 ± 0.01
	(ii), (iii)	223 (8)	0.18 ± 0.02	0.33 ± 0.01
MS		447(14)	0.61 ± 0.02	-0.25 ± 0.02
	(ii)	270 (13)	0.66 ± 0.03	-0.32 ± 0.02
	(iii)	389 (4)	0.61 ± 0.02	-0.21 ± 0.02
	(ii), (iii)	224 (6)	0.66 ± 0.03	-0.28 ± 0.02
TFR		447(23)	0.34 ± 0.01	2.03 ± 0.01
	(ii)	270 (5)	0.27 ± 0.02	2.07 ± 0.01
	(iii)	389 (21)	0.36 ± 0.01	2.01 ± 0.01
	(ii), (iii)	223 (7)	0.31 ± 0.02	2.03 ± 0.01
	(ii) to (v)	146 (1)	0.29 ± 0.02	2.01 ± 0.01

Notes. The B/D selection, which limits the sample to disk-dominated galaxies, is always applied. (1) Scaling relation fitted, (2) selection criteria used (see Sect. 6.1), (3) number of galaxies, with outliers shown in parentheses, (4) best-fit slope, and (5) best-fit zero point. Errors on fit parameters correspond to 1σ uncertainties.

methods take into account uncertainties on x and y , as well as the intrinsic scatter of each relation, but LTSFIT implements a robust method to identify and remove outliers from the fit. However, it currently does not have an option to fix the slope. Therefore, whenever we needed to fix the slope, we used MPFITEXY, removing beforehand outliers found by LTSFIT.

7.1. Impact of selection

We start by looking at how the aforementioned scaling relations are impacted by the different selection criteria used to select the MS and TFR samples. To do so, we fitted each scaling relation using the MS sample with LTSFIT, letting the slope free, and we looked at the impact of the size (ii) and/or S/N (iii) criteria on the best-fit results. Additionally, since we also apply the inclination (iv) and the mass modelling uncertainty (v) selections on the TFR, we also consider their impact on the slope and zero point of this relation. The results for each scaling relation are shown in Table 3. We also show in Fig. 10 the population of galaxies removed by each selection criterion, as well as the galaxies removed when applying a redshift cut $0.5 < z < 0.9$ (red upper triangles), and the remaining galaxies (black points). We find that the size-mass relation is mainly impacted by the size selection for both the slope and zero point, while the S/N criterion has a weaker effect. When removing small galaxies, the slope is biased towards lower values, and this effect is more important for field galaxies than for galaxies in other sub-samples. Similarly, the MS is mainly affected by the size selection while the S/N selection has almost no impact. This result may seem surprising given that, as can be seen in Fig. 10, size-removed (blue downward pointing triangles), and S/N-removed (orange squares) galaxies tend to lie along the MS, but on opposite parts. However, the size selection has a stronger impact since it mainly removes low mass galaxies, biasing the slope to larger values driven by more massive galaxies.

Finally, similarly to the size-mass and MS relations, the TFR is also mainly impacted by the size selection. Removing small

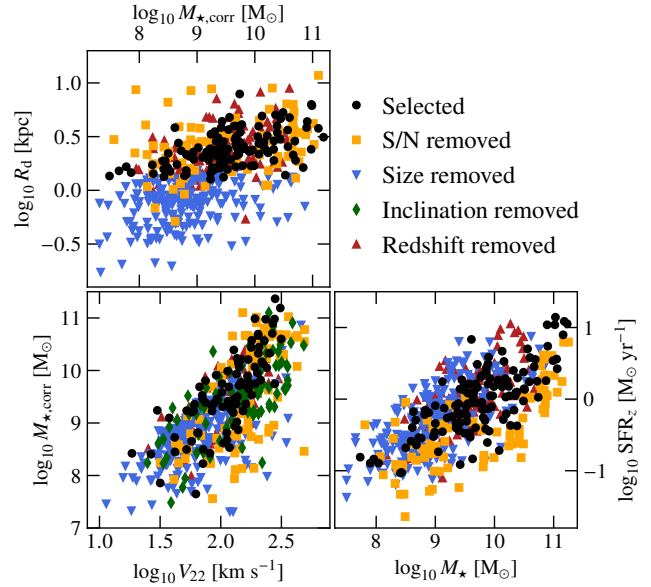


Fig. 10. Impact of the different selection criteria from Sect. 6.1 applied to the size-mass relation (*top left*), the TFR (*bottom left*), and the MS relation (*bottom right*). Black circles represent galaxies that remain when all the selection criteria are applied. Given that some selections remove similar galaxies, we show those removed by the S/N (orange squares), size (blue downward-pointing triangles), and redshift criteria (red triangles), in this order. Additionally, we also show the galaxies removed by the inclination selection (green diamonds) in the TFR before the redshift selection was applied.

galaxies changes the slope to lower values, driven by more massive galaxies. However, when applying the size and S/N selections, both the slope and zero point values become close to the original ones. Because of the mass models used, the TFR is quite tight and those criteria tend to remove almost symmetrically galaxies with low and high circular velocity as can be seen in Fig. 10, so that the remaining galaxies fall along the original TFR without any bias. Important selection criteria for the TFR are the inclination and mass modelling uncertainty (iv and v). Among the two, criterion (v) has the weakest impact since it only removes a handful of galaxies, whereas the inclination selection (iv) tends to remove a significant fraction of galaxies with larger circular velocities than the bulk of galaxies with stellar masses beyond $10^9 M_\odot$. These galaxies probably have overestimated circular velocities, so that including them in the fit of the TFR would lead to a slope biased towards larger values.

Because the size and S/N selection criteria were defined to select galaxies with reliable morphology and kinematics for the mass modelling, and because they can bias the slope and zero point of the size-mass and MS relations, we decided not to apply them to select the MS sample, as described in Sect. 6.1. However, these criteria, in combination with the inclination (iv) and mass modelling uncertainty (v) selections, are important to have an unbiased fit of the TFR. Thus, we decided to apply selection criteria from (i) to (v) to select the TFR sample in Sect. 6.1.

7.2. Impact of the environment on the size-mass relation

We fitted the sub-samples that target different environments by fixing the best-fit slope to the value from LTSFIT when

Table 4. Best-fit values for the size-mass and MS relations fitted on the MS sample.

Sub-sample (1)	Scaling relation (2)	Selection (3)	Nb. (4)	Prop. (%) (5)	α (6)	β (7)
Field	Size-Mass		250 (6)	57	0.33	0.23 ± 0.02
Small			54 (2)	13		0.22 ± 0.03
Large			133 (2)	30		0.19 ± 0.02
Field	Size-Mass	(vi)	237 (3)	63	0.41	0.26 ± 0.02
Small			48 (2)	13		0.24 ± 0.04
Large			93 (3)	24		0.24 ± 0.02
Field	Size-Mass	(vi), (vii)	77 (1)	45	0.34	0.26 ± 0.03
Large			84 (2)	49		0.23 ± 0.02
Field	MS		251 (5)	58	0.61	-0.19 ± 0.02
Small			55 (1)	13		-0.22 ± 0.05
Large			126 (9)	29		-0.36 ± 0.03
Field	MS	(vi)	239 (1)	63	0.78	-0.18 ± 0.02
Small			47 (3)	13		-0.15 ± 0.06
Large			91 (5)	24		-0.29 ± 0.04
Field	MS	(vi), (vii)	78 (0)	45	0.72	-0.22 ± 0.04
Large			83 (3)	48		-0.32 ± 0.04

Notes. Optionally, we apply a mass cut $M_\star \leq 10^{10} M_\odot$ (vi) and a redshift cut $0.5 \leq z \leq 0.9$ (vii). For each fit, the slope is fixed to the one from LTSFIT on the entire MS sample using the same selection criteria. We do not show the small structure sub-sample when applying the redshift cut since there remain too few galaxies to reliably constrain its zero point. Bold values correspond to those shown in Figs. 11 and 12 (full lines). (1) Sub-sample name, (2) scaling relation fitted, (3) selection criteria applied, (4) number of galaxies in each sub-sample, with outliers shown in parentheses, (5) proportion of galaxies in each sub-sample (after removing outliers), (6) fixed slope, and (7) best-fit zero point. Errors on fit parameters correspond to 1σ uncertainties.

considering the entire MS sample with the same selection criteria. We further applied two additional selection criteria, a mass cut $M_\star < 10^{10} M_\odot$ and a redshift cut $0.5 < z < 0.9$, in order to reduce the impact of different mass and redshift distributions between sub-samples on the best-fit zero points. We show in Table 4 the best-fit zero points as well as the slopes used for each fit and in Fig. 11 the size-mass relation and its best-fit line when applying the mass (vi) and redshift cuts (vii). We also provide in Fig. B.1 the size-mass relation and its best-fit line when only applying the mass cut, and when applying neither mass nor redshift cuts.

We find a small offset in the zero point between sub-samples. When applying both mass and redshift cuts, the difference amounts to 0.03 dex, which is at most 1σ significant⁷. Similarly, when applying only the mass cut, we get a 1σ significant difference between the field sub-sample and the small and large structure sub-samples. However, if we apply neither cuts, we get a slightly larger offset of 0.04 dex between the field and the large structure one, and almost similar zero points between the field and the small structure one. In Fig. 11 and in Table 4, we used the disk size to fit the size-mass relation, whereas other studies (e.g., Maltby et al. 2010) usually use a global radius. To check whether the choice of radius might have an impact on our results we fitted the size-mass relation, but using the global effective radius derived in Sect. 4.2. Even when using the global radius, we get the same trend as before, with an offset of 0.02 dex (1σ significant). If we use instead a more stringent richness threshold of $N = 20$ to separate galaxies between small and large structures, we do find a larger offset of 0.06 dex (2σ significant) between the field and the large structure sub-samples when using the disk radius as a size proxy, and a similar offset of 0.02 dex when using the global effective radius.

⁷ The term σ significant will always refer to the uncertainty on the zero point of the best-fit line.

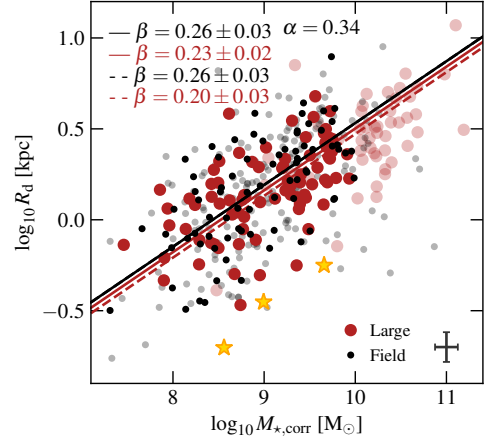


Fig. 11. Size-mass relation for galaxies from the MS sample with additional mass and redshift cuts applied (vi and vii). Symbols and colours are similar to those in Fig. 2, and orange stars represent galaxies identified as outliers from the fit done with LTSFIT. As an indication, we also show as semi-transparent symbols galaxies removed by the mass and redshift cuts. Best-fit lines are shown when using a richness threshold $N = 10$ (full lines) and $N = 20$ (dashed lines). The dashed black line is not visible since field galaxies have the same best-fit line for $N = 10$ and $N = 20$. We do not show galaxies in the small structure sub-sample since too few galaxies remain after selection criteria (vi) and (vii) are applied. We also provide in the *top left* the slope and best-fit zero point for each sub-sample (see Eq. (12) with $y = R_d$ and $x = M_\star$). The typical uncertainty on stellar mass and disk size is shown in the *bottom right* as a grey error bar. After controlling for differences in mass and redshift, we find a 1σ significant difference of 0.03 dex between sub-samples with $N = 10$, and a 2σ significant difference of 0.06 dex with $N = 20$.

Overall, if significant, the difference between the field and the largest structures when using $N = 10$ is quite small. We note that this result is different from what was found in previous studies such as Maltby et al. (2010) or Matharu et al. (2019). Indeed, such studies always found a weak but significant dependence of the size-mass relation with environment. For instance, Maltby et al. (2010) found spiral galaxies in the field to be about 15% larger than their cluster counterparts but, in our case, it would only amount to a size difference of roughly 7%. Instead, using the offset value with $N = 20$, we get a size difference of roughly 14%, consistent with previous findings from Maltby et al. (2010) that galaxies in the most massive structures are more compact than those in the field. Given the models used in the morphological analysis and because the bulge-to-disk ratio is fairly similar between sub-samples, the zero point of the size-mass relation directly translates in terms of the galaxies central surface mass density of the disk component (i.e. extrapolated from the Sérsic profile at $R = 0$). Assuming the flux of the disk component dominates at R_{22} , using a slope $\alpha = 0.34$ and a zero point β_{sm} , we get the following scaling relation for the disk component central surface mass density $\Sigma_{\text{M,d}}(0)$ as a function of stellar mass:

$$\log_{10} \Sigma_{\text{M,d}}(0) [\text{M}_\odot \text{kpc}^{-2}] \approx 0.32 \log_{10} M_{\star,\text{corr}} [\text{M}_\odot] + 5.65 - 2\beta_{\text{sm}}, \quad (13)$$

where $\beta_{\text{sm}} = 0.26 \pm 0.03$ for the field sub-sample and $\beta_{\text{sm}} = 0.20 \pm 0.03$ for the large structure sub-sample when using a richness threshold of $N = 20$. A change in the zero point of the size mass relation does not impact the slope of Eq. (13) but only its zero point. Thus, the 0.06 dex offset measured between the

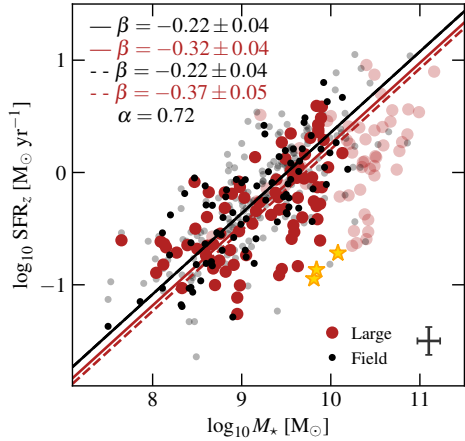


Fig. 12. SFR-stellar mass relation for galaxies from the MS sample with additional mass and redshift cuts applied (vi and vii). Symbols and colours are similar to those in Fig. 2, and orange stars represent galaxies identified as outliers from the fit done with LTSFIT. As an indication, we also show as semi-transparent symbols galaxies removed by the mass and redshift cuts. Best-fit lines are shown when using a richness threshold $N = 10$ (full lines) and $N = 20$ (dashed lines). We do not show galaxies in the small structure sub-sample since too few galaxies remain after selection criteria (vi) and (vii) are applied. The SFR is normalised to redshift $z_0 = 0.7$ (see Sect. 3.3). We also provide the slope and best-fit zero point for each sub-sample in the *top left* (see Eq. (12) with $y = \text{SFR}$ and $x = M_*$). The typical uncertainty on stellar mass and SFR is shown in the *bottom right* as a grey error bar. Even after controlling for differences in mass and redshift, we find a 2σ significant difference of 0.10 dex between sub-samples with $N = 10$, and a 3σ significant difference of 0.15 dex with $N = 20$.

field and the most massive structures results in a negative offset of -1.2 dex in Eq. (13). We note that this interpretation remains true as long as we can neglect the flux of the bulge at R_{22} . However, when we can no longer neglect it, then Eq. (13) will have an additional non-linear term that is a function of the bulge central surface mass density and effective radius. In this case, the interpretation would be more complex as galaxies could have different bulge or disk physical properties as a function of environment but still align on the same size-mass relation. However, as is visible in Fig. C.1, the bulge contribution at R_{22} is on average and independently of environment around 10% of the total flux, which amounts to a scatter in the size-mass relation of about 0.1 dex, which is sufficiently small to neglect at first order the bulge contribution in this relation.

7.3. Impact of the environment on the MS relation

To study the MS, we use the SED-based stellar mass and the [OII] SFR corrected for extinction and normalised to redshift $z_0 = 0.7$ as described in Sect. 3.3. For this relation, applying both a mass and a redshift cut is important. Indeed, as can be seen in Fig. A.3, the MS can be quite sensitive to redshift since there is still a small dichotomy between low and high redshift galaxies even after normalisation. The main reason for this effect is that the MAGIC survey is designed to blindly detect sources in a cone. The blind detection makes the survey flux-limited, which means we are missing faint, low SFR galaxies in the highest redshift bin. Besides, we expect to see an excess of massive galaxies in the most massive structures with respect to the field, which, in our sample, are all located at redshift $z \approx 0.7$. Thus, the survey

design tends to create a dichotomy in mass, which is visible in SFR as well since we are focussing on star-forming galaxies. Nevertheless, as can be seen in Table 4, the redshift cut has a much smaller effect than the mass cut, especially on the slope value from the best-fit line.

We show in Fig. 12 the MS with both cuts applied for the field and large structure sub-samples, as well as their best-fit lines and zero point values. We also provide in Fig. B.2 the MS and its best-fit line when only applying the mass cut, and when applying neither mass nor redshift cuts. Independently of whether we apply a mass and/or redshift cut or not, we find a more than 2σ significant difference in the zero point (~ 0.1 dex) between the field and large structure sub-samples. However, there is almost no difference in the zero point between the field and the small structure sub-samples. Independently of the cut applied, the field galaxies always have a larger zero point than the galaxies in the large structures. If we interpret this difference in terms of a SFR offset between the field and the largest structures, this would lead to an average SFR for the galaxies in the large structures that is about 1.3 times lower than that in the field. This factor is quite close to the recent value found by Old et al. (2020a,b) using the GOGREEN and GCLASS surveys at redshift $z \sim 1$. On the other hand, the reason why other studies such as Nantais et al. (2020) do not find any impact of the environment on the MS is still unclear. The effect of the redshift evolution of the MS might play a role, since Nantais et al. (2020) probe clusters at $z \sim 1.6$, which is beyond the $0.5 < z < 0.9$ redshift range we restricted our fit to. Similarly, the impact of the environment on the MS may be segregated between low and high mass galaxies. As was reported in Old et al. (2020a,b), the MS seems to be more impacted in the lowest mass regime. This explanation would be compatible with our result where we mainly probe low to intermediate mass galaxies since we remove massive galaxies not to bias the fit.

Similarly to Sect. 7.2, we performed the same fits but using a more stringent richness threshold of $N = 20$ to separate between structures. When using this threshold combined with both mass and redshift cuts, we find a roughly 3σ significant difference of 0.15 dex ($\beta_{\text{MS}} = -0.22 \pm 0.04$ for field galaxies, $\beta_{\text{MS}} = -0.37 \pm 0.05$ for galaxies in the largest structures), consistent with our previous finding that galaxies in the largest structures have reduced SFR with respect to the field. With this offset, we get an average SFR in the most massive structures that is about 1.5 times lower than that in the field, still quite close to the value from Old et al. (2020a,b).

7.4. Impact of the environment on the TFR

We look at the TFR as a function of the environment using the TFR sample. Since too few galaxies remain in the small structure sub-sample once all the selection criteria (i to v) are applied, we decided to focus this analysis on two sub-samples only. We fit the TFR using different richness thresholds ($N = 5, 10, 15$ and 20) to separate galaxies into a field and small structure and a large structure sub-samples. The best-fit zero points and the slopes values are shown in Table 5 and in Fig. 13. As a comparison, we also show on the bottom panel of Fig. 13 the TFR obtained using a simpler flat model for the rotation curve as defined in Abril-Melgarejo et al. (2021). This model allows us to measure the galaxies circular velocity without any prior on the baryon distribution and is therefore not affected by our mass modelling.

We find a similar trend between the TFR from the mass models and that from the flat model. Overall, the tightness of the relation using either model makes the zero point values well

Table 5. Best-fit values for the TFR fitted on the TFR sample.

Sub-sample (1)	Selec. (2)	Number (3)	Prop. (%) (4)	α_{TFR} (5)	β_{TFR} (6)	$\alpha_{\text{TFR}}^{\text{flat}}$ (7)	$\beta_{\text{TFR}}^{\text{flat}}$ (8)
Small-5		87 (1)	60	0.29	2.04 ± 0.01	0.32	2.00 ± 0.02
Large-5		58 (0)	40		1.99 ± 0.01		1.97 ± 0.01
Small-10		94 (1)	65		2.03 ± 0.01		2.00 ± 0.02
Large-10		51 (0)	35		2.00 ± 0.02		1.97 ± 0.01
Small-15		106 (1)	73		2.02 ± 0.01		1.99 ± 0.01
Large-15		39 (0)	27		2.00 ± 0.02		1.98 ± 0.02
Small-20		117 (1)	81		2.02 ± 0.01		1.99 ± 0.01
Large-20		28 (0)	19		1.98 ± 0.02		1.97 ± 0.02
Small-5		80 (1)	69	0.41	2.02 ± 0.02	0.49	1.98 ± 0.02
Large-5		36 (0)	31		1.98 ± 0.03		1.95 ± 0.03
Small-10		85 (1)	73		2.01 ± 0.02		1.98 ± 0.02
Large-10		31 (0)	27		1.99 ± 0.03		1.95 ± 0.03
Small-15	(vi)	89 (1)	77		2.01 ± 0.02		1.98 ± 0.02
Large-15		27 (0)	23		2.00 ± 0.03		1.95 ± 0.03
Small-20		98 (1)	84		2.01 ± 0.02		1.98 ± 0.02
Large-20		18 (0)	16		1.97 ± 0.04		1.92 ± 0.04
Small-5		27 (0)	48	0.36	2.02 ± 0.03	0.47	1.98 ± 0.03
Large-5		29 (0)	52		2.01 ± 0.03		1.96 ± 0.03
Small-10		27 (0)	48		2.02 ± 0.03		1.98 ± 0.03
Large-10	(vi)	29 (0)	52		2.01 ± 0.03		1.96 ± 0.03
Small-15	(vii)	29 (0)	52		2.02 ± 0.03		1.98 ± 0.03
Large-15		27 (0)	48		2.01 ± 0.03		1.95 ± 0.03
Small-20		38 (0)	68		2.03 ± 0.02		1.98 ± 0.03
Large-20		18 (0)	32		1.99 ± 0.04		1.93 ± 0.04

Notes. Optionally, we also apply a mass cut $M_* \leq 10^{10} M_\odot$ (vi) and a redshift cut $0.5 \leq z \leq 0.9$ (vii). For each fit, the slope is fixed to the one from LTSFIT on the entire kinematics sample using the same selection criteria. Bold values correspond to those shown in Fig. 13. (1) Sub-sample name, (2) additional selection criteria applied, (3) number of galaxies in each sub-sample, with outliers in parentheses, (4) proportion of galaxies in each sub-sample (after removing outliers), (5) fixed slope for the TFR using the velocity computed from the mass models, (6) best-fit zero point (mass models), (7) fixed slope using the velocity computed from a flat model, and (8) best-fit zero point (flat model). Errors on fit parameters correspond to 1σ uncertainties.

constrained, with typical uncertainties around 0.03 dex. When we do not apply any mass or redshift cut, the large structure sub-sample tends to systematically have a lower zero point between 0.02 dex and 0.04 dex with respect to the field sub-sample depending on the richness threshold⁸. This is shown in Table 5, as well as in Fig. B.3. However, when adding a mass and/or a redshift cut, this offset tends to disappear independently of the model and richness threshold used, as is shown in Fig. 13. When using $N = 20$, we nevertheless get a small 1σ significant offset of roughly 0.04 dex in both TFR. This result suggests that the larger offset values found when applying no cut are certainly the consequence of having different stellar mass distributions between the two sub-samples, or might be due to a small impact of the redshift evolution of the TFR.

Given the disk, bulge and DM halo mass models used to derive the circular velocity (see Sects. 5 and D), and assuming a constant B/D value of 3%, which is the median value found in the kinematics sample independently of environment, we can write the TFR as a function of the stellar mass $M_{*,\text{corr}}$ within R_{22} , the stellar fraction $f_*(R_{22}) = M_{*,\text{corr}}/[M_{*,\text{corr}} + M_{\text{DM}}(R_{22})]$, with

⁸ We fit the circular velocity against stellar mass (independent variable), but we show in Fig. 13 the inverse relation. Thus, the zero point offsets β given in the text and in Table 5 should be read horizontally in the figure.

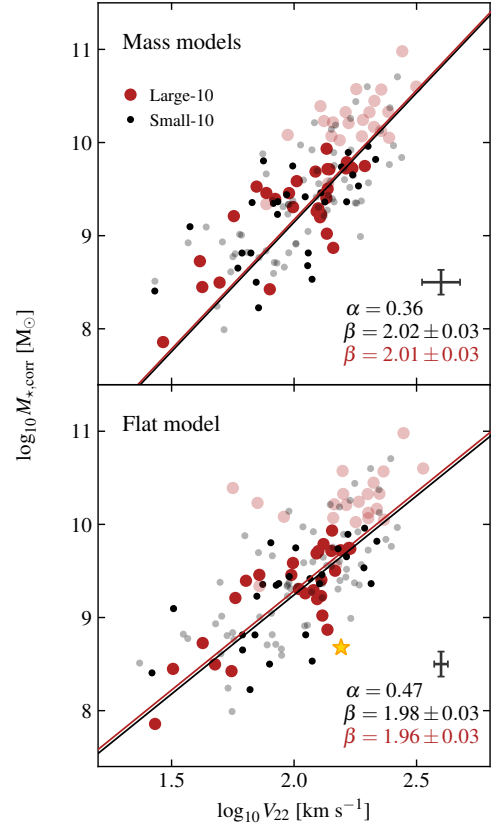


Fig. 13. Stellar mass TFR at R_{22} for galaxies from the TFR sample with mass and redshift cuts applied (vi and vii). The *top panel* shows the TFR using the velocity computed from the mass models, and the *bottom panel* shows the TFR using the velocity from a flat model. Galaxies are split between field and small structure (black points) and large structure (red circles) sub-samples using a richness threshold of $N = 10$. Orange stars represent galaxies identified as outliers from the fit done with LTSFIT. As an indication, we also show as semi-transparent symbols galaxies removed by the mass and redshift cuts. Best-fit linear relations for both sub-samples are shown as full lines. We provide in the *bottom part* of each panel the slope and best-fit zero points (see Eq. (12) with $y = V_{22}$ and $x = M_{*,\text{corr}}$). The typical uncertainty on stellar mass and velocity is shown as a grey error bar. After controlling for differences in mass and redshift, we do not find any impact of the environment on the zero point of either TFR.

M_{DM} the DM halo mass, both computed at R_{22} , and R_d as

$$\log_{10} \left(\frac{M_{*,\text{corr}}}{M_\odot} \right) \approx 2 \log_{10} \left(\frac{V_{22}}{\text{km s}^{-1}} \right) + \log_{10} \left(\frac{R_d}{\text{kpc}} \right) + \log_{10} \left(\frac{f_*}{1 + 0.15 f_*} \right) + 5.71. \quad (14)$$

In Eq. (14), we see the size-mass relation. Thus, rewriting Eq. (14) to make the central surface mass density of the disk component appear, and then inserting Eq. (13), we get

$$\log_{10} \left(\frac{M_{*,\text{corr}}}{M_\odot} \right) \approx 3.03 \log_{10} \left(\frac{V_{22}}{\text{km s}^{-1}} \right) + 1.52 \log_{10} \left(\frac{f_*}{1 + 0.15 f_*} \right) + 3.91 + 1.52 \beta_{\text{sm}}, \quad (15)$$

where β_{sm} is the size-mass relation zero point that was found to vary with environment in Sect. 7.2. In Eq. (15), we see that only two terms can contribute to an offset on the TFR:

- (i) different zero points on the size-mass relation as a function of environment,
- (ii) an offset on the stellar fraction measured within R_{22} between the field and the large structure sub-samples.

If we interpret any offset on the TFR zero point as being an offset on stellar mass at fixed circular velocity, given Eq. (15) we have

$$\Delta \log_{10} M_{\star, \text{corr}} [\text{M}_{\odot}] = 1.52 \left[\Delta \log_{10} \left(\frac{f_{\star}}{1 + 0.15 f_{\star}} \right) + \Delta \beta_{\text{sm}} \right], \quad (16)$$

where $\Delta \beta_{\text{sm}}$ is the offset on the zero point of the size-mass relation that is due to the contraction of baryons observed in the most massive structures. With a threshold $N = 20$, we have $\Delta \beta_{\text{sm}} = 0.06$ dex and an offset on the TFR, which is in circular velocity at fixed stellar mass, of 0.04 dex and 0.05 dex for the mass and flat models, respectively. The corresponding offset in stellar mass at fixed circular velocity is given by $-\Delta \beta_{\text{TFR}} / \alpha_{\text{TFR}} = 0.11$ dex for both models. For a typical galaxy in the kinematics sample with a stellar fraction of 20% this would give a difference between a galaxy in the field and one in the largest structures of roughly 4%. This result is quite close to the difference in stellar fraction (circles) seen in Fig. 14 where we have plotted its evolution computed from the mass models in bins of stellar mass between galaxies in the field and small structures (black) and those in large structures (red). We see that the stellar fraction increases as we go towards more massive galaxies, both in the field and in large structures. However, the difference remains small compared to the uncertainty of roughly 10%. Besides, the distributions tend to be quite spread out, as is shown by the grey error bars, even though there is a significant offset of the stellar fraction distribution and of its dispersion as we go towards larger stellar masses.

Contrary to what was found in [Abril-Melgarejo et al. \(2021\)](#), we cannot measure an impact of quenching on the TFR since our stellar mass offset is negative, meaning that galaxies in the largest structures would be on average more massive than those in the field. Nevertheless, the difference is quite small (~ 0.05 dex) and may not be particularly significant. However, we do measure a significant offset in the MS, which means that quenching does take place somehow within at least some of the galaxies in the largest structures. One way to explain the apparent discrepancy is to look at the timescale over which the SFR we used in the MS is probed. Indeed, we measure the SFR from the [O II] doublet, which mainly probes recent star formation (~ 10 Myr). On the other hand, if we consider that the field and large structure sub-samples do not have zero points more different than at most their uncertainty (0.02–0.03 dex), we can compute an upper bound on the quenching timescale in the large structures using Eq. (16) of [Abril-Melgarejo et al. \(2021\)](#). This gives us timescales between roughly 700 Myr and 1.5 Gyr, significantly larger than the ~ 10 Myr probed by the SFR from the [O II] doublet. Hence, the galaxies in the largest structures at $z \sim 0.7$ might have quite recently started being affected by their environment, and thus started being quenched, so that the impact on the TFR might not be visible yet with respect to the field galaxies.

Some authors also implement an asymmetric drift correction to take into account the impact of gas pressure on its dynamics (e.g., [Meurer et al. 1996](#); [Úbler et al. 2017](#); [Abril-Melgarejo et al. 2021](#); [Bouché et al. 2022](#)). Evaluated at R_{22} , the gas pressured corrected circular velocity for a double exponential density profile with a constant thickness writes ([Meurer et al. 1996](#); [Bouché et al. 2022](#))

$$V_{c,22} = \sqrt{V_{22}^2 + 2.2\sigma_V^2}, \quad (17)$$

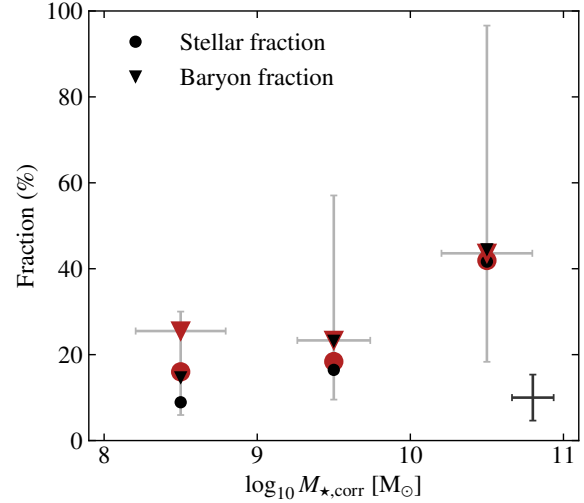


Fig. 14. Evolution of the median stellar and baryon fractions for galaxies from the TFR sample in the field (black points) and in large structures (red circles) as a function of stellar mass in mass bins of 1 dex. Light grey error bars correspond to the 16th and 84th percentiles of the baryon fraction distributions. The typical uncertainty on stellar mass and baryon fraction is shown as a dark grey error bar on the *bottom right*. Because we removed galaxies whose mass models have large uncertainties (selection criteria iv and v), the fractions we measure are probably slightly underestimated.

where V_{22} is the uncorrected circular velocity evaluated at R_{22} and σ_V is the velocity dispersion computed as the median value of the beam smearing and LSF corrected velocity dispersion map. Equation (17) is only an approximation of the real impact of gas pressure on the measured circular velocity since it only holds for turbulent gas disks with negligible thermal pressure. In the kinematics sample, the median value of the intrinsic velocity dispersion is around 30 km s^{-1} independently of environment. Thus, the impact of the asymmetric drift correction is quite small on the TFR. However, we find that the velocity dispersion is not constant but is correlated with stellar mass such that more massive galaxies are more impacted by the correction than low mass ones. In turn, this tends to align high and low mass galaxies onto a line with roughly the same slope, but with a slightly larger scatter. Indeed, when implementing the asymmetric drift correction, we find virtually the same zero point between the small and large structure sub-samples ($\beta_{\text{TFR}} \approx 2.07$ with the corrected velocity versus $\beta_{\text{TFR}} \approx 2.02$ with the uncorrected one), independently of the environment or the richness threshold used.

Additionally, we can also include the gas mass into the fit. We compute the gas mass using the Schmidt-Kennicutt relation ([Schmidt 1959](#); [Kennicutt 1998a](#)) assuming the gas is evenly distributed within a disk of radius R_{22} :

$$\log_{10} M_g [\text{M}_{\odot}] \approx 8.053 + 0.571 \log_{10} R_d [\text{kpc}] + 0.714 \log_{10} \text{SFR} [\text{M}_{\odot} \text{yr}^{-1}], \quad (18)$$

with M_g the gas mass and SFR the un-normalised SFR (see Sect. 3.3). If we replace the size and SFR variables in Eq. (18) by the size-mass and SFR-mass relations found before, we get a correlation between gas and stellar masses such that more massive galaxies also have a higher gas mass. In particular, the offset on the zero point found for the TFR between the field and the large structure sub-samples will also lead to a small offset in the gas mass-stellar mass relation. The impact of the gas mass

on the mass budget is shown in Fig. 14. We compare the stellar fraction (circles) with the total baryon fraction (triangles) for the field and large structure sub-samples. For most galaxies, the gas mass is non-negligible but has a small impact, leading to an offset between stellar and baryon fractions of roughly 5%. On the other hand, the gas mass has a slightly more significant impact on the lowest mass bin. While the impact is similar to other mass bins for the field sample (roughly 5%), the impact on the large structure sub-sample is stronger, reaching about 10%. This would suggest that the low mass galaxies are more gas rich in the large structures than in the field. However, only a handful of galaxies (~ 10) are located in the lowest mass bin in the large structure sub-sample. Besides, as is shown by the light grey error bars in Fig. 14, the distribution for the baryon fraction is quite large so that the difference in gas mass is probably not that significant. Another explanation for this slightly larger difference found at low mass might be that these galaxies are experiencing bursts of star formation, which would lead to overestimated gas masses, but this effect is not visible in the MS.

When the gas mass is included, we get a tighter TFR, with low mass galaxies that tend to be aligned onto the same line as the high mass ones. In turn, this brings the best-fit slope to a value of $\alpha = 0.31$ when applying the mass and redshift cuts, quite close to the $\alpha = 0.29$ value found when fitting the stellar mass TFR without applying any cut (i.e. driven by massive galaxies). The zero point is almost always similar between the field and small structure and large structure sub-samples ($\beta_{\text{TFR}} \approx 1.99$), independently of the richness threshold used to separate galaxies in the two sub-samples. Similarly to the stellar mass TFR, only when using a threshold $N = 20$ do we find a slightly more significant difference in zero point between the field and small structure sub-sample ($\beta_{\text{TFR}} = 2.00 \pm 0.02$) and the large structure sub-sample ($\beta_{\text{TFR}} = 1.98 \pm 0.02$). However, once we further include the asymmetric drift correction from Eq. (17), the difference vanishes for any richness threshold used ($\beta_{\text{TFR}} \approx 2.02$).

Thus, if there is an impact on the TFR, it is mostly driven by differences in terms of stellar mass or redshift distributions rather than the environment itself. We note that this result is consistent with Pelliccia et al. (2019), where they could not find an impact of the environment on the TFR as well, but is contradictory to what was found in Abril-Melgarejo et al. (2021). By comparing their sample to others, such as KMOS3D, KROSS, and ORELSE, they were able to find a significant offset in the TFR, which they attributed to the fact that different environments were probed. This offset was interpreted either as the effect of quenching, which reduces the amount of stellar mass in the most massive structures at fixed circular velocity, or as the effect of baryon contraction, which leads to an increase in circular velocity at fixed stellar mass. As discussed previously, baryon contraction and quenching are visible in our size-mass and MS relations, but not in the TFR. However, they noted that performing a consistent and reliable comparison between samples using different observing methods, models, tools, and selection functions was a difficult task and can lead to multiple sources of uncertainty. These can directly arise from the morphological and kinematics modelling, but can also be driven by uncertainties on the SED-based stellar masses, which, depending on the SED fitting code used and the assumptions made on the star formation history, can lead to systematics of the same order of magnitude as the offset found in Abril-Melgarejo et al. (2021). On the other hand, we argue that our result is quite robust since we have applied the same models, tools, assumptions and selection from the beginning to the end.

8. Conclusion

We have performed a morpho-kinematics modelling of 1142 [O II] emitters from the MAGIC survey using combined HST and MUSE data in the redshift range $0.25 < z < 1.5$. These galaxies are all located in the COSMOS field and have been attributed to structures of various richness (field, small, and large structures) using a FoF algorithm. We derived their global properties, such as their stellar mass, using the SED fitting code FAST and their SFR using the [O II] doublet. Their morphological modelling was performed with GALFIT on HST F814W images using a bulge and a disk decomposition. The best-fit models were later used to perform a mass modelling to constrain the impact of the baryons on the total rotation curve of the ionised gas. We included a mean prescription for the thickness of stellar disks as a function of redshift to correct for the impact of finite thickness on the mass and rotation curve of the disk component. The kinematics maps (line flux, velocity field, velocity dispersion, etc.) were extracted from the MUSE cubes using the [O II] doublet as kinematics tracer, and the 2D kinematics modelling was performed by fitting the baryon mass models combined with an NFW profile to describe the DM halo directly on the observed velocity field while modelling the impact of the beam smearing to compute the intrinsic velocity dispersion.

Our kinematics sample was divided into sub-samples, targeting different environments, and we decided to focus our analysis on three scaling relations, namely the size-mass relation, the MS relation, and the TFR. As a first step, we selected a sample of star-forming disk-like galaxies and studied how using different additional selection criteria, in terms of size, S/N, and/or redshift, would impact the best-fit slope and zero point for each relation. We found that the redshift and mass selection criteria were important in order not to bias the zero point when comparing between environments since their redshift and mass distributions differ. Additionally, the TFR requires additional criteria, especially in terms of inclination, to remove galaxies with poorly constrained kinematics.

We find a 1σ significant difference (0.03 dex) in the size-mass relation as a function of environment when using a richness threshold of $N = 10$ to separate between small and large structures, and a 2σ significant difference (0.06 dex) using $N = 20$. This result suggests that galaxies in the largest structures have, on average, smaller disks ($\sim 14\%$) than their field counterparts at $z \approx 0.7$, similar to what was found in the literature. Additionally, we get similar results when using the global effective radius rather than the disk effective radius for our disk sizes. Regarding the MS, we find a 2σ significant impact of the environment on the zero point of the MS (0.1 dex) when using $N = 10$ and a 3σ significant difference (0.15 dex) when using $N = 20$. These offsets are consistent with galaxies located in the large structures with SFRs reduced by a factor of 1.3 – 1.5 with respect to field galaxies at a similar redshift.

Finally, after applying mass and redshift cuts, we cannot find any difference in the zero point of the TFR between environments, except when using a richness threshold of $N = 20$ to separate between a field and small structure sub-sample and a large structure sub-sample. In this instance, we get an offset of 0.04 dex, which is significant to at most 1σ significance. By interpreting this offset as being an offset in stellar mass at fixed circular velocity, and by including the contribution of the size-mass relation in the interpretation of the TFR, we find that there must be a small difference of roughly 4% in stellar fraction between field galaxies and those in the largest structures. Because we measure a negative stellar mass offset in the TFR

between the field and the large structure sub-samples (galaxies in the large structures are more massive than those in the field), we can rule out the effect of quenching, as was suggested in [Abril-Melgarejo et al. \(2021\)](#), when using $N = 20$. On the other hand, because there is no measured difference in zero point with $N = 5, 10$, and 15 , we can compute upper bounds on the quenching timescale of the galaxies in the large structures using the typical uncertainty found on the TFR zero point. If quenching does indeed lead to a deficit in stellar mass in structures at $z \approx 0.7$ with respect to the field, this would suggest that galaxies have been impacted by the largest structures for at most between 700 Myr and 1.5 Gyr . When including the contribution of the gas in the mass budget of the TFR, we find a similarly significant offset of 0.02 dex between the field and the large structures (using $N = 20$). However, as previously discussed, quenching is still ruled out since this leads to a negative mass offset. Nevertheless, we note that these small differences in zero point vanish once we include the contribution of gas pressure in the dynamics (asymmetric drift correction).

The conclusion from our fully self-consistent study differs from that of [Abril-Melgarejo et al. \(2021\)](#), even though they investigated and took methodological biases between the samples they compared into account as much as possible. Such a difference might be due to uncontrolled biases when they compared the TFR between samples, or from a possible redshift evolution of the TFR since they could not control the redshift distribution of the various samples as much as we did in this analysis.

This outlines the importance of further reducing those biases by using similar datasets, selection functions, and analysis methods for galaxies in both low- and high-density environments to measure the impact of the environment on galaxy evolution.

Acknowledgements. We dedicate this article in memory of Hayley Finley. This work was supported by the Programme National Cosmology et Galaxies (PNCG) of CNRS/INSU with INP and IN2P3, co-funded by CEA and CNES. This work has been carried out through the support of the ANR FOGHAR (ANR-13-BS05-0010-02), the OCEVU Labex (ANR-11-LABX-0060), and the A*MIDEX project (ANR-11-IDEX-0001-02), which are funded by the “Investissements d’avenir” French government program managed by the ANR. This work has been carried out thanks to the support of the Ministry of Science, Technology and Innovation of Colombia (Minciencias) PhD fellowship program No. 756-2016. JCBP acknowledges financial support of Vicerrectoría de Investigación y Extensión de la Universidad Industrial de Santander under project 2494. This research has made use of MATPLOTLIB ([Hunter 2007](#)), SCIPY ([Virtanen et al. 2020](#)), NUMPY ([Harris et al. 2020](#)) and ASTROPY ([Astropy Collaboration 2013, 2018](#)). We acknowledge David Carton for his investment in the build-up of the project.

References

- Abril-Melgarejo, V., Epinat, B., Mercier, W., et al. 2021, *A&A*, **647**, A152
 Astropy Collaboration (Robitaille, T. P., et al.) 2013, *A&A*, **558**, A33
 Astropy Collaboration (Price-Whelan, A. M., et al.) 2018, *AJ*, **156**, 123
 Bacon, R., Conseil, S., Mary, D., et al. 2017, *A&A*, **608**, A1
 Balogh, M. L., van der Burg, R. F. J., Muzzin, A., et al. 2020, *MNRAS*, **500**, 358
 Bizyaev, D. V., Kautsch, S. J., Mosenkov, A. V., et al. 2014, *ApJ*, **787**, 24
 Boogaard, L. A., Brinchmann, J., Bouché, N., et al. 2018, *A&A*, **619**, A27
 Boselli, A., Epinat, B., Contini, T., et al. 2019, *A&A*, **631**, A114
 Bottinelli, L., Gouguenheim, L., Paturel, G., & de Vaucouleurs, G. 1983, *A&A*, **118**, 4
 Bouché, N., Murphy, M. T., Kacprzak, G. G., et al. 2013, *Science*, **341**, 50
 Bouché, N. F., Bera, S., Krajnovic, D., et al. 2022, *A&A*, **658**, A76
 Buchner, J., Georgakakis, A., Nandra, K., et al. 2014, *A&A*, **564**, A125
 Calzetti, D., Armus, L., Bohlin, R. C., et al. 2000, *ApJ*, **533**, 682
 Cappellari, M., Scott, N., Alatalo, K., et al. 2013, *MNRAS*, **432**, 1709
 Cardelli, J. A., Clayton, G. C., & Mathis, J. S. 1989, *ApJ*, **345**, 245
 Chabrier, G. 2003, *PASP*, **115**, 763
 Conroy, C., & Gunn, J. E. 2010, *ApJ*, **712**, 833
 Contini, T., Epinat, B., Bouché, N., et al. 2016, *A&A*, **591**, A49
 Cortese, L., Catinella, B., & Smith, R. 2021, *PASA*, **38**, e035
 Cowie, L. L., & McKee, C. F. 1977, *ApJ*, **211**, 135
 Cowie, L. L., & Songaila, A. 1977, *Nature*, **266**, 501
 Davé, R. 2009, in *Galaxy Evolution: Emerging Insights and Future Challenges*, eds. S. Jogee, I. Marinova, L. Hao, & G. A. Blanc, *ASP Conf. Ser.*, **419**, 347
 Dimauro, P., Huertas-Company, M., Daddi, E., et al. 2018, *MNRAS*, **478**, 5410
 Duncan, K., Conselice, C. J., Mundy, C., et al. 2019, *ApJ*, **876**, 110
 Epinat, B., Contini, T., Le Fèvre, O., et al. 2009, *A&A*, **504**, 789
 Epinat, B., Amram, P., Balkowski, C., & Marcelin, M. 2010, *MNRAS*, **401**, 2113
 Epinat, B., Tasca, L., Amram, P., et al. 2012, *A&A*, **539**, A92
 Epinat, B., Contini, T., Finley, H., et al. 2018, *A&A*, **609**, A40
 Erb, D. K., Shapley, A. E., Pettini, M., et al. 2006, *ApJ*, **644**, 813
 Erfanianfar, G., Popesso, P., Finoguenov, A., et al. 2016, *MNRAS*, **455**, 2839
 Feroz, F., & Hobson, M. P. 2008, *MNRAS*, **384**, 449
 Flores, H., Hammer, F., Puech, M., Amram, P., & Balkowski, C. 2006, *A&A*, **455**, 107
 Foster, C., van de Sande, J., D’Eugenio, F., et al. 2017, *MNRAS*, **472**, 966
 Freeman, K. C. 1970, *ApJ*, **160**, 811
 Freundlich, J., Combes, F., Tacconi, L. J., et al. 2019, *A&A*, **622**, A105
 Genzel, R., Price, S. H., Übler, H., et al. 2020, *ApJ*, **902**, 98
 Gilbank, D. G., Baldry, I. K., Balogh, M. L., Glazebrook, K., & Bower, R. G. 2010, *MNRAS*, **405**, 2594
 Gilbank, D. G., Baldry, I. K., Balogh, M. L., Glazebrook, K., & Bower, R. G. 2011, *MNRAS*, **412**, 2111
 Graham, A. W., Driver, S. P., Petrosian, V., et al. 2005, *AJ*, **130**, 1535
 Gray, M. E., Wolf, C., Barden, M., et al. 2009, *MNRAS*, **393**, 1275
 Guérou, A., Krajnović, D., Epinat, B., et al. 2017, *A&A*, **608**, A5
 Gunn, J. E., & Gott, J. R., III 1972, *ApJ*, **176**, 1
 Harris, C. R., Millman, K. J., van der Walt, S. J., et al. 2020, *Nature*, **585**, 357
 Heidmann, J., Heidmann, N., & de Vaucouleurs, G. 1972, *MNRAS*, **75**, 85
 Hernquist, L. 1990, *ApJ*, **356**, 359
 Hinton, S. 2016, MARZ: Redshifting Program, Astrophysics Source Code Library [record ascl:1605.001]
 Hopkins, A. M., & Beacom, J. F. 2006, *ApJ*, **651**, 142
 Hopkins, P. F., Quataert, E., & Murray, N. 2012, *MNRAS*, **421**, 3522
 Hunter, J. D. 2007, *Comput. Sci. Eng.*, **9**, 90
 Ilbert, O., Salvato, M., Le Floch, E., et al. 2010, *ApJ*, **709**, 644
 Inami, H., Bacon, R., Brinchmann, J., et al. 2017, *A&A*, **608**, A2
 Iovino, A., Petropoulou, V., Scodreggio, M., et al. 2016, *A&A*, **592**, A78
 Jaffe, W. 1983, *MNRAS*, **202**, 995
 Kelkar, K., Aragón-Salamanca, A., Gray, M. E., et al. 2015, *MNRAS*, **450**, 1246
 Kennicutt, R. C., Jr 1992, *ApJ*, **388**, 310
 Kennicutt, R. C., Jr 1998a, *ApJ*, **498**, 541
 Kennicutt, R. C., Jr 1998b, *ARA&A*, **36**, 189
 Kereš, D., Katz, N., Weinberg, D. H., & Davé, R. 2005, *MNRAS*, **363**, 2
 Knobel, C., Lilly, S. J., Iovino, A., et al. 2009, *ApJ*, **697**, 1842
 Knobel, C., Lilly, S. J., Iovino, A., et al. 2012, *ApJ*, **753**, 121
 Koekemoer, A. M., Aussel, H., Calzetti, D., et al. 2007, *ApJS*, **172**, 196
 Korsaga, M., Epinat, B., Amram, P., et al. 2019, *MNRAS*, **490**, 2977
 Kriek, M., van Dokkum, P. G., Labbé, I., et al. 2009, *ApJ*, **700**, 221
 Kuchner, U., Ziegler, B., Verdugo, M., Bamford, S., & Häußler, B. 2017, *A&A*, **604**, A54
 Laigle, C., McCracken, H. J., Ilbert, O., et al. 2016, *ApJS*, **224**, 24
 Leja, J., Johnson, B. D., Conroy, C., & Dokkum, P. V. 2018, *ApJ*, **854**, 62
 López-Sanjuan, C., Le Fèvre, O., Ilbert, O., et al. 2012, *A&A*, **548**, A7
 Lubin, L. M., Gal, R. R., Lemaux, B. C., Kocevski, D. D., & Squires, G. K. 2009, *ApJ*, **137**, 4867
 Maltby, D. T., Aragón-Salamanca, A., Gray, M. E., et al. 2010, *MNRAS*, **402**, 282
 Mantha, K. B., McIntosh, D. H., Brennan, R., et al. 2018, *MNRAS*, **475**, 1549
 Markwardt, C. B. 2009, in *Astronomical Data Analysis Software and Systems XVIII*, eds. D. A. Bohlender, D. Durand, & P. Dowler, *ASP Conf. Ser.*, **411**, 251
 Massey, R., Stoughton, C., Leauthaud, A., et al. 2010, *MNRAS*, **401**, 371
 Matharu, J., Muzzin, A., Brammer, G. B., et al. 2019, *MNRAS*, **484**, 595
 Meurer, G. R., Carignan, C., Beaulieu, S. F., & Freeman, K. C. 1996, *ApJ*, **111**, 1551
 Mowla, L. A., van Dokkum, P., Brammer, G. B., et al. 2019, *ApJ*, **880**, 57
 Muzzin, A., Wilson, G., Yee, H. K. C., et al. 2009, *ApJ*, **698**, 1934
 Muzzin, A., Marchesini, D., Stefanon, M., et al. 2013, *ApJ*, **777**, 18
 Nantais, J., Wilson, G., Muzzin, A., et al. 2020, *MNRAS*, **499**, 3061
 Navarro, J. F., Frenk, C. S., & White, S. D. M. 1995, *MNRAS*, **275**, 56
 Navarro, J. F., Frenk, C. S., & White, S. D. M. 1996, *ApJ*, **462**, 563
 Noeske, K. G., Weiner, B. J., Faber, S. M., et al. 2007, *ApJ*, **660**, L43
 Ocvirk, P., Pichon, C., & Teyssier, R. 2008, *MNRAS*, **390**, 1326
 Old, L. J., Balogh, M. L., van der Burg, R. F. J., et al. 2020a, *MNRAS*, **500**, 355
 Old, L. J., Balogh, M. L., van der Burg, R. F. J., et al. 2020b, *MNRAS*, **493**, 5987
 Osterbrock, D. E., & Ferland, G. J. 2006, *Astrophysics of Gaseous Nebulae and Active Galactic Nuclei* (Sausalito, CA: University Science Books)

- Padilla, N. D., Lagos, C., & Strauss, M. 2009, in *The Monster's Fiery Breath: Feedback in Galaxies, Groups, and Clusters*, eds. S. Heinz, & E. Wilcots, *Am. Inst. Phys. Conf. Ser.*, 1201, 100
- Pelliccia, D., Tresse, L., Epinat, B., et al. 2017, *A&A*, 599, A25
- Pelliccia, D., Lemaux, B. C., Tomczak, A. R., et al. 2019, *MNRAS*, 482, 3514
- Peng, C. Y., Ho, L. C., Impey, C. D., & Rix, H.-W. 2002a, *AJ*, 124, 266
- Peng, Q.-H., Peng, F., Chou, C.-K., & Lin, Y.-H. 2002b, *Ap&SS*, 282, 499
- Peng, Y. J., Lilly, S. J., Kova, K., et al. 2010, *ApJ*, 721, 193
- Plummer, H. C. 1911, *MNRAS*, 71, 460
- Rousseeuw, P. J., & Van Driessen, K. 2006, *Data Min. Knowl. Discovery*, 12, 29
- Schmidt, M. 1959, *ApJ*, 129, 243
- Schroetter, I., Bouché, N. F., Zabl, J., et al. 2019, *MNRAS*, 490, 4368
- Scoville, N., Aussel, H., Brusa, M., et al. 2007a, *ApJS*, 172, 1
- Scoville, N., Aussel, H., Benson, A., et al. 2007b, *ApJS*, 172, 150
- Shen, S., Mo, H. J., White, S. D. M., et al. 2003, *MNRAS*, 343, 978
- Soto, K. T., Lilly, S. J., Bacon, R., Richard, J., & Conseil, S. 2016, *MNRAS*, 458, 3210
- Speagle, J. S., Steinhardt, C. L., Capak, P. L., & Silverman, J. D. 2014, *ApJS*, 214, 15
- Tacconi, L. J., Genzel, R., Saintonge, A., et al. 2018, *ApJS*, 853, 179
- Tiley, A. L., Bureau, M., Cortese, L., et al. 2019, *MNRAS*, 482, 2166
- Toomre, A. 1963, *ApJ*, 138, 385
- Tremonti, C. A., Heckman, T. M., Kauffmann, G., et al. 2004, *ApJ*, 613, 898
- Trujillo, I., Conselice, C. J., Bundy, K., et al. 2007, *MNRAS*, 382, 109
- Tully, R. B., & Fisher, J. R. 1977, *A&A*, 54, 661
- Übler, H., Förster Schreiber, N. M., Genzel, R., et al. 2017, *ApJ*, 842, 121
- van der Wel, A., Franx, M., van Dokkum, P. G., et al. 2014a, *ApJ*, 788, 28
- van der Wel, A., Chang, Y.-Y., Bell, E. F., et al. 2014b, *ApJ*, 792, L6
- Ventou, E., Contini, T., Bouché, N., et al. 2017, *A&A*, 608, A9
- Ventou, E., Contini, T., Bouché, N., et al. 2019, *A&A*, 631, A87
- Vergani, D., Epinat, B., Contini, T., et al. 2012, *A&A*, 546, A118
- Virtanen, P., Gommers, R., Oliphant, T. E., et al. 2020, *Nat. Methods*, 17, 261
- Walter, F., Carilli, C., Neeleman, M., et al. 2020, *ApJ*, 902, 111
- Weilbacher, P. M., Palsa, R., Streicher, O., et al. 2020, *A&A*, 641, A28
- Whitaker, K. E., Franx, M., Leja, J., et al. 2014, *ApJ*, 795, 104
- Williams, M. J., Bureau, M., & Cappellari, M. 2010, *MNRAS*, 409, 1330
- Wuyts, S., Förster Schreiber, N. M., Lutz, D., et al. 2011, *ApJ*, 738, 106
- Yang, Y., Flores, H., Hammer, F., et al. 2008, *A&A*, 477, 789
- Zabl, J., Bouché, N. F., Schroetter, I., et al. 2019, *MNRAS*, 485, 1961
- Zhang, H., Primack, J. R., Faber, S. M., et al. 2019, *MNRAS*, 484, 5170

Appendix A: Additional plots and tables

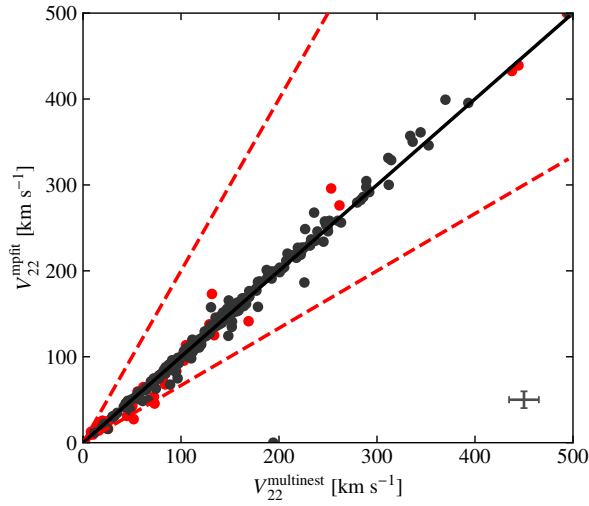


Fig. A.1. Comparison of the circular velocity $V_{22} = V(R_{22})$ using MOCKING between MULTINEST and MPFIT for galaxies from the MS sample. The rotation curve used was a flat model, and we removed galaxies whose circular velocity could not be reliably constrained (R_{22} falls outside the range where there is sufficient S/N in the MUSE data cube to derive the kinematics). Red points correspond to galaxies visually classified as having no apparent velocity field in their kinematics maps, and dashed red lines correspond to a 50% difference between the two methods. The typical uncertainty is shown in the bottom-right part of the plot. Overall, values are consistent within their error bars.

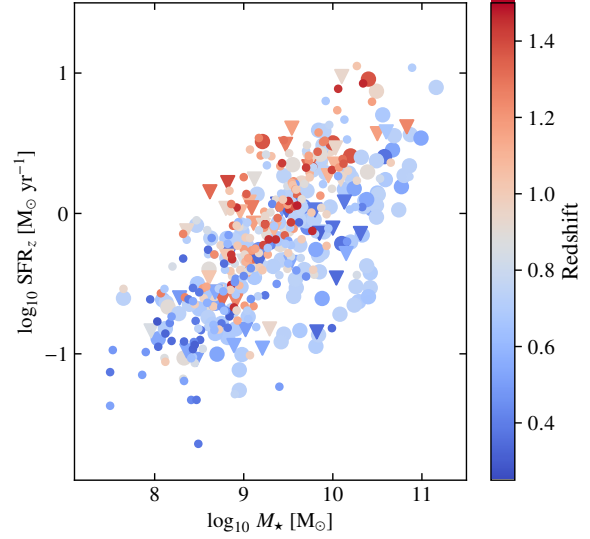


Fig. A.3. SFR-stellar mass relation for galaxies from the MS sample, colour-coded as a function of redshift. Despite the applied normalisation to redshift $z_0 = 0.7$, we still see a dichotomy. High redshift galaxies tend to align along lines with the largest specific star formation rate (sSFR), while low redshift galaxies tend to align along lines with the lowest sSFR because of the survey design.

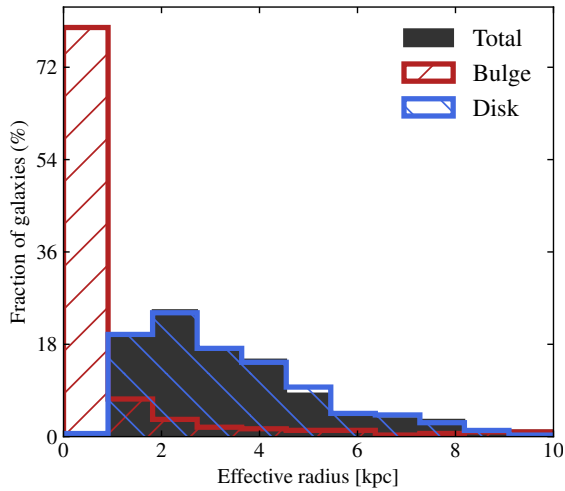


Fig. A.2. Distribution of effective radii for galaxies in the morphological sample. In grey (filled) we show the total size, in red (hatched) the bulge size, and in blue (hatched) the disk size. Disks are mostly found between roughly 1 kpc and 6 kpc, with very few galaxies with disk sizes beyond 10 kpc. The lack of disks below 1 kpc is due to the size selection criterion from Sect. 6.1. On the other hand, the majority of bulges are found below 2 kpc. The total size of galaxies is mainly driven by the disk component.

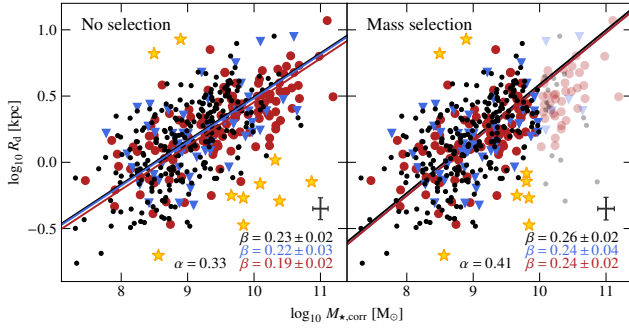
Appendix B: Impact of selection


Fig. B.1. Size-mass relation with and without applying the mass selection criterion (vi) on galaxies from the MS sample. The data points and best-fit lines are similar to Fig. 11. As an indication, we also show as semi-transparent symbols galaxies removed by the mass cut in the right panel. The typical uncertainty on stellar mass and disk size is shown on both panels as a grey error bar.

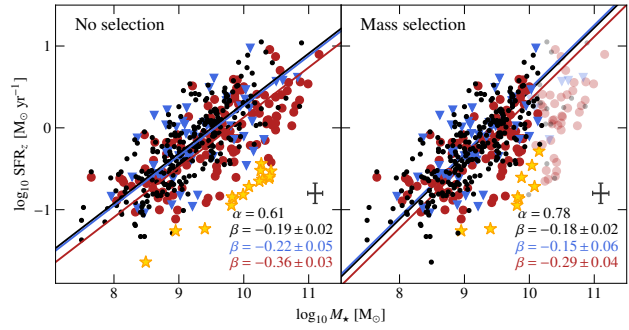


Fig. B.2. SFR-mass relation with and without applying the mass selection criterion (vi) on galaxies from the kinematics sample. The data points and best-fit lines are similar to Fig. 12. As an indication, we also show as semi-transparent symbols galaxies removed by the mass cut in the right panel. The typical uncertainty on stellar mass and SFR is shown on both panels as a grey error bar.

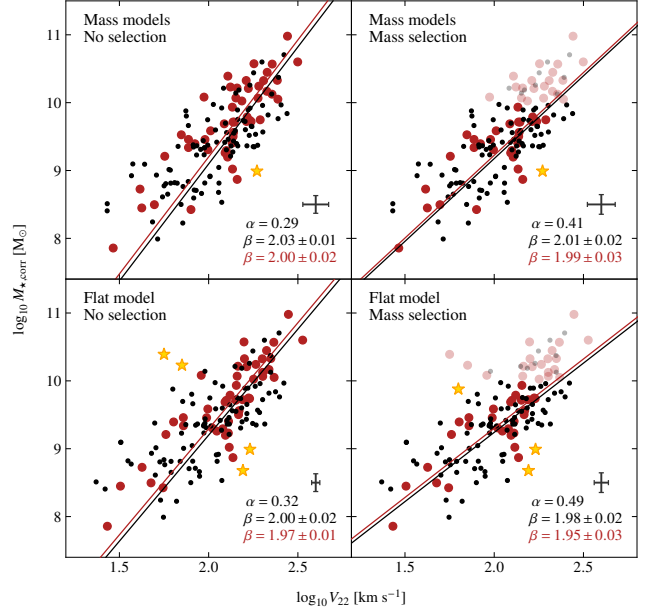


Fig. B.3. TFR with and without applying the mass selection criterion (vi) on galaxies from the TFR sample. The data points and best-fit lines are similar to Fig. 13. The first row shows the TFR using the velocity derived from the best-fit mass models, and the second row the TFR using the flat model. As an indication, we also show as semi-transparent symbols galaxies removed by the mass cut in the rightmost panels. The typical uncertainty on stellar mass and velocity is shown on each panel as a grey error bar.

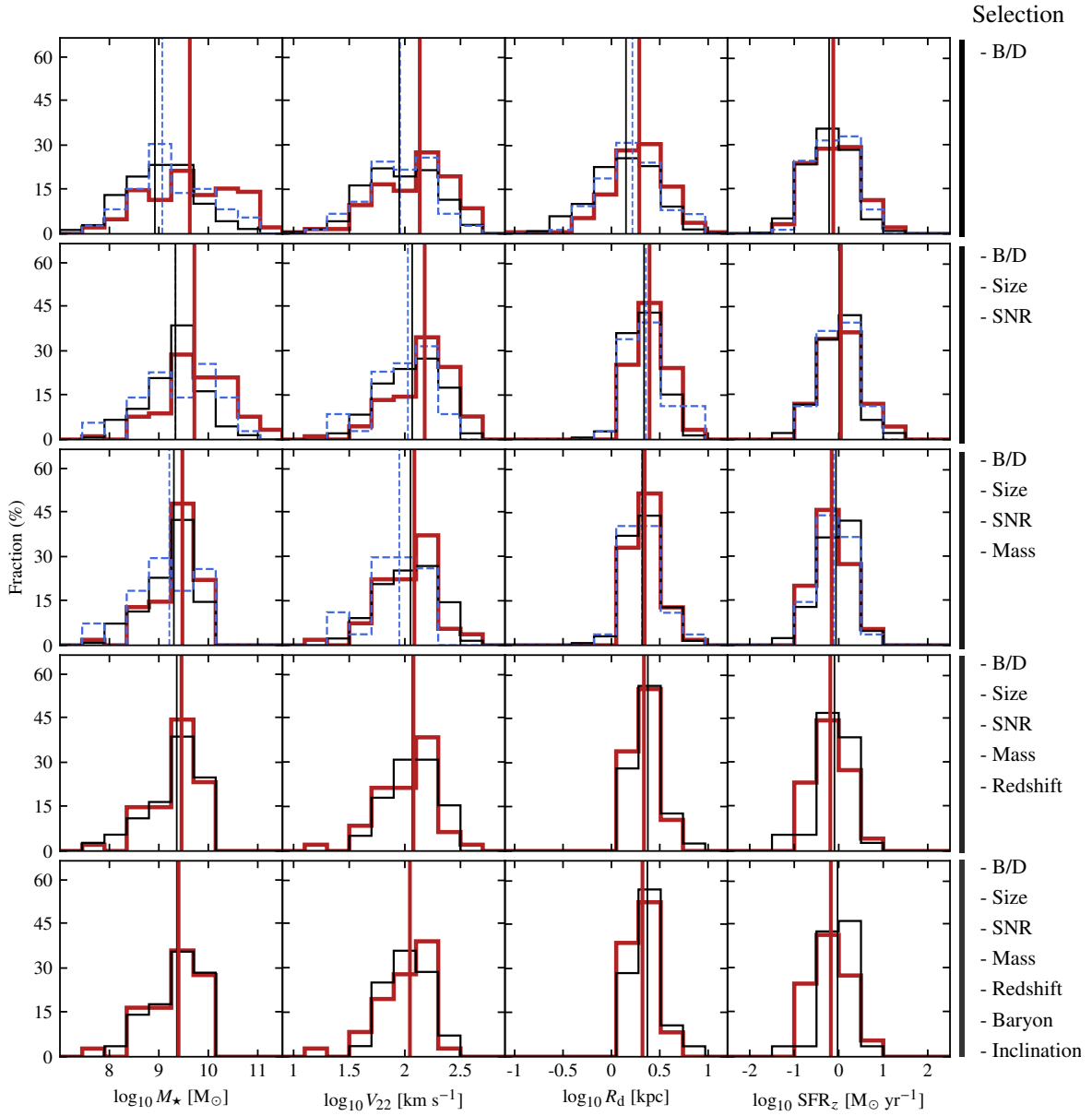


Fig. B.4. Impact of selection criteria on the main parameters distributions for galaxies from the kinematics sample. Each row represents a different selection. The black full line corresponds to the field galaxy sub-sample, the blue dashed line to the small structures and the red thick line to the large structures (using a threshold of $N = 10$ to separate between structures). We also show the median values for each sub-sample as vertical lines. We do not show the small structure sub-sample in the last two rows since there remain too few galaxies.

Appendix C: Bulge-disk decomposition

Figure C.1 represents the median value of the bulge-to-total flux ratio (B/T) for the morphological sample as a function of radius. We see that beyond one effective radius the disk dominates the flux budget. When computed near the centre, B/T is close to one, consistent with the bulge dominating the inner parts. Even though the disk dominates at large distances, B/T does not reach zero. This is a consequence of the chosen bulge-disk decomposition. Indeed, for a Sérsic profile with parameters $(n, \Sigma_{\text{eff}}, R_{\text{eff}})$, the integrated flux up to radius r is given by

$$F(< r) = 2\pi n \Sigma_{\text{eff}} R_{\text{eff}}^2 e^{b_n} \gamma\left(2n, b_n \left(r/R_{\text{eff}}\right)^{1/n}\right) / b_n^{2n}, \quad (\text{C.1})$$

where γ is the lower incomplete gamma function and where b_n is the solution of the equation $\Gamma(2n) = 2\gamma(2n, b_n)$ (Graham et al. 2005), with Γ the complete gamma function. Therefore, for a bulge-disk decomposition the total flux ratio between the two components is given by

$$B/T(r \rightarrow \infty) \approx \Sigma_{\text{eff,b}} R_{\text{eff,b}}^2 / (\Sigma_{\text{eff,b}} R_{\text{eff,b}}^2 + 0.527 \Sigma_{\text{eff,d}} R_{\text{eff,d}}^2), \quad (\text{C.2})$$

where $(\Sigma_{\text{eff,b}}, R_{\text{eff,b}})$ and $(\Sigma_{\text{eff,d}}, R_{\text{eff,d}})$ are the bulge and disk parameters, respectively. The only case for which Eq. C.2 vanishes is when the bulge contribution can be neglected with respect to the disk. Otherwise, when $B/T(\infty)$ is sufficiently larger than 0, this reflects a non-negligible contribution of the bulge to the overall flux budget. The fact that the median value for the morphological sample is around 0.2 is therefore a good indication of the relevance of performing a bulge-disk decomposition with respect to using a single disk model.

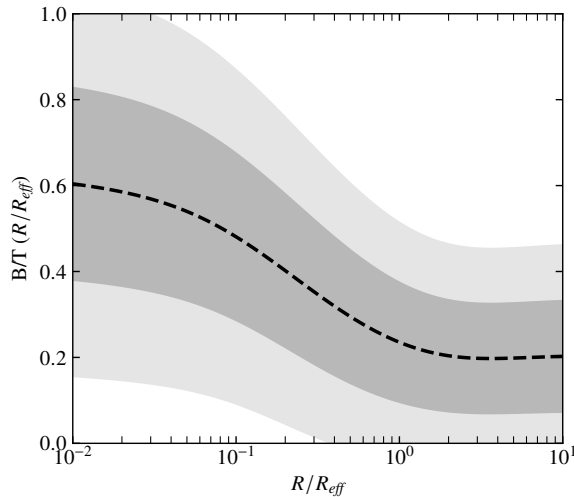


Fig. C.1. Mean B/T for galaxies in the morphological sample computed at various radii in units of R_{eff} . The areas correspond to the 1σ (dark grey) and 2σ (light grey) dispersions. The bulge component dominates the central parts of the galaxies whereas the disk takes over completely after roughly one effective radius. Even as far as $10R_{\text{eff}}$, we find a nearly constant non-zero $B/T \approx 0.2$ indicative of a non-negligible bulge contribution to the overall flux budget.

The half-light radius of a multi-component decomposition involving only Sérsic models does not necessarily have to be computed through numerical integration but can also be derived by finding the single zero of a given function. Indeed, for a bulge-disk decomposition, from the definition of the global half-light

radius (that is, the radius that encloses half of the total flux), we have

$$F_d(R_{\text{eff}}) + F_b(R_{\text{eff}}) = (F_{\text{tot,d}} + F_{\text{tot,b}}) / 2, \quad (\text{C.3})$$

where $F_d(R_{\text{eff}})$ and $F_b(R_{\text{eff}})$ are the disk and bulge fluxes at the global effective radius R_{eff} , and $F_{\text{tot,d}}, F_{\text{tot,b}}$ are the disk and bulge total fluxes, respectively. Given Eq. C.1, one can rewrite Eq. C.3 as

$$F_{\text{tot,d}} \left[\gamma\left(2, b_1 \frac{R_{\text{eff}}}{R_{\text{eff,d}}}\right) - 0.5 \right] + \frac{F_{\text{tot,b}}}{\Gamma(8)} \left[\gamma\left(8, b_4 \left(\frac{R_{\text{eff}}}{R_{\text{eff,b}}}\right)^{1/4}\right) - \Gamma(8)/2 \right] = 0. \quad (\text{C.4})$$

Furthermore, if one defines the total magnitude of a component i as $\text{mag}_i = -2.5 \log_{10} F_{\text{tot},i} + \text{zpt}$, where zpt is a zero point that is the same for all the components and normalises by the total flux, then Eq. C.4 simplifies to

$$f(R_{\text{eff}}) / f(\infty) = 0, \quad (\text{C.5})$$

with the function f defined as

$$f(x) = 10^{-\text{mag}_d/2.5} \left[\gamma\left(2, b_1 \frac{x}{R_{\text{eff,d}}}\right) - 0.5 \right] + 10^{-\text{mag}_b/2.5} \left[\gamma\left(8, b_4 \left(\frac{x}{R_{\text{eff,b}}}\right)^{1/4}\right) / \Gamma(8) - 0.5 \right]. \quad (\text{C.6})$$

Equation C.5 can be solved by searching for a zero in the range $[\min(R_{\text{eff,d}}, R_{\text{eff,b}}), \max(R_{\text{eff,d}}, R_{\text{eff,b}})]$. Indeed, if $R_{\text{eff}} > \max(R_{\text{eff,d}}, R_{\text{eff,b}})$, the flux at R_{eff} would be the sum of $F_d(R_{\text{eff}}) > F_{\text{d,tot}}/2$ and $F_b(R_{\text{eff}}) > F_{\text{b,tot}}/2$ such that it would be larger than the expected $F_{\text{tot}}/2$ value. Thus, R_{eff} cannot be greater than $\max(R_{\text{eff,d}}, R_{\text{eff,b}})$, and the same argument can be given for the case $R_{\text{eff}} < \min(R_{\text{eff,d}}, R_{\text{eff,b}})$.

Finally, there is only one zero that is a solution of Eq. C.5, and this can be shown by noticing that f is a monotonously increasing function of x whose normalised form $f(x)/f(\infty)$ is bounded between -1 for $x = 0$ and 1 for $x = \infty$.

Appendix D: Mass modelling

The methodology used in Abril-Melgarejo et al. (2021) to derive the galaxies dynamics is only an approximation of the intrinsic ionised gas kinematics. The flat model used for the rotation curve is ad hoc, based on observations of local and intermediate redshift rotation curves of DM-dominated galaxies. While being a good approximation for DM-dominated systems, this kinematics modelling does not take into account information from the morphological modelling. In theory, one should derive the ionised gas kinematics, assuming in our case that the gas is distributed within an infinitely thin disk, from the 3D mass distribution of the different galaxy components. Even though we do not have access to such distributions, we can nevertheless constrain the gas kinematics under a few assumptions. In Sect. 4.1 we assumed that the sky projected surface density of the stars can be described by a bulge-disk decomposition, where the surface density of stellar disk is represented by an exponential profile and the stellar bulge is assumed to be spherically symmetric with a surface density described by a de Vaucouleurs profile. If one can find 3D flux densities that, when projected onto the line of sight, become the corresponding surface densities, then one has found the corresponding mass densities up to a multiplicative factor that is the mass-to-light ratio $\Upsilon = (M/L)_*$.

D.1. Theoretical background

For any mass density $\rho_M(\mathbf{r})$, we can derive the corresponding potential Φ from Poisson equation

$$\nabla^2\Phi(\mathbf{r}) = 4\pi G\rho_M(\mathbf{r}). \quad (\text{D.1})$$

The observed velocity maps are derived from the ionised gas kinematics, which is assumed to be located within an infinitely thin disk; therefore, we are only interested in the velocity of the gas within the plane of the galaxy disk. If we further assume that the mass distribution ρ_M is in equilibrium within its gravitational potential, then the centrifugal acceleration caused by its rotation must balance the radial gradient of the potential Φ in the galaxy plane, that is,

$$\frac{V_{\text{circ}}^2}{R}(R) = -\frac{\partial\Phi}{\partial R}(R, z = 0), \quad (\text{D.2})$$

with V_{circ} the circular velocity, R the radial distance in the plane of the galaxy, and where we have assumed that the potential and circular velocity are independent of the azimuth because of the symmetry of the mass distributions used in the following. Since the mass distributions and therefore the potentials add up, the circular velocity can be simply written as

$$V_{\text{circ}}^2(R) = \sum_i V_{\text{circ},i}^2(R), \quad (\text{D.3})$$

where $V_{\text{circ},i}$ is the circular velocity of the component i obeying Eq. D.2 for the corresponding potential well. In our case, the components that will contribute the most to the rotation curve are the stellar disk, stellar bulge and the DM halo to account for constant or slowly declining observed rotation curves at large radii. We do not model the contribution of the gas, which will therefore slightly contribute to the DM halo profile. In the case of the stellar components, we transform from stellar light distributions ρ_i to mass distributions $\rho_{M,i}$ using

$$\rho_{M,i}(\mathbf{r}) = \Upsilon\rho_i(\mathbf{r}), \quad (\text{D.4})$$

where we have further assumed that the mass-to-light ratio, Υ , is constant throughout the galaxy, and we compute it using the SED-based estimator of the stellar mass as

$$\Upsilon = M_\star/F_{\text{SP}}(1.5''), \quad (\text{D.5})$$

where M_\star is the SED-based mass computed in a circular aperture of diameter $3''$, and $F_{\text{SP}}(1.5'')$ is the flux integrated on the plane of the sky in the same aperture. In this analysis, we assume a similar Υ for both disk and bulge because it would require at least two HST bands to constrain efficiently the M/L for both components individually as done for instance in [Dimauro et al. \(2018\)](#).

D.2. Razor-thin stellar disk

To begin with, we assume the stellar disk to be infinitely thin, so that the stellar light density can be written as

$$\rho(\mathbf{r}) = \Sigma_{\text{RT}}(R) \delta(z) \quad (\text{D.6})$$

$$\Sigma_{\text{RT}}(R) = \Sigma_{\text{RT}}(0) e^{-b_1[R/R_{\text{eff},d}]}, \quad (\text{D.7})$$

where Σ_{RT} represents the light distribution in the plane of the disk, with $\Sigma_{\text{RT}}(0)$ the central surface density, $b_1 \approx 1.6783$, $R_{\text{eff},d}$ the disk effective radius, and δ is the Dirac distribution. The rotation curve for such a distribution was computed for the first

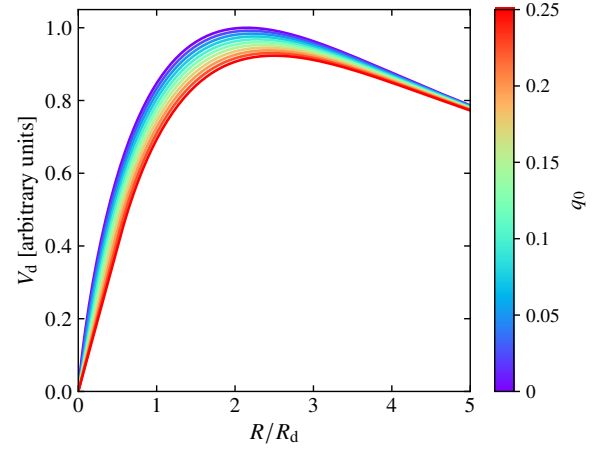


Fig. D.1. Impact of the thickness on the shape of the rotation curve for a thin disk. The finite thickness only impacts the inner parts and changes both the amplitude and the radius where the maximum is reached.

time by [Freeman \(1970\)](#) using the method described in [Toomre \(1963\)](#):

$$V_{\text{RT}}(R) = V_{\text{RT,max}} \times \frac{yf(y)}{1.075 f(1.075)}, \quad (\text{D.8})$$

with $f(y) = \sqrt{I_0(y)K_0(y) - I_1(y)K_1(y)}$ and $y = R/(2R_d)$. The effective radius of the disk is related to the disk scale length appearing in Eq. D.8 through $R_{\text{eff},d} = b_1R_d$. The maximum circular velocity is reached at a radius $R = 2.15R_d$ and is equal to

$$V_{\text{RT,max}} = 2.15f(1.075) \sqrt{\pi GR_d \Upsilon \Sigma_{\text{RT}}(0)}, \quad (\text{D.9})$$

where G is the gravitational constant.

D.3. Thin stellar disk

To refine the mass modelling of the stellar disk, we consider a disk model with a finite thickness. Assuming the light distribution can be correctly represented by a double exponential profile, we have

$$\rho(\mathbf{r}) = \Sigma_{\text{RT}}(R) e^{-|z|/h_z} / (2h_z), \quad (\text{D.10})$$

where h_z is the disk scale height. It can be shown ([Peng et al. 2002b](#)) that the potential in the plane of the galaxy for such a density can be written as

$$\Phi(R) = -(2\pi G/h_z) \int_{\mathbb{R}_+} dk (1/h_z + k)^{-1} J_0(kR) S_0(k), \quad (\text{D.11})$$

where $S_0(k)$ is the Hankel transform of order 0 of the surface density $\Sigma_d(R)$. For thin disks with small h_z , an approximation of the circular velocity in the plane of the galaxy is given by⁹

$$V_d^2(R) = V_{\text{RT}}^2(R) - V_{\text{corr,max}}^2 \times \frac{R e^{1-R/R_d}}{R_d}, \quad (\text{D.12})$$

where V_{RT} is the razor-thin circular velocity defined in Eq. D.8 and R_d is the disk scale length. For typical values of

⁹ For a derivation of this approximation, see Eq. 8.73 in Chapter 8 of Bovy J. Dynamics and Astrophysics of Galaxies. Princeton University Press, Princeton, NJ (in preparation) whose online version can be found at <https://galaxiesbook.org/>.

$h_z/R_d \approx 0.2 - 0.3$, this approximation gives a circular velocity that is different from numerical integration by less than 2% for most of the radial range, except near the central parts where the relative difference rises, though the absolute difference remains negligible in practice as the circular velocity quickly drops to zero near the centre. The maximum of the correction is reached at R_d (see Fig. D.1) and is given by

$$V_{\text{corr,max}} = \sqrt{2\pi G h_z \Upsilon \Sigma_{\text{RT}}(0)/e}. \quad (\text{D.13})$$

D.4. Impact of thickness on inclination and central surface density

In the case of a razor-thin disk projected at an inclination i with respect to the line of sight, the apparent central surface density $\Sigma_{\text{RT,obs}}(0)$ and axis ratio $q = b/a$, with a and b the semi-major and semi-minor axes, respectively, scale with the inclination as

$$\Sigma_{\text{RT,obs}}(0) = \Sigma_{\text{RT}}(0)/\cos i, \quad (\text{D.14})$$

$$q = \cos i. \quad (\text{D.15})$$

Writing Eq. D.14 is equivalent to saying that the total flux of the disk must be independent of its inclination on the sky, and Eq. D.15 comes from the fact that the isophotes of a projected razor-thin disk are ellipses. However, in the case of a disk with non-zero thickness the surface density profile gets more complicated, and must be computed as the integral of the inclined density distribution along the line of sight. We give in Appendix E a derivation of this integral in the general case. For the apparent central density, it simplifies to

$$\begin{aligned} \Sigma_{\text{d,obs}}(0) &= \frac{\Sigma_{\text{RT}}(0) R_d}{2h_z \sin i_0} \int_{\mathbb{R}} dv e^{-|v| (1+\beta)} \\ &= \frac{\Sigma_{\text{RT}}(0)}{q_0 \sin i_0 + \cos i_0}, \end{aligned} \quad (\text{D.16})$$

with $q_0 = h_z/R_d$ the real axis ratio, R_d the disk scale length, $\Sigma_{\text{RT}}(0)$ the central surface density if the galaxy was seen face-on, and i_0 the real inclination of the galaxy. We see that when the disk is infinitely thin (i.e. $h_z = 0$) we recover Eq. D.14, as should be expected. For a perfectly edge-on galaxy, that is, $i = 90^\circ$, Eq. D.14 diverges, which is due to the fact that a razor-thin disk seen edge-on does not have its flux distributed onto a surface anymore, but onto a line. For a disk with non-zero thickness, this is not the case, and therefore Eq. D.16 remains finite for an edge-on galaxy.

For a disk with finite thickness, there is no trivial way to relate the observed axis ratio q to the real one q_0 . In practice, the isophotes of a projected disk can be approximated by ellipses but with an ellipticity that depends on position, disk scale length, scale height, and inclination. Still, we expect the observed axis ratio to be 1 for a face-on galaxy, and equal to q_0 for a perfectly edge-on galaxy. For an oblate system, we can relate the observed axis ratio to the intrinsic one and the galaxy inclination i_0 as (Bottinelli et al. 1983):

$$\cos^2 i_0 = (q^2 - q_0^2)/(1 - q_0^2). \quad (\text{D.17})$$

Technically, the isodensity surfaces of a double exponential profile are not oblate but have a biconical shape, which means that Eq. D.17 is only an approximation of the real dependence of the observed axis ratio on q_0 and inclination. In Sect. 4.1 we fitted 2D profiles of galaxies using a bulge-disk decomposition, assuming that the disk is exponential with zero thickness. Its apparent central surface density is therefore given by Eq. D.14

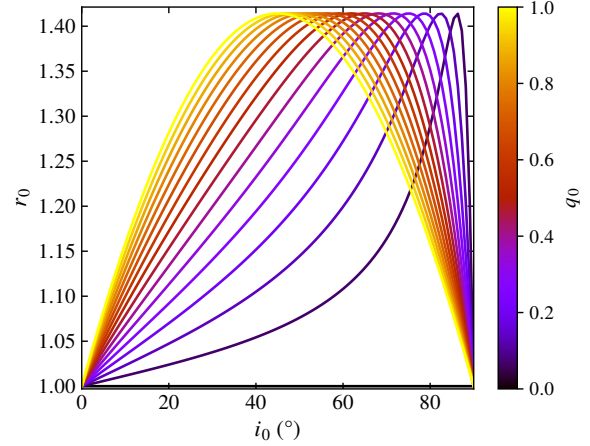


Fig. D.2. Ratio of the central density assuming a double exponential profile with that derived assuming a razor-thin disk exponential fit as a function of the galaxy's real inclination, i_0 , and intrinsic axis ratio, $q_0 = h_z/R_d$, with R_d the disk scale length. The maximum value is equal to $\sqrt{2}$ and is reached at $i_0 = \arctan(1/q_0)$.

with i the apparent inclination related to the observed axis ratio through Eq. D.15. If the stellar disk 3D distribution is actually described by a double exponential profile, then its apparent central surface density given by Eq. D.16 must match that of the fitted single exponential profile. Using Eq. D.17 to express the apparent inclination in terms of the real inclination i_0 and intrinsic axis ratio q_0 , we can derive the ratio r_0 of the central surface density computed using a double exponential profile against that computed from a single exponential fit as

$$r_0 = \frac{q_0 \sin i_0 + \cos i_0}{\sqrt{q_0^2 \sin^2 i_0 + \cos^2 i_0}}. \quad (\text{D.18})$$

The ratio of the central surface densities is plotted in Fig. D.2 as a function of the intrinsic axis ratio and real inclination. The central surface density derived in the case of a disk with non-zero thickness is always larger than its infinitely thin disk counterpart, the ratio reaching a maximum

$$\max_{i_0} r_0 = \sqrt{2} \quad (\text{D.19})$$

at $i_0 = \arctan(1/q_0)$. As is expected, when the disk becomes more and more flattened, the ratio reaches unity. Similarly, when the galaxy is viewed face-on, the central surface densities for both models are equal.

D.5. Correction in the inner parts

The Bovy approximation to the rotation curve of a double exponential profile given by Eq. D.12 has the disadvantage of reaching a null velocity as soon as the correction term on the right-hand side becomes larger than the velocity of the razor-thin disk that appears in the equation, that is, at $R > 0$. However, the real rotation curve would reach a null velocity at $R = 0$ if one integrates it numerically. The impact of using Eq. D.12 would be small since we lack the resolution in our MUSE data to model precisely the velocity in the inner parts and because beam-smearing strongly affects the velocity field near the centre. Nevertheless, it can be useful to slightly modify it in order to

have a rotation curve that behaves more physically in the inner parts.

To do so, we decided to replace the rotation curve for the double exponential profile near the centre with the tangential line to Bovy approximation, which passes through $R = 0$. This means that the rotation curve will behave linearly in the inner parts until it reaches the tangential point where Bovy approximation will take over. With R_0 the radius at which the corresponding tangential line passes through the point $R = 0$, the tangent must obey the following equation:

$$\frac{dV_d}{dR}(R_0) \times R = V_d(R_0) \times R/R_0. \quad (\text{D.20})$$

Defining $y = R/(2R_d)$ and $y_0 = R_0/(2R_d)$, this simplifies to

$$y_0 \times \frac{dV_d^2}{dy}(y_0) = 2V_d^2(y_0), \quad (\text{D.21})$$

with the derivative of V_d^2 given by

$$\begin{aligned} \frac{dV_d^2}{dy}(y_0) &= V_d^2(y_0)/y_0 + \\ &\alpha y_0 \left[f^2(y_0) + y_0 \frac{df^2}{dy}(y_0) + 2q_0 e^{-2y_0} \right], \end{aligned} \quad (\text{D.22})$$

where f is defined in Appendix D.2 and $\alpha = 4\pi GR_d Y \Sigma_{\text{RT}}(0)$. Furthermore, the derivative of f^2 is given by

$$\frac{df^2}{dy}(y_0) = 2I_1(y_0)K_0(y_0) + 2I_1(y_0)K_1(y_0)/y_0 - 2I_0(y)K_1(y_0). \quad (\text{D.23})$$

Thus, combining everything together, the equation one needs to solve to find $y_0 = R/R_d$ as a function of the disk thickness q_0 is

$$y_0^2 [I_1(y_0)K_0(y_0) - I_0(y_0)K_1(y_0)] + y_0 I_1(y_0)K_1(y_0) + q_0 (y_0 + 0.5) e^{-2y_0} = 0. \quad (\text{D.24})$$

Equation D.24 was solved numerically for a range of q_0 values and was then fitted by a polynomial function of degree five in order to get an analytical approximation of y_0 as a function of q_0 . We found that the best polynomial fit is given by

$$y_0 = 0.76679 + 0.86230q_0 - 0.13703q_0^2 - 0.02308q_0^3 + 0.00452q_0^4 + 0.00102q_0^5, \quad (\text{D.25})$$

and we show in Fig. D.3 the relative error on $y_0 = R/R_d$ between the analytical approximation given by Eq. D.25 and the numerical solution as a function of the disk thickness.

D.6. Stellar bulge

Galaxy bulges can be described by various 3D distributions such as Plummer or Jaffe profiles (Plummer 1911; Jaffe 1983), but the most interesting one remains the Hernquist profile (Hernquist 1990),

$$\rho_M(r) = \frac{M_b}{2\pi} \frac{a}{r} (r+a)^{-3}, \quad (\text{D.26})$$

with M_b the total bulge mass and a a scale radius related to the half-mass size $r_{1/2,M}$ through the relation $a = r_{1/2,M}/(1 + \sqrt{2})$. In the case of a light distribution, the total bulge mass M_b is

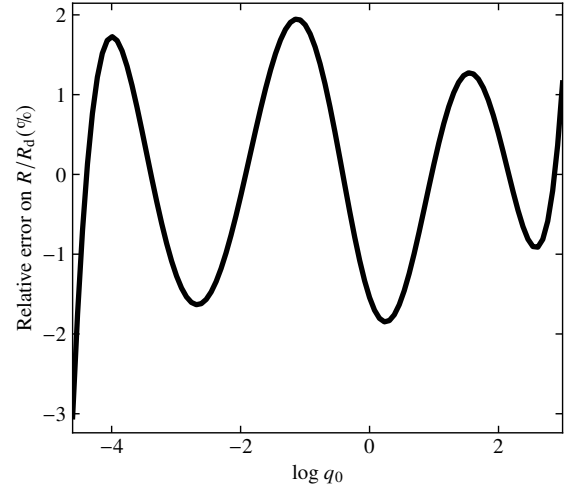


Fig. D.3. Relative error on R/R_d between the numerical solution of Eq. D.24 and the analytical approximation given by Eq. D.25 as a function of the disk thickness, q_0 . In the range of disk thicknesses we are interested in, the error does not exceed 2%.

replaced by the total bulge flux $F_b = M_b/Y$. This profile has the advantage of being spherically symmetric, with analytical forms of its gravitational potential and circular velocity, while having a line of sight projected surface density close to a de Vaucouleurs profile, except towards the inner parts. Therefore, describing the bulge 3D mass distribution as an Hernquist profile seems to be the most relevant choice. The circular velocity can be written as

$$V_b(r) = 2V_{b,\text{max}} \sqrt{ar} (a+r)^{-1}, \quad (\text{D.27})$$

where $V_{b,\text{max}} = 0.5 \times \sqrt{GYF_b/a}$ is the maximum circular velocity reached at a radius $r = a$.

D.7. Hernquist - de Vaucouleurs mapping

To compute the rotation curve of the bulge component, one needs to map the de Vaucouleurs parameters ($\Sigma_{\text{eff,b}}, R_{\text{eff,b}}$) from GALFIT with the parameters (F_b, a) of the Hernquist model whose line of sight projected surface brightness matches best that of the Sérsic model. We generated 2500 line of sight projected Hernquist models on a $\log_{10} a - \log_{10} F_b$ grid in the ranges $-1 \leq \log_{10} a/\text{kpc} \leq 1$ and $-4 \leq \log_{10} F_b/10^{-20} \text{ erg s}^{-1} \text{ \AA}^{-1} \leq 6$, and for each model, a de Vaucouleurs profile was fitted by minimizing the root mean square error using the Levenberg-Marquardt algorithm. The bounds for both parameters were chosen based on previous tests that showed that these values correspond to the typical sizes and surface brightnesses we have in our HST data. After inspection, it seems that the Hernquist parameters can be mapped to the Sérsic ones through the two following scaling relations:

$$\log_{10} a [\text{kpc}] = \alpha_a + \beta_a \log_{10} R_{\text{eff,b}} [\text{kpc}] \quad (\text{D.28})$$

$$\log_{10} F_b/\Sigma_{\text{eff,b}} [\text{cm}^2] = \alpha_F + \beta_F \log_{10} R_{\text{eff,b}} [\text{kpc}]. \quad (\text{D.29})$$

The error on these two scaling relations is shown in Fig. D.4. While not being perfect, for typical bulge sizes around 2 kpc the error is around 5%. We find the following best-fit scaling parameters: $\alpha_a = -0.454$, $\beta_a = 0.725$, $\alpha_F = 1.194$ and $\beta_F = 1.75$. Examples of Sérsic profiles and their associated projected Hernquist profiles using Eq. D.28 and D.29 are shown in Fig. D.5. The

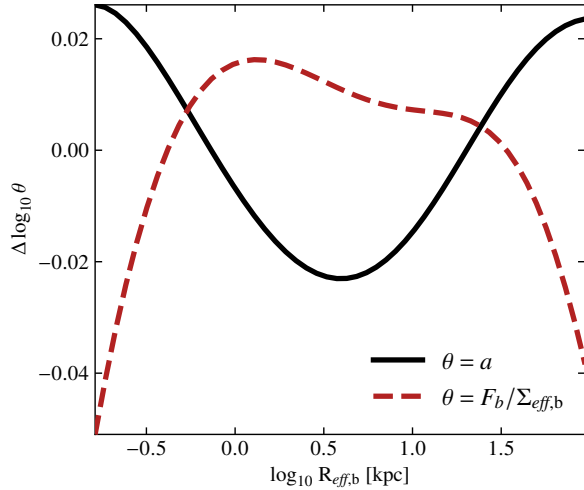


Fig. D.4. Log difference of the best-fit scaling relations from Eqs. D.28 and D.29 with the derived parameters $\theta \in \{a, F_b/\Sigma_{\text{eff},b}\}$ as a function of the bulge effective radius. The variation in the Hernquist parameters a and F_b with $R_{\text{eff},b}$ was derived by generating a grid of Hernquist models, projecting each model along the line of sight, and fitting them with de Vaucouleurs profiles. In the range of bulge sizes we are interested in, the error on the parameters is around 5%.

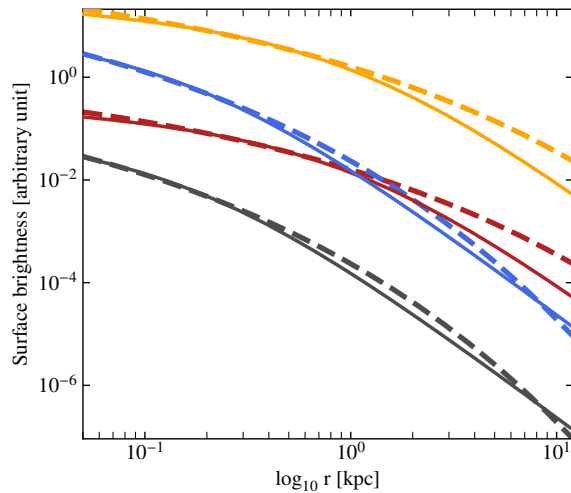


Fig. D.5. Examples of de Vaucouleurs profiles (dashed lines) and their corresponding sky projected Hernquist profiles (continuous lines) using the scaling relations in Eqs. D.28 and D.29. From top to bottom, the Sérsic parameters are $(\Sigma_{\text{eff}}, R_{\text{eff}}) = (10^{-3}, 0.5)$ (orange), $(10^{-3}, 6)$ (blue), $(0.1, 0.5)$ (red), and $(0.1, 6)$ (grey). Because the deviation of the projected Hernquist profile to the Sérsic one occurs mainly at large distances, where the surface brightness quickly drops, the overall fluxes are actually in quite good agreement.

two profiles start diverging towards large radii where the Sérsic profile drops more rapidly than the Hernquist one.

By construction, the Hernquist amplitude parameter F_b should be equal to the total de Vaucouleurs flux, but because the total flux is proportional to $R_{\text{eff},b}^2$ while F_b is proportional to $R_{\text{eff},b}^{1.75}$, in practice, this means that our parametrisation, while recovering the shape of a de Vaucouleurs profile for a broad part of the radial range, will underestimate or overestimate the real flux contribution, and therefore the maximum circular velocity

of the bulge component. Using Eq. C.1, D.29 and D.27, we can derive the error on $V_{b,\text{max}}$ as a function of the de Vaucouleurs parameters

$$\Delta V_{b,\text{max}}/V_{b,\text{max}}(F_{\text{tot}}) = 0.5 \left[1.174 \left(R_{\text{eff},b}/\text{kpc} \right)^{-0.125} - 1 \right], \quad (\text{D.30})$$

where $\Delta V_{b,\text{max}} = V_{b,\text{max}}(F_b) - V_{b,\text{max}}(F_{\text{tot}})$, with $V_{b,\text{max}}(F_b)$ and $V_{b,\text{max}}(F_{\text{tot}})$ the maximum circular velocities from Eq. D.27 using the Hernquist amplitude parameter and the total de Vaucouleurs flux, respectively. Therefore, our parametrisation overestimates the bulge circular velocity for bulge sizes $R_{\text{eff},b} \lesssim 3.6$ kpc, and underestimates it beyond, with a maximum relative difference of 50% when $R_{\text{eff},b} \rightarrow \infty$. Nevertheless, these differences need to be weighted out by two facts

- (i) as can be seen in Fig. A.2, bulges mainly have radii below 1.5 – 2 kpc where the difference is mostly negligible given the uncertainties on the other parameters and the assumption of a constant mass to light ratio,
- (ii) very small bulge sizes where we may expect the largest differences to arise are in practice associated with really weak bulge contribution, that is, $\Sigma_{\text{eff},b} \sim 0$, and therefore to a negligible rotation.

D.8. Dark matter halo

Apart from the baryonic disk and bulge components, we also model the galaxies DM halo with an NFW profile (Navarro et al. 1995),

$$\rho(r) = \delta_c \rho_{\text{crit}}(r/r_s)^{-1} (1 + r/r_s)^{-2}, \quad (\text{D.31})$$

where $r_s = r_{200}/c$ is the halo scale radius, with r_{200} the virial radius of the halo where the mean overdensity is equal to 200 and c the halo concentration, $\rho_{\text{crit}} = 3H_0^2/(8\pi G)$ the Universe closure density and δ_c the halo characteristic overdensity (Navarro et al. 1996). The associated circular velocity is given by

$$V_h(r) = \frac{V_{h,\text{max}}}{0.46499} \left[\frac{\ln(1 + r/r_s)}{r/r_s} - \frac{1}{1 + r/r_s} \right]^{1/2}, \quad (\text{D.32})$$

where $V_{h,\text{max}}$ is the maximum rotation velocity reached at a radius $r \approx 2.163r_s$.

Appendix E: Sky projection of a double exponential profile

We consider the double exponential disk model of the form $\rho_d(\mathbf{r}) = \rho_d(R, z)$ with R the radius in the plane of the disk and z the direction orthogonal to the disk. We define three new coordinates, (x', y', z') , such that $(x', y', 0)$ corresponds to the plane of the sky (see Fig. E.1). Furthermore, the axis defined by $x = x'$ corresponds to the intersection between the plane of the disk and the plane of the sky. Computing the surface density of the inclined 3D distribution at position (x', y') on the plane of the sky amounts to solving the following integral:

$$\Sigma_d(x', y') = \int_{\mathbb{R}} dz' \rho_d(R, z). \quad (\text{E.1})$$

Therefore, one must write R and z as functions of x', y' and z' . To do so, we define r , the distance of a point in the (y', z') plane, and θ , the angle between the r axis and y' , where θ is an oriented angle that varies between $-\pi/2$ and $\pi/2$. We have

$$y' = r \cos \theta, \quad z' = r \sin \theta, \quad (\text{E.2})$$

$$y = r \cos(\theta - i), \quad z = r \sin(\theta - i). \quad (\text{E.3})$$

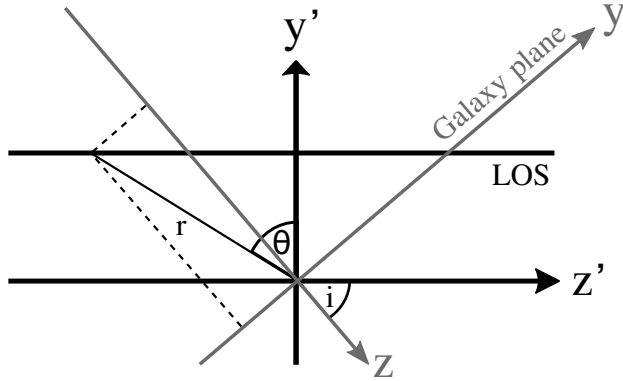


Fig. E.1. Geometry of the line of sight integration problem. For each point (x', y') in the plane of the sky, the 3D density disk distribution $\rho_d(x, y, z)$ must be integrated along a line of constant $R' = (x'^2 + y'^2)^{1/2}$. The angle θ is oriented such that it is positive for $z' > 0$ and negative otherwise.

Since the integral is computed along a line of constant y' , we can plug Eq. E.2 into Eq. E.3 after developing the cosine and sine terms to get

$$y = z' \sin i + y' \cos i, \quad (\text{E.4})$$

$$z = z' \cos i - y' \sin i. \quad (\text{E.5})$$

Using the expression for the double exponential profile (see Eqs. D.7 and D.10) we get

$$\Sigma_d(x', y') = \frac{\Sigma_d(0, 0)}{2h_z} \int_{\mathbb{R}} dz' \exp \left\{ -\frac{\sqrt{x'^2 + (z' \sin i + y' \cos i)^2}}{R_d} \right.$$

$$\left. -\frac{|z' \cos i - y' \sin i|}{h_z} \right\}. \quad (\text{E.6})$$

We can simplify this integral by making the change of variable $v = y/R_d$ and by defining the following parameters:

$$\alpha = x/R_d, \quad (\text{E.7})$$

$$\beta = (q_0 \tan i)^{-1}, \quad (\text{E.8})$$

$$\gamma = \frac{y'}{h_z} (\sin i + \cos^2 i / \sin i), \quad (\text{E.9})$$

with $q_0 = h_z/R_d$ the intrinsic axis ratio of the galaxy. The integral becomes

$$\Sigma_d(x', y') = \frac{\Sigma_d(0, 0)}{2q_0 \sin i} \int_{\mathbb{R}} dv \exp \{-\sqrt{\alpha^2 + v^2} - |\beta v - \gamma|\}. \quad (\text{E.10})$$

The original problem of solving Eq. E.1 for the double exponential profile required 6 free parameters, namely x' , y' , $\Sigma_d(0, 0)$, R_d , h_z and i , with $\Sigma_d(0, 0)$ only acting as an amplitude parameter, but Eq. E.10 reduces the dimensionality of the problem to 3 free parameters only to compute the integral. In the general case, there is no straightforward analytical solution or numerical approximation to the integral above, though a solution can be derived along the y' axis when $x = 0$:

$$\begin{aligned} \Sigma_d(0, y') &= \frac{\Sigma_d(0, 0)}{2q_0 \sin i} \int_{\mathbb{R}} dv \exp \{-|v| - |\beta v - \gamma|\} \\ &= \frac{\Sigma_d(0, 0)}{q_0 \sin i} \frac{e^{-\gamma} - \beta e^{-\gamma/\beta}}{1 - \beta^2}. \end{aligned} \quad (\text{E.11})$$

Appendix F: MAGIC catalogue
Table F.1. Column description of the MAGIC catalogue, which contains morpho-kinematics and physical parameters for the MS sample of 447 galaxies.

No.	Title	Description
1	ID	MUSE galaxy ID in the form X-CGRY, where X refers to the galaxy identification number within the field targeting COSMOS group CGRY
2	z	Spectroscopic systemic redshift derived from kinematics modelling
3	RA	J2000 Right Ascension of morphological centre in decimal degrees
4	Dec	J2000 Declination of morphological centre in decimal degrees
5	N	Number of galaxies in structures with more than three members
6	Reffd	Disk effective radius in kpc ($R_{\text{eff,d}}$)
7	Reffb	Bulge effective radius in kpc ($R_{\text{eff,b}}$)
8	Reff	Global effective radius in kpc (R_{eff})
9	logBD	Logarithm of the bulge-to-disk ratio at R_{eff}
10	q	Axis ratio of the disk (q)
11	PAm	Morphological position angle of the major axis in degrees
12	FWHM	Median PSF FWHM, corresponding to narrow band [O II] MUSE observations in arcsecond
13	OIIflux(R22)	[O II] flux derived from MUSE flux maps at $R_{22} = 1.311 \times R_{\text{eff,d}}$ in $10^{-21} \text{ erg s}^{-1} \text{ cm}^{-2}$
14	OIIflux	[O II] flux derived from MUSE flux maps at $3''$ in $10^{-21} \text{ erg s}^{-1} \text{ cm}^{-2}$
15	SNR	Total [O II] signal-to-noise ratio ($(S/N)_{\text{tot}}$)
16	i	Disk inclination corrected for thickness in degrees (i)
17	PAk	Kinematics position angle of the major axis in degrees
18	rs	NFW halo scale radius in kpc (r_s)
19	Vhmax	Maximum rotation velocity of the NFW rotation curve in km s^{-1} ($V_{\text{h,max}}$)
20	Vr22	Rotation velocity at R_{22} in km s^{-1} (V_{22})
21	sigma	Median velocity dispersion in km s^{-1} (σ_V)
22	Vc22	Corrected rotation velocity at R_{22} in km s^{-1} ($V_{c,22}$)
23	logM*	Logarithm of the stellar mass (M_{\star} / M_{\odot}) within an aperture of $3''$
24	logM*(R22)	Logarithm of the corrected stellar ($M_{\star,\text{corr}} / M_{\odot}$) inside R_{22}
25	logSFR	Logarithm of the SFR ($\text{SFR} / [M_{\odot} \text{ yr}^{-1}]$) at $3''$ using Gilbank et al. (2010, 2011) prescription
26	logMg	Logarithm of the gas mass (M_g / M_{\odot}) computed from the Schmidt-Kennicutt law and [O II] flux measured at R_{22}
27	logMdyn	Logarithm of the dynamical mass ($M_{\text{dyn}} / M_{\odot}$) computed at R_{22} from the mass model

Appendix G: Example of morpho-kinematics maps

We show below an example of a morpho-kinematics map. The maps for all the galaxies in the MS sample are sorted according to their (RA 2000, Dec 2000) coordinates and can be found online.

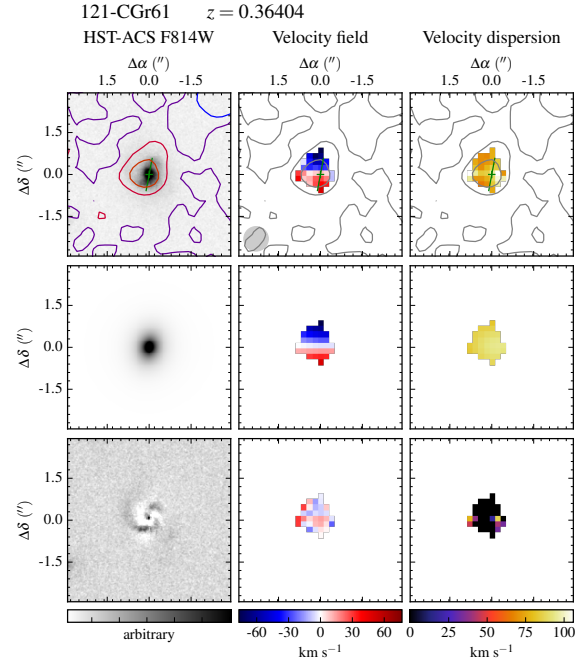


Fig. G.1. Morpho-kinematics map for galaxy 121-CGr61. From top to bottom and left to right: HST-ACS image, GALFIT model, HST residuals, CAMEL velocity field, MOCKING velocity field model, velocity field residuals, CAMEL velocity dispersion map, MOCKING beam smearing model (including spectral resolution broadening), and beam smearing and LSF corrected velocity dispersion map. The morpho-kinematics centre and the morphological PA are shown in the HST image and the CAMEL maps as a green cross and a green line whose length corresponds to R_{22} , respectively. The PSF FWHM is indicated as the grey disk in the velocity field. The [OII] surface brightness distribution is overlaid on top of the HST and MUSE [OII] flux maps, with contours at levels $\Sigma_{[\text{OII}]} = 2.5, 5, 10, 20, 40$ and $80 \times 10^{-18} \text{ erg s}^{-1} \text{ cm}^{-2} \text{ arcsec}^{-2}$.

Chapter 7

Angular momentum in the MAGIC survey

I present in this Chapter a nearly complete but still ongoing analysis of the angular momentum in MAGIC as a function of environment. This analysis is a follow-up study of the previous paper on major scaling relations discussed in Chapter 6. The angular momentum is an interesting dynamical tracer because it combines in one parameter the morphology and the kinematics of the galaxies. In [Mercier et al. \(2022\)](#), I showed that galaxies in MAGIC seem morphologically affected by the environment but that their kinematics is similar to that of the field galaxies at the same redshift. Therefore, it seemed interesting to see how this would translate into the angular momentum. Besides, not so many studies have tried to probe the impact of the environment on the angular momentum. One of the most recent is that of [Pelliccia et al. \(2019\)](#) where it was found that galaxies in structures have a deficit of roughly 1 dex in angular momentum at fixed stellar mass compared to galaxies in the field at the same redshift.

The advantages of MAGIC compared to other samples are similar to those already discussed for my first paper in Chapter 6: (i) I have a large and, most importantly, homogeneous sample of field galaxies and galaxies located in structures at intermediate redshift with high completeness (see Chapter 3), (ii) I can probe low-mass galaxies, and (iii) I can benefit from the high data quality offered by MUSE and HST. Also, as discussed in [Mercier et al. \(2022\)](#), because I apply the same method and the same sample selection for all the galaxies in the sample, any systematics that may arise are reduced to their minimum when comparing field galaxies to those in structures.

The analysis of the stellar angular momentum in MAGIC is not entirely complete yet. For the moment, a lot of efforts have been put into trying to improve as much as possible the sample selection and in deriving the stellar angular momentum as precisely as possible. On that particular point, my efforts have been aimed at using the galaxies' HST high-resolution images to alleviate the approximation of axisymmetry that is typically made in similar studies. Nevertheless, a full preliminary analysis with its associated early conclusion is presented in what follows.

Already a lot of verifications and variations of some figures and selection criteria have been tested to assess the strength of the current results, but there is still some remaining work before the paper is complete. First, I do not provide at the moment any discussion regarding the location of the small galaxies with respect to the selected sample. It would be interesting to see how these galaxies relate to V/σ , as was done in [Bouché et al. \(2022\)](#) for the angular momentum of the

ionised gas. In particular, a more thorough discussion regarding the visible bending of the Fall relation at the high-mass end would be needed, especially given that, to my current knowledge, it is not seen in the local Universe. From this first investigation, it might look like the effect of the environment might not be enough to explain this apparent bending. Furthermore, so far I have only focussed on the angular momentum evaluated at R_{22} which is the location where the disk's velocity peaks. However, this radius is not necessarily special, for instance because galaxies have a DM component and so their rotation curve might continue to rise beyond. Besides, it might also be interesting to probe the angular momentum at lower radii, that is closer to the bulge, as that there might be some interplay between the bulge fraction, the angular momentum, and the environment. There are also a few additional efforts that must be put into interpreting the change of shape of the Fall relation when integrating or not the bulge component. Already in [Mercier et al. \(2022\)](#), we had had the idea to implement a toy model to physically interpret the variations in zero point of the different scaling relations. In the end, we did not implement it into the analysis of the scaling relations, but now that we have the angular momentum on top of more precise estimates of the galaxies' environment, a possibility is to further develop this toy model to apply it to the Fall relation to better constrain the effect of the environment. All these ideas will not require tremendous efforts and will definitely bring more insights into our current results.

Impact of the environment on the angular momentum of $z \sim 0.25 - 1.5$ galaxies in the MAGIC survey[★]

W. Mercier^{1,★★}, B. Epinat^{2,3}, T. Contini¹, and MUSE collaboration

¹ Institut de Recherche en Astrophysique et Planétologie (IRAP), Université de Toulouse, CNRS, UPS, CNES, 31400 Toulouse, France

² Aix Marseille Univ, CNRS, CNES, LAM, Marseille, France

³ Canada-France-Hawaii Telescope, CNRS, 96743 Kamuela, Hawaii, USA

Received ; accepted

ABSTRACT

Aims. Group and cluster environments are thought to impact galaxy properties at intermediate redshift. Among these properties, the angular momentum is a useful proxy to trace environmental effects when the galaxies are infalling into their host structure.

Methods. We derive robust estimates of the angular momentum using Hubble Space Telescope images combined with spatially resolved kinematics from the Multi-Unit Spectroscopic Explorer for a sample of roughly 200 galaxies in groups, clusters, and in the field drawn from the MAGIC survey. Using various environmental tracers, we study the shape of the angular momentum-stellar mass (Fall) relation as a function of environment. We also study the impact of bulges on the angular momentum estimate.

Results. We find a significant impact of the environment on the zero-point of the Fall relation (0.12 dex without cut and 0.08 dex with mass and redshift cuts) consistent with galaxies in structures being depleted in angular momentum at fixed stellar mass. This effect seems driven by massive galaxies that are found in the densest regions of the structures and does not seem to correlate with their bulge fraction.

Conclusions. We find that galaxy groups and clusters at $z \sim 0.7$ seem on average to deplete their galaxy member's angular momentum with respect to the field. However, the lack of a current comparable sample of massive field galaxies prevent us from drawing clear conclusions. At the moment, we cannot eliminate the possibility that the observed zero point offsets are not mass-driven.

Key words. Galaxies: evolution – Galaxies: kinematics and dynamics – Galaxies: clusters: general – Galaxies: groups – Galaxies: high-redshift

1. Introduction

In the current paradigm of galaxy evolution, galaxies are expected to form through the condensation of baryons in the centres of DM haloes where, because of external tidal torques, the gas in the proto-galaxy acquires angular momentum before condensing into a disk and forming stars (e.g. Peebles 1969; Fall & Efstathiou 1980). The same is true for Dark Matter (DM) haloes that also acquire angular momentum during their linear phase of structure growth (e.g. Doroshkevich 1970; White 1984). Initially, it was thought that the angular momentum of the baryons (e.g. stars or gas) traces that of the DM component. However, recent simulations have shown that this picture is not entirely correct with processes that can either add or remove angular momentum independently of the halo and proto-galaxy early formation phase (e.g. Genel et al. 2015). For instance, there is strong evidence supporting the fact that galaxies must have smoothly accreted large amounts of cold gas from their circumgalactic medium (CGM) to sustain high values of star formation rate (SFR) across cosmic time (e.g. Bouché et al. 2013, 2016; Zabl et al. 2019). This accretion of fresh gas takes place predominantly in the disk plane of late-type galaxies and thus can

not only drive their star formation history but also the angular momentum growth of their baryonic component (e.g. Danovich et al. 2015; Cadiou et al. 2022). Similarly, feedback processes such as galactic winds have also been found as potential mechanisms to increase the angular momentum of the baryons in a galaxy (e.g. DeFelippis et al. 2017). In addition, galaxy mergers can also substantially redistribute angular momentum either by increasing that of the DM halo (e.g. Hetzner & Burkert 2006), or by redistributing the mass and thus either increasing the angular momentum of the baryons (e.g. Genel et al. 2015; Jiang et al. 2019) or increasing it if the spins of the two galaxies are aligned prior to the merger (e.g. Lagos et al. 2018).

Numerous studies have tried to constrain the angular momentum of the stellar and gas components in galaxies at various redshifts since the seminal work of Fall (1983) by studying the angular momentum-stellar mass relation, also known as the Fall relation. In the local Universe, some of these studies have focussed on the shape of the relation as a function of galaxy type (e.g. Fall 1983; Romanowsky & Fall 2012; Cortese et al. 2016; Rizzo et al. 2018), stellar mass (e.g. Posti et al. 2018; Di Teodoro et al. 2021), cold gas fraction (e.g. Mancera Piña et al. 2021b), or bulge fraction (e.g. Obreschkow & Glazebrook 2014; Fall & Romanowsky 2018). The general conclusion that can be drawn is that, in the local Universe, galaxies populate the Fall relation that can be described as a single linear relation in log-log space (i.e. no deviation at higher or lower stellar masses). The scatter of the Fall relation seems to be mainly driven by their

[★] Based on observations made with ESO telescopes at the Paranal Observatory under programs 094.A-0247, 095.A-0118, 096.A-0596, 097.A-0254, 099.A-0246, 100.A-0607, 101.A-0282, 102.A-0327, and 103.A-0563.

^{★★} e-mail: wilfried.mercier@irap.omp.eu

morphology, with ellipticals and disk galaxies with prominent bulges located below the relation followed by disk galaxies. The Fall relation has also been studied at higher redshift ($z \sim 1 - 2$, e.g. Burkert et al. 2016; Swinbank et al. 2017; Harrison et al. 2017; Bouché et al. 2021) where it is found to hold but with a lower zero-point that is consistent with galaxies gaining angular momentum with cosmic time. Interestingly, a recent analysis by Bouché et al. (2021) pointed out that there is a correlation between the zero-point of the Fall relation of the ionised gas and the dynamical state of the galaxies in the sense that dispersion dominated systems are located below the Fall relation of rotationally supported galaxies. This result was actually observed on a few other studies before (e.g. Contini et al. 2016; Burkert et al. 2016) and is consistent with the separation observed in the local Universe between spirals and ellipticals (e.g. Romanowsky & Fall 2012).

From a methodological perspective, simulations put aside, measuring the angular momentum in galaxies is not simple since it requires to know the full 3D mass distribution (stars, gas, and DM) as well as the amplitude and orientation of the velocity vector at each position in the galaxy. Hence, given the impossibility to derive the "true" angular momentum, proxies have been used in the literature that rely on various assumptions. The most common is that the gas and the stars are located in a disk that is dynamically stable because of its own rotation. With a few additional assumptions on the stars or gas kinematics and on the mass distribution in the disk, it is possible to derive the Romanowsky & Fall (2012, hereafter RF12) approximation that is widely used in the literature (e.g. Romanowsky & Fall 2012; Contini et al. 2016; Burkert et al. 2016; Swinbank et al. 2017; Rizzo et al. 2018). Though already mentioned in Romanowsky & Fall (2012) and in subsequent studies, a recent discussion was given in Bouché et al. (2021) where it is shown that, depending on the location where the angular momentum is measured, the RF12 estimator can overestimate the angular momentum by nearly 20%. Hence, because of that effect and of the increasing number of robust kinematics measurements throughout the last ten years, authors have started using more general estimates. Some have chosen to consider an axisymmetric disk model (typically exponential) and either to numerically integrate the expression of the angular momentum for a rotating disk galaxy (e.g. Posti et al. 2018; Bouché et al. 2021; Mancera Piña et al. 2021a,b) or by substituting the integral with a sum (e.g. Rizzo et al. 2018). Cortese et al. (2016) also proposed an interesting method slightly different from those previously mentioned in the sense that the numerical integration of the angular momentum is performed by summing the contribution of each spatial pixel (spaxel) in a data cube obtained through 3D spectroscopy. The advantage of such a method is that it alleviates the assumption of axial symmetry since the observed flux distribution is directly taken into account. However, its main drawback is that it suffers from the usually poor spatial resolution of 3D spectroscopic observations compared to high spatial resolution images obtained for instance by the Hubble Space Telescope (HST).

Finally, a few studies have tried to probe the impact of the environment on the galaxies' angular momentum (e.g. Pelliccia et al. 2019; Pérez-Martínez et al. 2021). The current picture that seems to emerge is that galaxies found in galaxy groups and galaxy clusters at $z \sim 1$ seem to have a deficit of angular momentum with respect to field galaxies located at the same redshift. Because physical mechanisms can affect the angular momentum of the baryons in different ways (i.e. increase or decrease it), an interpretation given in Pelliccia et al. (2019) is that this reduction of angular momentum at fixed stellar mass

could be due to galaxy mergers, in line with their prevalence in dense environments and with recent simulations (e.g. Lagos et al. 2018). However, these results were obtained on moderately large galaxy samples and they required to compare galaxies from different surveys/instruments (e.g. Pérez-Martínez et al. 2021) to reach these conclusions. As in Abril-Melgarejo et al. (2021) and Mercier et al. (2022), we argue that there might be systematic effects when doing so, mainly driven by different selection functions between different datasets. In this analysis, we propose to study the impact of the environment on the stellar angular momentum of galaxies in the MUSE-gAlaxy Groups In Cosmos (MAGIC) survey (Epinat et al., in prep.). As shown in Mercier et al. (2022), this survey is ideal to probe the environmental impact on galaxy dynamics at $z \sim 1$ because of the fact that we observe at the same time galaxies located in structures of varying density (i.e. galaxy groups and galaxy clusters) and foreground and background galaxies located in the field.

This paper is structured as follows. In Sect. 2, we give a brief description of the MAGIC sample, the HST and MUSE observations, how we performed the morphological and kinematics modellings, and how we characterised the galaxies' environment. More importantly, we also describe the sample selection used to study the angular momentum. In Sect. 3, we describe the method used to derive the angular momentum using HST images. Afterwards, we perform the analysis of the Fall relation in Sect. 4, where we first assess the reliability of our method in Sect. 4.1, then we study the impact of the environment without taking into account the contribution of bulges in Sect. 4.2, and finally we discuss the impact of bulges on the shape of the Fall relation and their link to the galaxies' environment in Sect. 4.3. Throughout this paper, we assume a Λ cold dark matter cosmology with $H_0 = 70 \text{ km s}^{-1} \text{ Mpc}^{-1}$, $\Omega_M = 0.3$, and $\Omega_\Lambda = 0.7$.

2. Sample selection and main properties

The sample used in this analysis is part of the MAGIC survey (Epinat et al., in prep.), a deep Multi-Unit Spectroscopic Explorer (MUSE) Guaranteed Time Observation (GTO) survey targeting 15 structures in the Cosmic Evolution Survey (Cosmos) area (Scoville et al. 2007) with 17 different MUSE pointings. The main goal is to study the impact of the environment on the properties of galaxies at intermediate redshift by combining multi-band photometry, in particular Hubble Space Telescope Advanced Camera for Surveys (HST-ACS) observations (Koeke-moer et al. 2007; Massey et al. 2010), with resolved spectroscopic properties from MUSE. The analysis performed in this paper is the continuation of two previous ones. The first was on the impact of the environment on the Tully-Fisher Relation (TFR) for a subsample of group galaxies (Abril-Melgarejo et al. 2021). The second focussed on the impact of the environment on various scaling relations such as the size-mass relation, the Main Sequence relation (MS), and the TFR for the full MAGIC sample by comparing between galaxies located in the field and those found in small and large groups (Mercier et al. 2022). We summarise the main observations and their characteristics below and we refer the reader to Epinat et al. (in prep.) for a complete description of the MAGIC survey.

2.1. Observations and physical parameters

The basis of the observations are 17 different MUSE data and variance cubes with a spatial sampling of $0.2''$ and a spectral sampling of 1.25 \AA over a spectral range ranging from 4750 \AA

to 9350 Å. Observing strategy and data reduction are fully described in Mercier et al. (2022) and Epinat et al. (in prep.). The MUSE Line Spread Function (LSF) was modelled with a second order polynomial function as in Bacon et al. (2017) and Guérou et al. (2017) and the MUSE Point Spread Function (PSF) was modelled by extracting 100 Å wide narrow-band images of stars in each MUSE field and by fitting them with a Moffat profile with free β index. The wavelength dependence of the PSF Full Width at Half Maximum (FWHM) was then derived field-by-field by fitting a linear relation to the median curve and the β parameter as the mean value of the various measurements weighted by their uncertainties.

The median value of the MUSE PSF FWHM for the 17 fields is 0.67'' at 4000 Å and 0.53'' at 8000 Å which correspond respectively to 4.8 kpc and 3.8 kpc at $z = 0.7$. Apart from the MUSE data we also have HST images that were used to model the galaxies' morphology. To that end, we used 4'' × 4'' stamps in the F814W filter since it provides the best spatial resolution possible (PSF FWHM below 0.1'', pixel scale of 0.03''). Similarly to what was done with MUSE, the HST PSF was measured by fitting a Moffat profile onto 27 non saturated stars found in the MUSE fields and by deriving the median profile. The final parameters used for the morphological modelling are $\text{FWHM}_{\text{HST}} = 0.0852''$ and $\beta = 1.9$.

Additionally, the two main physical parameters of interest for the previous analyses and for this one are the galaxies' stellar mass and star formation rate (SFR). They were derived from Spectral Energy Distribution (SED) fitting performed with the Code Investigating GALaxy Emission (CIGALE, see Boquien et al. 2019) using Bruzual & Charlot (2003) single stellar populations (SSPs) with a Salpeter (1955) initial mass function (IMF) and a single metallicity value of 0.02 dex, a truncated delayed exponential star formation history (SFH, described in Ciesla et al. 2018, 2021), and a Charlot & Fall (2000) attenuation law with a total to selective extinction ratio $R_V = 3.1$. More details about the grid of parameters and the choice of models will be given in Epinat et al. (in prep.). We note that these two parameters were derived differently in the previous papers. In Abril-Melgarejo et al. (2021), the stellar mass and SFR were derived from SED fitting performed with FAST. In Mercier et al. (2022), only the stellar mass from FAST was used and the SFR was derived from the Kennicutt (1992, 1998) law using the [O II] flux measured in the MUSE cubes in 3'' apertures after correcting for Galactic and intrinsic extinction using the Gilbank et al. (2010, 2011) prescription. Overall, we find consistent stellar masses within 0.5 dex when above $10^8 M_\odot$ and slightly larger differences below this value. Additionally, CIGALE tends to find on average larger stellar masses than FAST by roughly 0.05 dex, probably because of differences in the IMF or the SFH used.

2.2. Dynamical modelling

A complete dynamical modelling for the entire [O II] emitters sample in the MAGIC survey was done in Mercier et al. (2022). In this analysis, we define as the [O II] emitters sample galaxies that are found in the range $0.2 < z < 1.5$. Furthermore, those for which the [O II] doublet is indeed detected in the MUSE data form the kinematics sample, since we can use their [O II] doublet to extract the ionised gas kinematics. In what follows, we quickly summarise the main steps and in particular we emphasize what has changed since the previous analysis performed in Mercier et al. (2022). A complete description for the morpholog-

ical and kinematics modelling can be found in Sect. 4.1 and 5.1 of Mercier et al. (2022).

Starting from an initial sample of 1142 [O II] emitters, the first step was to model the galaxies' morphology. To that hand, bulge-disk decompositions were performed with GALFIT (Peng et al. 2002) using an exponential disk model for the disk component and a circular de Vaucouleur profile for the bulge. Initially, among the 1142 [O II] emitters 890 could be modelled with GALFIT. For each galaxy various morphological parameters were derived: (i) the effective radius R_{eff}^1 , (ii) the bulge-to-total flux ratio evaluated at one global effective radius (B/D), (iii) the disk major axis position angle (PA), and (iv) the apparent disk axis ratio $q = b/a$, with a and b the major and minor axes, respectively. In Mercier et al. (2022), we introduced two expressions to correct the central surface brightness of the disk, $\Sigma_{\text{d,bos}}(0)$, and the observed axis ratio q of the galaxy for the finite thickness of the disk. The average redshift dependence of the disk thickness q_0 was evaluated thanks to the method presented in Heidmann et al. (1972) and Bottinelli et al. (1983). The central surface brightness of the disk was then corrected assuming a double exponential 3D mass distribution and the disk inclination was derived using the correction given in Bottinelli et al. (1983). In addition, because the rotation velocity that was used for the TFR in Abril-Melgarejo et al. (2021) and Mercier et al. (2022) was measured at the radius $R_{22} = 2.2R_d$ in the plane of the disk, with R_d the disk scale length, we also introduced a corrected stellar mass ($M_{\star,\text{corr}}$) so that it is also evaluated at R_{22} . The correction assumes a constant mass-to-light ratio throughout the galaxy and takes into account the effect of sky projection and PSF convolution. We refer the reader to Sects. 4.3 and 4.4 and Appendix D.4, of Mercier et al. (2022) for more details. For this analysis and after inspecting the HST images, we decided to remodel the morphology for the 17 following galaxies: 85_CGR23, 82_CGR30, 97_CGR32, 35_CGR35, 74_CGR35, 127_CGR35, 94_CGR51, 36_CGR61, 39_CGR61, 52_CGR61, 121_CGR61, 41_CGR79, 23_CGR84, 122_CGR84, 79_CGR114, 31_CGR172, and 68_CGR172. Among these galaxies, we included a logarithmic spiral pattern to the disk component, available since version three of GALFIT, for the four following galaxies: 85_CGR23, 121_CGR61, 36_CGR61, and 79_CGR114. We did so because these galaxies showed strong spiral and bar features so that their previous disk morphological model used to fit the bar rather than the extended disk. Even if the modelling of the spiral arms and of the bar is not trivial and far from perfect, we did find more robust disk parameters once these features were included, especially for the disk axis ratio and PA. Overall, the remaining 13 galaxies had a center that was slightly misaligned with the bulge component which had the effect to mildly underestimate its contribution. With the updated models, we now have better constraints on the galaxy's centre and on the parameters of the bulge component. Furthermore, after trying to redo their morphology without more success than before, we decided to remove the 22 following galaxies: (i) 12_CGR61, 24_CGR32, 26_CGR61, 29_CGR23, 54_CGR79, 76_CGR30, 76_CGR84, 76_CGR172, 89_CGR79, 240_CGR30, and 240_CGR84 because they are strongly bulge-dominated (probably elliptical) whose disks are too faint to be efficiently constrained, (ii) 55_CGR61, 66_CGR30, 67_CGR87, 73_CGR61, 75_CGR84, 76_CGR172, 79_CGR61, 82_CGR87, and 97_CGR34 because their disks are detected but with too low S/N to be properly constrained, and (iii) 79_CGR30 and

¹ This corresponds to the global effective radius that takes into account both the disk and the bulge components given by Eq. 6 of Mercier et al. (2022).

84_CGR35 because they both show complex edge-on morphologies that do not match their velocity fields. Indeed, 79_CGR30 looks like two edge-on galaxies whose major axes are aligned but with a velocity field that spans the two objects and that shows undisturbed rotation with a PA rotated by 90° with respect to the stellar components. Similarly, galaxy 84_CGR35 seems to show multiple diffuse components that might be the result of a past merger or a stripping event even though its velocity field also shows an extended rotation which is not aligned with the brightest component visible in the HST image. Therefore, the morphological and mass models for these two objects would be too uncertain to compute their angular momentum.

The second step was to extract the ionised gas kinematics using the [O II] doublet as kinematics tracer. This was performed with CAMEL² by fitting the [O II] doublet spaxel per spaxel and then cleaning the maps to remove isolated spaxels and those with large velocity discontinuities. The detailed procedure of how this was done is described in Sect. 5.1 of Mercier et al. (2022). At the end of this step 271 galaxies were removed from the morphological sample because they had no remaining spaxels with a S/N in the [O II] doublet larger than five.

The last step of the modelling was to fit the velocity fields with MocKINg³ using mass models as in Sect. 5.1 of Mercier et al. (2022) where it is discussed in detail. The main difference with what we did in our previous analysis is that we re-modelled the ionised gas kinematics for the entire kinematics sample using the updated Moffat MUSE PSF profiles in each field. As in Mercier et al. (2022), we used prior information from the morphological modelling to constrain the contribution of the stellar disk and bulge to the total rotation curve. The remaining component was modelled with a Navarro-Frenk-White (NFW) profile (Navarro et al. 1996). This last component mostly describes the Dark Matter (DM) content of the galaxies but, since we have no constraints on their amount of gas, technically speaking it also includes the contribution of the gas. Given a rotation curve, we used MocKINg to model the ionised gas velocity field using the method of line moments (Epinat et al. 2010a) assuming the gas is located in a razor-thin disk. During the fitting process we fixed the parameters related to the disk and bulge models, and we fixed the centre and the inclination in order to remove degeneracies. Thus, the only free parameters are: (i) the DM halo parameters, its scale length r_s and maximum velocity $V_{h,max}$, (ii) the kinematics position angle, and (iii) the systemic redshift z_s . Once the best-fit velocity field model was found, MocKINg computed a correction map to account for the beam-smearing, an instrumental effect that increases the measured velocity dispersion where the velocity shear is large because of the smearing effect of the PSF, and removed it quadratically from the velocity dispersion map. At the end of this step, we removed four additional galaxies because they lied on the edge of the MUSE field-of-view or had signs of merger in their kinematics maps. Thus, we ended up with a kinematics sample of 571 galaxies.

2.3. Environment characterisation

The characterisation of the environment can be done in various ways, each method having its advantages and its drawbacks. For instance, the friends-of-friends (FoF) algorithm used in Knobel et al. (2012) and Iovino et al. (2016) is easy to implement but it only uses spectroscopic redshifts while the Voronoi tessellation Monte-Carlo mapping (VMC) technique discussed in

Lemaux et al. (2017, 2022) and Hung et al. (2020, 2021) combines both photometric and spectroscopic redshifts. Nevertheless, most techniques remain sensitive to the completeness of redshift measurements and the size of the studied fields.

The first step to characterise the galaxies' environment is to define the structures they belong to. This was done using a 3D FoF (as in Mercier et al. 2022) with a maximum sky projected separation of 450 kpc and a maximum line-of-sight velocity separation of 500 km s^{-1} . The location of the centre of the structures, their systemic redshift, and their dispersion σ_V are determined from the distribution of their galaxy members, and their radius is determined from their dispersion (see the survey paper Epinat et al., in prep. for more details). In this analysis we consider four different environmental tracers. The first is the simplest of all and was already used in Mercier et al. (2022): it corresponds to the richness of the structures. However, it is a quite crude tracer of the environment because it does not take into account the distribution of galaxies in the structures. The second tracer is called a global density estimator and is defined as (e.g. Noble et al. 2013; Pelliccia et al. 2019)

$$\eta = \frac{R_{\text{proj}}}{R_{200}} \times \frac{|\Delta v|}{\sigma_V}, \quad (1)$$

where R_{proj} is the projected distance of a galaxy with respect to the structure's centre, R_{200} is the radius where the density of the structure is equal to 200 times the critical density of the Universe, and Δv is the systemic velocity of the galaxy with respect to the structure. This tracer is global in the sense that it does not take into account the distribution of all the galaxies in the structures but only that of the galaxy of interest. However, it has the advantage to combine in a single parameter the distance of the galaxy and its velocity. Thus, it is interesting to probe the dynamics of the galaxy and how bound it is to its host structure.

The two last tracers are different from the others in the sense that they directly probe the density in the structures at the location of the galaxies. Both density estimates rely on the concept of Voronoi tessellations where a single cell is associated to each galaxy. A galaxy located in a low-density environment will have few neighbours and will therefore have a cell spanning a large area whereas the opposite is true for a galaxy located in a high-density environment. The density can then be calculated for each galaxy by taking the inverse of its associated cell's surface. The reason why we have two density estimates using Voronoi tessellations is because they do not take into account the same data, which can lead to slight variations in the way it is derived. The first density estimate uses the VMC approach by combining photometric redshifts from the Cosmos2015 catalogue of Laigle et al. (2016) and spectroscopic redshifts from zCOSMOS (Lilly et al. 2007) and VUDS (Le Fèvre et al. 2015). Using this method to derive the density of the structures has the advantage that it combines into a probabilistic model both photometric and spectroscopic redshifts that are sampled quite homogeneously throughout the Cosmos field. The method works by producing 100 Monte-Carlo realisations of the redshift distribution where the redshift of each galaxy is randomly assigned given their photometric or spectroscopic redshift and the associated uncertainty. For each realisation, 750 km s^{-1} wide redshift slices are produced per step of 150 km s^{-1} in the redshift range $0.2 < z < 1.5$. For each slice, Voronoi tessellations are produced and from them we reconstruct a density grid of 75 kpc wide pixels across the field. The final density map is then constructed as the mean of the 100 Monte-Carlo realisations. Finally, because the sampling might differ from one redshift slice to another (e.g.

² <https://gitlab.lam.fr/bepinat/CAMEL>

³ <https://gitlab.lam.fr/bepinat/MocKinG>

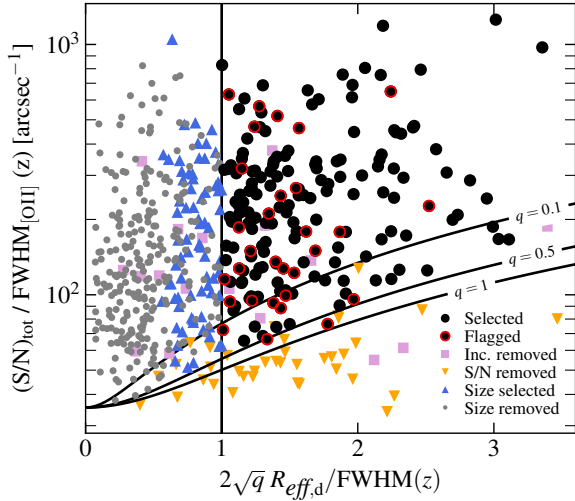


Fig. 1. Criteria used for the selection of the kinematics sample. The black points represent galaxies selected according to the surface, S/N, and inclination (removing face-on galaxies only) criteria. Removed galaxies are represented as follows and in this specific order: (i) those removed by the inclination criterion (pink squares), (ii) those removed by the S/N criterion among the remaining galaxies (orange downward pointing triangles), (iii) those removed by the surface criterion among the remaining galaxies but that would have been kept by our previous size criterion used in Mercier et al. (2022, blue upward pointing triangles), and (iv) those removed by the full selection and by our previous size criterion as well (grey dots). We also show galaxies flagged with peculiar kinematics with red contours. The vertical black line shows the surface selection criterion given in Eq. 3 and the other black lines represent the S/N selection for different disk axis ratios (see Eq.4).

due to completeness variations in spectroscopic redshifts), we rather use the overdensity parameter $\delta(z)$ defined as

$$1 + \delta(z) = \frac{\Sigma_{\text{VMC}}(z)}{\Sigma_{\text{med}}(z)}, \quad (2)$$

where $\Sigma_{\text{VMC}}(z)$ is the mean density map from the VMC method and $\Sigma_{\text{med}}(z)$ is the median of the pixels over the map, both at redshift z . The only caveat with this method is that we do not use neither the MUSE spectroscopic, nor the output of the FoF algorithm. To compensate for this problem and to take advantage of the high completeness of MUSE spectroscopic redshifts at $z < 1.5$ in the MUSE fields, we compute a second density estimate using a similar approach. For each structure detected by the FoF algorithm, we perform Voronoi tessellations using MUSE spectroscopic redshifts only and from that we derive the local density at the position of each galaxy. However, this method suffers from edge effects because galaxies on the edges of the MUSE fields or of the structures have undefined boundaries. Thus, to get more precise density estimates near the edges, we also included spectroscopic redshifts from the zCOSMOS catalogue that fall within the redshift range of the structures.

2.4. Sample selection

In Mercier et al. (2022) we showed that, depending on the scaling relation studied, different selection criteria had to be used in order to not be biased when fitting these relations. For the analysis of the TFR, we therefore had to remove bulge-dominated, small, and low S/N galaxies. Additionally, we applied two other

selections: the first in inclination and the second in stellar mass fraction. Indeed, we had to apply the three first criteria because such galaxies usually have poor constraints on their disk model, especially their half-light radius and axis ratio. Similarly, the inclination criterion was added to remove face-on galaxies whose line-of-sight kinematics is difficult to measure because of projection effects and edge-on galaxies because their mass models are much less constrained. The last selection criterion in Mercier et al. (2022) was used to select galaxies for which we might have overestimated the contribution of the stellar components to the total rotation curve. These galaxies were visually inspected and those that had consistent morphological and kinematics models (i.e. with an intrinsically high stellar mass fraction) were kept.

For this analysis, we have decided to update these selection criteria. Because each morphological model was re-inspected as part of the derivation of the angular momentum from HST maps (see Sect. 3.2) we manually picked bulge-dominated galaxies in the kinematics sample whose disk model was loosely constrained and removed them. Such galaxies will typically have very-low surface brightness disk components (below the noise level) that can either be due to substantially large magnitudes (i.e. low fluxes), or very large disk sizes that in both cases are inconsistent with the residuals image obtained when removing the bulge model from the initial HST image. These five galaxies are 24_CGR32, 29_CGR23, 240_CGR30, 240_CGR84, and 76_CGR172. Thus, in what follows, we do not apply the bulge-to-total flux ratio selection criterion as in Mercier et al. (2022). Furthermore, we also decided to update the size selection criterion. Indeed, the size selection was used to make sure that we had enough resolution elements in the MUSE kinematics maps to properly constrain the galaxies' kinematics. Thus, a criterion on the surface of the galaxy rather than on its size would be more appropriate, especially for edge-on galaxies. Therefore, in this analysis, galaxies are selected if their surface on the plane of the sky within an ellipse with major axis equal to one disk effective radius ($R_{\text{eff,d}}$) and apparent axis ratio (q) equal to that of the disk is larger than the surface of the MUSE PSF within its FWHM. Its simplified form writes

$$2\sqrt{q} \times R_{\text{eff,d}} / \text{FWHM}_{[\text{O II}]}(z) > 1, \quad (3)$$

where $\text{FWHM}_{[\text{O II}]}(z)$ is the MUSE PSF FWHM at the redshift of the galaxy and where $R_{\text{eff,d}}$ and $\text{FWHM}_{[\text{O II}]}$ must have the same unit. We remind that the $[\text{O II}]$ PSF FWHM in Eq. 3 was measured in the MUSE cubes whereas the disk effective radius and apparent axis ratio were both measured in high resolution HST images. This criterion naturally excludes galaxies with small sizes with respect to the MUSE PSF and edge-on galaxies because their axis ratio is small. Thus, we also updated the inclination criterion and only kept the part that removes face-on systems, that is we ask that the inclination follows $i \geq 25^\circ$, as in Mercier et al. (2022). This value seems a good compromise between removing galaxies that are too face-on to be well constrained and keeping a sufficiently large sample to perform the analysis. As an indication a more conservative criterion of $i > 30^\circ$ would only remove eight additional galaxies. Following the same argument, we also update the S/N criterion. In Mercier et al. (2022), we only kept galaxies that have an average S/N per spaxel of at least eight across one observed effective radius (i.e. taking into account the PSF). In this analysis, we update this criterion to take into account the ellipticity of the galaxy as follows

$$\frac{(S/N)_{\text{tot}}}{\text{FWHM}_{[\text{O II}]}(z)} \geq 20\sqrt{\pi} \left[(x^2 + 1)(qx^2 + 1) \right]^{1/4}, \quad (4)$$

where $x = 2R_{\text{eff,d}}/\text{FWHM}_{[\text{O II}]}(z)$, with $\text{FWHM}_{[\text{O II}]}(z)$ and $R_{\text{eff,d}}$ in arcsecond. We note that this new criterion, on top of being more physically motivated, actually adds 30 new galaxies that would have been removed by the previous S/N criterion. This number reduces to 15 when combined with the surface and inclination criteria. The new sample selection is shown in Fig. 1. Galaxies selected in surface, S/N, and inclination are shown in black and those removed by the selection with other symbols (one symbol per criterion). Because different criteria can remove the same galaxies, we show them in a specific order as follows: (i) galaxies removed by the inclination criterion with pink squares, (ii) among the remaining galaxies, those removed by the new S/N criterion with orange downward pointing triangles, (iii) among the remaining galaxies, those removed by the surface criterion that would have been kept by our previous size selection used in Mercier et al. (2022) with blue upward pointing triangles, and (iv) the remaining that are removed by our previous size selection as well (grey dots). The black vertical line shows the surface criterion defined in Eq. 3 and the other black lines show the S/N criterion defined in Eq. 4 for different disk axis ratios. The combination of the surface, S/N and inclination criteria yields a sample of 186 galaxies. As an indication, the previous selection used in Mercier et al. (2022) would have yielded 211 galaxies instead. Among them, those that would have been added by the size criterion are mostly located at the limit of the selection (thus quite small) and are significantly inclined ($i \gtrsim 60^\circ$).

Finally, rather than removing galaxies with large stellar mass fraction uncertainties, as was done in Mercier et al. (2022) we decided to visually inspect the kinematics maps and the rotation curves and to flag the 30 following galaxies: (i) 38_CGR172, 54_CGR51, 70_CGR79, 74_CGR172, 90_CGR23, 93_CGR114, 101_CGR32, 104_CGR28, 104_CGR172, 105_CGR114, 113_CGR23, 148_CGR30, 185_CGR30, 226_CGR84, 257_CGR84, 267_CGR84, 313_CGR84, 442_CGR32, and 454_CGR32 because there is no visible velocity gradient in their velocity fields so that their best-fit rotation curves probably do not correctly describe the intrinsic velocity of the gas, (ii) 28_CGR26, 96_CGR28, and 172_CGR32 because there is not central peak observed in the HST image as would be expected for an exponential disk even without a bulge so that the contribution of their disk component is overestimated in the inner parts, (iii) 23_CGR84 because it has a very massive disk whose contribution is overestimated in the inner parts so that its contribution to the total rotation curve is too high and therefore produces large velocity residuals, (iv) 87_CGR35 and 345_CGR32 because their velocity field and [O II] emission are quite off-centred from their morphological center so that their velocity gradient is not correctly fitted in the inner parts, (v) 37_CGR84, 85_CGR23, and 278_CGR84 because, even though they do show some signs of rotation, their velocity fields are too perturbed for a rotating razor-thin gas disk model to be appropriate enough, (vi) 106_CGR84 because there are two kinematically distinct components in its velocity field whose centres match the locations of two morphologically distinct component in its HST image (perhaps following a merging event), therefore rendering the kinematics model uncertain, and (vii) 85_CGR35 because it is a double-peaked galaxy in its HST image with little rotation and whose velocity field residuals show that a rotating razor-thin gas disk model is not sufficient. Nevertheless, contrary to Mercier et al. (2022) where we removed such galaxies, we do not do so in this analysis. Instead, we will keep these objects and we will identify them clearly during the analysis of the angular momentum to see how they scale with the other galaxies. This way, our sample

is comparable to others found in the literature where such objects are usually not excluded and we avoid adding a complex selection function that could bias our sample.

The choice of whether a galaxy has enough rotation in its velocity field to be flagged or not is ultimately a question of perspective. Thus, we have tried to remain as conservative as possible. Therefore, in the 156 galaxies that are not flagged there might still be a few objects that are at the edge of what could be called a rotating galaxy. To illustrate the difference between a galaxy that does not have clear signs of rotation and one that does, as well as galaxies at the limit, we show examples of dynamical models for such cases in Fig. 2. For each sub-figure the morphological model is shown in the leftmost column, the velocity field model in the middle one, and the velocity dispersion in the rightmost one. We show on the top left galaxy 18_CGR114 whose morphology and kinematics are sufficiently well fitted for the analysis of the angular momentum and on the top right 70_CGR79 that does not have any velocity gradient in its velocity field and was therefore flagged. On the bottom row, we also show on the left galaxy 17_CGR34 that has a small and slightly disturbed velocity field that was not flagged and on the right 278_CGR84, a massive galaxy with a large but quite disturbed velocity field as can be seen in its residuals. Because the rotating razor-thin gas disk model does not seem appropriate to model the kinematics of this galaxy, it is unlikely that we correctly constrain its intrinsic gas kinematics and we therefore also flagged it.

3. Deriving the angular momentum

3.1. General considerations

Deriving an accurate estimate of the stellar angular momentum J_\star in galaxies is not straightforward given that it involves knowing *a priori* the 3D stellar mass density ρ_M as well as the 3D velocity vector \mathbf{V} of the stars. Indeed, the most general form it can take when integrated in a volume \mathcal{V} is

$$\mathbf{J}_\star(\mathbf{r}) = \int_{\mathcal{V}} d^3r \rho_M(\mathbf{r}) \mathbf{r} \times \mathbf{V}(\mathbf{r}), \quad (5)$$

where \times represents the vector product operation. However, Eq. 5 is hardly usable in practice unless one is working with simulations (e.g. Brook et al. 2012; Stewart et al. 2013; Zavala et al. 2016; Cadiou et al. 2022) or in the vicinity of the Milky Way where 6D phase-space positions are available from Gaia (e.g. del Pino et al. 2021). Therefore, assumptions must be made on both the stellar mass density and the velocity of the stars in order to constrain their angular momentum from morphological and kinematics data. One of the most widely used expression is that of Romanowsky & Fall (2012) (hereafter RF12) which assumes that the stellar mass distribution can be described by a razor-thin exponential disk with a constant rotation curve. More recently, Posti et al. (2018) and Bouché et al. (2021) showed that the RF12 approximation is usually not precise enough to correctly compute the angular momentum of galaxies at intermediate redshift, especially in the case of low mass galaxies (typically $\log_{10} M_\star/M_\odot \lesssim 9 - 9.5$) since they tend to have shallower inner slopes in their rotation curve than their high mass counterparts. A more general expression than RF12 can be derived from Eq. 5 assuming a razor-thin disk under rotation only, that is neglecting radial and vertical motions (see Appendix B for a derivation), without any assumption on the rotation curve. It writes

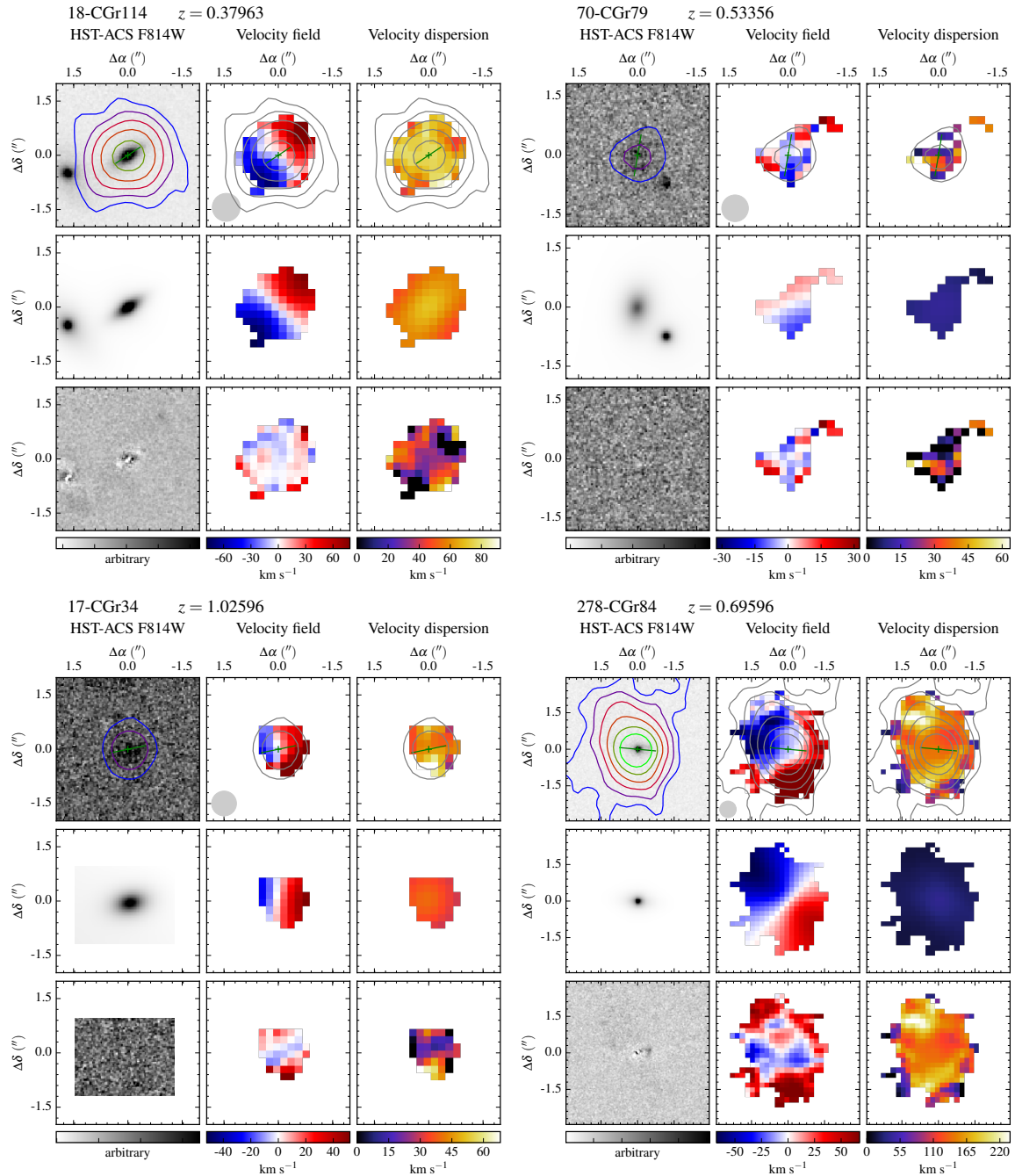


Fig. 2. Examples of dynamical models obtained in Mercier et al. (2022) and used in this analysis. For each sub-figure and from top to bottom we have the HST image, the GALFIT model, and the residuals in the leftmost column, the velocity field map extracted with CAMEL, the best-fit MOCNIG velocity field, and the residuals in the middle column, and the raw velocity dispersion map extracted with CAMEL, the beam-smearing model from MOCNIG, and the beam-smearing corrected velocity dispersion map from MOCNIG in the rightmost column. The top left sub-figure shows a galaxy with a seemingly correct dynamical model, the top right one shows a low S/N galaxy without any velocity gradient in its velocity field map that was flagged, the bottom left one shows a low S/N galaxy with a weak but non-negligible velocity gradient that was not flagged, and the bottom right one shows a massive galaxy with a kinematically disturbed velocity field that was flagged as well.

$$\mathbf{J}_\star = \int_S d\theta dR R^2 \Sigma_M(R, \theta) V_\theta(R, \theta) \hat{\mathbf{z}}, \quad (6)$$

where \mathcal{S} is the surface in the plane of the disk over which the angular momentum is integrated, R is the distance to the cen-

ter of the disk, θ is the azimuthal angle, Σ_M is the surface mass density given by the integral of the 3D mass distribution along the vertical direction, V_θ is the rotation velocity, and $\hat{\mathbf{z}}$ represents the direction perpendicular to the plane of the disk. Usually, the component of \mathbf{J}_\star orthogonal to the disk is normalised by the

galaxy or disk mass. It is called the specific angular momentum and it writes

$$j_{\star} = \frac{\int_{S_1} d\theta dR R^2 \Sigma_M(R, \theta) V_{\theta}(R, \theta)}{\int_{S_2} d\theta dR R \Sigma_M(R, \theta)}. \quad (7)$$

In Eq. 7, we have written two different surfaces S_1 and S_2 . A common practice is to integrate the normalisation factor on the whole disk surface (i.e. $\theta \in [0, 2\pi)$ and $R \in \mathbb{R}$) to get the total stellar mass or in a given aperture. However, we stress that the choice of the normalisation remains free and that different values of the stellar mass may be used depending on the context and the objectives of the analysis. Similarly, S_1 and S_2 do not have to be the same surface as long as it is relevant for the discussion. Besides, Eqs. 6 and 7 are technically speaking also valid for thick disks as long as they are (i) symmetric with respect to the plane of the disk and that (ii) it is possible to separate the vertical profile from the surface brightness distribution in the 3D stellar mass density (see Appendix B.1.1 for a more thorough discussion on that topic). If one further assumes a constant mass-to-light ratio throughout the galaxy and a rotation velocity that is independent of the azimuthal angle then the angular momentum integrated in a circular aperture of radius R_1 within the plane of the disk is given by

$$j_{\star}(R_1) = \frac{\int_0^{R_1} dR R^2 \Sigma(R, \theta) V_{\theta}(R)}{\int dR R \Sigma(R, \theta)}, \quad (8)$$

where Σ is the intrinsic surface brightness distribution (i.e. not sky projected) and where we have made implicit the limits of the integral for the normalisation factor since they are free to choose. We note that Eq. 8 is close to the expression used for instance in Bouché et al. (2021) and Mancera Piña et al. (2021a) that both rely on the assumption of a surface brightness distribution that only depends on R . On the other hand, our expression is slightly more general because it can account for both axisymmetric and non-axisymmetric disks (e.g. galaxies with spiral arms, bars or clumps). One potential caveat of using Eq. 8 is that it assumes a rotation velocity independent of θ which is unlikely for galaxies with non-axisymmetric features that will produce non-axisymmetric gravitational potentials. However, modelling such features is not straightforward even though technically possible (e.g. see Chemin et al. 2016) and is beyond the scope of this analysis. Besides, very few galaxies in our sample actually feature spiral arm and bar structures (less than 3%) and clumps will only locally affect the gravitational potential of their host galaxy so that their impact should be hardly visible in the velocity fields extracted from the MUSE cubes.

3.2. Angular momentum from HST maps

In the previous section we have defined the main equations used to derive the angular momentum. To extend beyond what was done in Bouché et al. (2021) or Mancera Piña et al. (2021a), we will use Eq. 8 in combination with HST maps to compute the angular momentum of galaxies in the MAGIC survey. There are two important quantities that must be derived beforehand: (i) the intrinsic surface brightness Σ and (ii) the rotation velocity V_{θ} . For the former we use the HST F814W images that were used in Mercier et al. (2022) to derive the galaxies' morphological parameters and for the latter the best-fit rotation curves also

derived in Mercier et al. (2022) from the mass modelling performed on the kinematics maps extracted from the MUSE cubes (see Sect. 2.2 for a summary). To do so, we approximate Eq. 8 by discretising it along the spatial dimensions x' and y' of the HST image. Thus, each pixel at position (x', y') has a specific angular momentum that writes

$$j_{\text{pix}}(x', y') = \frac{R F(x', y') V_{\theta}(R)}{\sum_{x', y'} F(x', y')}, \quad (9)$$

where $R = \sqrt{x'^2 + y'^2}$ is the distance of the pixel to the centre of the galaxy in the plane of the disk, with (x, y) the coordinates in the plane of the disk, and $F(x', y')$ is the flux in the pixel. Similarly to Eq. 8 we have let the bounds of the denominator implicit. The conversion from the apparent position (x', y') of a pixel on the plane of the sky to its location (x, y) in the plane of the disk is done by taking into account the position of the centre, the position angle (PA), and the inclination of the disk, all derived in Mercier et al. (2022) from the bulge-disk decomposition performed with GALFIT, assuming a razor-thin disk geometry (i.e. elliptical isophotes). The specific angular momentum measured in a circular aperture of radius R_1 in the plane of the disk is therefore just the sum of the specific angular momentum of each pixel that falls within the aperture:

$$j_{\star}(R_1) = \sum_{\{x', y' | R < R_1\}} j_{\text{pix}}(x', y'). \quad (10)$$

Contrary to the surface brightness, we cannot use in Eq. 8, 9 and 10 the velocity field extracted from the MUSE cubes because (i) the MUSE observations are much less spatially resolved than the HST data (0.2'' per spaxel for a PSF FWHM of 0.5'' on average for MUSE versus 0.03'' per pixel for a PSF FWHM of roughly 0.1'' for HST), (ii) the velocity fields extracted from the cubes are too severely affected by beam smearing, especially in the inner parts where the velocity gradient and the ionised gas flux are large, and (iii) the velocity fields are projected onto the sky and there is no trivial way to invert the projection, in particular along the minor axis. Thus, we use instead the rotation curves obtained from the forward mass models performed on the velocity fields in Mercier et al. (2022). These have the advantage of being unaffected by beam-smearing or projection effects and they can be interpolated to any radius R . However, the main drawback is that these rotation curves are that of the ionised gas whereas V_{θ} in Eqs. 8, 9, and 10 should be that of the stars. We provide in Sect. 3.3 a discussion regarding the reliability of such an estimate of the galaxies' stellar angular momentum.

3.3. Application of the HST formalism to MAGIC

Our goal for this analysis is to estimate the stellar angular momentum for intermediate redshift galaxies in the MAGIC survey. Given Eqs. 5, 8, 9, and 10, this means that we should measure the mass distribution and the kinematics of the stellar component. However, our sample is comprised of a majority of star-forming galaxies with strong emission lines (e.g. [O II]) so that we would be able to derive the stellar kinematics only for a small fraction of the entire sample. However, we do have a proxy for the stellar mass distribution through the galaxies' HST F814W images. Hence, our method is to estimate the stellar angular momentum using Eqs. 9 and 10 with the stellar flux distribution given by the galaxies' HST images but using the rotation curves derived from the [O II] doublet in Mercier et al. (2022). The underlying

assumption of this method is that there is co-rotation between the gas and the stars in the galaxies. We argue that this estimate should be close to the true stellar angular momentum for a couple of reasons. First, if the underlying assumptions behind the kinematics modelling performed in Mercier et al. (2022) are appropriate (e.g. rotating razor-thin disk) then the dynamics of the stars and the gas should be driven by the gravitational potential of the galaxy, which is the same for both components. Hence, their bulk dynamics (i.e. not taking into account local variations, for instance because of out-of-equilibrium motions) should match. The only effect that can differ between the gas and the stars is the impact of asymmetric drift. However, the asymmetric drift-corrected circular velocity is supposed to trace the total mass distribution and therefore, as long as we take that effect into account, using the ionised gas kinematics as a proxy for that of the stars should be appropriate enough. As an indication, a similar argument can be found in Guérou et al. (2017) where it is shown that the asymmetric drift-corrected stellar and ionised gas kinematics are consistent with each other for galaxies in the same redshift interval as ours.

We note that similar methods have already been used in a few previous studies (e.g. Cortese et al. 2016; Di Teodoro et al. 2021). However, they usually take into account the contribution of all the components (disk, bulge, spiral arms, bar, etc.) to the observed surface brightness distribution. Doing so may not be entirely appropriate because (i) the aforementioned equations are technically valid if the stellar mass is located in a disk, which is not the case for the bulge component, and (ii) bulges may be dispersion dominated systems in which case their angular momentum should be negligible. Thus, to not be biased by the bulge component that can contribute significantly to the flux in the inner parts, we remove from the HST image its best-fit GALFIT bulge model. In the few cases where the flux becomes negative near the centre in the new bulge-removed HST image, for instance because its contribution was slightly overestimated by GALFIT, we replace the pixels with negative values by the flux of the disk model at the same location. In what follows, we will nevertheless also investigate the impact of adding the bulge to the flux distribution to the Fall relation.

Finally, we must provide a last discussion regarding the impact of noise on our estimate. In Eqs. 9 and 10 we use the flux of the pixels to approximate Eq. 8 when using the HST images to derive the stellar angular momentum. However, HST images are affected by noise which can impact the angular momentum estimate. Because the background signal has already been removed from the images, either beforehand or by using an additional sky background component during the morphological modelling performed with GALFIT, we expect the noise to have an almost null mean value. Thus, if the integral in Eq. 8 or the sum in Eq. 10 are taken along a circle at fixed R and if there are a sufficiently large number of pixels along the path of integration/summation, then we expect the contribution of the noise to the angular momentum to be close to null as well. This argument does not hold near the centre where we do not have enough pixels to properly sample the noise distribution and because systematics may arise from the removal of bulges. However, because the rotation velocity is negligible in the inner parts, the angular momentum should be small at $R \approx 0$ and the noise contribution should still be negligible.

4. Analysis

For the analysis, we use the 186 galaxies from the kinematics sample, 30 of which have been flagged in Sect. 2.4 as having pe-

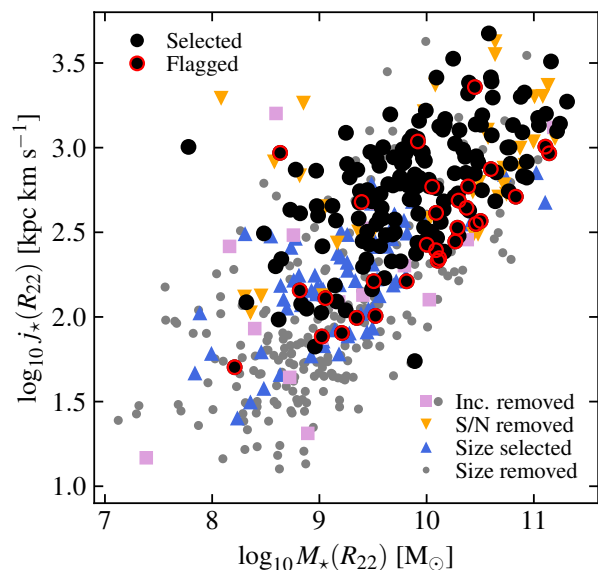


Fig. 3. Fall relation for the kinematics sample in the MAGIC survey using bulge-removed HST maps. The stellar mass, angular momentum, and its normalisation were all measured within R_{22} , and the normalisation corresponds to the mass of the disk component only. Galaxies selected from the kinematics sample are represented with black points and other symbols represent galaxies removed by different selection criteria (see Fig. 1 for more details). Black circles with red contours correspond to galaxies flagged with peculiar kinematics.

culiar kinematics. As discussed in the previous section, measuring the angular momentum of galaxies can mean multiple things depending on the way it is performed and the convention used. There are at least three important aspects that need to be discussed. First, where to measure the angular momentum? Should it be at infinity, thus at the cost of extrapolating the morphological and kinematics measurements? In one or two effective radii? At some kinematics radius such as R_{22} , the distance where the velocity induced by the disk component is the highest? Aspect number two is: which normalisation should we use? In the same radius where the angular momentum is measured or rather at infinity, once again at the cost of extrapolation? And finally, the last aspect is: how should we compute it? Should we use HST maps or analytical approximations? If the former, should we take into account the flux of the bulge or not? All these questions are important because they affect the value of the angular momentum and thus we address them in what follows. By default, we use the formalism based on HST maps discussed in Sect. 3.2, we measure the angular momentum within R_{22} , and similarly for the normalisation⁴. We also remove the contribution of the bulge to the HST map by default before deriving the angular momentum. Later on, we investigate whether changing the radius, the normalisation, or taking into account the bulge have an impact on our results and if so how.

To study the shape of the Fall relation, we use the same fitting methodology as in Mercier et al. (2022). We always fit the relation using the expression

$$\log_{10} j_{\star} [\text{kpc km s}^{-1}] = \beta + \alpha(\log_{10} M_{\star} [M_{\odot}] - p), \quad (11)$$

⁴ We note that photometric and kinematics measurements beyond this radius become less robust because of the significant drop in S/N.

where β acts as the zero point of the relation and α as the slope, p is the pivot point taken to be the decimal logarithm of the median stellar mass in the kinematics sample, and $\log_{10} j_{\star}$ is the dependent variable in the fit. Thus, we always use $p = 9.8$. The point of the pivot is to reduce the correlation between the slope and the zero point during the fit. Indeed, the further the data points are from the origin, the larger the zero point is impacted when there is a small variation in the slope. With a pivot, the data points are closer to the origin and the effect of the pivot is thus reduced. In what follows, we mainly consider the change in zero point between different Fall relations when fixing the slope unless there is a significant variation between subsamples, in which case we take it into account. To perform the fits we use a slightly updated version of `LrsFit`⁵ (Cappellari et al. 2013) that implements the Least Trimmed Squares (LTS) technique described in Rousseeuw & Driessen (2006) to find and remove outliers from the fit. The only feature that our updated version adds is the possibility to fit while fixing the slope at the same time. When fixing the slope, we use the following procedure: first, we fit the entire sample under consideration with a free slope and second, we fit each subsample separately using this slope. Another advantage of `LrsFit` is that it can take into account uncertainties on both the dependent (angular momentum) and independent (stellar mass) variables during the fit. For the stellar mass, we use the uncertainty from the SED fitting and, according to Mercier et al. (2022), we add a systematic uncertainty of 0.2 dex. For the angular momentum, we did not find in the literature (e.g. Bouché et al. 2021; Mancera Piña et al. 2021a) a typical systematic uncertainty that the authors add to perform the fit, though it is mentioned in Romanowsky & Fall (2012) that they use bootstrap resampling to estimate their uncertainties. After some tests, we found that adding no systematic uncertainty on the angular momentum can bias the fit because we treat asymmetrically the dependent and independent variables. Thus, we decided to add a systematic uncertainty of 0.1 dex on the angular momentum when fitting. This value is quite close to the typical uncertainty on the angular momentum evaluated by computing the difference between the HST-derived angular momentum estimates when using a rotation curve derived from the mass models and when using a simpler flat model rotation curve (see Sect. 4.1 for more details). Additionally, we also add quadratically for each galaxy an estimate of the uncertainty on j_{\star} due to the propagation of uncertainties taken as the standard deviation of 100 Monte-Carlo realisations of their HST map and kinematics parameters assuming Gaussian perturbations. This method nevertheless tends to under-predict the uncertainties on j_{\star} which therefore justifies the addition of a systematic uncertainty.

The Fall relation is shown in Fig. 3 for the kinematics sample. Similar symbols to Fig. 1 are used, with selected galaxies represented with black circles and flagged galaxies with red contours. The stellar mass (bulge plus disk), angular momentum, and its normalisation are all measured within $R_{22} = 2.2R_d$, with R_d the disk scale length, and we normalised the latter by the disk mass only. We recover the typical Fall relation with the angular momentum that seems to scale linearly with stellar mass. Our range of angular momentum values and the scatter in the relation are also consistent with recent results obtained with MUSE (e.g. Bouché et al. 2021). The main difference between our two studies is regarding the component that is traced by the angular momentum estimate since, in Bouché et al. (2021), it is that of the ionised gas that is traced, whereas in this analysis we try to estimate the stellar angular momentum. Still, we find a sim-

ilar Fall relation. Among the galaxies that would have been selected by the size criterion, the edge-on objects that would have been removed by the inclination selection (blue upward pointing triangles) tend to be spread out further than the selected galaxies above and below the relation. Those that would have been retained by the size and inclination selection criteria (orange downward pointing triangles) tend to be located throughout the Fall relation with more or less the same scatter, but populating more the low-mass end. Other galaxies that would have been removed anyhow by the size selection criterion (grey dots) mainly populate the low-mass and low-angular momentum part of the relation and even seem to be mostly found below the average relation. The fact that these galaxies are mostly found at low-mass is expected since, as was shown in Mercier et al. (2022), they fall on the size-mass relation. Finally, we note that flagged galaxies mostly populate the bottom part of the Fall relation which makes sense since the majority do not exhibit any visible velocity gradient. Thus, their rotation velocity is loosely constrained so that a DM halo with a nearly null maximum velocity is fitted to minimise the residuals. In other terms, the contribution of the stellar disk and bulge to the total rotation curve is likely overestimated for these galaxies.

4.1. Assessing the reliability of the method

First, we must ensure that we correctly measure the angular momentum when using HST maps. There are two main aspects that can change the value of the angular momentum with respect to more traditional estimates: (i) the fact that we derive the ionised gas kinematics and thus the total rotation curve using mass models. In Mercier et al. (2022), we showed that this could produce a limiting line on the TFR acting as a lower bound that had to be taken into account. And (ii) the fact that we use HST maps instead of assuming an axisymmetric surface brightness profile. Thus, in what follows we discuss how these two aspects impact the shape of the Fall relation. In our case, there are four different ways we can compute the angular momentum: (i) using the HST maps and the rotation curve derived from the mass modelling, (ii) using the HST maps and a simpler flat model rotation curve described in Wright et al. (2007); Epinat et al. (2009, 2010b); Abril-Melgarejo et al. (2021), see also Eq. B.9, which is not physically motivated but that can nevertheless robustly recover the rotation velocity for slowly declining or constant rotation curves at large radii, (iii) numerically integrating Eq. 8 using the best-fit axisymmetric exponential disk model and the rotation curve from the mass models, and (iv) using the analytical expression for the angular momentum of an exponential disk with a flat rotation curve that is given by Eqs. B.10 and B.13. The Fall relations for these four estimates are shown in Fig. 4. All are derived within R_{22} using the bulge-removed HST maps and similarly for the normalisation of j_{\star} . The same symbols have been used as for Fig. 1. This figure can be read along two directions. First, horizontally where the first row shows the Falls relations obtained with HST maps when using the rotation curve derived from mass models (top left) and when using a flat model for the rotation curve (top right). The second row shows instead the Fall relations when using an axisymmetric exponential disk surface brightness model with a rotation curve from mass models (bottom left) and with a flat rotation curve model (bottom right). Plots located on the same row therefore allow to see the effect of using different rotation curve models. The figure can also be read vertically, in which case the rotation curve model remains the same between the two plots and only the surface brightness map changes (HST on the top, exponential disk on the bottom).

⁵ <https://pypi.org/project/lrsfit/>

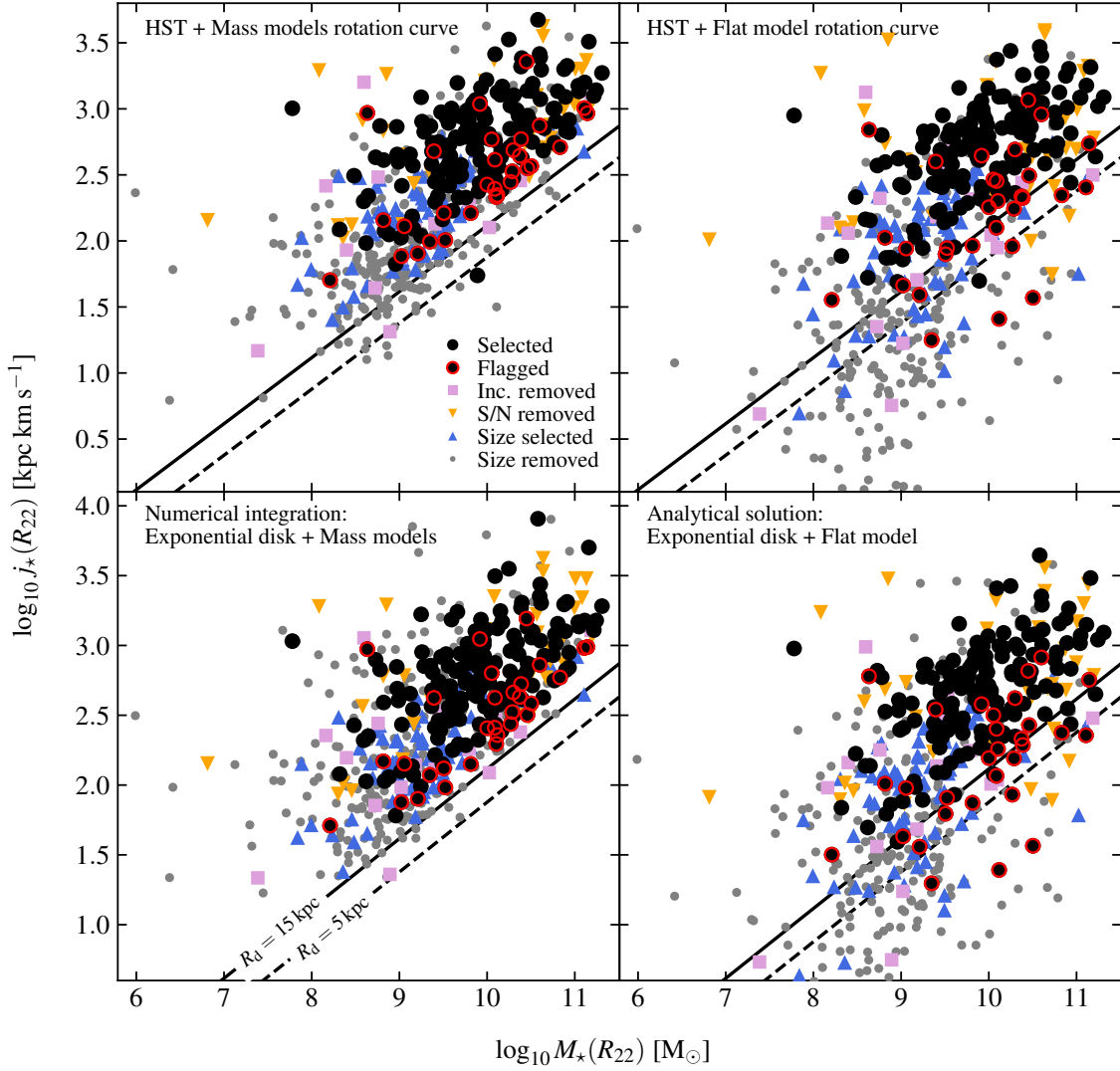


Fig. 4. Fall relation for the kinematics sample using various formalisms. On the top row is shown the angular momentum derived using HST maps and on the bottom row that derived using an exponential disk model. The leftmost column represents the Fall relation when using the rotation curve derived from the mass modelling and the rightmost column the Fall relation when using a flat model for the rotation curve. Stellar masses and angular momenta are all measured within R_{22} , as is the normalisation used for j_* . Galaxies selected for the analysis are shown as black points and those flagged with peculiar kinematics with red contours. Other symbols correspond to galaxies removed by the selection (see Fig. 1 for more details). The two black lines in each plot show the limit of the Fall relation for an exponential disk without DM halo and with two different disk scale lengths of 5 kpc (dashed line) and 15 kpc (plain line, see Eq. B.18).

Hence, this allows to see the effect of using non-axisymmetric HST maps compared to a more traditional axisymmetric exponential disk model

To begin with, we consider the effect of using mass models for the rotation curve. By comparing horizontally the plots in a same row in Fig. 4, we can see that there are large discrepancies found below roughly $10^9 M_\odot$ which correspond for the vast majority to galaxies removed by the sample selection, and in particular to galaxies with small sizes (grey dots). Above this stellar mass threshold, the two relations are more alike though slightly different. The selected galaxies (black points) are consistently spread along a line with a somewhat similar slope and zero point, though we can clearly see that the Fall relation obtained with mass models seems to have a lower limiting line similar to what could be seen for the TFR in Mercier et al. (2022). This effect

is striking for the galaxies flagged with peculiar kinematics (red contours) that are found for the majority along this limiting line when using mass models but that are spread across it when using the flat model. This result actually makes sense because most of the flagged galaxies are so because they lack a clear velocity gradient in their velocity field (e.g. 70-CGR79 in Fig. 2). This means that the contribution of the stellar components to the rotation curve of these galaxies is certainly overestimated in which case the kinematics model can only add a small fraction of DM. In turn, this produces a correlation between the galaxies' stellar mass and their stellar angular momentum. The only aspects that render this correlation not perfect are the non-axisymmetric features in the HST maps such as spiral arms or clumps and the relative contribution of the bulge component with respect to the disk.

Then, we investigate whether using HST maps instead of an exponential disk model has an important impact on the estimate of the angular momentum. This is shown by comparing vertically the plots in a same column in Fig. 4. Contrary to the previous comparison, we see that the HST maps have only a small impact on the Fall relation, with an average absolute difference in angular momentum below 0.1 dex which is about the same order of magnitude as the average uncertainty in the kinematics sample. Larger differences can be seen at the lowest stellar masses but they mostly concern small galaxies (grey dots) that certainly have loosely constrained disks. This result holds independently of whether we consider a rotation curve from mass models or from a flat model, which strengthens the conclusion that the choice of rotation curve is the leading factor that will affect the value of the derived angular momentum. We can also see the same kind of limiting lower line as for the HST maps when using mass models. We have previously mentioned that this line is due to galaxies whose baryon contribution was overestimated, which in turn produces a correlation between their stellar mass and their stellar angular momentum. For HST maps it is not trivial to derive an expression for this limiting line because it will depend on the flux distribution in the image. However, in the case where the angular momentum is derived through numerical integration, thus assuming an axisymmetric exponential disk, it is possible to derive an expression for this limiting line. More details are given in Appendix B.5, but basically the idea is to derive the expression of the angular momentum for a disk galaxy that has no DM halo. We do not take into account the impact of the bulge because the expression would already become much more complex. Besides, adding a bulge component will increase the flux and the rotation velocity which will in turn increase the angular momentum. For an exponential disk alone, the velocity of the ionised gas must compensate the disk’s gravity and so there is a link between its mass and its angular momentum. In the specific case where we measure the angular momentum within R_{22} , there is an analytical expression for the limiting line (see Eq. B.18 that depends on the disk’s mass and on its radius. The latter only affects the zero point of the line (smaller disks have less angular momentum at fixed stellar mass) but not its slope which is always equal to one-half. Two examples of such limiting lines are shown on the bottom right plot of Fig. 4 for galaxies with disk a scale length of 5 kpc or 15 kpc.

Hence, these two comparisons suggest that the choice of the rotation curve is what has the largest impact on the estimate of the angular momentum. In particular, we must be careful when using the mass models to not be biased by baryon-dominated galaxies that lie on the bottom of the Fall relation along the kind of limiting line that has been previously discussed. The same selection and kinematics modelling were applied to the entire sample independently of the characteristics of the galaxies’ environment so we expect the effect of this lower limiting line to be independent of environment. Therefore it should not bias this analysis unless perhaps if the fraction of baryon-dominated galaxies changes with environment. Besides, as shown in Fig. 4, selected galaxies from the kinematics sample are the least affected compared to very low-mass galaxies as they seem to populate similar Fall relations when using mass models or a flat one for the rotation curve.

4.2. Impact of environment

As discussed in Sect. 2.3, we have different proxies for the environment that we can use. Each proxy does not probe the environ-

ment in the same way and therefore it is interesting to consider all of them for this analysis.

4.2.1. Environment traced by structure richness

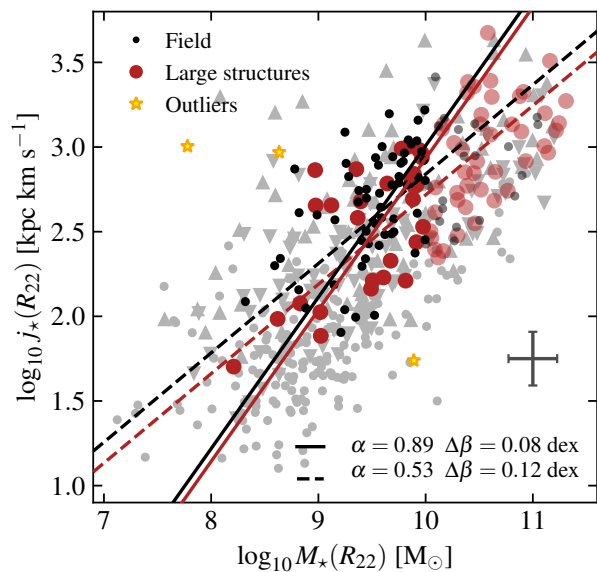


Fig. 5. Fall relation between galaxies in the field (black points) and those found in the richest structures (more than ten members - red circles). The stellar mass, angular momentum, and its normalisation are all measured within R_{22} and the normalisation corresponds to the mass of the disk component only. Galaxies beyond the mass cut at $M_* = 10^{10} M_\odot$ are shown with semi-transparent symbols and detected outliers are shown with yellow stars. Two best-lines are shown for each sub-sample (black line for the field and red for the structures). The dashed lines represent the best-fit Fall relations using the entire mass range whereas the plain lines correspond to the aforementioned stellar mass cut and an additional redshift cut $0.5 < z < 0.9$.

To begin with, we consider the simplest environment estimator that was used in Mercier et al. (2022) and that defines the environment in terms of the structures’ richness (i.e. number of galaxy members). We consider the two following sub-samples: (i) field galaxies, that is galaxies that were not associated to any structure by the FoF algorithm or that were associated to a structure with less than three members, and (ii) galaxies located in large structures that have at least ten galaxy members. As in Mercier et al. (2022), we do not consider smaller structures with less than ten members because we lack statistics for this sub-sample to properly constrain it. The Fall relation for these two sub-samples is illustrated in Fig. 5 with field galaxies shown with black points and those in structures with red circles. As discussed in our previous analysis of the TFR, there is an excess of massive galaxies found in large structures with respect to the field. This could be problematic because if the slope of the Fall relation is different for the high-mass end independently of environment, then it will mostly impact galaxies in the structures and we may wrongly interpret this result as an effect of environment. Hence, we fit the Fall relations with (plain lines) and without (dashed lines) a mass cut at $M_* < 10^{10} M_\odot$, which is the stellar mass below which the field galaxies and those in large structures have the same stellar mass distribution, to ensure we are not biased by the most massive galaxies. As in Mercier et al. (2022), we also applied a redshift cut $0.5 < z < 0.9$ to ensure

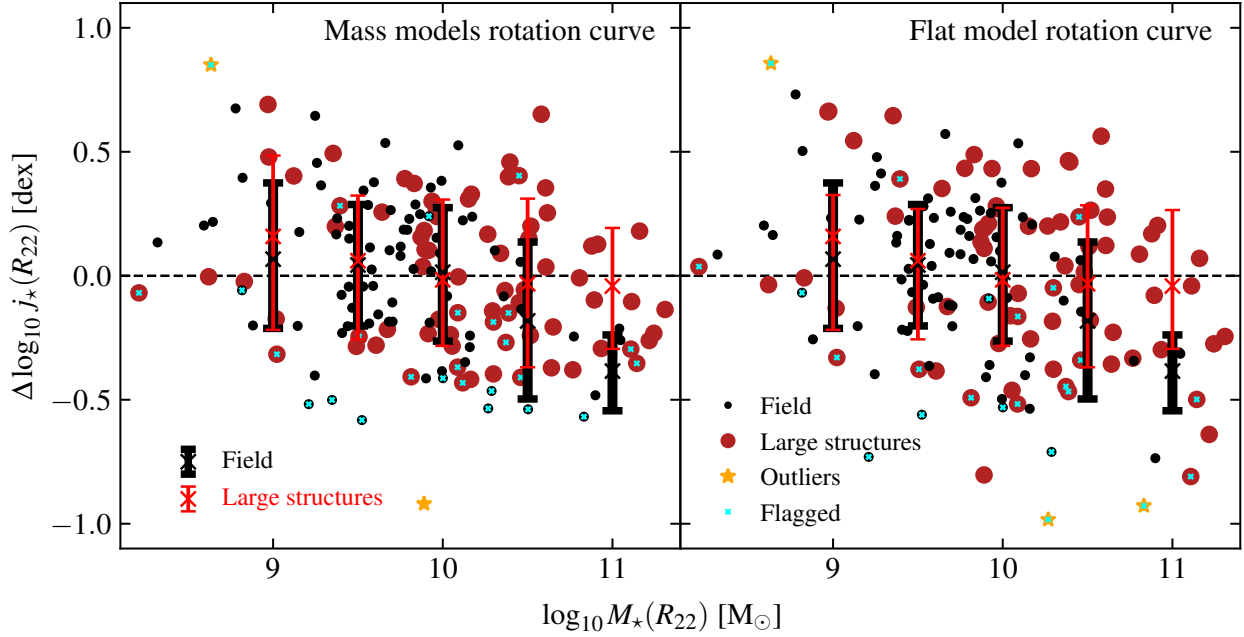


Fig. 6. Dispersion (data minus best-fit line, neither mass nor redshift cuts) along j_* as a function of stellar mass. Black points represent field galaxies, red circles those in structures, and yellow stars outliers. Galaxies flagged with peculiar kinematics are also shown with cyan crosses. The median, 16th, and 84th percentiles around the best-fit lines are shown as crosses and error bars for various 1 dex wide and partially overlapping stellar mass bins separated by 0.5 dex. We note that we used the best-fit line of each sub-sample separately (field or structures) to derive the galaxies’ dispersion. There is no significant difference in scatter between both subsamples, except in the last mass bin. However, we note that there are too few galaxies in the field around $10^{11} M_{\odot}$ to properly constrain this last bin. This result also holds when applying mass and redshift cuts.

we are not probing a potential redshift evolution of the relation given that galaxies in structures are mainly located at $z \approx 0.7$ whereas field galaxies are spread throughout the entire redshift range $0.2 \lesssim z \lesssim 1.5$. In Fig. 5, we directly show the best-fit linear relation (plain line) that takes into account both the stellar mass and the redshift cuts. However, we note that, even though the zero-points are higher when we only apply the mass cut, the offset between the two subsamples remains the same (0.08 dex), modulo a slightly steeper slope. As an indication, we also show the galaxies removed by the selection in the background with grey symbols and outliers detected by `LTSFIT` as yellow stars.

Interestingly, this first result may suggest that there is a visible impact of the environment on the Fall relation where field galaxies have a higher angular momentum (0.12 dex without any cut, 0.08 dex with mass and redshift cuts applied) than those in large structures at fixed stellar mass. We note that this result holds even when we apply the stellar mass and redshift cuts even though the slopes differ significantly. The zero-points are actually quite well constrained with an uncertainty of at most 0.02 dex, though their offset is significantly below the typical scatter in angular momentum of 0.3 dex measured in stellar mass bins of 1 dex. We also note that the result holds even when using the flat model rotation curve (see Fig. A.1). As discussed in Sect. 4.1, the advantage of the flat model is that it is not constrained by the mass modelling and thus it can probe galaxies that might be located below the Fall relation. Without mass and redshift cuts, we actually find a much larger difference of 0.22 dex (instead of 0.12 dex for mass models) between subsamples. However, when applying both cuts we recover the same 0.08 dex zero-points difference, modulo a slightly steeper slope. There may be two interpretations for this difference in zero point. Either there is a global shift of the Fall relation in the largest

structures with respect to the field or there is a larger scatter in a specific direction (seemingly towards lower angular momentum at fixed stellar mass for galaxies in structures). To investigate these interpretations, we computed the dispersion along j_* around the best-fit line for each sub-sample separately, as is shown in Fig. 6. On the left-hand side, we represent the dispersion around the best-fit line (without any cut) when using the rotation curve derived from the mass models, similarly to Fig. 5, and on the right-hand side the dispersion (without cuts as well) when using the flat model rotation curve (as in Fig. A.1). To help visualise the scatter around the Fall relation, we represent the median with crosses and the 16th and 84th percentiles with error bars for each sub-sample, computed in 1 dex wide stellar mass bins. Each bin is separated by 0.5 dex, starting at $10^9 M_{\odot}$ and ending at $10^{10.5} M_{\odot}$. We also performed the same exercise using the best-fit lines obtained when applying the mass and redshift cuts and we arrive at a similar conclusion. The only notable difference, which is visible in Fig. 5, is that nearly every massive galaxy is located below this line, but there is not visible trend with environment. We note that because we used four different best-fit Fall relations to derive the scatter (two for the two subsamples with the mass models and two for the two subsamples with the flat model), Fig. 6 only allows us to directly appreciate the dispersion around the relations and not offsets between different subsamples though, when combined with Figs. 5 and A.1, it is possible to draw some conclusions on that point. Looking at Fig. 6, we can notice that there is no significant difference between field galaxies and those in large structures in terms of scatter. For most of the stellar mass bins, the median value represented by the cross symbol is close to zero which shows that the slope is well constrained. Only for the highest mass bin can we see a significant difference. However, we note that in this mass

range there are very few galaxies found in the field and therefore we cannot draw clear conclusions for this bin. The same applies when using the flat model rotation curve and when applying a mass cut or mass and redshift cuts together. Similarly, removing galaxies flagged with peculiar kinematics before fitting the Fall relation does not change our conclusions in terms of zero-point difference and scatter around the best-fit relation. However, we note that there is a significant change in slope when doing so in the sense that the new value is much closer to the slope obtained when fitting the relation with a stellar mass cut. The effect is especially important for the Fall relation when using the flat model rotation curve. This indicates that flagged galaxies, because they mostly populate the bottom part of the Fall relation (mass models) or are located below it (flat models), tend to drive the slope towards a lower value.

Thus, the assumption that the difference in zero-points observed between subsamples is due to a larger scatter for the galaxies in the large structures does not seem to hold. Hence, this would point towards the other explanation that there is a global negative offset (in angular momentum at fixed stellar mass) of the relation for galaxies located in the largest structures with respect to the field. We note that there is a significant change in slope when we remove the most massive galaxies beyond $10^{10} M_{\odot}$ that make the best-fit Fall relation under-predict the angular momentum of low-mass galaxies below $10^9 M_{\odot}$ (see Fig. 5). The reason is that the best-fit line is actually driven by intermediate mass galaxies in the range $10^9 M_{\odot} < M_{\star} < 10^{10} M_{\odot}$. Hence, this global offset mostly applies for galaxies beyond $10^{10} M_{\odot}$.

4.2.2. Environment traced by other estimators

Using the structures' richness to probe the effect of the environment is an interesting first step but, for galaxies located in structures, it lacks some details. Indeed, depending on the type of structure (e.g. compact versus diffuse group) and the location of the galaxies in this structure, the environment can affect them differently. Thus, it is interesting to weigh our previous findings by looking at the Fall relation as a function of other environmental tracers.

First, we consider the global environment estimator η defined in Sect. 2.3. This estimator does not take into account the distribution of galaxies in the structures, but it allows to separate galaxies depending on their location and on their dynamics with respect to the structure they belong to. Low values of η means a galaxy is either located in the inner parts of the structure or that it has a low velocity relative to the structure's velocity dispersion (or both). Hence, by classifying galaxies using this parameter we can separate those that have certainly been largely affected by their environment from those that have been barely affected. In this analysis, we follow a similar classification to what was done in Pelliccia et al. (2019). We consider the three following classes:

- (i) $0.1 < \eta$ corresponding to "backsplash" galaxies, that is galaxies that have already passed the pericentre of their orbit once (e.g. Balogh et al. 2000; Gill et al. 2005) and that are thus expected to be highly affected by their environment,
- (ii) $0.1 < \eta < 0.4$ corresponding to recently accreted galaxies that may have started to be affected, and
- (iii) $\eta > 0.4$ corresponding to galaxies located in the outer parts and/or loosely bound to the structure (e.g. because of a large systemic velocity).

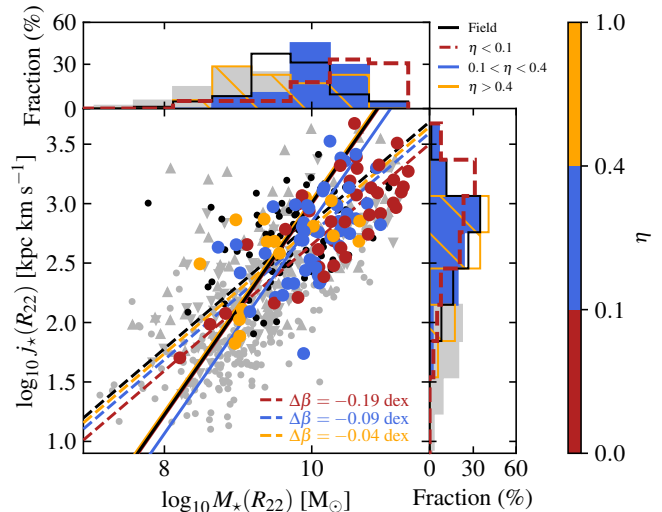


Fig. 7. Fall relation colour coded according to the global environment tracer η defined in Sect. 2.3. The stellar mass, angular momentum, and its normalisation are all measured within R_{22} , and the normalisation corresponds to the mass of the disk component only. We have used a similar classification as Pelliccia et al. (2019) with "backsplash" galaxies in red, recently accreted galaxies in blue, and galaxies in the outer regions of the structures in orange. Field galaxies are represented with black points. As an indication we also show galaxies removed by the selection in grey in the background. The best-fit line for each class of galaxies are shown with dashed lines when there is neither mass, nor redshift cut and with plain lines when there are both cuts applied. The stellar mass and angular momentum histograms are also shown on the sides of the figure.

The Fall relation for these three classes is shown in Fig. 7 with "backsplash" galaxies in red, those recently accreted in blue, and those loosely bound in orange. Field galaxies are also shown as black points and the stellar mass and angular momentum histograms for each class are represented on the sides of the main plot. The first striking feature is the difference in the stellar mass distributions between the field and the three aforementioned classes. We have already discussed in previous sections that galaxies located in structures populate the high-mass end of the Fall relation whereas only a handful of field galaxies are found beyond $10^{10} M_{\odot}$. In this figure, we actually see a clear transition from galaxies located in the outer parts of the structures, to recently accreted galaxies that populate mostly the $10^{9.5} M_{\odot} < M_{\star} < 10^{10.5} M_{\odot}$ range, and then to "backsplash" galaxies that are found at the high-mass end. This transition is also visible in the angular momentum histograms, though perhaps not as clearly. We note that there are only a few galaxies with $\eta > 0.4$ which makes it difficult to constrain their Fall relation. We have decided to keep them as a separate class rather than integrating them into the "recently accreted" class to avoid being potentially biased by the fact that these two populations of galaxies may be impacted by the environment in different ways.

To probe the impact of the environment, we fitted each class of galaxies separately, using the same slope found in Sect. 4.2.1. The best-fit lines are shown with (plain lines) and without (dashed lines) mass and redshift cuts applied, as in Fig. 5. We note that the best-fit lines with the mass and redshift cuts applied are difficult to interpret for various reasons. For "backsplash" galaxies, this is because most are located beyond $10^{10} M_{\odot}$. For recently accreted galaxies, there is a signif-

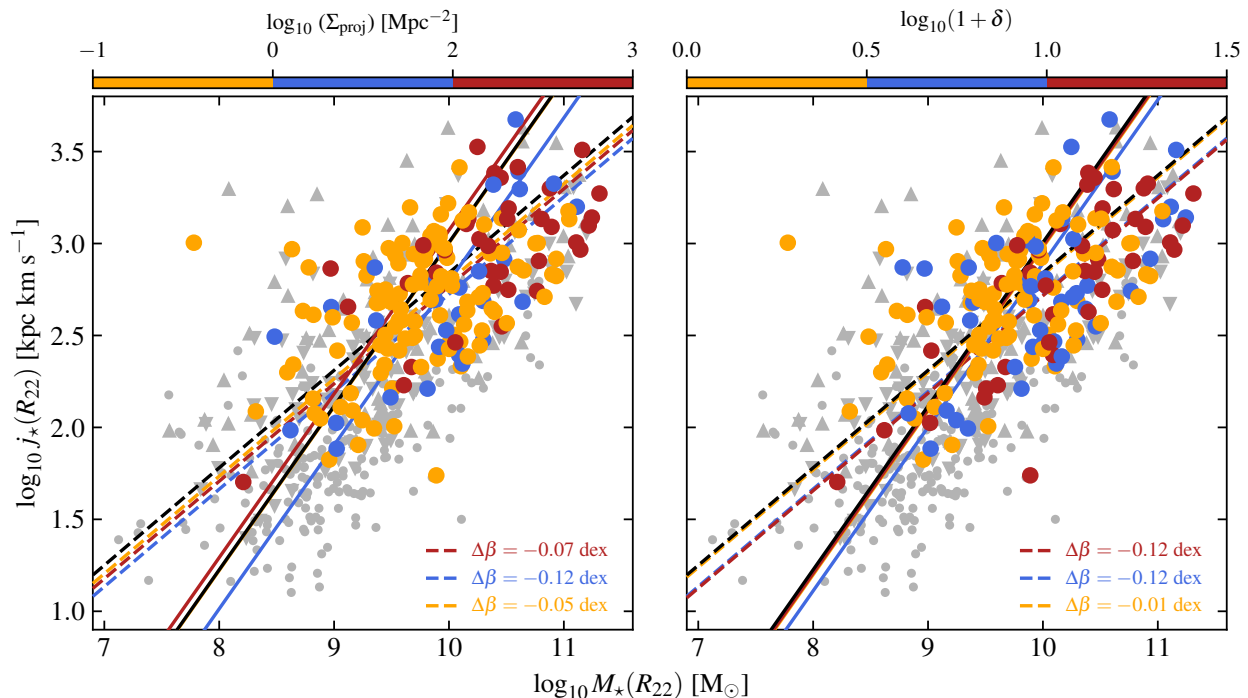


Fig. 8. Fall relation using the mass models rotation curve colour coded according to two local density estimates. On the left-hand side is shown the projected density (galaxies per unit area) when using MUSE and zCOSMOS spectroscopic redshifts only and on the right-hand side the overdensity using photometric and spectroscopic redshifts described in Sect. 2.3. Galaxies are split between low- (orange), medium- (blue), and high-density (red) environments. For each plot, the best-fit line for each class of galaxies is shown with a dashed line (plain line when mass and redshift cuts are applied). The stellar mass, angular momentum, and its normalisation are measured within R_{22} . The normalisation is taken as the mass of the disk component only.

icant fraction below $10^{10} M_{\odot}$, but the vast majority are clustered above $10^{9.5} M_{\odot}$ which makes it particularly difficult to fit a straight line without having large uncertainties on the zero-point. And for the last class, it is because, as discussed before, there is already few galaxies without any cut, thus even less remain after the cuts are applied. When no cut is applied, we find a visible impact of the environment on the zero-point of the relation with field galaxies that lie on the top, followed by galaxies in the outer parts of the structures (difference in zero-point of $\Delta\beta = -0.04$ dex with respect to the field), then by recently accreted galaxies ($\Delta\beta = -0.09$ dex), and finally by "backsplash" galaxies ($\Delta\beta = -0.19$ dex). However, as soon as we take into account the mass cut or both the mass and redshift cuts, these differences disappear. Only for the second class (recently accreted galaxies) do we find a large offset from the best-fit lines of the field galaxies and of those found in the two other classes, but we remind that, as discussed before, this class is by far the least constrained of the three, and so this result is not particularly significant. The same result applies when using the flat model rotation curve with a larger zero point difference without any cut ($\Delta\beta = -0.25$ dex) and a similar one with mass and redshift cuts ($\Delta\beta = -0.08$ dex), as illustrated in Fig. A.2. Combined with the previously mentioned fact that "backsplash" galaxies are clearly separated in stellar mass from the other galaxies, but not as much in angular momentum (see the two histograms in Fig. 7), this may be taken as an indication that massive "backsplash" galaxies deviate from the Fall relation found at lower stellar masses. We note that this interpretation is consistent with the variations of slope seen in Sect. 4.2.1 when applying or not the mass cut. However, this effect may not be necessarily environmentally-

driven. Because such galaxies are the only ones to occupy the high-mass end, we cannot eliminate the possibility that this deviation is solely caused by their mass, that is that if we had a larger sample of massive field galaxies we would find the same trend.

The parameter η provides us information regarding the location of the galaxies and/or how tightly bound they are to their structure. This can give us indications regarding the impact of the environment on the galaxies' angular momentum because we may expect a galaxy that has already completed an orbit through the structure to be more affected than a galaxy that has just started being accreted. However, structures such as galaxy groups are not completely isotropic and, depending on their exact location, galaxies may reside in more or less dense regions. In essence, the density of a region could mean that of the intra-cluster medium (ICM) or that of the galaxies (average number of galaxies per unit area). In our case, we are only able to probe the latter using one of the two local estimates discussed in Sect. 2.3. These two estimates are close but they do not probe exactly the same scales and they do not rely on the same data, so it is interesting to treat them in parallel. The VMC estimate uses a combination of photometric and spectroscopic redshifts (but not from MUSE) and derived the density within redshift slices with a fixed width whereas the other uses a combination of MUSE and zCOSMOS spectroscopic redshifts only and is derived structure-per-structure. Hence, the latter provides more precise density estimates but the former spans uniformly the entire field. In particular, because of depth variations from one redshift slice to another, we will consider the overdensity rather than the den-

sity for the estimate using the combination of photometric and spectroscopic redshifts (see Sect. 2.3 for more details).

We show the Fall relation for these two density estimates in Fig. 8. On the left-hand side the data are colour coded according to the estimator that uses the spectroscopic redshifts only (hence density estimate, noted Σ_{proj}) and on the right-hand side the data are colour coded according to the estimate using photometric and spectroscopic redshifts (hence overdensity, noted δ). For both plots, the Fall relation is split into three classes:

- (i) low-density environment where $\log_{10} \Sigma_{\text{proj}} < 0$ or $\log_{10}(1 + \delta) < 0.5$ (this also includes field galaxies),
- (ii) high-density environment where $\log_{10} \Sigma_{\text{proj}} > 2$ or $\log_{10}(1 + \delta) > 1$, and
- (iii) medium-density environment in-between the two previous classes.

The following results do not depend strongly on the criteria used to separate the galaxies into classes. For instance, only a handful of galaxies are added to the low-density environment when using $\log_{10} \Sigma_{\text{proj}} < 1$ instead of the aforementioned value. Nevertheless, we keep the criterion $\log_{10} \Sigma_{\text{proj}} < 0$ because it seems physically appropriate to separate low- from medium-density environments. We note that because of the size of the MUSE fields, this population of galaxies will be dominated by field galaxies. It is interesting to see that we recover similar results to what was previously seen in other figures. In particular, we find that massive galaxies are mostly located in high-density (or overdensity) environments, though the trend is not as clearly visible as in Fig. 7. By comparing Figs. 7 and 8, we can note that some galaxies identified as "backsplash" are found in low-density environments. This may be expected given that such galaxies can be classified as "backsplash" even if they are located far from the centre where the density is lower (e.g. because they have passed the pericentre and have now reached the apocentre of their orbit). When fitting each class separately, we find similar results to those obtained with the previously discussed environment tracers. Without any mass cut, we recover the transition from the field/low-density environment to the medium-/high-density ones. When using the density estimator (left-hand plot in Fig. 8), the zero-point of the medium- and high-density galaxy classes are switched compared to the result obtained with the parameter η . However, when using the overdensity parameter (right-hand side plot), the same zero-point is found for both classes. When applying the mass and redshift cuts, the differences between the field, the small-, and the large-density classes vanish. However, we note that for both estimators there is a significant zero-point offset ($\Delta\beta = -0.12$ dex with respect to the field) for the class probing medium-density environments. This offset is mainly driven by $M_{\star} \sim 10^9 - 10^{9.5} M_{\odot}$ galaxies which tend to populate the bottom part of the Fall relation when using both estimators.

4.2.3. Summary of the impact of the environment

It seems that, independently of the environmental tracer used, galaxies located in richer and denser structures and/or that are more dynamically bound to their host structure have less angular momentum at fixed stellar mass. Nevertheless, this effect seems to be mainly driven by the most massive galaxies. Indeed, those galaxies tend to be located below the Fall relation that is found for lower mass galaxies. This effect is even more striking when using an unconstrained rotation curve (flat model) to derive the angular momentum. Hence, this effect seems real and not induced by our method.

Because we lack a statistically significant sample of field galaxies in the highest stellar mass bin ($M_{\star} > 10^{10} M_{\odot}$), we cannot definitely reject the hypothesis that the observed difference in the zero-point of the Fall relation as a function of environment is not an effect of the galaxies' mass rather than environment. Still, we can note that there is a strong correlation with environment: these massive galaxies that show a deficit of angular momentum tend to be on average more dynamically bound to their host structure than their lower-mass counterparts and are located in denser environments. It is also interesting to note that a similar zero point offset of 0.1 dex between a sample of field galaxies and another of galaxies in structures was also obtained in Pelliccia et al. (2019) where the two samples have comparable stellar mass distributions at the high-mass end. Their interpretation of this result is that this loss of angular momentum is mainly due to gas-poor galaxy mergers happening in the structures. However, they also clearly state that other processes might be responsible for this observed angular momentum loss (e.g. tidal interactions). Galaxy mergers might be a viable explanation in our case as well because the effect seems more predominant in high-density environments where they are more likely to happen (e.g. Lin et al. 2010). But once again, without a comparable sample of field galaxies at the high-mass end, we cannot conclude for certain this effect is environmentally driven.

4.3. Impact of bulges

Some authors have argued that the presence of a bulge can affect the location of the galaxies on the Fall relation (e.g. Obreschkow & Glazebrook 2014; Fall & Romanowsky 2018). As plainly discussed by Obreschkow & Glazebrook (2014), galactic bulges can have some rotation but it is nevertheless usually much smaller than that of the disk component and therefore their contribution to the unnormalised angular momentum (i.e. not divided by the mass) is negligible. However, because a significant fraction of the stellar mass can be found in the bulge, especially when evaluated relatively close to the centre (e.g. at one effective radius), they can nevertheless impact the position of the galaxies on the Fall relation and they may even explain to some extent the dispersion seen in the relation (e.g. Fall & Romanowsky 2018). Hence, there are various ways we can look at the impact of bulges: (i) following Obreschkow & Glazebrook (2014) and Fall & Romanowsky (2018), we can explore the location of the galaxies on the Fall relation as a function of the bulge fraction and the environment, (ii) we can check the impact of the bulge when taking it into account for the normalisation of the angular momentum, and (iii) we can check the effect of keeping the bulge contribution in the HST maps when estimating the angular momentum, that is assuming the bulge co-rotates with the disk and that its flux distribution can be approximated as a thick disk. Each of these three approaches can potentially give us complementary information regarding the link between angular momentum, stellar mass, and bulge fraction, ideally as a function of the galaxies' environment.

4.3.1. Impact of normalisation

To begin with, we look at the position of the galaxies on the same Fall relation as before (i.e. normalising by the disk's mass) as a function of their bulge-to-disk flux ratio (B/D) and we check how this changes when we consider instead the total stellar mass for the normalisation. Indeed, so far we have always normalised the Fall relation using the disk's mass but what is usually done

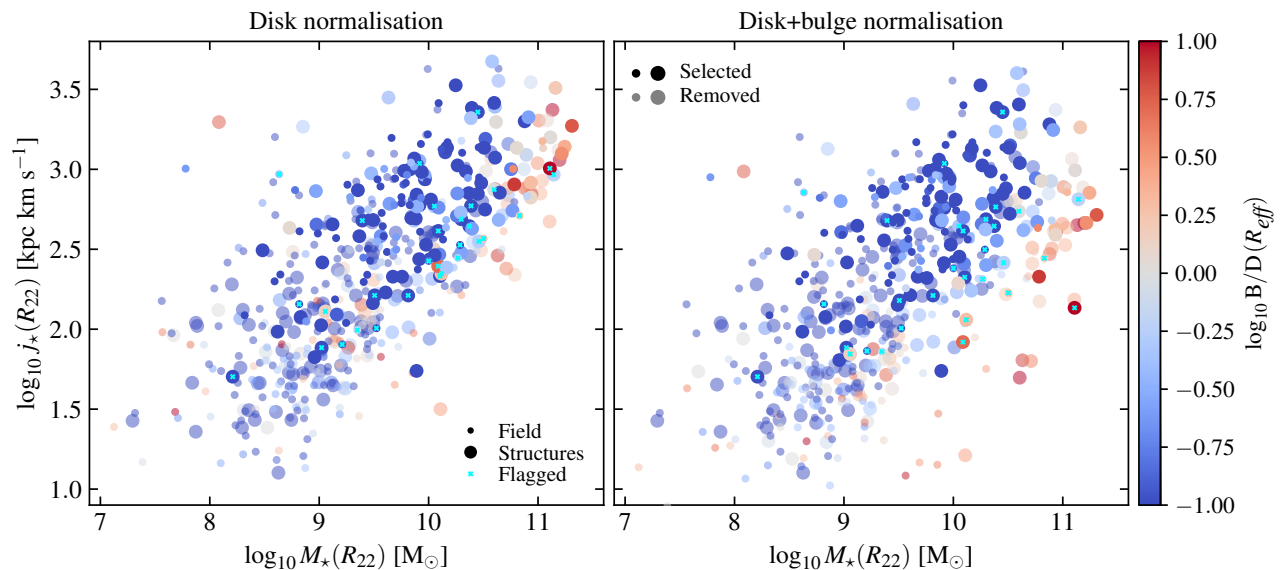


Fig. 9. Fall relation colour coded according to the bulge-to-disk flux ratio (B/D) evaluated at the global effective radius for the entire kinematics sample (selected galaxies with plain symbols and those removed by the selection criteria with semi-transparent symbols). The stellar mass, angular momentum, and its normalisation are all measured within R_{22} , and the normalisation corresponds to the mass of the disk only (left-hand side) or to the total mass (disk plus bulge, right-hand side). Galaxies are separated between those in the field (dots) and those in structures (circles). We note that, contrary to Figs. 5 and 6, we also include galaxies located in structures with less than ten members.

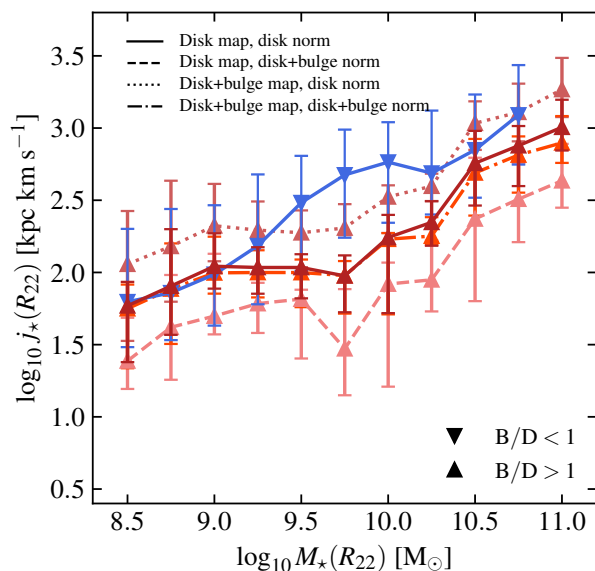


Fig. 10. Fall relation for the entire kinematics sample using the mass models rotation curve and binned in 0.5 dex wide stellar mass bins separated by 0.25 dex. The stellar mass, angular momentum, and its normalisation are all computed within R_{22} . Galaxies are split between those with a bulge-to-disk ratio (B/D) evaluated at one effective radius larger than one (red upward pointing triangles) and those with B/D below unity (blue downward pointing triangles). The different line styles represent various ways to derive the angular momentum. The plain and dashed correspond to the angular momentum derived using the bulge-removed HST map, whereas the dotted and dash-dotted lines represent that derived using the full HST map (i.e. including the bulge). Furthermore, the plain and dotted lines show the angular momentum derived with a normalisation taken as the disk mass only, whereas the dashed and dashed-dotted lines show that derived with the total mass (i.e. disk plus bulge).

in similar studies is to rather use the total stellar mass (e.g. Bouché et al. 2021; Mancera Piña et al. 2021b). Hence, we check whether this has an impact on our results or not. In this section, we still derive the angular momentum from the bulge-removed HST maps and only in Sect. 4.3.2 do we analyse the effect of including the flux of the bulge when deriving the angular momentum.

The Fall relation using the mass models rotation curve colour coded as a function of B/D evaluated at one global effective radius is shown in Fig. 9. On the left-hand side is shown the relation when using the disk mass within R_{22} as normalisation and on the right-hand side is shown the relation when using the total stellar mass within R_{22} as normalisation. Furthermore, galaxies are split between those in the field (points) and those in structures (circles). The full kinematics sample is shown but, for indication, we represent galaxies removed by the selection with semi-transparent symbols. Overall, galaxies are mainly disk dominated with $B/D < 1$ and bulge-dominated galaxies (defined here with $B/D > 1$) are mainly found at the highest stellar masses. There is nevertheless a non-negligible fraction of bulge-dominated galaxies throughout the entire stellar mass range. As already observed in Mercier et al. (2022), there is no obvious trend with environment, except for the highest stellar mass bin which is dominated by bulge-dominated galaxies. Yet, from visual inspection, it seems that lower mass bulge-dominated galaxies are mostly found on the bottom part of the Fall relation compared to disk-dominated galaxies. This is particularly clear when considering the Fall relation with the total stellar mass used as normalisation (right-hand side plot) since the inclusion of the bulge mass necessarily reduces more significantly the angular momentum for bulge-dominated galaxies than for the disk-dominated ones. This effect is also clearly visible in the Fall relation that uses the flat model rotation curve (see Fig. A.3).

To highlight this observation, we compute the median value along the Fall relation in 0.5 dex wide stellar mass bins sepa-

rated by steps of 0.25 dex, as shown in Fig. 10. We separate disk-dominated galaxies represented with downward pointing triangles from bulge-dominated galaxies represented with upward pointing triangles. The lines of interest for the current discussion are the two plain lines (disk mass as normalisation) and the dashed line (total stellar mass as normalisation), which for the latter is only shown for bulge-dominated galaxies since disk-dominated galaxies nearly unaffected. For each subsample, the 16th and 84th percentiles are also shown with error bars. It is clear that bulge-dominated galaxies are located on average well below the disk-dominated galaxies subsample and that the same applies for the scatter which is preferentially found below the median value. As already inferred from Fig. 9, the effect is amplified when the normalisation uses the total stellar mass. This result is actually similar to the dependence of the Fall relation with the bulge fraction presented in Fall & Romanowsky (2018). We also note that, based on previous findings in Sect. 4.2, the location of the most bulge-dominated galaxies is consistent with objects found in high-density environment and with the so-called "backplash" galaxies discussed in Sect. 4.2.2, though without a comparable sample of field galaxies in this mass range it is difficult to assess whether this is environmentally driven.

4.3.2. Effect of co-rotating bulges

Including bulges in the analysis of the angular momentum can be done by integrating them in the normalisation, as discussed in Sect. 4.3.1, and/or by including their contribution to the HST flux map used to compute the angular momentum. For the former, the net effect is to increase the normalisation and thus to reduce the angular momentum (for instance, see Fig. 9), whereas for the latter the expected net effect is to increase the flux (mostly in the inner parts) and thus to increase the angular momentum. If we consider that bulges are dispersion dominated systems, then it is more appropriate to remove their contribution to the HST image before deriving the galaxies' stellar angular momentum, as has been done so far. However, some simulations seem to suggest that the stellar mass may be partially redistributed from the disk to the bulge component after a wet merger (e.g. Lagos et al. 2018), producing a rotating bulge. If this scenario is correct, then it is interesting to compare the location of the bulge-dominated galaxies when including the bulge component in our derivation of the angular momentum, assuming it is co-rotating with the disk. To do so, we derive the angular momentum using the complete HST maps (i.e. without removing the bulge) and using the mass models rotation curve. When doing so, bulge-dominated galaxies are actually brought back along the Fall relation of disk-dominated galaxies when using the disk mass as normalisation, as illustrated by the dotted line in Fig. 10, and closer, though mostly still below, when using the total stellar mass as normalisation (dashed-dotted line in Fig. 10). Overall, there is a good agreement between disk- and bulge-dominated galaxies when using either normalisation, except at intermediate stellar mass where there is still a deficit of angular momentum in bulge-dominated galaxies compared to the disk-dominated ones. The difference observed in the lowest stellar mass bins when using the disk mass as normalisation is driven by a few outlier bulge-dominated galaxies located above the main Fall relation because the statistics are lower for these bins.

To interpret these results, let us consider two galaxies that have similar disks and DM haloes but the second galaxy has a more massive bulge component. The second galaxy will always move towards higher stellar masses in the Fall relation because we consider the total stellar mass in the relation. Then,

the second galaxy might further move depending on the relation that is considered: (i) in the Fall relation that uses the disk-only flux map and the disk mass as normalisation, the second galaxy will not move along j_* because the bulge does not intervene. For bulge-dominated galaxies ($B/D > 1$), this means a stellar mass offset of at least 0.3 dex which brings back the most massive bulge-dominated galaxies to a similar Fall relation as the disk-dominated ones. (ii) The second galaxy will have a lower j_* because the bulge contributes only to the normalisation when using the disk-only flux map and the total stellar mass for the normalisation of the Fall relation. For bulge-dominated galaxies, this will produce an offset in j_* of at least -0.3 dex which is what is seen in Fig. 10. (iii) For the Fall relation that uses the total flux map (i.e. including the bulge flux) but the disk mass as normalisation, the second galaxy will move towards higher values of j_* because the flux will be higher. The expected offset cannot be derived as simply as before because the impact on the angular momentum will depend on the shapes and amplitudes of the rotation curve and of the bulge component. Still, as a crude estimate, if we double the mass of the disk component, which should give us a sort of upper limit, it will produce the same offset of 0.3 dex. (iv) Finally, when we take the contribution of the bulge into account both in the normalisation and in the flux map, then the two effects should, at least partially, compensate each other. This is also what we see in Fig. 10. Hence, depending on the mass range probed, the variation in zero point between disk- and bulge-dominated galaxies when varying the way the Fall relation is derived can be explained. For massive bulge-dominated galaxies, the picture seems consistent with galaxies having their angular momentum nearly entirely in their disk component since, based on the arguments presented above, including the bulge as a co-rotating component over-predicts the angular momentum compared to disk-dominated galaxies at a similar disk's mass. For lower mass galaxies, the picture seems different. This is particularly true at intermediate stellar masses ($M_* \sim 10^{9.5} - 10^{10} M_\odot$) where even co-rotating bulges seem to under-predict compared to disk-dominated galaxies. However, contrary to high-mass galaxies, these objects would have been removed for the majority by our selection and so necessarily have a higher intrinsic uncertainty on their angular momentum. Hence, this difference may not be completely significant for this population of galaxies.

5. Conclusions

In this analysis, we have studied the environmental dependence of the angular momentum-stellar mass (Fall) relation for a sample of nearly 200 intermediate redshift ($0.2 \lesssim z \lesssim 1.5$) galaxies from the MAGIC survey that are found either in the field or in structures of varying density. These galaxies were chosen from a larger sample of [O II] emitters in MAGIC using robust selection criteria. We have modelled the galaxies morphology using their HST F814W images and their ionised gas kinematics from their MUSE cubes using the [O II] doublet as kinematics tracer. We develop a new method to estimate the galaxies' stellar angular momentum that combines our robust rotation curves obtained from MUSE with high-resolution HST images. This approach allows us to alleviate the assumption of axisymmetry for the disk component and therefore to derive more precise values of the angular momentum.

After discussing the impact of the sample selection and assessing the reliability of this method compared to simpler approaches to measure the angular momentum, we discuss the impact of the environment and of the galaxies' bulge component on

the Fall relation. First, we fit the Fall relation, separating galaxies between those in the field and those in rich structures, and we find a significant 0.12 dex offset that reduces to 0.08 dex when applying mass and redshift cuts. This result indicates that galaxies in the richest structures are depleted in angular momentum by roughly 20% compared to those in the field at the same redshift and in the same stellar mass range, consistent with other studies (e.g. Pelliccia et al. 2019). There is no clear indication that this result is correlated to the scatter found in the relation. However, it is more significant when massive galaxies are taken into account. Because such galaxies are predominantly found in structures, we argue that it may be an indication that they are more impacted by the environment than their lower mass counterparts. This result is further strengthened when comparing the location of the galaxies on the Fall relation as a function of various environmental tracers. Using global and local density estimates, we find that massive galaxies are indeed found below the Fall relation observed at lower stellar masses and that these objects are associated to the population of so-called "backsplash" galaxies and to the highest density parts of their host structure. We also show that the shape of the Fall relation and the location of bulge-dominated galaxies can significantly change when normalising by either the disk or the total stellar mass and when taking the contribution of the bulge component in the flux distribution into account for the derivation of the angular momentum. We find that high mass bulge dominated galaxies are consistent with a scenario where their angular momentum is nearly entirely found in their disk component. For lower mass galaxies, the lack of well constrained statistics prevent us from drawing any conclusions.

Thus, this analysis hints at the fact that there might be a visible impact of the environment on the Fall relation. However, our current lack of a complete sample of massive galaxies found at the same redshift prevents us from drawing clear conclusions. It may be that massive galaxies in structures suffer from a depletion of angular momentum, but without comparable field galaxies, we cannot eliminate the other possibility that this effect is mass-driven. To provide a definite answer, we will need to assemble a large sample of massive field galaxies from similar MUSE surveys that probe an even much larger volume than MAGIC currently does.

Acknowledgements. We dedicate this article in memory of Hayley Finley. This work was supported by the Programme National Cosmologie et Galaxies (PNCG) of CNRS/INSU with INP and IN2P3, co-funded by CEA and CNES. This work has been carried out through the support of the ANR FOGHAR (ANR-13-BS05-0010-02), the OCEVU Labex (ANR-11-LABX-0060), and the A*MIDEX project (ANR-11-IDEX-0001-02), which are funded by the "Investissements d'avenir" French government program managed by the ANR. This work has been carried out thanks to the support of the Ministry of Science, Technology and Innovation of Colombia (MINCIENCIAS) PhD fellowship program No. 756-2016. This research has made use of MATPLOTLIB (Hunter 2007), SCIPY (Virtanen et al. 2020), NUMPY (Harris et al. 2020) and ASTROPY (Astropy Collaboration et al. 2013, 2018). We acknowledge David Carton for his investment in the build-up of the project.

References

- Abril-Melgarejo, V., Epinat, B., Mercier, W., et al. 2021, *A&A*, 647, A152
 Astropy Collaboration, Price-Whelan, A. M., Sipőcz, B. M., et al. 2018, *AJ*, 156, 123
 Astropy Collaboration, Robitaille, T. P., Tollerud, E. J., et al. 2013, *A&A*, 558, A33
 Bacon, R., Conseil, S., Mary, D., et al. 2017, *A&A*, 608, A1
 Balogh, M. L., Navarro, J. F., & Morris, S. L. 2000, *ApJ*, 540, 113
 Boquien, M., Burgarella, D., Roehly, Y., et al. 2019, *Astronomy & Astrophysics*, 622, A103
 Bottinelli, L., Gouguenheim, L., Paturel, G., & de Vaucouleurs, G. 1983, *A&A*, 118, 4
 Bouché, N., Finley, H., Schroetter, I., et al. 2016, *The Astrophysical Journal*, 820, 121
 Bouché, N., Murphy, M. T., Kacprzak, G. G., et al. 2013, *Science*, 341, 50
 Bouché, N. F., Genel, S., Pellissier, A., et al. 2021, *Astronomy & Astrophysics*, 654, A49
 Brook, C. B., Stinson, G., Gibson, B. K., et al. 2012, *Monthly Notices of the Royal Astronomical Society*, 419, 771
 Bruzual, G. & Charlot, S. 2003, *Monthly Notices of the Royal Astronomical Society*, 344, 1000
 Burkert, A., Förster Schreiber, N. M., Genzel, R., et al. 2016, *The Astrophysical Journal*, 826, 214
 Cadiou, C., Dubois, Y., & Pichon, C. 2022, *Monthly Notices of the Royal Astronomical Society*, 514, 5429
 Cadiou, C., Pontzen, A., & Peiris, H. V. 2022, *Stellar angular momentum can be controlled from cosmological initial conditions*, arXiv:2206.11913 [astro-ph]
 Cappellari, M., Scott, N., Alatalo, K., et al. 2013, *MNRAS*, 432, 1709
 Charlot, S. & Fall, S. M. 2000, *The Astrophysical Journal*, 539, 718
 Chemin, L., Huré, J.-M., Soubiran, C., et al. 2016, *Astronomy & Astrophysics*, 588, A48
 Ciesla, L., Buat, V., Boquien, M., et al. 2021, *Astronomy & Astrophysics*, 653, A6
 Ciesla, L., Elbaz, D., Schreiber, C., Daddi, E., & Wang, T. 2018, *Astronomy & Astrophysics*, 615, A61
 Contini, T., Epinat, B., Bouché, N., et al. 2016, *A&A*, 591, A49
 Cortese, L., Fogarty, L. M. R., Bekki, K., et al. 2016, *MNRAS*, 463, 170
 Cortese, L., Fogarty, L. M. R., Bekki, K., et al. 2016, *Monthly Notices of the Royal Astronomical Society*, 463, 170
 Danovich, M., Dekel, A., Hahn, O., Ceverino, D., & Primack, J. 2015, *Monthly Notices of the Royal Astronomical Society*, 449, 2087
 DeFelippis, D., Genel, S., Bryan, G. L., & Fall, S. M. 2017, *The Astrophysical Journal*, 841, 16
 del Pino, A., Fardal, M. A., van der Marel, R. P., et al. 2021, *The Astrophysical Journal*, 908, 244
 Di Teodoro, E. M., Posti, L., Ogle, P. M., Fall, S. M., & Jarrett, T. 2021, *Monthly Notices of the Royal Astronomical Society*, 507, 5820
 Doroshkevich, A. G. 1970, *Astrofizika*, 6, 581
 Epinat, B., Amram, P., Balkowski, C., & Marcelin, M. 2010a, *MNRAS*, 401, 2113
 Epinat, B., Amram, P., Balkowski, C., & Marcelin, M. 2010b, *Monthly Notices of the Royal Astronomical Society*, 401, 2113
 Epinat, B., Contini, T., Le Fèvre, O., et al. 2009, *Astronomy & Astrophysics*, 504, 789
 Fall, S. M. 1983, in *Internal Kinematics and Dynamics of Galaxies*, ed. E. Athanassoula, Vol. 100, 391–398
 Fall, S. M. & Efstathiou, G. 1980, *Monthly Notices of the Royal Astronomical Society*, 193, 189
 Fall, S. M. & Romanowsky, A. J. 2018, *The Astrophysical Journal*, 868, 133
 Genel, S., Fall, S. M., Hernquist, L., et al. 2015, *The Astrophysical Journal Letters*, 804, L40
 Gilbank, D. G., Baldry, I. K., Balogh, M. L., Glazebrook, K., & Bower, R. G. 2010, *MNRAS*, no
 Gilbank, D. G., Baldry, I. K., Balogh, M. L., Glazebrook, K., & Bower, R. G. 2011, *MNRAS*, 412, 2111
 Gill, S. P. D., Knebe, A., & Gibson, B. K. 2005, *Monthly Notices of the Royal Astronomical Society*, 356, 1327
 Graham, A. W., Driver, S. P., Petrosian, V., et al. 2005, *AJ*, 130, 1535
 Guérou, A., Krajnović, D., Epinat, B., et al. 2017, *A&A*, 608, A5
 Harris, C. R., Millman, K. J., van der Walt, S. J., et al. 2020, *Nature*, 585, 357
 Harrison, C. M., Johnson, H. L., Swinbank, A. M., et al. 2017, *MNRAS*, 467, 1965
 Heidmann, J., Heidmann, N., & de Vaucouleurs, G. 1972, *Memoirs of the Royal Astronomical Society*, 75, 85
 Hetzner, H. & Burkert, A. 2006, *Monthly Notices of the Royal Astronomical Society*, 370, 1905
 Hung, D., Lemaux, B. C., Gal, R. R., et al. 2020, *Monthly Notices of the Royal Astronomical Society*, 491, 5524
 Hung, D., Lemaux, B. C., Gal, R. R., et al. 2021, *Monthly Notices of the Royal Astronomical Society*, 502, 3942
 Hunter, J. D. 2007, *Computing in Science & Engineering*, 9, 90
 Iovino, A., Petropoulou, V., Scodreggio, M., et al. 2016, *Astronomy & Astrophysics*, 592, A78
 Jiang, F., Dekel, A., Kneller, O., et al. 2019, *Monthly Notices of the Royal Astronomical Society*, 488, 4801
 Kennicutt, Jr., R. C. 1992, *ApJ*, 388, 310
 Kennicutt, Jr., R. C. 1998, *ARA&A*, 36, 189
 Knobel, C., Lilly, S. J., Iovino, A., et al. 2012, *The Astrophysical Journal*, 753, 121

- Koekemoer, A. M., Aussel, H., Calzetti, D., et al. 2007, *ApJS*, 172, 196
- Lagos, C. d. P., Stevens, A. R. H., Bower, R. G., et al. 2018, *MNRAS*, 473, 4956
- Laigle, C., McCracken, H. J., Ilbert, O., et al. 2016, *The Astrophysical Journal Supplement Series*, 224, 24
- Le Fèvre, O., Tasca, L. A. M., Cassata, P., et al. 2015, *Astronomy & Astrophysics*, 576, A79
- Lemaux, B. C., Cucchiati, O., Le Fèvre, O., et al. 2022, *Astronomy & Astrophysics*, 662, A33
- Lemaux, B. C., Tomczak, A. R., Lubin, L. M., et al. 2017, *Monthly Notices of the Royal Astronomical Society*, 472, 419
- Lilly, S. J., Fevre, O. L., Renzini, A., et al. 2007, *The Astrophysical Journal Supplement Series*, 172, 70
- Lin, L., Cooper, M. C., Jian, H.-Y., et al. 2010, *ApJ*, 718, 1158
- Mancera Piña, P. E., Posti, L., Fraternali, F., Adams, E. A. K., & Oosterloo, T. 2021a, *Astronomy & Astrophysics*, 647, A76
- Mancera Piña, P. E., Posti, L., Pezzulli, G., et al. 2021b, *Astronomy & Astrophysics*, 651, L15
- Massey, R., Stoughton, C., Leauthaud, A., et al. 2010, *MNRAS*, 401, 371
- Mercier, W., Epinat, B., Contini, T., et al. 2022, arXiv:2204.08724 [astro-ph], arXiv: 2204.08724
- Navarro, J. F., Frenk, C. S., & White, S. D. M. 1996, *ApJ*, 462, 563
- Noble, A. G., Webb, T. M. A., Muzzin, A., et al. 2013, *The Astrophysical Journal*, 768, 118
- Obreschkow, D. & Glazebrook, K. 2014, *The Astrophysical Journal*, 784, 26
- Peebles, P. J. E. 1969, *Astrophysical Journal*, 155, 393
- Pelliccia, D., Lemaux, B. C., Tomczak, A. R., et al. 2019, *Monthly Notices of the Royal Astronomical Society*, 482, 3514
- Peng, C. Y., Ho, L. C., Impey, C. D., & Rix, H.-W. 2002, *The Astronomical Journal*, 124, 266
- Pérez-Martínez, J. M., Ziegler, B., Dannerbauer, H., et al. 2021, *A&A*, 646, A53
- Posti, L., Fraternali, F., Di Teodoro, E. M., & Pezzulli, G. 2018, *Astronomy & Astrophysics*, 612, L6
- Rizzo, F., Fraternali, F., & Iorio, G. 2018, *MNRAS*, 476, 2137
- Romanowsky, A. J. & Fall, S. M. 2012, *The Astrophysical Journal Supplement*, 203, 17
- Romanowsky, A. J. & Fall, S. M. 2012, *The Astrophysical Journal Supplement Series*, 203, 17
- Rousseeuw, P. & Driessen, K. 2006, *Data Min. Knowl. Discov.*, 12, 29
- Salpeter, E. E. 1955, *The Astrophysical Journal*, 121, 161
- Scoville, N., Aussel, H., Brusa, M., et al. 2007, *ApJS*, 172, 1
- Sérsic, J. L. 1963, *Boletín de la Asociación Argentina de Astronomía La Plata Argentina*, 6, 41
- Stewart, K. R., Brooks, A. M., Bullock, J. S., et al. 2013, *The Astrophysical Journal*, 769, 74
- Swinbank, A. M., Harrison, C. M., Trayford, J., et al. 2017, *MNRAS*, 467, 3140
- Virtanen, P., Gommers, R., Oliphant, T. E., et al. 2020, *Nature Methods*, 17, 261
- White, S. D. M. 1984, *Astrophysical Journal*, 286, 38
- Wright, S. A., Larkin, J. E., Barczys, M., et al. 2007, *The Astrophysical Journal*, 658, 78
- Zabl, J., Bouché, N. F., Schroetter, I., et al. 2019, *Monthly Notices of the Royal Astronomical Society*, 485, 1961
- Zavala, J., Frenk, C. S., Bower, R., et al. 2016, *Monthly Notices of the Royal Astronomical Society*, 460, 4466

Appendix A: Additional figures

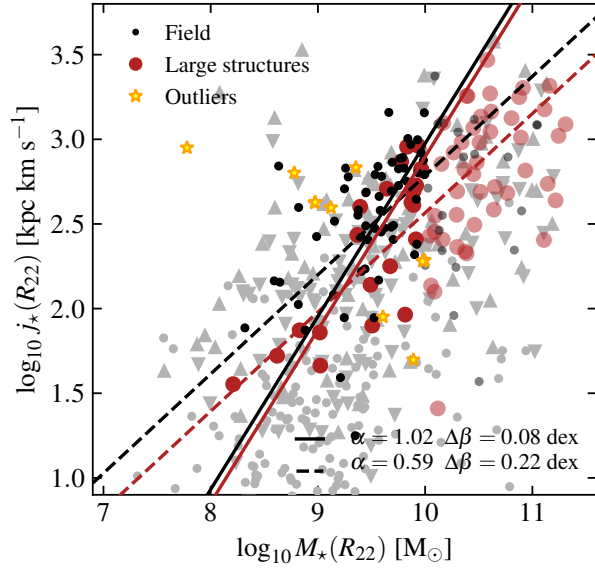


Fig. A.1. Fall relation between galaxies in the field (black points) and those found in the richest structures (more than ten members - red circles) using the flat model rotation curve. See Fig. 5 for details regarding the legend.

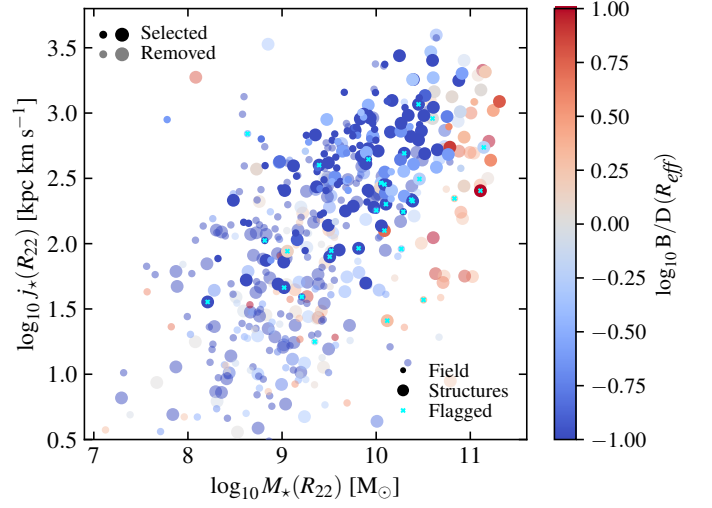


Fig. A.3. Fall relation using the flat model rotation curve colour coded according to the bulge-to-disk ratio (B/D) evaluated at the global effective radius for the entire kinematics sample. The stellar mass, angular momentum, and its normalisation are all measured within R_{22} , and the normalisation corresponds to the mass of the disk only. See Fig. 9 for the details of the legend.

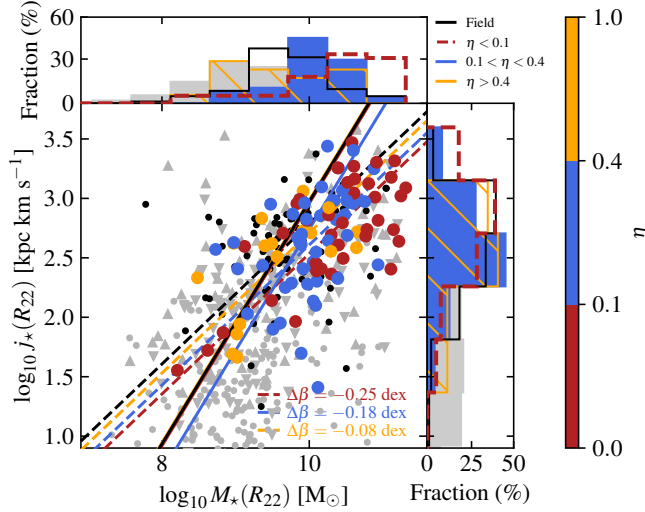


Fig. A.2. Fall relation colour coded according to the global environment tracer η using the flat model rotation curve. See Fig. 7 regarding the details of the legend.

Appendix B: Deriving angular momentum

Our goal is to derive the angular momentum of the stars in the MAGIC survey. We can split distribution of stars into two main components: the stellar disk and the stellar bulge. Among the two, the disk is the simplest to derive its angular momentum because of the assumptions that are usually made on its geometry and on its kinematics. Besides, bulges are usually thought of as stellar systems dynamically supported by random motions. In our case, because we model the bulge component as a spherical system, this means that its angular momentum should be nearly null. Thus, we will make the assumption that the bulge component does not possess any angular momentum and we will focus on deriving that of the disk component only.

Appendix B.1: General derivation

The angular momentum of a system is defined from its 3D mass distribution $\rho(\mathbf{r})$ and 3D velocity field $\mathbf{V}(\mathbf{r})$ as

$$\mathbf{J} = \int_{\mathcal{V}} d\tau \rho(\mathbf{r}) \mathbf{r} \times \mathbf{V}(\mathbf{r}), \quad (\text{B.1})$$

where \mathcal{V} represents the volume over which the integral is computed. In cylindrical coordinates, the cross product writes

$$\mathbf{r} \times \mathbf{V}(\mathbf{r}) = R V_{\theta} \hat{\mathbf{z}} + (z V_R - R V_z) \hat{\boldsymbol{\theta}} - z V_{\theta} \hat{\mathbf{R}}, \quad (\text{B.2})$$

where $\mathbf{V}(\mathbf{r}) = V_R \hat{\mathbf{R}} + V_{\theta} \hat{\boldsymbol{\theta}} + V_z \hat{\mathbf{z}}$. Assuming we want to derive the angular momentum of a disk-like distribution where only the tangential component of the velocity field is non-zero and does not depend on z , that is $V_R = V_z = 0$ and $V_{\theta} = V_{\theta}(R, \theta)$, then the angular momentum simplifies to

$$\mathbf{J} = \int_{\mathcal{V}} d\theta dR dz \rho(\mathbf{r}) \left[R^2 V_{\theta}(R, \theta) \hat{\mathbf{z}} - R z V_{\theta}(R, \theta) \hat{\mathbf{R}} \right]. \quad (\text{B.3})$$

Appendix B.1.1: Angular momentum of thick disks

The angular momentum of a disk galaxy with a non-zero thickness profile $f(z)$ is similar to that of a razor-thin disk galaxy with the same surface mass density $\Sigma_M(R)$ if the three following criteria are met:

- (i) $\rho(\mathbf{r}) = \Sigma_M(R, \theta) f(z)$,
- (ii) $\int_{\mathbb{R}} dz f(z) = 1$,
- (iii) $f(z) = f(-z)$.

Criterion (i) means that it is possible to separate the surface mass density profile from the thickness profile. For instance, this is the case for a double exponential profile where $f(z) = \exp\{-|z/h_z|\}/h_z$. Among the three conditions, criterion (ii) is always met since it is required in order to recover the surface mass density when integrating the 3D mass distribution along the vertical axis with respect to the disk plane, that is $\Sigma_M(R, \theta) = \int_{\mathbb{R}} dz \rho(\mathbf{r})$. Finally, criterion (iii) is usually assumed to simplify the shape of the vertical profile. If these three conditions are met, one can see that the rightmost integral in Eq. B.3 vanishes when integrating along the vertical axis, whereas only the R and θ integrations remain in the leftmost one. Thus, we

⁶ In the following, when the velocity field is fully described by V_{θ} , we will refer to it as the galaxy rotation curve.

get an angular momentum integral similar to that of a razor-thin disk⁷

$$\mathbf{J} = \int_{\mathcal{S}} d\theta dR R^2 \Sigma_M(R, \theta) V_{\theta}(R, \theta) \hat{\mathbf{z}}, \quad (\text{B.4})$$

where \mathcal{S} represents the surface over which the R and θ integrations are carried out. It is common practice to normalise the angular momentum by the total stellar mass to define a specific angular momentum $j = |\mathbf{J}|/M_{\star}$ (e.g. Fall 1983; Romanowsky & Fall 2012; Bouché et al. 2021) but it is also possible to normalise it by the mass of the disk only. For instance, if we normalise the angular momentum measured over some surface \mathcal{S} by the total disk mass, we get

$$j = \frac{\int_{\mathcal{S}} d\theta dR R^2 \Sigma_M(R, \theta) V_{\theta}(R, \theta)}{\int_{[0, 2\pi) \times \mathbb{R}_+} d\theta dR R \Sigma_M(R, \theta)}, \quad (\text{B.5})$$

or in the case where there is no dependence on θ for both the surface mass density and the velocity:

$$j = \frac{\int_{\mathbb{R}_+} dR R^2 \Sigma_M(R) V_{\theta}(R)}{\int_{\mathbb{R}_+} dR R \Sigma_M(R)}. \quad (\text{B.6})$$

Appendix B.2: Angular momentum for special rotation curves

In most general terms, if one wants to compute the specific angular momentum for any surface mass density and velocity profile, one needs to numerically integrate Eq. B.5 or B.6 depending on whether there is a θ dependence or not. However, there exist for a few specific velocity profiles simplified formulae which can be computed either numerically or analytically in certain cases. We present in the following simplified expressions for some rotation curves, assuming no θ dependence on both the surface mass density and the rotation curve.

Appendix B.2.1: Constant rotation curve

If one assumes a constant rotation curve $V_{\theta}(R) = V_{\theta}$, then the angular momentum up to radius r is given by

$$j(r) = V_{\theta} \times M_2\{\Sigma_M\}_0^r / M_1\{\Sigma_M\}_0^{\infty}, \quad (\text{B.7})$$

where $M_k\{\Sigma_M\}_{\alpha}^{\beta}$ is the k^{th} radial moment of the surface brightness distribution Σ_M integrated between α and β , that is

$$M_k\{\Sigma_M\}_{\alpha}^{\beta} = \int_{\alpha}^{\beta} dR R^k \Sigma_M(R). \quad (\text{B.8})$$

Appendix B.2.2: Flat model

If one assumes the rotation curve to be a flat model as in Abril-Melgarejo et al. (2021), that is described by the following formula:

$$V_{\theta}(R) = V_t \times \begin{cases} R/R_t, & \text{if } R < R_t \\ 1, & \text{otherwise} \end{cases} \quad (\text{B.9})$$

⁷ For a razor-thin disk we have $f(z) = \delta(z)$, with δ a Dirac distribution, so criteria (i) to (iii) are also met.

then the angular momentum is given by

$$j(r) = \frac{V_t}{R_t M_1 \{\Sigma_M\}_0^\infty} \times \begin{cases} M_3 \{\Sigma_M\}_0^R, & \text{if } R < R_t \\ M_3 \{\Sigma_M\}_0^{R_t} + R_t M_2 \{\Sigma\}'_{R_t}, & \text{otherwise} \end{cases} \quad (\text{B.10})$$

Appendix B.3: Angular momentum for a Sérsic profile

If the surface mass density can be further described by a Sérsic profile (Sérsic 1963) with Sérsic index n , effective radius R_{eff} and central surface mass density $\Sigma_{M,0}$, then we have

$$\mathbf{J} = \Sigma_{M,0} \int_R dR R^2 e^{-b_n(R/R_{\text{eff}})^{1/n}} \int_\theta d\theta V_\theta(R, \theta) \hat{z}, \quad (\text{B.11})$$

where b_n is the solution of the equation $\Gamma(2n) = 2\gamma(2n, b_n)$ (Graham et al. 2005), with γ and Γ the lower incomplete and complete gamma functions, respectively. Without any θ dependence, the specific angular momentum writes

$$j = \frac{2 b_n^{2n}}{(2n)!} \int_R dR (R/R_{\text{eff}})^2 V_\theta(R) e^{-b_n(R/R_{\text{eff}})^{1/n}}, \quad (\text{B.12})$$

where the normalisation factor comes from the analytical expression for the total mass of a Sérsic profile (e.g. Mercier et al. 2022). In the case of a flat rotation curve as in Eq. B.9, it is possible to compute analytically Eq. B.8 and therefore Eq. B.10. Indeed, we have

$$M_k \{\Sigma_M\}_\alpha^\beta = \frac{n \Sigma_{M,0} R_{\text{eff}}^{k+1}}{b_n^{n(k+1)}} \left[\gamma \left(n(k+1), b_n \left(\frac{\beta}{R_{\text{eff}}} \right)^{1/n} \right) - \gamma \left(n(k+1), b_n \left(\frac{\alpha}{R_{\text{eff}}} \right)^{1/n} \right) \right]. \quad (\text{B.13})$$

Appendix B.4: Recovering the RF12 approximation

The Romanowsky & Fall (2012) approximation, hereafter referred as RF12, assumes an exponential disk with a constant rotation curve and computes the angular momentum at infinity. Thus, we can use Eq. B.10 and B.13 to check whether we recover it. First, we can see that for a flat model and in the limit where the rotation curve becomes constant, that is $R_t \rightarrow 0$, Eq. B.10 reduces to B.7. Furthermore, evaluated at infinity and for an exponential disk model (i.e. $n = 1$) Eq. B.13 simplifies to

$$M_k \{\Sigma_M\}_0^\infty = \Sigma_{M,0} R_d^{k+1} \Gamma(k+1), \quad (\text{B.14})$$

where Γ is the complete gamma function and $R_d = R_{\text{eff,d}}/b_1$ is the disk scale length, with $b_1 \approx 1.6783$. Thus, given Eq. B.7, we do recover the Romanowsky & Fall (2012) approximation

$$j = 2V_\theta R_d. \quad (\text{B.15})$$

Appendix B.5: Angular momentum for an exponential disk in equilibrium

It can be interesting to derive the angular momentum for an exponential disk model that is stable against its own gravity, that is without any DM halo or bulge component. We consider the case where the normalisation is taken at the same radius as the angular momentum. Given the expression of the integrated mass and circular velocity for such a model (see Eqs. C.1, D.8, and D.9 of Mercier et al. (2022), its integral writes

$$j(R) = \frac{\sqrt{\pi G R_d \Sigma_{M,d}(0)}}{2\pi R_d^3 \gamma(2, R/R_d)} \int_0^R dr r^3 e^{-r/R_d} f\left(\frac{r}{2R_d}\right), \quad (\text{B.16})$$

where G is the gravitational constant, R_d is the disk scale length, $\Sigma_{M,d}(0)$ is the central surface mass density of the disk, γ is the lower incomplete gamma function, and f is a function of Bessel functions defined in Appendix D of Mercier et al. (2022). If we define $y = x/R_d$, then it simplifies to

$$j(R) = \frac{\sqrt{G M_d(R) R_d}}{2\sqrt{2}\pi \gamma^2(2, R/R_d)} \times \int_0^{R/R_d} dy y^3 e^{-y} f(y/2), \quad (\text{B.17})$$

where $M_d(R)$ is the mass of the disk within the radius R . At $R_{22} = 2.2R_d$, the radius of maximum velocity for the disk, both γ and the integral on the right-hand side become constants and Eq. B.17 further reduces to

$$j(R_{22}) [\text{kpc km s}^{-1}] \approx 3.373 \times 10^{-4} \times \sqrt{M_d(R_{22}) R_d}, \quad (\text{B.18})$$

where $M_d(R_{22})$ is in M_\odot and R_d in kpc.

Chapter 8

A new method for a detailed study of the dark matter content in galaxies

At the end of the first year of this Thesis was discussed the possibility to produce resolved stellar mass maps from SED fitting with the aim to better constrain the distribution of DM within galaxies. Indeed, as discussed in Chapter 5, we can use MUSE cubes to extract the galaxies' kinematics maps which can then be used to model the rotation of their ionised gas. If mass models are used, as was done in [Mercier et al. \(2022\)](#) and in Chapter 6, we can then constrain the fraction of DM found in these galaxies. However, deriving precise constraints on the DM fraction is difficult. Among the different sources of uncertainty that can propagate, an important one comes from the distribution of the stellar mass between the disk and the bulge components. Indeed, based on the implementation of the mass models for the analyses of the scaling relations and of the angular momentum presented in Chapter 7, there are three components that contribute to the total rotation curve: (i) the stellar bulge, (ii) the stellar disk, and (iii) the DM halo. To be complete we should also take into account the contribution of the gas, especially given that at intermediate to high redshift its content in galaxies is larger than in the local Universe (e.g. [Padmanabhan & Kulkarni 2017](#); [Wang et al. 2022](#)). However, we do not have constraints on the amount of gas at these redshifts. An important point is that, when modelling the ionised gas kinematics, the DM halo is what is truly fitted¹, being unknown, and the stellar components are fixed based on the morphological models as discussed in Sect. 5.3.3. Thus, to properly constrain the kinematics parameters of the DM halo and therefore its mass distribution we need first to have robust constraints on the distribution of mass in the stellar disk and bulge.

In [Mercier et al. \(2022\)](#), the disk and bulge morphological parameters were derived from a single HST map in the F814W band. These parameters (more specifically each component's central surface brightness) were then converted in units of mass assuming a constant M/L throughout the galaxy. This M/L was derived by dividing the SED-based stellar mass with the total flux integrated in the same aperture as where the mass was evaluated. Thus, there are two potentially

¹Because we do not constrain the gas, it technically corresponds to the combination of the DM halo and the gas distribution.

strong assumptions that had to be made: (i) that the F814W band traces well enough the distribution of mass and (ii) that the M/L is constant throughout the galaxies. The first assumption is not completely correct because at the redshifts we are concerned with ($0.2 \lesssim z \lesssim 1.5$) the central wavelength of this band corresponds to a rest-frame wavelength that falls between roughly 3300 Å and 6800 Å. Hence, the F814W band misses the red part of the spectrum that traces best the stellar mass. This is certainly one of the most important limitations of the modelling that I performed in [Mercier et al. \(2022\)](#) and it was a strong motivation to develop a framework to produce resolved stellar mass maps. The second assumption is certainly not correct as well but its effect will rather be on the relative amount of stellar mass found in the stellar disk with respect to the bulge. Indeed, with a constant M/L we implicitly assume that both components can be described by the same stellar population. However, we expect the bulge component to be redder than the disk because it is supposed to host a majority of older low-mass stars (e.g. [Quilley & de Lapparent 2022](#)) whose M/L is higher. Thus, with a constant M/L and if the disk dominates the total flux, in particular the massive young stars if there is star formation in the disk, we might underestimate the amount of mass located in the bulge. As an indication, this is typically what is seen when producing resolved stellar mass maps of spiral galaxies as described in Sect. 8.1.2.3, with M/L values that can vary between the stellar bulge and disk components by roughly a factor of five on average.

A first solution that could not be applied in [Mercier et al. \(2022\)](#) because we lacked high-resolution infrared bands but that could be done with future data would be to use two different bands to estimate two M/L values, one for the disk and one for the bulge (e.g. [Junais et al. 2020](#)). Though, this would still assume that the two bands would trace sufficiently well each component separately. But, if there are not just two but multiple bands all the way through from the UV to the IR then it would be even more efficient to use the full information contained in each of these bands to derive the stellar mass in each pixel separately rather than trying to estimate the M/L directly. This is the option that we decided to investigate and it will be referred to in the next parts as resolved or pixel-per-pixel SED fitting. Besides, such a method does not reduce to the sole estimation of the stellar mass in each pixel. Indeed, since it involves SED fitting, it is technically speaking possible to produce resolved maps for any physical parameters that comes out of the SED modelling. Notably, this applies for the SFR for which it might also be interesting to know its spatial distribution to improve the kinematics modelling. Producing resolved stellar mass maps is not completely new. For instance, early works did so on local galaxies by parametrising the M/L in a given band as a function of multiple colours (e.g. [Zibetti et al. 2009](#)) or by directly building SED templates and then applying them on the pixel level (e.g. [Welikala et al. 2008](#)). Follow-up studies also applied the same technique to higher redshift galaxies (e.g. [Welikala et al. 2011](#); [Wuyts et al. 2012](#); [Lang et al. 2014](#); [Tacchella et al. 2018](#)), while other works rather focussed on constraining from multi-band photometry 1D M/L radial profiles which can then be used to reconstruct resolved stellar mass maps (e.g. [Suess et al. 2019](#)).

8.1 Resolved maps from multi-band HST photometry

The first step of this project was to select a small sample of galaxies that would be used to test the method and compare the results of the morphological and kinematics models when using the resolved stellar mass maps with the ones derived from a single band and a with constant M/L value. The two important constraints to select this sample were (i) to have multiple high-resolution bands from the UV to the IR and (ii) to have well resolved morphological and

kinematics maps for these galaxies, in the sense that we should have enough spaxels in both cases to test the impact of the mass maps on the morphological and kinematics model outputs.

We decided to use a sample of 12 galaxies, nine of which are from the MXDF survey (Bacon et al. 2021) and the remaining three are located in the MOSAIC of the MUSE-HUDF survey (Bacon et al. 2017). The nine galaxies of the MXDF were selected in Bouché et al. (2022) from the [OII] emitters catalogue of Inami et al. (2017) keeping those with the highest S/N and eliminating face-on objects to properly constrain their kinematics. In Bouché et al. (2022), these galaxies were used to model their morphology with GALFIT and their kinematics with the GALPAK^{3D} code in order to constrain the shape of their DM halo profile in the inner parts (cusp-core problem). Thus, they were specifically chosen to have well resolved morphology and kinematics. Besides, these galaxies are all located in the MXDF which is itself found within the HUDF for which the nine following HST photometric bands are available (from UV to NIR): F435W, F606W, F775W, F814W, F850LP, 105W, 125W, 140W, and 160W. Additionally, since we had contributed to the analysis performed in Bouché et al. (2022), especially on the morphological modelling of the nine MXDF galaxies with GALFIT, it further made sense to select these galaxies as part of the test sample. The main characteristics of this sample are presented in Table 8.1 with their (1) ID, (2) MUSE spectroscopic redshift, (3) total exposure time, (4) [OII] S/N, (5) total stellar mass, (6) SFR derived from SED fitting (Bouché et al. 2022) using the code Multi-wavelength Analysis of Galaxy Physical Properties (MAGPHYS)², (7) stellar disk inclination derived from GALFIT, (8) B/T evaluated at two effective radii (based on the GALFIT best-fit model), and (9) global effective radius derived from a single Sérsic profile fit on their F160W HST map. The HST images for the 12 galaxies in the different HST bands are also represented in Figs. 8.1 and 8.2. The largest galaxy is ID1 and it has a quite massive bulge in the central parts (roughly $1.5 \times 10^{10} M_{\odot}$ at two effective radii, that is around 35% of the total stellar mass; see Table 8.1 for more details). Thus, it will be used as the main test galaxy in what follows, especially in Sect. 8.2 for the machine learning application. We see that there is a non-negligible fraction of edge-on systems in the test sample and galaxies with various bulge contributions, as is also shown in Table. 8.1. Among the galaxies there are two special cases with nearby companions: ID3 and ID943. For both galaxies the companions have been masked using segmentation maps (see Sect. 8.1.2.1 for more details). Most of the galaxies in the sample are quite red with HST images in the reddest band (F160W) brighter by at least 1 mag (galaxy ID37) and by at most 4 mag (galaxy ID 15) than in the bluest band (F435W). Looking at galaxy ID1 we can also see that the bluest bands (435W and 606W) tend to trace the spiral arms and clumps where star formation is most likely to happen. On the other hand, these features tend to fade in the IR bands where the bulk of the stellar mass is probed.

In order to perform the SED fitting and extract maps of physical parameters, we relied on two codes: LEPHARE and CIGALE. Among the two, CIGALE is the most recent and probably the most versatile. Initially, LEPHARE was designed to derive photometric redshifts but it is also possible to use it with a fixed redshift to estimate physical parameters. Broadly speaking, the two codes work in the same way and include similar models. The only difference is that CIGALE is an energy-balance code, meaning that the energy of the stars and gas absorbed by dust in the UV and in the optical is re-emitted entirely by the dust model in the mid-infrared (MIR) and far-infrared (FIR). The development of the framework to produce resolved stellar mass and SFR maps was started in 2021 as part of H. Plombat’s Master project that I supervised. In addition, previous data processing of the 12 selected galaxies to align images and match their pixel scale

²<http://www.iap.fr/magphys/>

Table 8.1: Main characteristics of the test sample used for resolved SED fitting. The table is adapted from [Bouché et al. \(2022\)](#) and H. Plombat’s Master project.

ID	z	t_{exp} h	S/N	$\log_{10} M_{\star}$ M_{\odot}	$\log_{10} \text{SFR}$ $M_{\odot} \text{ yr}^{-1}$	i °	B/T %	R_{eff} "
(1)	(2)	(3)	(4)	(5)	(6)	(7)	(8)	(9)
MXDF								
3	0.62	42	15	$10.08^{+0.02}_{-0.06}$	$2.62^{+0.80}_{-1.20}$	64	4	0.83
15	0.67	136	9	$10.23^{+0.02}_{-0.10}$	$0.99^{+2.53}_{-0.99}$	86	0	0.82
37	0.98	136	61	$8.87^{+0.06}_{-0.17}$	$0.80^{+1.22}_{-0.18}$	56	0	0.45
912	0.62	136	124	$9.19^{+0.19}_{-0.06}$	$1.29^{+1.60}_{-0.30}$	27	0	0.28
919	1.10	136	98	$9.83^{+0.02}_{-0.06}$	$4.28^{+0.52}_{-0.55}$	28	21	0.40
937	0.73	44	18	$9.35^{+0.08}_{-0.06}$	$1.50^{+0.34}_{-0.36}$	82	16	0.74
943	0.66	136	32	$9.28^{+0.06}_{-0.06}$	$1.00^{+0.57}_{-0.40}$	77	0	0.73
982	1.10	92	22	$9.75^{+0.09}_{-0.07}$	$3.25^{+0.84}_{-0.97}$	70	43	0.59
1002	0.99	47	35	$9.43^{+0.02}_{-0.07}$	$1.18^{+0.02}_{-0.26}$	73	21	0.52
mosaic								
1	0.62			$10.65^{+0.06}_{-0.08}$	$8.19^{+3.07}_{-2.34}$	36	35	1.45
7	0.62			$10.05^{+0.05}_{-0.04}$	$5.51^{+1.17}_{-1.08}$	40	26	0.55
13	1.00			$9.92^{+0.06}_{-0.06}$	$2.63^{+0.90}_{-0.69}$	32	0	0.39

Notes: (1) ID from [Inami et al. \(2017\)](#), (2) MUSE spectroscopic redshift, (3) exposure time, (4) signal-to-noise ratio for [O II], (5) total stellar mass, (6) star formation rate, (7) disk inclination, (8) bulge-to-total flux ratio in the F160W HST band evaluated at two effective radii, and (9) global effective radius. The MUSE data for galaxy ID3 are from the MOSAIC of the MUSE-HUDF because it lies on the side of the MXDF FoV so that the deepest data are in the MOSAIC.

and their resolution was performed by J. C. B. Pineda. Afterwards, I kept working on the project and developed a proper python implementation.

In what follows, I will discuss the framework that we developed, starting in Sect. 8.1.1 by mentioning the fundamental principles that are shared between SED fitting codes. The properties of multi-band photometric observations and how they are handled by such codes will be discussed and, in Sect. 8.1.2, I will mention the pre-processing steps performed by J. C. B. Pineda, as well as how the HST maps errors were handled for the SED fitting part. Afterwards, a comparison will be made between the stellar mass maps reconstructed from resolved SED fitting and the distribution of mass inferred from single-band observations assuming a constant M/L throughout the galaxies. Finally, the python implementation of the framework will be discussed in Sect. 8.1.3. In particular,

examples of automatic pixel-per-pixel SED fitting modellings performed with both LEPHARE and CIGALE will be shown and differences between the two implementations will be mentioned.

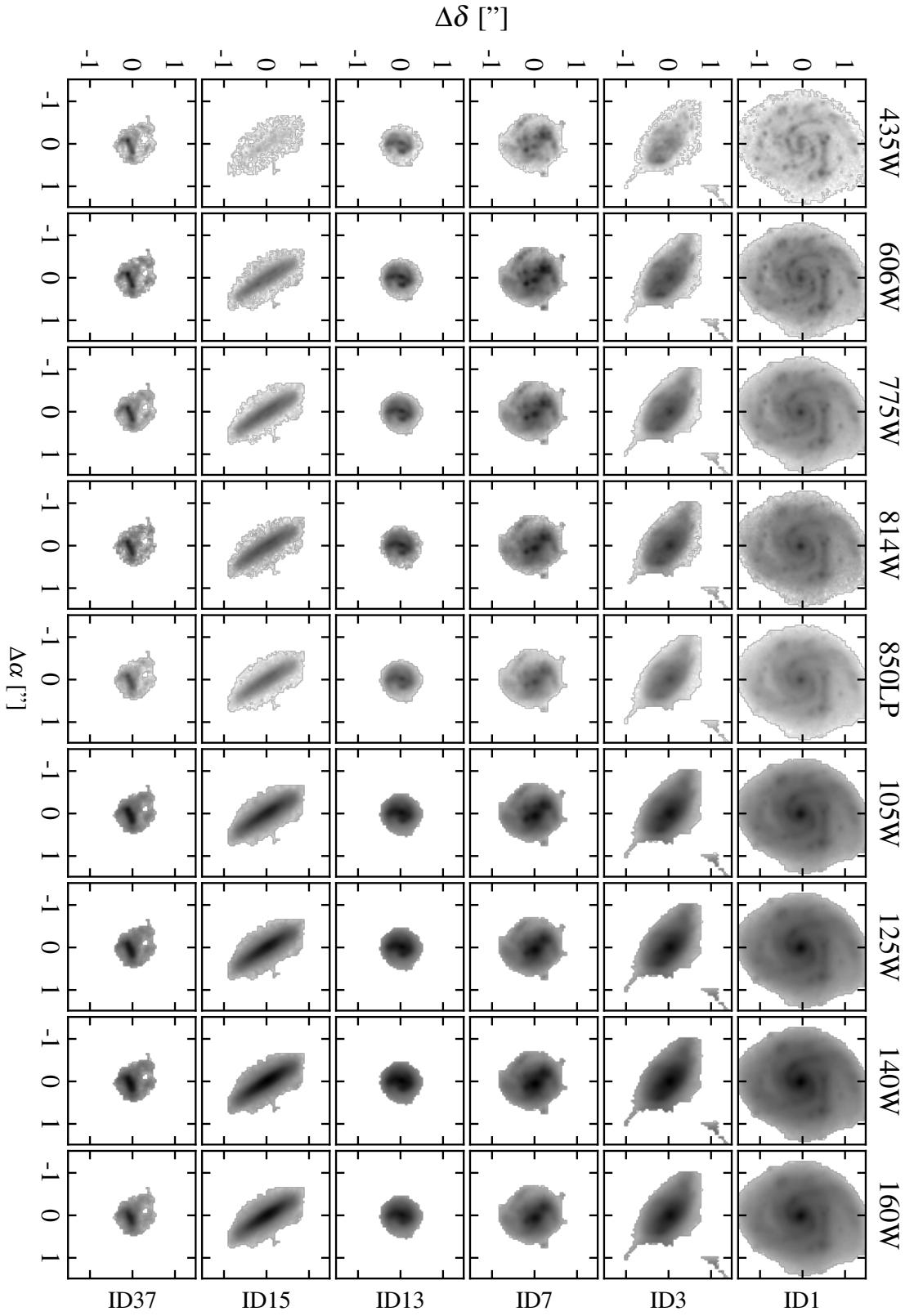


Figure 8.1: HST images in the nine available bands for the first six galaxies in the test sample used for resolved SED fitting. For each galaxy the same logarithmic scale is used for the nine bands. All of the images are shown in their coarsest pixel scale (0.06" per pixel) but in their original resolution and have already been masked using segmentation maps from SEXTRACTOR.

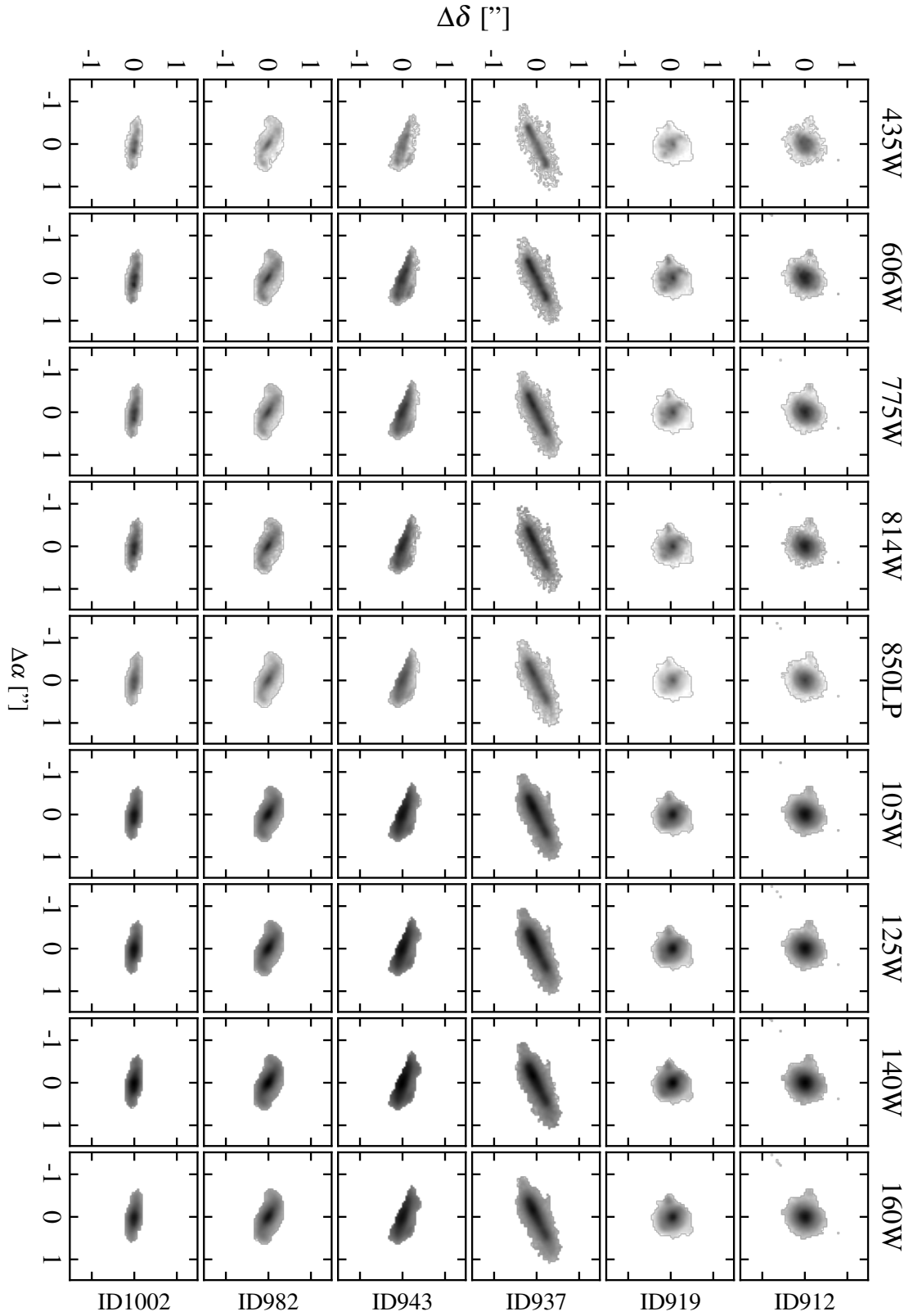


Figure 8.2: HST images for the remaining six galaxies in the test sample used for resolved SED fitting. See Fig. 8.1 for the description.

8.1.1 Fundamental principles of SED fitting

Before delving into the implementation we used to perform pixel-per-pixel SED fitting, I must first discuss the basic principles behind the concept of SED fitting and how it is possible to derive physical parameters such as stellar masses or SFRs from multi-band photometric observations. Because the two codes we are interested in that are `LEPHARE` and `CIGALE` only handle photometric data, that is fluxes measured in filters, and not spectra nor a combination of both, I will solely focus on the implementation of such codes.

8.1.1.1 Multi-band photometric observations

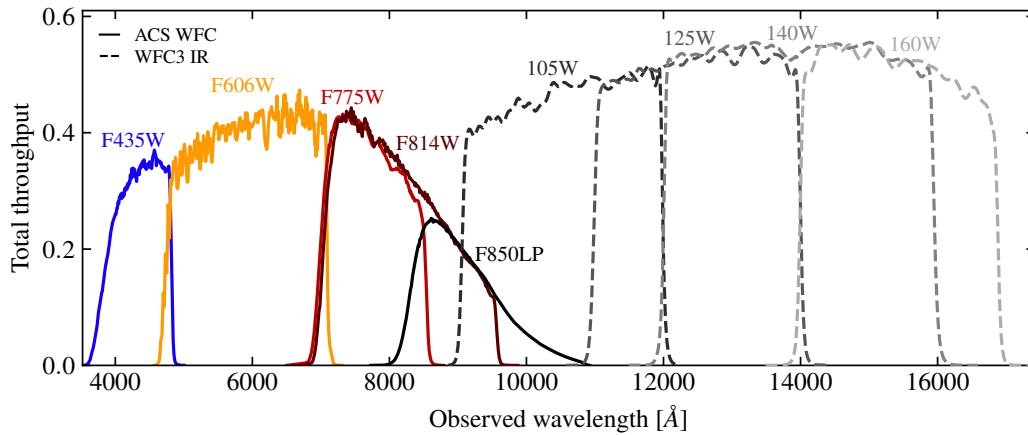


Figure 8.3: Illustration of the total throughput (filter, mirrors, and instrument) for the nine HST filters used to derive resolved stellar mass maps. The lines are approximately coloured by that of their central wavelength, except for the infrared filters which are coloured by shades of grey (the lighter the longer the central wavelength). Filters corresponding to the ACS WFC instrument are shown with solid lines whereas those from the WFC3 instrument in its IR channel are shown with dashed lines.

The input data that handle SED fitting codes are multi-band photometric observations, that is fluxes or magnitudes measured in a given band. By nature, the constituents of a galaxy (e.g. stars, gas, dust, etc.) emit and absorb (e.g. gas, dust) light in a continuum of wavelengths which is what is referred to as a spectrum. The spectrum of a galaxy is therefore the combination of the spectra of each of its constituents, for instance of all its stars of different ages and metallicity, of the different phases of gas (atomic, molecular, or ionised), or of the dust. In addition, these components can interact with each other. Typically, the dust will partially obscure the optical part of the spectrum emitted by the stars and the gas and will re-emit it in the IR. Thus, a photometric observation in a single band is no more than integrating the redshifted spectrum of the galaxy in the spectral window of the band.

This picture would be correct if there was no loss of light along the optical path all the way through to the detector. However, because of the optics of the telescope, the instrument, the detector, etc., some light is lost along the way. This is what is called throughput: the amount of

light that is preserved when passing through some part or the entirety of the system. In addition, the filters themselves are not perfect boxcar filters that let through 100% of the light in their targeted wavelength range. Thus, depending on the filter and the instrument used the spectrum of the galaxy will be more or less impacted as a function of wavelength which will change its shape and therefore the flux measured in a given band. This is illustrated in Fig. 8.3 where I show the total throughput, that is including the filter, the mirrors, and the instrument, for the nine HST filters that we used to produce resolved maps. Those from the Hubble Space Telescope Advanced Camera for Surveys (HST-ACS) that are located in the optical are represented with a color that roughly matches their wavelength whereas the IR filters from the Hubble Space Telescope Wide Field Camera 3 (HST-WFC3) are shown with varying shades of grey and with a dashed line. Hence, a first key ingredient in SED fitting codes is to provide, if not already present, the total throughput as a function of wavelength for each band that is going to be used in the modelling.

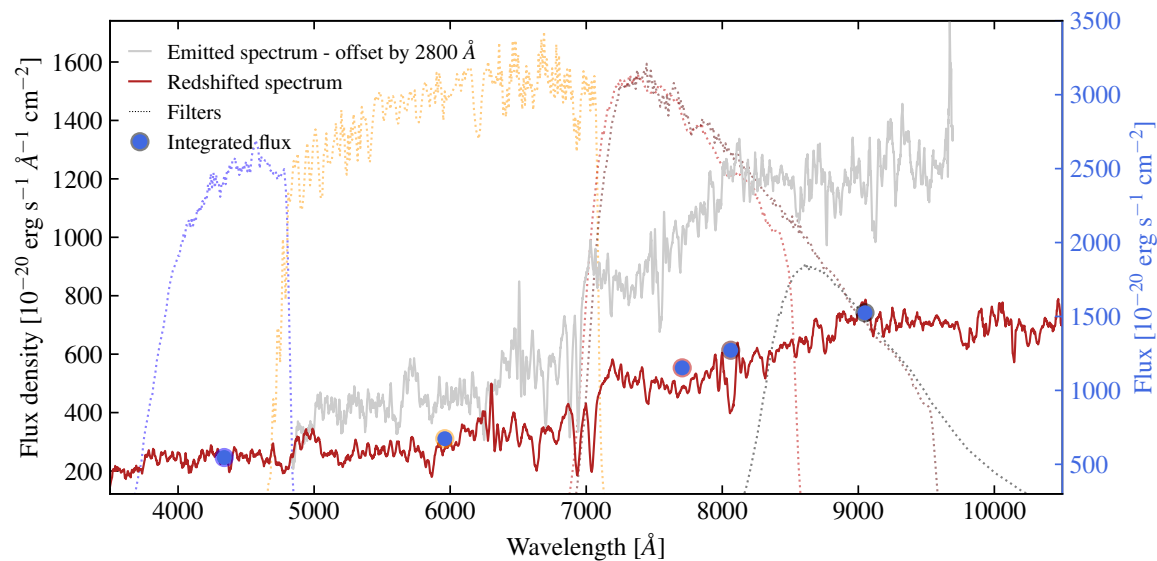


Figure 8.4: Illustration of the impact of redshifting and integrating a spectrum in various HST filters on a galaxy’s SED. The grey line represents a fictitious rest-frame spectrum at $z = 0.7$ adapted from the MUSE spectrum of galaxy 328_CGR84 which, for readability, has been offset by 2800 Å. The red line represents the redshifted spectrum as it would be observed and the blue data points show the integrated flux in the five HST ACS WFC filters that we used (flux scale is shown in blue on the right hand-side). For illustration, the various filters’ total throughput curves are shown as faint dotted line in the background.

So, to convert a high-resolution spectrum into a SED, that is a combination of observed fluxes in multiple bands, at least two steps must be taken: (i) take into account the impact of cosmology by redshifting the spectrum to the galaxy’s cosmological redshift and (ii) integrate it into each band taking into account the total throughput. Based on Sect. 1.1, there are two aspects to take into account to perform the first step. First, we need to scale appropriately the amplitude of the spectrum according to whether it is measured in units of frequency or wavelength. Second, we

must redshift its wavelength range, the effect of which will be to shift it redward and to dilate it. The fact that it is dilated is important because if we consider a filter with a given spectral window then it will probe a smaller rest-frame spectral range for higher redshift galaxies. I show an illustration of how a fictitious spectrum is affected by these steps in Fig. 8.4. The spectrum has been adapted from that of galaxy 328_CGR84. In grey is represented the rest-frame spectrum offset by 2800 Å so that it is visible in the wavelength range of the redshifted spectrum ($z = 0.7$) shown in red. The integrated fluxes in the five HST ACS WFC bands that we used (from shorter to longer wavelengths: F435W, F606W, F775W, F814W, and F850LP) are shown with blue circle. The filters' throughput curves are also shown as faint dotted lines in the background. As discussed previously we see the effects of redshifting the spectrum, in particular how it spreads it into a larger wavelength range. We can also see that, even if the global shape of the spectrum is retained in the SED, we lose substantial details compared to the original spectrum which therefore limits the complexity of the modelling that can be applied.

Transforming a high-resolution spectrum into a SED technically requires a few more steps than those I have discussed above. Indeed, if we consider a SED that is made of space-based and ground-based observations then the latter will be affected in different ways than the former because of the impact of the atmosphere that will both absorb and emit, and that as a function of wavelength. For instance, the atmosphere will emit thermal radiation in the IR that will change throughout the night as the atmosphere cools down. Furthermore, independently of whether the observations are space-based or ground-based there are further aspects that need to be taken into account such as, for instance, the attenuation by dust in the Milky Way or the zodiacal light. The former can be modelled using a Galactic attenuation curve and an amplitude, typically taken as A_V (see discussion in Sect. 8.1.1.2). Since dust is primarily located in the disk of the Galaxy, it will more severely affect observations made therein and thus a map of the spatial distribution of dust and its properties must also be taken into account (e.g. [Planck Collaboration et al. 2014](#)). The latter effect is rather due to dust located in the ecliptic plane of the Solar System that scatters light emitted from the Sun and produces a faint glow. Such additional effects may or may not be included in SED fitting codes depending on the implementation. As an example, CIGALE assumes that fluxes have already been pre-treated beforehand and therefore does not take them into account whereas LEPHARE does include a mean atmospheric extinction when computing the throughput of the filters.

8.1.1.2 Key concepts: IMF, SSPs, SFH, and dust attenuation

Now that we know how to transform a high-resolution spectrum into a SED, we need to actually produce models of spectra to fit the observed SEDs. This is the core concept of SED fitting codes: produce high-resolution spectra from models, degrade them to match the different bands, and fit them onto the observed SED to find the best solution. To produce such models there are at least four key ingredients that are shared between every SED fitting code: the IMF, SSP, SFH, and dust absorption. I will quickly go through each one to explain how they are used in combination with the others to produce composite models of galaxies' spectra.

SED fitting codes such as CIGALE were initially designed to model SEDs from integrated photometry, that is the SEDs combining the light coming from the entire galaxies or from most of their extension. Thus, the light that is received is the combination of a very large number of stars, dust, and gas particles whose spatial distribution is not very well constrained and it would therefore be vain to try to model each star or dust and gas particles separately. Instead, the

concept of SSPs was developed. A SSP is a population of stars that was born at the same time from the same gas cloud. Thus, a SSP is composed of a large number of stars with different masses but with the same age and metallicity that will evolve along an isochrone. In practice, a SSP is stored as a spectrum that changes with time as stars evolve along and out of the stellar main sequence. Massive blue stars will burn their fuel faster and therefore will leave the main sequence and “die” quicker than older red stars. Thus, the SSP spectrum will tend to get redder with cosmic time. Usually, different SSP spectra with a different evolution are provided for discrete values of metallicity, though implementations may vary between SED fitting codes. For instance, in CIGALE the following metallicities are available: $\log_{10}(\text{O}/\text{H}) = 10^{-4}$, 4×10^{-4} , 4×10^{-3} , 8×10^{-3} , 2×10^{-2} , and 5×10^{-2} dex. Furthermore, SSP spectra are normalised so that their amplitude with wavelength only depends on the proportion of stars in each mass bin, which is also an important parameter for a SSP. Indeed, depending on how many stars there are in low-mass or high-mass bins, the shape of the spectrum will necessarily be affected. Thus, we also need to have a function that tells us how likely it is to sample a star of a given mass from a collapsing gas cloud. This function is called the IMF. Commonly used IMFs are those of [Salpeter \(1955\)](#), [Kroupa \(2002\)](#), or [Chabrier \(2003\)](#). Once an IMF is chosen the SSP can be derived for a given metallicity using a stellar evolution code that will sample it, evolve the stellar population along its isochrone, and compute the total spectrum at each time step. Typical SSPs used in SED fitting codes are those of [Bruzual & Charlot \(2003\)](#) and [Maraston \(2005\)](#). Discussing the origin of the differences between these SSPs is beyond the scope of this discussion but I can just note that they can be affected by lots of different treatments from, for instance, the modelling of the IMF, the treatment of the post and pre-stellar main sequence phases, to whether they integrate the contribution of multiple-stars systems.

However, SSPs are not sufficient in themselves to create synthetic spectra because the spectrum of a galaxy is not just due to a single population of stars but to the sum of the spectra of all the stellar populations in the galaxy with different ages. Because these populations have different ages their spectrum will not evolve by the same amount and it will therefore differ in shape from one age to another. Furthermore, this sum must be weighted by the amount of stars created at each time step. The function that describes how many stars are born as a function of cosmic time is referred to as the SFH. When measured at a given time step or across a certain period it is rather called the SFR. There is a multitude of SFHs that can be used such as an exponentially declining star-formation law, a delayed exponential law that includes a rising part before the exponential decline, periodic, or even empirically calibrated laws (e.g. see [Boquien et al. 2019](#)). These examples pertain to the class of parametric models, that is models for which we assume a certain parametrised shape of the SFH. Another class of SFH models not implemented in LEPHARE and CIGALE but that is for instance in PROSPECTOR³ ([Leja et al. 2019](#); [Johnson et al. 2021](#)) or STARLIGHT⁴ ([Cid Fernandes et al. 2005](#)) is non-parametric models. These models are non-parametric in the sense that they do not assume a shape of the SFH or rather than they assume a SFH that is piecewise constant. The amplitude of each piece being a free parameter, these models are therefore usually as parametric if not more than parametric models. Nevertheless, they can be useful to better constrain the shape of the SFH though their use can be limited with only broad-band photometry ([Leja et al. 2019](#)). The production of a full galaxy’s spectrum is then quite simple once we know the SFH. Indeed, let us assume that a galaxy with an age t_{age} can be modelled with a SSP that we will note $\text{SSP}(t)$ ($t = 0$ corresponds to the beginning

³<https://prospect.readthedocs.io/en/latest/index.html>

⁴<http://www.starlight.ufsc.br/>

of the galaxy and $t = t_{\text{age}}$ corresponds to the time when the light that reaches us was emitted), and with a SFH that can be split in three parts: $\text{SFH}(0)$, $\text{SFH}(t_1)$, and $\text{SFH}(t_{\text{age}})$, with $0 < t_1 < t_{\text{age}}$. At $t = 0$, the spectrum of the galaxy will be given by $\text{SSP}(0) \times \text{SFH}(0)$. At $t = t_1$, the SSP emitted at $t = 0$ will evolve into $\text{SSP}(t_1)$ and a new SSP will emit (thus its spectrum will be that given by $\text{SSP}(0)$) with an amount of stars given by $\text{SFH}(t_1)$. Hence, the spectrum at $t = t_1$ writes $\text{SSP}(t_1)\text{SFH}(0) + \text{SSP}(0)\text{SFH}(t_1)$. Finally, at $t = t_{\text{age}}$, the first SSP will evolve to $\text{SSP}(t_{\text{age}})$, the second to $\text{SSP}(t_1)$, and a new one will emit with an amount of stars given by $\text{SFH}(t_{\text{age}})$. Hence, the final spectrum is $\text{SSP}(t_{\text{age}})\text{SFH}(0) + \text{SSP}(t_1)\text{SFH}(t_1) + \text{SSP}(0)\text{SFH}(t_{\text{age}})$. If we generalise to continuous SSPs and SFHs, then we get the general expression to compute the model galaxy's spectrum:

$$F_\lambda = \int_0^{t_{\text{age}}} dt \text{SSP}_\lambda(t) \text{SFH}(t_{\text{age}} - t), \quad (8.1)$$

where I have used the subscript λ for the SSP to emphasize that it is per unit wavelength as for F_λ on the left-hand side of the equation.

To be complete, we need at the very least one more aspect to take into account. We need to consider the fact that the spectrum of galaxies are affected by the absorption and the scattering by dust that reduces the amount of flux we receive in the UV and in the optical and increases it in the FIR. The sheer effect of absorption and scattering by dust irrespective of the geometry of the stars, gas, and dust is called dust absorption. In essence, the more dust along the LOS, that is the higher its column density, the larger the dust absorption. On the other hand, the complex modelling of the interplay between the light of the obscured and unobscured stars, the ISM, and the dust, taking into account their spatial distribution, and potential scattering back onto the LOS is referred to as dust attenuation. This is what SED fitting codes implement. To do so, they must know the amplitude of the attenuation which is related to the column density of the dust, and its shape, that is by how much is attenuated the emitted light as a function of wavelength. The former is parametrised by the attenuation in the V-band, noted A_V , that was already discussed in Sect. 3.2.5.2 and the latter by the attenuation curve, noted A_λ/A_V . The modelling of the attenuation curve is complex and depends on the properties of the ISM, on the distribution of the stars and the grains, and on the chemistry of the grains among other things. Thus, I will not extend further and I will refer to [Salim & Narayanan \(2020\)](#) for a review on the topic. Two typical attenuation laws that are used are those of [Calzetti et al. \(2000\)](#) and [Charlot & Fall \(2000\)](#). These four components (IMF, SSP, SFH, and dust attenuation) are the key ingredients of SED fitting but, depending on the code and its objectives, there can be other components that might be in some cases as important. For instance, in both LEPHARE and CIGALE the contribution of emission lines can be modelled and integrated into the galaxy's spectrum model using recipes that change from one code to another. Another example in CIGALE is its treatment of the dust emission in the FIR with various dust emission models and using the principle of energy balance where the absorbed energy from the stars and the gas is used as input for the energy emitted by the dust.

8.1.1.3 Fitting galaxies' SEDs with LePHARE and Cigale

Both codes will find the best-fit solution in the same way. Given the models and the list of values for their parameters they will generate a multi-dimensional grid of normalised SED model. The best-fit solution is therefore the one that minimises the following χ^2 expression:

$$\chi^2 = \sum_i \left(\frac{f_i - \alpha \times m_i}{\sigma_i} \right)^2, \quad (8.2)$$

where f_i , m_i , and σ_i are the observed flux, normalised SED model, and photometric uncertainty in the band i , respectively, and α is the de-normalisation factor for the model that writes (Boquien et al. 2019)

$$\alpha = \frac{\sum_i f_i m_i / \sigma_i^2}{\sum_i m_i^2 / \sigma_i^2}. \quad (8.3)$$

CIGALE uses a slightly more general expression but that reduces to Eqs. 8.2 and 8.3 in our case. The scale factor α is then used to scale appropriately the normalised extensive physical properties (e.g. stellar mass or SFR) associated to the best-fit model. Therefore, in both codes both the stellar mass and the SFR are products of the SED fitting rather than parameters that are fitted. Finally, CIGALE implements a Bayesian method to estimate more robustly some physical parameters. For each model in the grid CIGALE computes a likelihood as $\exp(-\chi^2/2)$ and then likelihood weighted mean and standard deviation estimates for each parameter.

8.1.2 Application to resolved SED fitting

8.1.2.1 Pre-processing steps

A few pre-processing steps were applied by J. C. B. Pineda on the HST images of the 12 selected galaxies. Originally, each band had its own resolution and pixel scale. The images in the F435W, F606W, F775W, F814W, and F850LP ACS WFC bands had the finest pixel scale of 0.03'' per pixel, though they were also available at 0.06'' per pixel, whereas the remaining four F105W, F125W, F140W, and F160W WFC3 IR bands had a coarser scale of 0.06'' per pixel. Additionally, the images' world coordinate systems (WCS) were aligned between the bands of the same instrument (ACS WFC or WFC3) but not between the two instruments. Finally, some objects had companions in their HST images that needed to be masked. Therefore there was a need to equate the resolutions and the pixel scales of the images and align them before producing resolved maps. The way this was achieved is as follows: (i) the sky background was estimated in empty regions of the images and subtracted for each image in each band, (ii) the HST PSF FWHM was derived in each band by fitting as many stars as possible, the retained value being the median FWHM of all the fits (see Table 8.2 for the full list of values), (iii) for each galaxy, East-West and North-South offsets were measured in each band using the images at a scale of 0.06'' per pixel and a correction was applied to align the images, (iv) the images were convolved by a Gaussian kernel⁵ to match the worst resolution in our data, that is in the F160W band with a FWHM of 0.22'', and (v) the images were masked using segmentation maps from Inami et al. (2017) derived with the Source-Extractor (SEXTRACTOR)⁶ software (Bertin & Arnouts 1996) using multiple HST bands (see also Rafelski et al. 2015).

The images were originally given in units of electrons per second so they needed to be converted in physical units before being handled by LEPHARE or CIGALE. The former accepts magnitudes in the AB system (Oke 1974) whereas the latter accepts flux densities in Jy, that is per unit

⁵A Moffat profile might have been more appropriate but a Gaussian kernel was simpler to match the resolution between each band.

⁶<https://www.astromatic.net/software/sextractor/>

HST band	Zero point AB magnitude	PSF FWHM "
(1)	(2)	(3)
F435W	25.68	0.110
F606W	26.51	0.134
F775W	25.69	0.123
F814W	25.94	0.129
F850LP	24.87	0.120
F105W	26.27	0.208
F125W	26.23	0.211
F140W	26.45	0.219
F160W	26.94	0.220

Table 8.2: Zero point and PSF FWHM values for the nine HST bands used for the derivation of the resolved maps. The table is adapted from H. Plombat’s Master project.

Notes: (1) HST band, (2) zero point in the AB magnitude system, and (3) HST PSF FWHM. The zero point values are those used in Eq. 8.5 to convert the HST maps from electron counts to AB magnitudes and/or flux densities.

frequency. Formally, AB magnitudes are defined as the magnitude m_{AB} corresponding to an equivalent flux density F_ν that would produce the same observed count rate but with a flat spectrum per unit of frequency. Its expression is

$$m_{\text{AB}} = -2.5 \log_{10} F_\nu - 48.6, \quad (8.4)$$

where F_ν must be in $\text{erg s}^{-1} \text{Hz}^{-1} \text{cm}^{-2}$. To convert images from electrons per second to AB magnitudes one can use the following formula:

$$m_{\text{AB}} = -2.5 \log_{10} \text{CR} + \text{Zpt}_{\text{AB}}, \quad (8.5)$$

where CR is the count rate measured in electrons per second and Zpt_{AB} is the zero point value that must be used to get AB magnitudes. This zero point can be derived using two keywords given in HST image headers: an inverse sensitivity noted PHOTFLAM and a pivot wavelength noted PHOTPLAM. Its expression is given by

$$\text{Zpt}_{\text{AB}} = -2.5 \log_{10} \text{PHOTFLAM} - 5 \log_{10} \text{PHOTPLAM} - 2.408, \quad (8.6)$$

where PHOTFLAM must be in $\text{erg } \text{\AA}^{-1} \text{e}^{-1} \text{cm}^{-2}$ and PHOTPLAM in \AA . The different zero points are listed in Table 8.2 for the nine HST bands. With Eqs. 8.4, 8.5, and 8.6 it is possible to convert from count rates to fluxes and magnitudes and vice versa.

8.1.2.2 Handling flux uncertainties

An important aspect for any kind of fit, including SED fitting, is to properly estimate the uncertainty on the observations. This is particularly true for SED fitting because we do not want

a band with a large uncertainty to contribute too much to the estimation of the galaxy’s physical parameters. This is even more true in the case of pixel-per-pixel SED fitting. Indeed, if we assume that the photons that hit the detector follow Poisson’s statistics, then we know that the standard deviation for a signal S will be given by $N = \sqrt{S}$. This gives us an estimate of the uncertainty on the signal and therefore on the noise level in the absence of additional noise sources. The S/N is then equal to \sqrt{S} which means the more signal the relatively more precise it becomes. Incidentally, this also means that the S/N in each individual pixel will be lower than that of the integrated signal coming from the entire galaxy and therefore that we need more precise estimates of the noise than we would with an integrated SED to have precise constraints on the stellar mass and SFR in each pixel.

To do so, we started from the weight maps given alongside the HST images that correspond to the inverse of the variance of the images, excluding the contribution of the noise due to the signal (i.e. Poisson’s noise). However, these are not standard images since they have been treated through a drizzling program (Illingworth et al. 2013) called MULTIDRIZZLE and described in Koekemoer et al. (2003). This drizzling step allows to combine multiple dithered images of the same FoV to produce a final image that has a smaller pixel scale than the original images but at the cost of introducing correlations between the noise in each of the new pixels (Casertano et al. 2000). This renders the modelling of the propagation of the signal-induced noise difficult. Besides, as argued in Casertano et al. (2000), the relevant noise, for instance to decide on the significance of a detection, is rather the background noise. Hence, the noise induced by the signal was not implemented in their weight maps, which in turn produces error maps that are relatively flat. Nevertheless, even if the background noise is sufficiently high, we would expect the signal-induced noise to be larger where the flux of the galaxy peaks. Therefore, we decided to include an estimate of Poisson’s noise into these maps. If the detector measures a count rate S over an exposure time T_e , then the signal corresponding to the detected number of electrons is $S_e = S \times T_e$. If we assume that the electrons obey Poisson’s statistics, then this signal must also be equal to its variance. In addition, because HST images are given in units of electrons per second, the HST weight maps provide us with variance maps (noted σ^2) for the background signal in units of electrons squared per second squared. Thus, the total variance due to the background signal over the entire exposure time is $\sigma_b^2 = T_e^2 \times \sigma^2$. The total variance σ_{tot}^2 will be the sum of the two and the corresponding variance $\sigma_{e^-/s}^2$ in electrons per second will therefore write

$$\begin{aligned}\sigma_{e^-/s}^2 &= \frac{\sigma_{\text{tot}}^2}{T_e^2} \\ &= \sigma^2 + \frac{S}{T_e},\end{aligned}\tag{8.7}$$

where S is the signal in electrons per second and σ^2 is the variance in electrons squared per second squared coming from the HST weight maps. As already discussed above, the drizzling step changes the pixels’ dimensions and introduces correlations into the noise so that Eq. 8.7 is only an approximation of the real variance. A last important aspect is to properly take into account the effect of convolution. Indeed, the HST images were convolved to the worst resolution available in the F160W band (see Sect. 8.1.2.1). As long as we can neglect the covariance between pixels, the variance map must also be convolved but using the square of the kernel that was used for the images (see in Appendix D for a demonstration):

$$\sigma^2(x_0, y_0) = \sum_{x,y} K^2(x_0 - x, y_0 - y) \sigma^2(x, y) + \sum_{\substack{x,x',y,y' \\ x \neq x' \wedge y \neq y'}} K(x_0 - x, y_0 - y) K(x_0 - x', y_0 - y') Cov((x, y), (x', y')), \quad (8.8)$$

where $\sigma^2(x_0, y_0)$ is the variance of the convolved signal and $Cov((x, y), (x', y'))$ is the covariance between two pixels at position (x, y) and (x', y') . If the covariance is null or negligible, then the variance of the convolved signal is given by the variance map convolved by the square of the kernel. In theory, neglecting the covariance is not entirely appropriate since we know there must be some, though we do not know how much there is. Still, neglecting it is at least consistent with the previous assumption that the signal follows Poisson's statistics.

8.1.2.3 Pixel-per-pixel SED fitting with LEPHARE and Cigale

Once the pre-processing steps were done and the variance maps correctly estimated, the last part was to extract the flux in each pixel and in each band, produce tables according to the input format required by LEPHARE and CIGALE, define the models and their parameters for the SED fitting, run the fit, and finally recover the output tables, reconstruct the resolved maps, and analyse them. Discussing the variation of the results when using different SED fitting models is important and shall be done in a future analysis. Instead, in what follows, the goal is to see how much impact resolved stellar mass maps have on the galaxies' morphology and on the derived fraction of mass found in their DM component when propagating their best-fit morphological model to their kinematics modelling compared to the previous assumption of a constant M/L throughout the galaxies. Thus, this constant M/L used in the following parts will be derived with the same SED fitting models as those used to produce the resolved maps. For LEPHARE, we used the Bruzual & Charlot (2003) SSP library available as an additional package with a Calzetti et al. (2000) attenuation law. In LEPHARE, the galaxy spectra are automatically computed for a given SSP library with fixed metallicity values, IMF, and SFH. Thus, for the Bruzual & Charlot (2003) library it comes with a Chabrier (2003) IMF, three metallicity values, and an exponentially declining SFH. For CIGALE we also used a Bruzual & Charlot (2003) SSP library with a Chabrier (2003) IMF, a fixed metallicity of 0.02 dex, a delayed exponential SFH with a final burst-quenching phase (see Sect. 3.2.5.2), and a dust attenuation that is modelled with a single powerlaw for both young and old stars with an adjustable attenuation amplitude between both. Finally, we also included the nebular module to take into account the contribution of emission lines.

Three examples of resolved stellar mass maps for galaxies ID1, ID13, and ID1002 are shown in Fig. 8.5. On the leftmost column is shown the map derived using LEPHARE, on the second column from the left the map derived with CIGALE, on the third column the stellar mass map obtained when multiplying the HST map in the F160W band by the M/L derived using CIGALE's total mass, and on the rightmost column the same as the F160W HST map but using the F435W band. The same mass scale has been used for each image and each galaxy. As already discussed in Sect. 8.1, we can see that the F160W band seems to trace much more robustly the stellar mass distribution than the F435W band. Overall, LEPHARE and CIGALE find consistent stellar mass maps between each other and their total mass derived by summing up the contribution of each unmasked pixel is nearly the same between the two codes. Furthermore, we checked whether the

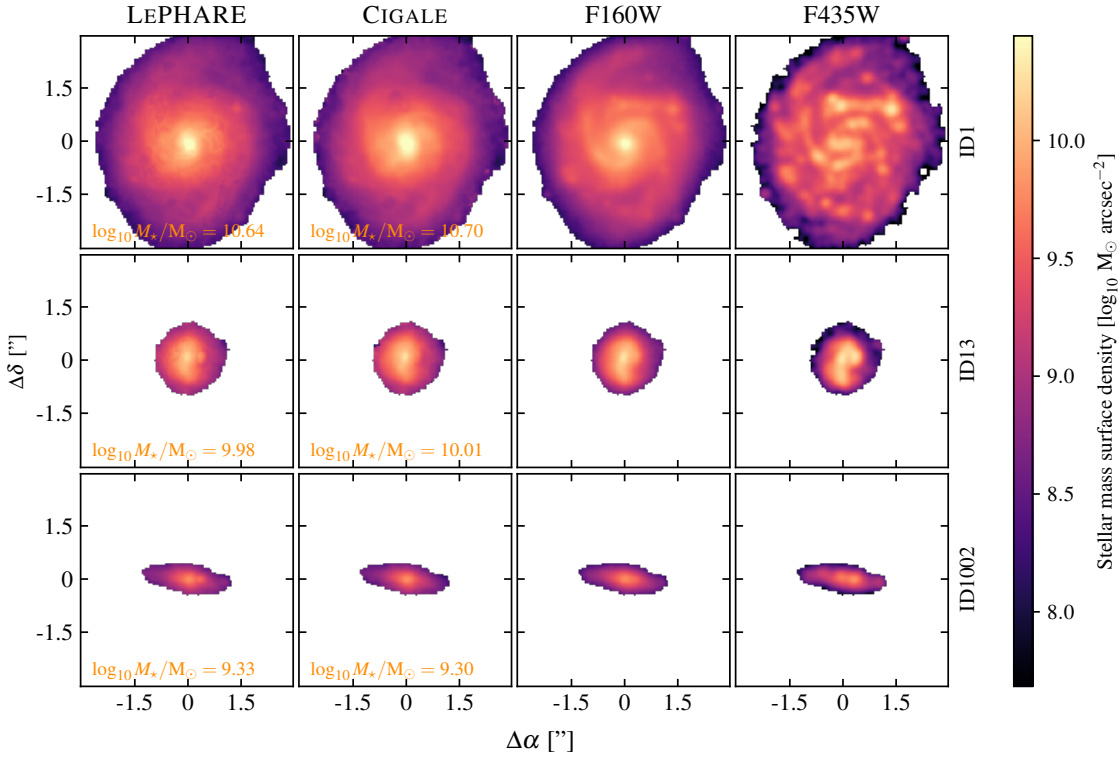


Figure 8.5: Examples of resolved stellar mass maps (mass per pixel) produced with LEPHARE (leftmost column) and CIGALE (second column from the left) for galaxies ID1, ID13, and ID1002. Also represented are the stellar mass maps obtained with a constant M/L value when using the F160W (third column from the left) and F435W (rightmost column) band images. For these two latter maps the total stellar mass used to compute the M/L was that of CIGALE. The value of the total stellar mass integrated over all pixels is given in the maps derived with LEPHARE and CIGALE.

total stellar mass derived in this manner was consistent with the stellar mass we would get if we performed the SED fitting on the integrated SED rather than on each pixel individually and we do find consistent results. On average CIGALE finds slightly larger pixel-per-pixel stellar mass uncertainties (around 25%) than LEPHARE (around 15%) but this difference may not be entirely significant given that LEPHARE adds by default lower systematic uncertainties on the fluxes than CIGALE does⁷ before performing the SED fitting. These systematic uncertainties are ubiquitous in SED fitting codes and are important to not underestimate the uncertainty on the fluxes. In some way, they can be seen as the uncertainty on the models rather than on the input data. The difference between the two codes is mostly found in the details. Looking at galaxy ID1, we can see that LEPHARE finds much more structure than CIGALE or said otherwise that the stellar mass map derived with CIGALE is smoother than that derived with LEPHARE. The reason

⁷Note however that these are the typical values used but we could have chosen the same value for both.

behind that is not entirely clear yet and it is still being investigated at the moment. The fact that we use different SFHs might play a role. It would not be so much about the final burst-quenching phase that happens so late that it effectively only affects the SFR and not the stellar mass, but rather that the SFH used in CIGALE is delayed. What might be more likely though is that LEPHARE allows for three metallicity values whereas we fixed the metallicity in CIGALE to one value only. If the metallicity is different then it may also affect the age because of the age-metallicity degeneracy which in turn will affect the amount of stellar mass that is created. A more thorough analysis of the reliability of the stellar mass maps derived using different codes and models shall be carried out in the near future. For now, we will keep using these maps and we will investigate their effect on the morphological and kinematics parameters in Sect. 8.1.4. But before doing so, I will quickly discuss in the following section the current implementation of the code.

8.1.3 A python library to easily produce resolved maps from pixel-per-pixel SED fitting

Once we had converged on how to implement the framework to produce resolved maps of physical parameters, I implemented it into a python module⁸. This module has the advantage of producing resolved maps in a simple way by automatising as much as possible the entire pipeline while still retaining the flexibility that is required to deal with different SED fitting codes and potentially with different input data. Originally, the code only worked with LEPHARE but it has been updated since then to also work with CIGALE. No plan has been made yet to integrate other SED fitting codes but the modular design of the module should allow any one who is interested to do so in a relatively simple way. Thus I will focus on CIGALE and LEPHARE implementations below⁹. In essence, there are five key python objects that must be used to produce and handle resolved maps with this module: `Filter`, `FilterList`, `Catalogue`, `SED`, and `Output`. The `Filter` object corresponds to a single band and contains the data as well as the variance map and zero point to convert input data into fluxes or magnitudes. All the `Filter` objects must be assembled into a `FilterList` with a common mask, the code that is going to be used for the SED fitting, the redshift of the galaxy, and a few more optional keywords. The `FilterList` must then be converted into a `Catalogue` object, either `CigaleCat` for CIGALE or `LePhareCat` for LEPHARE. It essentially contains the data that has already been pre-formatted to be correctly handled by either SED fitting codes. Once the data have been prepared accordingly, the SED fitting can be run by first creating a `SED` object and then calling it. Each code has its own `SED` object: `CigaleSED` or `LePhareSED`. These two objects do not expect the same input parameters since the SED fitting codes do not work exactly in the same way. I will quickly discuss each separately below. Nevertheless, a `SED` object contains all the modules and physical parameters that are needed to perform the SED fitting. Once created, either can be run and it will launch the corresponding SED fitting code on the data contained in the `Catalogue`. At the end, they will both return an `Output` object (`CigaleOutput` or `LePhareOutput`) that will read the result and store it. If the SED fitting has already been done beforehand, it is also possible to directly load the result without having to redo it. For LEPHARE, the code will perform some transforms to

⁸<https://github.com/WilfriedMercier/SED>

⁹This is not a SED fitting code since it relies on LEPHARE and CIGALE. Thus, it cannot work adequately if neither codes are properly set up first. Please check that the SED fitting codes work in stand-alone with the intended modules on a test case first before using this module. As an example, if one wants to use LEPHARE with the external Bruzual & Charlot (2003) SSP library that can be recovered on LEPHARE's website, then please check that the external library is properly installed before trying to use it.

the data before creating the `Catalogue` so it is recommended to use the `SED.link` method to directly transfer the transforms so that it can correctly produce resolved maps with the right unit. It is also possible to provide them manually if necessary. For `CIGALE`, the only thing the `SED.link` method does is to provide the shape of the input/output data to produce resolved maps. Once again, the shape can also be given manually if required. More details about the specific input for each object and each method can be found in the online documentation¹⁰. An example of the code that has been used to produce the stellar mass map for galaxy ID1 represented in Fig. 8.5 is shown below. It is split in three parts as follows: (i) a common part that spans the creation of the `Filter` objects all the way through to the `Catalogue`, (ii) a part specific to `LEPHARE`, and (iii) another part specific to `CIGALE`. Given that `LEPHARE` pre-computes the models in multiple steps before running the SED fitting, it is possible to skip them to speed up the process if the correct models have already been generated (e.g. in a previous fit). This can be done so using the keywords `skipSEDgen`, `skipFiltergen`, `skipMagQSO`, `skipMagStar`, and `skipMagGal` when calling the `LePhareSED` object. Multiple properties, such as the libraries to use, the filters to consider, or the systematic error to add can be set using the `properties` keyword when generating the `LePhareSED` object. For `CIGALE`, it works slightly differently. Because `CIGALE` is built using a modular design, the same has been used for `CigaleSED`. The `SFH`, `SSP`, `nebular`, and `attenuation` modules must be provided when creating the `CigaleSED` object using the corresponding `SED.cigmod` objects. A list of at least one module must be given for each. When calling the `CigaleSED` object additional parameters can be given such as the bands to use for the fit or the number of cores for parallelisation. All the details with specific examples can be found in the documentation.

¹⁰<https://wilfriedmercier.github.io/SED/>

```

1 from astropy.io import fits
2 import os.path as opath
3 import SED
4
5 # HST zero points
6 zeropoints = [25.68, 26.51, 25.69, 25.94, 24.87, 26.27, 26.23, 26.45, 25.94]
7
8 # HST bands (same order as zero points)
9 bands = ['435', '606', '775', '814', '850', '105', '125', '140', '160']
10
11 # Bands names in Cigale
12 band_names = [f'F{band}LP' if band == '850' else f'F{band}W' for band in bands]
13
14 # Band names in LePhare
15 #band_names = [f'{band}LP' if band == '850' else f'{band}W' for band in bands]
16
17 dataFiles = [] # Flux maps
18 data2Files = [] # Flux maps convolved by the PSF squared
19 varFiles = [] # Variance maps
20
21 # Get input file names
22 for band in bands:
23
24     file = opath.abspath(f'1_{band}_smooth.fits')
25     dataFiles.append(file)
26
27     file2 = opath.abspath(f'1_{band}_kernel_squared.fits')
28     data2Files.append(file2)
29
30     vfile = opath.abspath(f'1_{band}_variance_sm.fits')
31     varFiles.append(vfile)
32
33 # Get mask file
34 mfile = opath.abspath(f'mask_1.fits')
35
36 with fits.open(mfile) as hdul:
37     mask = hdul[0].data == 0 # True where data must be masked
38
39 # Generate a list of Filter objects
40 filts = []
41 for band, data, data2, var, zpt in zip(band_names, dataFiles, data2Files, varFiles, zeropoints):
42     filts.append(SED.Filter(band, data, data2, var, zpt))
43
44 # Create the FilterList object
45 # scaleFactor is a parameter important for LePhare only. Cigale does not use it.
46 # cleanMethod handles pixels with negative values in different ways
47 flist = SED.FilterList(filts, mask,
48                        code = SED.SEDcode.CIGALE,
49                        redshift = 0.622,
50                        cleanMethod = SED.CleanMethod.ZERO,
51                        scaleFactor = 1,
52                        texpFac = 4
53                        )
54
55 # Convert to CigaleCat or LePhareCat. The conversion to the correct catalogue is
56 # done based on the code given in FilterList
57 catalogue = flist.toCatalogue(galName)

```

Code 8.1: First part of the example of a python script to perform SED fitting.

```

1 # Custom properties
2 filt_used = [opath.join('hst_filters', i) for i in ['HST_ACS_WFC.F435W', 'HST_ACS_WFC.F606W',
3                                                    'HST_ACS_WFC.F775W', 'HST_ACS_WFC.F814W',
4                                                    'HST_ACS_WFC.F850LP', 'HST_WFC3_IR.F105W',
5                                                    'HST_WFC3_IR.F125W', 'HST_WFC3_IR.F140W',
6                                                    'HST_WFC3_IR.F160W']]
7
8 # Systematic error set to 0.03 in this case
9 # See LePhareSED docstring for other parameters
10 properties = {'FILTER_LIST' : filt_used,
11              'ERR_SCALE'   : [0.03]*len(filt_used)}
12
13 # Create LePhare SED object
14 sedobj      = sed.LePhareSED(f'{gal}', properties=properties)
15
16 # Output parameters to keep
17 oparams     = ['K_COR()', 'MASS_BEST', 'MASS_INF', 'MASS_MED', 'MASS_SUP', 'SFR_BEST', 'SFR_INF',
18              'SFR_MED', 'SFR_SUP', 'SSFR_BEST', 'SSFR_INF', 'SSFR_MED', 'SSFR_SUP', 'AGE_BEST',
19              'AGE_INF', 'AGE_MED', 'AGE_SUP']
20
21 # Run SED fitting
22 # skipXXX parameters allow to skip the models generation if already done in a previous
23 # run to save time
24 # Comment if the SED fitting has already been done
25 output      = sedobj(catalogue,
26                    outputParams = oparams,
27                    skipSEDgen   = False,
28                    skipFilterGen = False,
29                    skipMagQSO   = False,
30                    skipMagStar  = False,
31                    skipMagGal   = False
32                    )
33
34 # Uncomment to load the result if SED fitting has already been done
35 #output      = sed.LePhareOutput('1/1.out')
36
37 # Recommended with LePhare
38 output.link(filterList)
39
40 # Generate a resolved stellar mass map
41 mstar = output.toImage('mass_med')

```

Code 8.2: Second part of the example of a python script to perform SED fitting that is specific to LEPHARE.

```

1 # Modules are given as lists because Cigale accepts multiple modules
2 # e.g. multiple SSPs or SFHs
3
4 SFH = [SED.cigmod.SFHDELAYEDBQmodule(tau_main = [250, 500, 1000, 2000, 4000, 6000, 8000],
5                                     age_main = [2500, 5000, 7500, 10000, 12500],
6                                     age_bq   = [10, 25, 50, 75, 100, 150, 200],
7                                     r_sfr    = [0.0, 0.2, 0.4, 0.6, 0.8, 1.0, 1.25, 1.5,
8                                               1.75, 2.0, 5.0, 10.0],
9                                     sfr_A    = [1.0],
10                                    normalise = True
11                                    )]
12
13 SSP = [SED.cigmod.BC03module(imf         = SED.IMF.CHABRIER,
14                             separation_age = [8],
15                             metallicity  = [0.02]
16                             )]
17
18 nebular = [SED.cigmod.NEBULARmodule(logU           = [-2.0],
19                                     f_esc          = [0.0],
20                                     f_dust         = [0.0],
21                                     lines_width    = [300.0],
22                                     include_emission = True
23                                     )]
24
25 attenuation = [SED.cigmod.DUSTATT_POWERLAWmodule(Av_young = [0.0, 0.25, 0.5, .75, 1.0,
26                                                            1.25, 1.5, 1.75, 2.0, 2.25,
27                                                            2.5, 2.75, 3.0],
28                                                    Av_old_factor   = [0.44],
29                                                    uv_bump_wavelength = [217.5],
30                                                    uv_bump_width      = [35.0],
31                                                    uv_bump_amplitude  = [0.0, 1.5, 3.0],
32                                                    powerlaw_slope   = [-0.7],
33                                                    filters         = '&'.join(band_names)
34                                                    )]
35
36 # Create the Cigale SED object
37 sedobj = SED.CigaleSED(galName, band_names,
38                       uncertainties = [True]*len(band_names),
39                       SFH          = SFH,
40                       SSP          = SSP,
41                       nebular      = nebular,
42                       attenuation  = attenuation,
43                       flux_uncertainty = 0.1
44                       )
45
46 # Run SED fitting
47 # Comment if the SED fitting has already been done
48 output = sedobj(catalogue,
49                ncores           = 16,           # Number of threads to use
50                physical_properties = None,     # None means all properties will be computed
51                bands            = band_names,  # Estimate the flux for all the bands
52                save_best_sed     = False,
53                save_chi2        = False,
54                lim_flag          = False,
55                redshift_decimals = 2,
56                blocks            = 1,
57                )
58
59 # Generate a resolved stellar mass map
60 mass_star = output.toImage('bayes.stellar.m_star', shape=(100, 100))

```

Code 8.3: Third part of the example of a python script to perform SED fitting that is specific to CIGALE.

8.1.4 A quick look at the impact of resolved maps on morphological and kinematics models

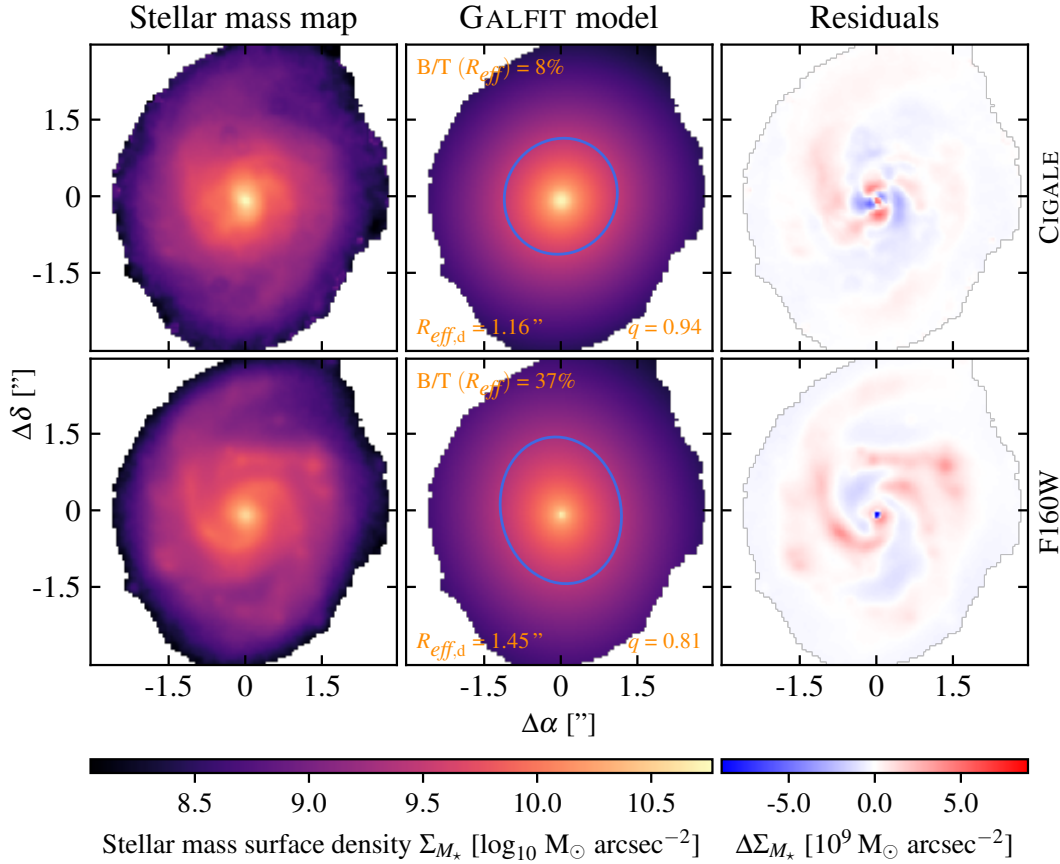


Figure 8.6: Comparison of the best-fit GALFIT results for galaxy ID1 when using CIGALE's stellar mass map (top row) and when using the F160W HST band (bottom row). For comparison, the images in the F160W band have been transformed into mass maps by multiplying by the M/L derived using CIGALE's total mass. The disk size, the disk axis ratio, and the B/T computed at one effective radius are given for each fit and the ellipsis that encircles one effective radius is shown on each model as a blue line. The residuals (observations - model) are shown on the rightmost column.

To conclude this section, a quick analysis of the impact of resolved maps on the morphological and kinematics parameters derived with the formalisms discussed in Chapters 4 and 5 is presented. A more statistically significant analysis shall be done first on the entire test sample and then on a larger sample of galaxies in the MUSE-HUDF in the future. In the meantime, below is shown a comparison of the morphology and the kinematics of galaxy ID1, that is the largest galaxy in the test sample which has, based on its F160W map, a non-negligible bulge

contribution. Besides, this galaxy will also be used as benchmark for the machine learning application in Sect. 8.2, thus it makes sense to perform its full dynamical modelling with this framework. The best-fit GALFIT bulge-disk decompositions for galaxy ID1 using the resolved stellar mass map derived with CIGALE (top row) and the F160W map (bottom row) are shown in Fig. 8.6. The images in the F160W band have been converted into stellar masses using the M/L derived using the total stellar mass from CIGALE. The rightmost column represents the residuals in absolute units, hence observations minus model. As an indication, the ellipsis encircling half of the disk’s total mass is shown with a blue line. As can be seen, the model from CIGALE finds a smaller disk and a weaker bulge contribution than the M/L model at the galaxy’s half-light radius. The disk ellipticity is also smaller, meaning that the galaxy is found to be more face-on, which should have an impact on the kinematics model when de-projecting the circular velocity. The reason why the model of the stellar mass map finds a smaller but more prominent disk is because it fits a denser disk model in the inner parts that forces the bulge component to be smaller to fit the remaining residuals near the centre. Thus, at one global effective radius the disk already significantly dominates the flux budget. On the other hand, the central peak visible in the F160W band is rather fitted by the bulge component, certainly because it is steeper so that the disk alone is not sufficient to fit the inner parts. Thus, this leaves the disk with the possibility to have a shallower core and rather fit the outer parts, hence increasing its radius. The residuals are quite similar between the two models. The stellar mass in the arms is underestimated and that in the inter-arms region is overestimated which is expected given that we do not try to model the arms or the clumps but only a smooth disk. The spirals arms are more visible in the residuals of the F160W band modelling but that is only because there is more structure visible in this band than in the stellar mass map.

GALFIT was originally designed to fit photometric observations in unit of electrons or flux and not in unit of mass. Nevertheless, by tweaking some header keywords in the input file, it is possible to use it to fit stellar mass maps. However, there is one more aspect that must be handled correctly: the variance map that is used to weight the value of each pixel during the fit. By default, GALFIT will convert the input map in electrons and then it will assume that the pixels follow Poisson’s statistics unless a variance map is provided by the user. However, it is unlikely that our maps simply follow Poisson’s statistics and it is not yet clear whether the uncertainty on the mass in each pixel that comes out of the SED fitting is sufficient for the morphological modelling given that it is mostly dominated by the systematic uncertainty added by CIGALE before the fit is done. In turn, this will generate correlations between the stellar mass and its uncertainty in each pixel which will therefore produce relatively flat stellar mass S/N maps. Such maps are quite different from what would be expected for Poisson’s statistics and it will therefore have an impact on the fit. As an indication, Poisson’s statistics was assumed in Fig. 8.6. Instead, if we provide the uncertainty from the SED fitting, we get the following morphological parameters: $R_{eff,d} = 1.29''$, $B/T(R_{eff}) = 52\%$, and $q = 0.92$ which are closer to the values found using the F160W map, except for the disk axis ratio that remains nearly unchanged. This example illustrates the importance of the weight map on the best-fit parameters, which is one of the last aspects that we are currently working on.

Finally, we can also check the impact of using the stellar mass map, compared to the F160W HST band, on the best-fit velocity field model and on the derived DM fraction when propagating the bulge and disk components to the kinematics modelling of the ionised gas component. This comparison performed on galaxy ID1 is shown in Fig. 8.7. The two velocity fields and their residuals are shown on the second and third columns with respect to the left-hand side. The

result based on CIGALE is shown on the top row and that based on the F160W band is shown on the bottom row. Note that the same disk inclination of 20° has been used for both models even though the best-fit GALFIT model on the F160W band found a larger inclination of roughly 36° . This way, we can compare more easily the impact of different bulge and disk parameters provided by the resolved stellar mass map independently of variations in inclination that will also affect the amplitude of the rotation curve. Besides, using an inclination of 36° has nearly no impact of the projected velocity field and residuals but it does affect the amplitude of the DM halo rotation curve by lowering it and therefore reducing the DM fraction. The two velocity field models shown in Fig. 8.7 and their residuals are very similar with differences of the order of a few kilometres per second, even though the contribution of the various components are different. In particular, we can note the different contribution of the bulge in the inner parts. In the case of CIGALE, the bulge is less massive than in the F160W map but peaks significantly closer to the centre, thus producing a fast rise of the rotation curve in the inner parts. Nevertheless, the total rotation curves remain close between the two models which, combined with the smoothing effect of beam smearing, produce similar velocity field models.

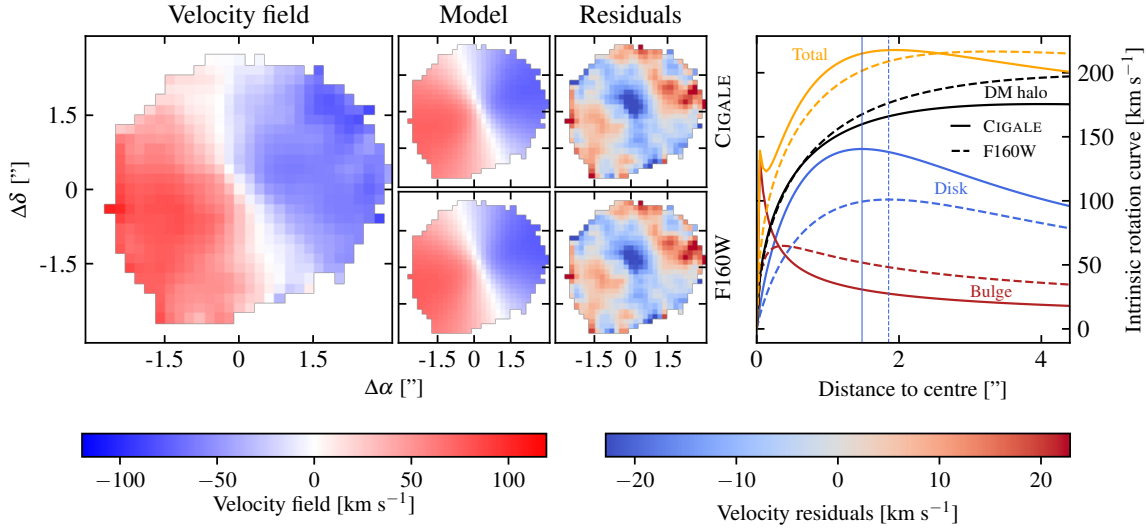


Figure 8.7: Comparison of the best-fit MOCKING velocity field models for galaxy ID1 when using CIGALE’s stellar mass map and when using the F160W HST band. The velocity field is shown on the left-hand side and the best-fit model and corresponding residuals are represented when using the disk and bulge morphological parameters from the stellar mass map derived with CIGALE to constrain the ionised gas kinematics (top row) and when using those derived from the morphological modelling on the F160W HST band (bottom row). On the right-hand side is also shown the intrinsic rotation curve when using the morphological parameters derived from the CIGALE map (solid lines) and those derived from the F160W band (dashed lines). The total rotation curve is shown as an orange line and the bulge, disk, and DM halo components are represented in red, blue, and black, respectively. The vertical lines represent R_{22} , that is the radius where the maximum of the disk rotation curve is reached.

The two DM halo rotation curves are mostly similar below R_{22} which is the position where the maximum rotation velocity of the disk is reached and where the DM fraction is typically estimated. At this radius, the model that uses the parameters from CIGALE finds a DM fraction of $f_{\text{DM}} \approx 65\%$ whereas the model using the parameters from the F160W band finds $f_{\text{DM}} \approx 75\%$ instead. Such a difference is nevertheless only mildly significant. Indeed, we can derive a rough estimate of the uncertainty of the DM fraction by loosening the bounds on the DM parameters during the kinematics modelling and see how that changes the value of f_{DM} . When doing so using the best-fit morphological parameters derived from CIGALE’s stellar mass map, we find a new value $f_{\text{DM}} \approx 73\%$. This gives an uncertainty on the DM fraction of the order of 10% which is close to the difference observed between the two best-fit models previously discussed. Furthermore, it is important to stress that this galaxy is not an optimal example to check the impact of stellar mass maps on the gas kinematics since it is nearly face-on. In practice, this means that a small change in the stellar disk inclination can have a large impact on the best-fit parameters.

8.2 Machine learning application with Self Organising Maps

At the beginning of the project, we had started thinking about improving the production of spatially resolved maps of physical parameters by implementing machine learning techniques. After discussing with collaborators, we converged towards an algorithm that is sufficiently simple to handle while remaining powerful enough to produce such maps by preserving the topology of the input data used for training (i.e. close input data such as fluxes or magnitudes should be mapped to close output data, i.e. stellar masses or SFR values): self-organising maps (SOMs). This work was started after the end of the first phase of the project, that is after H. Plombat had successfully produced our first results on resolved stellar mass maps during his internship. Since implementing such an algorithm requires a substantial amount of work, we supervised a second Master student to help us in this task: M. Tarrasse. The machine learning algorithm was developed by using the resolved SED library discussed in Sect. 8.1.3 as back-end with LEPHARE first, and then with CIGALE. In what follows, I will only discuss the current implementation of the SOM trained on input data from CIGALE.

Though the method has technically already produced positive results, it still remains currently in development. The test phase, (but not the training phase, see Sect. 8.2.5), were only carried out on a single galaxy (ID1) and thus are not to be taken as definite proof but rather as an indication of how the algorithm performs. We still need to assess its performance on a larger sample of galaxies, in particular in terms of speed-up compared to the classical framework discussed in Sect. 8.1, as well as better characterise its performance when dealing with noisy data.

8.2.1 A general overview of Self Organising Maps

A SOM is an unsupervised and competitive machine learning algorithm that can be seen as an early neural network with a single layer of neurons. It was invented by Teuvo Kohonen and described for the first time in Kohonen (1982). Its design and architecture was highly influenced by the development of biologically-influenced artificial neural networks of the 1970s and 1980s. The key feature that rendered SOMs different from contemporary early neural networks such as Perceptrons (McCulloch & Pitts 1943; Rosenblatt 1957) was that they were designed to preserve

the topology of the input space. As previously mentioned, the SOM is an unsupervised algorithm, meaning that it learns from the input space without having to provide labelled data. In other words, the algorithm learns the structure of the data by itself during the training phase and does not rely on a “ground-truth” (labels) that it could compare to in order to improve its performance. Additionally, the SOM is also a competitive learning algorithm, meaning that, at each step during the training phase, neurons will be in competition with each other and one of them will be selected as the best (see below for more details). In essence, the SOM can be seen as a clustering algorithm that will map input data to their closest neuron. Thus, if two data points in an N -dimensional input space are close to each other, so will they be on the neuron layer, hence topology is preserved. Because of that feature, a very common use of SOMs is to perform a reduction of dimensionality, mapping a N -dimensional input space into a simpler two-dimensional output space, similarly to what could be done with principal component analysis (PCA). This is typically done to visualise the clustering of data in datasets with a large number of dimensions. Another use, which is what we are interested in here, is classification. In this case, the idea is to apply *a posteriori* a label to each neuron after the training phase is completed. Afterwards, when a new data is presented to the SOM, the label corresponding to the closest neuron will be attributed to it. This application is the most common in the extragalactic literature. Examples would be to perform source (stars versus galaxies, Miller & Coe 1996) or morphological classification (Naim et al. 1997), to use multi-band photometric observations to derive photometric redshifts (e.g. Geach 2012; Way & Klose 2012; Carrasco Kind & Brunner 2014; Masters et al. 2015; Speagle & Eisenstein 2017; Davidzon et al. 2019), to infer spectroscopic properties (Jafariyazani et al. 2022), or to derive global physical properties (e.g. Hemmati et al. 2019; Davidzon et al. 2019). In our case, we extend the latter use to derive resolved maps of physical properties. In particular, I will solely focus on producing resolved stellar mass maps using SOMs since we have not tackled yet the production of SFR maps.

8.2.1.1 Key concepts for the SOM

A SOM contains a single layer of neurons (also called units or weights) regularly spaced onto a 2D surface. A classical layout is to consider that the neurons are laid on a flat Euclidean surface so that those located on opposite sides are far away from each other, though other types of surfaces can be used (e.g. cylindrical). The Euclidean surface is the most common and it is therefore the one that we have worked with. Let us refer to the layer of neurons (weights) as w . Then, the location of each neuron on the layer can be characterised by two numbers (i, j) and the neuron is noted $\vec{w}_{i,j}$. The coordinates (i, j) do not correspond to “physical” dimensions or dimensions in input space (e.g. fluxes, magnitudes, etc.) but to the location of the neuron on the neuron layer/map. The dimensions of the layer are ultimately free (hyper-)parameters that must be optimised (see the discussion on hyper-parameters below). Nevertheless, as a rule of thumb, we can keep in mind the few following points: (i) it is useless to have more neurons than input data because the “optimal” coverage of input space that the SOM can do is to map a single neuron to each data point, (ii) fewer neurons means faster convergence and learning phase but less precision on the inferred physical properties, and (iii) beyond a certain point, too many neurons means lower convergence without improvement in learning (i.e. we reach the irreducible error). As an indication, a 1×3 neurons’ layer is shown on the top of Fig. 8.8. This dimension therefore characterises the proximity of neurons on the layer. Furthermore, each neuron acts as a vector in input space. Thus, if the input data is N -dimensional then so are the neurons, that is we have

$\vec{w}_{i,j} = (w_{i,j,0}, \dots, w_{i,j,N})$. In our case, the input space will typically be the pixels' fluxes or magnitudes (hence $N = 9$ bands) or colours ($N = 8$ for colours between nine successive bands), but in practice any type of data can be used (e.g. redshift, spectral features, etc.). Because neurons are located in the same space as the input data, it is possible to compute a distance between a data point and a neuron. For a given data point, the closest neuron in input space is called the best-matching unit (BMU).

As described in more details in Sect. 8.2.1.2, the goal of the SOM is to iterate through the input data one by one, find the selected data's BMU, and move the latter (in input space) towards the given data point. The BMU will be displaced in the sense that its coordinates in input space will be modified, but its location on the neurons' layer will always remain the same. To preserve the topology of the input data, not only will the data point attract its BMU towards it but it will also attract every other neuron with an amplitude that is lower for those located far away from the BMU. Let us consider the same example as in Fig. 8.8 and let us assume that the BMU is the neuron located at the position $(0, 1)$, i.e. the middle one. Then, the amplitude of the displacement will be the same for each of the two neurons on both sides since they are equidistant from the BMU (as quantified by the (i, j) coordinates). Instead, if the BMU was the neuron located at position $(0, 2)$, then the neuron at position $(0, 1)$ would be more affected than the one at position $(0, 0)$ because it would be closer to the BMU on the neurons' layer. This mechanism is what allows the preservation of the topology of the input data. In practice, the function that characterises the amplitude of the displacement of a neuron is called the neighbourhood function and it is noted $\beta_{i,j}$. A typical choice that we used in our implementation is a Gaussian neighbourhood that writes

$$\beta_{i,j} = \exp \left\{ -\frac{d^2}{\sigma^2} \right\}, \quad (8.9)$$

where d is the distance between the neuron and the BMU on the neurons' layer and σ is a free hyper-parameter called the neighbourhood radius. The distance between neurons ultimately depends upon the choice of the geometry used for the neurons' layer. In our case, we used a Euclidean surface so d is simply the Euclidean distance between two neurons on the layer, that is $d = \sqrt{(i - i')^2 + (j - j')^2}$ for two neurons at positions (i, j) and (i', j') . The neighbourhood radius characterises the strength of the neighbourhood sphere of influence. A large radius means distant neurons will be more affected than with a small radius. If $\sigma = 0$, then there is no neighbourhood and if $\sigma \rightarrow \infty$, then the same displacement is applied to all the neurons.

Based on what has been said, it would not be certain that the SOM would converge to a final position after a finite number of iterations since each data point would attract the neurons towards itself, indefinitely. To counteract this effect, we must reduce the amplitude of the displacement at each iteration so that it will sufficiently converge to stop the learning phase. The function that reduces the amplitude with each iteration is called the learning rate and it is noted α . In our case, for a maximum number of iterations τ , the learning rate will linearly decrease with each iteration t . In other words, we have $\alpha(t) = 1 - t/\tau$ (e.g. see the evolution of the amplitude of the arrows in Fig. 8.8). Other implementations exist (e.g. exponential decline) but the linear decrease is quite common.

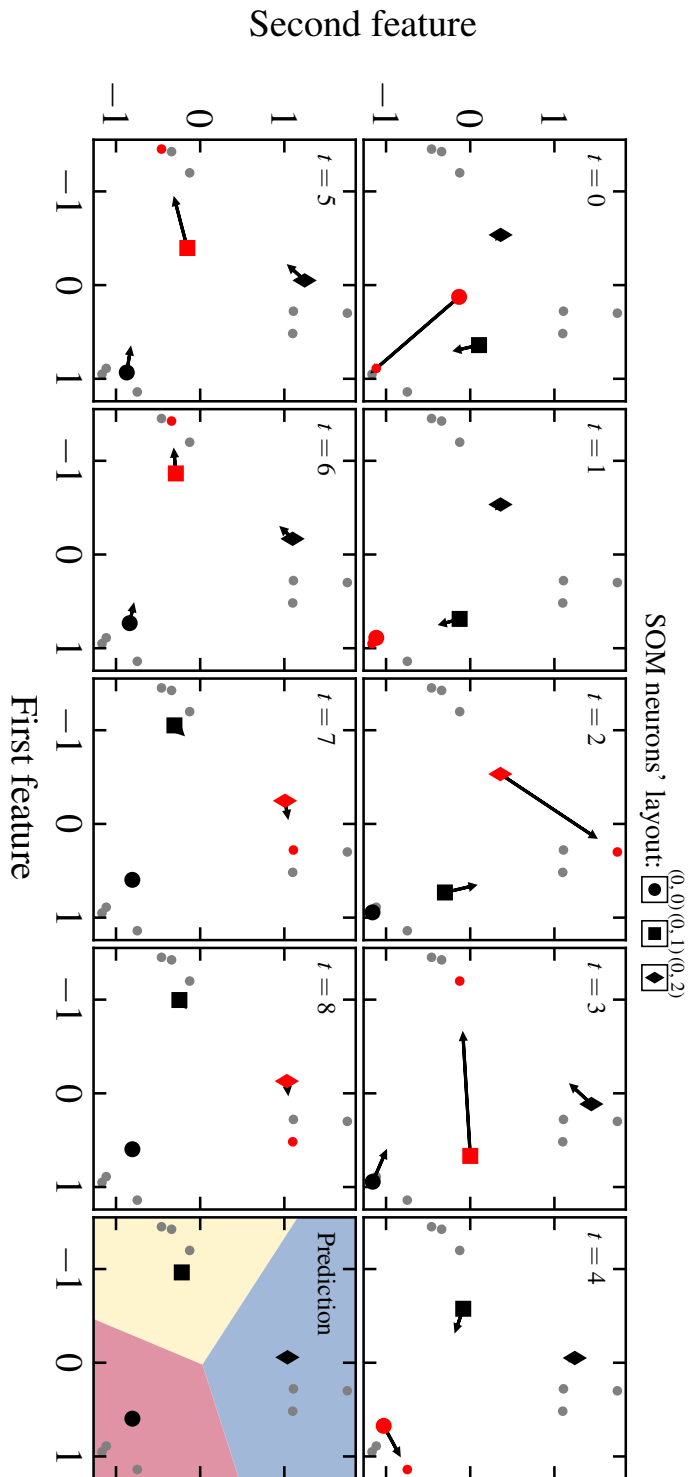


Figure 8.8: Illustration of the learning phase for a 1×3 SOM ($\sigma = 0.7$) using synthetic data. The 2-dimensional data are represented with grey points and the SOM's neurons with large symbols. For each iteration t , a data point is randomly chosen (highlighted in red) and the BMU is found (in red as well). Then, all the neurons are moved to their new location represented by their arrow. In this example, after nine iterations the SOM is stopped ($t = 8$). The last subplot represents which neuron would be attributed as BMU to a new data point as a function of the position in input space. At $t = 0$, the first (circle) and last (diamond) neurons do not have a large impact on each other because they are located the furthest apart on the neuron's layer (see layout on the top). A different layout and σ would yield different results.

8.2.1.2 Learning phase

Now, we turn towards the learning phase. Let us consider a N -dimensional input space (e.g. galaxy magnitudes or colours) with K input data \vec{x}_k . These form a matrix $X = (\vec{x}_0, \dots, \vec{x}_K)$ where each vector $\vec{x}_k = (x_{k,0}, \dots, x_{k,N})$ corresponds to a single data (in our case a pixel). The first step before the learning phase begins is to initialise the neurons' values in input space. To avoid that one input feature¹¹ dominates over the others during the training phase, for instance because of the range of values the data take, the input data X must be normalised first as follows

$$\tilde{X} = \frac{X - \langle X \rangle_{\vec{x}}}{\sqrt{\text{Var}(X)_{\vec{x}}}}, \quad (8.10)$$

where $\tilde{X} = (\tilde{x}_0, \dots, \tilde{x}_K)$ is the normalised data, $\langle X \rangle_{\vec{x}}$ is the mean vector taken as the average of each feature (e.g. average of fluxes in a single band), and $\sqrt{\text{Var}(X)_{\vec{x}}}$ is the standard deviation taken as the standard deviation of each feature. This kind of normalisation is typical in machine learning because it allows each feature to have a null mean and a standard deviation of unity. Once the data have been normalised, the neurons' initial coordinates in input space can simply be drawn randomly from the uniform distribution $\mathcal{U}[-1, 1]$. Because this first step is non-deterministic, each new run of the SOM will initialise the neurons to different coordinates. Thus, this will have an impact on the learning phase and on the outcome. This effect can be used to estimate the uncertainty induced by the algorithm itself by running multiple times the same SOM on the same data. To perform the learning phase, the SOM will first select a single input data \tilde{x}_k and then it will compute the Euclidean distance in input space between the data point and each neuron $\vec{w}_{i,j}$ as

$$\|\tilde{x}_k - \vec{w}_{i,j}(t)\| = \sqrt{\sum_n [\tilde{x}_{k,n} - \vec{w}_{i,j,n}(t)]^2}, \quad (8.11)$$

where \tilde{x}_k is the normalised input vector and $\vec{w}_{i,j}(t)$ is the neuron's coordinates in input space at step t . Afterwards, the SOM will find the BMU (closest neuron, i.e. smallest distance), it will determine the distance d on the neurons' layer between the BMU and all the remaining neurons, it will compute the neighbourhood function, and it will update the learning rate. Finally, it will update the position of all the neurons using the formula

$$\vec{w}_{i,j}(t+1) = \vec{w}_{i,j}(t) + \alpha(t)\beta_{i,j}(t) [\tilde{x}_k - \vec{w}_{i,j}(t)], \quad (8.12)$$

where $\vec{w}_{i,j}(t+1)$ is the new position of the neuron in input space that will be used in the next iteration. Once all the neurons updated, the SOM will start the next iteration by selecting a new data and performing the same steps again. If the data points are selected randomly, the common rule is that it is done with replacement (i.e. a pixel can eventually be selected multiple times). An illustration of the learning process for a 1×3 SOM with nine synthetic input data is shown in Fig. 8.8. Each step t is represented from left to right and top to bottom (from $t = 0$ to $t = 8$). For each step, the selected data point and the BMU are both highlighted in red and the displacement of the different neurons are shown with arrows. The last subplot (bottom right) shows the clustering prediction of the SOM for the entire input space, with each class represented with a different colour.

¹¹In machine learning jargon a feature is a single dimension in a multi-dimensional input space.

8.2.2 Using the SOM for predictions

The SOM is a clustering algorithm so, once the learning phase is done, it can be used on new input data to find their BMU. Each neuron will therefore act as a potential cluster onto which new data will be mapped. Note that the mapping to a BMU after training is independent of whether the given neuron could be matched to any input data during the training phase. This means that it is possible, especially when there are many neurons or a sparsely populated input space with empty regions, that a neuron is identified as the BMU of a new data point during the prediction phase even though it was never the BMU of any of the input data during the training phase. This mapping can be used to predict unknown properties of the new data. For instance, let us assume that we trained a SOM on galaxy colours and that we also know the M/L of the galaxies in the training sample. If one of the neurons is mapped to n galaxies in the sample after the training phase, then we can assign to this neuron a M/L value by taking, for instance, the median M/L of the n galaxies. Afterwards, if we want to predict the M/L values of a new sample of galaxies for which we only know their colours, we can find for each galaxy in the sample the corresponding BMU and attribute to the galaxy the BMU's M/L value. In machine learning terminology, we say that we use the SOM to predict the M/L of the new galaxies.

8.2.3 Optimisation of the SOM

The SOM has a few hyper-parameters that can be tuned to improve its performance for a specific task. Namely, in our implementation these are: (i) the dimensions of its neurons' layer (2D hence two hyper-parameters), (ii) the neighbourhood radius, and (iii) the maximum number of iterations. The dimensions of the SOM are important in two regards. First, the more neurons, the longer the training and the predictions will take. Second, if there are too many neurons on a too sparsely populated input space, a large number of neurons will never match any input data point and will therefore be useless for the prediction step since we will not be able to assign to them any value (e.g. stellar mass to use the same example as in Sect. 8.2.2). Hence, there is a trade off between having many neurons, thus potentially a lot of precision (because few input data will be mapped to each neuron), but with plenty of unusable neurons, or fewer neurons but with less precision when using the SOM to make predictions. Furthermore, note that it is technically possible to use SOMs with a neurons' layer with a single dimension or with more than two. For the former, it is similar to the 2D case where there is a single row or a single column in the layer. Hence, our implementation can naturally reduce to the 1D case if this is the most efficient solution. For SOMs with more than two dimensions, even though it is possible to use them, we have not tried to do so. The only caveat is that the visualisation of the SOM becomes more tedious. The neighbourhood radius is also an important hyper-parameter in the sense that even small changes in its value can have a large impact on the training phase and thus on the output. Finally, the maximum number of iterations is also an important hyper-parameter to tune. Indeed, for very large training samples, it is useless in practice to train on the entire sample since convergence will be achieved sufficiently quickly. Thus, limiting the maximum number of iterations can help in reducing the time taken to perform the training phase. Additionally, there is a risk of overfitting for large numbers of iterations, which means the neurons would become too optimised for the training sample and would not be able to properly generalise to new data.

8.2.4 The need for a fast implementation

Various SOM implementations are available in python, some given as stand-alone codes, others as extra-packages that can be used in combination with already existing machine learning frameworks. Codes such as SUSI¹² or SOMOCLU¹³ have the advantage of being optimised and are usually quite complete in terms of available features but they cannot be easily combined with common machine learning frameworks. On the other hand, extra-packages such as SKLEARN-SOM¹⁴ are made to be used with these frameworks (in this case SCIKIT-LEARN¹⁵, see Pedregosa et al. 2011; Buitinck et al. 2013). During the development of the project, we decided to use SKLEARN-SOM as it seemed to be the simplest solution. However, it became quickly clear that this code was not optimised for large datasets. Thus, we had to either use another code or try to improve its performance. A quick inspection showed that, even though it had been written with NUMPY¹⁶ (Harris et al. 2020), it could be substantially optimised. Hence, after rewriting a significant portion of the code, we produced our own version that pushes its optimisation to its limits. Though the details of the optimisation are not especially important, we can nevertheless mention that it mostly consists in reducing as much as possible the number of loops in the code, maximising the use of the vectorisation capabilities of NUMPY, and using smarter computations with access to fewer resources whenever possible. As an indication, for a SOM with a grid of 50×50 neurons trained on 14 000 data points, SKLEARN-SOM finishes the training in roughly 2 min whereas the same result is achieved in 7 s with the optimised version. This yields a significant speedup of more than 17, which increases with the dimensions of the SOM. With this new version, a training phase that would have taken an hour before only takes four minutes to complete now. This new version of the code, dubbed SOMPTIMISED¹⁷, is not only an optimised version of the previous code. It also incorporates useful additional features that are explained in details and with examples in the online documentation¹⁸. First, the code now follows a modular design that allows more flexibility regarding the specific implementations that different people may want to use. The core class is labelled `SOM`, the method `SOM.fit` can be called to perform the training phase, and the method `SOM.predict` can be called to perform a prediction on new data. Additional new features that have been implemented are the possibilities to (i) set extra properties (e.g. stellar masses) to the neurons with the `SOM.set` method and to retrieve them later on with the `SOM.get` method and (ii) serialise (i.e. locally save on the computer) the `SOM` object using the `SOM.write` method and retrieve it using the `SOM.read` method. This last feature is particularly useful because it allows to locally store the python object after the training phase and to recover it later, as if the training phase had just been done. Typically, this can be used to archive previous versions that may have different parameters or handle different input data and compare them with a newer SOM version without having to perform the training phase again. Concerning the code design, there are only three modules that the `SOM` object requires: (i) the `LearningStrategy` module that defines the type of learning rate α to use and its parameters. Only two options are available at the moment: `LinearLearningStrategy` for a linearly decreasing function (see Sect. 8.2.1.1) and `ExponentialLearningStrategy` for an exponentially declining

¹²<https://felixriese.github.io/susi/>

¹³<https://peterwittek.github.io/somoclu/>

¹⁴<https://pypi.org/project/sklearn-som/>

¹⁵<https://scikit-learn.org/stable/index.html>

¹⁶<https://numpy.org/>

¹⁷<https://pypi.org/project/SOMptimised/>

¹⁸<https://wilfriedmercier.github.io/SOMptimised/index.html>

function. (ii) The `NeighbourhoodStrategy` module that defines the type of neighbourhood radius σ to use and its parameters. Two options are available as well: `ConstantRadiusStrategy` for a constant neighbourhood radius (see Sect. 8.2.1.1) and `ExponentialRadiusStrategy` for an exponentially declining radius. And (iii) the metric used to compute the distance in input space between a data point and the neurons. Three options are available: `euclidianMetric()` which corresponds to the classical Euclidean distance in an N -dimensional space (discussed in Sect. 8.2.1.2), `chi2Metric()` that implements a “distance” using the classical χ^2 formula that takes into account the uncertainties on the input data, and `chi2CigaleMetric()` that implements a “distance” using the χ^2 formula used in CIGALE. As discussed in Sect. 8.2.5, the last metric was included to have a SOM that maps neurons to input data in a similar fashion to how CIGALE fits its SED models to the observations.

8.2.5 Current implementation of the SOM

Our goal is to use the SOM to produce resolved stellar mass maps without running any SED fitting code. To do so, the procedure is as follows: (i) construct a training dataset $X = (\vec{x}_0, \dots, \vec{x}_K)$, where each vector \vec{x}_k corresponds to the data of a single pixel (e.g. the fluxes in the nine HST bands), (ii) use it to train the SOM, (iii) attach to each neuron of the SOM the median CIGALE-derived stellar mass of the pixels of the training data set that are mapped to the given neuron, and finally (iv) use this trained SOM to predict the stellar mass of future pixels (e.g. new galaxies). To apply this procedure, we must define two things. First, we have to choose which data to use (e.g. fluxes, magnitudes, colours, etc.) and second, we must choose the values of the hyper-parameters of the SOM.

We tested plenty of SOM variations during the development of the algorithm. Originally, the plan was to have a single SOM that would take the fluxes (or a quantity that holds similar information, e.g. magnitudes) and the redshift of the pixels and use that information to estimate the pixels’ stellar mass values. For various reasons, this design was difficult to implement. For instance, it induces unnecessary uncertainties during the prediction phase because, in some sense, it is as if the SOM approximates the redshift of the pixels even if they are perfectly constrained (e.g. MUSE spectroscopic redshift). An early solution to this problem was to predict the M/L in the reddest band rather than the stellar mass directly since both quantities (mass and luminosity) scale equally with redshift, that is the M/L is redshift independent to first order (besides its intrinsic evolution). To improve the efficiency of the algorithm, we also decided to use colours computed as the difference between the magnitudes in successive bands, hence reducing the dimensionality of the problem by one. The argument behind their use is as follows: (i) let us imagine a galaxy but now it is located twice further away from us. Its M/L will remain the same since the galaxy has not changed, but its flux will be reduced. In practice, the change in flux is not simple to compute. Indeed, there will be a reduction of its amplitude but there will also be a shift of the galaxy’s spectrum (i.e. k-correction). So, depending on the spectrum’s shape, the flux may not necessarily be reduced¹⁹. Hence, in flux space, the galaxy will not be located at the same position because of the change in distance even though it has the same M/L. When using colours, this is not the case any more because the impact of the distance on the fluxes cancel each other out (modulo the k-correction, see below). (ii) Now, let us imagine two galaxies with the same spectrum and at the same distance from us but one of them has twice the luminosity (in the

¹⁹At the time, we had not yet thought about the impact of k-correction so the argument that follows only applied to the amplitude (see discussion below regarding the k-correction)

reddest band) of the other. To first order, this implies that its stellar mass will be twice as massive and thus that they have the same M/L. Hence, the galaxies will not be located at the same position in flux space even though they share the same M/L. Once again, with colours this is not the case any more because the same scale factor between the fluxes of the two galaxies will apply for each band. (iii) A last argument is that it is likely that successive bands will suffer from a roughly similar extinction, though in practice it does depend on how close the bands are to each other, so using colours should minimise the impact of extinction as well.

Therefore, the first designs of the SOM that we tested used the pixels' colours as input data, including or not the redshift information. However, they failed at addressing one important issue mentioned above: the impact of the k-correction. Because galaxies located at different redshifts will have their spectrum differently shifted (offset plus dilation), this means we will not probe the same intrinsic wavelength range. To correct for this effect we would need to apply the k-correction to recover the intrinsic fluxes but this would require a spectrum model which we do not have. Incorporating the redshift among the input features and using fluxes instead of colours would not change the problem because the k-correction would still affect the data. The solution that was chosen is to build a library of SOMs where each SOM is optimised for a given redshift slice. For slices with a step $\Delta z = (1 + z) \times 1\%$ ²⁰ in the redshift range $0.6 < z < 1.5$, corresponding to the range of the test sample (see Table. 8.1), this amounts to optimising 46 SOMs. Furthermore, in order to have a fair comparison, we wanted to reduce as much as possible the systematics between the results produced by the SOM and those produced by CIGALE. Thus, we included in SOMPTIMISED the possibility to use the same χ^2 metric as in CIGALE to determine the BMU among the neurons. The metric can be used for the training and/or for the prediction on new data. Initially, we directly used the colours of the pixels in the 12 galaxies of the test sample as training data set but we soon realised that this was not the optimal choice to make. Indeed, the problem is that the SEDs of the pixels in these galaxies do not represent the variety of SED models built by CIGALE. Thus, there was a clear risk of overfitting only a subset of CIGALE's models. However, a clear advantage of using real data for the training phase is that they come with a variety of S/N values that would force the SOM to adapt to the impact of noise during the training phase. However, based on early tests, the risk of overfitting was too great and we therefore decided to use the SED models produced by CIGALE when using its `savefluxes` mode as training data set. For each redshift slice we produced a catalogue of 69 000 SED models using the same grid of parameters as the one used when producing resolved maps with CIGALE. For each slice we trained the SOM on a grid of hyper-parameters in order to find the combination that gives the best result. We always considered a SOM with dimensions varying from 22×27 to 83×82 neurons and we tested a few values of neighbourhood radius between roughly $\sigma = 0.5$ and $\sigma = 3$ before settling to $\sigma = 3$ to speed-up the optimisation phase as it seemed to nearly always converge towards this value. The dimensions of the SOM were chosen based on the number of available training data so that there would be enough neurons to precisely map the data but not too many to avoid having a large number of empty neurons (i.e. neurons that are mapped to no data).

8.2.6 First results and perspectives

The algorithm described in Sect. 8.2.5 has been tested so far on a few galaxies in the test sample but only a single galaxy has been studied in details: galaxy ID1. Hence, it is difficult to extrapolate the results without considering a larger sample of galaxies. Besides, our algorithm has

²⁰This corresponds to a constant step $\Delta\lambda/\lambda_{\text{obs}}$, where λ_{obs} is the observed wavelength.

technically been optimised for 46 different redshift slices but galaxy ID1 is logically located only in a single slice. Furthermore, the training dataset can also have an impact on the performance of the SOM and this will be discussed in more details in the perspectives.

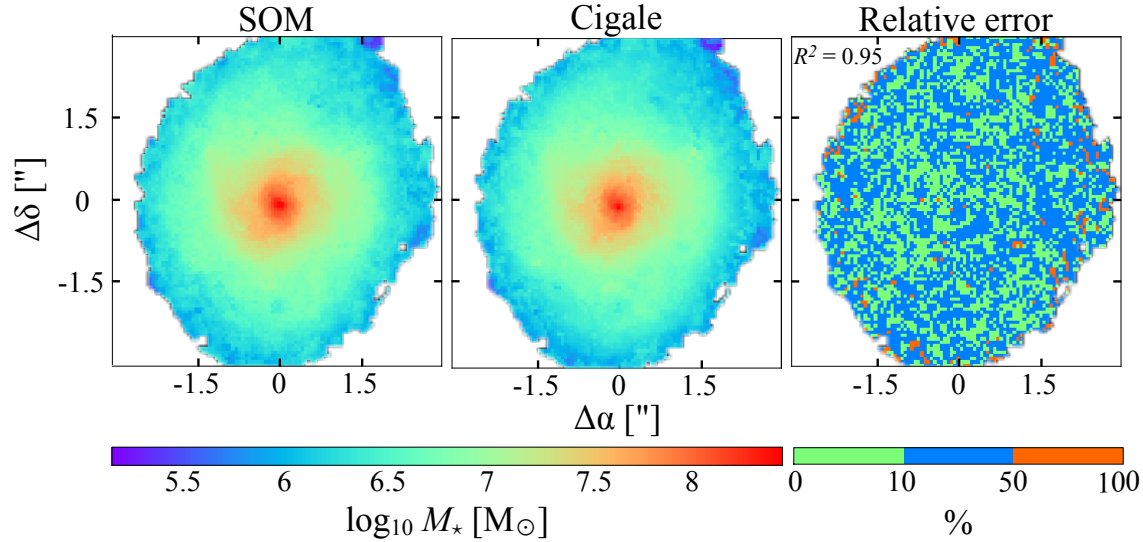


Figure 8.9: Example of a resolved stellar mass map, adapted from M. Tarrasse’s Master project, using the SOM described in Sect. 8.2.5 (left-hand side) compared with the result from CIGALE (middle). The relative difference between the SOM and CIGALE is shown on the right-hand side. The algorithm was trained and optimised on the same grid of 69 000 models that CIGALE used to perform the pixel-per-pixel SED fitting. Different dimensions of SOM and values of neighbourhood radius σ were tested to find the best optimisation before producing the map. In the end, the best hyper-parameters are a dimension of 74×74 neurons and $\sigma = 3$.

As mentioned in the previous section, we trained the SOM on SED models produced by CIGALE. Once the algorithm was optimised, we attributed to each neuron in the SOM the median M/L of the input data that were matched to the neurons. We used the reddest band available to compute the M/L as we thought it would better match the galaxies’ stellar mass distribution. We then used the SOM to predict the M/L of each pixel in galaxy ID1 and then converted it to a stellar mass to reconstruct the galaxy’s stellar mass map. The result of this process is shown in Fig. 8.9. On the left-hand side is represented the stellar mass map produced by the SOM, in the middle is shown the stellar mass map produced by the pixel-per-pixel SED fitting library discussed in Sect. 8.1.3 using CIGALE, and on the right-hand side is shown the relative difference between the two maps (hereafter error) split in three different bins: small error (less than 10%), mild error (between 10% and 50%), and large error (more than 50%). Based on this example, it seems clear that, once optimised, the SOM can reproduce very accurately the results of CIGALE. The error is quite flat which means that the uncertainty induced by the SOM on the logarithm of the stellar mass is roughly constant, hence that it does not fail or perform better in specific parts of the galaxy (e.g. bulge or spiral arms). The relative error between the two maps may seem a bit high but note that an error of 50% only amounts to about 0.2 dex which is quite acceptable. Besides, these correspond to pixel-per-pixel errors but once integrated on the entire surface of the galaxy, the

two stellar masses are completely consistent with each other within 0.05 dex (i.e. less than 10%).

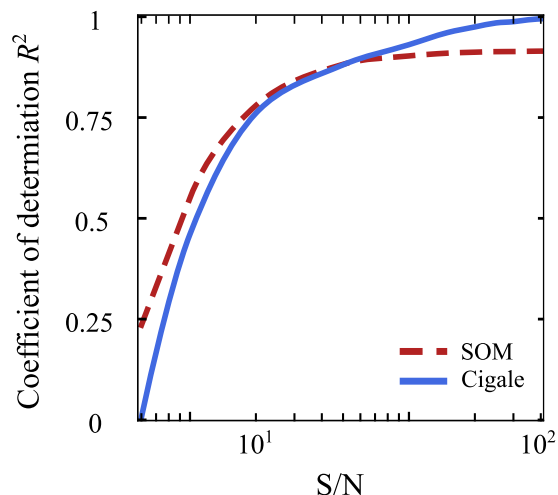


Figure 8.10: Performance of the SOM measured with the coefficient of determination as a function of S/N, adapted from M. Tarrasse’s Master project. The algorithm was trained on noiseless input data from CIGALE’s SED models but the association of the M/L values for each neuron took the noise into account. The performance of the SOM (red dashed line) is compared with the performance for the traditional pixel-per-pixel SED fitting performed with CIGALE (blue solid line). Both were measured by evaluating the coefficient of determination (the closer to unity the better) on noisy input data. For low S/N values, hence noisy data, the SOM actually reproduces more efficiently the stellar mass maps on average whereas the opposite is true at high S/N.

In the very last phase of the project, we also started investigating the performance of the SOM in the presence of noisy data. Though current results seem particularly promising, it must be stressed that this work is still ongoing. We wondered whether it is better to train and optimise the SOM on noisy data and if so what kind of noise should we consider and in what range of S/N values. The noise can affect the SOM in two different parts: (i) during the training phase, that is when providing noisy fluxes or colours as input data so that the algorithm can learn how to cluster the neurons by taking the impact of the noise into account, and (ii) during the association of the M/L values to the neurons. The two are independent in the sense that, by construction, the SOM is a clustering algorithm. Hence, it is technically possible to train the SOM on noiseless data and afterwards use noisy data to assign a M/L to each neuron in the SOM. This is what we have done so far. The next step that shall be taken in the future is to include the noise in the input data during the training and optimisation phases so that the SOM can learn to cluster on noisy data. Thus, to estimate the performance of the algorithm on noisy data we applied the following steps: (i) we trained and optimised the SOM for each redshift slice in the same way as before, that is without adding noise to the input data, (ii) we assigned to each neuron the median M/L value of the input data that are mapped to this neuron after perturbing the input data set with a Gaussian noise (i.e. the flux in each band and therefore the colours but also the M/L). The noise level was chosen based on the typical S/N values measured in the different HST maps in the test sample, taking into account S/N variations between different bands. We varied the S/N from low values (noise-dominated) to high-values (noiseless) to see how the algorithm performs with different types of data. And (iii) we evaluated its performance on new realisations of noisy input data for different S/N values. We also performed the last step with the pixel-per-pixel SED fitting algorithm using CIGALE to compare the performance of the two techniques. The result of this first analysis is shown in Fig. 8.10 where the performance of the SOM is represented with the red dashed line and that of CIGALE with the blue solid line. In this figure, the performance is measured through the coefficient of determination R^2 which can be seen as one minus the ratio of

the residuals over the variance in the input data. Hence, the higher its value, the better the model can reproduce the input data. As is visible, at high S/N values CIGALE performs the best. This result is naturally expected since we are testing its performance on its own (slightly noisy) models. However, at lower S/N values (≤ 50), the SOM becomes more efficient. There are at least two explanations for this effect. First, because the SOM has much less neurons than the number of models used in CIGALE it must necessarily average its prediction which in turn smooths the output stellar mass map (e.g. see Fig. 8.9). Second, the M/L (but not the clustering for the moment) takes into account noisy fluxes or colours which will force its prediction to be closer to the true value. Beside its performance, another interesting quantity is the time it takes to produce the resolved maps. In this regard, the SOM can be quite effective because, if one uses models to train the algorithm, the optimisation can be done before the data are available. We can even imagine creating different type of SOMs, each using different SED models (e.g. IMF, SFH, etc.) and grid of parameters, and saving them locally to re-use them later on. As an indication, once the best hyper-parameters have been found, the training phase (to associate physical parameters to the neurons) is quicker than CIGALE and the prediction phase is nearly instantaneous. But once again, the training does not need to be performed each time the SOM is used since it can be saved at any time in its current state.

The previous discussion is based on quite early results and much still remains to be done. To begin with, we still need to assess whether the current implementation is robust for the 46 different redshift slices and for different types of galaxies. In particular, our results strongly depend on the grid of models that are used for the training phase and it is not yet clear whether the current implementation is well adapted for both star-forming and quiescent galaxies. We also need to assess in a much more quantitative way the impact of noise on the performance of the algorithm. Finally, we should certainly investigate much further the current design of the algorithm, in particular regarding the fact that we need to use redshift slices to solve the k-correction problem. If there is at least one thing that the current implementation has shown is that it is possible to recover resolved stellar mass maps given a redshift slice combined with fluxes or colours. Hence, we technically have all the necessary information to produce such maps using a single SOM layer. The complexity in doing so is the large number of input data that will be required to smoothly sample the input space, especially along the redshift dimension. A possible solution to this problem would be an hybrid approach where we sample the redshift dimension of the input space with a fixed number of steps and then train a single but larger SOM on this new data set by providing fluxes or colours and the redshift of the galaxies.

Concluding remarks and perspectives

In this manuscript, I have presented the work that I have carried out throughout the three years of this Thesis regarding the impact of the environment on the dynamical properties of galaxies across cosmic time. I have shown how I was able, combining MUSE and HST data, to constrain the morphology and the kinematics of roughly 400 galaxies in the MAGIC survey. In particular, I have highlighted in Chapter 3 how valuable the MAGIC survey is to probe the impact of the environment on galaxy properties given its large homogeneity in the way precise physical, morphological, and dynamical properties are collected for a large sample of galaxies found both in the field and in environments of varying density (galaxy groups, and galaxy clusters). This has allowed me to contribute significantly to two already published papers (Abril-Melgarejo et al. 2021; Mercier et al. 2022) and to two nearly complete analyses, the first on the angular momentum in MAGIC, presented in Chapter 7, and the second on the MAGIC survey discussed in Chapter 3. Thanks to the MAGIC survey design, the powerful capabilities of MUSE, and to the precise morphological and dynamical modellings that I performed (see Chapters 4 and 5), this work has enabled me to put the most precise constraints up to date on the impact of the environment on major scaling relations at intermediate redshift. From these analyses, I have managed to highlight the environmental effect on the morphology and star formation rate of galaxies found in large structures. I have also shown that, at intermediate redshift, the environment does not have a visible impact on the galaxies kinematics (rotational velocity) but that it does seem to affect the angular momentum of the most massive galaxies found in the densest parts of their host structure.

Nevertheless, much still remains to be done. Besides, as discussed in Chapter 8, we have developed throughout the last two years a new methodology that could significantly help us to much better constrain the dynamics of intermediate redshift galaxies with MUSE and, more importantly, of high-redshift galaxies with next-generation IFS instruments such as ERIS, HARMONI, or MOSAIC that will be installed on the VLTs and ELTs. Thus, in what follows, I provide a brief account of the continuity of my research project on the short-, mid-, and long-term, in this specific order.

Completing the analysis of the angular momentum

The shortest-term perspective that I can discuss is regarding the analysis of the angular momentum in MAGIC. As already mentioned, the analysis presented in Chapter 7 is still

preliminary. Already we can draw some early conclusions regarding the impact of the environment, stellar mass, or bulges, but there is still some work that needs to be done before a definite conclusion can be reached. In particular, one aspect that has not been discussed is the impact of the radius where the angular momentum is measured. Other radii beside R_{22} may also be appropriate to probe the impact of the environment. Thus, it would be interesting to see (i) if I recover the same results when measuring the angular momentum for instance in one effective radius, or when extrapolating to infinity, and (ii) if there is some variation with environment or bulge fraction when computing the cumulative angular momentum (i.e. angular momentum versus radial distance). A second aspect that has not been discussed so far is how the population of small galaxies removed by the selection criteria compares to the Fall relation found at low stellar masses. It would be interesting to investigate whether such galaxies are found on the same relation or whether they are located below (as the Fall relation using the flat model rotation curve seems to indicate at first glance). If so, then it would be valuable to investigate whether this is physical or whether it is related to loose constraints on the galaxies' M/L, disk inclination, disk and/or bulge flux distributions, ionised gas kinematics, etc.

I will pursue these investigations and complete them in the next couple of months.

Prospects for MAGIC, MUSCATEL, and other MUSE surveys

The MAGIC survey is now complete (Epinat et al., in prep.) and the analysis of the impact of the environment on the scaling relations, in particular the TFR and the Fall relation has already been investigated. However, as discussed in both Chapters 6 and 7, probing the impact of the environment on the dynamics of galaxies with MAGIC is entirely doable but drawing definite conclusions can be difficult for the moment. The main reason is that it seems that the differences observed between low- and high-density environments is mostly visible at high stellar masses where we lack field galaxies. Hence, it would be interesting to complement these two first studies with additional data from other MUSE surveys. The most promising one is obviously MUSE Cosmic Assembly survey Targeting Extragalactic Legacy fields (MUSCATEL) that has already been presented in Sect. 2.2.3 and that I was originally supposed to use during this Thesis. This new survey should be available soon and will provide us with deep MUSE observations with AO for four parallel fields of the HUBBLE Frontier Fields (HFF). These observations are split between four very deep (25 h), 16 deep (5 h) and 36 shallower (around 2 h) MUSE pointings spanning an area of roughly 36 arcmin^2 . Thus, with this large spatial coverage we should expect to find a significant fraction of massive field galaxies as well as a few structures at higher redshift. Hence, this survey will be perfectly complementary to MAGIC. It will greatly extend our current sample and will allow us to probe a wider variety of environment than currently probe with MAGIC alone. Combined with other surveys, either very deep (e.g. MXDF) or shallower but spanning a larger area (e.g. HUDF and MUSE-WIDE), this should allow us to put even stronger constraints on the impact of the environment on the dynamics of galaxies at $z \sim 1$ and we might even be able to disentangle the effect of the environment from the redshift evolution of the galaxy scaling relations discussed throughout this Thesis (size-mass, MS, TFR, and Fall relations).

Beside what has been previously said, MAGIC can also be used for other purposes than probing the effect of the environment on galaxy properties. For instance, a few years back, some evidence has arisen regarding the potential existence of a few DM-poor galaxies at high redshift (e.g. Lang

et al. 2017; Genzel et al. 2017) but other authors have argued in the meantime that this may be caused by systematics induced by the method used (e.g. Tiley et al. 2019b). However, recently Mancera Piña et al. (2022) has found an ultra-diffuse galaxy in the local Universe whose baryonic mass distribution (i.e. stars plus gas) is sufficient to recover the observed kinematics. They do argue that the inclination they measure is a large source of uncertainty but that, even when taking that into account, the galaxy’s kinematics is not compatible neither with the existence of a cold dark matter halo around the galaxy, nor with MOND. Hence, if such a population of DM-poor galaxies exists, then it might be a challenge to MOND, but certainly also to the current Λ CDM paradigm of galaxy evolution. If not, then it would be particularly interesting to understand why some galaxies do appear seemingly DM-poor. MAGIC, potentially combined with other surveys such as MUSCATEL, can help in that matter because we do actually see in our sample what we called in Mercier et al. (2022) baryon-dominated (i.e. DM-poor) galaxies. However, our early investigations have led us to believe that these galaxies are not intrinsically baryon-dominated but that they appear so because of the propagation of uncertainties in our mass modelling. Still, I personally think that it would be enlightening to investigate these objects on a galaxy-per-galaxy basis. Because of the homogeneity of the MAGIC sample, of its high completeness, and because we have already acquired plenty of information regarding these galaxies (e.g. properties of their host environment, their location on various scaling relations, their morphology, etc.), I believe we have all the required information in MAGIC to study these galaxies in more details. Independently of whether we find that all these objects can be accounted for by methodological biases or systematic effects, which seems the most likely explanation at the moment, or whether some galaxies do appear intrinsically DM-poor after all, the conclusion will remain interesting either way. This is particularly true because, even if the former explanation is retained (i.e. biases, systematics, etc.), we do expect such objects to be seen at higher redshift in the intermediate-future with the development of the ELTs and their first-light instruments such as HARMONI on the ELT and in the near-future with the JWST or ERIS.

Paving the way for next-generation IFS instruments

The methods presented in Chapters 5 and 8 of this Thesis, in particular the part regarding the production of spatially resolved maps of physical properties, can already be applied onto MUSE and HST data. For instance, it will be possible to use it with MUSCATEL because there is ultra deep multi-band HST observations in the parallel fields of the HFF. However, the real objective is to improve the method so that we are prepared for the next-generation of IFS (e.g. HARMONI, MOSAIC) and imaging instruments such as the Multi-AO Imaging Camera for Deep Observations (MICADO) on the future ELTs. HARMONI and MOSAIC will both observe in the NIR with medium to high spectral resolving power and will therefore target high-redshift galaxies. The former instrument is really optimised for high spatial resolution observations of distant galaxies and will therefore observe one object at a time over a relatively narrow FoV. On the other hand, the latter will have a MOS IFS mode with eight-ten IFUs that shall be deployed over a large FoV but with a coarser spatial sampling similar to that of MUSE (i.e. about $0.2''$ per spaxel). In the meantime, it will be possible to apply and further test our methodology on the new generation of instruments such as NIRSPEC and MIRI on board of the JWST that both host an IFS observing mode or ERIS that will be soon available on the VLT. These instruments will provide us with integral field spectroscopy on a galaxy-per-galaxy basis in the NIR (MIR for MIRI) with a better spatial resolution and spatial sampling that MUSE currently allows.

A first plan which is still on relatively short term is to test our current methodology on a galaxy as if it was observed with HARMONI. To do so, we will use Fourier-transform spectroscopy observations obtained with the Spectromètre Imageur à Transformée de Fourier pour l'Etude en Long et en Large de raies d'Emission (SITELE) combined with MEGACAM and Wide-field InfraRed Camera (WIRCAM) images of M95 to simulate how this galaxy would be observed by HARMONI if it lay at high redshift. Then, we will be able to use these mock observations to assess the reliability of our current method (including the pixel-per-pixel SED fitting and the machine learning application discussed in Chapter 8). I note that it may also be doable in a slightly more distant future to perform the same tests but using outputs from simulations rather than high-resolution observations of local galaxies.

Apart from what has already been discussed, there is also the work regarding the implementation of the machine learning algorithm that needs to continue. A lot of efforts have already been put into the SOM, but there is still some work that needs to be done. We need to assess in details the advantages and drawbacks of using such a method over the more traditional pixel-per-pixel SED fitting technique, verify whether there is not a more advantageous design for the algorithm, and finally we need to test the algorithm over a large sample of galaxies, possibly from MUSCATEL. Depending on how many people work on this and how much effort is put into it, this could lead to another publication in the next one or two years. I note that this exercise will be particularly interesting because it will definitely benefit us when large surveys from next-generation instruments will become available in the medium/long-term.

Finally, I will conclude with a last prospect which is regarding the dynamical modelling of high-redshift galaxies. Indeed, with the incoming wealth of 3D spectroscopic data in the NIR, it is likely that there will be a time, perhaps in ten years from now, perhaps even before, when it will become custom to extract spatially resolved kinematics of galaxies using rest-frame optical and UV emission lines at redshifts $z \gtrsim 6$. Actually, with NIRSPEC it is theoretically possible to reach $z \approx 12$ and, with space-based observations in the MIR such as those performed by MIRI, galaxies could be observed with relatively high spatial and spectral resolutions up to $z \approx 30$. Obviously, such observations would be limited not so much by the apparent size of the galaxies but by the scaling of the flux with redshift. Nevertheless, the point is that it will become more and more common to study the dynamics of very high redshift galaxies but, based on our current understanding of galaxy evolution and on simulations, these objects are likely to be very different from intermediate redshift galaxies. In particular, we might expect to probe a large fraction of gas-rich morphologically and kinematically disturbed galaxies. In this context, the rotationally supported disk approximation that is used in nearly all dynamical studies might begin to fail and if so it will become much harder to precisely constrain the DM fraction found in very high redshift galaxies. Hence, in my view, there should be efforts put into building dynamical models of non-axisymmetric galaxies, perhaps based on high-resolution observations of local irregular or peculiar galaxies or on outputs from simulations. The clear difficulty in doing so is that the complexity of such models will be greatly impacted by various limitations (spatial and/or spectral resolution, S/N, etc.) and by the loss of information due to integration along the LOS. Perhaps the solution will be to combine the information found in various types of data (e.g. SED, high-resolution images, data cubes, etc.) into a grand physical-morphological-dynamical model applied on spatially resolved scales, that is similarly to what is done with pixel-per-pixel SED fitting but by taking the geometry of the galaxy and its dynamics into account.

Conclusions et perspectives

Dans ce manuscrit, j'ai présenté le travail que j'ai effectué au cours de ces trois dernières années concernant l'impact de l'environnement sur les propriétés dynamiques des galaxies au cours des dix derniers milliards d'années. J'ai montré comment j'ai été capable, en combinant des données MUSE et HST, de contraindre la morphologie et la cinématique de presque 400 galaxies dans le relevé MAGIC. En particulier, j'ai mis en avant dans le Chapitre 3 l'efficacité du relevé MAGIC pour sonder l'impact de l'environnement sur les propriétés des galaxies grâce à sa grande homogénéité dans la manière dont les propriétés physiques, morphologiques et cinématiques des galaxies sont mesurées pour un grand échantillon de galaxies à la fois dans les champs et dans des environnements de densité variable (groupes et amas de galaxies). Ceci m'a permis de contribuer fortement à deux articles déjà publiés (Abril-Melgarejo et al. 2021; Mercier et al. 2022) et à deux autres analyses quasiment terminées, la première sur le moment angulaire dans MAGIC présentée au Chapitre 7, et la seconde sur le relevé MAGIC discutées au Chapitre 3. Grâce à la conception du relevé MAGIC, aux capacités incroyables de MUSE et aux modélisations morphologiques et dynamiques précises que j'ai effectuées (voir Chapitres 4 et 5), ce travail m'a permis de poser les contraintes les plus précises à ce jour sur l'impact de l'environnement sur plusieurs relations d'échelles de galaxies à redshift intermédiaire. À partir de ces analyses, j'ai pu mettre en lumière l'effet de l'environnement sur la morphologie et le taux de formation stellaire dans les structures. J'ai aussi montré que, à redshift intermédiaire, l'environnement ne semble pas affecter la cinématique des galaxies (vitesse de rotation) mais qu'il semble avoir un impact sur le moment angulaire des galaxies les plus massives que l'on trouve dans les parties les plus denses des structures.

Néanmoins, beaucoup de travail reste encore à effectuer. Qui plus est, comme discuté au Chapitre 8, nous avons développé au cours des deux dernières années une nouvelle méthodologie qui pourrait nous aider grandement à mieux contraindre la dynamique des galaxies à redshift intermédiaire avec MUSE et, de manière encore plus importante, des galaxies à grand redshift avec la prochaine génération de spectrographes à intégrale de champs tels que ERIS, HARMONI ou MOSAIC qui seront installés sur les très grands télescopes actuels et sur les télescopes extrêmement grands du futur. Ainsi, dans ce qui suit, je discute rapidement de la continuité de mon projet de recherche à la fois sur le court, moyen et long termes.

Finaliser l'analyse du moment angulaire

La perspective sur le plus court terme possible que je peux discuter concerne l'analyse du moment angulaire dans MAGIC. Comme précédemment discuté, l'analyse présentée au Chapitre 7 est encore préliminaire. Il est possible de tirer quelques premières conclusions concernant l'impact de

l'environnement, de la masse stellaire, ou encore des bulbes, mais il reste encore du travail avant de pouvoir conclure définitivement. En particulier, un aspect qui n'a pas été discuté est l'impact du rayon où le moment angulaire est mesuré. Des rayons autres que R_{22} pourraient aussi être considérés pour sonder l'impact de l'environnement. Ainsi, il serait intéressant de tester (i) si je retrouve les mêmes résultats quand je mesure le moment angulaire par exemple à un rayon effectif, ou quand j'extrapole à l'infini, et (ii) s'il y a des variations avec l'environnement ou la fraction de masse dans le bulbe quand je calcule le moment angulaire cumulatif (c'est-à-dire le moment angulaire en fonction de la distance radiale). Un autre aspect qui n'a pas été discuté pour le moment est où se situent les petites galaxies enlevées par la sélection par rapport à la relation de Fall trouvée à faibles masses stellaires. Il serait intéressant de voir si de telles galaxies se trouvent sur la même relation ou si elles sont situées en-dessous (comme le relation de Fall obtenue en utilisant les courbes de rotation issues du modèle « flat » semble indiquer). Si c'est le cas, alors cela mériterait d'étudier si l'effet est physique ou si c'est lié à des contraintes faibles sur le rapport masse-lumière des galaxies, sur leurs distributions de flux dans le disque ou le bulbe, sur la cinématique du gaz ionisé, etc.

Je compte continuer ces investigations et arriver à des conclusions définitives dans les mois qui suivent.

Perspectives concernant MAGIC, MUSCATEL et d'autres relevés MUSE

Le survey MAGIC est à présent terminé (Epinat et al., in prep.) et l'analyse de l'impact de l'environnement sur les relations d'échelles, en particulier les relations de Tully-Fisher et de Fall, a été effectuée. Cependant, comme discuté dans les Chapitres 6 et 7, sonder l'impact de l'environnement sur la dynamique des galaxies avec MAGIC est entièrement faisable, mais conclure définitivement peut être difficile pour le moment. La raison principale est qu'il semble que les différences observées entre les galaxies dans les environnements à basse et à haute densité soient majoritairement visibles à grande masse stellaire où nous manquons de galaxies de champs. Ainsi, il serait intéressant de compléter ces deux premières études avec des données supplémentaires issues d'autres relevés MUSE. Le plus prometteur est évidemment MUSCATEL qui a déjà été présenté en Sect. 2.2.3 et dont j'étais censé utiliser les données pendant cette Thèse. Ce nouveau relevé devrait être disponible bientôt et fournira des observations MUSE profondes avec optique adaptative pour quatre champs parallèles du HFF. Ces observations sont séparées entre quatre champs MUSE très profonds (25 h), 16 profonds (5 h), et 36 moins profonds (environ 2 h) qui couvriront au total une surface de 36 arcmin². Ainsi, avec cette grande couverture spatiale on devrait s'attendre à trouver une fraction significative de galaxies de champs massives ainsi que quelques structures à plus haut redshift. De fait, ce relevé sera parfaitement complémentaire de MAGIC. Il permettra d'étendre grandement notre échantillon actuel et nous permettra de sonder une plus grande variété d'environnements que ce que MAGIC peut faire seul actuellement. Combiné avec d'autres relevés MUSE, soit très profonds (ex : MXDF), soit un peu moins mais couvrant une plus grande surface (ex : HUDF et MUSE-WIDE), cela devrait nous permettre de poser des contraintes encore plus fortes sur l'impact de l'environnement sur la dynamique des galaxies à $z \sim 1$, et l'on peut même imaginer séparer l'effet de l'environnement d'une potentielle évolution en redshift des relations d'échelle discuté au cours de cette Thèse (relation masse-taille, séquence principale, relation Tully-Fisher, relation de Fall).

Au-delà ce qui a été dit, MAGIC peut aussi être utilisé pour d'autres objectifs que sonder l'impact de l'environnement sur les propriétés des galaxies. Par exemple, quelques années en arrière, certaines études ont semblé montrer l'existence potentielle de quelques galaxies pauvres en matière noire à grand redshift (e.g. [Lang et al. 2017](#); [Genzel et al. 2017](#)) mais d'autres auteurs ont montré par la suite que cela pourrait être dû à des effets systématiques induits par la méthode utilisée (e.g. [Tiley et al. 2019b](#)). Cependant, [Mancera Piña et al. \(2022\)](#) ont trouvé récemment une galaxie ultra diffuse dans l'Univers local dont la distribution de matière baryonique (c'est-à-dire étoiles plus gaz) est suffisante pour reconstruire la cinématique observée. Ils discutent bien du fait que l'inclinaison de la galaxie qu'ils mesurent est une grande source d'incertitude, néanmoins, ils affirment que, même en prenant cela en compte, la cinématique n'est compatible ni avec un halo de matière noire froide, ni avec MOND. Ainsi, si une telle population de galaxies pauvres en matière noire existe, alors cela pourrait être un challenge pour le paradigme actuel Λ CDM concernant l'évolution des galaxies et, si ce n'est pas le cas, alors il serait particulièrement intéressant de comprendre pourquoi certaines galaxies semblent apparaître pauvre en matière noire. MAGIC, potentiellement combiné avec d'autres relevés MUSE comme MUSCATEL, peuvent aider parce que nous observons en effet dans notre échantillon ce que nous appelons dans [Mercier et al. \(2022\)](#) des galaxies dominées par les baryons (c'est-à-dire pauvres en matière noire). Cependant, nos premières investigations nous ont amené à conclure que ces galaxies ne sont pas intrinsèquement dominées par les baryons mais plutôt qu'elles apparaissent ainsi à cause de la propagation d'incertitudes jusque dans notre modélisation de masse. Et pourtant, je pense personnellement qu'il serait intéressant d'étudier au cas par cas ces objets. Grâce à la grande homogénéité de notre échantillon MAGIC, de sa haute complétude, et parce que nous avons acquis de nombreuses informations sur ces galaxies (ex : propriété de leur environnement, leur localisation dans plusieurs relations d'échelle, leur morphologie, etc.), je pense que nous avons en notre possession toutes les informations nécessaires pour étudier ces galaxies plus en détail. Indépendamment du résultat (effet systématique pour toutes les galaxies ou certaines d'entre elles sont intrinsèquement pauvres en matière noire), la conclusion sera dans tous les cas enrichissante. Cela est particulièrement vrai, même si la première explication s'avère la bonne (ex : biais systématiques), parce que l'on s'attend à ce que de tels objets soient détectés à haut redshift dans le futur à moyen terme avec le développement des télescopes extrêmement grands et leur instruments de première lumière comme HARMONI sur l'ELT et dans le future proche avec le JWST ou encore ERIS.

Préparer le chemin pour les spectrographes à intégrale de champs de prochaine génération

Les méthodes présentées aux Chapitres 5 et 8 de cette Thèse, en particulier concernant la production de cartes spatialement résolues de propriétés physiques, peuvent déjà être appliquées sur des données MUSE et HST. Par exemple, il sera possible de l'utiliser avec MUSCATEL car il y a des observations HST multi-bandes ultra profondes dans les champs parallèles du HFF. Cependant, le véritable objectif est d'améliorer la méthode de telle sorte qu'elle soit disponible pour les prochaines générations de spectrographes à intégrale de champs (ex : HARMONI, MOSAIC) et d'imageurs haute résolution tel que MICADO sur les futures télescopes extrêmement grands. HARMONI et MOSAIC observeront tous les deux dans le proche infrarouge avec des résolutions spectrales moyennes et hautes et pourront de fait cibler des

galaxies à haut redshift. Le premier des deux instruments est vraiment optimisé pour des observations à haute résolution spatiale de galaxies distantes et observera donc un objet à la fois sur un champ de vue relativement petit. À l'inverse, le second instrument aura un mode spectroscopie à intégrale de champs multi-objets composé de huit à dix unités d'intégrale de champs (IFU) qui seront déployées sur un grand champ de vue mais avec une moins bonne résolution spatiale, similaire à celle de MUSE (c'est-à-dire environ $0.2''$ par spaxel). En attendant, il sera possible d'appliquer et de tester notre méthodologie sur les instruments de nouvelle génération que sont NIRSPEC et MIRI sur le JWST, qui tout les deux ont un mode spectroscopie à intégrale de champs, ou encore ERIS qui sera bientôt disponible sur le VLT. Ces instruments nous fourniront des observations dans le proche infrarouge (infrarouge moyen pour MIRI) avec une meilleure résolution spatiale que ce que MUSE offre actuellement.

À relativement court terme, je testerai notre méthodologie sur une galaxie comme si elle était observée avec HARMONI. Pour ce faire, nous allons utiliser des observations de spectroscopie à transformée de Fourier de M95 obtenues avec SITELLE combinées avec des images issues de MEGACAM et WIRCAM pour simuler comment cette galaxie nous apparaîtrait si elle était située à grand redshift et vue par HARMONI. Ensuite, nous serons en mesure d'utiliser ces observations synthétiques pour estimer l'efficacité de notre méthode (incluant la technique d'ajustement pixel par pixel et son application d'apprentissage machine discutés au Chapitre 8). Je précise qu'il serait aussi possible dans une avenir légèrement plus lointain d'effectuer ce même type de tests sur des données issues de simulations plutôt que sur des observations à haute résolution de galaxies dans l'Univers local.

Au-delà de ce qui a déjà été dit, il reste encore du travail concernant l'implémentation de l'algorithme d'apprentissage machine qui doit être terminée. Beaucoup d'efforts ont déjà été fournis dans le SOM, mais il reste encore du travail. Nous devons déterminer en détails les avantages et les inconvénients d'une telle méthode par rapport à des techniques plus classiques d'ajustement pixel par pixel, vérifier qu'il n'existe pas une manière plus efficace d'utiliser l'algorithme et enfin le tester sur un grand échantillon de galaxies, potentiellement avec MUSCATEL. En fonction de combien de personnes travailleront dessus et de l'effort général qui sera fourni, cela pourrait mener à une autre publication dans les deux prochaines années à venir. Cet exercice sera particulièrement intéressant car ce qu'il en ressortira sera d'autant plus utile pour les grands relevés à venir issus des futurs instruments sur le moyen/long terme.

Finalement, je conclurai avec une dernière perspective concernant la modélisation dynamique des galaxies à grand redshift. En effet, avec l'avènement prochain de nombreuses données 3D dans le proche infrarouge, il est plus que probable qu'il adviendra une époque, peut-être dans une dizaine d'années, où il sera coutume d'extraire la cinématique spatialement résolue de galaxies à l'aide de raies d'émission dans l'ultra-violet ou le visible (au repos) à des redshifts $z \gtrsim 6$. En principe, avec NIRSPEC il est déjà théoriquement possible d'atteindre des redshifts $z \approx 12$ et, avec des observations spatiales dans l'infrarouge moyen comme celles fournies par MIRI, des galaxies pourraient être observées avec une relativement haute résolution spatiale jusqu'à $z \approx 30$.

Évidemment, de telles observations seraient limitées non pas vraiment par la taille apparente des galaxies mais plutôt par l'évolution du flux avec le redshift. Néanmoins, l'argument reste qu'il sera de plus en plus commun d'étudier la dynamique de galaxies à très grand redshift mais, basé sur notre connaissance actuelle de leur évolution et sur les résultats de simulations, ces objets sont censés être très différents de ceux à redshift intermédiaire. En particulier, on peut s'attendre à observer une fraction importante d'objets riches en gaz et perturbés morphologiquement et cinématiquement. Dans ce contexte, l'approximation de disques supportés par leur propre

rotation qui est utilisée dans la plupart des études pourrait ne plus être valide, auquel cas il deviendrait d'autant plus difficile de contraindre correctement la fraction de matière noire à grand redshift. Ainsi, de mon point de vue, il devrait y avoir des efforts mis dans la conception de modèles dynamiques de galaxies non-axisymétriques, peut-être en se basant sur des observations de galaxies locales irrégulières ou particulières ou via des résultats de simulations. La difficulté évidente dans cet effort est que la complexité de tels modèles sera fortement impactée par la perte d'information due à l'intégration le long de la ligne de visée. Peut-être que la solution serait de combiner les informations contenues dans différents types de données (ex : distribution d'énergie spectrale, images haute résolution, cubes de données, etc.) dans un super modèle physico-morphologico-dynamique qui serait appliqué sur des échelles résolues, dans la veine de ce qui est actuellement fait avec l'ajustement de distribution d'énergie spectrale pixel par pixel mais en prenant en compte la géométrie de la galaxie et sa dynamique.

Bibliography

- Abril-Melgarejo, V., Epinat, B., Mercier, W., et al. 2021, *Astronomy & Astrophysics*, **647**, [A152](#)
- Adamczyk, P. 2021, PhD thesis, Aix-Marseille Université, thèse de doctorat dirigée par Amram, Philippe et Epinat, Benoît Physique et sciences de la matière. Astrophysique et cosmologie Aix-Marseille 2021
- Allen, J. T., Croom, S. M., Konstantopoulos, I. S., et al. 2015, *Monthly Notices of the Royal Astronomical Society*, **446**, [1567](#)
- Ambartsumian, V. A. 1968, in *Non-stable Phenomena in Galaxies*, Vol. 29, 11
- Baade, W. 1944, *Astrophysical Journal*, **100**, [147](#)
- Baade, W. & Minkowski, R. 1954a, *Astrophysical Journal*, **119**, [206](#)
- Baade, W. & Minkowski, R. 1954b, *Astrophysical Journal*, **119**, [215](#)
- Bacon, R., Adam, G., Baranne, A., et al. 1995, *Astronomy & Astrophysics Supplement*, **113**, 347
- Bacon, R., Adam, G., Baranne, A., et al. 1988, *Very Large Telescopes and their Instrumentation, ESO Conference and Workshop Proceedings, Proceedings of a ESO Conference on Very Large Telescopes and their Instrumentation, held in Garching, March 21-24, 1988, Garching: European Southern Observatory (ESO), 1185*
- Bacon, R., Brinchmann, J., Richard, J., et al. 2015, *Astronomy & Astrophysics*, **575**, [A75](#)
- Bacon, R., Conseil, S., Mary, D., et al. 2017, *Astronomy & Astrophysics*, **608**, [A1](#)
- Bacon, R., Copin, Y., Monnet, G., et al. 2001, *Monthly Notices of the Royal Astronomical Society*, **326**, [23](#)
- Bacon, R., Emsellem, E., Combes, F., et al. 2001, *Astronomy & Astrophysics*, **371**, [409](#)
- Bacon, R., Emsellem, E., Monnet, G., & Nieto, J. L. 1994, *Astronomy & Astrophysics*, **281**, 691
- Bacon, R., Mary, D., Garel, T., et al. 2021, *Astronomy & Astrophysics*, **647**, [A107](#)
- Bacon, R., Vernet, J., Borisova, E., et al. 2014, *The Messenger*, **157**, 13
- Baldry, I. K., Balogh, M. L., Bower, R. G., et al. 2006, *Monthly Notices of the Royal Astronomical Society*, **373**, [469](#)
- Balogh, M. L., Gilbank, D. G., Muzzin, A., et al. 2017, *Monthly Notices of the Royal Astronomical Society*, **470**, [4168](#)
- Baxter, D. C., Cooper, M. C., Balogh, M. L., et al. 2022, *Monthly Notices of the Royal Astronomical Society*, **515**, [5479](#)
- Begeman, K. G. 1987, PhD thesis, University of Groningen, Kapteyn Astronomical Institute
- Behroozi, P. S., Wechsler, R. H., & Conroy, C. 2013, *The Astrophysical Journal*, **770**, [57](#)
- Belfiore, F., Maiolino, R., Maraston, C., et al. 2017, *Monthly Notices of the Royal Astronomical Society*, **466**, [2570](#)
- Bellhouse, C., Jaffé, Y. L., Hau, G. K. T., et al. 2017, *The Astrophysical Journal*, **844**, [49](#)
- Bertin, E. & Arnouts, S. 1996, *Astronomy and Astrophysics Supplement*, **117**, [393](#)
- Bina, D., Pelló, R., Richard, J., et al. 2016, *Astronomy & Astrophysics*, **590**, [A14](#)
- Binney, J. & Tremaine, S. 2008, *Galactic Dynamics: Second Edition* (Princeton University Press)
- Bizyaev, D. & Mitronova, S. 2002, *Astronomy & Astrophysics*, **389**, [795](#)
- Bizyaev, D., Tatarsnikov, A., Shatsky, N., et al. 2020, *Astronomische Nachrichten*, **341**, [314](#)
- Bizyaev, D., Walterbos, R. A. M., Yoachim, P., et al. 2017, *The Astrophysical Journal*, **839**, [87](#)

- Bizyaev, D. V., Kautsch, S. J., Mosenkov, A. V., et al. 2014, *The Astrophysical Journal*, **787**, [24](#)
- Boissier, S., Boselli, A., Duc, P. A., et al. 2012, *Astronomy & Astrophysics*, **545**, [A142](#)
- Boldrini, P. 2021, *Galaxies*, **10**, [5](#)
- Boogaard, L. A., Brinchmann, J., Bouché, N., et al. 2018, *Astronomy & Astrophysics*, **619**, [A27](#)
- Boquien, M., Burgarella, D., Roehlly, Y., et al. 2019, *Astronomy & Astrophysics*, **622**, [A103](#)
- Boselli, A., Boissier, S., Cortese, L., et al. 2006, *The Astrophysical Journal*, **651**, [811](#)
- Boselli, A., Epinat, B., Contini, T., et al. 2019, *Astronomy & Astrophysics*, **631**, [A114](#)
- Boselli, A., Lupi, A., Epinat, B., et al. 2021, *Astronomy & Astrophysics*, **646**, [A139](#)
- Bosma, A. 1978, PhD thesis, University of Groningen, Netherlands
- Bosma, A. 1981a, *Astronomical Journal*, **86**, [1791](#)
- Bosma, A. 1981b, *Astronomical Journal*, **86**, [1825](#)
- Bottinelli, L., Gouguenheim, L., Paturel, G., & de Vaucouleurs, G. 1983, *Astronomy and Astrophysics*, **118**, [4](#)
- Bouché, N., Carfantan, H., Schroetter, I., Michel-Dansac, L., & Contini, T. 2015, *The Astronomical Journal*, **150**, [92](#)
- Bouché, N., Dekel, A., Genzel, R., et al. 2010, *The Astrophysical Journal*, **718**, [1001](#)
- Bouché, N., Finley, H., Schroetter, I., et al. 2016, *The Astrophysical Journal*, **820**, [121](#)
- Bouché, N. F., Bera, S., Krajnović, D., et al. 2022, *Astronomy & Astrophysics*, **658**, [A76](#)
- Bouché, N. F., Genel, S., Pellissier, A., et al. 2021, *Astronomy & Astrophysics*, **654**, [A49](#)
- Brinchmann, J., Abraham, R., Schade, D., et al. 1998, *The Astrophysical Journal*, **499**, [112](#)
- Broadhurst, T. J., Ellis, R. S., & Shanks, T. 1988, *Monthly Notices of the Royal Astronomical Society*, **235**, [827](#)
- Bruzual, G. & Charlot, S. 2003, *Monthly Notices of the Royal Astronomical Society*, **344**, [1000](#)
- Bryant, J. J., Bland-Hawthorn, J., Lawrence, J., et al. 2016, in *Society of Photo-Optical Instrumentation Engineers (SPIE) Conference Series*, Vol. 9908, *Ground-based and Airborne Instrumentation for Astronomy VI*, ed. C. J. Evans, L. Simard, & H. Takami, 99081F
- Buchner, J., Georgakakis, A., Nandra, K., et al. 2014, *Astronomy & Astrophysics*, **564**, [A125](#)
- Buitinck, L., Louppe, G., Blondel, M., et al. 2013, in *ECML PKDD Workshop: Languages for Data Mining and Machine Learning*, 108–122
- Bundy, K., Bershady, M. A., Law, D. R., et al. 2015, *The Astrophysical Journal*, **798**, [7](#)
- Burkert, A. 1995, *The Astrophysical Journal*, **447**
- Burkert, A., Förster Schreiber, N. M., Genzel, R., et al. 2016, *The Astrophysical Journal*, **826**, [214](#)
- Burkert, A. & Silk, J. 1997, *The Astrophysical Journal*, **488**, [L55](#)
- Butcher, H. & Oemler, A., J. 1978, *Astrophysical Journal*, **219**, [18](#)
- Butcher, H. & Oemler, A., J. 1984, *Astrophysical Journal*, **285**, [426](#)
- Calvi, R., Vulcani, B., Poggianti, B. M., et al. 2018, *Monthly Notices of the Royal Astronomical Society*, **481**, [3456](#)
- Calzetti, D., Armus, L., Bohlin, R. C., et al. 2000, *The Astrophysical Journal*, **533**, [682](#)
- Calzetti, D., Kennicutt, R. C., Engelbracht, C. W., et al. 2007, *The Astrophysical Journal*, **666**, [870](#)
- Cameron, M., Weitzel, L., Krabbe, A., Genzel, R., & Drapatz, S. 1993, in *American Astronomical Society Meeting Abstracts*, Vol. 183, *American Astronomical Society Meeting Abstracts*, 117.02
- Camm, G. L. 1950, *Monthly Notices of the Royal Astronomical Society*, **110**, [305](#)
- Cappellari, M., Emsellem, E., Bacon, R., et al. 2007, *Monthly Notices of the Royal Astronomical Society*, **379**, [418](#)
- Cappellari, M., Emsellem, E., Krajnović, D., et al. 2011a, *Monthly Notices of the Royal Astronomical Society*, **413**, [813](#)
- Cappellari, M., Emsellem, E., Krajnović, D., et al. 2011b, *Monthly Notices of the Royal Astronomical Society*, **416**, [1680](#)

- Cardelli, J. A., Clayton, G. C., & Mathis, J. S. 1989, *The Astrophysical Journal*, **345**, 245
- Carrasco Kind, M. & Brunner, R. J. 2014, *Monthly Notices of the Royal Astronomical Society*, **438**, 3409
- Casertano, S., de Mello, D., Dickinson, M., et al. 2000, *The Astronomical Journal*, **120**, 2747
- Chabrier, G. 2003, *The Publications of the Astronomical Society of the Pacific*, **115**, 763
- Champagne, J. B., Casey, C. M., Zavala, J. A., et al. 2021, *The Astrophysical Journal*, **913**, 110
- Charlot, S. & Fall, S. M. 2000, *The Astrophysical Journal*, **539**, 718
- Charlot, S. & Fall, S. M. 2000, *The Astrophysical Journal*, **539**, 718
- Chemin, L., de Blok, W. J. G., & Mamon, G. A. 2011, *The Astronomical Journal*, **142**, 109
- Chen, Y.-C., Ho, S., Freeman, P. E., Genovese, C. R., & Wasserman, L. 2015, *Monthly Notices of the Royal Astronomical Society*, **454**, 1140
- Chiang, Y.-K., Overzier, R. A., Gebhardt, K., & Henriques, B. 2017, *The Astrophysical Journal Letters*, **844**, L23
- Chu, A., Durret, F., & Márquez, I. 2021, *Astronomy & Astrophysics*, **649**, A42
- Cid Fernandes, R., Mateus, A., Sodré, L., Stasińska, G., & Gomes, J. M. 2005, *Monthly Notices of the Royal Astronomical Society*, **358**, 363
- Ciesla, L., Buat, V., Boquien, M., et al. 2021, *Astronomy & Astrophysics*, **653**, A6
- Ciesla, L., Elbaz, D., Schreiber, C., Daddi, E., & Wang, T. 2018, *Astronomy & Astrophysics*, **615**, A61
- Closs, M. F., Ferruit, P., Lobb, D. R., et al. 2008, in *Space Telescopes and Instrumentation 2008: Optical, Infrared, and Millimeter*, ed. J. M. O. Jr., M. W. M. de Graauw, & H. A. MacEwen, Vol. 7010, International Society for Optics and Photonics (SPIE), 701011
- Clowe, D., Gonzalez, A., & Markevitch, M. 2004, *The Astrophysical Journal*, **604**, 596
- Conroy, C. & Gunn, J. E. 2010, *The Astrophysical Journal*, **712**, 833
- Consolandi, G., Gavazzi, G., Fossati, M., et al. 2017, *Astronomy & Astrophysics*, **606**, A83
- Contini, T., Epinat, B., Bouché, N., et al. 2016, *Astronomy & Astrophysics*, **591**, A49
- Contini, T., Garilli, B., Le Fèvre, O., et al. 2012, *Astronomy & Astrophysics*, **539**, A91
- Cortese, L., Catinella, B., & Smith, R. 2021, *Publications of the Astronomical Society of Australia*, **38**, e035
- Costantin, L., Pérez-González, P. G., Méndez-Abreu, J., et al. 2022, arXiv e-prints, arXiv:2202.02332
- Courteau, S. & Dutton, A. A. 2015, *The Astrophysical Journal Letters*, **801**, L20
- Courtes, G. 1982, *International Astronomical Union Colloquium*, **67**, 123–128
- Cowie, L. L. & Songaila, A. 1977, *Nature*, **266**, 501
- Cowie, L. L., Songaila, A., & Hu, E. M. 1991, *Nature*, **354**, 460
- Crain, R. A., Schaye, J., Bower, R. G., et al. 2015, *Monthly Notices of the Royal Astronomical Society*, **450**, 1937
- Cresci, G., Hicks, E. K. S., Genzel, R., et al. 2009, *The Astrophysical Journal*, **697**, 115
- Croom, S. M., Lawrence, J. S., Bland-Hawthorn, J., et al. 2012, *Monthly Notices of the Royal Astronomical Society*, **421**, 872
- Croom, S. M., Owers, M. S., Scott, N., et al. 2021, *Monthly Notices of the Royal Astronomical Society*, **505**, 991
- Daddi, E., Dickinson, M., Morrison, G., et al. 2007, *The Astrophysical Journal*, **670**, 156
- Daddi, E., Valentino, F., Rich, R. M., et al. 2021, *Astronomy & Astrophysics*, **649**, A78
- Dalcanton, J. J. & Stilp, A. M. 2010, *The Astrophysical Journal*, **721**, 547
- Dale, D. A., Helou, G., Magdis, G. E., et al. 2014, *The Astrophysical Journal*, **784**, 83
- Darragh Ford, E., Laigle, C., Gozaliasl, G., et al. 2019, *Monthly Notices of the Royal Astronomical Society*, **489**, 5695
- Darvish, B., Mobasher, B., Sobral, D., Scoville, N., & Aragon-Calvo, M. 2015, *The Astrophysical Journal*, **805**, 121
- Darvish, B., Scoville, N. Z., Martin, C., et al. 2020, *The Astrophysical Journal*, **892**, 8

- Davidzon, I., Laigle, C., Capak, P. L., et al. 2019, *Monthly Notices of the Royal Astronomical Society*, **489**, 4817
- Davies, R., Esposito, S., Schmid, H. M., et al. 2018, in *Society of Photo-Optical Instrumentation Engineers (SPIE) Conference Series*, Vol. 10702, *Ground-based and Airborne Instrumentation for Astronomy VII*, ed. C. J. Evans, L. Simard, & H. Takami, 1070209
- Davis, M. & Djorgovski, S. 1985, *Astrophysical Journal*, **299**, 15
- Davis, M., Guhathakurta, P., Konidaris, N. P., et al. 2007, *The Astrophysical Journal*, **660**, L1
- de Blok, W. J. G. & McGaugh, S. S. 1997, *Monthly Notices of the Royal Astronomical Society*, **290**, 533
- de La Vieuville, G., Bina, D., Pello, R., et al. 2019, *Astronomy & Astrophysics*, **628**, A3
- de Vaucouleurs, G. 1948, *Annales d'Astrophysique*, **11**, 247
- de Vaucouleurs, G. 1958, *Nature*, **182**, 1478
- de Vaucouleurs, G. 1974, in *The Formation and Dynamics of Galaxies*, ed. J. R. Shakeshaft, Vol. 58, 1
- Deb, T., Verheijen, M. A. W., Poggianti, B. M., et al. 2022, arXiv e-prints, arXiv:2208.12950
- Di Matteo, T., Springel, V., & Hernquist, L. 2005, *Nature*, **433**, 604
- Di Teodoro, E. M. & Fraternali, F. 2015, *Monthly Notices of the Royal Astronomical Society*, **451**, 3021
- Dickinson, M. 1995, *Imaging Clusters of Galaxies at z > 1*, HST Proposal ID 5967. Cycle 5
- Dickinson, M., Giavalisco, M., & GOODS Team. 2003, in *The Mass of Galaxies at Low and High Redshift*, ed. R. Bender & A. Renzini, 324
- Diener, C., Wisotzki, L., Schmidt, K. B., et al. 2017, *Monthly Notices of the Royal Astronomical Society*, **471**, 3186
- Divoy, C., Contini, T., Pérez-Montero, E., et al. 2014, *Astronomy & Astrophysics*, **569**, A64
- Djorgovski, S. & Davis, M. 1987, *Astrophysical Journal*, **313**, 59
- D'Onghia, E., Besla, G., Cox, T. J., & Hernquist, L. 2009, *Nature*, **460**, 605
- Dressler, A., Oemler, Augustus, J., Butcher, H. R., & Gunn, J. E. 1994a, *Astrophysical Journal*, **430**, 107
- Dressler, A., Oemler, Augustus, J., Sparks, W. B., & Lucas, R. A. 1994b, *Astrophysical Journal Letters*, **435**, L23
- Durret, F., Pecontal, E., Petitjean, P., & Bergeron, J. 1994, *Astronomy & Astrophysics*, **291**, 392
- Dutton, A. A., Macciò, A. V., Dekel, A., et al. 2016, *Monthly Notices of the Royal Astronomical Society*, **461**, 2658
- Ebeling, H., Stephenson, L. N., & Edge, A. C. 2014, *The Astrophysical Journal Letters*, **781**, L40
- Einasto, J. 1965, *Trudy Astrofizicheskogo Instituta Alma-Ata*, **5**, 87, aDS Bibcode: 1965TrAlm...5...87E
- Einasto, J., Joeveer, M., & Saar, E. 1980, *Nature*, **283**, 47
- El-Zant, A., Shlosman, I., & Hoffman, Y. 2001, *The Astrophysical Journal*, **560**, 636
- El-Zant, A. A., Freundlich, J., & Combes, F. 2016, *Monthly Notices of the Royal Astronomical Society*, **461**, 1745
- Elbaz, D., Daddi, E., Le Borgne, D., et al. 2007, *Astronomy and Astrophysics*, **468**, 33
- Ellis, R. & Dawson, K. 2019, in *Bulletin of the American Astronomical Society*, Vol. 51, 45
- Emsellem, E. 1999, in *Astronomical Society of the Pacific Conference Series*, Vol. 182, *Galaxy Dynamics - A Rutgers Symposium*, ed. D. R. Merritt, M. Valluri, & J. A. Sellwood, 45
- Emsellem, E., Cappellari, M., Krajnović, D., et al. 2007, *Monthly Notices of the Royal Astronomical Society*, **379**, 401
- Emsellem, E., Krajnovic, D., & Sarzi, M. 2014, *Monthly Notices of the Royal Astronomical Society*, **445**, L79
- Epinat, B., Amram, P., Balkowski, C., & Marcelin, M. 2010, *Monthly Notices of the Royal Astronomical Society*, **401**, 2113
- Epinat, B., Amram, P., Marcelin, M., et al. 2008, *Monthly Notices of the Royal Astronomical Society*, **388**, 500
- Epinat, B., Contini, T., Finley, H., et al. 2018, *Astronomy & Astrophysics*, **609**, A40
- Epinat, B., Contini, T., Le Fèvre, O., et al. 2009, *Astronomy & Astrophysics*, **504**, 789
- Epinat, B., Tasca, L., Amram, P., et al. 2012, *Astronomy & Astrophysics*, **539**, A92

- Erb, D. K., Shapley, A. E., Pettini, M., et al. 2006, *The Astrophysical Journal*, **644**, 813
- Evans, C. J., Puech, M., Barbuy, B., et al. 2014, in *Society of Photo-Optical Instrumentation Engineers (SPIE) Conference Series*, Vol. 9147, *Ground-based and Airborne Instrumentation for Astronomy V*, ed. S. K. Ramsay, I. S. McLean, & H. Takami, 914796
- Ewen, H. I. & Purcell, E. M. 1951, *Nature*, **168**, 356
- Faber, S. M. & Jackson, R. E. 1976, *Astrophysical Journal*, **204**, 668
- Faber, S. M., Phillips, A. C., Kibrick, R. I., et al. 2003, in *Society of Photo-Optical Instrumentation Engineers (SPIE) Conference Series*, Vol. 4841, *Instrument Design and Performance for Optical/Infrared Ground-based Telescopes*, ed. M. Iye & A. F. M. Moorwood, 1657–1669
- Feltre, A., Bacon, R., Tresse, L., et al. 2018, *Astronomy & Astrophysics*, **617**, A62
- Feng, S., Shen, S.-Y., Yuan, F.-T., Riffel, R. A., & Pan, K. 2020, *The Astrophysical Journal Letters*, **892**, L20
- Feroz, F. & Hobson, M. P. 2008, *Monthly Notices of the Royal Astronomical Society*, **384**, 449
- Ferrarese, L. & Merritt, D. 2000, *The Astrophysical Journal*, **539**, L9
- Finley, H., Bouché, N., Contini, T., et al. 2017, *Astronomy & Astrophysics*, **608**, A7
- Flores, H., Hammer, F., Puech, M., Amram, P., & Balkowski, C. 2006, *Astronomy & Astrophysics*, **455**, 107
- Flores, H., Puech, M., Hammer, F., Garrido, O., & Hernandez, O. 2004, *Astronomy & Astrophysics*, **420**, L31
- Förster Schreiber, N. M., Genzel, R., Bouché, N., et al. 2009a, *The Astrophysical Journal*, **706**, 1364
- Förster Schreiber, N. M., Genzel, R., Bouché, N., et al. 2009b, *The Astrophysical Journal*, **706**, 1364
- Förster Schreiber, N. M., Genzel, R., Eisenhauer, F., et al. 2006a, *The Messenger*, **125**, 11
- Förster Schreiber, N. M., Genzel, R., Lehnert, M. D., et al. 2006b, *The Astrophysical Journal*, **645**, 1062
- Förster Schreiber, N. M., Genzel, R., Newman, S. F., et al. 2014, *The Astrophysical Journal*, **787**, 38
- Förster Schreiber, N. M., Renzini, A., Mancini, C., et al. 2018, *The Astrophysical Journal Supplement Series*, **238**, 21
- Förster Schreiber, N. M. & Wuyts, S. 2020, *Annual Review of Astronomy and Astrophysics*, **58**, 661
- Fossati, M., Fumagalli, M., Boselli, A., et al. 2016, *Monthly Notices of the Royal Astronomical Society*, **455**, 2028
- Fossati, M., Fumagalli, M., Lofthouse, E. K., et al. 2019, *Monthly Notices of the Royal Astronomical Society*, **490**, 1451
- Foster, C., Mendel, J. T., Lagos, C. D. P., et al. 2021, *Publications of the Astronomical Society of Australia*, **38**, e031
- Freeman, K. C. 1970, *The Astrophysical Journal*, **160**, 811
- Freundlich, J., Dekel, A., Jiang, F., et al. 2020, *Monthly Notices of the Royal Astronomical Society*, **491**, 4523
- Freundlich, J., Jiang, F., Dekel, A., et al. 2020, *Monthly Notices of the Royal Astronomical Society*, **499**, 2912
- Friedmann, A. 1922, *Zeitschrift fur Physik*, **10**, 377
- Friedmann, A. 1924, *Zeitschrift fur Physik*, **21**, 326
- Fritz, J., Moretti, A., Gullieuszik, M., et al. 2017, *The Astrophysical Journal*, **848**, 132
- Fujita, Y. 2004, *Publications of the Astronomical Society of Japan*, **56**, 29
- Galárraga-Espinosa, D., Aghanim, N., Langer, M., Gouin, C., & Malavasi, N. 2020, *Astronomy & Astrophysics*, **641**, A173
- Geach, J. E. 2012, *Monthly Notices of the Royal Astronomical Society*, **419**, 2633
- Genzel, R., Price, S. H., Übler, H., et al. 2020, *The Astrophysical Journal*, **902**, 98
- Genzel, R., Schreiber, N. M. F., Übler, H., et al. 2017, *Nature*, **543**, 397
- Gialalisco, M., Macchetto, F. D., Madau, P., & Sparks, W. B. 1995, *Astrophysical Journal Letters*, **441**, L13
- Gilbank, D. G., Baldry, I. K., Balogh, M. L., Glazebrook, K., & Bower, R. G. 2010, *Monthly Notices of the Royal Astronomical Society*, **no-no**
- Gilbank, D. G., Baldry, I. K., Balogh, M. L., Glazebrook, K., & Bower, R. G. 2011, *Monthly Notices of the Royal Astronomical Society*, **412**, 2111
- Gilmore, G., Wilkinson, M. I., Wyse, R. F. G., et al. 2007, *The Astrophysical Journal*, **663**, 948

- Gnerucci, A., Marconi, A., Cresci, G., et al. 2011, *Astronomy & Astrophysics*, **528**, [A88](#)
- Gordon, K. J. 1969, *Quarterly Journal of the Royal Astronomical Society*, **10**, 293
- Graham, A. W., Driver, S. P., Petrosian, V., et al. 2005, *The Astronomical Journal*, **130**, [1535](#)
- Graham, M. T., Cappellari, M., Li, H., et al. 2018, *Monthly Notices of the Royal Astronomical Society*, **477**, [4711](#)
- Green, A. W., Croom, S. M., Scott, N., et al. 2018, *Monthly Notices of the Royal Astronomical Society*, **475**, [716](#)
- Gruppioni, C., Béthermin, M., Loiacono, F., et al. 2020, *Astronomy & Astrophysics*, **643**, [A8](#)
- Guérou, A., Emsellem, E., Krajnović, D., et al. 2016, *Astronomy & Astrophysics*, **591**, [A143](#)
- Gunn, J. E. & Gott, J. Richard, I. 1972, *Astrophysical Journal*, **176**, [1](#)
- Gunn, J. E. & Knapp, G. R. 1993, in *Astronomical Society of the Pacific Conference Series*, Vol. 43, *Sky Surveys. Protostars to Protogalaxies*, ed. B. T. Soifer, 267
- Guo, Q., White, S., Li, C., & Boylan-Kolchin, M. 2010, *Monthly Notices of the Royal Astronomical Society*, **404**, [1111](#)
- Guérou, A., Krajnović, D., Epinat, B., et al. 2017, *Astronomy & Astrophysics*, **608**, [A5](#)
- Haider, M., Steinhäuser, D., Vogelsberger, M., et al. 2016, *Monthly Notices of the Royal Astronomical Society*, **457**, [3024](#)
- Harris, C. R., Millman, K. J., van der Walt, S. J., et al. 2020, *Nature*, **585**, [357](#)
- Harrison, C. M., Johnson, H. L., Swinbank, A. M., et al. 2017, *Monthly Notices of the Royal Astronomical Society*, **467**, [1965](#)
- Hemmati, S., Capak, P., Pourrahmani, M., et al. 2019, *The Astrophysical Journal*, **881**, [L14](#)
- Henault, F., Bacon, R., Bonneville, C., et al. 2003, in *Society of Photo-Optical Instrumentation Engineers (SPIE) Conference Series*, Vol. 4841, *Instrument Design and Performance for Optical/Infrared Ground-based Telescopes*, ed. M. Iye & A. F. M. Moorwood, 1096–1107
- Herenz, E. C., Urrutia, T., Wisotzki, L., et al. 2017, *Astronomy & Astrophysics*, **606**, [A12](#)
- Hernquist, L. 1990, *The Astrophysical Journal*, **356**, [359](#)
- Hinton, S., Davis, T. M., Lidman, C., Glazebrook, K., & Lewis, G. 2016, *Astronomy and Computing*, **15**, [61](#)
- Hopkins, A. M. 2004, *The Astrophysical Journal*, **615**, [209](#)
- Hopkins, A. M. & Beacom, J. F. 2006, *The Astrophysical Journal*, **651**, [142](#)
- Hopkins, P. F., Kereš, D., Oñorbe, J., et al. 2014, *Monthly Notices of the Royal Astronomical Society*, **445**, [581](#)
- Hubble, E. 1929, *Proceedings of the National Academy of Science*, **15**, [168](#)
- Hubble, E. P. 1925, *Popular Astronomy*, **33**, 252
- Hubble, E. P. 1926, *Astrophysical Journal*, **64**, [321](#)
- Hubble, E. P. 1930, *The Astrophysical Journal*, **71**, [231](#)
- Hung, D., Lemaux, B. C., Gal, R. R., et al. 2020, *Monthly Notices of the Royal Astronomical Society*, **491**, [5524](#)
- Hung, D., Lemaux, B. C., Gal, R. R., et al. 2021, *Monthly Notices of the Royal Astronomical Society*, **502**, [3942](#)
- Husser, T.-O., Kamann, S., Dreizler, S., et al. 2016, *Astronomy & Astrophysics*, **588**, [A148](#)
- Ilbert, O., Salvato, M., Le Floch, E., et al. 2010, *The Astrophysical Journal*, **709**, [644](#)
- Illingworth, G. D., Magee, D., Oesch, P. A., et al. 2013, *The Astrophysical Journal Supplement*, **209**, [6](#)
- Inami, H., Bacon, R., Brinchmann, J., et al. 2017, *Astronomy & Astrophysics*, **608**, [A2](#)
- Iovino, A., Petropoulou, V., Scodreggio, M., et al. 2016, *Astronomy & Astrophysics*, **592**, [A78](#)
- Jafariyazani, M., Masters, D., Teplitz, H., & Faisst, A. 2022, in *American Astronomical Society Meeting Abstracts*, Vol. 54, *American Astronomical Society Meeting Abstracts*, 412.02
- Jedrzejewski, R. I. 1987, *Monthly Notices of the Royal Astronomical Society*, **226**, [747](#)
- Jin, Y., Chen, Y., Shi, Y., et al. 2016, *Monthly Notices of the Royal Astronomical Society*, **463**, [913](#)
- Johnson, B. D., Leja, J., Conroy, C., & Speagle, J. S. 2021, *The Astrophysical Journal Supplement Series*, **254**, [22](#)

- Joy, A. H. 1939, *Astrophysical Journal*, **89**, 356
- Junais, Boissier, S., Epinat, B., et al. 2020, *Astronomy & Astrophysics*, **637**, A21
- Kamann, S., Husser, T. O., Brinchmann, J., et al. 2016, *Astronomy & Astrophysics*, **588**, A149
- Kamann, S., Husser, T. O., Dreizler, S., et al. 2018, *Monthly Notices of the Royal Astronomical Society*, **473**, 5591
- Karman, W., Caputi, K. I., Caminha, G. B., et al. 2017, *Astronomy & Astrophysics*, **599**, A28
- Karman, W., Caputi, K. I., Grillo, C., et al. 2015, *Astronomy & Astrophysics*, **574**, A11
- Katz, N., Hernquist, L., & Weinberg, D. H. 1992, *Astrophysical Journal Letters*, **399**, L109
- Kauffmann, G., White, S. D. M., & Guiderdoni, B. 1993, *Monthly Notices of the Royal Astronomical Society*, **264**, 201
- Kennicutt, Robert C., J. 1998, *Annual Review of Astronomy and Astrophysics*, **36**, 189
- Kennicutt, Jr., R. C. 1992, *The Astrophysical Journal*, **388**, 310
- Kennicutt, Jr., R. C. 1998, *The Astrophysical Journal*, **498**, 541
- Kerr, F. J. & Hindman, J. V. 1953, *Astronomical Journal*, **58**, 218
- Knobel, C., Lilly, S. J., Iovino, A., et al. 2012, *The Astrophysical Journal*, **753**, 121
- Knobel, C., Lilly, S. J., Iovino, A., et al. 2009, *The Astrophysical Journal*, **697**, 1842
- Koekemoer, A. M., Fruchter, A. S., Hook, R. N., & Hack, W. 2003, in *HST Calibration Workshop : Hubble after the Installation of the ACS and the NICMOS Cooling System*, 337
- Kohonen, T. 1982, *Biological Cybernetics*, **43**, 59
- Kormendy, J. 1985, *Astrophysical Journal*, **295**, 73
- Kormendy, J. & Bender, R. 1996, *Astrophysical Journal Letters*, **464**, L119
- Kormendy, J. & Bender, R. 2012, *The Astrophysical Journal Supplement*, **198**, 2
- Kormendy, J., Fisher, D. B., Cornell, M. E., & Bender, R. 2009, *The Astrophysical Journal Supplement Series*, **182**, 216
- Korsaga, M., Amram, P., Carignan, C., & Epinat, B. 2019a, *Monthly Notices of the Royal Astronomical Society*, **482**, 154
- Korsaga, M., Carignan, C., Amram, P., Epinat, B., & Jarrett, T. H. 2018, *Monthly Notices of the Royal Astronomical Society*, **478**, 50
- Korsaga, M., Epinat, B., Amram, P., et al. 2019b, *Monthly Notices of the Royal Astronomical Society*, **490**, 2977
- Krabbe, A., Weitzel, L., Kroker, H., et al. 1995, in *Society of Photo-Optical Instrumentation Engineers (SPIE) Conference Series, Vol. 2475, Infrared Detectors and Instrumentation for Astronomy*, ed. A. M. Fowler, 172–183
- Krajnović, D., Emsellem, E., den Brok, M., et al. 2018, *Monthly Notices of the Royal Astronomical Society*, **477**, 5327
- Krajnović, D., Weilbacher, P. M., Urrutia, T., et al. 2015, *Monthly Notices of the Royal Astronomical Society*, **452**, 2
- Kravtsov, A. V., Vikhlinin, A. A., & Meshcheryakov, A. V. 2018, *Astronomy Letters*, **44**, 8
- Kriek, M., van Dokkum, P. G., Labbé, I., et al. 2009, *The Astrophysical Journal*, **700**, 221
- Krolewski, A., Ho, S., Chen, Y.-C., et al. 2019, *The Astrophysical Journal*, **876**, 52
- Kroupa, P. 2002, *Science*, **295**, 82
- Kuchner, U., Ziegler, B., Verdugo, M., Bamford, S., & Häußler, B. 2017, *Astronomy & Astrophysics*, **604**, A54
- Kusakabe, H., Blaizot, J., Garel, T., et al. 2020, *Astronomy & Astrophysics*, **638**, A12
- Kuzmin, G. 1956, *Astron. zh*, **33**, 27
- La Penna, P., Aller Carpentier, E., Argomedo, J., et al. 2016, in *Society of Photo-Optical Instrumentation Engineers (SPIE) Conference Series, Vol. 9909, Adaptive Optics Systems V*, ed. E. Marchetti, L. M. Close, & J.-P. Véran, 99092Z
- Lachize-Rey, M. 1980, *Premier Colloque du Comité Français du ST^a Applications de la photométrie bidimensionnelle à l'Astrophysique*
- Lagattuta, D. J., Richard, J., Clément, B., et al. 2017, *Monthly Notices of the Royal Astronomical Society*, **469**, 3946
- Laigle, C., McCracken, H. J., Ilbert, O., et al. 2016, *The Astrophysical Journal Supplement Series*, **224**, 24

- Lang, P., Förster Schreiber, N. M., Genzel, R., et al. 2017, *The Astrophysical Journal*, **840**, 92
- Lang, P., Wuyts, S., Somerville, R. S., et al. 2014, *The Astrophysical Journal*, **788**, 11
- Larkin, J., Barczys, M., Krabbe, A., et al. 2006, in *Society of Photo-Optical Instrumentation Engineers (SPIE) Conference Series*, Vol. 6269, Society of Photo-Optical Instrumentation Engineers (SPIE) Conference Series, ed. I. S. McLean & M. Iye, 62691A
- Larkin, J. E., Moore, A. M., Barton, E. J., et al. 2010, in *Society of Photo-Optical Instrumentation Engineers (SPIE) Conference Series*, Vol. 7735, *Ground-based and Airborne Instrumentation for Astronomy III*, ed. I. S. McLean, S. K. Ramsay, & H. Takami, 773529
- Larkin, J. E., Quirrenbach, A., & Graham, J. R. 2000, in *Astronomical Society of the Pacific Conference Series*, Vol. 195, *Imaging the Universe in Three Dimensions*, ed. W. van Breugel & J. Bland-Hawthorn, 508
- Larson, R. B. 1974, *Monthly Notices of the Royal Astronomical Society*, **169**, 229
- Laurikainen, E., Salo, H., Buta, R., Knapen, J. H., & Comerón, S. 2010, *Monthly Notices of the Royal Astronomical Society*
- Lavalley, C. 2000, PhD thesis, Université Joseph Fourier Grenoble, France
- Law, D. R., Belfiore, F., Bershad, M. A., et al. 2022, *The Astrophysical Journal*, **928**, 58
- Law, D. R., Steidel, C. C., Chen, Y., et al. 2018, *The Astrophysical Journal*, **866**, 119
- Law, D. R., Steidel, C. C., Erb, D. K., et al. 2009, *The Astrophysical Journal*, **697**, 2057
- Law, D. R., Steidel, C. C., Shapley, A. E., et al. 2012, *The Astrophysical Journal*, **745**, 85
- Le Fèvre, O., Tasca, L. A. M., Cassata, P., et al. 2015, *Astronomy & Astrophysics*, **576**, A79
- Le Fèvre, O., Vettolani, G. P., Maccagni, D., et al. 1998, in *Society of Photo-Optical Instrumentation Engineers (SPIE) Conference Series*, Vol. 3355, *Optical Astronomical Instrumentation*, ed. S. D'Odorico, 8–19
- Leavitt, H. S. 1908, *Annals of Harvard College Observatory*, 60, 87
- Leavitt, H. S. & Pickering, E. C. 1912, *Harvard College Observatory Circular*, 173, 1
- Leclercq, F., Bacon, R., Wisotzki, L., et al. 2017, *Astronomy & Astrophysics*, **608**, A8
- Leclercq, F., Verhamme, A., Epinat, B., et al. 2022, *Astronomy & Astrophysics*, **663**, A11
- Ledoux, C., Theodore, B., Petitjean, P., et al. 1998, *Astronomy & Astrophysics*, 339, L77
- Leja, J., Carnall, A. C., Johnson, B. D., Conroy, C., & Speagle, J. S. 2019, *The Astrophysical Journal*, **876**, 3
- Lelli, F., McGaugh, S. S., & Schombert, J. M. 2016, *The Astronomical Journal*, **152**, 157
- Lemaître, G. 1927, *Annales de la Société Scientifique de Bruxelles*, 47, 49
- Lemaître, G. 1931, *Monthly Notices of the Royal Astronomical Society*, **91**, 483
- Lemaux, B. C., Cucciati, O., Le Fèvre, O., et al. 2022, *Astronomy & Astrophysics*, **662**, A33
- Lemaux, B. C., Tomczak, A. R., Lubin, L. M., et al. 2017, *Monthly Notices of the Royal Astronomical Society*, **472**, 419
- Lequeux, J., Peimbert, M., Rayo, J. F., Serrano, A., & Torres-Peimbert, S. 1979, *Astronomy and Astrophysics*, 80, 155
- Li, P., Lelli, F., McGaugh, S., & Schombert, J. 2020, *The Astrophysical Journal Supplement Series*, **247**, 31
- Lilly, S. J., Carollo, C. M., Pipino, A., Renzini, A., & Peng, Y. 2013, *The Astrophysical Journal*, **772**, 119
- Lilly, S. J., Fevre, O. L., Renzini, A., et al. 2007, *The Astrophysical Journal Supplement Series*, **172**, 70
- Lilly, S. J., Le Fèvre, O., Hammer, F., & Crampton, D. 1996, *Astrophysical Journal Letters*, **460**, L1
- Livio, M. 2011, *Nature*, **479**, 171
- Longair, M. 2019, in *Under One Sky: The IAU Centenary Symposium*, ed. C. Sterken, J. Hearnshaw, & D. Valls-Gabaud, Vol. 349, 3–24
- Longair, M. & Giacconi, R. 2007, *Physics Today*, **60**, 64
- Longair, M. S. 2008, *Galaxy Formation* (Berlin, Heidelberg: Springer Berlin Heidelberg)
- Longhetti, M., Saracco, P., Severgnini, P., et al. 2007, *Monthly Notices of the Royal Astronomical Society*, **374**, 614
- Longobardi, A., Boselli, A., Fossati, M., et al. 2020, *Astronomy & Astrophysics*, **644**, A161
- Lopez-Coba, C., Sanchez, S. F., Lin, L., et al. 2022, arXiv e-prints, arXiv:2207.07906

- López-Sanjuan, C., Le Fèvre, O., Tasca, L. A. M., et al. 2013a, *Astronomy & Astrophysics*, **553**, [A78](#)
- López-Sanjuan, C., Le Fèvre, O., Tasca, L. A. M., et al. 2013b, *Astronomy & Astrophysics*, **553**, [A78](#)
- Lotz, J. M., Koekemoer, A., Coe, D., et al. 2017, *The Astrophysical Journal*, **837**, [97](#)
- Luber, N., Müller, A., van Gorkom, J. H., et al. 2022, *The Astrophysical Journal*, **927**, [39](#)
- Lubin, L. M., Gal, R. R., Lemaux, B. C., Kocevski, D. D., & Squires, G. K. 2009, *The Astronomical Journal*, **137**, [4867](#)
- Lundmark, K. 1926, *Arkiv for Matematik, Astronomi och Fysik*, **19**, 1
- Lusso, E., Fumagalli, M., Fossati, M., et al. 2019, *Monthly Notices of the Royal Astronomical Society*, **485**, [L62](#)
- MacLaren, I., Ellis, R. S., & Couch, W. J. 1988, *Monthly Notices of the Royal Astronomical Society*, **230**, [249](#)
- Madau, P. & Dickinson, M. 2014, *Annual Review of Astronomy and Astrophysics*, **52**, [415](#)
- Madau, P., Ferguson, H. C., Dickinson, M. E., et al. 1996, *Monthly Notices of the Royal Astronomical Society*, **283**, [1388](#)
- Madau, P., Shen, S., & Governato, F. 2014, *The Astrophysical Journal*, **789**, [L17](#)
- Mahler, G., Richard, J., Clément, B., et al. 2018, *Monthly Notices of the Royal Astronomical Society*, **473**, [663](#)
- Maiolino, R., Nagao, T., Grazian, A., et al. 2008, *Astronomy & Astrophysics*, **488**, [463](#)
- Maltby, D. T., Aragón-Salamanca, A., Gray, M. E., et al. 2010, *Monthly Notices of the Royal Astronomical Society*, **402**, [282](#)
- Mancera Piña, P. E., Fraternali, F., Oosterloo, T., et al. 2022, *Monthly Notices of the Royal Astronomical Society*, **512**, [3230](#)
- Mancini, C., Förster Schreiber, N. M., Renzini, A., et al. 2011, *The Astrophysical Journal*, **743**, [86](#)
- Mannucci, F., Cresci, G., Maiolino, R., et al. 2009, *Monthly Notices of the Royal Astronomical Society*, **398**, [1915](#)
- Maraston, C. 2005, *Monthly Notices of the Royal Astronomical Society*, **362**, [799](#)
- Marinoni, C., Davis, M., Newman, J. A., & Coil, A. L. 2002, *The Astrophysical Journal*, **580**, [122](#)
- Markarian, B. E. 1963, *Communications of the Byurakan Astrophysical Observatory*, **34**, 3
- Markwardt, C. B. 2009, in *Astronomical Society of the Pacific Conference Series*, Vol. 411, *Astronomical Data Analysis Software and Systems XVIII*, ed. D. A. Bohlender, D. Durand, & P. Dowler, 251
- Martinsson, T. P. K., Verheijen, M. A. W., Westfall, K. B., et al. 2013, *Astronomy & Astrophysics*, **557**, [A131](#)
- Maseda, M. V., Bacon, R., Lam, D., et al. 2020, *Monthly Notices of the Royal Astronomical Society*, **493**, [5120](#)
- Masters, D., Capak, P., Stern, D., et al. 2015, *The Astrophysical Journal*, **813**, [53](#)
- Matharu, J., Muzzin, A., Brammer, G. B., et al. 2019, *Monthly Notices of the Royal Astronomical Society*, **484**, [595](#)
- Matthee, J., Sobral, D., Gronke, M., et al. 2020, *Monthly Notices of the Royal Astronomical Society*, **492**, [1778](#)
- Mcculloch, W. & Pitts, W. 1943, *Bulletin of Mathematical Biophysics*, **5**, 127
- McNab, K., Balogh, M. L., van der Burg, R. F. J., et al. 2021, *Monthly Notices of the Royal Astronomical Society*, **508**, [157](#)
- McPartland, C., Ebeling, H., Roediger, E., & Blumenthal, K. 2016, *Monthly Notices of the Royal Astronomical Society*, **455**, [2994](#)
- Mendes de Oliveira, C., Plana, H., Amram, P., Bolte, M., & Boulesteix, J. 1998, *The Astrophysical Journal*, **507**, [691](#)
- Mercer, E. P., Clemens, D. P., Rathborne, J. M., et al. 2007, *The Astrophysical Journal*, **656**, [242](#)
- Mercier, W., Epinat, B., Contini, T., et al. 2022, *arXiv:2204.08724 [astro-ph]*, *arXiv: 2204.08724*
- Milgrom, M. 1983, *Astrophysical Journal*, **270**, [365](#)
- Miller, A. S. & Coe, M. J. 1996, *Monthly Notices of the Royal Astronomical Society*, **279**, [293](#)
- Miller, B. W., Bureau, M., Verolme, E., et al. 2000, in *Astronomical Society of the Pacific Conference Series*, Vol. 195, *Imaging the Universe in Three Dimensions*, ed. W. van Breugel & J. Bland-Hawthorn, 158

- Monnet, G. 2002, *The Messenger*, 108, 2
- Monreal-Ibero, A. & Walsh, J. R. 2020, *Astronomy & Astrophysics*, 634, A47
- Moore, B. 1994, *Nature*, 370, 629
- Moore, B., Ghigna, S., Governato, F., et al. 1999, *The Astrophysical Journal*, 524, L19
- More, A., Cabanac, R., More, S., et al. 2012, *The Astrophysical Journal*, 749, 38
- Mortonson, M. J., Hu, W., & Huterer, D. 2011, *Physical Review D*, 83, 023015
- Mosenkov, A. V., Sotnikova, N. Y., Reshetnikov, V. P., Bizyaev, D. V., & Kautsch, S. J. 2015, *Monthly Notices of the Royal Astronomical Society*, 451, 2376
- Mowla, L. A., van Dokkum, P., Brammer, G. B., et al. 2019, *The Astrophysical Journal*, 880, 57
- Muzzin, A., Marchesini, D., Stefanon, M., et al. 2013, *The Astrophysical Journal*, 777, 18
- Muzzin, A., Wilson, G., Yee, H. K. C., et al. 2012, *The Astrophysical Journal*, 746, 188
- Muzzin, A., Wilson, G., Yee, H. K. C., et al. 2009, *The Astrophysical Journal*, 698, 1934
- Naim, A., Ratnatunga, K. U., & Griffiths, R. E. 1997, *The Astrophysical Journal Supplement Series*, 111, 357
- Navarro, J. F., Frenk, C. S., & White, S. D. M. 1996, *The Astrophysical Journal*, 462, 563
- Navarro, J. F., Frenk, C. S., & White, S. D. M. 1997, *The Astrophysical Journal*, 490, 493
- Neichel, B., Hammer, F., Puech, M., et al. 2008, *Astronomy & Astrophysics*, 484, 159
- Newman, S. F., Buschkamp, P., Genzel, R., et al. 2014, *The Astrophysical Journal*, 781, 21
- Newman, S. F., Genzel, R., Förster-Schreiber, N. M., et al. 2012, *The Astrophysical Journal*, 761, 43
- Newman, S. F., Genzel, R., Förster-Schreiber, N. M., et al. 2013, *The Astrophysical Journal*, 767, 104
- Nipoti, C. & Binney, J. 2014, *Monthly Notices of the Royal Astronomical Society*, 446, 1820
- Noble, A. G., Webb, T. M. A., Muzzin, A., et al. 2013, *The Astrophysical Journal*, 768, 118
- Noeske, K. G., Weiner, B. J., Faber, S. M., et al. 2007, *The Astrophysical Journal*, 660, L43
- Oke, J. B. 1974, *Astrophysical Journal Supplement*, 27, 21
- Old, L. J., Balogh, M. L., van der Burg, R. F. J., et al. 2020a, *Monthly Notices of the Royal Astronomical Society*, 500, 355
- Old, L. J., Balogh, M. L., van der Burg, R. F. J., et al. 2020b, *Monthly Notices of the Royal Astronomical Society*, 493, 5987
- Ostriker, J. P. & Peebles, P. J. E. 1973, *Astrophysical Journal*, 186, 467
- Ostriker, J. P., Peebles, P. J. E., & Yahil, A. 1974, *Astrophysical Journal*, 193, L1
- Padmanabhan, H. & Kulkarni, G. 2017, *Monthly Notices of the Royal Astronomical Society*, 470, 340
- Pasquini, L., Avila, G., Allaert, E., et al. 2000, in *Society of Photo-Optical Instrumentation Engineers (SPIE) Conference Series*, Vol. 4008, *Optical and IR Telescope Instrumentation and Detectors*, ed. M. Iye & A. F. Moorwood, 129–140
- Pasquini, L., Avila, G., Blecha, A., et al. 2002, *The Messenger*, 110, 1
- Patrício, V., Richard, J., Verhamme, A., et al. 2016, *Monthly Notices of the Royal Astronomical Society*, 456, 4191
- Pedregosa, F., Varoquaux, G., Gramfort, A., et al. 2011, *Journal of Machine Learning Research*, 12, 2825
- Pelliccia, D., Lemaux, B. C., Tomczak, A. R., et al. 2019, *Monthly Notices of the Royal Astronomical Society*, 482, 3514
- Peng, C. Y., Ho, L. C., Impey, C. D., & Rix, H.-W. 2002, *The Astronomical Journal*, 124, 266
- Peng, Y.-j., Lilly, S. J., Kovač, K., et al. 2010, *The Astrophysical Journal*, 721, 193
- Perlmutter, S., Aldering, G., Goldhaber, G., et al. 1999, *The Astrophysical Journal*, 517, 565
- Pettini, M., Smith, L. J., Hunstead, R. W., & King, D. L. 1994, *Astrophysical Journal*, 426, 79
- Planck Collaboration, Abergel, A., Ade, P. A. R., et al. 2014, *Astronomy & Astrophysics*, 571, A11
- Planck Collaboration, Aghanim, N., Akrami, Y., et al. 2020, *Astronomy & Astrophysics*, 641, A6
- Planck Collaboration, Aghanim, N., Akrami, Y., et al. 2021, *Astronomy & Astrophysics*, 652, C4

- Poggianti, B. M., Moretti, A., Gullieuszik, M., et al. 2017, *The Astrophysical Journal*, **844**, 48
- Pohlen, M. & Trujillo, I. 2006, *Astronomy & Astrophysics*, **454**, 759
- Price, S. H., Shimizu, T. T., Genzel, R., et al. 2021, *The Astrophysical Journal*, **922**, 143
- Puech, M., Flores, H., Hammer, F., & Lehnert, M. D. 2006a, *Astronomy & Astrophysics*, **455**, 131
- Puech, M., Flores, H., Hammer, F., et al. 2008a, *Astronomy & Astrophysics*, **484**, 173
- Puech, M., Flores, H., Hammer, F., et al. 2008b, *Astronomy & Astrophysics*, **484**, 173
- Puech, M., Hammer, F., Flores, H., et al. 2010, *Astronomy & Astrophysics*, **510**, A68
- Puech, M., Hammer, F., Flores, H., Östlin, G., & Marquart, T. 2006b, *Astronomy & Astrophysics*, **455**, 119
- Puech, M., Hammer, F., Hopkins, P. F., et al. 2012, *The Astrophysical Journal*, **753**, 128
- Puech, M., Hammer, F., Lehnert, M. D., & Flores, H. 2007, *Astronomy & Astrophysics*, **466**, 83
- Puech, M., Hammer, F., Rodrigues, M., et al. 2014, *Monthly Notices of the Royal Astronomical Society*, **443**, L49
- Quilley, L. & de Lapparent, V. 2022, arXiv e-prints, arXiv:2206.04707
- Rafelski, M., Teplitz, H. I., Gardner, J. P., et al. 2015, *The Astronomical Journal*, **150**, 31
- Raimond, E. & Volders, L. M. J. S. 1957, *Bulletin of the Astronomical Institutes of the Netherlands*, 14, 19
- Read, J. I. & Gilmore, G. 2005, *Monthly Notices of the Royal Astronomical Society*, **356**, 107
- Regis, M., Taoso, M., Vaz, D., et al. 2021, *Physics Letters B*, **814**, 136075
- Reynolds, J. H. 1913, *Monthly Notices of the Royal Astronomical Society*, **74**, 132
- Richard, J., Bacon, R., Blaizot, J., et al. 2019, arXiv e-prints, arXiv:1906.01657
- Richard, J., Claeysens, A., Lagattuta, D., et al. 2021, *Astronomy & Astrophysics*, **646**, A83
- Richard, J., Patricio, V., Martinez, J., et al. 2015, *Monthly Notices of the Royal Astronomical Society*, **446**, L16
- Rieke, G. H., Wright, G. S., Böker, T., et al. 2015, *Publications of the Astronomical Society of the Pacific*, **127**, 584
- Riess, A. G. 1998, in *American Astronomical Society Meeting Abstracts*, Vol. 192, *American Astronomical Society Meeting Abstracts #192*, 17.06
- Roberts, M. S., Hogg, D. E., Bregman, J. N., Forman, W. R., & Jones, C. 1991, *Astrophysical Journal Supplement*, **75**, 751
- Roberts, M. S. & Rots, A. H. 1973, *Astronomy & Astrophysics*, 26, 483
- Rocca-Volmerange, B., Adam, G., Ferruit, P., & Moy, E. 2000, in *Astronomical Society of the Pacific Conference Series*, Vol. 195, *Imaging the Universe in Three Dimensions*, ed. W. van Breugel & J. Bland-Hawthorn, 341
- Rodrigues, M., Hammer, F., Flores, H., et al. 2008, *Astronomy & Astrophysics*, **492**, 371
- Rogstad, D. H. & Shostak, G. S. 1972, *Astrophysical Journal*, **176**, 315
- Romano-Díaz, E., Shlosman, I., Hoffman, Y., & Heller, C. 2008, *The Astrophysical Journal*, **685**, L105
- Rood, H. J., Page, T. L., Kintner, E. C., & King, I. R. 1972, *The Astrophysical Journal*, **175**, 627
- Rosenblatt, F. 1957, *The Perceptron, a Perceiving and Recognizing Automaton Project Para*, Report: Cornell Aeronautical Laboratory (Cornell Aeronautical Laboratory)
- Rubin, V. C., Ford, W. K., J., Strom, K. M., Strom, S. E., & Romanishin, W. 1978a, *Astrophysical Journal*, **224**, 782
- Rubin, V. C., Ford, W. K., J., & Thonnard, N. 1978b, *Astrophysical Journal*, **225**, L107
- Rubin, V. C., Ford, W. K., J., & Thonnard, N. 1980, *Astrophysical Journal*, **238**, 471
- Rutten, R. 2000, *The Newsletter of the Isaac Newton Group of Telescopes*, 2, 24
- Salim, S. & Narayanan, D. 2020, *Annual Review of Astronomy and Astrophysics*, **58**, 529
- Salpeter, E. E. 1955, *The Astrophysical Journal*, **121**, 161
- Salucci, P. 2001, *Monthly Notices of the Royal Astronomical Society*, **320**, L1
- Sánchez, S. F., García-Benito, R., Zibetti, S., et al. 2016, *Astronomy & Astrophysics*, **594**, A36

- Sandage, A. & Binggeli, B. 1984, *Astronomical Journal*, **89**, 919
- Sanders, R. H. 2010, *The Dark Matter Problem: A Historical Perspective* (Cambridge University Press)
- Sarron, F., Adami, C., Durret, F., & Laigle, C. 2019, *Astronomy & Astrophysics*, **632**, A49
- Sarron, F. & Conselice, C. J. 2021, *Monthly Notices of the Royal Astronomical Society*, **506**, 2136
- Schaye, J., Crain, R. A., Bower, R. G., et al. 2015, *Monthly Notices of the Royal Astronomical Society*, **446**, 521
- Schechter, P. 1976, *Astrophysical Journal*, **203**, 297
- Schmidt, M. 1959, *The Astrophysical Journal*, **129**, 243
- Schroetter, I., Bouché, N., Wendt, M., et al. 2016, *The Astrophysical Journal*, **833**, 39
- Schroetter, I., Bouché, N. F., Zabl, J., et al. 2019, *Monthly Notices of the Royal Astronomical Society*, **490**, 4368
- Schroetter, I., Bouché, N. F., Zabl, J., et al. 2021, *Monthly Notices of the Royal Astronomical Society*, **506**, 1355
- Scott, N., van de Sande, J., Croom, S. M., et al. 2018, *Monthly Notices of the Royal Astronomical Society*, **481**, 2299
- Scoville, N., Aussel, H., Benson, A., et al. 2007, *The Astrophysical Journal Supplement Series*, **172**, 150
- Sérsic, J. L. 1963, *Boletín de la Asociación Argentina de Astronomía La Plata Argentina*, **6**, 41
- Shapiro, K. L., Genzel, R., Förster Schreiber, N. M., et al. 2008, *The Astrophysical Journal*, **682**, 231
- Shapiro, K. L., Genzel, R., Quataert, E., et al. 2009, *The Astrophysical Journal*, **701**, 955
- Shapley, H. & Ames, A. 1926, *Harvard College Observatory Circular*, **294**, 1
- Shapley, H. & Curtis, H. D. 1921, *Bulletin of the National Research Council*, **2**, 171
- Sharma, G., Salucci, P., Harrison, C. M., van de Ven, G., & Lapi, A. 2021, *Monthly Notices of the Royal Astronomical Society*, **503**, 1753
- Sharples, R., Bender, R., Bennett, R., et al. 2005, *The Messenger*, **122**, 2
- Sharples, R. M., Bender, R., Lehnert, M. D., et al. 2004, in *Society of Photo-Optical Instrumentation Engineers (SPIE) Conference Series*, Vol. 5492, *Ground-based Instrumentation for Astronomy*, ed. A. F. M. Moorwood & M. Iye, 1179–1186
- Sheen, Y.-K., Smith, R., Jaffé, Y., et al. 2017, *The Astrophysical Journal Letters*, **840**, L7
- Silk, J. & Rees, M. J. 1998, *Astronomy and Astrophysics*, **331**, L1
- Simard, L. & Pritchett, C. J. 1998, *The Astrophysical Journal*, **505**, 96
- Skillman, E. D., Kennicutt, R. C., & Hodge, P. W. 1989, *Astrophysical Journal*, **347**, 875
- Skrutskie, M. F., Cutri, R. M., Stiening, R., et al. 2006, *The Astronomical Journal*, **131**, 1163
- Slipher, V. M. 1913, *Lowell Observatory Bulletin*, **2**, 56
- Slipher, V. M. 1915, *Popular Astronomy*, **23**, 21
- Smith, R. J., Lucey, J. R., Hammer, D., et al. 2010, *Monthly Notices of the Royal Astronomical Society*, **408**, 1417
- Smith, R. W. 2009, *Journal for the History of Astronomy*, **40**, 71
- Snyder, G. F., Lotz, J. M., Rodriguez-Gomez, V., et al. 2017, *Monthly Notices of the Royal Astronomical Society*, **468**, 207
- Soto, K. T., Lilly, S. J., Bacon, R., Richard, J., & Conseil, S. 2016, *Monthly Notices of the Royal Astronomical Society*, **458**, 3210
- Soucail, G. 1987, *The Messenger*, **48**, 43
- Soucail, G., Fort, B., Mellier, Y., & Picat, J. P. 1987, *Astronomy and Astrophysics*, **172**, L14
- Speagle, J. S. & Eisenstein, D. J. 2017, *Monthly Notices of the Royal Astronomical Society*, **469**, 1205
- Speagle, J. S., Steinhardt, C. L., Capak, P. L., & Silverman, J. D. 2014, *The Astrophysical Journal Supplement Series*, **214**, 15
- Spitzer, Jr., L. 1942, *The Astrophysical Journal*, **95**, 329
- Springel, V., Pakmor, R., Pillepich, A., et al. 2018, *Monthly Notices of the Royal Astronomical Society*, **475**, 676
- Springel, V., White, S. D. M., Jenkins, A., et al. 2005, *Nature*, **435**, 629

- Steidel, C. C. & Hamilton, D. 1993, *Astronomical Journal*, **105**, 2017
- Stone, C. J., Arora, N., Courteau, S., & Cuillandre, J.-C. 2021, *Monthly Notices of the Royal Astronomical Society*, **508**, 1870
- Stott, J. P., Swinbank, A. M., Johnson, H. L., et al. 2016, *Monthly Notices of the Royal Astronomical Society*, **457**, 1888
- Strigari, L. E. & Wechsler, R. H. 2012, *The Astrophysical Journal*, **749**, 75
- Ströbele, S., La Penna, P., Arsenault, R., et al. 2012, in *Society of Photo-Optical Instrumentation Engineers (SPIE) Conference Series*, Vol. 8447, *Adaptive Optics Systems III*, ed. B. L. Ellerbroek, E. Marchetti, & J.-P. Véran, 844737
- Suess, K. A., Kriek, M., Price, S. H., & Barro, G. 2019, *The Astrophysical Journal*, **877**, 103
- Swedenborg, E. 1734, *Principia rerum naturalium sive Novorum tentaminum phaenomena mundi elementaris philosophice explicandi...*, *Principia rerum naturalium sive Novorum tentaminum phaenomena mundi elementaris philosophice explicandi No. v. 3* (sumptibus Friderici Hekelii)
- Swinbank, A. M., Harrison, C. M., Trayford, J., et al. 2017, *Monthly Notices of the Royal Astronomical Society*, **467**, 3140
- Swinbank, A. M., Vernet, J. D. R., Smail, I., et al. 2015, *Monthly Notices of the Royal Astronomical Society*, **449**, 1298
- Tacchella, S., Carollo, C. M., Schreiber, N. M. F., et al. 2018, *The Astrophysical Journal*, **859**, 56
- Tacchella, S., Lang, P., Carollo, C. M., et al. 2015, *The Astrophysical Journal*, **802**, 101
- Tacconi, L. J., Genzel, R., & Sternberg, A. 2020, *Annual Review of Astronomy and Astrophysics*, **58**, 157
- Tasca, L. A. M., Le Fèvre, O., López-Sanjuan, C., et al. 2014, *Astronomy & Astrophysics*, **565**, A10
- Tecza, M., Thatte, N., Clarke, F., & Freeman, D. 2009, in *Astrophysics and Space Science Proceedings*, Vol. 9, *Science with the VLT in the ELT Era*, 267
- Thatte, N., Tecza, M., Clarke, F., et al. 2010, in *Society of Photo-Optical Instrumentation Engineers (SPIE) Conference Series*, Vol. 7735, *Ground-based and Airborne Instrumentation for Astronomy III*, ed. I. S. McLean, S. K. Ramsay, & H. Takami, 77352I
- Thatte, N. A., Tecza, M., Eisenhauer, F., et al. 1998, in *Society of Photo-Optical Instrumentation Engineers (SPIE) Conference Series*, Vol. 3353, *Adaptive Optical System Technologies*, ed. D. Bonaccini & R. K. Tyson, 704–715
- Tiley, A. L., Bureau, M., Cortese, L., et al. 2019a, *Monthly Notices of the Royal Astronomical Society*, **482**, 2166
- Tiley, A. L., Gillman, S., Cortese, L., et al. 2021, *Monthly Notices of the Royal Astronomical Society*, **506**, 323
- Tiley, A. L., Swinbank, A. M., Harrison, C. M., et al. 2019b, *Monthly Notices of the Royal Astronomical Society*, **485**, 934
- Tomono, D., Weisz, H., & Hofmann, R. 2003, in *Society of Photo-Optical Instrumentation Engineers (SPIE) Conference Series*, Vol. 4841, *Instrument Design and Performance for Optical/Infrared Ground-based Telescopes*, ed. M. Iye & A. F. M. Moorwood, 390–397
- Toomre, A. 1963, *The Astrophysical Journal*, **138**, 385
- Tremaine, S., Gebhardt, K., Bender, R., et al. 2002, *The Astrophysical Journal*, **574**, 740
- Tremonti, C. A., Heckman, T. M., Kauffmann, G., et al. 2004, *The Astrophysical Journal*, **613**, 898
- Trujillo, I. & Aguerri, J. A. L. 2004, *Monthly Notices of the Royal Astronomical Society*, **355**, 82
- Trujillo, I., Conselice, C. J., Bundy, K., et al. 2007, *Monthly Notices of the Royal Astronomical Society*, **382**, 109
- Trujillo, I., Förster Schreiber, N. M., Rudnick, G., et al. 2006, *The Astrophysical Journal*, **650**, 18
- Trumpler, R. J. 1930, *Publications of the Astronomical Society of the Pacific*, **42**, 214
- Tully, R. B., de Marseille, O., & Fisher, J. R. 1975, in *Bulletin of the American Astronomical Society*, Vol. 7, 426
- Umehata, H., Fumagalli, M., Smail, I., et al. 2019, *Science*, **366**, 97
- Urrutia, T., Wisotzki, L., Kerutt, J., et al. 2019, *Astronomy & Astrophysics*, **624**, A141
- van den Bergh, S. 1976, *Astrophysical Journal*, **206**, 883
- van der Burg, R. F. J., Rudnick, G., Balogh, M. L., et al. 2020, *Astronomy & Astrophysics*, **638**, A112

- van der Kruit, P. C. & Searle, L. 1981a, *Astronomy & Astrophysics*, **95**, 105
- van der Kruit, P. C. & Searle, L. 1981b, *Astronomy and Astrophysics*, **95**, 105, aDS Bibcode: 1981A&A....95..105V
- van der Wel, A., Bell, E. F., Häussler, B., et al. 2012, *The Astrophysical Journal Supplement Series*, **203**, **24**
- van der Wel, A., Chang, Y.-Y., Bell, E. F., et al. 2014a, *The Astrophysical Journal*, **792**, **L6**
- van der Wel, A., Franx, M., van Dokkum, P. G., et al. 2014b, *The Astrophysical Journal*, **788**, **28**
- Vanderriest, C. 1980, *Publications of the Astronomical Society of the Pacific*, **92**, **858**
- Ventou, E., Contini, T., Bouché, N., et al. 2017, *Astronomy & Astrophysics*, **608**, **A9**
- Ventou, E., Contini, T., Bouché, N., et al. 2019, *Astronomy & Astrophysics*, **631**, **A87**
- Vergani, D., Epinat, B., Contini, T., et al. 2012, *Astronomy & Astrophysics*, **546**, **A118**
- Vogelsberger, M., Genel, S., Springel, V., et al. 2014, *Monthly Notices of the Royal Astronomical Society*, **444**, **1518**
- Vogel, K., Hilker, M., Baumgardt, H., et al. 2016, *Monthly Notices of the Royal Astronomical Society*, **460**, **3384**
- Vogt, N. P., Forbes, D. A., Phillips, A. C., et al. 1996, *Astrophysical Journal Letters*, **465**, **L15**
- Walcher, J., Groves, B., Budavári, T., & Dale, D. 2011, *Astrophysics and Space Science*, **331**, **1**
- Walsh, J. R., Monreal-Ibero, A., Barlow, M. J., et al. 2016, *Astronomy & Astrophysics*, **588**, **A106**
- Walter, F., Carilli, C., Neeleman, M., et al. 2020, *The Astrophysical Journal*, **902**, **111**
- Wang, E. & Lilly, S. J. 2022, Coplanar gas inflow can be hidden within warped galactic gas disks, number: arXiv:2205.04215 arXiv:2205.04215 [astro-ph]
- Wang, T.-M., Magnelli, B., Schinnerer, E., et al. 2022, *Astronomy & Astrophysics*, **660**, **A142**
- Way, M. J. & Klose, C. D. 2012, *Publications of the Astronomical Society of the Pacific*, **124**, **274**
- Weaver, J. R., Kauffmann, O. B., Ilbert, O., et al. 2022, *The Astrophysical Journal Supplement Series*, **258**, **11**
- Wechsler, R. H. & Tinker, J. L. 2018, *Annual Review of Astronomy and Astrophysics*, **56**, **435**
- Weilbacher, P. M., Palsa, R., Streicher, O., et al. 2020, *Astronomy & Astrophysics*, **641**, **A28**
- Welikala, N., Connolly, A. J., Hopkins, A. M., Scranton, R., & Conti, A. 2008, *The Astrophysical Journal*, **677**, **970**
- Welikala, N., Hopkins, A. M., Robertson, B. E., et al. 2011, arXiv e-prints, arXiv:1112.2657
- Wells, M., Pel, J.-W., Glasse, A., et al. 2015, *Publications of the Astronomical Society of the Pacific*, **127**, **646**
- Wernli, F., Emsellem, E., & Copin, Y. 2002, *Astronomy & Astrophysics*, **396**, **73**
- Whitaker, K. E., Franx, M., Leja, J., et al. 2014, *The Astrophysical Journal*, **795**, **104**
- White, S. D. M. & Frenk, C. S. 1991, *Astrophysical Journal*, **379**, **52**
- White, S. D. M. & Rees, M. J. 1978a, *Monthly Notices of the Royal Astronomical Society*, **183**, **341**
- White, S. D. M. & Rees, M. J. 1978b, *Monthly Notices of the Royal Astronomical Society*, **183**, **341**
- Williams, R. E., Blacker, B. S., Dickinson, M., et al. 1996, in *Science with the Hubble Space Telescope - II*, ed. P. Benvenuti, F. D. Macchetto, & E. J. Schreier, 33
- Winkel, N., Husemann, B., Davis, T. A., et al. 2022, *Astronomy & Astrophysics*, **663**, **A104**
- Wisnioski, E., Förster Schreiber, N. M., Fossati, M., et al. 2019, *The Astrophysical Journal*, **886**, **124**
- Wisnioski, E., Förster Schreiber, N. M., Wuyts, S., et al. 2015, *The Astrophysical Journal*, **799**, **209**
- Wisotzki, L., Bacon, R., Blaizot, J., et al. 2016, *Astronomy & Astrophysics*, **587**, **A98**
- Wright, G. S., Rieke, G. H., Colina, L., et al. 2004, in *Society of Photo-Optical Instrumentation Engineers (SPIE) Conference Series*, Vol. 5487, *Optical, Infrared, and Millimeter Space Telescopes*, ed. J. C. Mather, 653–663
- Wright, S. A., Larkin, J. E., Barczys, M., et al. 2007, *The Astrophysical Journal*, **658**, **78**
- Wright, S. A., Larkin, J. E., Graham, J. R., & Ma, C.-P. 2010, *The Astrophysical Journal*, **711**, **1291**

- Wright, S. A., Larkin, J. E., Law, D. R., et al. 2009, The Astrophysical Journal, [699](#), [421](#)
- Wright, T. & Rafinesque, C. 1837, The Universe and the Stars: Being an Original Theory on the Visible Creation, Founded on the Laws of Nature (C. Wetherill)
- Wuyts, E., Kurk, J., Förster Schreiber, N. M., et al. 2014, The Astrophysical Journal Letters, [789](#), [L40](#)
- Wuyts, E., Wisnioski, E., Fossati, M., et al. 2016, The Astrophysical Journal, [827](#), [74](#)
- Wuyts, S., Förster Schreiber, N. M., Genzel, R., et al. 2012, The Astrophysical Journal, [753](#), [114](#)
- Yang, Y., Flores, H., Hammer, F., et al. 2008, Astronomy & Astrophysics, [477](#), [789](#)
- Zabl, J., Bouché, N. F., Schroetter, I., et al. 2019, Monthly Notices of the Royal Astronomical Society, [485](#), [1961](#)
- Zabl, J., Bouché, N. F., Wisotzki, L., et al. 2021, Monthly Notices of the Royal Astronomical Society, [507](#), [4294](#)
- Zeldovich, I. B. 1978, in Large Scale Structures in the Universe, ed. M. S. Longair & J. Einasto, Vol. 79, 409
- Zhang, H., Primack, J. R., Faber, S. M., et al. 2019, Monthly Notices of the Royal Astronomical Society, [484](#), [5170](#)
- Zhao, H. 1997, Monthly Notices of the Royal Astronomical Society, [287](#), [525](#)
- Zibetti, S., Charlot, S., & Rix, H.-W. 2009, Monthly Notices of the Royal Astronomical Society, [400](#), [1181](#)
- Zoutendijk, S. L., Brinchmann, J., Boogaard, L. A., et al. 2020, Astronomy & Astrophysics, [635](#), [A107](#)
- Zoutendijk, S. L., Brinchmann, J., Bouché, N. F., et al. 2021a, Astronomy & Astrophysics, [651](#), [A80](#)
- Zoutendijk, S. L., Júlio, M. P., Brinchmann, J., et al. 2021b, arXiv e-prints, arXiv:2112.09374
- Zwicky, F. 1933, Helvetica Physica Acta, 6, 110
- Zwicky, F. 1937, The Astrophysical Journal, [86](#), [217](#)
- Übler, H., Förster Schreiber, N. M., Genzel, R., et al. 2017, The Astrophysical Journal, [842](#), [121](#)

Observatories, instruments, and surveys

- 2MASS** The Two Micron All Sky Survey is a NIR photometric survey carried out between 1997 and 2001 that observed nearly completely the celestial sphere. [53](#)
- 3D-MPE** An early German IFS instrument that integrated an image slicer with a long-slit and that was deployed at the WHT, at the observatory of Calar Alto in Andalusia, Spain, and at the 2.2 m MPG-ESO telescope in La Silla, Chile. [52](#)
- AEGIS** All-Wavelength Extended Groth Strip International Survey is a multi-wavelength ground- and space-based survey that studies the evolution of galaxies at $z \sim 1$. [53](#)
- AIP** The Leibniz Institute for Astrophysics Potsdam is an astrophysics research institute located in Potsdam, Germany. [54](#)
- ALMA** Atacama Large Millimeter/submillimeter Array is an international observatory comprised of 66 radio telescopes observing at millimetre and sub-millimetre wavelengths and located in the Chajnantor plateau, Chile. [7](#)
- AMAZE** Assessing the Mass-Abundance redshift[-Z] Evolution is an ESO large program spectroscopic survey obtained with SINFONI whose goal was to study the mass-metallicity relation in the range $3 < z < 5$. [52](#)
- ATLAS^{3D}** A multi-wavelength survey from the radio to the optical of 260 early type galaxies whose stellar and ionised gas kinematics has been derived from SAURON observations. [52](#)
- BLUEMUSE** A future IFS instrument for the VLT similar to MUSE but optimised to observe in the blue part of the spectrum. [59](#)
- CALIFA** Calar Alto Legacy Integral Field Area Survey is a large IFS survey of galaxies in the local Universe carried out at the Calar Alto 3.5 m telescope. [44](#)
- CANDELS** The Cosmic Assembly Near-infrared Deep Extragalactic Legacy Survey is a HST imaging survey observing galaxies at high redshift. [92](#)
- CFHT** Canada-France-Hawaii Telescope is a Canadian-French-Hawaiian observatory and a 3.5 m telescope located on mount Mauna Kea in Hawaii. [33](#), [49–51](#)

- COSMOS** Cosmic Evolution Survey, a two square degree photometric survey from X-ray to radio bands designed to probe the evolution of galaxies as a function of cosmic time. The version of the catalogue is usually appended with the year of its release, that is COSMOS2015 for the old version and COSMOS2020 for the new one. [6](#), [53](#), [58](#), [61](#), [63](#), [65](#), [68](#), [73](#), [75](#), [84](#)
- CRAL** The Centre de Recherche Astrophysique de Lyon is an astrophysics research institute located in Lyon, France. [54](#)
- ELTs** Extremely Large Telescopes are the next-generation 30 – 40 m class telescopes that should be available around the years 2030 – 2040. [49](#), [58](#), [59](#), [237](#), [239](#)
- ELT** Extremely Large Telescope, the next-generation extremely large European (ESO) telescope with a 39 m diameter telescope located at Cerro Armazones, Chile, and that should be launched around the year 2025. [59](#), [239](#), [243](#)
- ERIS** The Enhanced Resolution Imager and Spectrograph is a new instrument installed on the UT4 platform of the VLT that has an integral field spectroscopy mode from the J to the K bands. [59](#), [60](#), [237](#), [239](#), [241](#), [243](#), [244](#)
- ESA** The European Space Agency is a European organisation begun in 1975 that is dedicated to the exploration of space. [33](#)
- ESO** European Southern Observatory is an intergovernmental European research organisation specialised in ground-based astronomy in the southern hemisphere. [32](#), [52–54](#), [58](#), [59](#), [61](#)
- ETH** Eidgenössische Technische Hochschule Zürich is a University located in Zürich, Switzerland. [54](#)
- FLAMES** Fibre Large Array Multi-Element Spectrograph is a fiber facility installed on the UT2 platform of the VLT. It hosts two different spectrographs: GIRAFFE and UVES. [52](#), [53](#)
- GALACSI** The AO facility associated to MUSE at the VLT. [55](#), [61](#)
- GALEX** An American UV telescope launched in 2003 and designed to study star formation in the Universe. [34](#)
- GASP** GAs Stripping Phenomena in galaxies with MUSE is a MUSE survey designed to study gas stripping in local galaxies. [6](#)
- GIRAFFE** A medium-high resolution spectrograph in the visible fed by FLAMES. It can either offer simultaneous spectroscopy for 132 targets in its MEDUSA mode, or perform IFU spectroscopy for simultaneously 15 targets, or perform a single IFU observation on a larger FoV. [52](#), [53](#), [58](#), [59](#)
- GOODS** Great Observatories Origins Deep Survey is a multi-wavelength ground- and space-based survey that studies the evolution of galaxies over a large FoV combining optical, IR, and X-ray data. [53](#)
- GAIA** A space mission that performs precise astrometry and proper motion measurement of mainly stars. [89](#)

- HARMONI** High Angular Resolution Monolithic Optical and Near-infrared Integral field spectrograph will be one of the first-light instrument on the future ELT that will perform diffraction-limited integral field spectroscopy across the optical and the IR. [59](#), [237](#), [239–241](#), [243](#), [244](#)
- HDFS** The Hubble Deep Field South is a deep HST multi-wavelength observation of a portion of the sky visible in the southern hemisphere that followed the Hubble Deep Field observations. [5](#)
- HDF** The Hubble Deep Field is the first deep HST multi-wavelength observation performed in the Northern Hemisphere. [33](#)
- HST-ACS** Hubble Space Telescope Advanced Camera for Surveys is a third generation camera installed on the HST since 2002 that can observe from the UV to the IR. [207](#)
- HST-WFC3** Hubble Space Telescope Wide Field Camera 3 is a fourth generation camera installed on the HST since 2009 designed for its large FoV and high sensitivity that can observe from the UV to the IR. [207](#)
- HST** Hubble Space Telescope is a 2.4 m diameter telescope operating from UV to near-IR with spectroscopy and imaging capabilities. [6](#), [33](#), [34](#), [64](#), [67](#), [92](#), [105](#), [173](#), [199](#), [201](#), [202](#), [207](#), [208](#), [211–214](#), [222](#), [231](#), [234](#), [237](#), [239](#), [241](#), [243](#)
- HUDF** The Hubble Ultra Deep Field survey is a deep HST survey that targeted a low density region of the sky first with the ACS instrument and later with WFC3 in the infrared. [33](#), [201](#), [238](#), [242](#)
- IAG** The Institute for Astrophysics and Geophysics is an astrophysics and geophysics research institute located in Göttingen, Germany. [54](#)
- IMAGES** Intermediate MAss Galaxy Evolution Sequence, an ESO large program spectroscopic survey performed with FLAMES-GIRAFFE multi-IFU instrument designed to probe the dynamics of 63 intermediate redshift ($0.4 < z < 0.75$) galaxies. [53](#)
- IRAP** The Institut de Recherche en Astrophysique et Planétologie is an astrophysics research institute located in Toulouse, France. [54](#)
- IRIS** The Infrared Imaging Spectrograph is a future first-light IFS instrument on the TMT that will perform diffraction-limited observations in the NIR. [59](#)
- JWST** James Webb Space Telescope is a new-generation space-based telescope observing the in IR with a primary mirror of 6.5 m launched in 2021 and operational since mid-2022. [59](#), [239](#), [243](#), [244](#)
- KMOS3D** K-band Multi Object Spectrograph 3D, an integral field spectroscopic survey performed with KMOS on more than 600 galaxies in the redshift range $0.7 < z < 2.7$. The goal was to build a large sample of galaxies with spatially resolved kinematics at intermediate to high redshift using the high capabilities of KMOS. [58](#), [137](#)
- KMOS** K-band Multi Object Spectrograph is a second-generation near-infrared spectrograph mounted on the UT1 platform of the VLT that can perform integral field spectroscopy on 24 targets at the same time. [53](#), [56](#), [58](#), [59](#)

- KROSS** KMOS Redshift One Survey, an ESO GTO KMOS survey targeting 795 star forming galaxies around redshift $z \sim 0.9$. 58, 137
- KECK telescopes** Two 10 m-class American telescopes located on Mauna Kea in Hawaii and operated by Caltech and NASA. 52, 53
- LAM** Laboratoire d'Astrophysique de Marseille is a French astrophysics research institute located in Marseille. 131
- LSD** Lyman-break galaxies Stellar populations and Dynamics, a spectroscopic survey performed with SINFONI whose goal was to have integral field spectroscopic observations for a complete sample of Lyman-break galaxies at $z \sim 3$. 52
- MAGPI** Middle Ages Galaxy Properties with Integral Field Spectroscopy is a MUSE survey dedicated to studying resolved properties and kinematics of 60 central galaxies and roughly 100 satellites in dense environments at $z \approx 0.3$ where the impact of the environment on galaxies is supposed to be the most prominent. 7
- MASSIV** Mass Assembly Survey with SINFONI in VVDS is a spectroscopic survey performed with SINFONI in the VIMOS VLT Deep Survey whose goal was to probe the kinematics and chemical content of a representative sample of galaxies at $1 \lesssim z \lesssim 2$. 44, 52
- MAUVE** MUSE and ALMA Unveiling the Virgo Environment is a future MUSE survey that will observe massive disk galaxies in the Virgo cluster in combination with ALMA to study the link between environment and star-formation. 7
- MEGAFLOW** MusE GAs FLOW and Wind survey is a MUSE survey that observes galaxy-quasar pairs to study gas inflows and outflows in the range $0.4 < z < 1.4$. 6
- MICADO** Multi-AO Imaging Camera for Deep Observations will be one of the first-light instrument on the future ELT that will take images at a diffraction-limited spatial resolution in the NIR. 239, 243
- MIRI** The JWST Mid-Infrared Instrument is a spectrograph mounted on the JWST and observing in the MIR between roughly $5 \mu\text{m}$ and $28 \mu\text{m}$. 59, 239, 240, 244
- MOSAIC** A future MOS and IFS instrument that will be located on the ELT. 59, 237, 239, 241, 243
- MUDF** The MUSE Ultra Deep Field is a deep survey of 200 h on-source integration time composed of two largely overlapping MUSE fields that targeted various structures along with two bright quasars. 7
- MUSE-HDFS** The MUSE Hubble Deep Field South is a deep 27 h integration time early MUSE survey that targeted the HDFS region of the sky. 5, 58, 64, 65, 68, 71
- MUSE-HUDF** The MUSE Hubble Ultra Deep Field survey is a deep MUSE survey that targeted ten fields in the HUDFS area. 5, 56, 58, 65, 68, 71, 201, 221
- MUSE-WIDE** A complementary survey to MUSE-HUDF that performed shallow observations of 1 h exposure but over a large FoV comprised of 24 different MUSE fields. 5, 58, 238, 242

- MUSE-FAINT** MUSE-FAINT is a MUSE survey of ultra-faint dwarf galaxies designed to put constraints on DM properties. 45
- MUSE** Multi-Unit Spectroscopic Explorer is an IFS spectrograph with large FoV of one arc minute square. It is a second generation instrument mounted on the UT4 platform on the VLT. 5–7, 9, 43, 47, 49, 53–61, 63–65, 67–69, 71–73, 83–85, 105, 109, 110, 119, 122, 125, 128, 131, 134, 137, 138, 173, 199, 201, 207, 231, 237–239, 241–244, 272
- MXDF** The MUSE Extremely Deep Field is an ultra deep MUSE survey of 140 h of integration time located in the HUDF field. 6, 46, 56, 58, 201, 238, 242
- MANGA** Mapping Nearby Galaxies at APO is an ongoing survey that uses 17 different fibre-based IFUs to observe local galaxies that are part of the SDSS. 58
- MEGACAM** A wide-field optical imager installed on the CFHT which is complementary to WIRCAM. 240, 244
- NASA** The National Aeronautics and Space Administration is an American agency founded in 1958 dedicated to space exploration. 33
- NIRSPEC** The JWST Near-Infrared Spectrograph is a spectrograph mounted on the JWST and observing in the NIR between roughly 0.9 μm and 5 μm . 59, 239, 240, 244
- OASIS** Optically Adaptive System for Imaging Spectroscopy, the second IFS instrument developed in Lyon under the supervision of Roland Bacon that was installed on the CFHT. 50–52
- OHP** Observatory of Haute-Provence is a French observatory located in Provence, France. 50
- ORELSE** Observations of Redshift Evolution in Large-Scale Environments is a photometric and spectroscopic survey of galaxies located in 20 clusters in the redshift range $0.6 < z < 1.3$ designed to probe the impact of the environment on galaxy properties over a large range of environments. 48, 137
- OSIRIS** OH-Suppressing Infra-Red Imaging Spectrograph is an IFS instrument that observes in the infrared and is mounted on one of the Keck telescopes. 53
- SAMI** Sydney-AAO Multi-object Integral field spectrograph is a MOS and IFS instrument that combines 13 deployable fibre bundles. It is also the name of a large IFS survey of galaxies in the nearby Universe. 44, 59
- SAURON** Spectroscopic Areal Unit for Research on Optical Nebulae was an early IFS instrument built in collaboration between the observatories of Lyon, Leiden, and Durham with a large FoV designed to study the dynamics of galaxies. 51, 52
- SAURON project** A survey of 72 spiral, lenticular, and elliptical galaxies observed with SAURON. 51
- SDSS** DEep Imaging Multi-Object Spectrograph is a MOS slit spectrograph mounted on the Keck II telescope. 48

- SDSS** The Sloan Digital Sky Survey is a large FoV deep spectroscopic multi-band survey observing galaxies in the local Universe. [37](#), [41](#), [53](#), [58](#), [92](#), [94](#)
- SINFONI** A second-generation IFS instrument located on the UT4 platform at the VLT that observed in the infrared. [52](#), [54](#), [60](#)
- SINS** Spectroscopic Imaging survey in the Near-infrared with SINFONI is a survey performed with SINFONI aimed at studying the dynamics of galaxies at high redshift ($z \gtrsim 2$). [52](#)
- SITELLE** Spectromètre Imageur à Transformée de Fourier pour l'Etude en Long et en Large de raies d'Emission is an imaging Fourier-transform spectrograph installed at the CFHT. [240](#), [244](#)
- SPARCS** Spitzer Photometry and Accurate Rotation Curves is a sample of nearby galaxies with high-quality rotation curves and SPITZER photometry. [44](#)
- SPITZER** An American infrared telescope launched in 2003. [6](#), [34](#)
- TIGER** Traitement Intégral des Galaxies par l'Etude de leurs Raies, the first IFS prototype imagined by Georges Courtès in 1982, developed between the observatories of Lyon and Marseille, and installed on the CFHT and then on the WHT. [49–52](#)
- TMT** The Thirty Meter Telescope is a future American extremely large telescope that will host a 30 m primary mirror. [59](#)
- VIMOS** Visible Multi-Object Spectrograph was a large FoV imager, multi-object spectrograph, and IFU instrument previously mounted on the UT3 platform of the VLT. [52](#), [65](#)
- VLTS** Very Large Telescopes, a generation of 8 – 10 m class telescopes. [34](#), [59](#), [237](#)
- VLT** Very Large Telescope, a 8 m ground-based large telescope operated by ESO on Cerro Paranal in Chile. [52](#), [55](#), [58](#), [59](#), [61](#), [239](#), [244](#)
- VUDS** The VIMOS Ultra-Deep Survey is a large spectroscopic survey of roughly 10 000 galaxies at $2 \lesssim z \lesssim 6$ carried out with VIMOS. [84](#)
- WHT** William Herschel Telescope is a 4.2 m telescope located at the Roque de los Muchachos Observatory in La Palma, Spain. [51](#), [52](#)
- WIRCAM** The Wide-field InfraRed Camera is a NIR imager installed at the CFHT which is complementary to MEGACAM. [240](#), [244](#)
- zC-SINF** zCOSMOS-SINFONI is a spectroscopic survey that combined SINFONI observations with the zCOSMOS information to study a sample of massive star forming galaxies around $z \approx 2$. [52](#)
- zCOSMOS** A 600 h ESO Large Program carried out with the VIMOS spectrograph to provide a spectroscopic follow-up to roughly 20 000 galaxies between redshift 0.2 and 3. The sample with about 20 000 galaxies is sometimes referred as the 20K sample whereas the earlier version with only 10 000 galaxies is named 10K sample. [61](#), [65](#), [84](#), [85](#)

Gemini The Gemini Observatory is composed of two 8 m-class telescopes, one located at Cerro Pachón in Chile and the other at Mauna Kea in Hawaii, thus covering almost the entire sky. [52](#)

MPE A German research institute in astrophysics located in Garching. [52](#)

Glossary

- [\$\Lambda\$ CDM](#)** A Cold Dark Matter is the current cosmological model that assumes an homogeneous and isotropic Universe with a dark matter component and a cosmological constant that acts as dark energy and is responsible for the current accelerated expansion of the Universe. [23–25](#), [28](#), [44–46](#), [239](#), [243](#)
- [CIGALE](#)** Code Investigating GALaxy Emission, a SED fitting code initially written in Fortran but rewritten in Python that can fit SEDs from the X-ray/UV to the radio bands. [73](#), [75](#), [78](#), [80–83](#), [134](#), [201](#), [203](#), [206](#), [208–211](#), [214–217](#), [222–224](#), [231–235](#)
- [EAGLE](#)** The Evolution and Assembly of GaLaxies and their Environments project is a large cosmological hydrodynamical simulation from the Virgo consortium. [35](#)
- [FAST](#)** A SED fitting code written in IDL that can work in combination with the photometric redshift code EAZY. [73](#), [74](#), [78](#), [80](#), [82](#)
- [FIRE](#)** Feedback In Realistic Environments is a suite of high-resolution cosmological designed to probe star formation and feedback processes on spatially resolved scales. [35](#)
- [GALPAK^{3D}](#)** Galaxy parameters and kinematics is a full 3D kinematics fitting code based on a parametric disk model and MCMC sampling that directly fits the data cubes to extract the intrinsic kinematics of a galaxy. [130](#), [131](#), [201](#)
- [GALFIT](#)** A widely used 2D fitting software optimised to fit the surface brightness distribution of galaxies from single-band photometry. [72](#), [87](#), [132](#), [133](#), [201](#), [222](#)
- [HFF](#)** The HUBBLE Frontier Fields are ultra deep HST and SPITZER observations that focus on six massive high-magnification lensing clusters as well as six blank parallel fields. This survey provides the deepest HST observation ever taken. [6](#), [238](#), [239](#), [242](#), [243](#)
- [ILLUSTRISTNG](#)** The Next Generation Illustris Simulations is new version of ILLUSTRIS that covers boxes of different volume and spatial resolution. [35](#)
- [ILLUSTRIS](#)** A large cosmological hydrodynamical simulation designed to study the evolution of galaxies. [35](#)
- [LEPHARE](#)** A SED fitting/photometric redshift code written in Fortran used in particular for the COSMOS catalogue. [73](#), [75](#), [201](#), [203](#), [206](#), [208–211](#), [214–217](#), [224](#)

- MAGIC** The MUSE-gAlaxy Groups In Cosmos is a deep MUSE survey targeting already known groups in the COSMOS field and designed to probe the impact of the environment on galaxy properties. 6, 9, 41–43, 57, 58, 61, 63–65, 68, 69, 71, 72, 77, 83, 84, 87, 97, 101, 105, 109, 110, 119, 122, 130–134, 137, 138, 173, 237–239, 241–243
- MARZ** Manual and Automatic Redshifting Software is a template-matching automatic and manual redshifting software. 65
- MUSCATEL** The MUSE Cosmic Assembly survey Targeting Extragalactic Legacy fields is a MUSE survey targeting the four HFF fields with deep 25 h observations surrounded by a mosaic of shallower MUSE fields. 6, 238–240, 242–244
- MAGPHYS** Multi-wavelength Analysis of Galaxy Physical Properties is SED fitting code written in Fortran77 that can model SEDs from the UV to the IR. 201
- MILLENIUM** The first large semi-analytical cosmological simulation from the Virgo consortium. 35
- MULTIDRIZZLE** A program used on HST observations that perform various tasks to combine dithered images. 213
- PROSPECTOR** A SED fitting code that performs Bayesian inference on highly flexible models and that can combine photometric and spectroscopic data. 209
- SEXTRACTOR** Source-Extractor is a program that automatically creates catalogues of objects from images. 211
- ZAP** Zurich Atmosphere Purge is a sky subtraction software for integral field spectroscopy data that uses PCA analysis, wavelength segmentation and masking. 65
- ^{3D}BAROLO** 3D-Based Analysis of Rotating Object via Line Observation is a full 3D fitting code that uses the tilted-ring formalism to model and fit an input cube. 130
- STARLIGHT** A stellar spectral synthesis code that estimates stellar physical parameters from spectra. 209
- absolute magnitude** Noted M , it is defined as the apparent magnitude if the object was seen at 10 pc from us. Depending on the definitions it can also be corrected of the extinction and the k-correction. In essence, it is a proxy for the intrinsic luminosity of the object. 74
- AGN** An active galactic nucleus is a luminous compact region in the central parts of a galaxy that emits all across the wavelength range from radio to gamma rays and is supposedly associated to a supermassive black-hole surrounded by an accretion disk. 35, 38, 46, 53, 56
- angular diameter distance** A distance in cosmology used to derive the physical extension of an object onto the sky. 27, 28
- AO** Adaptive Optics, a technology used in modern ground-based telescopes to actively compensate for atmospheric distortion by deforming the mirror. 6, 50, 52, 53, 55, 59, 60, 65, 238

- apparent magnitude** Noted m , it is defined as -2.5 times the decimal logarithm of the observed flux. 74
- asymmetric drift** The tendency of a test particle to rotate slower than the circular velocity it should have because of non-streaming motions. The asymmetric drift is usually associated to an inward radial pressure gradient that compensates parts of the inward gravitational force and therefore lead to a reduction of the rotation velocity. 109, 112, 113
- attenuation curve** The curve that describes the strength of the dust attenuation as a function of wavelength. 208, 210
- B/T** Bulge-to-disk flux ratio, the ratio between the integrated flux of the bulge component and that of the sum of all the components in a galaxy and in a given aperture. 97, 99, 101, 201
- Balmer line** A set of hydrogen lines corresponding to an energy transition from the second level to a higher one (absorption) or vice-versa (emission). 57, 65
- beam smearing** An instrumental effect that affects kinematics maps extracted from data cubes by convolving nearby pixels with different flux and line-of-sight velocity. Its effect is particularly relevant for the velocity dispersion whose value is increased where the flux and the velocity gradient are the highest. 39, 69, 119, 129–131, 223
- bias frame** An image generated instantaneously that only contains undesired signal from the electronics independently of the exposure. 65
- BMU** The best-matching unit is the closest neuron in a SOM to a given data point. 226, 228, 229, 232
- Boltzmann's equation** An equation of conservation of mass along a flow in phase space derived by Boltzmann in 1872. 25–27
- Burkert** A core DM profile first proposed by Andreas Burkert to fit DM haloes of dwarf spiral galaxies. 118
- CCD** Charge-Coupled Devices are a type of light detector that converts incoming photons into electrons that can then be read and stored on a device. 54
- CDM** Cold Dark Matter, the most massive type of DM which is currently part of the standard cosmological model. Its high mass means it must have a low thermal velocity and thus it is "cold". 44
- CGM** The gas located beyond the extent of a galaxy stellar disk but still gravitationally bound that is thought to be source of accreted cold gas. 41
- circular velocity** Rotation velocity of a test particle in equilibrium embedded in the gravitational potential generated by a mass distribution so that its centrifugal acceleration compensates the inward force generated by the mass distribution. 112, 114
- CMB** The cosmic microwave background is an electromagnetic signal coming from the youngest detectable age of the Universe, the epoch of recombination, when protons and electrons recombined into neutral hydrogen. 24, 44

- colour excess** A measurement of the excess of colour, that is reduction in flux, between two bands because of their differential dust extinction. 74
- comoving distance** The distance to an object that is measured with respect to a reference distance that stretches with the expansion of the Universe. Thus, this distance remains constant with cosmic time if the object has no proper motion. 24, 27
- core** A family of DM profiles that exhibit a core in their central parts. 46, 118–120
- COSMOS-WALL** A large scale filamentary structure located at $z \approx 0.73$ in the COSMOS field. 61, 65
- critical density** The density that is required to compensate the expansion of the Universe when there is no cosmological constant. It corresponds to the density of such a Universe without curvature. 25
- cuspid-core problem** A current problem in extragalactic astrophysics where DM-only simulations predict cuspy DM profiles whereas observations favour cored profiles instead. 46, 118, 201
- cuspy** A family of DM profiles that exhibit a cusp in their central parts. 46, 118, 119
- dark energy** A component of the Universe to which is attributed the acceleration of its expansion. 25
- dark frame** An image taken for a given exposure time in complete darkness that contains dark current signal plus electronics signal. The bias frame is usually removed from the dark frame to produce a new dark frame that only contains the dark current signal. 65
- de Vaucouleurs profile** A surface brightness profile first proposed by Gérard de Vaucouleurs in 1948. 36, 89, 99, 115
- Dekel-Zhao** Another parametric DM profile of the family of the Zhao profiles with fewer parameters and first proposed by Jonathan Freundlich. 118
- DM** Dark Matter, an hypothetical transparent component visible in galaxies and galaxy clusters through its impact on galaxies dynamics via gravity. 6, 23, 33, 35, 37–40, 42–46, 87, 110, 114, 118–120, 133, 134, 138, 139, 174, 199, 201, 214, 222–224, 238–240
- double exponential disk** A thick disk model represented by the product of two exponential laws, one along the radial direction in the plane of the disk, the other along the vertical direction. 94–96, 113, 114, 133
- Einasto** A parametric cuspy/core model defined by Jaan Einasto to describe stellar systems that has been used to model DM haloes. 118, 119
- exponential disk** A disk model whose surface brightness follows an exponential law, usually combined with a Dirac delta to produce a razor-thin disk for morphological and mass models. 89, 94, 95, 97, 99, 113

- extinction** The drop in flux, or equivalently the increase in magnitude, due to the absorption of a part of the emitted light by dust. There are two different type of extinctions: (i) the intrinsic extinction that affects the rest-frame light due to the dust embedded in the observed galaxy and (ii) the Galactic extinction that affects the observed/redshifted light because of the dust located in the Milky Way. [74](#)
- Faber-Jackson relation** A scaling relation observed for elliptical galaxies between their luminosity or stellar mass and their velocity dispersion. [36](#)
- Fabry-Pérot spectroscopy** A type of spectroscopic observation where the spectrum of an object is taken by varying the distance between two semi-reflective blades. [48](#)
- FIR** Far-infrared, a sub-portion of the IR part of the spectrum that goes beyond 25 μm . [201](#), [210](#)
- flat-field** Correcting pixel-per-pixel sensitivity variations so that a uniform input signal produces a uniform image on the detector. [65](#)
- FLRW** Friedmann-Lemaître-Robertson-Walker metric is the exact solution of Einstein's field equations for a homogeneous, isotropic, and expanding Universe. [24-27](#)
- flux calibration** Processing step that transforms an input signal in ADUs or electrons into a physical units. [65](#)
- FoF** Friends of Friends are a type of grouping algorithm that associate objects to the same group. To objects belong to the same group if they are separated by a distance which is less than the linking length, a free parameter chosen beforehand. [83-85](#), [139](#)
- FoV** Field of View, the area over which an observation is made. [6](#), [9](#), [49-56](#), [58-61](#), [63-65](#), [71](#), [84](#), [85](#), [213](#), [239](#)
- Freeman's disk** Another name for the razor-thin exponential disk. Named after Kenneth Charles Freeman after his derivation of the expression of the circular velocity required to compensate the gravitational force generated by this mass distribution. [114](#), [115](#), [118](#)
- FTS** A type of spectroscopic observation where the spectrum of an object is taken by varying the distance between the two arms of a Michelson interferometer. The resulting observation is the Fourier transform of the incoming spectrum. [48](#)
- fundamental plane** A multivariate scaling relations that links the luminosity, velocity dispersion and size of elliptical galaxies by placing them on a plane. [36](#)
- FWHM** Full Width at Half Maximum, a measure of the width of a distribution where its value equals half its maximum. It is used for a PSF to describe the quality of an image. [51](#), [53](#), [55](#), [61](#), [71](#), [72](#), [122](#), [125](#), [131](#), [132](#), [211](#)
- galaxy harassment** The effect of gravitational interactions with multiple galaxies in a clusters across a few fly-bys. [38](#), [41](#)
- geodesic** The path of shortest distance in an arbitrary geometry. For instance, in a Euclidian space it corresponds to a straight line whereas on a sphere it corresponds to a great circle. [26](#)

- GLAO** Ground Layer Adaptive Optics, a type of AO technology that uses a single deformable mirror and whose correction only applies for atmospheric distortion close to the ground. 61
- GR** General Relativity is a geometrical theory of gravity developed by Albert Einstein in 1915 that expands upon Special Relativity. 24, 25, 30
- grating** An optical element composed of a multitude of equally spaced ridges or slits that act as a dispersive system in spectrographs. 48, 59
- green valley** A population of scarce galaxies that lie between the blue and red sequences, probably in a transition from an active to a passive state. 77
- grism** An optical element made of the combination of a prism and a dispersion grating used in modern spectrographs. 48, 52
- GTO** Guaranteed Time Observation, a fixed amount of guaranteed observing hours provided by ESO to a consortium that has provided software or hardware solutions. 5, 6, 57, 58, 61
- Hernquist's model** A spherical mass distribution derived by Lars Hernquist that is close to a de Vaucouleurs profile once projected onto the sky. 114, 115, 133
- Hubble modified** A cored DM profile whose surface brightness approximates the Hubble-Reynolds law for elliptical galaxies. 119
- ICM** The intra-cluster medium is a medium mainly composed of hot X-ray emitting gas located between galaxies in galaxy clusters. 41, 44
- IDL** Interactive Data Language is a dynamic proprietary language mainly used for data analysis and data visualisation. 131
- IFS** Integral Field Spectrograph, an instrument that combines spectroscopy and photometry by splitting the FoV in multiple parts that are fed to spectrographs to recover one spectrum per spatial element, thus producing a data cube. 49–53, 55–60, 237, 239
- IFU** Integral Field Unit, an instrument that performs integral field spectroscopy. Some IFS instruments combine multiple IFUs together to observe a large FoV with good spatial resolution. 53, 54, 58–60, 239, 244
- IMF** Initial mass function, the mass distribution of stars originating from a single star formation event when entering the stellar Main Sequence. It describes how likely it is to get a star of a given mass on the stellar Main Sequence as a result of star formation. 73, 75, 80, 82, 208–210, 214, 235
- intrinsic axis ratio** The intrinsic ratio between the scale height and the scale length of a thick disk. This ratio is different from the observed axis ratio on the plane of the sky since the latter is impacted by projection effects. 94, 117, 119
- IR** Infrared, the part of the spectrum located between the visible and the submillimeter that roughly spans from 8000 Å (or similarly 0.8 μm) to 300 μm. 6, 34, 47, 52, 53, 58, 60, 200, 201, 206–208

- ISM** The gaseous and dusty medium located in a galaxy in-between stars. 35, 41, 210
- isochrone** A line of constant age in a stellar evolution diagram. 209
- isophotal fitting** A technique which consists in fitting circular or elliptical isophotes on an image of a galaxy to measure key properties such as its flux, size, or axis ratio. 101
- Jeans' equations** A set of four equations derived by Jeans in 1915 from Boltzmann's equation which describe the dynamics of collisionless particles whose mass is conserved along a flow in phase space. 11, 25–28
- k-correction** A correction that needs to be applied to the flux measured in a given band of redshifted galaxies to recover their intrinsic flux in the band. Indeed, redshifted galaxies see a reduction of their flux and a scaling of the wavelength of their emitted light because of cosmological redshift. Thus, the flux measured in a given band does corresponds to the flux emitted in a narrower band located at shorter wavelengths. To recover the intrinsic flux in the observed band, a correction must be applied that assumes a galaxy's spectrum. 74, 231, 232
- Kuzmin's disk** A theoretical razor-thin disk model with an analytical potential derived by Grigori Kuzmin in 1956. 88, 114
- LBGs** Lyman-break galaxies are galaxies selected from photometric observations in multiple UV and optical filters given that their signal significantly drops below the Lyman limit at 912 Å in rest-frame, since below this limit the radiation is sufficiently energetic to be almost completely absorbed by the neutral gas content of the galaxies. 52
- long-slit spectroscopy** A type of spectroscopic observation where the spectrum of an object is taken along a slit, thus giving 1D spatial plus spectral information at the same time. 48
- LOS** line-of-sight. 6, 24, 27, 32, 83, 125, 126, 210, 240
- LSF** Line Spread Function, the response of a spectrograph to a source whose spectrum is Dirac delta distribution. 51, 69, 71, 125–131
- luminosity distance** A distance in cosmology that appears in the expression relating the luminosity and the flux of an object. 27, 28
- M/L** Mass-to-light ratio defined as the ratio between the mass and the luminosity (or flux depending on definitions) in a given aperture. The mass-to-light ratio can be assumed constant throughout a galaxy or varying. 115, 134, 199, 200, 202, 214, 222, 229, 231–235, 238
- MACHOs** Massive astrophysical compact halo objects are DM candidates that would be composed of baryonic but low-luminosity matter such as black holes, neutron stars, white dwarfs, or brown dwarfs. 45
- MIR** Mid-infrared, a sub-portion of the IR part of the spectrum that spans roughly from 3 μm to 25 μm. 201, 239, 240

- Moffat profile** A PSF profile used to better characterise the outer parts, first derived by Anthony F. J. Moffat in 1969. [72](#), [134](#), [211](#)
- MOND** Modified Newtonian dynamics is a theory of modified gravity proposed by Mordehai Milgrom to account for the missing mass problem in galaxies without relying on DM. [45](#), [239](#)
- MOS** Multi-Object Spectrographs, an instrument that perform spectroscopy on multiple targets at the same time, usually using a bundle of fibres whose position can be placed on the FoV. [34](#), [52](#), [53](#), [59](#), [239](#)
- MS** The Galaxies main sequence is a scaling relation that relates the galaxies' stellar mass to their star formation rate, galaxies with larger stellar masses are also found to be more star-forming. Quenched galaxies are found below the MS and starburst galaxies are found above. [5](#), [6](#), [34](#), [37](#), [38](#), [42](#), [57](#), [73](#), [77](#), [78](#), [80–83](#), [138](#), [238](#)
- MZR** The mass-metallicity relation is a scaling relation observed at low- and high-redshift between stellar mass and gas metallicity. [33](#), [34](#)
- NFW** Navarro-Frenk-White profile, a cuspy DM profile predicted from numerical simulations and extensively used in the literature. [46](#), [114](#), [118](#), [119](#), [133](#), [134](#), [139](#)
- NIR** Near-infrared, a sub-portion of the IR part of the spectrum that goes up to roughly 3 μm . [53](#), [58](#), [59](#), [201](#), [239](#), [240](#)
- OB** Observing Block, a unit observation made of multiple combined single observations with fixed integration time. [6](#), [64](#), [65](#)
- PA** Position angle, the angle between the major axis and a reference direction (usually the north). There two types of PA: (i) the morphological PA which measures the direction of the morphological major axis and (ii) the kinematics PA which measures the direction of the velocity field major axis. [133](#)
- PCA** Principal component analysis is a statistical technique that allows to define a new orthogonal basis where the first vector shares the most variance of the input data, the second vector the second most variance, and so on. [225](#)
- photometric redshift** Redshift measured from a SED obtained from multi-band photometric observation, usually through Bayesian inference. [65](#)
- proper distance** The distance to an object that is measured with respect to a reference distance that does not scale with the expansion of the Universe. Thus, this distance is varies when the Universe is expanding. [24](#), [27](#)
- pseudo isothermal sphere** A cored extension of the isothermal sphere model that avoid that singularity at the centre and that can be used to model DM haloes. [118–120](#)
- PSF** Point Spread Function, the response of an optical system to a point source. [53](#), [55](#), [61](#), [65](#), [69](#), [71](#), [72](#), [127–129](#), [131](#), [134](#), [211](#)

- QSOs** Quasi-stellar objects are particularly luminous AGNs powered by the accretion of material onto a supermassive black hole. 33
- ram-pressure stripping** The removal of cold gas found in galaxies because of the pressure exerted by the ICM. 6, 38, 41
- red sequence** A population of red, passive and mostly elliptical galaxies that is seen in colour-magnitude diagrams and in the MS. 77, 78
- S/N** Signal to Noise ratio, defined as the ratio between the true signal and the noise in an image or in a spectrum. It is a indicator of data quality. 105, 125, 130, 133, 201, 213, 222, 232, 234, 235, 240
- scale height** Scale parameter for the thickness profile of thick disks which can be either a constant or vary with the radius in the plane of the disk. 94, 117
- sech law** A thickness profile derived in the approximation of an isothermal sheet represented by a sech function. 25, 28, 94, 95, 113
- SED** Spectral Energy Distribution, the wavelength or frequency variation of the flux or energy of a source for multiple broad-band filters. 29, 33, 73–75, 78, 80, 139, 199–203, 206–217, 222, 224, 231–235, 240
- SFH** Star formation history, the evolution of the SFR across cosmic time. 73, 75, 77, 78, 80, 82, 208–210, 214, 216, 235
- SFR** Star Formation Rate, a measure of the total mass of new stars being born in a given amount of time. 33, 34, 37–42, 47, 65, 69, 73–75, 77, 78, 80–83, 138, 200, 201, 206, 209, 211, 213, 216, 224, 225
- SHMR** The stellar-to-halo mass relation is a scaling relation that links on a statistical level the stellar mass of the galaxies with the mass of their host dark matter halo. 119, 120
- sky subtraction** Processing step that removes from input data signal coming from foreground and background unresolved sources. 65
- SMF** The stellar mass function is a measure of the comoving stellar mass density as a function of stellar mass. It characterises how many galaxies with a given mass there are. 41
- SOM** A self-organising map, also called Kohonen map, is an unsupervised machine learning algorithm originally created to reduce the number of dimensions in a multi-dimensional dataset. 224–226, 228–235, 240, 244
- spaxel** Spatial pixel, the name given for a pixel in a data cube for a given spectral slice. A spaxel can only vary in space, not in wavelength. 51, 53, 55, 59, 69, 71, 122–126, 128–130, 133, 201, 239, 244
- spexel** Spectral pixel, the name given for a pixel in a data cube along the spectral dimension, that is at a fixed spatial position. 51, 55, 67, 69, 124, 126

- SSP** Single Stellar population, a cluster of stars with various ages all born as a result of the same star formation event. By extension, it designates the spectrum of the whole cluster as a function of time. To model a SSP, one must use a model for stellar evolution and assume given IMF and metallicity. [73](#), [75](#), [208–210](#), [214](#), [216](#)
- starvation** The cessation of cold gas accretion from the CGM. [41](#)
- strangulation** A synonym of starvation. [41](#)
- Sérsic profile** A general parametric profile used to describe the surface brightness distribution of disk-like and elliptical galaxies, derived by José Luis Sérsic.. [88](#), [89](#), [97](#), [99](#), [102](#), [113](#), [201](#)
- TFR** Tully-Fisher relation, a scaling relation between stellar mass or luminosity and velocity first described by Richard Brent Tully and James Richard Fisher in 1977. [6](#), [33–35](#), [37](#), [39](#), [43](#), [80](#), [137](#), [138](#), [238](#)
- thermal evaporation** The removal of the cold gas in a galaxy through heating when interacting with the hot ICM. [38](#), [41](#)
- throughput** The efficiency of an optical system to let light pass through. It characterises the loss of incoming flux from the beginning of the optics to the detector at the end. [51](#), [206](#), [207](#)
- total-to-selective extinction ratio** R_V , the ratio of the total extinction in the V band over the difference between the extinctions in the B and V bands.. [74](#), [75](#)
- UV** Ultraviolet, the part of the spectrum located between the X-ray part and the visible that roughly spans from 100 Å to 3000 Å. [33](#), [34](#), [58](#), [200](#), [201](#), [210](#), [240](#)
- WCS** World coordinate system, the physical coordinates attached to some observations to locate them on the sky. [211](#)
- WDM** Warm Dark Matter, an type of DM that has a theoretical mass below that of CDM but above that of neutrinos. [44](#)
- wide-field mode** The largest of the two observing modes for MUSE with a $1' \times 1'$ FoV and pixel scale of $0.2''$. [61](#)
- Zhao** A parametric DM profile first suggested by HongSheng Zhao. [118](#)

First author or significant contributions

- Epinat et al. (in prep.)** MAGIC: MUSE-gALaxy Groups In Cosmos - I. A survey of galaxies in groups at intermediate redshift
Paper describing the MAGIC survey. It includes the observing strategy, an evaluation of its completeness, a description of the spectroscopic redshift determination, the structure determination, and a thorough discussion of the morpho-physical properties of the galaxies as a function of environment.
Contribution: Morphological and kinematics modellings of the galaxies, measurements of their key properties ([OII] flux, bulge-to-total flux ratio, size, DM fraction, velocity dispersion, etc.), pre-analysis of the morpho-dynamics dependence of galaxies with environment
Keywords: *Galaxy morpho-dynamics, large spectroscopic survey, galaxy groups/clusters, structure characterisation, red sequence, HST, MUSE, MAGIC*
- Mercier et al. (in prep., 2023)** Impact of the environment on the angular momentum of $z \sim 0.25 - 1.5$ galaxies in the MAGIC survey
Analysis of the stellar angular momentum as a function of environment, bulge fraction, and stellar mass for intermediate redshift galaxies in the MAGIC survey. This paper includes a new method to derive the galaxies' angular momentum that uses high-resolution HST images and robust kinematics mass models derived from MUSE data. This analysis discusses mainly the impact of the environment on the Fall relation and how this relates to the fraction of mass found in galactic bulges. We show that massive galaxies are depleted in angular momentum by $\sim 20\%$ with respect to the field and that it correlates with high-density environments.
Contribution: Nearly everything. Including for the major parts: the development of the new method to measure angular momentum, the sample selection, assessment of the method performance, analysis, and writing of the entire paper.
Keywords: *Galaxy dynamics, angular momentum, Fall relation, galaxy groups/clusters, bulges, HST, MUSE, MAGIC*
- Mercier et al. (2022)** Scaling relations of $z \sim 0.25 - 1.5$ galaxies in various environments from the morpho-kinematics analysis of the MAGIC sample
A self-consistent joint analysis of the size-mass relation, MS relation, and TFR for galaxies in the field and in environments of various density. The galaxies' morphology is obtained from high-resolution HST images and the ionised gas kinematics from deep MUSE observations of intermediate redshift galaxies in the MAGIC survey using a mass modelling approach. Our self-consistent analysis and robust sample selection allow us to put the strongest constraints up to date on the impact of the environment on these scaling relation at $z \sim 0.7$. We find that there is a visible impact of massive structures on the size and SFR of galaxies at fixed stellar mass but that their dynamics is unaffected.
Contribution: Nearly everything. Including for the major parts: the morpho-kinematics modelling, sample selection, full analysis, and redaction of the entire paper. Excluding: data reduction.
Keywords: *Galaxy morpho-kinematics modelling, mass models, ionised gas, size-mass relation, main sequence relation, Tully-Fisher relation, galaxy groups/clusters, quenching, baryon contraction, dark matter fraction, 3D spectroscopy, HST, MUSE, MAGIC*
- Bouché et al. (2022)** The MUSE Extremely Deep Field: Evidence for SFR-induced cores in dark-matter dominated galaxies at $z \approx 1$
A dynamical analysis of nine $z \approx 1$ emission line galaxies in the ultra deep MXDF survey using a mass modelling approach. The high S/N of these galaxies combined with our robust 3D modelling approach allowed to constrain the shape of DM haloes at intermediate redshift. We find that DM cores are preferred over cuspy profiles and that they correlate with higher SFR, showing an interplay between feedback processes and the formation of cored DM profiles in intermediate redshift galaxies.
Contribution: Morphological modelling used in the mass models and in the kinematics modelling of the ionised gas
Keywords: *Galaxy dynamics, mass modelling, ionised gas, dark matter, cusp-core problem, 3D spectroscopy, HST, MUSE, MXDF*
- Abril-Melgarejo et al. (2021)** The Tully-Fisher relation in dense groups at $z \sim 0.7$ in the MAGIC survey
First analysis with the MAGIC survey of the TFR as a function of environment. Our MUSE-derived galaxies' kinematics is compared to that of other galaxies in shallower groups. An effect of the environment is found, consistent with baryon contraction and/or quenching.
Contribution: Morphological characterisation and sample selection for the analysis of the TFR as a function of environment.
Keywords: *Galaxy morphology & 2D kinematics, 3D spectroscopy, MUSE, HST, TFR, large spectroscopic survey, ionised gas*
- Richard et al. (2021)** An atlas of MUSE observations towards twelve massive lensing clusters
A large and deep spectroscopic survey of 12 massive lensing clusters observed with MUSE providing spatially resolved observations of galaxies in clusters and magnified background sources.
Contribution: Led the Toulouse redshift determination team.
Keywords: *Galaxy clusters, strong lensing, 3D spectroscopy, MUSE, large spectroscopic survey, redshift measurement*

Minor contributions

- Langan et al. (in prep., 2023)** MusE GAS FLOW and Wind (MEGAFLOW) IX. The impact of gas flows on the relations between the mass, star formation rate and metallicity of galaxies
A joint analysis of the MS relation, MZR, and FMR for galaxies with and without gas inflows/outflows at intermediate redshift. Current results suggest a link between (i) the SFR and inflow event and (ii) the metal content and outflow events, visible in the three scaling relations.
Keywords: *Gas flows, MgII absorption, main sequence relation, mas-metallicity relation, fundamental metallicity relation, MUSE, X-SHOOTER*
- Bouché et al. (2021)** The MUSE Hubble Ultra Deep Field Survey. XVI. The angular momentum of low-mass star-forming galaxies: A cautionary tale and insights from TNG50
A joint analysis of the angular momentum of the ionised gas for galaxies in the MUSE-HUDF survey and in the TNG50 simulation. The key result is the discovery of a correlation between the scatter in the relation and the dynamical states of galaxies.
Keywords: *Galaxy dynamics, angular momentum, Fall relation, ionised gas, MUSE, TNG50*

Proceedings

- Bouché et al. (2021)** Cored dark-matter profiles in $z \approx 1$ star forming galaxies
Presentation of the analysis of the shape of the dark matter haloes for nine galaxies in the MXDF survey.
Keywords: *Galaxy dynamics, mass modelling, dark matter, core-cusp problem, ionised gas, MUSE, MXDF*
- Mercier et al. (2021)** Morpho-kinematics of galaxies in various environments at $z \sim 0.2 - 1.5$
Presentation of the first results of the analysis of the impact of the environment on the dynamics of galaxies at intermediate redshift in the MAGIC survey.
Keywords: *Galaxy dynamics, mass modelling, Tully-Fisher relation, ionised gas, MUSE, MAGIC*

Appendices

Appendix A

List of major MUSE surveys

Below are listed¹ the main GTO and non-GTO MUSE surveys that are related to the study of galaxy evolution.

A.1 Main GTO MUSE surveys

Several important GTO surveys have been carried out thanks to MUSE. On the topic of galaxy evolution the main ones are:

- (i) MUSE-HDFS described in [Bacon et al. \(2015\)](#), the first deep observation (27 h) carried out with MUSE over a portion of the Hubble Deep Field South (HDFS) and whose goal was to assess the performance of the instrument for long integration times during its commissioning. Its most significant scientific results were the first ionised gas kinematics analysis of intermediate redshift galaxies that especially probed low-mass galaxies ([Contini et al. 2016](#)) and the discovery of extended Ly α haloes at high redshift ([Wisotzki et al. 2016](#)).
- (ii) MUSE-WIDE ([Herenz et al. 2017](#); [Urrutia et al. 2019](#)), a shallow survey (1 h integration time) targeting a large area made of 100 different MUSE pointings following the release of the MUSE-HDFS. It is complementary to the MUSE-HUDF survey.
- (iii) MUSE-HUDF ([Bacon et al. 2017](#)), a deep and ultra-deep MUSE survey following the release of the MUSE-HDFS that was complementary to MUSE-WIDE. Its approach was to observe first a mosaic of nine MUSE fields (hereafter MOSAIC) with a total integration time of roughly 10 h over an area of almost 10 square arcminutes and then a tenth field (hereafter UDF-10) that partially overlap the MOSAIC with an ultra-deep integration time of 31 h. Significant contributions concerning intermediate and/or high redshift galaxies were the first spatially resolved stellar kinematics modelling at $0.2 \lesssim z \lesssim 0.8$ ([Gu erou et al. 2017](#)), the study of galactic winds at $z \approx 1.3$ ([Finley et al. 2017](#)), the measurement of the evolution of the fraction of galaxy mergers up to redshift $z \approx 6$ ([Ventou et al. 2017](#)), constraining the low-mass end of the galaxy MS relation ([Boogaard et al. 2018](#)), exploring the physical origin

¹The list is not intended to be exhaustive but rather to give a census of the important surveys that have impacted the field.

of Mg II emission seen in some star-forming galaxies (Feltre et al. 2018), or studying the angular momentum of the ionised gas in galaxies as a function of their redshift and dynamical state (Bouché et al. 2021).

- (iv) MusE GAs FLOW and Wind survey (MEGAFLOW) that observed 79 Mg II absorbers located along the LOS of 22 selected quasars to study galactic super-winds, inflows, and outflows in intermediate redshift galaxies (Schroetter et al. 2016, 2019, 2021; Bouché et al. 2016; Zabl et al. 2019, 2021).
- (v) MXDF (Bacon et al. 2021), an extremely deep survey located within the MOSAIC and that partially overlaps the UDF-10 field and uses AO. Its design that involves a rotation of the FoV of a few degrees between each OB allows extremely deep observations of 140 h in an inner circle of 1' in diameter and deep observations of around 10 h in the outer parts. Among important results we can cite the detection of Ly α emission that traces the cosmic web at redshift $3 \lesssim z \lesssim 4.5$ (Bacon et al. 2021), constraining the DM profile inner slope of $z \approx 1$ star-forming galaxies (Bouché et al. 2022), or the serendipitous detection of a large Mg II emission nebula that spans the intra-group medium of a galaxy group located at $z \approx 1.3$ (Leclercq et al. 2022).
- (vi) MAGIC (Epinat et al., in prep.), a deep survey of 17 MUSE fields that was specifically designed to study the impact of the environment on the dynamics of galaxies at $z \sim 0.7$ by targeting already known structures in the COSMOS field as well as foreground and background sources (see Chapter 3 for more details). Current publications concern the first detection of ram-pressure stripping at $z \sim 0.7$ (Boselli et al. 2019), the serendipitous detection of a unique large ionised gas structure in a galaxy group (Epinat et al. 2018), and the study of the impact of the environment on the TFR, MS relation, and size-mass relation at intermediate redshift (Abril-Melgarejo et al. 2021; Mercier et al. 2022).
- (vii) MUSCATEL (PIs: Lutz Wisotzki, Roland Bacon, and Thierry Contini), an ongoing deep MUSE survey with AO targeting four parallel fields in the HFF survey (Lotz et al. 2017). The design is composed of one deep 25 h observation per parallel field surrounded by four 5 h FoVs and nine shallower FoVs of roughly 2 h that map the entire four parallel fields observed by the HST and SPITZER. The fact that the survey targets parallel fields allows to minimise the effect of lensing while still having access to the deepest HST observations ever taken combined with deep IR SPITZER data. Expected science cases are the study of the physical mechanisms at the origin of high-redshift Ly α haloes and their dependence on environment, as well as building a statistically significant large sample of intermediate redshift galaxies to study their spatially resolved dynamics.

A.2 Main non-GTO MUSE surveys

Similarly, important non-GTO surveys that probe the evolution of galaxies have also been carried out with MUSE, including:

- (i) GAs Stripping Phenomena in galaxies with MUSE (GASP) described in Poggianti et al. (2017), a survey aimed at studying with MUSE gas stripping phenomena by observing galaxies in the local Universe. It has led to a significant series of publications on that topic,

starting with Poggianti et al. (2017) and currently continuing with Luber et al. (2022) and Deb et al. (2022).

- (ii) Middle Ages Galaxy Properties with Integral Field Spectroscopy (MAGPI) described in Foster et al. (2021), an ongoing survey targeting 60 central galaxies and around 100 satellites located in galaxy clusters at $z \approx 0.3$. Based on predictions from simulations, this survey was specifically designed to maximise the chance to probe the impact of the environment on galaxy properties.
- (iii) MUSE Ultra Deep Field (MUDF) described in Lusso et al. (2019) and Fossati et al. (2019), an extremely deep survey of 200 h on-source integration time made of two largely overlapping MUSE field. The survey targeted a region of the sky with multiple structures and two bright quasars that allowed the detection of seven galaxy groups at $0.5 < z < 1.5$, four of which showed the presence of cold gas in the intra-group medium through Mg II absorption.
- (iv) MUSE and ALMA Unveiling the Virgo Environment (MAUVE)², a future survey that will combine MUSE and Atacama Large Millimeter/submillimeter Array (ALMA) observations of 40 massive disk galaxies in the Virgo cluster. The survey is designed to study the link between the cold gas found in galaxies, star formation, and the galaxies' environment.

²<https://astronomyaustralia.org.au/blog/news/australian-based-astronomers-to-take-a-deep-dive-into-the-cosmos-with-time-awarded-on-one-of-esos-most-powerful-instruments/>

Appendix B

MAGIC field-of-views

Here are shown the MUSE FoVs for the 15 targeted groups. Even though these figures illustrate the MAGIC survey and are discussed in various parts of Sect. 3, I moved them to their own appendix to save space in the main part of the manuscript.

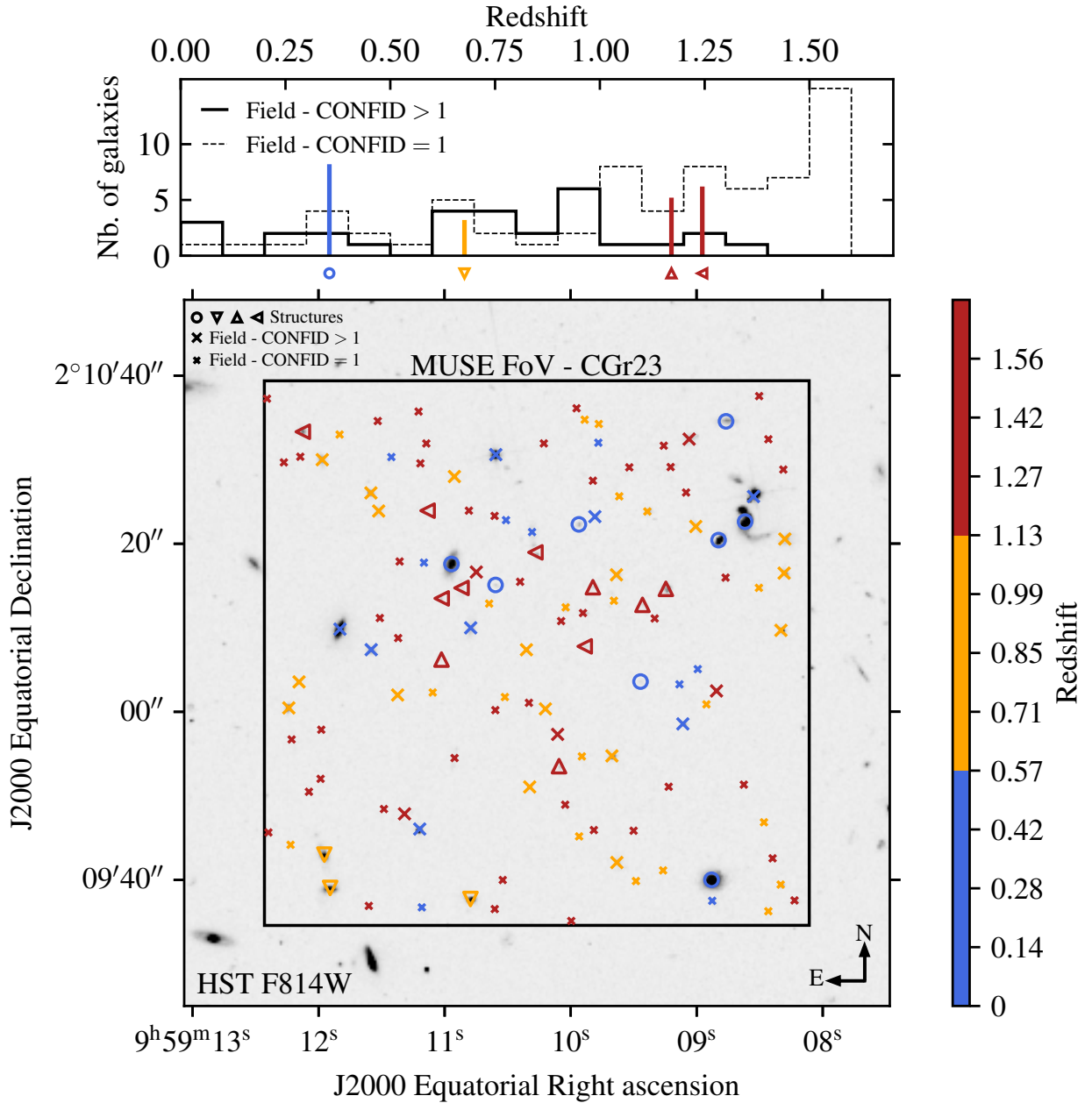


Figure B.1: HST image of the MUSE observation CGR23. The main MUSE FoV is represented as a square with dimensions roughly equal to $1' \times 1'$, with north and east pointing up and left, respectively. The galaxies observed in the FoV are colour-coded according to their MUSE spectroscopic redshift. Field galaxies are shown with crosses whereas each structure is shown with its own marker (see the top left part of the main plot). Field galaxies with low confidence flag (CONFID) are shown with smaller markers (by definition there are no such galaxies in the structures). On the top is shown the redshift histogram for field galaxies, segregated between low (black dashed line) and high (black solid line) CONFID value. The structures are shown with vertical lines with the same colour as that of the galaxies in the main plot and below each line is shown the corresponding symbol used in the main plot.

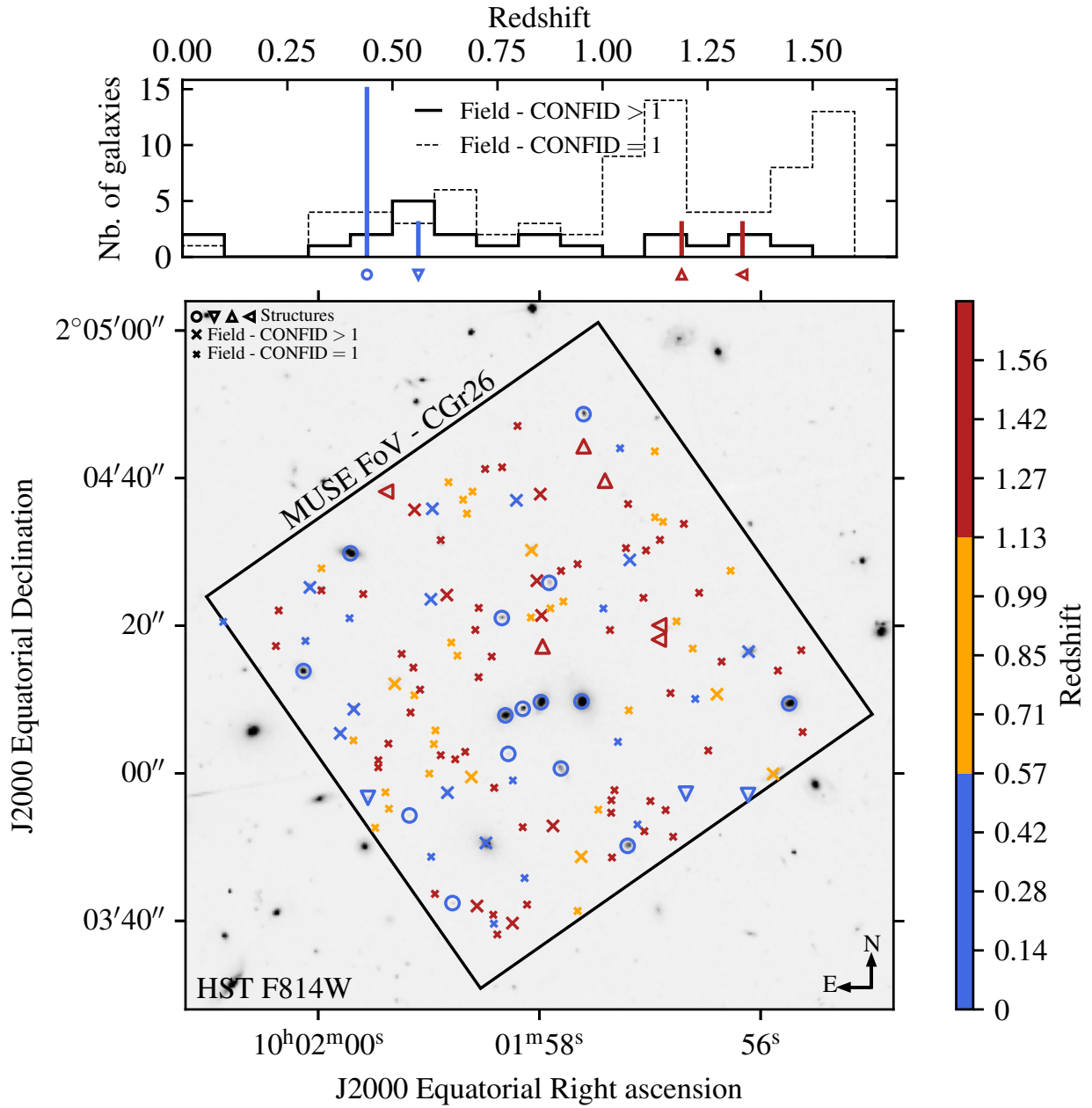


Figure B.2: HST image of the MUSE observation CGR26. See Fig. B.1 for the legend.

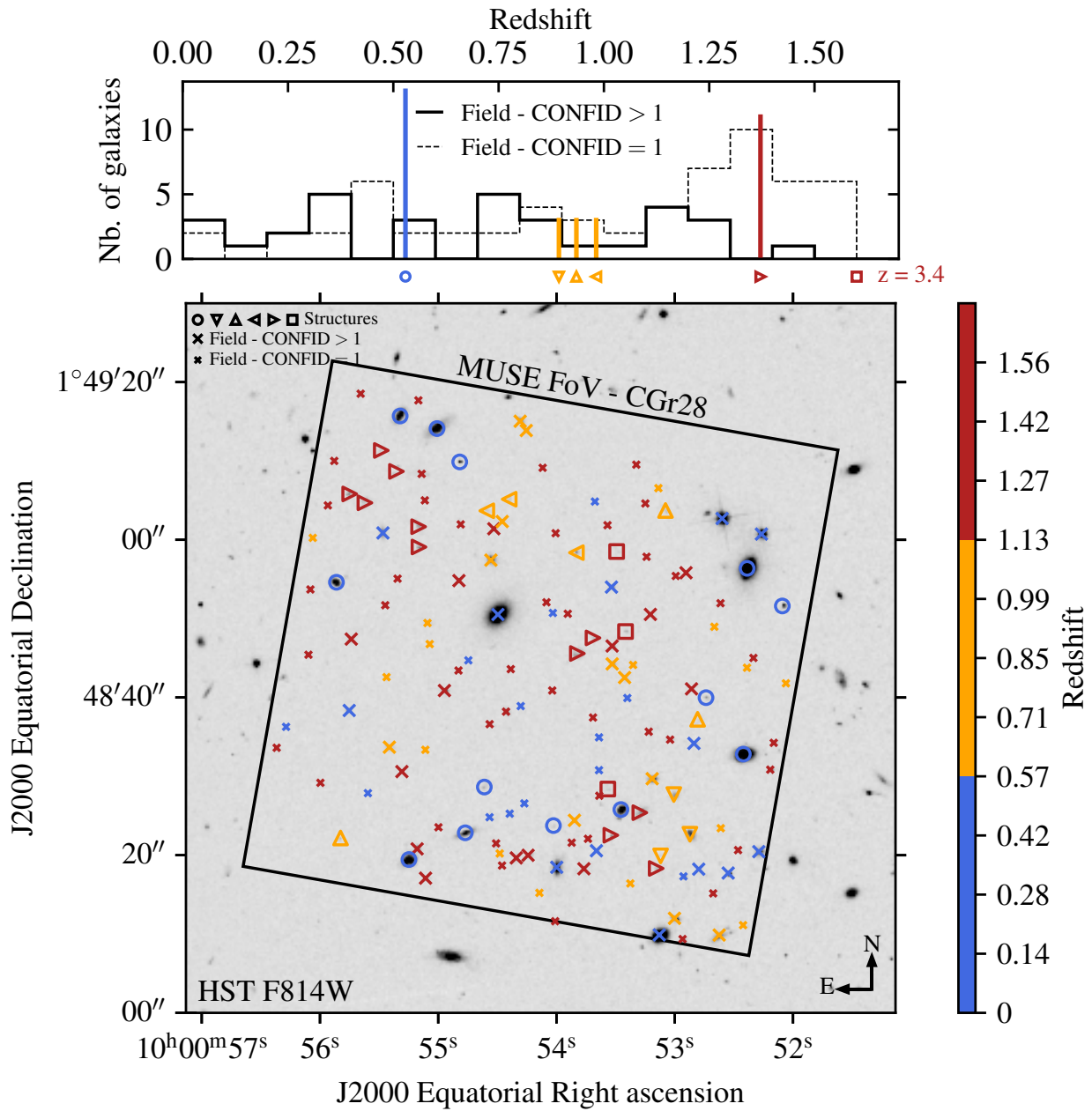


Figure B.3: HST image of the MUSE observation CGR28. See Fig. B.1 for the legend. One group is not shown in the histogram because its redshift is beyond the plot limits but its symbol and its redshift are indicated below.

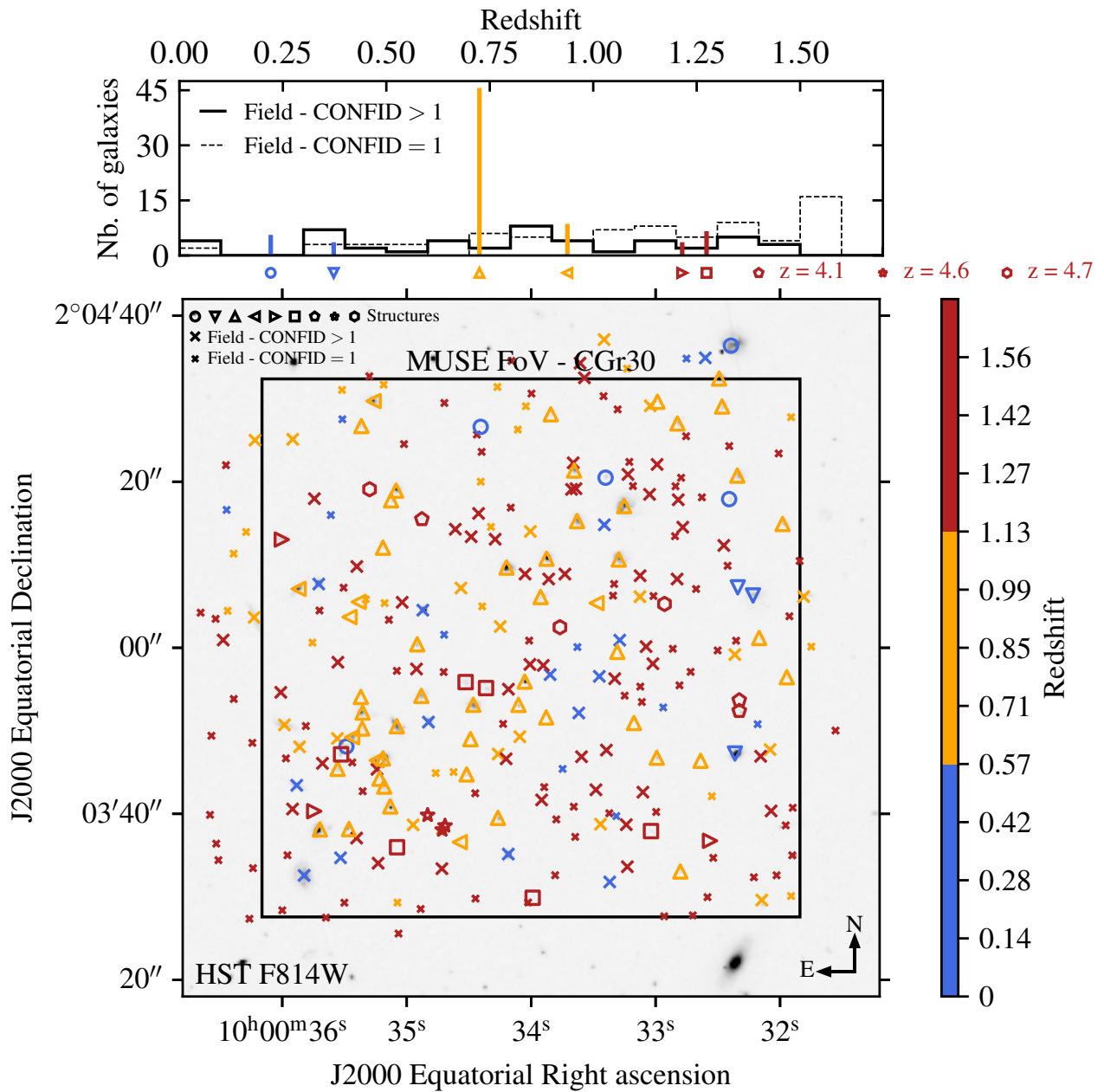


Figure B.4: HST image of the MUSE observation CGR30. See Fig. B.1 for the legend. Three groups are not shown in the histogram because their redshift is beyond the plot limits, but their symbol and their redshift are indicated below. The reason why a large number of galaxies is found beyond the FoV limits is that these galaxies were observed in an early snapshot at the result of which the FoV was rotated by roughly 30° and its centre was moved to the south west.

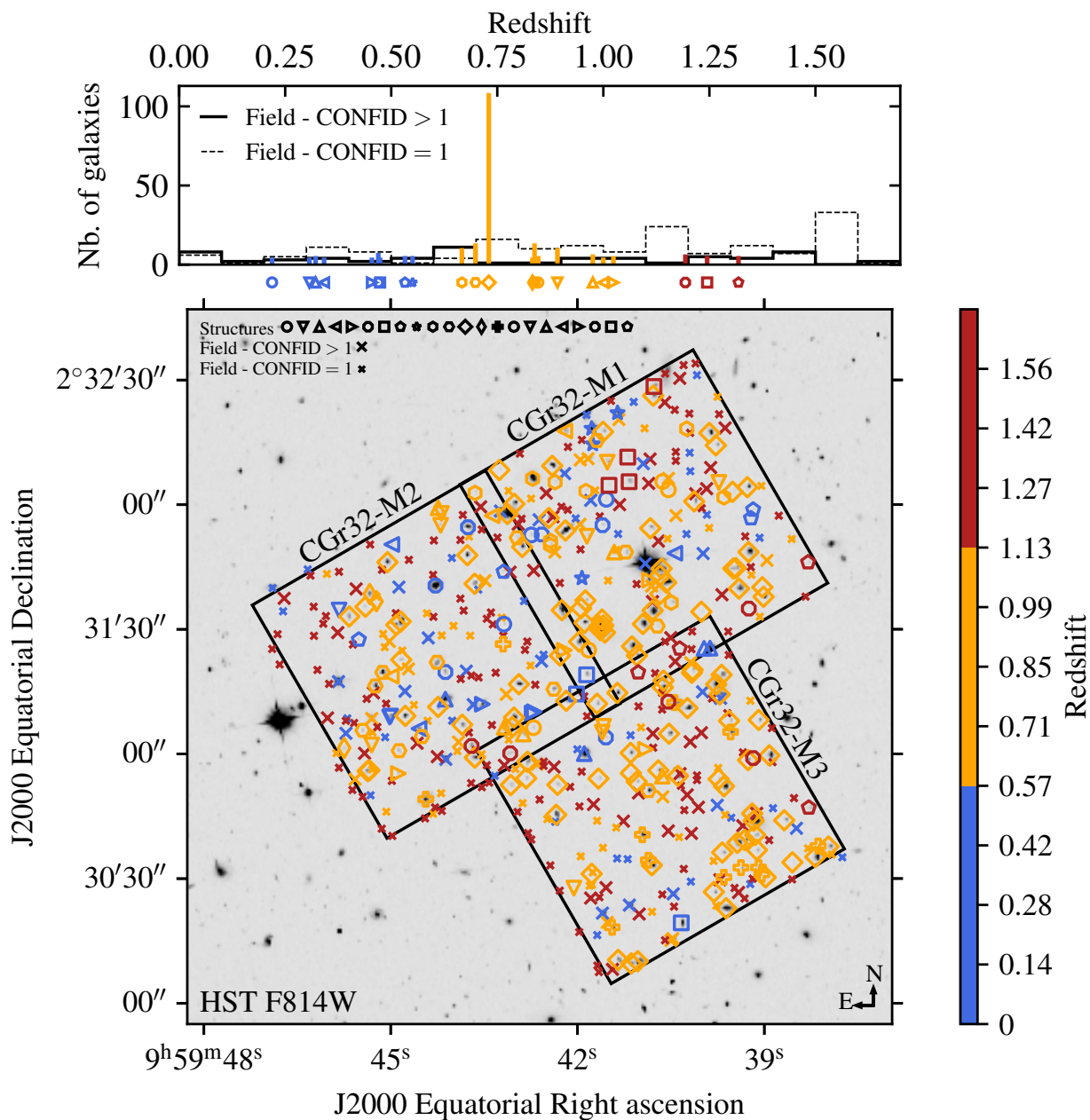


Figure B.5: HST image of the MUSE observation CGR32. See Fig. B.1 for the legend.

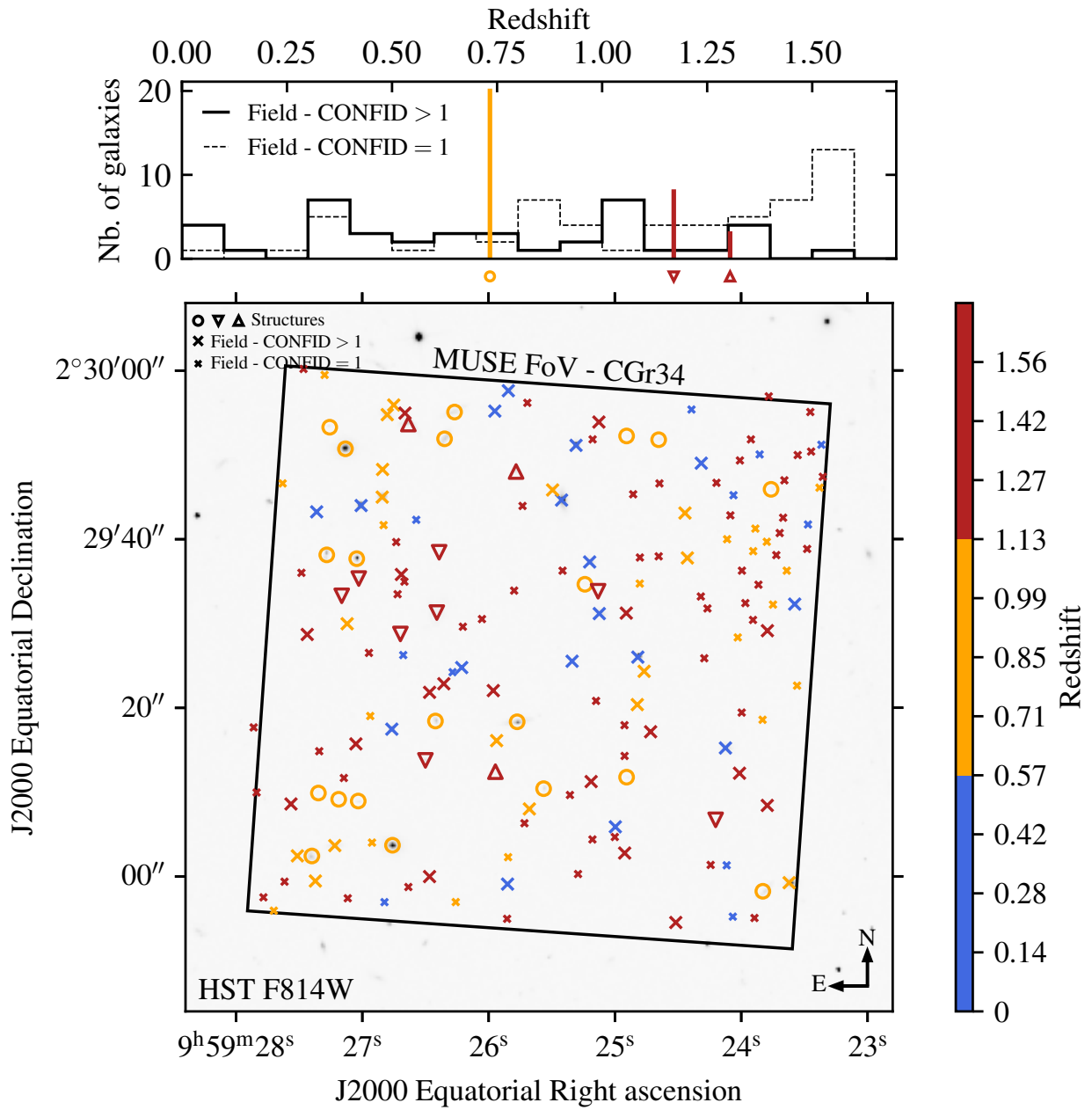


Figure B.6: HST image of the MUSE observation CGR34. See Fig. B.1 for the legend.

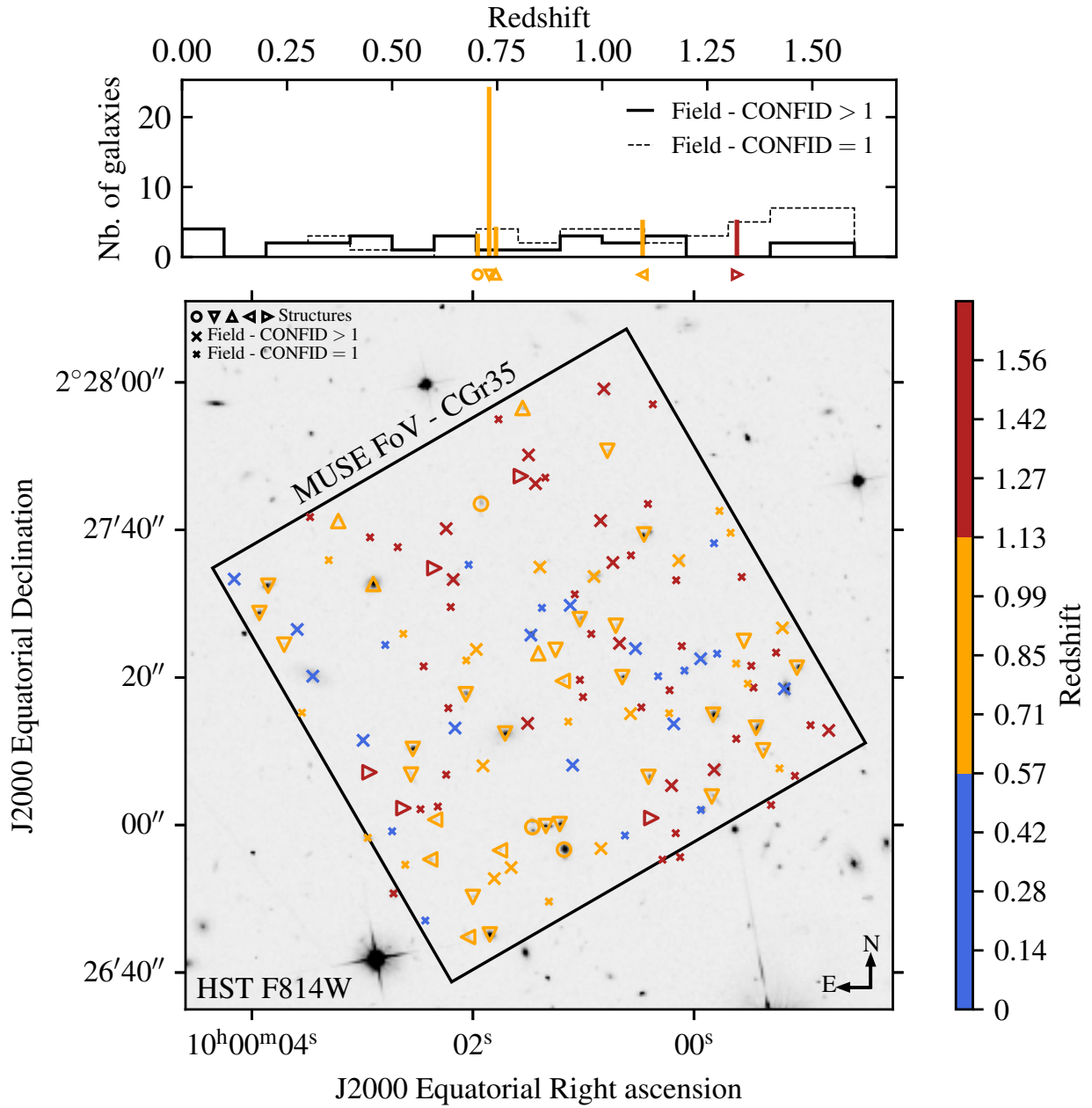


Figure B.7: HST image of the MUSE observation CGR35. See Fig. B.1 for the legend.

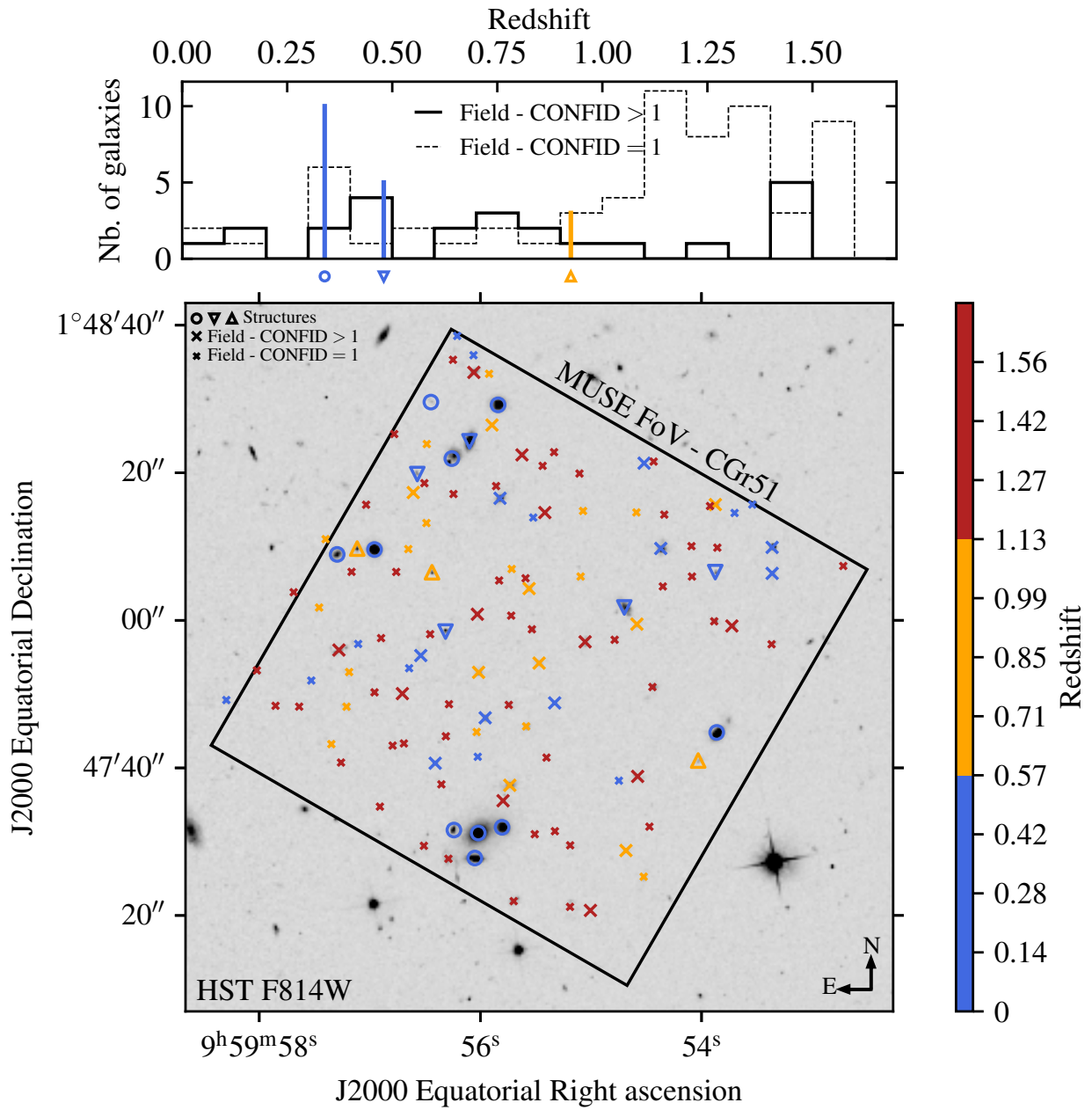


Figure B.8: HST image of the MUSE observation CGR51. See Fig. B.1 for the legend.

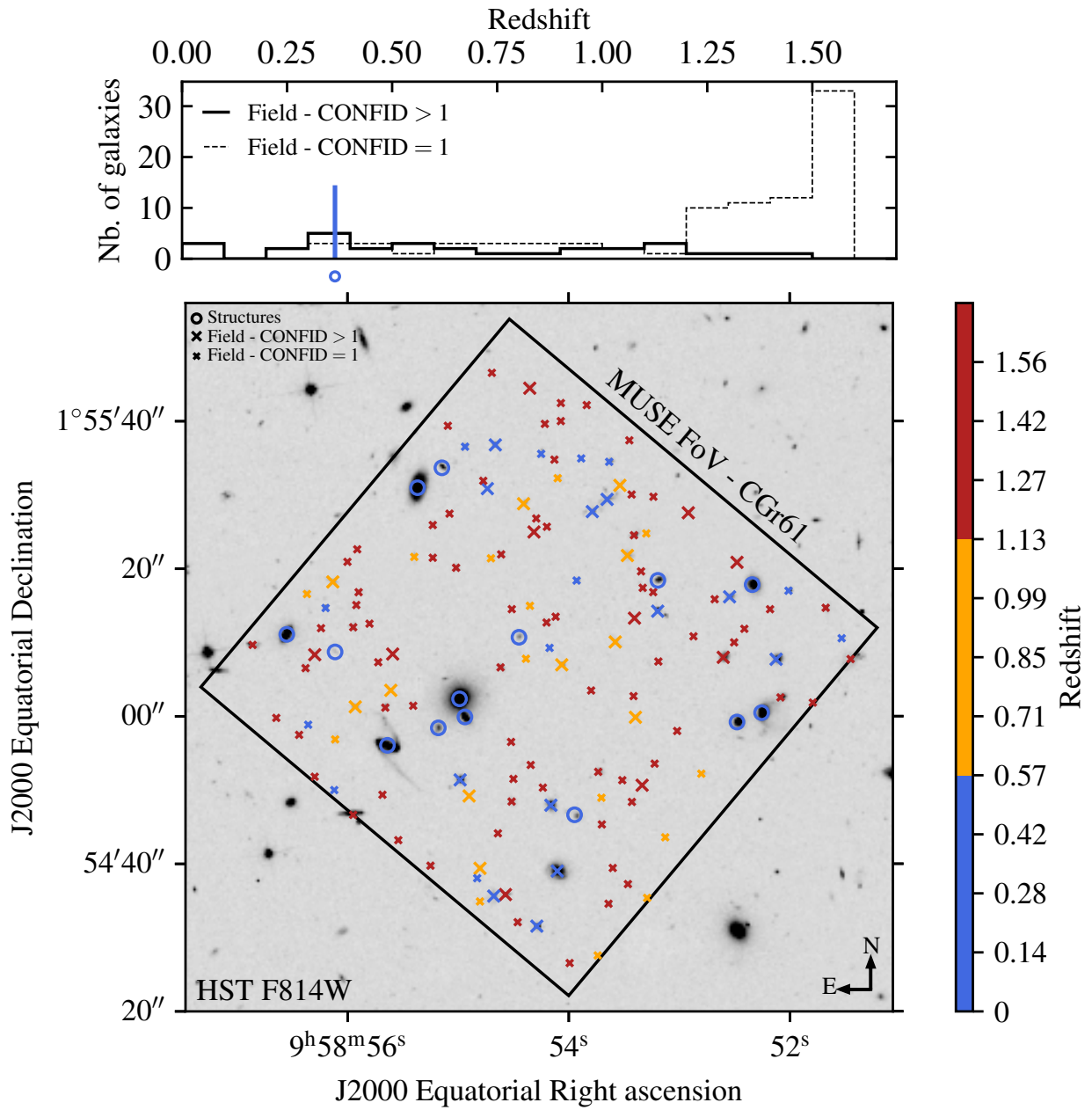


Figure B.9: HST image of the MUSE observation CGR61. See Fig. B.1 for the legend.

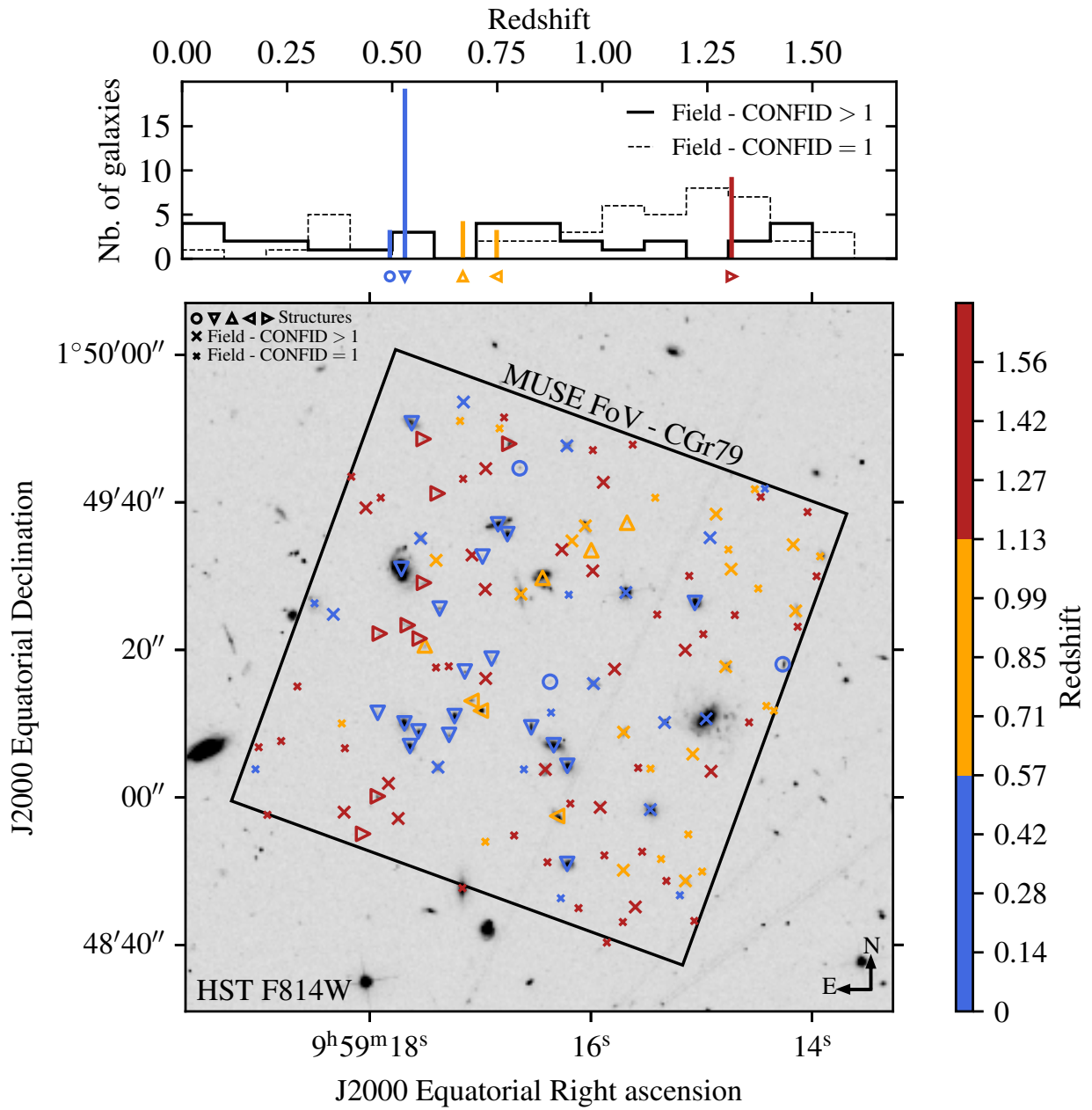


Figure B.10: HST image of the MUSE observation CGR79. See Fig. B.1 for the legend.

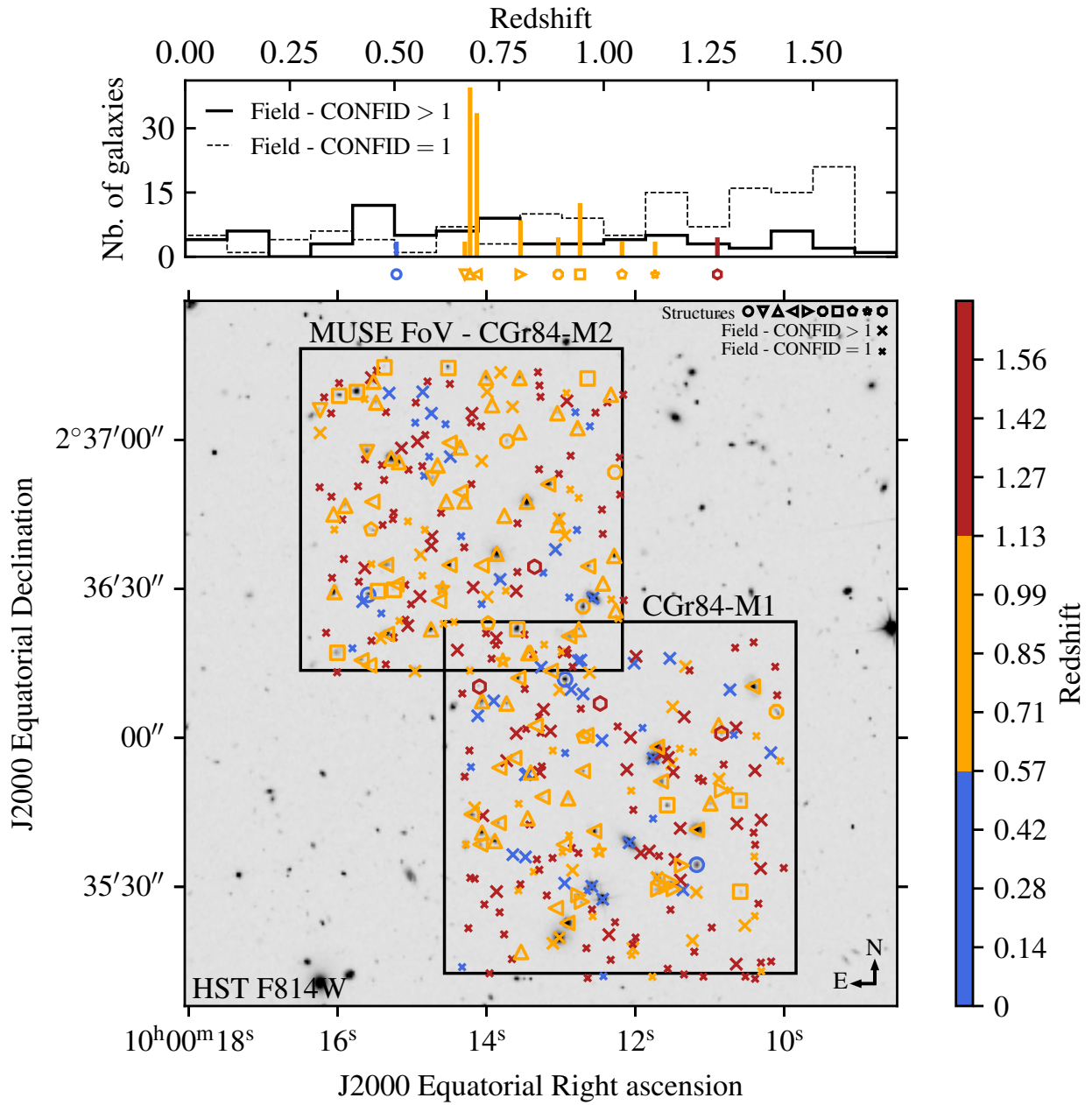


Figure B.11: HST image of the MUSE observations CGR84-M1 and CGR84-M2. See Fig. B.1 for the legend.

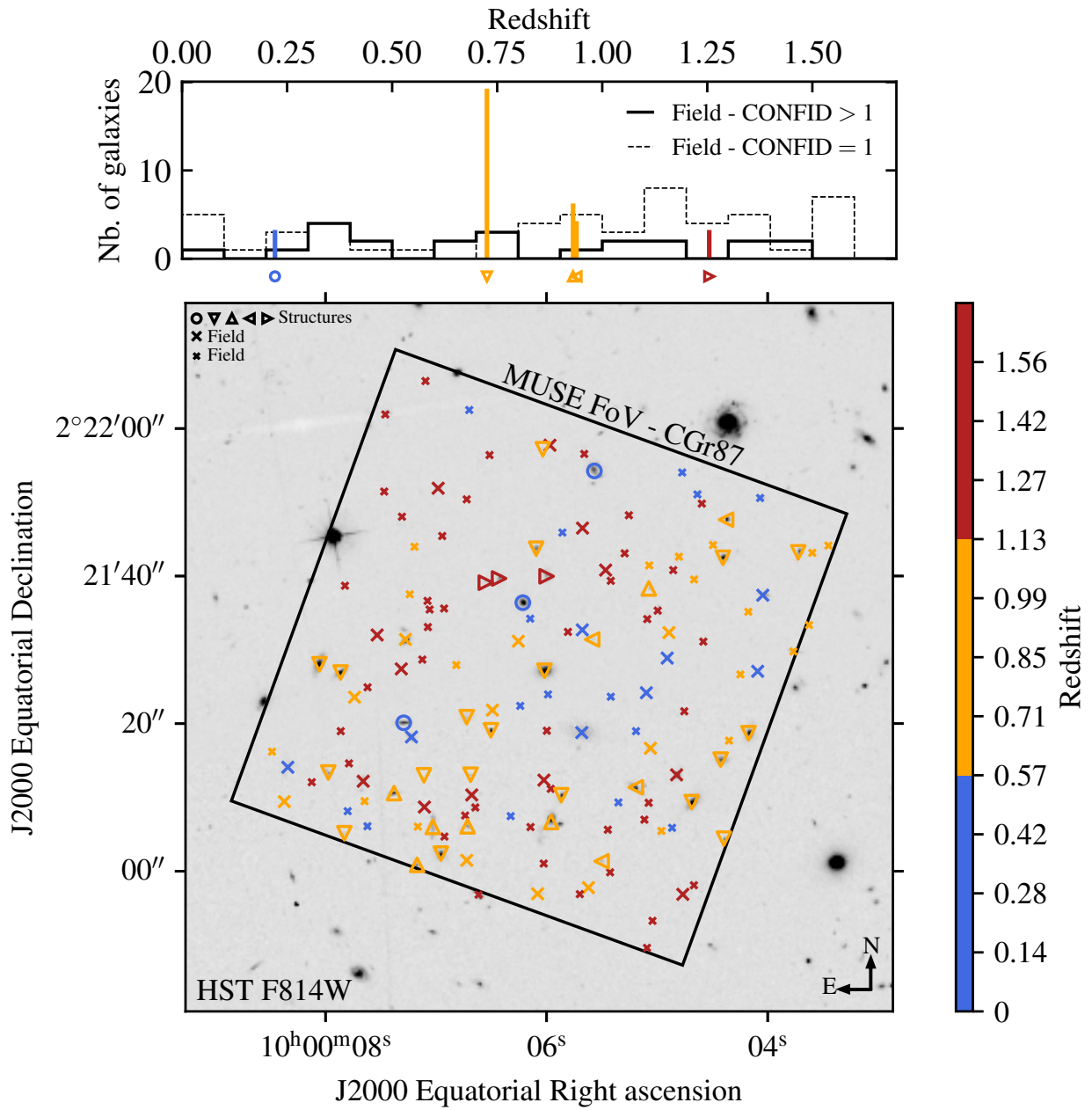


Figure B.12: HST image of the MUSE observation CGR87. See Fig. B.1 for the legend.

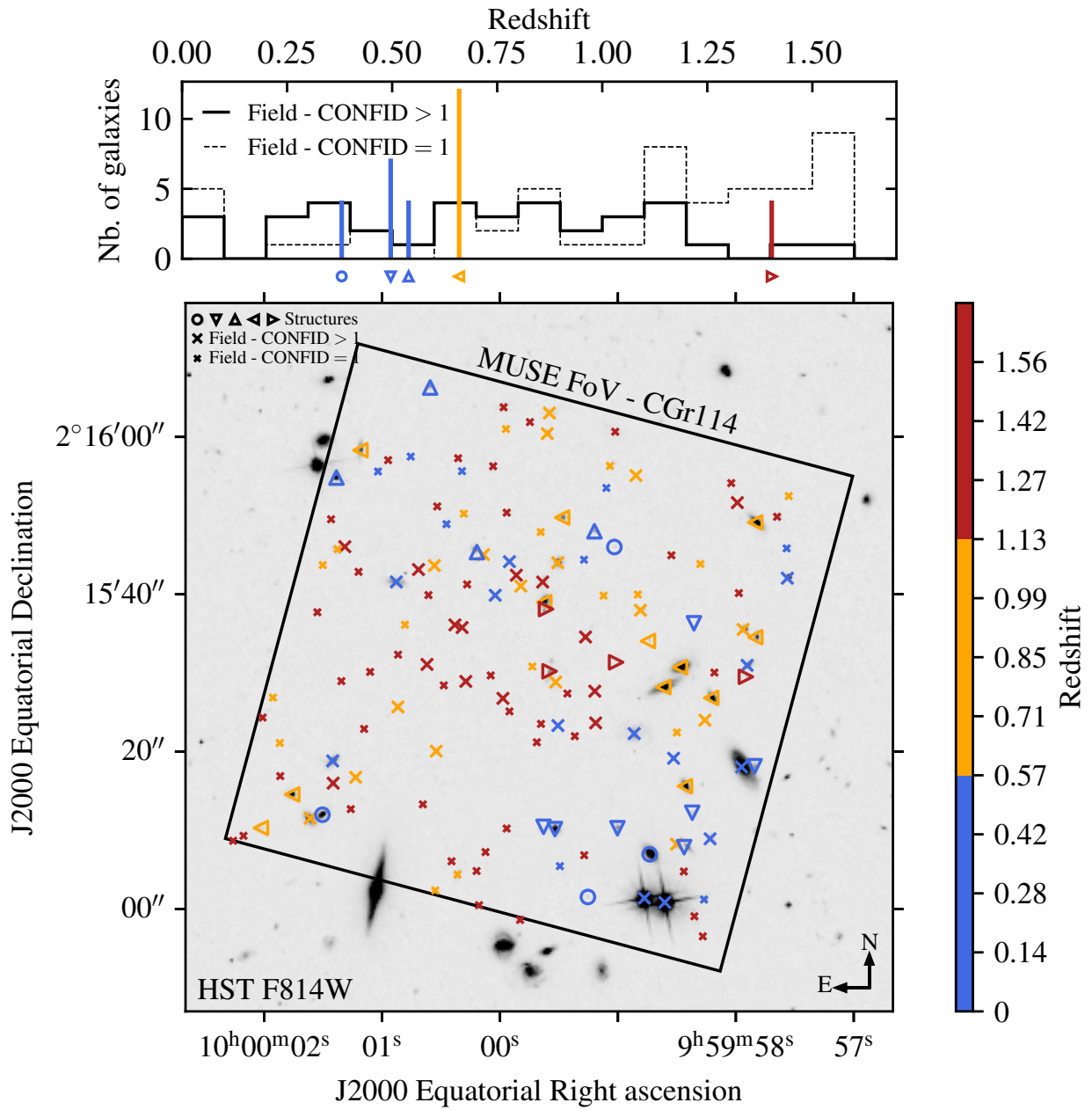


Figure B.13: HST image of the MUSE observation CGR114. See Fig. B.1 for the legend.

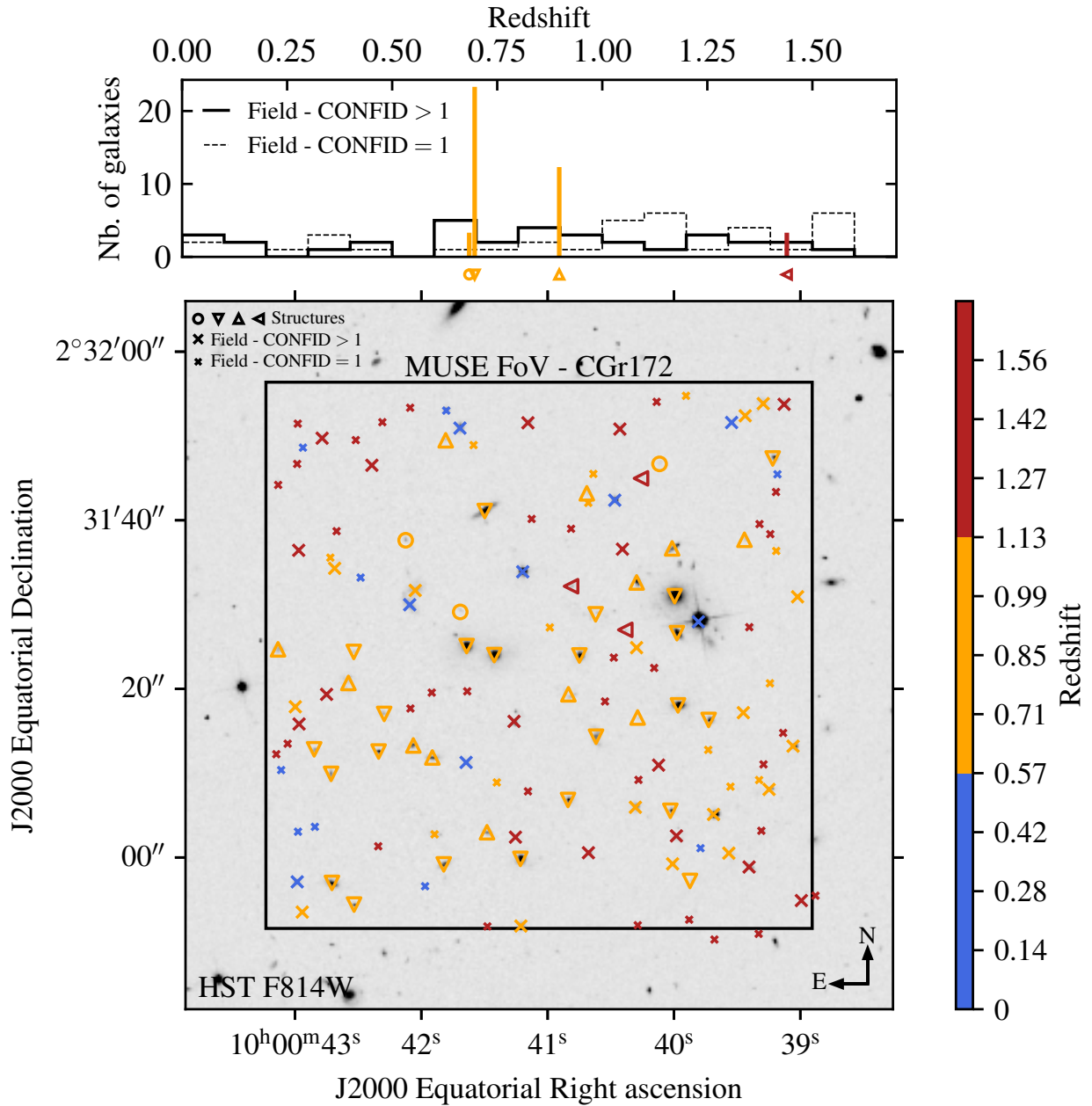


Figure B.14: HST image of the MUSE observation CGR172. See Fig. B.1 for the legend.

Appendix C

Derivation of the Jeans' equations and their applications

In this section, we provide a complete derivation of the theoretical thickness profile one can get for a disk galaxy when making the isothermal sheet approximation. This derivation was first proposed by [Spitzer \(1942\)](#) and [Camm \(1950\)](#) as an analytical solution for a self-gravitating distribution of stars. Here, the term "isothermal sheet" refers to the assumption that the velocity dispersion and thus the temperature do not vary with z , where z represents the vertical coordinate with respect to the $x - y$ plane of symmetry of the disk galaxy. The reason to provide the derivation in this appendix was twofold: (i) to give a quick access for any reader having a look at [Sect. 4.1.2.2](#) who might be interested in the derivation of the sech law and (ii) to have a concise and hopefully clear version of the demonstration that uses more modern notations for some parts.

C.1 From Boltzmann's to Jeans' equations

First, let us start with the derivation of the Jeans' equations since they are the basis for both the asymmetric drift correction discussed in [Sect. 5.2.2](#) and the theoretical thickness profile for the isothermal sheet in [Sect. 4.1.2.2](#). The starting point of the derivation is to consider that stars are collisionless particles that can be described by their distribution function $f(t, \vec{x}, \vec{v})$ and that their mass is conserved along a flow in phase space, that is $df/dt = 0$. This is the so-called Boltzmann's equation:

$$\frac{\partial f}{\partial t} + \frac{d\vec{x}}{dt} \cdot \vec{\nabla} f + \frac{d\vec{v}}{dt} \cdot \vec{\nabla}_{\vec{v}} f = 0, \quad (\text{C.1})$$

where we have made the following definitions

$$\vec{\nabla} = \sum_i \frac{\partial f}{\partial x_i} \hat{e}_i \quad \vec{\nabla}_{\vec{v}} = \sum_i \frac{\partial f}{\partial v_i} \hat{e}_i \quad (\text{C.2})$$

$$d\vec{x}/dt = \sum_i \frac{dx_i}{dt} \hat{e}_i \quad d\vec{v}/dt = \sum_i \frac{dv_i}{dt} \hat{e}_i. \quad (\text{C.3})$$

The first line corresponds to the gradient operators in position and velocity space, respectively, and the second line represents the vectors of the time derivative of the position and velocity vector coordinates, respectively. We note that, depending on the coordinate system used, these two vectors may not correspond to the velocity and acceleration vectors since they do not take into account the time derivative of the basis vectors. In other terms, based on the coordinate system used, the following equalities may not hold: $d\vec{x}/dt = d\vec{x}/dt$ and $d\vec{v}/dt = d\vec{v}/dt$.

C.2 Jeans' equations in Cartesian coordinates

In Eq. C.1, we see the acceleration which, in Cartesian coordinates, matches the gradient of the gravitational potential Φ , and we also have $\vec{v} = d\vec{x}/dt$. Thus, Boltzmann's equation becomes

$$\frac{\partial f}{\partial t} + \vec{v} \cdot \vec{\nabla} f - \vec{\nabla} \Phi \cdot \vec{\nabla}_{\vec{v}} f = 0. \quad (\text{C.4})$$

Let us remind a few important properties of the distribution function. To start with, depending on the convention used, the integral of f in phase space yields either the total number of stars or the total stellar mass at time t . In what follows, we will use the latter convention. Thus, it follows that the integral of f in velocity space yields the stellar mass density ρ_M , that is

$$\rho_M = \int_{\vec{v} \in \mathbb{R}^3} d^3 \vec{v} f. \quad (\text{C.5})$$

Another useful property is that for all i, j the integral of $v_j \partial f / \partial v_i$ in velocity space always yields 0 if $i \neq j$ and $-\rho_M$ otherwise since we have

$$\begin{aligned} \int_{\vec{v} \in \mathbb{R}^3} d^3 \vec{v} v_j \frac{\partial f}{\partial v_i} &= \underbrace{[v_j f]_{-\infty}^{+\infty}}_0 - \int_{\vec{v} \in \mathbb{R}^3} d^3 \vec{v} \underbrace{\frac{\partial v_j}{\partial v_i}}_{\delta_{ij}} f \\ &= -\delta_{ij} \rho_M, \end{aligned} \quad (\text{C.6})$$

where we have used the constraint that the distribution function should rapidly vanish at infinity. To compute the first Jeans' equations, we also need to define the average velocity vector $\langle \vec{v} \rangle$ at each position in space. Here, the average must be understood as the mean velocity of all the stars given their distribution function f , thus for any component $\langle v_i \rangle$ we have

$$\langle v_i \rangle = \frac{1}{\rho_M} \int_{\vec{v} \in \mathbb{R}^3} d^3 \vec{v} v_i f. \quad (\text{C.7})$$

The first Jeans' equations can be derived by integrating Eq. C.4 in velocity space:

$$\frac{\partial \rho_M}{\partial t} + \vec{\nabla} \cdot (\rho_M \langle \vec{v} \rangle) = 0, \quad (\text{C.8})$$

where we have used that $\vec{\nabla} \cdot (f \vec{v}) = \vec{\nabla} f \cdot \vec{v}$, with $\vec{\nabla}$ the divergence operator. The second Jeans' equations (which is actually a set of three equations) can be obtained by multiplying Eq. C.4 by \vec{v} and integrating in velocity space:

$$\frac{\partial(\rho_M \langle \vec{v} \rangle)}{\partial t} + \vec{\nabla} \cdot (\rho_M \langle \vec{v} \otimes \vec{v} \rangle) + \rho_M \vec{\nabla} \Phi = 0, \quad (\text{C.9})$$

where we have used the fact that $\partial(f\vec{v})/\partial t = \vec{v} \partial f/\partial t$ and where \otimes denotes the tensor product operation. Alternatively, the second Jeans' equations can be rewritten by developing the first term in Eq. C.9, using Eq. C.8 and defining the stress tensor $\overline{\sigma^2}$ as

$$\begin{aligned} \overline{\sigma^2} &= \langle (\vec{v} - \langle \vec{v} \rangle) \otimes (\vec{v} - \langle \vec{v} \rangle) \rangle \\ &= \langle \vec{v} \otimes \vec{v} \rangle - \langle \vec{v} \rangle \otimes \langle \vec{v} \rangle. \end{aligned} \quad (\text{C.10})$$

The alternate form for the second Jeans' equations therefore writes

$$\rho_M \frac{\partial \langle \vec{v} \rangle}{\partial t} + \rho_M (\langle \vec{v} \rangle \cdot \vec{\nabla}) \langle \vec{v} \rangle + \vec{\nabla} \cdot (\rho_M \overline{\sigma^2}) + \rho_M \vec{\nabla} \Phi = 0. \quad (\text{C.11})$$

C.3 Jeans' equations in cylindrical coordinates

Now we turn to the Jeans' equations written in cylindrical coordinates since this coordinate system is more appropriate for rotating axisymmetric disks in galaxies. To do so, we need to write Boltzmann's equation in cylindrical coordinates this time. Using Eq. 5.4 for the expression of the acceleration and equating with the gradient of the gravitational potential, we get

$$\frac{\partial v_R}{\partial t} = \frac{v_\theta^2}{R} - \frac{\partial \Phi}{\partial R}, \quad (\text{C.12})$$

$$\frac{\partial v_\theta}{\partial t} = -\frac{1}{R} \left(\frac{v_R v_\theta}{R} + \frac{\partial \Phi}{\partial \theta} \right), \quad (\text{C.13})$$

$$\frac{\partial v_z}{\partial t} = -\frac{\partial \Phi}{\partial z}, \quad (\text{C.14})$$

which we can plug into Eq. C.1 to retrieve its expression in cylindrical coordinates

$$\begin{aligned} \frac{\partial f}{\partial t} + v_R \frac{\partial f}{\partial R} + \frac{v_\theta}{R} \frac{\partial f}{\partial \theta} + v_z \frac{\partial f}{\partial z} + \left(\frac{v_\theta^2}{R} - \frac{\partial \Phi}{\partial R} \right) \frac{\partial f}{\partial v_R} \\ - \frac{1}{R} \left(v_R v_\theta + \frac{\partial \Phi}{\partial \theta} \right) \frac{\partial f}{\partial v_\theta} - \frac{\partial \Phi}{\partial z} \frac{\partial f}{\partial v_z} = 0. \end{aligned} \quad (\text{C.15})$$

For an axisymmetric disk, Eq. C.15 can be further simplified by considering that the mass density ρ_M and therefore the distribution function f and the gravitational potential Φ must be independent of the azimuthal angle θ . Then, integrating Eq. C.15 in velocity space yields the first Jeans' equations in cylindrical coordinates for an axisymmetric disk:

$$\frac{\partial \rho_M}{\partial t} + \frac{1}{R} \frac{\partial(\rho_M R \langle v_R \rangle)}{\partial R} + \frac{\partial(\rho_M \langle v_z \rangle)}{\partial z} = 0. \quad (\text{C.16})$$

The three other Jeans' equations can be derived by integrating in velocity space the product of Eq. C.15 with each of the three velocity vector components and using the same tricks as in Sect. C.2

$$\frac{\partial(\rho_M \langle v_R \rangle)}{\partial t} + \frac{\partial(\rho_M \langle v_R^2 \rangle)}{\partial R} + \frac{\partial(\rho_M \langle v_R v_z \rangle)}{\partial z} + \rho_M \left[\frac{\langle v_R^2 \rangle - \langle v_\theta^2 \rangle}{R} + \frac{\partial \Phi}{\partial R} \right] = 0, \quad (\text{C.17})$$

$$\frac{\partial(\rho_M \langle v_\theta \rangle)}{\partial t} + \frac{\partial(\rho_M \langle v_R v_\theta \rangle)}{\partial R} + \frac{\partial(\rho_M \langle v_\theta v_z \rangle)}{\partial z} + \frac{2\rho_M}{R} \langle v_R v_\theta \rangle = 0, \quad (\text{C.18})$$

$$\frac{\partial(\rho_M \langle v_z \rangle)}{\partial t} + \frac{\partial(\rho_M \langle v_R v_z \rangle)}{\partial R} + \frac{\partial(\rho_M \langle v_z^2 \rangle)}{\partial z} + \rho_M \left[\frac{\langle v_R v_z \rangle}{R} + \frac{\partial \Phi}{\partial z} \right] = 0. \quad (\text{C.19})$$

C.4 Isothermal sheet thickness profile

A common vertical profile used for disk galaxies is the isothermal sheet profile. This profile can be derived by considering a sheet at a given position R in steady state with a constant temperature and therefore velocity dispersion. The vertical support of this sheet is described by Eq. C.19 after getting rid of derivatives with respect to t and R and by assuming a diagonal stress tensor (i.e. $\langle v_R v_z \rangle = 0$):

$$\frac{d\rho_M}{dz} = -\frac{\rho_M}{\langle v_z^2 \rangle} \frac{\partial \Phi}{\partial z}. \quad (\text{C.20})$$

This equation can be solved using Poisson's equation. Similarly to Jeans' equations, the vertical gradient will mostly contribute to the dynamical support of the sheet and therefore Poisson's equation can be written as

$$\frac{\partial^2 \Phi}{\partial z^2} = -4\pi G \rho_M. \quad (\text{C.21})$$

The differential equation to solve in order to find the vertical profile therefore writes

$$\frac{d^2 \log \rho_M}{dz^2} = \frac{4\pi G \rho_M}{\langle v_z^2 \rangle}. \quad (\text{C.22})$$

Considering the boundary condition $\rho_M(z \rightarrow \infty) = 0$, the solution of Eq. C.22 is given by (Spitzer 1942; Camm 1950)

$$\rho_M(R, z) = \rho_{M,0}(R) \operatorname{sech}^2(z/z_0(R)), \quad (\text{C.23})$$

where $z_0(R) = \sqrt{\langle v_z^2 \rangle / (2\pi G \rho_{M,0}(R))}$ with $\rho_{M,0}(R) = \rho_M(R, z = 0)$ the mass density in the plane of the disk. This solution is usually referred to as the sech law.

Appendix D

Impact of convolution on the variance

In this appendix, I derive the impact of the convolution of a signal S by a kernel K on its variance map. This result was used in Sect. 8.1.2.2 to produce resolved map using pixel-per-pixel SED fitting. We consider a signal that is represented by a random variable $S(x_0, y_0)$ at position (x_0, y_0) on an image. By definition, we can estimate its variance as $Var_S = \sum_i (S_i - \bar{S})^2 / n$, where S_i is a single realisation of the random variable, n is the number of realisations, and \bar{S} is its average value. We could also use $n - 1$ instead of n to have an unbiased estimator but the demonstration would remain the same. Now, we consider a new signal S' that has been convolved with a kernel K , hence

$$\begin{aligned} S'(x_0, y_0) &= [S \otimes K](x_0, y_0) \\ &= \sum_{x,y} S(x, y) K(x_0 - x, y_0 - y). \end{aligned} \quad (\text{D.1})$$

Its variance can be estimated in the same way. If we develop the terms we have

$$Var_{S'}(x_0, y_0) = \frac{1}{n} \sum_i \left[\sum_{x,y} S_i(x, y) K(x_0 - x, y_0 - y) - \frac{1}{n} \sum_j \sum_{x,y} S_j(x, y) K(x_0 - x, y_0 - y) \right]^2. \quad (\text{D.2})$$

Inverting the two sums in the last term and combining the sum along x and y for the two terms, we get

$$Var_{S'}(x_0, y_0) = \frac{1}{n} \sum_i \left[\sum_{x,y} K(x_0 - x, y_0 - y) [S_i(x, y) - \bar{S}(x, y)] \right]^2. \quad (\text{D.3})$$

The square can be written as the product of a sum along x and y with a sum along x' and y' , in which case we can rewrite it as a first sum when $x = x'$ and $y = y'$ and a second sum when $x \neq x'$ and/or $y \neq y'$, that is

$$\begin{aligned}
Var_{S'}(x_0, y_0) = \frac{1}{n} \sum_i \left[\sum_{x,y} K^2(x_0 - x, y_0 - y) [S_i(x, y) - \bar{S}(x, y)]^2 + \right. \\
\left. \sum_{\substack{x, x', y, y' \\ x \neq x' \wedge y \neq y'}} K(x_0 - x, y_0 - y) K(x_0 - x', y_0 - y') [S_i(x, y) - \bar{S}(x, y)] [S_i(x', y') - \bar{S}(x', y')] \right].
\end{aligned} \tag{D.4}$$

If we invert the order of the first and the two inner sums, we finally get

$$\begin{aligned}
Var_{S'}(x_0, y_0) = \sum_{x,y} K^2(x_0 - x, y_0 - y) Var_S(x, y) + \\
\sum_{\substack{x, x', y, y' \\ x \neq x' \wedge y \neq y'}} K(x_0 - x, y_0 - y) K(x_0 - x', y_0 - y') Cov_S((x, y), (x', y')),
\end{aligned} \tag{D.5}$$

where $Cov_S((x, y), (x', y'))$ is the covariance between two pixels at position (x, y) and (x', y') . If the covariance is null or negligible, then the variance of the convolved signal is given by the variance map convolved by the square of the kernel.